Quantum control of electron and nuclear circulations, ring currents, and induced magnetic fields in atoms, ions, and molecules by circularly polarized laser pulses

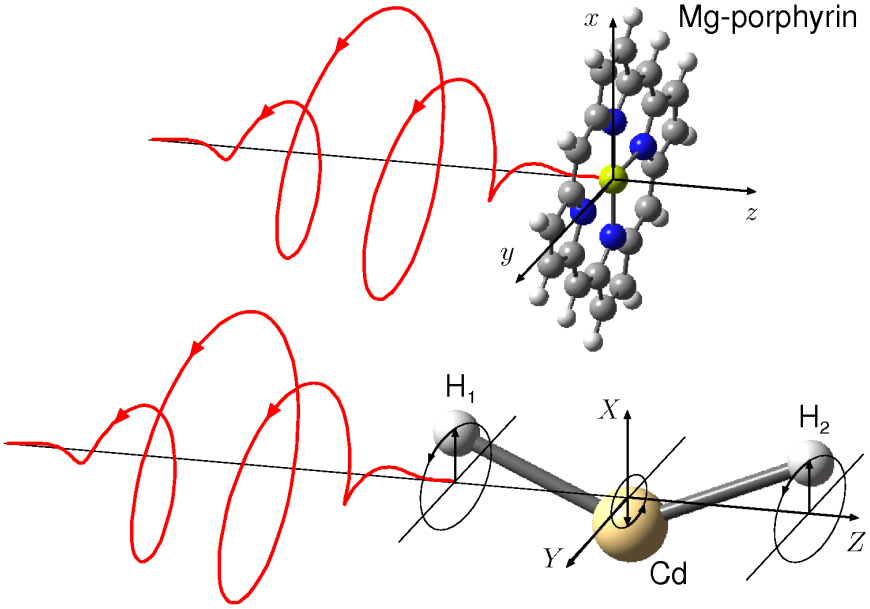

INAUGURAL – DISSERTATION

zur Erlangung des Doktorgrades
der Freien Universität Berlin
Fachbereich Biologie, Chemie, Pharmazie

vorgelegt von

Ingo Barth

aus Berlin

2009

Erstgutachter:	Prof. Dr. Jörn Manz
Zweitgutachter:	Prof. Dr. Peter Saalfrank
Tag der Disputation:	15.06.2009

Publications

1. (a) I. Barth, J. Manz, *Periodic Electron Circulation Induced by Circularly Polarized Laser Pulses: Quantum Model Simulations for Mg-porphyrin*, Angew. Chem. Int. Ed. **45**, 2962–2965 (2006) [26 times cited]

   (b) I. Barth, J. Manz, *Anregung periodischer Elektronen-Kreisbewegung durch circular polarisierte Laserpulse: quantenmechanische Modell-Simulationen für Mg-porpyhrin*, Angew. Chem. **118**, 3028–3031 (2006)

2. I. Barth, J. Manz, Y. Shigeta, K. Yagi, *Unidirectional Electronic Ring Current Driven by a Few Cycle Circularly Polarized Laser Pulse: Quantum Model Simulations for Mg-Porphyrin*, J. Am. Chem. Soc. **128**, 7043–7049 (2006) [32 times cited]

3. I. Barth, J. Manz, *Design of Circularly Polarized Laser Pulses for Periodic Electron Circulation in Mg-Porphyrin*, in: A. W. Castleman, Jr., M. L. Kimble (eds.), *Femtochemistry VII: Fundamental Ultrafast Processes in Chemistry, Physics, and Biology* (Elsevier, Amsterdam, 2006), pp. 441–454

4. I. Barth, L. González, C. Lasser, J. Manz, T. Rozgonyi, *Laser Control of Nuclear and Electron Dynamics: Bond Selective Photodissociation and Electron Circulation*, in: B. Lasorne, G. A. Worth (eds.), *Coherent Control of Molecules* (CCP6, Daresbury, 2006), pp. 18–27

5. I. Barth, J. Manz, *Electric ring currents in atomic orbitals and magnetic fields induced by short intense circularly polarized π laser pulses*, Phys. Rev. A **75**, 012510-1–012510-9 (2007) [7 times cited]

6. I. Barth, J. Manz, G. K. Paramonov, *Time-dependent extension of Koopmans' picture for ionisation by a laser pulse: application to $H_2(B\,^1\Sigma_u^+)$*, Mol. Phys. **106**, 467–483 (2008) [1 time cited]

7. I. Barth, J. Manz, P. Sebald, *Spinning a pseudorotating molecular top by means of a circularly polarized infrared laser pulse: Quantum simulations for $^{114}CdH_2$*, Chem. Phys. **346**, 89–98 (2008) [2 times cited]

8. I. Barth, J. Manz, L. Serrano-Andrés, *Quantum simulations of toroidal electric ring currents and magnetic fields in linear molecules induced by circularly polarized laser pulses*, Chem. Phys. **347**, 263–271 (2008) [2 times cited]

9. X. Xie, A. Scrinzi, M. Wickenhauser, A. Baltuška, I. Barth, M. Kitzler, *Internal Momentum State Mapping using High Harmonic Radiation*, Phys. Rev. Lett. **101**, 033901-1–033901-4 (2008) [3 times cited]

10. I. Barth, J. Manz, G. Pérez-Hernández, P. Sebald, *Towards Toroidal Hydrogen Bonds*, Z. Phys. Chem. **222**, 1311–1331 (2008) [1 time cited]

11. I. Barth, L. Serrano-Andrés, T. Seideman, *Nonadiabatic orientation, toroidal current, and induced magnetic field in BeO molecules*, J. Chem. Phys. **129**, 164303-1–164303-12 (2008), Erratum: J. Chem. Phys. **130**, 109901-1–109901-1 (2009) [3 times cited]

12. N. Elghobashi-Meinhardt, L. González, I. Barth, T. Seideman, *Few-cycle laser pulses to obtain spatial separation of OHF^- dissociation products*, J. Chem. Phys. **130**, 024310-1–024310-9 (2009) [0 time cited]

13. I. Barth, C. Lasser, *Trigonometric pulse envelopes for laser induced quantum dynamics*, Phys. Rev. A (2009), submitted

14. I. Barth, H.-C. Hege, H. Ikeda, A. Kenfack, M. Koppitz, J. Manz, F. Marquardt, G. K. Paramonov, *Concerted Quantum Effects of Electronic and Nuclear Fluxes in Molecules*, Chem. Phys. Lett. (2009), submitted

Talks

1. I. Barth, *Electronic ring currents and electron circulations driven by circularly polarized few cycle laser pulses*, Tag der Chemie, TU Berlin, Germany, 28.06.2006

2. I. Barth, J. Manz, *Quantum simulations of effects of few cycle as to near fs laser pulses on valence electrons: Ring currents, electron circulations, and ionization*, Attosecond Science Workshop, KITP, UCSB, Santa Barbara, USA (A. D. Bandrauk), 28.08.2006

3. I. Barth, J. Manz, *Electron circulation, ring currents, and induced magnetic fields in atoms and molecules driven by circularly polarized laser pulses*, International Workshop on Atomic Physics, MPI Dresden, Germany (J.-M. Rost), 01.12.2006

4. I. Barth, J. Manz, *Electron circulation, electric ring currents, and induced magnetic fields excited by circularly polarized laser pulses: Quantum simulations for atoms and molecules*, Forschungsseminar "Ultra", Universität Kassel, Germany (T. Baumert), 18.12.2006

5. I. Barth, J. Manz, *Quantum simulations of laser driven electron circulation and ring currents in molecules and atoms*, Theory Seminar, FHI Berlin, Germany (B. Friedrich), 22.02.2007

6. I. Barth, J. Manz, *Quantum control of electric ring currents by circularly polarized laser pulses*, DPG Tagung, Symposium "Quantum control of functional molecules", Universität Düsseldorf, Germany (E. Riedle), 21.03.2007

7. I. Barth, J. Manz, *Quantum control of electric ring currents in molecular excited states*, International Symposium "Molecular response to electronic excitation", Bad Münstereifel, Germany (C. M. Marian), 17.04.2007

8. I. Barth, J. Manz, *Quantum control of electron circulation, ring currents, and induced magnetic fields*, James Franck Symposium on Spectroscopy and Quantum Control of Molecular Systems, Schloss Hohenkammer, Germany (Z. Rosenwaks, G. Gerber, K. L. Kompa), 08.10.2007

9. I. Barth, J. Manz, *Intense magnetic fields from laser induced electron and nuclear currents in molecules and in atomic or molecular ions*, 11^{th} International Conference on Multiphoton Processes (ICOMP), Heidelberg, Germany (R. Moshammer, J. Ullrich), 23.09.2008

10. I. Barth, J. Manz, *Quantum control by laser pulses: from nuclear to electron dynamics, and back*, Workshop on Quantum Control of Light and Matter, KITP, UCSB, Santa Barbara, USA (D. J. Tannor), 22.04.2009

Posters

1. I. Barth, J. Manz, Y. Shigeta, K. Yagi, *Quantum ignition of uni-directional electronic ring current and cyclic electron transfer in oriented Mg-porphyrin by circularly polarized π- and $\pi/2$- laser pulse*, 4^{th} International Workshop on Optimal Control of Dynamics, Ringberg, Germany (M. Motzkus), 05.12.2005

2. I. Barth, J. Manz, Y. Shigeta, K. Yagi, *Quantum ignition of uni-directional electronic ring currents and electron circulations in oriented Mg-porphyrin by circularly polarized π and $\pi/2$ laser pulses*, Biannual Conference on Chemistry Chem.04, Cairo University, Egypt (R. H. Hilal), 08.03.2006

3. I. Barth, L. González, J. Manz, G. K. Paramonov, L. Serrano-Andrés, Y. Shigeta, K. Yagi, *Electronic ring currents and electron circulations driven by circularly polarized few cycle laser pulses*, 12^{th} International Congress of Quantum Chemistry, Kyoto University, Japan (H. Nakatsuji), 22.05.2006

4. I. Barth, L. González, J. Manz, G. K. Paramonov, L. Serrano-Andrés, Y. Shigeta, K. Yagi, *Electronic ring currents and electron circulations driven by circularly polarized few cycle laser pulses*, Tag der Chemie, TU Berlin, Germany, 28.06.2006

5. I. Barth, L. González, J. Manz, G. K. Paramonov, L. Serrano-Andrés, Y. Shigeta, K. Yagi, *Control of electronic ring currents and electron circulations by circularly polarized few cycle laser pulses*, CCP6 Workshop on Coherent Control of Molecules, Birmingham, UK (G. Worth), 03.07.2006

6. I. Barth, J. Manz, L. Serrano-Andrés, Y. Shigeta, K. Yagi, *Quantum control of electron circulation, ring currents, and induced magnetic fields*, James Franck Symposium on Spectroscopy and Quantum Control of Molecular Systems, Schloss Hohenkammer, Germany (Z. Rosenwaks, G. Gerber, K. L. Kompa), 08.10.2007

7. X. Xie, A. Scrinzi, M. Wickenhauser, A. Baltuška, I. Barth, M. Kitzler, *Strong-field momentum state mapping*, 11^{th} International Conference on Multiphoton Processes (ICOMP), Heidelberg, Germany (R. Moshammer, J. Ullrich), 22.09.2008

8. I. Barth, H.-C. Hege, H. Ikeda, A. Kenfack, M. Koppitz, J. Manz, F. Marquardt, G. K. Paramonov, B. Paulus, *Concerted Quantum Effects of Electronic and Nuclear Fluxes in Molecules*, Tag der Chemie, Universität Potsdam, 04.06.2009

Abstract

This work develops concepts for quantum control of electron and nuclear dynamics in atoms, ions, and aligned/oriented molecules by means of circularly polarized laser pulses. The main goal is the generation of stationary electronic and nuclear ring currents in electronic and vibrational excited degenerate states, respectively. Here, the expectation values of electronic and nuclear (pseudorotational) angular momenta are non-zero. The theory of stationary ring currents in excited degenerate states of atomic and molecular systems is developed first. As examples, I compute electronic ring currents in atomic orbitals of the hydrogen atom and one-electron ions, in the first excited degenerate states $|A\,^1\Pi_\pm\rangle$ of oriented AlCl and BeO molecules, and in several excited states $|n\,^1E_{u\pm}\rangle$ $(n = 2, 4, 5)$ of the aligned ring-shaped molecule Mg-porphyrin. These ring currents can be excited by means of circularly polarized UV/visible optimized π laser pulses from electronic non-degenerate ground states, where the direction of the ring current is determined by the circular polarization. Likewise, nuclear ring currents in pseudorotational excited degenerate anharmonic bending states of aligned linear triatomic molecules FHF^- and $^{114}CdH_2$ can be achieved by means of circularly polarized IR optimized π laser pulses. After the end of the laser pulse, the electronic or nuclear ring current, circulating about the axis of symmetry, persists throughout the lifetime of the excited state. In the course of these investigations, I discovered a new type of hydrogen bonds, i.e. so-called toroidal bonds, in which the protons are not located on the axis connecting two neighboring heavy atoms, as usual, but are circulating toroidally about this axis. As a consequence, magnetic fields are induced which may be even stronger than the strongest permanent magnetic fields that can be produced with present-day technology. This approach is further extended to control electron circulations and nuclear pseudorotations in superpositions of several electronic and vibrational states, respectively. This control can be realized by means of modified circularly polarized UV/visible and IR laser pulses for electronic and vibrational excitations, respectively. Finally, the control of nonadiabatic orientation of AlCl and BeO molecules by means of short half-cycle linearly polarized laser pulses is also achieved.

Zusammenfassung

Diese Arbeit entwickelt Konzepte für die Quantenkontrolle von Elektronen- und Kerndynamik in Atomen, Ionen und ausgerichteten/orientierten Molekülen durch zirkular polarisierte Laserpulse. Das Hauptziel ist die Erzeugung stationärer elektronischer und nuklearer Ringströme in angeregten entarteten Elektronen- und Vibrationszuständen. Hierbei sind die Erwartungswerte der elektronischen und der die Pseudorotation betreffenden nuklearen Drehimpulse von Null verschieden. Die Theorie der stationären Ringströme in angeregten entarteten Zuständen von atomaren und molekularen Systemen wird zuerst erarbeitet. Als Beispiele werden elektronische Ringströme in den Atomorbitalen des Wasserstoffatoms und der Einelektronenionen, in den ersten angeregten entarteten Zuständen $|A\,^1\Pi_\pm\rangle$ der orientierten AlCl- und BeO-Molekülen und in einigen angeregten Zuständen $|n\,^1E_{u\pm}\rangle$ $(n = 2, 4, 5)$ des ausgerichteten Ringmoleküls Mg-Porphyrin berechnet. Diese Ringströme können durch zirkular polarisierte UV/sichtbare optimierte π Laserpulse von elektronischen nicht-entarteten Grundzuständen aus angeregt werden, wobei die Richtung der Ringströme durch die zirkulare Polarisation bestimmt wird. Ähnlich können nukleare Ringströme in Pseudorotationszuständen angeregter entarteter anharmonischer Biegezustände der ausgerichteten linearen dreiatomigen Molekülen FHF^- und $^{114}CdH_2$ durch zirkular polarisierte IR optimierte π Laserpulse erzielt werden. Nach dem Ende des Laserpulses bleibt der elektronische oder nukleare Ringstrom, der um die Symmetrieachse zirkuliert, innerhalb der Lebensdauer des angeregten Zustandes bestehen. Damit wird auch eine neue Art von Wasserstoffbrückenverbindungen entdeckt, bei den die Protonen nicht wie üblich auf der Verbindungsachse zwischen den benachbarten Schweratomen sitzen, sondern um diese Achse torusförmig kreisen. Als Folge werden Magnetfelder induziert, welche sogar stärker sein können als die stärksten permanenten Magnetfelder, die mit heutiger Technologie produziert werden. Die Erweiterung dieser Methode ist die Kontrolle von Elektronenzirkulationen bzw. nuklearen Pseudorotationen in Superpositionen von einigen Elektronen- bzw. Vibrationszuständen. Das kann durch modifizierte zirkular polarisierte UV/sichtbare oder IR Laserpulse für Elektronen- oder Vibrationsanregungen verwirklicht werden. Zum Schluss wird auch die Kontrolle der nicht-adiabatischen Orientierung von AlCl- und BeO-Molekülen durch kurze linear polarisierte Halbzyklus-Laserpulse erzielt.

Contents

Chapter 1

Introduction

This chapter contains a brief introduction to attosecond science (Section 1.1), followed by highlights on quantum control of nuclear and electron dynamics (Section 1.2). Finally, the goals and structure of this work will be presented in Sections 1.3 and 1.4, respectively.

1.1 Attosecond science

Attosecond science is a new emerging research field of physics and chemistry in the last decade [1–6]. In this hot topic field, physcial processes are described on the attosecond timescale ($1\,\mathrm{as} = 10^{-18}$), on which the motion of the electron in atoms, ions, and molecules plays an important role. The electron rest mass ($m_e = 9.109382 \cdot 10^{-31}\,\mathrm{kg}$), charge ($q = -e = 1.602176 \cdot 10^{-19}\,\mathrm{C}$), and spin ($s = \frac{1}{2}\,\hbar$) define the atomic units of mass, charge, and (half of) the angular momentum or action, respectively. The corresponding atomic units of length and energy are Bohr radius $a_0 = 4\pi\varepsilon_0\hbar^2/(m_e e^2) = 5.291772 \cdot 10^{-11}\,\mathrm{m}$ and Hartree energy $E_h = \hbar^2/(m_e a_0^2) = 27.21138\,\mathrm{eV}$, respectively. Thus, the atomic unit of time, $\hbar/E_h = 24.18884\,\mathrm{as}$, is on the attosecond timescale. To put this time in perspective: If the atomic unit of time is stretched so that it takes one second, one second would take 1.3 billion years on the same scale, i.e. about twice the age of the first complex multicelled lifeforms on the Earth. Furthermore, the electron motion is much faster than nuclear vibrations and molecular rotations on femtosecond ($1\,\mathrm{fs} = 10^{-15}\,\mathrm{s}$) and picosecond ($1\,\mathrm{ps} = 10^{-12}\,\mathrm{s}$) timescales, respectively. Thus, molecular rotation can be considered frozen on fs- and as-timescales. Similarly, on the as-timescale, the nuclei can be considered frozen (Born-Oppenheimer approximation [7, 8]). A list of different timescales with several examples is shown in Table 1.1.

timescale	SI unit and conversion	examples
exasecond	$1\,\mathrm{Es} = 10^{18}\,\mathrm{s} \approx 32 \cdot 10^9\,\mathrm{a}$	estimated total lifetime of the closed universe
petasecond	$1\,\mathrm{Ps} = 10^{15}\,\mathrm{s} \approx 32 \cdot 10^6\,\mathrm{a}$	age of the Earth and the Universe
terasecond	$1\,\mathrm{Ts} = 10^{12}\,\mathrm{s} \approx 32000\,\mathrm{a}$	age of Homo sapiens
gigasecond	$1\,\mathrm{Gs} = 10^9\,\mathrm{s} \approx 32\,\mathrm{a}$	lifespans of humans and sequoia trees
megasecond	$1\,\mathrm{Ms} = 10^6\,\mathrm{s} \approx 11.6\,\mathrm{d}$	orbital periods of Moon and inner planets
kilosecond	$1\,\mathrm{ks} = 10^3\,\mathrm{s} \approx 16.7\,\mathrm{min}$	Earth's rotation around its own axis
second	$1\,\mathrm{s}$	heartbeat, 100 m sprint
millisecond	$1\,\mathrm{ms} = 10^{-3}\,\mathrm{s}$	blink of an eye, human reflex
microsecond	$1\,\mu\mathrm{s} = 10^{-6}\,\mathrm{s}$	thunderbolt
nanosecond	$1\,\mathrm{ns} = 10^{-9}\,\mathrm{s}$	access time of computer main memory
picosecond	$1\,\mathrm{ps} = 10^{-12}\,\mathrm{s}$	molecular rotation
femtosecond	$1\,\mathrm{fs} = 10^{-15}\,\mathrm{s}$	nuclear dynamics, chemical reaction
attosecond	$1\,\mathrm{as} = 10^{-18}\,\mathrm{s}$	electron dynamics
zeptosecond	$1\,\mathrm{zs} = 10^{-21}\,\mathrm{s}$	relativistic electron dynamics

Table 1.1: Overview of different timescales.

To monitor ultrafast electronic processes in atoms, ions, molecules [9], chemical reactions, condensed-matter systems and on surfaces [10], e.g. ionization [11], electron tunneling [12], electron transfer [13], and electron circulation, sub-femtosecond laser pulses are required. A review of attosecond spectroscopy can be found in Ref. [14]. The generation of sub-femtosecond laser pulses was already predicted in 1994 [15, 16]. In 2001, these ultrashort attosecond laser pulses were produced experimentally by high harmonic generation (HHG), using visible (1.6 eV) 7 fs laser pulses [17, 18]. Other applications of HHG are the tomographic imaging of molecular orbitals [19–22], the probing of nuclear dynamics and structural rearrangement of the molecule on the attosecond timescale [23, 24], as well as the monitoring of vibrational [25–27] and rotational [28–30] dynamics on fs- and ps-timescales, respectively.

In the recollision model of HHG [31–34], the valence electron is steered by means of a few-cycle infrared (IR) or visible laser pulse with field amplitude $\mathcal{E}_0$ and carrier frequency ω in three steps. First, an electron in the atom or molecule is ionized with zero initial velocity (tunnel ionization [31, 32, 35–38] or above-threshold ionization (ATI) [33, 39, 40]). Second, the electron accelerates in the electric field of the driven laser pulse and returns if the electric field is redirected. Finally, the electron recombines with the parent ion via stimulated emission and a photon with energy $N\hbar\omega$ is subsequently emitted, where $N = 1, 2, 3, \ldots$

is the harmonic order. For atoms and molecules with inversion symmetry, the selection rule for electron recombination implies that only odd harmonics $N = 1, 3, 5, \ldots$ are allowed for linearly polarized driven laser pulses while only harmonics $N = kN_{sym} \pm 1$ ($k = 0, 1, 2, \ldots$) are generated for circularly polarized driven laser pulses with sufficiently long pulse duration, where N_{sym} is the symmetry number of the molecule [41]. For benzene with D_{6h} symmetry ($N_{sym} = 6$), only photons of harmonics $N = 1, 5, 7, 11, 13, \ldots$ are emitted [42, 43] (for 1D and 2D models of benzene, see Refs. [44, 45]). The HHG for nanotubes with different N_{sym} can be found in Refs. [46, 47]. However, for short pulse durations of circularly polarized laser pulses, other harmonics can also be observed. The selection rule also implies, that there are no HHG for atoms and aligned linear molecules with infinite symmetry number, $N_{sym} = \infty$, driven by circularly polarized laser pulses. The HHG driven by elliptically polarized laser pulses is demonstrated in Refs. [48, 49]. The HHG spectra are usually calculated using Fourier transform of the expectation value of either the dipole moment [50, 51] or the dipole acceleration [52]. Recently, quantum electrodynamical theory has shown that the intensity of the HHG spectrum is proportional to the squared magnitude of the Fourier transform of the expectation value of the dipole velocity [53]. This provides closest agreement of HHG results for dipole velocity in Ref. [54]. These three HHG spectra (dipole moment, dipole velocity, and dipole acceleration) for the hydrogen atom have recently been compared [55]. In general, the HHG spectrum shows a plateau and a subsequent cutoff region at high photon energies. The HHG spectrum depends on the molecular orientation and has a structural minimum in the plateau region, due to multi-center destructive interference [54, 56–61]. Furthermore, the HHG spectrum also depends on the symmetry of the molecular orbital [26, 62–66]. For atoms, the maximum energy of the emitted photon is given by $N_{max}\hbar\omega = I_p + 3.17\,U_p$, where I_p and $U_p = e^2\mathcal{E}_0^2/(4m_e\omega^2)$ are the ionization potential and the ponderomotive energy, respectively [31, 32]. For molecules, the energy of the emitted photon can exceed this maximum, i.e. the cutoff of the spectrum of molecular HHG is larger [67–69], because the ionized electron from the parent atom can recombine with another atom of the molecule. This electronic process is called laser induced electron transfer (LIET) [67].

To achieve an attosecond laser pulse, a spectral filter is used to select high photon energies in the HHG plateau and cutoff regions broadly, according to the inverse Fourier transform of the laser pulse. A pulse duration of 80 as can currently be achieved in experiments [70]. The pulse duration of attosecond laser pulses can be measured and controlled [70–74], see the review [75]. The polarization of the generated attosecond laser pulse is often linear, but the generation of elliptically (or near circularly) polarized attosecond laser pulses has also been predicted [76–78] and experimentally realized [79]. Of course, the laser frequency of few-cycle attosecond laser pulses is in extreme ultraviolet (XUV) or X-ray regimes, for example the photon energy corresponding to the period of

a laser cycle of 0.1 fs is 41.4 eV. However, the generation of intense few-cycle 3.7 fs laser pulses in the deep ultraviolet (UV) regime (4.6 eV) with adjustable polarization by HHG is experimentally realized [80]. We will show that these laser pulses with circular polarization are useful for excitation of electronic ring currents in atoms, ions, and molecules.

1.2 Quantum control

Controlling electron and nuclear dynamics in different physical and chemical systems is an important task for physicsts and chemists [81,82]. Highlights can be found in experimental rewiews on coherent control in femtochemistry [83, 84] and on femtosecond time-resolved photoelectron spectroscopy [85]. Pioneering works on quantum control of nuclear dynamics are pump-dump and optimal control of chemical reactions [86, 87], coherent control of unimolecular reactions [88], IR control of dissociation of vibrationally excited molecular resonances [89], optimal control of selective vibrational excitation [90,91], of selective rotational excitation using evolutionary learning algorithm [92], and of vibrational-rotational excitations [93], see the review on optimal control theory [94]. Further examples include population switching control in three-level systems via stimulated Raman adiabatic passage (STIRAP) [95], see reviews [96, 97], control of molecular dissociation by chirped IR laser pulses [98] and by IR+UV laser pulses [99], control of isomerization and hydrogen transfer by pump-dump IR π laser pulses [100–102] (for generalized π pulses, see Ref. [103]), femtosecond control of unimolecular reactions and their transition states [104], see the review on femtochemistry [105], selective preparation of enantiomers from a racemate [106–108] e.g. by means of circularly polarized π laser pulses [107], carrier envelope phase (CEP) control of chemical reactions [109], optimal control of photoassociation of ultracold molecules [110], IR+UV control of bond selective and spatial separation of dissociation of hydrogen-bonded triatomic anions [111–113], and coherent control of interferences of wavepackets (wavepacket interferometry) [114, 115].

Quantum control of electron dynamics was established based on advances in the field of control of nuclear dynamics. The first paper was published in 1989, in which the phase-coherent control of photocurrent direction in semiconductors was devised [116]. In the following years, various control schemes for electrons were devised, for example dipole switching control in molecules and in open systems [117,118], magnetization switching control in quantum rings [119], optimal control of population transfer in polyatomic molecules [120], attosecond control of charge migration in small peptides [13], coherent control of electric currents in superlattices and molecular wires [121, 122], chiral control of electron transmission (current transfer) through molecules [123,124], and coherent spin

control of matrix isolated molecules by IR+UV laser pulses [125]. Quantum control of HHG includes restricted optimal control of attosecond laser pulse synthesis from HHG using chirped driven laser pulses [126], IR+UV control of HHG [127], CEP control of HHG [22, 68, 70, 72, 128], optimal control of HHG by pulse-shaped laser pulses [129, 130], and control of polarization direction of HHG by phase-locked, orthogonal two-color laser fields [131, 132]. Finally, quantum control of ionization and dissociation includes strong field control of landscapes (SFCL) involving multiphoton ionization of the K atom by selective population of dressed states (SPODS) using pulse-shaped laser pulses [133, 134], optimal control of multiphoton ionization of K_2 by ultrafast polarization shaping [135], IR+UV control of electron localization in dissociation of H_2^+ [136], IR+UV control of photoelectron spectroscopy of electron tunneling in H_2^+ [137], CEP control of photodissociation of D_2^+ [138, 139], laser control of symmetry breaking of dissociation of H_2 [140], control of unidirectional rescattering of electrons in H atom [141], and CEP control of directionality of ionization of the H atom [142] and the K_2^+ molecule [143] by means of circularly polarized laser pulses.

This work develops concepts for quantum control of electron and nuclear dynamics by means of circularly polarized laser pulses. Specifically, optimized π pulses are used for the control of unidirectional stationary electronic and nuclear ring currents about the axis of symmetry with associated induced magnetic fields, while optimized $\pi/2$ pulses are used for the control of unidirectional electron circulations and nuclear pseudorotations. Note that the electronic or nuclear ring currents are defined as the fraction of the electron or nucleus passing through a perpendicular half plane (at fixed azimuthal angle) per time, respectively. The electronic ring currents occur, in general, in electronic degenerate excited states, e.g. for atoms and ions [144], for oriented linear molecules [145, 146], and for aligned, ring-shaped, achiral molecules [147–152] with non-zero electronic angular momentum. However, electron circulation can also be generated in two-dimensional nanosized quantum rings by means of picosecond laser pulses. Examples of these laser pulses are two shaped time-delayed half-cycle laser pulses (HCP) with perpendicular linear polarizations [153], circularly polarized laser pulses [154, 155], and optimized laser pulses designed through optimal control theory [156]. Electron circulation in chiral aromatic molecules can also be controlled by means of linearly polarized laser pulses, but the direction of the circulation alternates periodically after the end of the laser pulses because the electronic excited states are not exactly degenerate [157, 158]. Recently, the generation of electron circulation in the oriented LiH molecule about the molecular axis by means of two orthogonal linearly polarized laser pulses with phase shift of $\pi/2$ has been predicted [159]; for coherent control of LiH, see Ref. [160]. For exciton (electron-hole pair) recurrence motion in ring-shaped aggregate complexes induced by circularly polarized laser fields, see Ref. [161]. Electron circulation of coherent superpositions of high-lying Rydberg states has already been demonstrated in Refs. [162–167]. This electron motion about the nu-

cleus is very slow, i.e. on ps- to ms-timescales and can be described classically. Revivals of localized Rydberg wavepackets are investigated in Refs. [168, 169]. In general, electron circulation and electronic ring currents can be actively controlled by means of laser pulses with adjustable laser parameters, e.g. amplitude of the electric field, pulse duration, and laser frequency. Furthermore, the electronic ring current depends, in general, on the electronic state of the atomic or molecular system. In contrast to this active control, there is also passive control of rather weak electronic ring currents induced by permanent magnetic fields [170–185], see reviews [186–188]. Extension to magnetically induced relativistic ring currents was recently introduced [189]. Moreover, it has a unique structure for a given molecule and depends linearly only on the strength of the time-independent magnetic field. We note that light-induced electronic ring currents in degenerate states and, in particular, their directions could be detected by HHG by means of elliptically polarized laser pulses [77], for HHG by a driven mesoscopic ring with a localized impurity, see Ref. [190].

Similar quantum control for nuclear dynamics is the control of unidirectional intramolecular rotation by laser pulses. This is an important topic in molecular engineering [191–194]. Pioneering works on control of unidirectional chiral molecular motors, also called molecular rotors or propellers, by means of linearly polarized IR laser pulses [195–199] (somewhat analogous to control of electron circulation in chiral aromatic molecules [157, 158]) and by means of IR+UV laser pulses [200] have already been developed. A complementary example is the control of nuclear pseudorotation in the electronic excited state of the triangular molecule $Na_3(B)$ by means of linearly polarized laser pulses [201–205]. The theory of pseudorotation in ring systems can be found in Ref. [206]. However, the linearly polarized laser pulse induces interfering pseudorotations with opposite (left and right) directions, i.e. the nuclei of $Na_3(B)$ circulate about three equivalent minima of the potential energy surface (PES) of the electronic excited state without control achieving the goal of unidirectionality. To solve this problem, we developed the control of unidirectional nuclear pseudorotation in the electronic ground and vibrational (bending and pseudorotational) degenerate excited state of pre-aligned linear triatomic molecules $^{114}CdH_2$ and FHF^- by means of a right or left circularly polarized IR laser pulse, propagating along the molecular axis [207, 208]. It is analogous to the quantum control of electron circulation and electronic ring currents by means of circularly polarized laser pulses [144–150]. The corresponding nuclei of the excited bent molecule with a non-zero pseudorotational quantum number ($l \neq 0$) circulate anti-clockwise ($l > 0$) or clockwise ($l < 0$) about the pre-aligned molecular axis, i.e. the probability of finding a nucleus on this axis is zero. For FHF^-, the hydrogen bond in the first pseudorotational state, excited by means of a right or left circularly polarized optimized π laser pulse, is no longer linear and is, thus, a new type of hydrogen bond, called a toroidal hydrogen bond [208], see the review on hydrogen bonds e.g. Ref. [209].

Finally, quantum control of molecular rotation is important for many applications described above. For example, the molecule must be oriented or aligned during short electronic or vibrational excitations by means of circularly polarized laser pulses in order to induce unidirectional electronic or nuclear circulations. The field-free alignment [210–214] and orientation [113, 146, 215–217] of the non-polar and polar molecules can be controlled nonadiabatically by means of a linearly polarized ultrashort HCP, respectively. Extensions are e.g. field-free 3D alignment of polyatomic molecules by means of two linearly [218–221] or elliptically [222] polarized laser pulses, see also Ref. [223], and adapative optimization of field-free molecular alignment by means of an optimized laser pulse through an evolutionary algorithm [224]. After the end of the laser pulse, there is a rotational revival pattern, i.e. the rotational wavepackt dephases and rephases periodically at intervals of the rotational revival time τ_{rev} [225], where the duration of the molecular alignment or orientation is comparatively short, typically less than $0.1\,\tau_{rev}$. Furthermore, rotation-vibration effects are also observed on longer timescales (ns-timescale) due to rotational-vibrational coupling [226].

1.3 Goals of this work

This Section outlines four main directions of this work:

1. The first goal of this work is the laser control of unidirectional electronic and nuclear ring currents in atoms, ions, and molecules by means of circularly polarized optimized π laser pulses. These ring currents then induce magnetic fields. The concept, illustrated schematically in Fig. 1.1, is related to the inverse Faraday effect [227–229], i.e. the magnetic field is induced by the circularly polarized electric field. Here, the electronic or vibrational (pseudorotational) degenerate state, representing a stationary electronic or nuclear ring current, is excited selectively and completely from the ground state by means of a circularly polarized UV/visible or IR optimized π laser pulse, respectively. We have developed the theory of the laser control of electronic ring currents in the hydrogen atom and one-electron ions [144], oriented linear molecules AlCl [145] and BeO [146], and aligned ring-shaped molecule Mg-porphyrin [148] as well as the control of nuclear ring currents in the aligned linear triatomic molecule FHF^- [208]. In this work, the theory will be reviewed and also extended to other applications, such as control of electronic ring currents in different excited states of Mg-porphyrin.

2. The second goal is the derivation of analytic expressions for electronic and nuclear probability and current densities, corresponding electric ring currents (defined as the

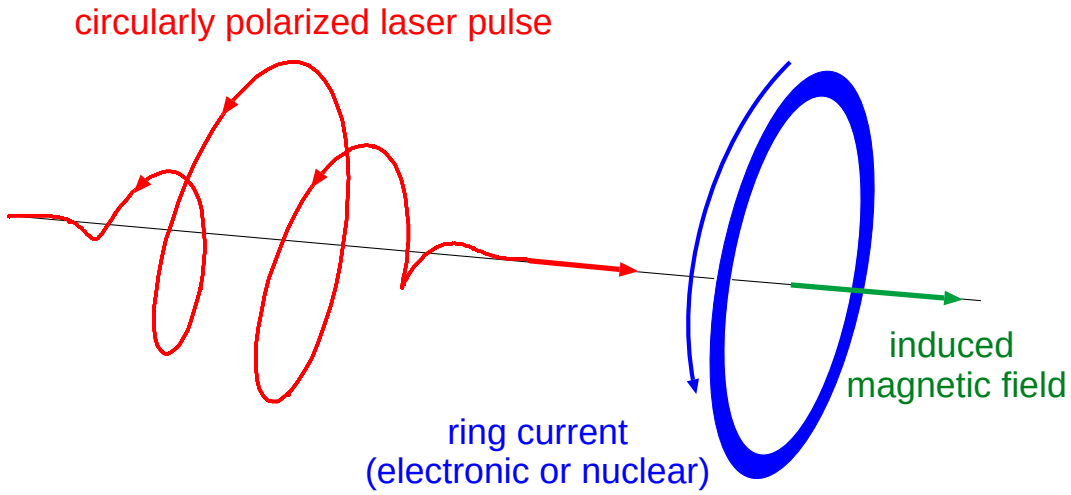

Figure 1.1: Schematic illustration of the electronic or nuclear ring current and the induced magnetic field by a circularly polarized laser pulse.

product of the electronic or nuclear ring current and the electron or nuclear charge, respectively), mean ring current radii, and induced magnetic fields. This derivation is carried out in particular for electronic ring currents in the hydrogen atom and one-electron ions [144], and for nuclear ring currents in linear triatomic molecules with $D_{\infty h}$ symmetry. Several expressions require evaluations of demanding integrals involving Gaussian functions, associated Laguerre polynomials, and confluent hypergeometric functions. Based on these analytic results, we choose atomic or molecular systems with very strong electronic or nuclear ring currents which induce very strong magnetic fields, even stronger than the strongest permanent magnetic fields which can be generated in present-day experiments, ca. 90 T [230].

3. The third goal is the laser control of unidirectional electron circulation and nuclear pseudorotation by means of circularly polarized laser pulses. The laser pulse excites a superposition of several electronic or pseudorotational states, which represent electron circulation or nuclear pseudorotation, respectively. After the end of the laser pulse, the time-dependent electron or nuclear wavepacket circulates about the axis of symmetry. In this framework, the electronic circulation in the aligned molecule Mg-porphyrin by means of a circularly polarized optimized $\pi/2$ laser pulse has been extensively investigated [147, 149, 150]. The nuclear pseudorotation in the superposition of several bending and pseudorotational states of the aligned linear triatomic molecule $^{114}CdH_2$ by means of a circularly polarized IR 50 fs laser pulse has been presented in Ref. [207]. In this work, the theory will be reviewed and also extended to other applications, e.g. electron circulation in the hydrogen atom, one-electron ions, and linear molecules.

4. The fourth goal is the control of nonadiabatic orientation [113, 146, 215–217] of diatomic molecules AlCl and BeO [146] by means of a HCP-like linearly polarized ultrashort laser pulse. The molecular orientation or alignment is required for subsequent laser control of electron and nuclear circulation and ring currents in molecules. However, the control of nonadiabatic alignment [210–214] of non-polar molecules, e.g. Mg-porphyrin, FHF^-, and $^{114}CdH_2$, is not investigated in this work.

1.4 Structure of this work

This work is organized as follows. Chapter 2 presents the theory of electronic ring currents and corresponding induced magnetic fields in electronic excited degenerate states (Section 2.2). The following theory is that of laser control of electronic ring currents and electron circulation by means of circularly polarized laser pulses (Section 2.3). Then, the theory of nuclear ring currents and associated induced magnetic fieles in excited bending and pseudorotational states of linear triatomic molecules is developed (Section 2.4), following the theory of laser control of nuclear ring currents and pseudorotation by means of circularly polarized laser pulses (Section 2.5). At the end of this Chapter, the theory of control of nonadiabatic molecular orientation is presented, in particular for polar diatomic molecules AlCl and BeO (Section 2.6). Applications of these theories are presented in Chapter 3, i.e. for electronic ring currents and electron circulation in atomic orbitals (Section 3.2), linear molecules AlCl and BeO (Section 3.3), and ring-shaped molecule Mg-porphyrin (Section 3.4), as well as for nuclear ring currents and pseudorotation in linear triatomic moleculs FHF^- and $^{114}CdH_2$ (Section 3.5). The conclusions of this work with an outlook for future work are summarized in Chapter 4. Finally, evaluations of rather demanding integrals involving Gaussian functions, associated Laguerre polynomials, and confluent hypergeometric functions are documented in Appendix A.

Chapter 2

Theory

2.1 Overview

In Section 2.2 we investigate electronic ring currents and corresponding induced magnetic fields in electronic degenerate states in atoms, ions and aligned or oriented molecules which can be excited by circularly polarized laser pulses described in Section 2.3. Then, in Section 2.4 we extend the theory of electronic ring currents to nuclear ring currents and corresponding induced magnetic fields in vibrational and pseudorotational states specifically for the aligned linear triatomic molecule ABA. The induction of nuclear pseudorotation by means of a circularly polarized laser pulse is described in Section 2.5. Finally, the orientation of a linear polar molecule by means of a linearly polarized laser pulse is discussed in Section 2.6.

2.2 Electronic states

2.2.1 Time-independent electronic Schrödinger equation

The time-independent treatment of electronic states is based on the time-independent non-relativistic electronic Schrödinger equation (TISE)

$$\hat{H}_{el}|\Psi_i\rangle = E_i|\Psi_i\rangle \tag{2.1}$$

where E_i is the eigenenergy of the stationary (time-independent) electronic state $|\Psi_i\rangle$ with the corresponding set of electronic quantum numbers (i). The electronic Hamiltonian $\hat{H}_{el}$

of the arbitrary atomic or molecular system contains the kinetic operator of the electrons, the repulsive Coulomb potential between nuclei, the attractive Coulomb potential between nuclei and electrons, and the repulsive Coulomb potential between electrons, that is

$$\begin{aligned}\hat{H}_{el} &= -\frac{\hbar^2}{2m_e}\sum_{n=1}^{N}\nabla_{\mathbf{r}_n}^2 \\ &+\frac{e^2}{4\pi\varepsilon_0}\left(\sum_{\substack{\alpha,\beta=1\\ \beta>\alpha}}^{N'}\frac{Z_\alpha Z_\beta}{|\mathbf{R}_\alpha-\mathbf{R}_\beta|}-\sum_{n=1}^{N}\sum_{\alpha=1}^{N'}\frac{Z_\alpha}{|\mathbf{r}_n-\mathbf{R}_\alpha|}+\sum_{\substack{n,m=1\\ m>n}}^{N}\frac{1}{|\mathbf{r}_n-\mathbf{r}_m|}\right)\end{aligned} \tag{2.2}$$

where $\mathbf{r}_n\,(n=1,\ldots,N)$ and $\mathbf{R}_\alpha\,(\alpha=1,\ldots,N')$ are the positions of N electrons and N' nuclei with charges $Z_\alpha\,(\alpha=1,\ldots,N')$, respectively. The second and last terms in Eq. (2.2) vanish for an atom or ion with one nucleus ($N'=1$) and for the one-electron system ($N=1$), respectively.

Including electronic spin, the electronic states

$$|\Psi_i\rangle = |\Psi_{qSM_S}\rangle \tag{2.3}$$

with sets of orbital quantum numbers q and spin quantum numbers $S=0,\frac{1}{2},1,\frac{3}{2},2,\ldots$, $M_S=-S,-S+1,\ldots,S-1,S$ are the common eigenstates of the spin-free electronic Hamiltonian $\hat{H}_{el}$ (Eqs. (2.1), (2.2)) and the spin operators $\hat{S}^2$, $\hat{S}_z$

$$\hat{S}^2|\Psi_i\rangle = S(S+1)\hbar^2|\Psi_i\rangle \tag{2.4}$$

$$\hat{S}_z|\Psi_i\rangle = M_S\hbar|\Psi_i\rangle. \tag{2.5}$$

In this work, only singlet states ($S=M_S=0$) for many-electron systems are considered for which the electronic ground states are singlet states.

2.2.2 Electronic wavefunction

The exact electronic configuration interaction (CI) wavefunctions $\Psi_i^{CI}(\mathbf{q}_1,\ldots,\mathbf{q}_N)$ of the singlet state $|\Psi_i\rangle = |\Psi_{qS=0M_S=0}\rangle$ (Eq. (2.3)) depending on all space and spin variables $\mathbf{q}_n=(\mathbf{r}_n,\sigma_n)=(x_n,y_n,z_n,\sigma_n)$ $(n=1,\ldots,N)$ of N electrons can be written as a linear combination $\Psi_i^{CI}=\sum_k C_{k,i}\Phi_k$ of the configuration functions Φ_k with the same symmetry properties as the state $|\Psi_i\rangle$, i.e.

$$\Psi_i^{CI} = C_{0,i}^{HF}\Phi_0^{HF}+\sum_{a=1}^{N/2}\sum_{b=N/2+1}^{\infty}{}^{S}C_{a,i}^{b}\,{}^{S}\Phi_a^b+\ldots \tag{2.6}$$

where Φ_0^{HF} and ${}^{S}\Phi_a^b$ are the restricted Hartree-Fock (HF) wavefunction and singly excited configuration functions with corresponding coefficients $C_{0,i}^{HF}$ and ${}^{S}C_{a,i}^{b}$ respectively. The

sum in Eq. (2.6) includes, in principle, also more, e.g. doubly excited configuration functions [231]. The simple approximation of CI wavefunctions (Eq. (2.6)) are wavefunctions

$$\Psi_i^{CIS} = C_{0,i}^{HF}\Phi_0^{HF} + \sum_{a=1}^{N/2}\sum_{b=N/2+1}^{\infty} {}^{S}C_{a,i}^{b}\,{}^{S}\Phi_a^b \tag{2.7}$$

including only the singly excited configuration functions (CIS) [117,118,120,231–233]. In this work, this CIS approximation is mainly used.

The CIS wavefunction of the electronic singlet ground state Ψ_0^{CIS} is equal to the restricted HF wavefunction $\Phi_0^{HF}(\mathbf{q}_1,\ldots,\mathbf{q}_N)$ ($C_{0,0}^{HF}=1$, ${}^{S}C_{a,0}^{b}=0$). It is given by the Slater determinant

$$\begin{aligned}\Psi_0^{CIS} &= \Phi_0^{HF} \\ &= |\varphi_1\alpha\ \varphi_1\beta\ \ldots\ \varphi_{N/2}\alpha\ \varphi_{N/2}\beta| \\ &= \frac{1}{\sqrt{N!}}\begin{vmatrix} \varphi_1(\mathbf{r}_1)\alpha(\sigma_1) & \varphi_1(\mathbf{r}_1)\beta(\sigma_1) & \ldots & \varphi_{N/2}(\mathbf{r}_1)\alpha(\sigma_1) & \varphi_{N/2}(\mathbf{r}_1)\beta(\sigma_1) \\ \varphi_1(\mathbf{r}_2)\alpha(\sigma_2) & \varphi_1(\mathbf{r}_2)\beta(\sigma_2) & \ldots & \varphi_{N/2}(\mathbf{r}_2)\alpha(\sigma_2) & \varphi_{N/2}(\mathbf{r}_2)\beta(\sigma_2) \\ \ldots & \ldots & \ldots & \ldots & \ldots \\ \varphi_1(\mathbf{r}_N)\alpha(\sigma_N) & \varphi_1(\mathbf{r}_N)\beta(\sigma_N) & \ldots & \varphi_{N/2}(\mathbf{r}_N)\alpha(\sigma_N) & \varphi_{N/2}(\mathbf{r}_N)\beta(\sigma_N) \end{vmatrix}\end{aligned} \tag{2.8}$$

where φ_a ($a=1,\ldots,N/2$) and α, β are occupied spatial atomic or molecular orbitals (AO or MO) and spinors, respectively. The CIS wavefunctions of the electronic singlet excited states Ψ_i^{CIS} ($i>0$) are ($C_{0,i}^{HF}=0, i>0$)

$$\Psi_i^{CIS} = \sum_{a=1}^{N/2}\sum_{b=N/2+1}^{\infty} {}^{S}C_{a,i}^{b}\,{}^{S}\Phi_a^b \qquad (i>0) \tag{2.9}$$

where

$${}^{S}\Phi_a^b = \frac{1}{\sqrt{2}}\left(|\ldots\ \varphi_b\alpha\ \varphi_a\beta\ \ldots| + |\ldots\ \varphi_a\alpha\ \varphi_b\beta\ \ldots|\right) \tag{2.10}$$

are the so-called singlet configuration state functions (CSF) [117, 118, 120, 231, 233, 234] in which an electron with spin α or β is excited from an occupied orbital $\varphi_a\alpha$ or $\varphi_a\beta$ to an unoccupied orbital $\varphi_b\alpha$ or $\varphi_b\beta$, respectively. The normalization conditions for CIS excited states $|\Psi_i^{CIS}\rangle$ (Eq. (2.9)) are

$$\sum_{a=1}^{N/2}\sum_{b=N/2+1}^{\infty} |{}^{S}C_{a,i}^{b}|^2 = 1. \tag{2.11}$$

For the special case in which an electron is excited from different occupied orbitals φ_a ($a=1,\ldots,N/2$) to the only unoccupied orbital φ_b, the CIS wavefunction (Eq. (2.9)) reduces to

$$\Psi_{i,\to b}^{CIS} = \sum_{a=1}^{N/2} {}^{S}C_{a,i}^{b}\,{}^{S}\Phi_a^b. \tag{2.12}$$

For another special case in which an electron is excited from the only occupied orbital φ_a to different unoccupied orbitals φ_b ($b = N/2+1, \ldots, \infty$), the CIS wavefunction (Eq. (2.9)) becomes

$$\Psi^{CIS}_{i,a\rightarrow} = \sum_{b=N/2+1}^{\infty} {}^{S}C^{b}_{a,i}\, {}^{S}\Phi^{b}_{a}. \tag{2.13}$$

If the CIS excited state is dominated by the transition of an electron from an occupied orbital φ_a to an unoccupied orbital φ_b, then it is simply equal to the singlet CSF (Eq. (2.10))

$$\Psi^{CIS}_{i,a\rightarrow b} = {}^{S}\Phi^{b}_{a}. \tag{2.14}$$

2.2.3 Electronic probability density

The one-electron probability density $\rho_i(\mathbf{r} = \mathbf{r}_1)$ of the stationary eigenstate $|\Psi_i\rangle$ is given by

$$\rho_i(\mathbf{r}) = N \int \ldots \int |\Psi_i|^2 d\sigma_1 d\mathbf{q}_2 \ldots d\mathbf{q}_N \tag{2.15}$$

where the symbol $\int \ldots \int$ indicates integration over the other $N-1$ space $\mathbf{r}_n$ ($n = 2, \ldots, N$) and all spin variables σ_n ($n = 1, \ldots, N$) of N electrons [235].

For the CIS approximation (Eq. (2.7)), the one-electron probability density of the electronic singlet ground state ($i = 0$) is (cf. Eq. (2.8))

$$\begin{aligned} \rho^{CIS}_0(\mathbf{r}) &= N \int \ldots \int |\Psi^{CIS}_0|^2 d\sigma_1 d\mathbf{q}_2 \ldots d\mathbf{q}_N \\ &= N \int \ldots \int |\Phi^{HF}_0|^2 d\sigma_1 d\mathbf{q}_2 \ldots d\mathbf{q}_N \\ &= 2 \sum_{a=1}^{N/2} |\varphi_a|^2, \end{aligned} \tag{2.16}$$

i.e. it is equal to the sum of the probability densities of the occupied spatial orbitals φ_a multiplied by 2 for two electrons occupying each orbital [235]. The one-electron probability densities of the CIS excited states ($i > 0$) (Eqs. (2.9) and (2.10)) are derived, using the normalization condition (Eq. (2.11)) and Eq. (2.16), according to

$$\begin{aligned} \rho^{CIS}_i(\mathbf{r}) &= N \int \ldots \int |\Psi^{CIS}_i|^2 d\sigma_1 d\mathbf{q}_2 \ldots d\mathbf{q}_N \\ &= \sum_{a,c=1}^{N/2} \sum_{b,d=N/2+1}^{\infty} {}^{S}C^{b}_{a,i}\, ({}^{S}C^{d}_{c,i})^{*}\, N \int \ldots \int {}^{S}\Phi^{b}_{a}\, ({}^{S}\Phi^{d}_{c})^{*} d\sigma_1 d\mathbf{q}_2 \ldots d\mathbf{q}_N \\ &= \sum_{a,c=1}^{N/2} \sum_{b,d=N/2+1}^{\infty} {}^{S}C^{b}_{a,i}\, ({}^{S}C^{d}_{c,i})^{*} \left(2\delta_{ac}\delta_{bd} \sum_{f=1}^{N/2} |\varphi_f|^2 + \delta_{ac}\varphi_b\varphi^{*}_d - \delta_{bd}\varphi_a\varphi^{*}_c \right) \end{aligned} \tag{2.17}$$

$$
\begin{aligned}
&= \rho_0^{CIS}(\mathbf{r}) + \sum_{a,c=1}^{N/2} \sum_{b,d=N/2+1}^{\infty} {}^{S}C_{a,i}^{b}\, ({}^{S}C_{c,i}^{d})^{*}\, (\delta_{ac}\varphi_b\varphi_d^{*} - \delta_{bd}\varphi_a\varphi_c^{*}) \\
&= \rho_0^{CIS}(\mathbf{r}) + \sum_{b=N/2+1}^{\infty} \left(\sum_{a=1}^{N/2} |{}^{S}C_{a,i}^{b}|^2 \right) |\varphi_b|^2 - \sum_{a=1}^{N/2} \left(\sum_{b=N/2+1}^{\infty} |{}^{S}C_{a,i}^{b}|^2 \right) |\varphi_a|^2 \\
&\quad + \sum_{\substack{b,d=N/2+1 \\ b\neq d}}^{\infty} \left(\sum_{a=1}^{N/2} {}^{S}C_{a,i}^{b}\, ({}^{S}C_{a,i}^{d})^{*} \right) \varphi_b\varphi_d^{*} - \sum_{\substack{a,c=1 \\ a\neq c}}^{N/2} \left(\sum_{b=N/2+1}^{\infty} {}^{S}C_{a,i}^{b}\, ({}^{S}C_{c,i}^{b})^{*} \right) \varphi_a\varphi_c^{*}.
\end{aligned}
$$

The one-electron probability density of the excited state $|\Psi_i^{CIS}\rangle$ $(i > 0)$ is, therefore, equal to the density of the ground state $|\Psi_0^{CIS}\rangle$ plus those of the unoccupied orbitals φ_b with weights $\sum_{a=1}^{N/2}|{}^{S}C_{a,i}^{b}|^2$ minus the densities of the occupied orbitals φ_a with weights $\sum_{b=N/2+1}^{\infty}|{}^{S}C_{a,i}^{b}|^2$, plus the additional interference contributions of the probability densities of the mixed orbitals. For the special approximations of the CIS excited wavefunctions, Eqs. (2.12), (2.13) and (2.14), the corresponding electronic probability densities are

$$
\rho_{i,\to b}^{CIS}(\mathbf{r}) = \rho_0^{CIS}(\mathbf{r}) + |\varphi_b|^2 - \sum_{a=1}^{N/2} |{}^{S}C_{a,i}^{b}|^2\, |\varphi_a|^2 - \sum_{\substack{a,c=1 \\ a\neq c}}^{N/2} {}^{S}C_{a,i}^{b}\, ({}^{S}C_{c,i}^{b})^{*}\, \varphi_a\varphi_c^{*}, \tag{2.18}
$$

$$
\rho_{i,a\to}^{CIS}(\mathbf{r}) = \rho_0^{CIS}(\mathbf{r}) + \sum_{b=N/2+1}^{\infty} |{}^{S}C_{a,i}^{b}|^2\, |\varphi_b|^2 - |\varphi_a|^2 + \sum_{\substack{b,d=N/2+1 \\ b\neq d}}^{\infty} {}^{S}C_{a,i}^{b}\, ({}^{S}C_{a,i}^{d})^{*}\, \varphi_b\varphi_d^{*}, \tag{2.19}
$$

$$
\rho_{i,a\to b}^{CIS}(\mathbf{r}) = \rho_0^{CIS}(\mathbf{r}) + |\varphi_b|^2 - |\varphi_a|^2, \tag{2.20}
$$

respectively.

2.2.4 Electronic current density

The one-electron current density $\mathbf{j}_i(\mathbf{r} = \mathbf{r}_1)$ of the state $|\Psi_i\rangle$ is given by

$$
\mathbf{j}_i(\mathbf{r}) = \frac{i\hbar}{2m_e} N \int \ldots \int (\Psi_i \nabla \Psi_i^{*} - \Psi_i^{*} \nabla \Psi_i)\, d\sigma_1 d\mathbf{q}_2 \ldots d\mathbf{q}_N \tag{2.21}
$$

where the symbol $\int \ldots \int$ has the same meaning as in Eq. (2.15) and $\nabla = \nabla_{\mathbf{r}}$. The current density of the CIS singlet ground state $|\Psi_0^{CIS}\rangle$ can be derived from Eqs. (2.8) and (2.21),

$$
\begin{aligned}
\mathbf{j}_0^{CIS}(\mathbf{r}) &= \frac{i\hbar}{2m_e} N \int \ldots \int \left(\Psi_0^{CIS} \nabla (\Psi_0^{CIS})^{*} - (\Psi_0^{CIS})^{*} \nabla \Psi_0^{CIS} \right) d\sigma_1 d\mathbf{q}_2 \ldots d\mathbf{q}_N \\
&= \frac{i\hbar}{2m_e} N \int \ldots \int \left(\Phi_0^{HF} \nabla (\Phi_0^{HF})^{*} - (\Phi_0^{HF})^{*} \nabla \Phi_0^{HF} \right) d\sigma_1 d\mathbf{q}_2 \ldots d\mathbf{q}_N \\
&= \frac{i\hbar}{m_e} \sum_{a=1}^{N/2} (\varphi_a \nabla \varphi_a^{*} - \varphi_a^{*} \nabla \varphi_a) \\
&= 2 \sum_{a=1}^{N/2} \mathbf{j}_{\varphi_a}(\mathbf{r}),
\end{aligned} \tag{2.22}
$$

where

$$\mathbf{j}_{\varphi_a}(\mathbf{r}) = \frac{i\hbar}{2m_e}\left(\varphi_a \nabla\varphi_a^* - \varphi_a^* \nabla\varphi_a\right) \tag{2.23}$$

is the electronic current density of the orbital φ_a. Thus, the current density of the ground state is equal to the sum of the electronic current densities of the occupied orbitals φ_a multiplied by 2 for two electrons occupying each orbital. The derivation of the current densities of the CIS excited states $|\Psi_i^{CIS}\rangle$ $(i > 0)$ (Eqs. (2.9) and (2.10)) from Eq. (2.21) is analogous to the derivation of the probability densities (Eq. (2.17)), i.e.

$$\begin{aligned}
\mathbf{j}_i^{CIS}(\mathbf{r}) &= \frac{i\hbar}{2m_e} N \int \ldots \int \left(\Psi_i^{CIS} \nabla (\Psi_i^{CIS})^* - (\Psi_i^{CIS})^* \nabla \Psi_i^{CIS}\right) d\sigma_1 d\mathbf{q}_2 \ldots d\mathbf{q}_N \qquad (2.24)\\
&= \frac{i\hbar}{2m_e} \sum_{a,c=1}^{N/2} \sum_{b,d=N/2+1}^{\infty} {}^S C_{a,i}^b \, ({}^S C_{c,i}^d)^* \\
&\qquad N \int \ldots \int \left({}^S\Phi_a^b \nabla ({}^S\Phi_c^d)^* - ({}^S\Phi_c^d)^* \nabla \, {}^S\Phi_a^b\right) d\sigma_1 d\mathbf{q}_2 \ldots d\mathbf{q}_N \\
&= \mathbf{j}_0^{CIS}(\mathbf{r}) + \frac{i\hbar}{2m_e} \sum_{a,c=1}^{N/2} \sum_{b,d=N/2+1}^{\infty} {}^S C_{a,i}^b \, ({}^S C_{c,i}^d)^* \\
&\qquad \left(\delta_{ac}\left(\varphi_b \nabla\varphi_d^* - \varphi_d^* \nabla\varphi_b\right) - \delta_{bd}\left(\varphi_a \nabla\varphi_c^* - \varphi_c^* \nabla\varphi_a\right)\right) \\
&= \mathbf{j}_0^{CIS}(\mathbf{r}) + \sum_{b=N/2+1}^{\infty} \left(\sum_{a=1}^{N/2} |{}^S C_{a,i}^b|^2\right) \mathbf{j}_{\varphi_b}(\mathbf{r}) - \sum_{a=1}^{N/2} \left(\sum_{b=N/2+1}^{\infty} |{}^S C_{a,i}^b|^2\right) \mathbf{j}_{\varphi_a}(\mathbf{r}) \\
&\qquad + \frac{i\hbar}{2m_e} \sum_{\substack{b,d=N/2+1 \\ b\neq d}}^{\infty} \left(\sum_{a=1}^{N/2} {}^S C_{a,i}^b \, ({}^S C_{a,i}^d)^*\right) \left(\varphi_b \nabla\varphi_d^* - \varphi_d^* \nabla\varphi_b\right) \\
&\qquad - \frac{i\hbar}{2m_e} \sum_{\substack{a,c=1 \\ a\neq c}}^{N/2} \left(\sum_{b=N/2+1}^{\infty} {}^S C_{a,i}^b \, ({}^S C_{c,i}^b)^*\right) \left(\varphi_a \nabla\varphi_c^* - \varphi_c^* \nabla\varphi_a\right).
\end{aligned}$$

This result is analogous to the result of the probability density (Eq. (2.17)), i.e. the current density of the excited state $|\Psi_i^{CIS}\rangle$ $(i > 0)$ is equal to the current density of the ground state $|\Psi_0^{CIS}\rangle$ plus those of the unoccupied orbitals φ_b with weights $\sum_{a=1}^{N/2} |{}^S C_{a,i}^b|^2$ minus the current densities of the occupied orbitals φ_a with weights $\sum_{b=N/2+1}^{\infty} |{}^S C_{a,i}^b|^2$. There are also additional interference contributions of the current densities of the mixed orbitals. The approximations of CIS excited wavefunctions, Eqs. (2.12), (2.13) and (2.14), lead to the corresponding electronic current densities

$$\begin{aligned}
\mathbf{j}_{i,\to b}^{CIS}(\mathbf{r}) &= \mathbf{j}_0^{CIS}(\mathbf{r}) + \mathbf{j}_{\varphi_b}(\mathbf{r}) - \sum_{a=1}^{N/2} |{}^S C_{a,i}^b|^2 \, \mathbf{j}_{\varphi_a}(\mathbf{r}) \qquad (2.25)\\
&\qquad - \frac{i\hbar}{2m_e} \sum_{\substack{a,c=1 \\ a\neq c}}^{N/2} {}^S C_{a,i}^b \, ({}^S C_{c,i}^b)^* \, \left(\varphi_a \nabla\varphi_c^* - \varphi_c^* \nabla\varphi_a\right)
\end{aligned}$$

$$\mathbf{j}^{CIS}_{i,a\rightarrow}(\mathbf{r}) = \mathbf{j}^{CIS}_{0}(\mathbf{r}) + \sum_{b=N/2+1}^{\infty} |{}^{S}C^{b}_{a,i}|^{2}\, \mathbf{j}_{\varphi_b}(\mathbf{r}) - \mathbf{j}_{\varphi_a}(\mathbf{r}) + \frac{i\hbar}{2m_e} \sum_{\substack{b,d=N/2+1 \\ b\neq d}}^{\infty} {}^{S}C^{b}_{a,i}\, ({}^{S}C^{d}_{a,i})^{*}\, (\varphi_b \nabla \varphi^{*}_{d} - \varphi^{*}_{d} \nabla \varphi_b) \tag{2.26}$$

$$\mathbf{j}^{CIS}_{i,a\rightarrow b}(\mathbf{r}) = \mathbf{j}^{CIS}_{0}(\mathbf{r}) + \mathbf{j}_{\varphi_b}(\mathbf{r}) - \mathbf{j}_{\varphi_a}(\mathbf{r}), \tag{2.27}$$

respectively.

2.2.5 Electronic ring currents

For the real wavefunction $\Psi_i = \Psi^{*}_{i}$, the electronic current density $\mathbf{j}_i(\mathbf{r})$ (Eq. (2.21)) vanishes exactly because the term $\Psi_i \nabla \Psi^{*}_{i} - \Psi^{*}_{i} \nabla \Psi_i = \Psi_i \nabla \Psi_i - \Psi_i \nabla \Psi_i$ is equal to zero. Each non-degenerate state can be represented by real orbitals, therefore the current densities of non-degenerate states are always zero. In particular, each singlet ground state, i.e. $|X\,{}^{1}S\rangle$ for atoms or atomic ions, $|X\,{}^{1}\Sigma\rangle$ for linear molecules, and $|X\,{}^{1}A\rangle$ for non-linear molecules, is not degenerate. Thus, the electronic current densities of the singlet ground states are always zero, i.e.

$$\mathbf{j}_0(\mathbf{r}) = \mathbf{j}^{CIS}_{0}(\mathbf{r}) = \mathbf{0}, \tag{2.28}$$

cf. Eqs. (2.21) and (2.22).

If there are orbitally degenerate states, i.e. if two or more eigenstates $|\Psi_i\rangle, |\Psi_j\rangle, \ldots$ with the same spin quantum numbers S, M_S have the same eigenenergies $E_i = E_j = \ldots$, then all possible linear combinations $|\tilde{\Psi}_i\rangle, |\tilde{\Psi}_j\rangle, \ldots$ of the orbitally degenerate states $|\Psi_i\rangle, |\Psi_j\rangle, \ldots$ are again stationary electronic eigenstates with the same spin quantum numbers S, M_S and the same eigenenergies $\tilde{E}_i = \tilde{E}_j = \ldots = E_i = E_j = \ldots$. Thus, the electronic probability densities (Eq. (2.15)) and current densities (Eq. (2.21)) of the new degenerate states $|\tilde{\Psi}_i\rangle, |\tilde{\Psi}_j\rangle, \ldots$ are also stationary.

In the present work, we consider non-zero electronic ring currents and associated induced magnetic fields in atoms, ions, and molecules. Note that the electronic ring current, defined as the fraction of the electron passing through the perpendicular half plane per time, should not be confused with the electronic current density $\mathbf{j}_i(\mathbf{r})$ (Eq. (2.21)) and the electric ring current, which, in the case of electrons, is the product of the electronic ring current and the electron charge, cf. Eq. (2.55), whereas for nuclei, it is the product of the nuclear ring current times the nuclear charge, cf. Eq. (2.327). In order to obtain non-zero stationary electronic current density $\mathbf{j}_i(\mathbf{r}) \neq 0$, an orbitally degenerate state $|\Psi_i\rangle = |\Psi_{qSM_S}\rangle$ must be suitably chosen, cf. Ref. [236]. The condition $\mathbf{j}_i(\mathbf{r}) \neq 0$

implies that the wavefunction of the degenerate state $|\Psi_i\rangle$ be complex. For example, the linear combinations

$$|\Psi_\pm\rangle \;=\; \frac{1}{\sqrt{2}}\left(|\Psi_x\rangle \pm i|\Psi_y\rangle\right) \tag{2.29}$$

of two real orbitally degenerate states $|\Psi_x\rangle$ and $|\Psi_y\rangle$ with the same spin quantum numbers S, M_S satisfy the condition given above, i.e. the wavefunctions $\Psi_\pm$ are complex. They have non-zero electronic current densities, derived from Eq. (2.21)

$$\mathbf{j}_\pm(\mathbf{r}=\mathbf{r}_1) \;=\; \pm\frac{\hbar}{2m_e}\,N\int\ldots\int\left(\Psi_x\nabla\Psi_y-\Psi_y\nabla\Psi_x\right)d\sigma_1 d\mathbf{q}_2\ldots d\mathbf{q}_N. \tag{2.30}$$

Hence, the complex wavefunctions $\Psi_\pm$ (Eq. (2.29)) represent stationary electronic ring currents about the axis of symmetry, i.e. the z-axis. Note that the sign $\pm$ determines the direction of the electronic ring current. Nevertheless, the electronic probability densities of the degenerate states $|\Psi_\pm\rangle$ (Eq. 2.15)

$$\rho_\pm(\mathbf{r}=\mathbf{r}_1) \;=\; \frac{N}{2}\int\ldots\int\left(|\Psi_x|^2+|\Psi_y|^2\right)d\sigma_1 d\mathbf{q}_2\ldots d\mathbf{q}_N \tag{2.31}$$

are independent of the sign $\pm$.

The complex wavefunctions $\Psi_\pm$ (Eq. (2.29)) can be constructed using non-degenerate real orbitals as well as degenerate complex ones, e.g.

$$\varphi_\pm \;=\; \frac{1}{\sqrt{2}}\left(\varphi_x \pm i\varphi_y\right), \tag{2.32}$$

where φ_x and φ_y are the degenerate real orbitals. The current density of the orbital $\mathbf{j}_\varphi(\mathbf{r})$ is zero for the real orbitals, and non-zero for the complex orbitals such as $\varphi_\pm$, i.e.

$$\begin{aligned}\mathbf{j}_{\varphi_\pm}(\mathbf{r}) \;&=\; \frac{i\hbar}{2m_e}\left(\varphi_\pm\nabla\varphi_\pm^*-\varphi_\pm^*\nabla\varphi_\pm\right) \\ &=\; \pm\frac{\hbar}{2m_e}\left(\varphi_x\nabla\varphi_y-\varphi_y\nabla\varphi_x\right)\neq 0.\end{aligned} \tag{2.33}$$

For atoms, atomic ions, and linear molecules, there is axial symmetry, i.e. the orbitals in the complex representation can be rewritten as (Eq. (2.32))

$$\varphi_{M_L} \;=\; \tilde{\varphi}_{M_L}e^{iM_L\phi}, \tag{2.34}$$

where ϕ and $M_L = 0, \pm1, \pm2, \ldots$ are the azimuthal angle and magnetic quantum number, respectively, and $\tilde{\varphi}_{M_L}$ is independent of ϕ. The angular momentum operator

$$\hat{L}_z \;=\; -i\hbar\frac{\partial}{\partial\phi} \tag{2.35}$$

has the eigenvalues $M_L\hbar = 0, \pm\hbar, \pm 2\hbar, \ldots$. The current density of the orbital φ_M is calculated using the Nabla operator in spherical

$$\nabla = \frac{\partial}{\partial r}\mathbf{e}_r + \frac{1}{r}\frac{\partial}{\partial\theta}\mathbf{e}_\theta + \frac{1}{r\sin\theta}\frac{\partial}{\partial\phi}\mathbf{e}_\phi \tag{2.36}$$

or cylindrical coordinates ($\rho = r\sin\theta$)

$$\nabla = \frac{\partial}{\partial\rho}\mathbf{e}_\rho + \frac{1}{\rho}\frac{\partial}{\partial\phi}\mathbf{e}_\phi + \frac{\partial}{\partial z}\mathbf{e}_z, \tag{2.37}$$

i.e.

$$\begin{aligned}\mathbf{j}_{\varphi_{M_L}}(\mathbf{r}) &= \frac{i\hbar}{2m_e}\left(\varphi_{M_L}\nabla\varphi^*_{M_L} - \varphi^*_{M_L}\nabla\varphi_{M_L}\right) \\ &= \frac{M_L\hbar}{m_e}\frac{|\varphi_{M_L}|^2}{\rho}\mathbf{e}_\phi.\end{aligned} \tag{2.38}$$

Note that the cylindrical coordinate ρ and electronic probability density $\rho(\mathbf{r})$ should not be confused. The current density of the non-degenerate real ($M_L = 0$) or degenerate complex orbitals ($M_L \neq 0$) is zero and non-zero, respectively. Furthermore, it is proportional to the magnetic quantum number M_L. Its ϕ-component is the only one which does not vanish, and it is independent of ϕ. Thus, the orbital φ_{M_L} (Eq. (2.34)) represents the stationary toroidal electronic ring current about the axis of symmetry (z-axis). The direction of the electronic ring current of the orbital φ_{M_L} is determined by the sign of M_L but it has no influence on the electronic probability density $\rho(\mathbf{r})$ (Eq. (2.15)).

If the CIS degenerate complex wavefunctions Ψ_i^{CIS} (Eq. (2.9)) consists of several CSFs (Eq. (2.10)) described by the excitations of an electron from an occupied degenerate complex orbital φ_a to an unoccupied degenerate complex orbital φ_b, then the current density $\mathbf{j}_i^{CIS}(\mathbf{r})$ (Eq. (2.24)) has non-zero contributions from the current densities of the occupied and unoccupied complex orbitals. For example, if the wavefunction Π_+ of a linear molecule is governed by an electronic transition from an occupied complex orbital $\pi_+ = \tilde{\pi}_+ e^{i\phi}$ to an unoccupied complex orbtial $\delta_+ = \tilde{\delta}_+ e^{2i\phi}$ (Eq. (2.14)) where $\tilde{\pi}_+$ and $\tilde{\delta}_+$ are independent of ϕ, then the corresponding current density (Eq. (2.27)) is derived, using $\mathbf{j}_0(\mathbf{r}) = 0$ (Eq. (2.28)) and Eq. (2.38),

$$\mathbf{j}^{CIS}_{i,\pi_+\rightarrow\delta_+}(\mathbf{r}) = \frac{\hbar}{m_e}\frac{1}{\rho}\left(2|\delta_+|^2 - |\pi_+|^2\right)\mathbf{e}_\phi. \tag{2.39}$$

The ring current has two contributions of the spatially separated electronic ring currents with opposite directions, say the positive electronic ring current of the orbital δ_+ plus the negative one of the orbital π_+, which is mathematically equivalent to the positive one of the orbital π_- (Eq. (2.38) and $|\varphi_{M_L}|^2 = |\varphi_{-M_L}|^2$) because the occupied orbital π_- still remains in the CIS wavefunction. Note that the electronic current density of this type

of state $|\Pi_+\rangle$ is not proportional to the magnetic quantum number M_L. These so-called bidirectional electronic ring currents are, however, not studied in this work.

Here, we consider only the CIS singlet degenerate excited states $|\Psi_i^{CIS}\rangle$ in which the dominant electronic excitations are the transitions from different occupied real orbitals φ_a to an unoccupied complex orbital $\varphi_{b\pm}$ or from an occupied complex orbital $\varphi_{a\pm}$ to different unoccupied real orbitals φ_b. The corresponding electronic current densities are thus (Eqs. (2.25)–(2.27))

$$\mathbf{j}^{CIS}_{i,\rightarrow b\pm}(\mathbf{r}) = \mathbf{j}_{\varphi_{b\pm}}(\mathbf{r}), \tag{2.40}$$

$$\mathbf{j}^{CIS}_{i,a\pm\rightarrow}(\mathbf{r}) = -\mathbf{j}_{\varphi_{a\pm}}(\mathbf{r}) = \mathbf{j}_{\varphi_{a\mp}}(\mathbf{r}). \tag{2.41}$$

These expressions have rather simple forms with just one term, i.e. the electronic current density of the CIS degenerate state $|\Psi_i^{CIS}\rangle$ is equal to the electronic current density of the only unoccoupied or occupied complex orbital $\varphi_{b\pm}$ or $\varphi_{a\mp}$ (Eq. (2.33)), respectively. For atoms, atomic ions, or linear molecules, it is proportional to the magnetic quantum number M_L (Eq. (2.38)), and the degenerate states $|\Psi_i\rangle$ represent the stationary unidirectional electronic ring currents about the axis of symmetry where the current direction is determined by the sign of M_L.

Now, let us specify the degenerate states (Eq. (2.29)) and degenerate orbitals (Eqs. (2.32) and (2.34)) in complex representation for atoms, atomic ions, linear molecules and non-linear molecules. First, for atoms and atomic ions with spherical symmetry, the electronic states $|P\rangle$, $|D\rangle$, $|F\rangle$, ... are 3-, 5-, and 7-fold orbitally degenerate, respectively. The simplest degenerate states are thus $|P\rangle$ states which can be represented in real or complex forms. The real degenerate states are well-known as $|P_x\rangle$, $|P_y\rangle$, and $|P_z\rangle$, and the corresponding complex representation of $|P\rangle$ states can also be written as $|P_0\rangle = |P_z\rangle$ ($M_L = 0$) and, according to Eq. (2.29),

$$|P_\pm\rangle = |P_{\pm1}\rangle = \frac{1}{\sqrt{2}}\left(|P_x\rangle \pm i|P_y\rangle\right) \tag{2.42}$$

which possess magnetic quantum numbers $M_L = \pm1$. For the special case for which the $|P_{\pm1}\rangle$ state has the dominant contribution of the electronic transition from different occupied real orbitals such as ns orbitals to an unoccupied orbital $p_{\pm1}$, i.e.

$$p_\pm = p_{\pm1} = \frac{1}{\sqrt{2}}\left(p_x \pm ip_y\right) = \tilde{p}_{\pm1}e^{\pm i\phi}, \tag{2.43}$$

where p_x and p_y are the degenerate real orbitals (Eqs. (2.32) and (2.34)), see Fig. 2.1, and $\tilde{p}_{\pm1}$ is independent of ϕ, the electronic current density is (Eqs. (2.38) and (2.40))

$$\mathbf{j}^{CIS}_{P_{\pm1},\rightarrow p_{\pm1}}(\mathbf{r}) = \pm\frac{\hbar}{m_e}\frac{|p_{\pm1}|^2}{\rho}\mathbf{e}_\phi, \tag{2.44}$$

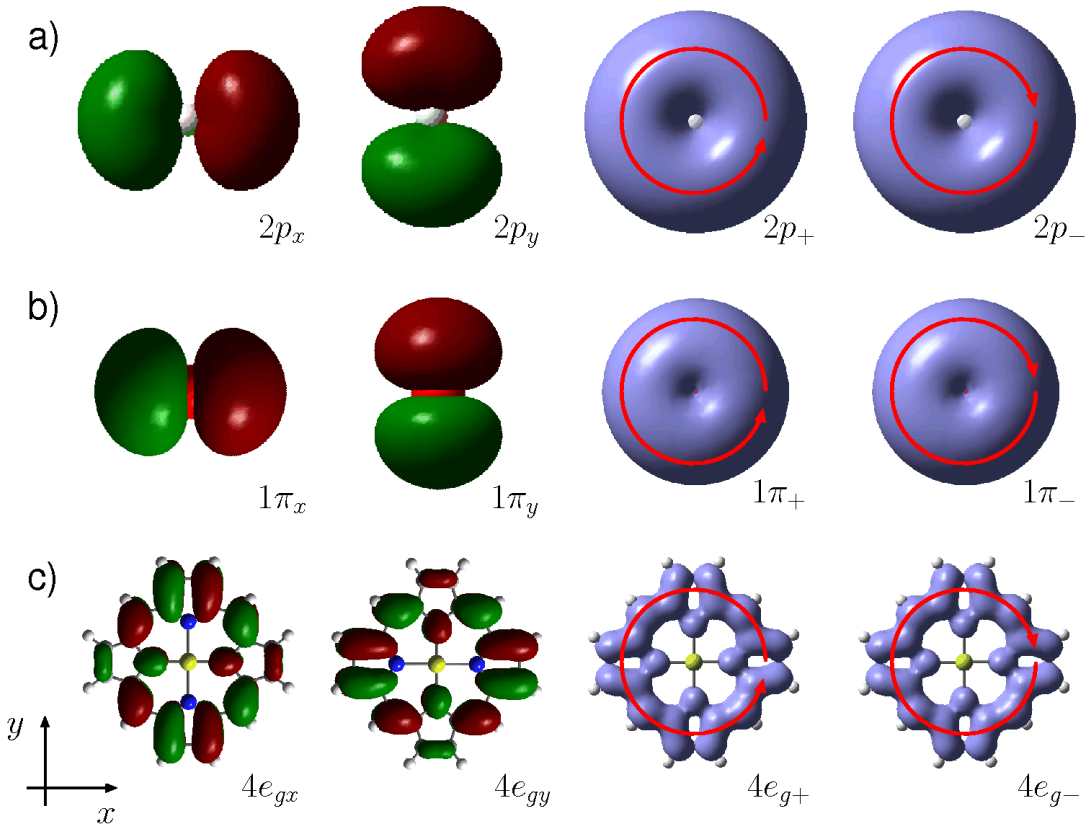

Figure 2.1: a) Real p_x, p_y, and complex $p_\pm = (p_x \pm ip_y)/\sqrt{2}$ (Eq. (2.43)) degenerate orbitals for atoms and atomic ions (here: $2p_x$, $2p_y$, and $2p_\pm$ orbitals for the hydrogen atom); b) real π_x, π_y, and complex $\pi_\pm = (\pi_x \pm i\pi_y)/\sqrt{2}$ (Eq. (2.47)) degenerate orbitals for linear molecules (here: $1\pi_x$, $1\pi_y$, and $1\pi_\pm$ orbitals for BeO molecule for which the Be nucleus is located behind the O nucleus (red)); c) real e_x, e_y, and complex $e_\pm = (e_x \pm ie_y)/\sqrt{2}$ (Eq. (2.50)) degenerate orbitals for non-linear molecules (here: $4e_{gx}$, $4e_{gy}$, and $4e_{g\pm}$ orbitals for Mg-porphyrin). All orbitals are drawn in the x/y plane; the z-axis is perpendicular to the plane of the figure. Red arrows indicate the directions of the electronic ring currents.

which is proportional to $M_L = \pm 1$. For electronic transitions from an occupied orbital $p_{\mp 1}$ to different unoccupied real orbitals such as ns orbitals, the corresponding current density of the state $|P_{\pm 1}\rangle$ is (Eqs. (2.38) and (2.41))

$$\mathbf{j}^{CIS}_{P_{\pm 1}, p_{\mp 1}\rightarrow}(\mathbf{r}) \;=\; \pm \frac{\hbar}{m_e} \frac{|p_{\pm 1}|^2}{\rho} \mathbf{e}_\phi, \tag{2.45}$$

which has exactly the same form as Eq. (2.44). Analogous considerations hold for the other degenerate states such as $|D_{M_L}\rangle$ ($M_L = \pm 1, \pm 2$), $|F_{M_L}\rangle$ ($M_L = \pm 1, \pm 2, \pm 3$), ... with dominant electronic transitions from different occupied real orbitals to an unoccupied complex orbital such as $d_{M_L} = \tilde{d}_{M_L} e^{iM_L\phi}$ ($M_L = \pm 1, \pm 2$), $f_{M_L} = \tilde{f}_{M_L} e^{iM_L\phi}$ ($M_L = \pm 1, \pm 2, \pm 3$), ..., or vice versa, respectively. The corresponding electronic current densities of the states $|D_{M_L}\rangle$, $|F_{M_L}\rangle$, ... are given by Eq. (2.38) and they are proportional to M_L. Note that the states with $M_L = 0$, for example $|S\rangle$, $|P_0\rangle$, $|D_0\rangle$, $|F_0\rangle$, ... do not have any electronic ring currents.

Next, let us consider linear molecules with cylindrical symmetry, i.e. molecular symmetries $C_{\infty v}$ and $D_{\infty h}$, the electronic states $|\Pi\rangle$, $|\Delta\rangle$, $|\Phi\rangle$, ... are orbitally twofold degenerate whereas the states $|\Sigma\rangle$ are orbitally non-degenerate. For example, the complex representations of the $|\Pi\rangle$ states are (Eq. (2.29))

$$|\Pi_\pm\rangle \;=\; \frac{1}{\sqrt{2}}\left(|\Pi_x\rangle \pm i|\Pi_y\rangle\right), \tag{2.46}$$

where $|\Pi_x\rangle$ and $|\Pi_y\rangle$ are the corresponding real representations of the $|\Pi\rangle$ states. These complex states $|\Pi_\pm\rangle$ have non-zero magnetic quantum numbers $M_L = \pm 1$. If the electronic transitions from different occupied real orbitals $n\sigma$ to an unoccupied complex orbital $\pi_\pm$, i.e.

$$\pi_\pm \;=\; \frac{1}{\sqrt{2}}\left(\pi_x \pm i\pi_y\right) \;=\; \tilde{\pi}_\pm e^{\pm i\phi}, \tag{2.47}$$

are dominant, or vice versa, where π_x and π_y are the real representations of the complex orbitals $\pi_\pm$ (Eqs. (2.32), (2.34)), see Fig. 2.1, and $\tilde{\pi}_\pm$ is independent of ϕ, then the electronic current density of the state $|\Pi_\pm\rangle$ is calculated as (Eqs. (2.38), (2.40), (2.41))

$$\mathbf{j}^{CIS}_{\Pi_\pm,\rightarrow\pi_\pm}(\mathbf{r}) \;=\; \mathbf{j}^{CIS}_{\Pi_\pm,\,\pi_\mp\rightarrow}(\mathbf{r}) \;=\; \pm\frac{\hbar}{m_e}\frac{|\pi_\pm|^2}{\rho}\mathbf{e}_\phi. \tag{2.48}$$

The current density is proportional to $M_L = \pm 1$. This derivation can be easily extended to other degenerate states such as $|\Delta_\pm\rangle$ ($M_L = \pm 2$), $|\Phi_\pm\rangle$ ($M_L = \pm 3$), ... with dominant electronic transitions from different occupied real orbitals $n\sigma$ to an unoccupied orbital such as $\delta_\pm = \tilde{\delta}_\pm e^{\pm 2i\phi}$, $\phi_\pm = \tilde{\phi}_\pm e^{\pm 3i\phi}$, ..., or vice versa, respectively. The current densities of these states are given by Eq. (2.38), and they are propotional to M_L. Only the states $|\Sigma\rangle$ ($M_L = 0$) do not have any electronic ring currents.

Finally, for non-linear molecules with high molecular symmetries C_{nv}, C_{nh}, D_{nh} ($n \geq 3$), D_{nd} ($n \geq 2$), T_h, T_d and O_h, orbitally twofold degenerate states $|E\rangle$ can be written as $|E_x\rangle$ and $|E_y\rangle$ states in real representation. The corresponding complex states are the same as Eq. (2.29), i.e.

$$|E_\pm\rangle \;=\; \frac{1}{\sqrt{2}}\left(|E_x\rangle \pm i|E_y\rangle\right). \tag{2.49}$$

For dominant electronic transitions from the unoccupied real orbials to an occupied complex orbital $e_\pm$, i.e.

$$e_\pm \;=\; \frac{1}{\sqrt{2}}\left(e_x \pm ie_y\right), \tag{2.50}$$

or vice versa, where e_x and e_y are the degenerate real orbitals (Eq. (2.32)), see Fig. 2.1, the current density of the state $|E_\pm\rangle$ is (Eqs. (2.33), (2.40), (2.41))

$$\mathbf{j}^{CIS}_{E_\pm,\rightarrow e_\pm}(\mathbf{r}) \;=\; \mathbf{j}^{CIS}_{E_\pm,\,e_\mp\rightarrow}(\mathbf{r}) \;=\; \pm\frac{\hbar}{2m_e}\left(e_x\nabla e_y - e_y\nabla e_x\right), \tag{2.51}$$

$$\mathbf{j}^{CIS}_{E_\pm,\rightarrow e_\mp}(\mathbf{r}) \;=\; \mathbf{j}^{CIS}_{E_\pm,\,e_\pm\rightarrow}(\mathbf{r}) \;=\; \mp\frac{\hbar}{2m_e}\left(e_x\nabla e_y - e_y\nabla e_x\right), \tag{2.52}$$

depends on the symmetry of the initial and final real orbitals. For example, the excited state $|4\,^1E_{u+}\rangle$ of Mg-porphyrin with D_{4h} symmetry has the dominant electronic transition $3a_{2u} \rightarrow 4e_{g+}$, but the excited states $|3\,^1E_{u+}\rangle$ and $|5\,^1E_{u+}\rangle$ have the dominant electronic transitions $2b_{2u} \rightarrow 4e_{g-}$ and $3e_{g+} \rightarrow 2b_{1u}$, respectively. This difference in transition symmetry is that the real a ($a_{1g}, a_{2g}, a_{1u}, a_{2u}$) and b ($b_{1g}, b_{2g}, b_{1u}, b_{2u}$) orbitals have different symmetry properties, i.e. different eigenvalues $+1$ and -1 of the symmetry operator $\hat{C}_4(z)$ for molecules with D_{4h} symmetry,

$$\hat{C}_4(z)a(x,y,z) = a(-y,x,z) = a(x,y,z), \tag{2.53}$$

$$\hat{C}_4(z)b(x,y,z) = b(-y,x,z) = -b(x,y,z), \tag{2.54}$$

respectively. Thus, in contrast to a orbitals, the direct product of both symmetries b and $e_{\mp} = 1/\sqrt{2}(e_x \mp ie_y)$ yields the opposite symmetry $e_{\pm} = 1/\sqrt{2}(e_x \pm ie_y)$. The z-component of the angular momentum for non-linear molecules is not conserved, thus there are no magnetic quantum numbers M_L. Each state $|E_{\pm}\rangle$ has a different expectation value of $\hat{L}_z$ (Eq. (2.35)). Hence, the formulas for electronic current densities (Eqs. (2.51) and (2.52)) do not contain the factor M_L. The sign $\pm$ determines, however, the direction of the electronic ring current. The $|E_{\pm}\rangle$ states represent the stationary symmetric electronic ring currents about the axis of symmetry. These ring currents are no longer toroidal. Note that only the non-degenerate states $|A\rangle$, $|B\rangle$, $|A'\rangle$, $|A''\rangle$ do not have any electronic ring currents.

In addition, there are orbitally threefold degenerate states $|T\rangle$ specifically for non-linear molecules with higher molecular symmetries T_h, T_d, O_h and I_h. The real representation of these $|T\rangle$ states are $|T_x\rangle$, $|T_y\rangle$ and $|T_z\rangle$ (similar to the $|P\rangle$ states of atoms and atomic ions), which can be converted into the corresponding complex forms $|T_0\rangle = |T_z\rangle$ and $|T_{\pm}\rangle = 1/\sqrt{2}(|T_x\rangle \pm i|T_y\rangle)$ (cf. Eq. (2.42)). The molecules with highest molecular symmetry I_h, for example the C_{60} molecule, also have orbitally fourfold and fivefold degenerate states $|G\rangle$ and $|H\rangle$, respectively, but these states $|T\rangle$, $|G\rangle$, $|H\rangle$ are not further studied in this work.

The electric ring current $I_{\pm}$ in the degenerate state $|\Psi_{\pm}\rangle$ (Eq. (2.29)) can be calculated using the simple formula

$$I_{\pm} = -e \int\int \mathbf{j}_{\pm}(\mathbf{r}) \cdot d\mathbf{S}, \tag{2.55}$$

where the integral is over the half plane perpendicular to the x/y plane at fixed arbitrary azimuthal angle ϕ with domains $\rho \in [0,\infty)$, $z \in (-\infty,\infty)$ in cylindrical coordinates ($d\mathbf{S} = d\rho\, dz\, \mathbf{e}_\phi$) or $r \in [0,\infty)$, $\theta \in [0,\pi]$ in spherical coordinates ($d\mathbf{S} = r\, dr\, d\theta\, \mathbf{e}_\phi$), and the z-axis is the axis of symmetry, see Fig. 2.2. If the electronic current density is zero ($\mathbf{j}(\mathbf{r}) = 0$), e.g. for all non-degenerate states, then the electric ring current is also

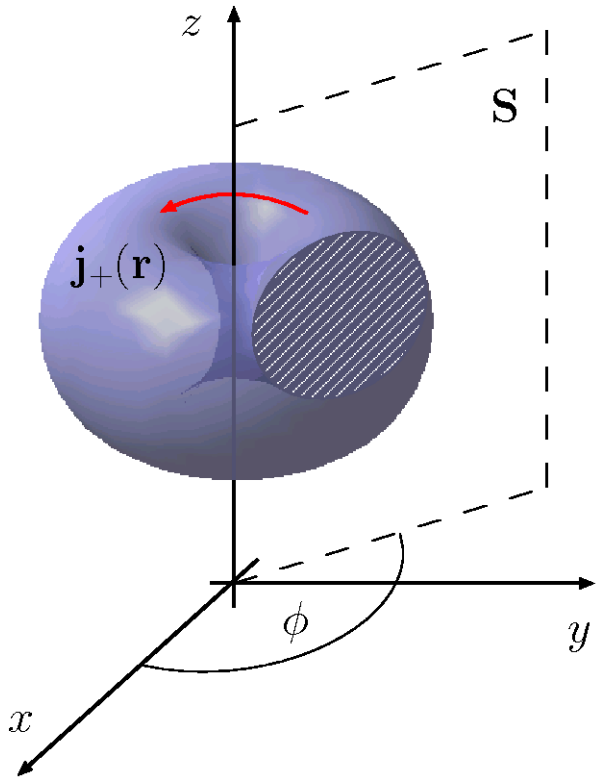

Figure 2.2: Magnitude (blue torus) and direction (red arrow) of the electronic current density $\mathbf{j}_+(\mathbf{r})$ about the axis of symmetry (z-axis). The surface $\mathbf{S}$ indicates the area through which the electric ring current I_+ (Eq. (2.55)) is evaluated.

zero ($I = 0$). For atoms, atomic ions, and linear molecules, $\mathbf{j}_\pm(\mathbf{r}) \cdot d\mathbf{S}$ is independent of the azimuthal angle ϕ (cf. Eqs. (2.38), (2.39), (2.44), (2.45), (2.48)), thus the electric ring current is also independent of ϕ. For non-linear molecules without axial symmetry, $\mathbf{j}_\pm(\mathbf{r}) \cdot d\mathbf{S}$ generally depends on ϕ but the integral in Eq. (2.55) for an arbitrary stationary current density $\mathbf{j}(\mathbf{r})$ does not depend on ϕ. This ϕ-independence of the electric ring current can be proved using the general continuity equation

$$\frac{\partial}{\partial t}\rho(\mathbf{r},t) + \nabla\mathbf{j}(\mathbf{r},t) \quad = \quad 0 \tag{2.56}$$

where $\rho(\mathbf{r},t)$ and $\mathbf{j}(\mathbf{r},t)$ are the time-dependent electronic probability density and time-dependent electronic current density, respectively. For stationary states, the probability density $\rho(\mathbf{r},t) = \rho(\mathbf{r})$ (cf. Eq. (2.15)) and the current density $\mathbf{j}(\mathbf{r},t) = \mathbf{j}(\mathbf{r})$ (cf. Eq. (2.21)) are independent of the time t, thus the time-dependent continuity equation (Eq. (2.56)) reduces to the time-independent continuity equation

$$\nabla\mathbf{j}(\mathbf{r}) \quad = \quad 0. \tag{2.57}$$

Next, we integrate Eq. (2.57) over the volume V ($dV = \rho\, d\rho\, d\phi\, dz$) with domains $\rho \in [0, \infty)$, $\phi \in [\phi_1, \phi_2]$ ($\phi_1 < \phi_2$), $z \in (-\infty, \infty)$ and use Gauss' theorem ($d\mathbf{S} = d\rho\, dz\, \mathbf{e}_\phi$)

$$\begin{aligned} 0 &= \int\int\int \nabla \mathbf{j}(\rho, \phi, z)\, dV \\ &= \int\int \mathbf{j}(\rho, \phi_2, z) \cdot d\mathbf{S} - \int\int \mathbf{j}(\rho, \phi_1, z) \cdot d\mathbf{S} \end{aligned} \tag{2.58}$$

with the fact that the surface integrals for $z \to \pm\infty$ and $\rho \to \infty$ are zero due to the wavefunction and current density vanishing in these infinite domains. Eq. (2.58) yields

$$\begin{aligned} I(\phi_1) &= -e \int\int \mathbf{j}(\rho, \phi_1, z) \cdot d\mathbf{S} \\ &= -e \int\int \mathbf{j}(\rho, \phi_2, z) \cdot d\mathbf{S} \\ &= I(\phi_2). \end{aligned} \tag{2.59}$$

Eq. (2.59) shows that the electric ring current $I_\pm$ (Eq. (2.55)) of the stationary current density $\mathbf{j}_\pm(\mathbf{r})$ is independent of the azimuthal angle ϕ. Finally, in the CIS approximation, the mean period T of an electron occupying a degenerate orbital about the axis of symmetry is calculated according to

$$T = \frac{e}{|I_\pm|}. \tag{2.60}$$

2.2.6 Induced magnetic fields

From electrodynamics we know that the electric ring current $I_\pm$ (Eq. (2.55)) or electronic current density $\mathbf{j}_\pm(\mathbf{r})$ (Eq. (2.30)) of the degenerate state $|\Psi_\pm\rangle$ (Eq. (2.29)) induces a magnetic field $\mathbf{B}_\pm(\mathbf{r})$. The well-known Biot-Savart law

$$\mathbf{B}_\pm(\mathbf{r}) = -\frac{\mu_0 e}{4\pi} \int\int\int \frac{\mathbf{j}_\pm(\mathbf{r}') \times (\mathbf{r} - \mathbf{r}')}{|\mathbf{r} - \mathbf{r}'|^3}\, dV' \tag{2.61}$$

is strictly valid only for time-independent electronic current density also within relativistic theory [237–239]. Using the cylindrical coordinates (ρ, ϕ, z), we have

$$\begin{aligned} \mathbf{r} &= \rho \cos\phi\, \mathbf{e}_x + \rho \sin\phi\, \mathbf{e}_y + z\, \mathbf{e}_z \\ &= \rho\, \mathbf{e}_\rho + z\, \mathbf{e}_z \end{aligned} \tag{2.62}$$

and ($\Delta\phi = \phi - \phi'$)

$$\begin{aligned} \mathbf{r}' &= \rho' \cos\phi'\, \mathbf{e}_x + \rho' \sin\phi'\, \mathbf{e}_y + z'\, \mathbf{e}_z \\ &= \rho' \mathbf{e}_{\rho'} + z'\, \mathbf{e}_z \\ &= \rho' \cos\Delta\phi\, \mathbf{e}_\rho - \rho' \sin\Delta\phi\, \mathbf{e}_\phi + z'\, \mathbf{e}_z, \end{aligned} \tag{2.63}$$

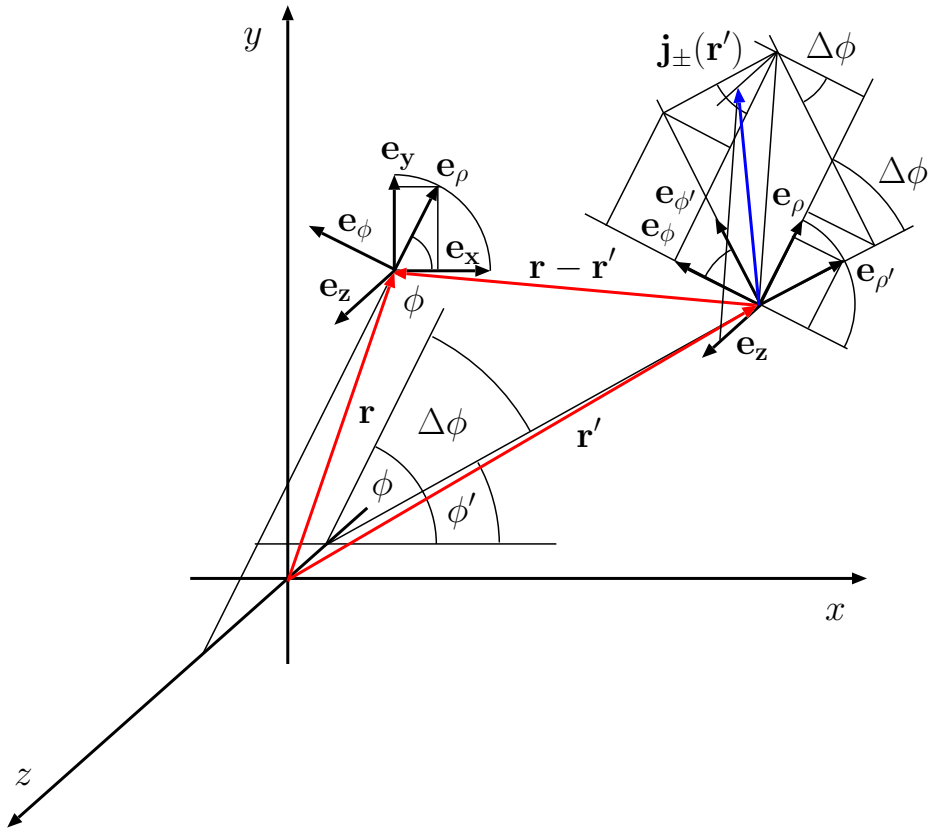

Figure 2.3: Position vectors $\mathbf{r}$, $\mathbf{r}'$ and $\mathbf{r}-\mathbf{r}'$ (red arrows) (Eqs. (2.62), (2.63), (2.68)) and electronic current density $\mathbf{j}_\pm(\mathbf{r}')$ (blue arrow) (Eqs. (2.71)–(2.74)) in a cylindrical coordinate system $(\mathbf{e}_\rho, \mathbf{e}_\phi, \mathbf{e}_z)$.

where the transformations for basis vectors between Cartesian $(\mathbf{e}_x, \mathbf{e}_y, \mathbf{e}_z)$ and cylindrical $(\mathbf{e}_\rho, \mathbf{e}_\phi, \mathbf{e}_z)$ coordinate systems

$$\mathbf{e}_\rho = \cos\phi\,\mathbf{e}_x + \sin\phi\,\mathbf{e}_y \tag{2.64}$$

$$\mathbf{e}_\phi = -\sin\phi\,\mathbf{e}_x + \cos\phi\,\mathbf{e}_y \tag{2.65}$$

and between two distorted cylindrical $(\mathbf{e}_\rho, \mathbf{e}_\phi, \mathbf{e}_z)$ and $(\mathbf{e}_{\rho'}, \mathbf{e}_{\phi'}, \mathbf{e}_z)$ coordinate systems

$$\mathbf{e}_{\rho'} = \cos\Delta\phi\,\mathbf{e}_\rho - \sin\Delta\phi\,\mathbf{e}_\phi \tag{2.66}$$

$$\mathbf{e}_{\phi'} = \sin\Delta\phi\,\mathbf{e}_\rho + \cos\Delta\phi\,\mathbf{e}_\phi \tag{2.67}$$

are illustrated in Fig. 2.3. Eqs. (2.62) and (2.63) yield ($\Delta z = z - z'$)

$$\mathbf{r}-\mathbf{r}' = (\rho - \rho'\cos\Delta\phi)\mathbf{e}_\rho + \rho'\sin\Delta\phi\,\mathbf{e}_\phi + \Delta z\,\mathbf{e}_z \tag{2.68}$$

and

$$|\mathbf{r}-\mathbf{r}'|^3 = \left(\rho^2 + \rho'^2 - 2\rho\rho'\cos\Delta\phi + (\Delta z)^2\right)^{3/2}. \tag{2.69}$$

The decomposition of $\mathbf{j}_\pm(\mathbf{r}')$ in cylindrical components is

$$\mathbf{j}_\pm(\mathbf{r}') = j_{\rho'\pm}(\mathbf{r}')\mathbf{e}_{\rho'} + j_{\phi'\pm}(\mathbf{r}')\mathbf{e}_{\phi'} + j_{z'\pm}(\mathbf{r}')\mathbf{e}_z, \tag{2.70}$$

where the ρ'- and z'-components $j_{\rho'\pm}(\mathbf{r}')$ and $j_{z'\pm}(\mathbf{r}')$ vanish only for atoms, atomic ions, and linear molecules (cf. Eqs. (2.38), (2.39), (2.44), (2.45), (2.48)). Using the transformations for basis vectors $\mathbf{e}_{\rho'}$, $\mathbf{e}_{\phi'}$ and $\mathbf{e}_{z'}$ (Eqs. (2.66) and (2.67)), the current density $\mathbf{j}_\pm(\mathbf{r}')$ (Eq. (2.70)) becomes

$$\begin{aligned}\mathbf{j}_\pm(\mathbf{r}') &= (j_{\rho'\pm}(\mathbf{r}')\cos\Delta\phi + j_{\phi'\pm}(\mathbf{r}')\sin\Delta\phi)\,\mathbf{e}_\rho \\ &\quad + (j_{\phi'\pm}(\mathbf{r}')\cos\Delta\phi - j_{\rho'\pm}(\mathbf{r}')\sin\Delta\phi)\,\mathbf{e}_\phi + j_{z'\pm}(\mathbf{r}')\mathbf{e}_z \\ &= j_{\rho\pm}(\mathbf{r}')\mathbf{e}_\rho + j_{\phi\pm}(\mathbf{r}')\mathbf{e}_\phi + j_{z\pm}(\mathbf{r}')\mathbf{e}_z,\end{aligned} \tag{2.71}$$

where the components of $\mathbf{j}_\pm(\mathbf{r}')$ with respect to the distorted cylindrical coordinate system $(\mathbf{e}_\rho, \mathbf{e}_\phi, \mathbf{e}_z)$ are

$$j_{\rho\pm}(\mathbf{r}') = j_{\rho'\pm}(\mathbf{r}')\cos\Delta\phi + j_{\phi'\pm}(\mathbf{r}')\sin\Delta\phi \tag{2.72}$$

$$j_{\phi\pm}(\mathbf{r}') = j_{\phi'\pm}(\mathbf{r}')\cos\Delta\phi - j_{\rho'\pm}(\mathbf{r}')\sin\Delta\phi \tag{2.73}$$

$$j_{z\pm}(\mathbf{r}') = j_{z'\pm}(\mathbf{r}'), \tag{2.74}$$

see Fig. 2.3. The vector product of $\mathbf{j}_\pm(\mathbf{r}')$ (Eq. (2.71)) and $\mathbf{r} - \mathbf{r}'$ (Eq. (2.68)) with use of the usual rules for basis vectors $\mathbf{e}_z \times \mathbf{e}_\rho = \mathbf{e}_\phi$, $\mathbf{e}_\rho \times \mathbf{e}_\phi = \mathbf{e}_z$ and $\mathbf{e}_\phi \times \mathbf{e}_z = \mathbf{e}_\rho$ leads to

$$\begin{aligned}\mathbf{j}_\pm(\mathbf{r}') \times (\mathbf{r} - \mathbf{r}') &= (j_{\phi\pm}(\mathbf{r}')\Delta z - j_{z\pm}(\mathbf{r}')\rho'\sin\Delta\phi)\mathbf{e}_\rho \\ &\quad + (j_{z\pm}(\mathbf{r}')(\rho - \rho'\cos\Delta\phi) - j_{\rho\pm}(\mathbf{r}')\Delta z)\mathbf{e}_\phi \\ &\quad + (j_{\rho\pm}(\mathbf{r}')\rho'\sin\Delta\phi - j_{\phi\pm}(\mathbf{r}')(\rho - \rho'\cos\Delta\phi))\mathbf{e}_z \\ &= (j_{\phi'\pm}(\mathbf{r}')\Delta z\cos\Delta\phi - j_{\rho'\pm}(\mathbf{r}')\Delta z\sin\Delta\phi - j_{z'\pm}(\mathbf{r}')\rho'\sin\Delta\phi)\mathbf{e}_\rho \\ &\quad + (j_{z'\pm}(\mathbf{r}')(\rho - \rho'\cos\Delta\phi) - j_{\rho'\pm}(\mathbf{r}')\Delta z\cos\Delta\phi \\ &\qquad\qquad - j_{\phi'\pm}(\mathbf{r}')\Delta z\sin\Delta\phi)\mathbf{e}_\phi \\ &\quad + (j_{\phi'\pm}(\mathbf{r}')\rho' - j_{\phi'\pm}(\mathbf{r}')\rho\cos\Delta\phi + j_{\rho'\pm}(\mathbf{r}')\rho\sin\Delta\phi)\mathbf{e}_z.\end{aligned} \tag{2.75}$$

In general, e.g. for non-linear molecules, the induced magnetic field $\mathbf{B}_\pm(\mathbf{r})$ at the position $\mathbf{r}$ (Eq. (2.61)) can be evaluated numerically, together with Eqs. (2.69), (2.75) and the volume element $dV' = \rho'\,d\rho'\,d\phi'\,dz'$.

However, for atoms, atomic ions, and linear molecules, the expressions in Eq. (2.75) can be simplified considerably since the ρ'- and z'-components of $\mathbf{j}_\pm(\mathbf{r}')$ vanish, i.e. $j_{\rho'\pm}(\mathbf{r}') = 0$ and $j_{z'\pm}(\mathbf{r}') = 0$, and the ϕ'-component of $\mathbf{j}_\pm(\mathbf{r}')$ is independent of ϕ', i.e. $j_{\phi'\pm}(\mathbf{r}') = j_{\phi'\pm}(\rho', z')$. In this case, we obtain from Eq. (2.75)

$$\mathbf{j}_\pm(\mathbf{r}') \times (\mathbf{r} - \mathbf{r}') = j_{\phi'\pm}(\rho', z')(\Delta z(\cos\Delta\phi\,\mathbf{e}_\rho - \sin\Delta\phi\,\mathbf{e}_\phi) + (\rho' - \rho\cos\Delta\phi)\mathbf{e}_z). \tag{2.76}$$

Then, we apply Eqs. (2.69), (2.76) and the Biot-Savart law (2.61), and notice that the integral

$$\int_0^{2\pi} \frac{\sin\Delta\phi}{(\rho^2+\rho'^2-2\rho\rho'\cos\Delta\phi+(\Delta z)^2)^{3/2}}\,d\phi' \tag{2.77}$$
$$= -\int_{\phi}^{\phi-2\pi} \frac{\sin\Delta\phi}{(\rho^2+\rho'^2-2\rho\rho'\cos\Delta\phi+(\Delta z)^2)^{3/2}}\,d\Delta\phi$$
$$= \int_{\phi-2\pi}^{\phi} \frac{\sin\Delta\phi}{(\rho^2+\rho'^2-2\rho\rho'\cos\Delta\phi+(\Delta z)^2)^{3/2}}\,d\Delta\phi$$
$$= \int_{-\pi}^{\pi} \frac{\sin\Delta\phi}{(\rho^2+\rho'^2-2\rho\rho'\cos\Delta\phi+(\Delta z)^2)^{3/2}}\,d\Delta\phi = 0$$

after replacing the cyclic domain $[\phi-2\pi,\phi]$ by $[-\pi,\pi]$ is zero because the integrand is an odd function with respect to $\Delta\phi$. Thus, the induced magnetic field $\mathbf{B}_\pm(\mathbf{r})$ for atoms, atomic ions, and linear molecules is given by (Eq. (2.61))

$$\mathbf{B}_\pm(\mathbf{r}) = -\frac{\mu_0 e}{4\pi}\int_0^\infty \rho'\,d\rho' \int_{-\infty}^{\infty} j_{\phi'\pm}(\rho',z')\,dz' \tag{2.78}$$
$$\int_0^{2\pi} \frac{(z-z')\cos\Delta\phi\,\mathbf{e}_\rho + (\rho'-\rho\cos\Delta\phi)\mathbf{e}_z}{(\rho^2+\rho'^2-2\rho\rho'\cos\Delta\phi+(z-z')^2)^{3/2}}\,d\Delta\phi$$

where the cyclic domain $[0,2\pi]$ replaces $[\phi-2\pi,\phi]$ (cf. Eq. (2.77)). The induced magnetic field $\mathbf{B}_\pm(\mathbf{r})$ is independent of the azimuthal angle ϕ (cylindrical symmetry) and has no ϕ-component.

Now we focus on the calculation of the induced magnetic field $\mathbf{B}_\pm(z)$ along the axis of symmetry, i.e. $\mathbf{r}=z\mathbf{e}_z$ (Eq. (2.62)), first for the general case, i.e. for non-linear molecules. Using $\rho=0$ and setting $\phi=0$ arbitrarily for the z-axis, we have (Eq. (2.69))

$$|\mathbf{r}-\mathbf{r}'|^3 = \left(\rho'^2+(\Delta z)^2\right)^{3/2} \tag{2.79}$$

and (Eq. (2.75))

$$\mathbf{j}_\pm(\mathbf{r}')\times(\mathbf{r}-\mathbf{r}') = (j_{\phi'\pm}(\mathbf{r}')\Delta z\cos\phi' + j_{\rho'\pm}(\mathbf{r}')\Delta z\sin\phi' + j_{z'\pm}(\mathbf{r}')\rho'\sin\phi')\mathbf{e}_\rho$$
$$-(j_{z'\pm}(\mathbf{r}')\rho'\cos\phi' + j_{\rho'\pm}(\mathbf{r}')\Delta z\cos\phi' - j_{\phi'\pm}(\mathbf{r}')\Delta z\sin\phi')\mathbf{e}_\phi$$
$$+j_{\phi'\pm}(\mathbf{r}')\rho'\,\mathbf{e}_z. \tag{2.80}$$

Since $|\mathbf{r}-\mathbf{r}'|^3$ (Eq. (2.79)) no longer depends on ϕ', the integration over ϕ' in Eq. (2.61) can be carried out.

Next, we show that the integrals of the ρ- and ϕ-components of $\mathbf{j}_\pm(\mathbf{r}')\times(\mathbf{r}-\mathbf{r}')$ (Eq. (2.80)) over ϕ' with domain $\phi'=[0,2\pi]$ are zero. In general, e.g. for non-linear molecules, the components $j_{\rho'\pm}(\mathbf{r}')$, $j_{\phi'\pm}(\mathbf{r}')$ and $j_{z'\pm}(\mathbf{r}')$ depend on all cylindrical coordinates ρ', ϕ'

and z'. For molecules with symmetry number $n \geq 2$, the electronic current density is periodic with respect to the azimuthal angle ϕ', i.e.

$$\mathbf{j}_{\pm}(\rho', \phi', z') \;=\; \mathbf{j}_{\pm}\left(\rho', \phi' + 2\pi\frac{m}{n}, z'\right) \qquad (m = 0, \pm1, \pm2, \ldots), \tag{2.81}$$

thus their ρ'-, ϕ'- and z'-components are also periodic. The periodic current density $\mathbf{j}_{\pm}(\rho', \phi', z')$ (Eq. (2.81)) can be expanded in terms of the sinus and cosinus functions, i.e.

$$\begin{aligned}
\mathbf{j}_{\pm}(\mathbf{r}') &= \mathbf{a}_{0\pm}(\rho', z') + \sum_{k=1}^{\infty} \left(\mathbf{a}_{k\pm}(\rho', z')\cos(k\phi') + \mathbf{b}_{k\pm}(\rho', z')\sin(k\phi')\right) \qquad (2.82)\\
&= \mathbf{a}_{0\pm}(\rho', z') + \sum_{k=1}^{\infty} \left(\mathbf{a}_{k\pm}(\rho', z')\cos\left(k\phi' + 2\pi\frac{km}{n}\right)\right.\\
&\qquad \left. + \mathbf{b}_{k\pm}(\rho', z')\sin\left(k\phi' + 2\pi\frac{km}{n}\right)\right)\\
&= \mathbf{a}_{0\pm}(\rho', z') + \sum_{k=n,2n,\ldots}^{\infty} \left(\mathbf{a}_{k\pm}(\rho', z')\cos(k\phi') + \mathbf{b}_{k\pm}(\rho', z')\sin(k\phi')\right),
\end{aligned}$$

i.e. the coefficients $\mathbf{a}_{k\pm}(\rho', z')$ and $\mathbf{b}_{k\pm}(\rho', z')$ must be zero for $k \neq n, 2n, 3n, \ldots$ $(n \geq 2)$. Hence, the current density $\mathbf{j}_{\pm}(\mathbf{r}')$ contains the ϕ'-independent term $\mathbf{a}_0(\rho', z')$ and terms of the trigonometric functions $\cos(k\phi')$ and $\sin(k\phi')$ $(k = n, 2n, 3n, \ldots)$. The integrals for $n \geq 2$

$$\begin{aligned}
&\int_0^{2\pi} \mathbf{j}_{\pm}(\mathbf{r}')\cos(\phi')\,d\phi' \;=\; \mathbf{a}_{0\pm}(\rho', z')\int_0^{2\pi}\cos\phi' d\phi' \qquad (2.83)\\
&+ \sum_{k=n,2n,\ldots}^{\infty}\left(\mathbf{a}_{k\pm}(\rho', z')\int_0^{2\pi}\cos(k\phi')\cos\phi'\,d\phi' + \mathbf{b}_{k\pm}(\rho', z')\int_0^{2\pi}\sin(k\phi')\cos\phi'\,d\phi'\right) = \mathbf{0}
\end{aligned}$$

and

$$\begin{aligned}
&\int_0^{2\pi} \mathbf{j}_{\pm}(\mathbf{r}')\sin(\phi')\,d\phi' \;=\; \mathbf{a}_{0\pm}(\rho', z')\int_0^{2\pi}\sin\phi' d\phi' \qquad (2.84)\\
&+ \sum_{k=n,2n,\ldots}^{\infty}\left(\mathbf{a}_{k\pm}(\rho', z')\int_0^{2\pi}\cos(k\phi')\sin\phi'\,d\phi' + \mathbf{b}_{k\pm}(\rho', z')\int_0^{2\pi}\sin(k\phi')\sin\phi'\,d\phi'\right) = \mathbf{0}
\end{aligned}$$

vanish because all trigonometric integrals in Eqs. (2.83) and (2.84) are zero due to the orthogonality of the trigonometric functions. Thus, the integrals of the ρ- and ϕ-components of $\mathbf{j}_{\pm}(\mathbf{r}') \times (\mathbf{r} - \mathbf{r}')$ (Eq. (2.80)) over ϕ' are zero.

The induced magnetic field $\mathbf{B}_{\pm}(z)$ along the z-axis for non-linear molecules using Eqs. (2.61), (2.79), (2.80), (2.82)–(2.84) is given by

$$\mathbf{B}_{\pm}(z) \;=\; -\frac{\mu_0 e}{2}\int_0^{\infty}\rho'^2\,d\rho'\int_{-\infty}^{\infty}\frac{\overline{j_{\phi'\pm}(\rho', z')}}{\left(\rho'^2 + (z - z')^2\right)^{3/2}}\,dz'\,\mathbf{e}_z \tag{2.85}$$

where

$$\overline{j_{\phi'\pm}(\rho', z')} \;=\; \frac{1}{2\pi}\int_0^{2\pi} j_{\phi'\pm}(\rho', \phi', z')\,d\phi' \tag{2.86}$$

is the ϕ' component of the electronic current density $j_{\phi'\pm}(\mathbf{r}')$ averaged over the azimuthal angle ϕ'. There are no ρ- and ϕ-components of the induced magnetic field $\mathbf{B}_\pm(z)$, i.e. it is directed towards the z-axis. Only the averaged current density $\overline{j_{\phi'\pm}(\rho', z')}$ determines the value of $\mathbf{B}_\pm(z)$. For atoms, atomic ions, and linear molecules with infinite symmetry number $n \to \infty$, the ϕ'-component of the electronic current density $j_{\phi'\pm}(\mathbf{r}')$ does not depend on the azimuthal angle ϕ' (cf. Eqs. (2.38), (2.39), (2.44), (2.45), (2.48)), i.e. for $n \to \infty$ all coefficients $\mathbf{a}_{k\pm}(\rho', z')$ and $\mathbf{b}_{k\pm}(\rho', z')$ ($k = 1, 2, 3, \ldots$) must be zero (Eq. (2.82)). Thus, it yields $\overline{j_{\phi'\pm}(\rho', z')} = j_{\phi'\pm}(\rho', z')$ (Eq. (2.86)) and

$$\mathbf{B}_\pm(z) = -\frac{\mu_0 e}{2} \int_0^\infty \rho'^2 \, d\rho' \int_{-\infty}^\infty \frac{j_{\phi'\pm}(\rho', z')}{\left(\rho'^2 + (z - z')^2\right)^{3/2}} \, dz' \, \mathbf{e}_z \tag{2.87}$$

which can also be obtained from Eq. (2.78), using $\rho = 0$.

For example, the excited state $|\Pi_\pm\rangle$ of the linear molecule with dominant electronic transitions from occupied $n\sigma$ orbitals to an unoccupied orbital $\pi_\pm$ has the electric ring current (Eqs. (2.48), (2.55))

$$I_\pm = \mp\frac{e\hbar}{m_e} \int_0^\infty \frac{d\rho}{\rho} \int_{-\infty}^\infty |\pi_\pm(\rho, \phi, z)|^2 \, dz \tag{2.88}$$

and the induced magnetic field (Eqs. (2.48), (2.78))

$$\begin{aligned} \mathbf{B}_\pm(\mathbf{r}) = \mp\frac{\mu_0 e\hbar}{4\pi m_e} \int_0^\infty d\rho' \int_{-\infty}^\infty |\pi_\pm(\rho', \phi', z')|^2 \, dz' \\ \int_0^{2\pi} \frac{(z - z')\cos\Delta\phi \, \mathbf{e}_\rho + (\rho' - \rho\cos\Delta\phi)\mathbf{e}_z}{\left(\rho^2 + \rho'^2 - 2\rho\rho'\cos\Delta\phi + (z - z')^2\right)^{3/2}} \, d\Delta\phi \end{aligned} \tag{2.89}$$

and for $\rho = 0$ (Eqs. (2.48), (2.87))

$$\mathbf{B}_\pm(z) = \mp\frac{\mu_0 e\hbar}{2m_e} \int_0^\infty \rho' \, d\rho' \int_{-\infty}^\infty \frac{|\pi_\pm(\rho', \phi', z')|^2}{\left(\rho'^2 + (z - z')^2\right)^{3/2}} \, dz' \, \mathbf{e}_z \tag{2.90}$$

where the orbital density $|\pi_\pm(\rho, \phi, z)|^2$ is independent of the azimuthal angle ϕ.

For the calculation of the approximate induced magnetic field, the ϕ-component of the electronic current density in the current loop model is given by

$$j_{\phi\pm}(\rho, \phi, z) = \pm j_0 \, \delta(\rho - R)\delta(z - Z) \tag{2.91}$$

where $I = -ej_0 < 0$, R and $(0, 0, Z)$ are the electric ring current, the ring current radius and the position of the center of the current loop, respectively. The formula for the induced magnetic field $\mathbf{B}_\pm(z)$ along the z-axis (Eq. (2.85)) is thus simplified to

$$\mathbf{B}_\pm(z) = \pm\frac{\mu_0 I}{2} \frac{R^2}{\left(R^2 + (z - Z)^2\right)^{3/2}} \, \mathbf{e}_z, \tag{2.92}$$

and for $z = Z$, i.e. the induced magnetic field at the center of the current loop is [240]

$$\mathbf{B}_{\pm}(Z) \;=\; \pm\frac{\mu_0 I}{2R}\,\mathbf{e}_z. \tag{2.93}$$

In the case in which an electron with angular momentum $L_z = m_e R^2\omega$ circulates in the current loop, the electric ring current is calculated clasically as

$$I \;=\; -\frac{e}{T} \;=\; -\frac{e\omega}{2\pi} \;=\; -\frac{eL_z}{2\pi m_e R^2} \tag{2.94}$$

where T and $\omega = 2\pi/T$ are the period and the angular velocity, respectively.

2.2.7 Mean ring current radius

For non-zero electronic ring currents, there are different versions for the calculation of the mean ring current radius

$$R_1 \;=\; \langle\rho\rangle_j \;=\; \frac{-e\int\int\rho\,\mathbf{j}_{\pm}(\mathbf{r})\cdot d\mathbf{S}}{I_{\pm}}, \tag{2.95}$$

$$R_{-1} \;=\; \langle\rho^{-1}\rangle_j^{-1} \;=\; \frac{I_{\pm}}{-e\int\int\rho^{-1}\mathbf{j}_{\pm}(\mathbf{r})\cdot d\mathbf{S}}, \tag{2.96}$$

$$R_{-2} \;=\; \langle\rho^{-2}\rangle_j^{-1/2} \;=\; \sqrt{\frac{I_{\pm}}{-e\int\int\rho^{-2}\mathbf{j}_{\pm}(\mathbf{r})\cdot d\mathbf{S}}} \tag{2.97}$$

where the index j means that the distribution in the integral is the electronic current density $\mathbf{j}_{\pm}(\mathbf{r})$ instead of the electronic probability density $\rho_{\pm}(\mathbf{r})$. Since the mean radius $\tilde{R} = \langle\rho\rangle = \langle\Psi_i|\rho|\Psi_i\rangle = \int\int\int\rho\rho_i(\mathbf{r})dV$ can also be calculated for non-degenerate states without carrying electronic ring currents, the mean radius $\tilde{R}$ and the mean ring current radii R_1, R_{-1} and R_{-2} are, in general, different. For atoms, atomic ions, and linear molecules the mean ring current radii R_1, R_{-1} and R_{-2} of the degenerate orbital ($l \neq 0$) are smaller than the mean radius $\tilde{R}$ of the same orbital because the electronic current density contains the additional factor $1/\rho$ (cf. Eqs. (2.38), (2.39), (2.44), (2.45), (2.48)). Nevertheless, for large ring-shaped molecules the mean radius of the π-conjugated orbitals is similar to the mean ring current radius of the corresponding electronic ring currents, i.e. in this case $\langle\rho\rangle \approx R_1 \approx R_{-1} \approx R_{-2}$. For the calculation of the approximate induced magnetic fields and electric ring currents in the current loop model, the mean ring current radius R_{-1} and R_{-2} should be used instead of R_1 because the induced magnetic field at the center of the current loop and the electric ring current are inversely proportional to R (Eq. (2.93)) and R^2 (Eq. (2.94)), respectively.

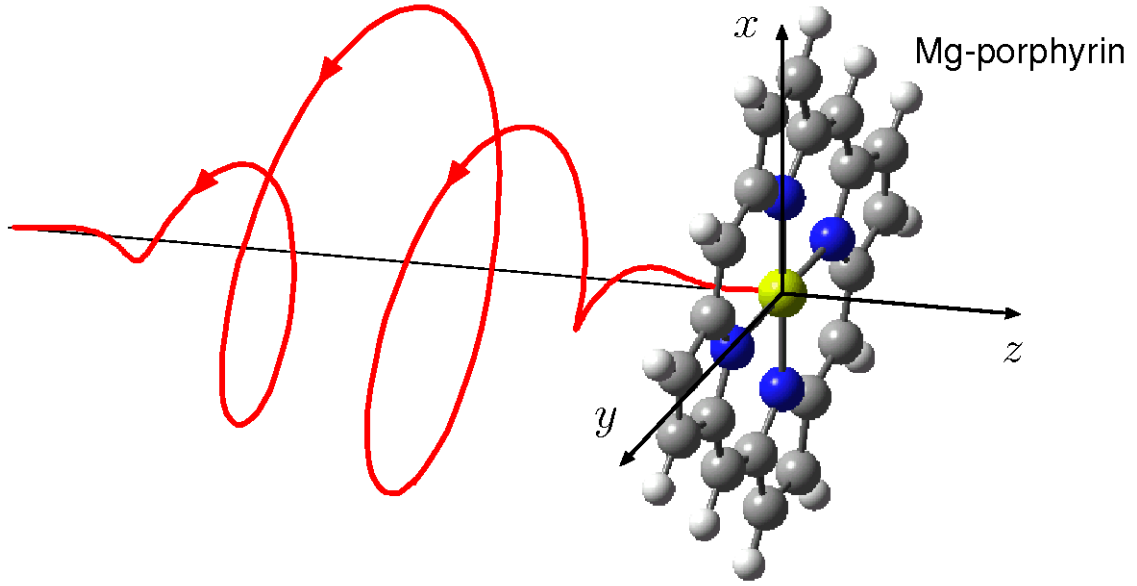

Figure 2.4: A right (+) circularly polarized laser pulse impinging on the aligned ring-shaped molecule Mg-porphyrin and propagating along the axis of symmetry (z-axis). The arrows indicate the central sequence of laser cycles as they would be "seen" by the molecule when the pulse passes by.

2.3 Electron dynamics

2.3.1 Circularly polarized laser pulses

A right (+) or left (−) circularly polarized laser pulse propagating along the axis of symmetry is the natural choice for the electronic excitation from the non-degenerate ground singlet state, i.e. $|X\,^1S\rangle$ for atoms and atomic ions, $|X\,^1\Sigma\rangle$ for linear molecules, and $|X\,^1A\rangle$ for ring-shaped molecules, to the degenerate excited singlet state, i.e. $|^1P_+\rangle$ or $|^1P_-\rangle$ for atoms and atomic ions, $|^1\Pi_+\rangle$ or $|^1\Pi_-\rangle$ for linear molecules, and $|^1E_+\rangle$ or $|^1E_-\rangle$ for ring-shaped molecules, respectively. These degenerate states carry anti-clockwise (+) or clockwise (−) electronic ring currents with non-zero z-components of the angular momentum $\langle\hat{L}_z\rangle \neq 0$. The laser-driven dynamics is illustrated in Fig. 2.4 schematically for the aligned ring-shaped molecule Mg-porphyrin.

Note that for molecules, the propagating axis of the circularly (c) polarized laser pulse is chosen such that it is parallel to the axis of symmetry of the molecule, i.e. the non-polar or polar molecule has to be pre-aligned or pre-oriented along the z-axis by means of a linearly (l) polarized laser pulse, respectively, see Section 2.6.

Starting from the time-dependent right (+) or left (−) circularly polarized vector potential centered at the time t_c and propagating along the z-axis

$$\mathbf{A}_{c\pm}(t) = -\frac{\mathcal{E}_c}{\omega_c} s_n(t-t_c) \begin{pmatrix} \sin(\omega_c(t-t_c)+\eta_c) \\ \mp\cos(\omega_c(t-t_c)+\eta_c) \\ 0 \end{pmatrix}, \tag{2.98}$$

we derive the time-dependent right (+) or left (−) circularly polarized electric field

$$\begin{aligned} \mathbf{E}_{c\pm}(t) &= -\frac{d}{dt}\mathbf{A}_{c\pm}(t) \qquad (2.99) \\ &= \mathcal{E}_c s_n(t-t_c) \begin{pmatrix} \cos(\omega_c(t-t_c)+\eta_c) \\ \pm\sin(\omega_c(t-t_c)+\eta_c) \\ 0 \end{pmatrix} + \frac{\mathcal{E}_c}{\omega_c}\dot{s}_n(t-t_c) \begin{pmatrix} \sin(\omega_c(t-t_c)+\eta_c) \\ \mp\cos(\omega_c(t-t_c)+\eta_c) \\ 0 \end{pmatrix} \end{aligned}$$

with amplitude $\mathcal{E}_c$ and laser frequency ω_c. We will show in Section 2.3.2 that the phase η_c is irrelevant for circularly polarized laser pulses, and is set to zero in all of the applications discussed here.

The laser envelope $s_n(t)$ is given by

$$s_n(t-t_c) = \begin{cases} \cos^n\left(\frac{\pi(t-t_c)}{t_{p,c}}\right) & \text{for } |t-t_c| \le \frac{t_{p,c}}{2} \\ 0 & \text{for } |t-t_c| > \frac{t_{p,c}}{2} \end{cases} \tag{2.100}$$

where $n > 0$ and $t_{p,c}$ are the exponent of the trigonometric envelope and the total pulse duration, respectively [241]. Thus, the initial and final times of the laser pulse are set to $t_0 = t_c - t_{p,c}/2$ and $t_f = t_c + t_{p,c}/2$, respectively. The full width at half maximum (FWHM) τ of $s_n^2(t)$, i.e. $s_n^2(\tau/2) = \frac{1}{2}$, is

$$\tau = \frac{f_n t_{p,c}}{\pi} \tag{2.101}$$

where

$$f_n = 2\arccos\left(2^{-\frac{1}{2n}}\right). \tag{2.102}$$

The FWHM τ is denoted as the effective pulse duration of the laser envelope. The corresponding Gaussian envelope centered at the time t_c with the same effective pulse duration τ is

$$s(t-t_c) = e^{-2\ln(2)(t-t_c)^2/\tau^2} \tag{2.103}$$

for $t \in (-\infty, \infty)$. We have shown that for the same effective pulse duration τ the trigonometric envelope $s_n(t-t_c)$ (Eq. (2.100)) converges to the Gaussian envelope $s(t-t_c)$ (Eq. (2.103)) as n tends to infinity, i.e.

$$s(t-t_c) = \lim_{n\to\infty} s_n(t-t_c), \tag{2.104}$$

and we determined that the deviation between the trigonometric envelope for $n = 20$ and the Gaussian envelope is already very small, i.e. $\max(s(t) - s_{20}(t)) = 0.0077$ [241]. Trigonometric envelopes are advantageous because of their finite pulse durations and will be used in the following applications, in particular for $n = 2$ and $n = 20$. The Fourier transform of the trigonometric envelope $s_n(t)$ for $n > 0$ is [241]

$$\hat{s}_n(k) = \frac{1}{\sqrt{2\pi}} \int_{-\infty}^{\infty} s_n(t) e^{-ikt}\, dt = \frac{2^{-n-1/2}\sqrt{\pi}\,\Gamma(n+1)\tau}{f_n \Gamma\left(1 + \frac{n}{2} - \frac{k\tau}{2f_n}\right) \Gamma\left(1 + \frac{n}{2} + \frac{k\tau}{2f_n}\right)} \quad (2.105)$$

where $\Gamma(x)$ is the Gamma function. Again, $\hat{s}_n(k)$ converges to the Fourier transform of the Gaussian envelope $\hat{s}(t)$ [241]

$$\hat{s}(k) = \lim_{n\to\infty} \hat{s}_n(k) = \frac{1}{\sqrt{2\pi}} \int_{-\infty}^{\infty} s(t) e^{-ikt}\, dt = \frac{\tau}{2\sqrt{\ln(2)}}\, e^{-k^2\tau^2/(8\ln(2))}. \quad (2.106)$$

The FWHM κ_n of $\hat{s}_n^2(k)$, i.e. $\hat{s}_n^2(\kappa_n/2)/\hat{s}_n^2(0) = \frac{1}{2}$, and the spectral width $\Gamma_n = \kappa_n\hbar$ must be solved numerically because the corresponding equation is non-linear and includes polynomials and trigonometric functions whereas the corresponding spectral width $\Gamma = \kappa\hbar$ of the Gaussian envelope, where κ is the FWHM of $\hat{s}^2(k)$, can be solved analytically, i.e. the relation between the spectral width Γ and the effective pulse duration τ of the Gaussian envelope is

$$\Gamma\tau = 4\ln 2\,\hbar \approx 2.773\,\hbar, \quad (2.107)$$

and the corresponding relations for trigonometric envelopes, e.g. for $n = 2$ and $n = 20$, are [241]

$$\Gamma_2\tau \approx 3.295\,\hbar \quad (2.108)$$

$$\Gamma_{20}\tau \approx 2.826\,\hbar. \quad (2.109)$$

Furthermore, the spectral width of the trigonometric envelope converges to that of the Gaussian envelope, i.e.

$$\Gamma = \lim_{n\to\infty} \Gamma_n \quad (2.110)$$

because of the convergence of $\hat{s}_n(k)$ (Eq. (2.106)).

The electric field (Eq. (2.99)) satisfies the condition of the far-field approximation of Maxwell's equations automatically [141, 242, 243], i.e.

$$\int_{-\infty}^{\infty} \mathbf{E}_{c\pm}(t)\, dt = \mathbf{0}. \quad (2.111)$$

Using the dimensionsless variables $y = t/\tau$, $y_c = t_c/\tau$ and $m_c = \omega_c\tau$ where y and y_c are times in units of τ and $m_c/(2\pi)$ is approximately equal to the number of laser cycles

during τ, the electric field (Eq. (2.99)) can be rewritten as

$$\begin{aligned}\mathbf{E}_{c\pm}(y) &= \mathcal{E}_c \tilde{s}_n(y-y_c) \begin{pmatrix} \cos(m_c(y-y_c)+\eta_c) \\ \pm\sin(m_c(y-y_c)+\eta_c) \\ 0 \end{pmatrix} \\ &\quad + \frac{\mathcal{E}_c}{m_c}\left(\frac{d}{dy}\,\tilde{s}_n(y-y_c)\right) \begin{pmatrix} \sin(m_c(y-y_c)+\eta_c) \\ \mp\cos(m_c(y-y_c)+\eta_c) \\ 0 \end{pmatrix}\end{aligned} \tag{2.112}$$

where

$$\tilde{s}_n(y-y_c) = \begin{cases} \cos^n\left((y-y_c)f_n\right) & \text{for } |y-y_c| \le \frac{\pi}{2f_n} \\ 0 & \text{for } |y-y_c| > \frac{\pi}{2f_n} \end{cases} . \tag{2.113}$$

Thus, for laser pulses with many laser cycles ($m_c \gg 1$) the second term of the electric field (Eqs. (2.99) and (2.112)) can be neglected and the condition (2.111) is approximately valid whereas for few-cycle laser pulses the second term of the electric field must be included. Moreover, for $n > 2$ the electric field (Eqs. (2.99) and (2.112)) is continuously differentiable [241].

The time-dependent intensity is calculated as [244]

$$I_c(t) = c\varepsilon_0 |\mathbf{E}_{c\pm}(t)|^2 \tag{2.114}$$

which is independent of the polarization sense. For laser pulses with many cycles ($m_c \gg 1$) the time-dependent intensity is approximately given by

$$I_c(t) \approx c\varepsilon_0 \mathcal{E}_c^2 s_n^2(t). \tag{2.115}$$

The corresponding peak values are $I_{max,c} = c\varepsilon_0 \max|\mathbf{E}_{c\pm}(t)|^2$ and $I_{max,c} \approx c\varepsilon_0\mathcal{E}_c^2$ ($m_c \gg 1$). The FWHM of the intensity is denoted as the effective pulse duration of the laser pulse τ_c and for laser pulses with many cycles it is approximately equal to the effective pulse duration of the laser envelope τ (Eq. (2.101)). In the following applications for the induction of electronic ring currents in the electronic excited degenerate states, the effective pulse durations τ_c should be shorter than the vibrational periods in the excited states, thus we can assume that the nuclei are frozen during the Franck-Condon (FC) electronic excitations by means of the right or left circularly polarized laser pulse.

2.3.2 Time-dependent electronic Schrödinger equation

The laser-driven electron dynamics for fixed nuclei is described by the time-dependent non-relativistic electronic Schrödinger equation (TDSE) within the electric dipole ap-

proximation

$$i\hbar\frac{\partial}{\partial t}\,|\Psi(t)\rangle \;=\; \hat{H}_{el}(t)|\Psi(t)\rangle \tag{2.116}$$

where $\hat{H}_{el}(t)$ is the time-dependent electronic Hamiltonian

$$\hat{H}_{el}(t) \;=\; \hat{H}_{el} - \mathbf{M}\cdot\mathbf{E}_{c\pm}(t). \tag{2.117}$$

$\hat{H}_{el}$, $\mathbf{E}_{c\pm}(t)$ and $\mathbf{M}$ are the time-independent electronic Hamiltonian (Eq. (2.2)), the time-dependent right (+) or left (−) circularly polarized electric field (Eq. (2.99)) and the electric dipole operator

$$\mathbf{M} \;=\; -e\sum_{n=1}^{N}\mathbf{r}_n + \sum_{\alpha=1}^{N'} Z_\alpha \mathbf{R}_\alpha, \tag{2.118}$$

respectively. Since the z-component of the electic field $\mathbf{E}_{c\pm}(t)$ (Eq. (2.99)) is zero, the interaction term becomes

$$-\mathbf{M}\cdot\mathbf{E}_{c\pm}(t) \;=\; -M_x E_{c\pm,x}(t) - M_y E_{c\pm,y}(t) \tag{2.119}$$

where M_x, M_y and $E_{c\pm,x}(t)$, $E_{c\pm,y}(t)$ are the x- and y-components of the dipole operator $\mathbf{M}$ and electric field $\mathbf{E}_{c\pm}(t)$, respectively. Thus, the interaction term (Eq. (2.119)) is independent of the z-component of the dipole operator M_z.

The time-dependent electronic state $|\Psi(t)\rangle$ in Eq. (2.116) can be expanded in terms of electronic eigenstates $|\Psi_i\rangle$ of $\hat{H}_{el}$ (Eq. (2.1)) with electronic quantum numbers $i = 0, 1, 2, \ldots$ and corresponding eigenenergies E_i, i.e.

$$|\Psi(t)\rangle \;=\; \sum_{i=0}^{i_{max}} C_i(t)|\Psi_i\rangle e^{-iE_i(t-t_0)/\hbar} \tag{2.120}$$

where $C_i(t)$ and $i_{max}+1$ are the time-dependent coefficients of electronic states $|\Psi_i\rangle$ and the total number of electronic states included in this epxansion, respectively. The initial condition at the initial time t_0 is given by

$$|\Psi(t_0)\rangle \;=\; |\Psi_0\rangle \tag{2.121}$$

where $|\Psi_0\rangle$ is the electronic ground state, for example $|X\,^1S\rangle$ for atoms and atomic ions, $|X\,^1\Sigma\rangle$ for linear molecules, and $|X\,^1A\rangle$ for ring-shaped molecules. The time-dependent electronic state $|\Psi(t)\rangle$ (Eq. (2.120)) does not include any continuum states describing the ionization because we have assumed that the ionization potentials are very high compared to the small excitation energies of target degenerate states carrying electronic ring currents and the maximum intensity of the laser pulse $I_{max,c}$ is well below the Keldysh limit [36].

Inserting the ansatz (Eqs. (2.120) and (2.121)) into the Schrödinger equation (Eqs. (2.116) and (2.117)) yields the equivalent set of differential equations for the time-dependent coefficients

$$i\hbar\frac{d}{dt}C_i(t) = \sum_{j=0}^{i_{max}} H_{ij}(t)C_j(t) \qquad (i=0,1,2,\ldots,i_{max}) \tag{2.122}$$

with initial condition

$$C_i(t_0) = \delta_{0i} \qquad (i=0,1,2,\ldots,i_{max}) \tag{2.123}$$

and time-dependent matrix elements

$$H_{ij}(t) = -\mathbf{M}_{ij}\cdot\mathbf{E}_{c\pm}(t)e^{-i\omega_{ji}(t-t_0)} \qquad (i,j=0,1,2,\ldots,i_{max}), \tag{2.124}$$

where

$$\omega_{ji} = \frac{E_j - E_i}{\hbar} \qquad (i,j=0,1,2,\ldots,i_{max}) \tag{2.125}$$

and

$$\mathbf{M}_{ij} = \langle\Psi_i|\mathbf{M}|\Psi_j\rangle \qquad (i,j=0,1,2,\ldots,i_{max}) \tag{2.126}$$

are the transition frequencies and the transition dipole matrix elements, respectively. Again, since $E_{c\pm,z}=0$ (Eq. (2.99)) the matrix elements (Eq. (2.124)) are rewritten as

$$H_{ij}(t) = -(M_{ij,x}E_{c\pm,x}(t)+M_{ij,y}E_{c\pm,y}(t))e^{-i\omega_{ji}(t-t_0)} \qquad (i,j=0,1,2,\ldots,i_{max}) \tag{2.127}$$

and are independent of the z-component of the transition dipole matrix elements $M_{ij,z}$. Note that for symmetry reasons (atoms, atomic ions, aligned linear and ring-shaped molecules), the diagonal elements of the x- and y-components of the dipole matrix are zero, $M_{ii,x}=M_{ii,y}=0$, thus all diagonal matrix elements $H_{ii}(t)$ are also zero, i.e. $H_{ii}(t)=0$.

The electronic transition from the state $|\Psi_i\rangle$ to the state $|\Psi_j\rangle$ is dipole-allowed if the corresponding x- or y-components of the transition dipole matrix element are non-zero, i.e. $M_{ij,x}\neq 0$ or $M_{ij,y}\neq 0$, respectively. Thus, such electronic transitions $|^1S\rangle \leftrightarrow |^1P_\pm\rangle$, $|^1P_+\rangle \leftrightarrow |^1D_{+2}\rangle$, $|^1P_-\rangle \leftrightarrow |^1D_{-2}\rangle$, $|^1P_\pm\rangle \leftrightarrow |^1D_0\rangle,\ldots$ for atoms and atomic ions, $|^1\Sigma^+\rangle \leftrightarrow |^1\Pi_\pm\rangle$, $|^1\Sigma^-\rangle \leftrightarrow |^1\Pi_\pm\rangle$, $|^1\Pi_+\rangle \leftrightarrow |^1\Delta_+\rangle$, $|^1\Pi_-\rangle \leftrightarrow |^1\Delta_-\rangle,\ldots$ for aligned linear molecules with molecular symmetry $C_{\infty v}$ and $|^1A_{1g}\rangle \leftrightarrow |^1E_{u\pm}\rangle$, $|^1A_{2g}\rangle \leftrightarrow |^1E_{u\pm}\rangle$, $|^1B_{1g}\rangle \leftrightarrow |^1E_{u\pm}\rangle$, $|^1B_{2g}\rangle \leftrightarrow |^1E_{u\pm}\rangle$, $|^1A_{1u}\rangle \leftrightarrow |^1E_{g\pm}\rangle$, $|^1A_{2u}\rangle \leftrightarrow |^1E_{g\pm}\rangle$, $|^1B_{1u}\rangle \leftrightarrow |^1E_{g\pm}\rangle$, $|^1B_{2u}\rangle \leftrightarrow |^1E_{g\pm}\rangle$ for aligned ring-shaped molecules with molecular symmetry D_{4h} are allowed whereas other electronic transitions in electric dipole approximation are forbidden. For example, the dipole matrix element (Eq. (2.126)) of the dipole-allowed electronic transition $|\Psi_{ts}\rangle \leftrightarrow |\Psi_\pm\rangle$ ($|\Psi_{ts}\rangle$ is the total symmetric state), such as $|\,^1S\rangle \leftrightarrow |^1P_\pm\rangle$,

$|\,^1\Sigma^+\rangle \leftrightarrow |^1\Pi_\pm\rangle$, and $|\,^1A_{1g}\rangle \leftrightarrow |^1E_{u\pm}\rangle$, using Eq. (2.29), is evaluated as

$$\begin{aligned}\langle\Psi_{ts}|\mathbf{M}|\Psi_\pm\rangle &= \frac{1}{\sqrt{2}}\left(\langle\Psi_{ts}|\mathbf{M}|\Psi_x\rangle \pm i\langle\Psi_{ts}|\mathbf{M}|\Psi_y\rangle\right) \\ &= \frac{1}{\sqrt{2}}\left(\langle\Psi_{ts}|M_x|\Psi_x\rangle\mathbf{e}_x \pm i\langle\Psi_{ts}|M_y|\Psi_y\rangle\mathbf{e}_y\right) \\ &= \frac{\langle\Psi_{ts}|M_x|\Psi_x\rangle}{\sqrt{2}}\begin{pmatrix}1\\ \pm i\\ 0\end{pmatrix}\end{aligned} \tag{2.128}$$

where for symmetry reasons $\langle\Psi_{ts}|M_x|\Psi_x\rangle = \langle\Psi_{ts}|M_y|\Psi_y\rangle$. Since $\langle\Psi_\pm|\mathbf{M}|\Psi_{ts}\rangle = \langle\Psi_{ts}|\mathbf{M}|\Psi_\pm\rangle^*$, it is the conjugate form of Eq. (2.128), i.e.

$$\langle\Psi_\pm|\mathbf{M}|\Psi_{ts}\rangle = \frac{\langle\Psi_{ts}|M_x|\Psi_x\rangle}{\sqrt{2}}\begin{pmatrix}1\\ \mp i\\ 0\end{pmatrix} \tag{2.129}$$

where $\langle\Psi_{ts}|M_x|\Psi_x\rangle = \langle\Psi_x|M_x|\Psi_{ts}\rangle$ is real.

The differential equations (Eq. (2.122)) with initial condition (Eq. (2.123)) are then solved by means of the Runge-Kutta method of fourth order (Simpson rule) [245] with a small time step size of $\Delta t = 1\,\text{as}$. Note that the total number of electronic states $i_{max}+1$ should be large enough such that the numerical results converge well. Finally, the time-dependent populations of electronic states $|\Psi_i\rangle$ are calculated as

$$P_i(t) = |C_i(t)|^2 \qquad (i = 0, 1, 2, \ldots, i_{max}). \tag{2.130}$$

Next, let us show that the time-dependent populations $P_i(t)$ for atoms, atomic ions, aligned linear and ring-shaped molecules are independent of the phase η_c of the circularly polarized laser pulse (Eq. (2.99)), which is now defined as $\mathbf{E}_{c\pm}(t,\eta_c)$. Using the unitary matrix

$$D(\eta_c) = \begin{pmatrix}\cos\eta_c & -\sin\eta_c & 0\\ \sin\eta_c & \cos\eta_c & 0\\ 0 & 0 & 1\end{pmatrix}, \tag{2.131}$$

the time- and phase-dependent electric field $\mathbf{E}_{c\pm}(t,\eta_c)$ (Eq. (2.99)) is equal to the product of the unitary matrix $D(\pm\eta_c)$ and the vector of the electric field without phase $\mathbf{E}_{c\pm}(t,\eta_c = 0)$, i.e.

$$\mathbf{E}_{c\pm}(t,\eta_c) = D(\pm\eta_c)\mathbf{E}_{c\pm}(t,\eta_c = 0), \tag{2.132}$$

since

$$
\begin{aligned}
D(\pm\eta_c)\mathbf{E}_{c\pm}(t,\eta_c=0) &= \mathcal{E}_c s_n(t-t_c)\begin{pmatrix} \cos\eta_c & \mp\sin\eta_c & 0 \\ \pm\sin\eta_c & \cos\eta_c & 0 \\ 0 & 0 & 1 \end{pmatrix}\begin{pmatrix} \cos(\omega_c(t-t_c)) \\ \pm\sin(\omega_c(t-t_c)) \\ 0 \end{pmatrix} \\
&\quad + \frac{\mathcal{E}_c}{\omega_c}\,\dot{s}_n(t-t_c)\begin{pmatrix} \cos\eta_c & \mp\sin\eta_c & 0 \\ \pm\sin\eta_c & \cos\eta_c & 0 \\ 0 & 0 & 1 \end{pmatrix}\begin{pmatrix} \sin(\omega_c(t-t_c)) \\ \mp\cos(\omega_c(t-t_c)) \\ 0 \end{pmatrix} \qquad (2.133) \\
&= \mathcal{E}_c s_n(t-t_c)\begin{pmatrix} \cos(\omega_c(t-t_c))\cos\eta_c - \sin(\omega_c(t-t_c))\sin\eta_c \\ \pm\cos(\omega_c(t-t_c))\sin\eta_c \pm \sin(\omega_c(t-t_c))\cos\eta_c \\ 0 \end{pmatrix} \\
&\quad + \frac{\mathcal{E}_c}{\omega_c}\,\dot{s}_n(t-t_c)\begin{pmatrix} \sin(\omega_c(t-t_c))\cos\eta_c + \cos(\omega_c(t-t_c))\sin\eta_c \\ \pm\sin(\omega_c(t-t_c))\sin\eta_c \mp \cos(\omega_c(t-t_c))\cos\eta_c \\ 0 \end{pmatrix} \\
&= \mathcal{E}_c s_n(t-t_c)\begin{pmatrix} \cos(\omega_c(t-t_c)+\eta_c) \\ \pm\sin(\omega_c(t-t_c)+\eta_c) \\ 0 \end{pmatrix} \\
&\quad + \frac{\mathcal{E}_c}{\omega_c}\,\dot{s}_n(t-t_c)\begin{pmatrix} \sin(\omega_c(t-t_c)+\eta_c) \\ \mp\cos(\omega_c(t-t_c)+\eta_c) \\ 0 \end{pmatrix} \\
&= \mathbf{E}_{c\pm}(t,\eta_c).
\end{aligned}
$$

Then, the time- and phase-dependent matrix elements $H_{ij}(t,\eta_c)$ (Eq. (2.124)) are rewritten as

$$
\begin{aligned}
H_{ij}(t,\eta_c) &= -\mathbf{M}_{ij}^T D(\pm\eta_c)\mathbf{E}_{c\pm}(t,\eta_c=0)e^{-i\omega_{ji}(t-t_0)} \qquad (2.134) \\
&= -(M_{ij,x},M_{ij,y},M_{ij,z})\begin{pmatrix} \cos\eta_c & \mp\sin\eta_c & 0 \\ \pm\sin\eta_c & \cos\eta_c & 0 \\ 0 & 0 & 1 \end{pmatrix}\mathbf{E}_{c\pm}(t,\eta_c=0)e^{-i\omega_{ji}(t-t_0)} \\
&= -\begin{pmatrix} M_{ij,x}\cos\eta_c \pm M_{ij,y}\sin\eta_c \\ \mp M_{ij,x}\sin\eta_c + M_{ij,y}\cos\eta_c \\ 0 \end{pmatrix}\cdot\mathbf{E}_{c\pm}(t,\eta_c=0)e^{-i\omega_{ji}(t-t_0)}
\end{aligned}
$$

where its z-component is zero because of zero z-component of the circularly polarized electric field. For example, for right (+) circularly polarized electric field, the matrix elements for the electronic transitions $|\Psi_i\rangle = |\Psi_{i,ts}\rangle \leftrightarrow |\Psi_j\rangle = |\Psi_{j,+}\rangle$ and

$|\Psi_i\rangle = |\Psi_{i,ts}\rangle \leftrightarrow |\Psi_k\rangle = |\Psi_{k,-}\rangle$, using Eq. (2.128), are

$$\begin{aligned} H_{ij}(t,\eta_c) &= -\begin{pmatrix} M_{ij,x}\cos\eta_c + M_{ij,y}\sin\eta_c \\ -M_{ij,x}\sin\eta_c + M_{ij,y}\cos\eta_c \\ 0 \end{pmatrix} \cdot \mathbf{E}_{c+}(t,\eta_c=0)e^{-i\omega_{ji}(t-t_0)} \qquad (2.135) \\ &= -\frac{\langle\Psi_{i,ts}|M_x|\Psi_{j,x}\rangle}{\sqrt{2}} \begin{pmatrix} \cos\eta_c + i\sin\eta_c \\ -\sin\eta_c + i\cos\eta_c \\ 0 \end{pmatrix} \cdot \mathbf{E}_{c+}(t,\eta_c=0)e^{-i\omega_{ji}(t-t_0)} \\ &= -\frac{\langle\Psi_{i,ts}|M_x|\Psi_{j,x}\rangle}{\sqrt{2}} \begin{pmatrix} 1 \\ i \\ 0 \end{pmatrix} \cdot \mathbf{E}_{c+}(t,\eta_c=0)e^{-i\omega_{ji}(t-t_0)}e^{i\eta_c} \\ &= -\mathbf{M}_{ij}\cdot\mathbf{E}_{c+}(t,\eta_c=0)e^{-i\omega_{ji}(t-t_0)}e^{i\eta_c} \\ &= H_{ij}(t,\eta_c=0)e^{i\eta_c} \end{aligned}$$

and

$$H_{ik}(t,\eta_c) = H_{ik}(t,\eta_c=0)e^{-i\eta_c}, \qquad (2.136)$$

respectively. The differential equations (Eq. (2.122)) for the time- and phase-dependent coefficients $C_i(t,\eta_c)$, $C_j(t,\eta_c)$, $C_k(t,\eta_c)$, ... of the electronic states $|\Psi_i\rangle = |\Psi_{i,ts}\rangle$, $|\Psi_j\rangle = |\Psi_{j,+}\rangle$, $|\Psi_k\rangle = |\Psi_{k,-}\rangle$, ..., respectively, are

$$i\hbar\frac{d}{dt}C_i(t,\eta_c) = \sum_j H_{ij}(t,\eta_c=0)C_j(t,\eta_c)e^{i\eta_c} + \sum_k H_{ik}(t,\eta_c=0)C_k(t,\eta_c)e^{-i\eta_c} + \cdots, \qquad (2.137)$$

$$i\hbar\frac{d}{dt}C_j(t,\eta_c) = \sum_i H_{ji}(t,\eta_c=0)C_i(t,\eta_c)e^{-i\eta_c} + \cdots, \qquad (2.138)$$

$$i\hbar\frac{d}{dt}C_k(t,\eta_c) = \sum_i H_{ki}(t,\eta_c=0)C_i(t,\eta_c)e^{i\eta_c} + \cdots, \qquad (2.139)$$

$$\cdots = \cdots.$$

Multiplying $e^{i\eta_c}$ and $e^{-i\eta_c}$ in Eqs. (2.138) and (2.139) yields the corresponding differential equations

$$i\hbar\frac{d}{dt}\tilde{C}_i(t,\eta_c) = \sum_j H_{ij}(t,\eta_c=0)\tilde{C}_j(t,\eta_c) + \sum_k H_{ik}(t,\eta_c=0)\tilde{C}_k(t,\eta_c) + \cdots, \qquad (2.140)$$

$$i\hbar\frac{d}{dt}\tilde{C}_j(t,\eta_c) = \sum_i H_{ji}(t,\eta_c=0)\tilde{C}_i(t,\eta_c) + \cdots, \qquad (2.141)$$

$$i\hbar\frac{d}{dt}\tilde{C}_k(t,\eta_c) = \sum_i H_{ki}(t,\eta_c=0)\tilde{C}_i(t,\eta_c) + \cdots, \qquad (2.142)$$

$$\cdots = \cdots$$

where $\tilde{C}_i(t,\eta_c) = C_i(t,\eta_c)$, $\tilde{C}_j(t,\eta_c) = C_j(t,\eta_c)e^{i\eta_c}$, $\tilde{C}_k(t,\eta_c) = C_k(t,\eta_c)e^{-i\eta_c}$, ... Since these coefficients are just the solutions for $\eta_c = 0$, i.e. $\tilde{C}_i(t,\eta_c) = C_j(t,\eta_c = 0)$, $\tilde{C}_j(t,\eta_c) = C_j(t,\eta_c = 0)$, $\tilde{C}_k(t,\eta_c) = C_k(t,\eta_c = 0)$, ... (Eqs. (2.137)–(2.142)), we obtain the time-dependent coefficients $C_i(t,\eta_c) = C_i(t,\eta_c = 0)$, $C_j(t,\eta_c) = C_j(t,\eta_c = 0)e^{-i\eta_c}$, $C_k(t,\eta_c) = C_k(t,\eta_c = 0)e^{i\eta_c}$, ... of the electronic states $|\Psi_i\rangle = |\Psi_{i,ts}\rangle$, $|\Psi_j\rangle = |\Psi_{j,+}\rangle$, $|\Psi_k\rangle = |\Psi_{k,-}\rangle$, ..., and the corresponding populations are independent of the phase η_c, i.e.

$$\begin{aligned}
P_i(t,\eta_c) &= |C_i(t,\eta_c)|^2 = |C_i(t,\eta_c = 0)|^2 = P_i(t,\eta_c = 0) && (2.143)\\
P_j(t,\eta_c) &= |C_j(t,\eta_c)|^2 = |C_j(t,\eta_c = 0)e^{-i\eta_c}|^2 = |C_j(t,\eta_c = 0)|^2 = P_j(t,\eta_c = 0) && (2.144)\\
P_k(t,\eta_c) &= |C_k(t,\eta_c)|^2 = |C_k(t,\eta_c = 0)e^{i\eta_c}|^2 = |C_k(t,\eta_c = 0)|^2 = P_k(t,\eta_c = 0) && (2.145)\\
\cdots &= \cdots,
\end{aligned}$$

respectively. It can be shown for other electronic states with different symmetries, for example $|^1D_{\pm 2}\rangle$, $|^1\Sigma^-\rangle$, $|^1\Delta_\pm\rangle$, $|^1B_{1g}\rangle$, ..., that the populations of all electronic states are independent of the phase η_c of the circularly polarized electric field (Eq. (2.99)).

2.3.3 Three-state model

For the dominant electronic transition from the ground (total symmetric) singlet state $|\Psi_0\rangle$ to the excited degenerate state $|\Psi_+\rangle$ or $|\Psi_-\rangle$ by means of a circularly polarized laser pulse, the effective pulse duration τ should be chosen such that the corresponding spectral width Γ (estimated from Eqs. (2.107)–(2.109) depending on the exponent n of the trigonometric envelope) is smaller than the energy gap between the target state $|\Psi_\pm\rangle$ and neighboring states with the same symmetry. In this case, the ansatz for the time-dependent electronic state $|\Psi(t)\rangle$ (Eq. (2.120)) reduces to approximately three dominant contributions of $|\Psi_0\rangle$ and $|\Psi_\pm\rangle$ states, i.e.

$$|\Psi(t)\rangle \approx C_0(t)|\Psi_0\rangle e^{-iE_0(t-t_0)/\hbar} + C_+(t)|\Psi_+\rangle e^{-iE_+(t-t_0)/\hbar} + C_-(t)|\Psi_-\rangle e^{-iE_-(t-t_0)/\hbar}. \quad (2.146)$$

Inserting this ansatz into the differential equation (2.122) for the time-dependent coefficients C_0, C_+, and C_- yields

$$\begin{aligned}
i\hbar\frac{d}{dt}C_0(t) &= H_{0+}(t)C_+(t) + H_{0-}(t)C_-(t), && (2.147)\\
i\hbar\frac{d}{dt}C_+(t) &= H_{+0}(t)C_0(t), && (2.148)\\
i\hbar\frac{d}{dt}C_-(t) &= H_{-0}(t)C_0(t). && (2.149)
\end{aligned}$$

Note that the electronic transition $|\Psi_+\rangle \leftrightarrow |\Psi_-\rangle$ is dipole-forbidden. Using Eqs. (2.124), (2.128), and (2.129) for the matrix elements $H_{ij}(t)$ and dipole matrix elements $\mathbf{M}_{ij}$ with

$$M = \frac{\langle\Psi_0|M_x|\Psi_x\rangle}{\sqrt{2}}, \tag{2.150}$$

respectively, we obtain

$$i\hbar\frac{d}{dt}C_0(t) = -M\left((E_{c\pm,x}+iE_{c\pm,y})C_+(t)+(E_{c\pm,x}-iE_{c\pm,y})C_-(t)\right)e^{-i\omega(t-t_0)}, \tag{2.151}$$

$$i\hbar\frac{d}{dt}C_+(t) = -M(E_{c\pm,x}-iE_{c\pm,y})C_0(t)e^{i\omega(t-t_0)}, \tag{2.152}$$

$$i\hbar\frac{d}{dt}C_-(t) = -M(E_{c\pm,x}+iE_{c\pm,y})C_0(t)e^{i\omega(t-t_0)}. \tag{2.153}$$

where $\omega = \omega_{+0} = \omega_{-0}$ (Eq. (2.125)) is the transition frequency. For the right circularly polarized laser pulse with resonant frequency $\omega_c = \omega$, zero phase $\eta_c = 0$, and many laser cycles ($m_c \gg 1$), i.e. the second term of the electric field (Eq. (2.99)) is neglected, the differential equations are simplified to

$$i\hbar\frac{d}{dt}C_0(t) = -M\mathcal{E}_c s_n\left(t-t_0-\frac{t_{p,c}}{2}\right)\left(C_+(t)e^{-i\omega t_{p,c}/2}+C_-(t)e^{-i2\omega t}e^{i\omega(2t_0+t_{p,c}/2)}\right), \tag{2.154}$$

$$i\hbar\frac{d}{dt}C_+(t) = -M\mathcal{E}_c s_n\left(t-t_0-\frac{t_{p,c}}{2}\right)C_0(t)e^{i\omega t_{p,c}/2}, \tag{2.155}$$

$$i\hbar\frac{d}{dt}C_-(t) = -M\mathcal{E}_c s_n\left(t-t_0-\frac{t_{p,c}}{2}\right)C_0(t)e^{2i\omega t}e^{-i\omega(2t_0+t_{p,c}/2)} \tag{2.156}$$

where $t_c = t_0 + t_{p,c}/2$ was used. Applying the rotating wave approximation (RWA), i.e. neglecting the rapidly oscillating terms $e^{\pm 2i\omega t}$ (cf. Refs. [246–249]), we obtain

$$i\hbar\frac{d}{dt}C_0(t) = -M\mathcal{E}_c s_n\left(t-t_0-\frac{t_{p,c}}{2}\right)C_+(t)e^{-i\omega t_{p,c}/2} \tag{2.157}$$

$$i\hbar\frac{d}{dt}C_+(t) = -M\mathcal{E}_c s_n\left(t-t_0-\frac{t_{p,c}}{2}\right)C_0(t)e^{i\omega t_{p,c}/2}, \tag{2.158}$$

$$i\hbar\frac{d}{dt}C_-(t) = 0. \tag{2.159}$$

Starting from $C_0(t_0) = 1$, $C_+(t_0) = 0$, and $C_-(t_0) = 0$, the analytical solutions for the time-dependent coefficients and the corresponding populations are

$$C_0(t) = \cos\left(\frac{M\mathcal{E}_c}{\hbar}\int_{t_0}^{t} s_n\left(t'-t_0-\frac{t_{p,c}}{2}\right)dt'\right) \tag{2.160}$$

$$C_+(t) = i\sin\left(\frac{M\mathcal{E}_c}{\hbar}\int_{t_0}^{t} s_n\left(t'-t_0-\frac{t_{p,c}}{2}\right)dt'\right)e^{i\omega t_{p,c}/2} \tag{2.161}$$

$$C_-(t) = 0 \tag{2.162}$$

and

$$P_0(t) = \cos^2\left(\frac{M\mathcal{E}_c}{\hbar}\int_{t_0}^{t} s_n\left(t'-t_0-\frac{t_{p,c}}{2}\right)dt'\right) \tag{2.163}$$

$$P_+(t) = \sin^2\left(\frac{M\mathcal{E}_c}{\hbar}\int_{t_0}^{t} s_n\left(t'-t_0-\frac{t_{p,c}}{2}\right)dt'\right) \tag{2.164}$$

$$P_-(t) = 0 \tag{2.165}$$

for $t_0 \leq t \leq t_f = t_0 + t_{p,c}$, respectively. Equations (2.163)–(2.165) describe a transfer of population selectively from the ground state $|\Psi_0\rangle$ to the excited state $|\Psi_+\rangle$ ($|\Psi_-\rangle$) by means of a right (left) circularly polarized laser pulse, neglecting any population of the $|\Psi_-\rangle$ ($|\Psi_+\rangle$) state. For the laser pulse with $n = 2$, denoted as the reference pulse, the integral, using Eq. (2.100), becomes

$$\begin{aligned}
\int_{t_0}^{t} s_2\left(t' - t_0 - \frac{t_{p,c}}{2}\right) dt' &= \int_{t_0}^{t} \cos^2\left(\pi\left(\frac{t'-t_0}{t_{p,c}} - \frac{1}{2}\right)\right) dt' \\
&= \frac{t_{p,c}}{\pi} \int_{-\frac{\pi}{2}}^{\pi\left(\frac{t-t_0}{t_{p,c}} - \frac{1}{2}\right)} \cos^2 x \, dx \\
&= \frac{t_{p,c}}{\pi}\left(\frac{x}{2} + \frac{1}{4}\sin(2x)\right)\Big|_{-\frac{\pi}{2}}^{\pi\left(\frac{t-t_0}{t_{p,c}} - \frac{1}{2}\right)} \\
&= \frac{t-t_0}{2} + \frac{t_{p,c}}{4\pi}\sin\left(2\pi\left(\frac{t-t_0}{t_{p,c}} - \frac{1}{2}\right)\right).
\end{aligned} \tag{2.166}$$

At the final time $t_f = t_0 + t_{p,c}$, the integral yields

$$\int_{t_0}^{t_f} s_2\left(t' - t_0 - \frac{t_{p,c}}{2}\right) dt' = \frac{t_{p,c}}{2}. \tag{2.167}$$

If the population is completely transferred from the ground state $|\Psi_0\rangle$ to the target state $|\Psi_+\rangle$, i.e.

$$P_0(t_f) = \cos^2\left(\frac{M\mathcal{E}_c t_{p,c}}{2\hbar}\right) = 0 \tag{2.168}$$

$$P_+(t_f) = \sin^2\left(\frac{M\mathcal{E}_c t_{p,c}}{2\hbar}\right) = 1 \tag{2.169}$$

$$P_-(t_f) = 0, \tag{2.170}$$

then the condition

$$\frac{|M\mathcal{E}_c t_{p,c}|}{\hbar} = \pi \tag{2.171}$$

must be satisfied. If the laser amplitude $\mathcal{E}_c$ and the pulse duration $t_{p,c}$ are chosen such that the condition (2.171) is fulfilled, then the laser pulse is denoted as a right (left) circularly polarized π laser pulse. On the other hand, the half population transfer from the ground state $|\Psi_0\rangle$ to the excited state $|\Psi_+\rangle$

$$P_0(t_f) = \cos^2\left(\frac{M\mathcal{E}_c t_{p,c}}{2\hbar}\right) = \frac{1}{2} \tag{2.172}$$

$$P_+(t_f) = \sin^2\left(\frac{M\mathcal{E}_c t_{p,c}}{2\hbar}\right) = \frac{1}{2} \tag{2.173}$$

$$P_-(t_f) = 0, \tag{2.174}$$

yields the condition for a right (left) circularly polarized $\pi/2$ laser pulse

$$\frac{|M\mathcal{E}_c t_{p,c}|}{\hbar} = \frac{\pi}{2}. \tag{2.175}$$

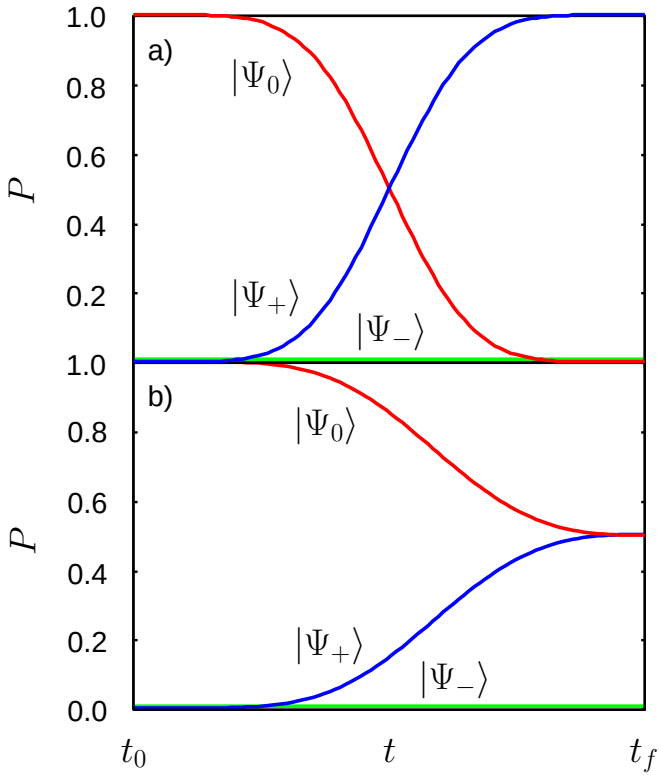

Figure 2.5: Time-dependent populations $P_0(t)$ (red), $P_+(t)$ (blue), $P_-(t)$ (green) (Eqs. (2.163)–(2.165)) of three states $|\Psi_0\rangle$, $|\Psi_+\rangle$, $|\Psi_-\rangle$ starting from $P_0(t_0) = 1$, $P_+(t_0) = 0$, $P_-(t_0) = 0$ for a right circularly polarized (a) π (Eq. (2.171)) or (b) $\pi/2$ (Eq. (2.175)) laser pulse ($n = 2$).

Inserting condition (2.171) or (2.175) in Eqs. (2.163)–(2.165) for the complete or half population transfer by means of a right circularly polarized π or $\pi/2$ laser pulse ($n = 2$), respectively, yields the corresponding time-dependent populations $P_0(t)$, $P_+(t)$, $P_-(t)$ (Eqs. (2.163)–(2.165)) of three states $|\Psi_0\rangle$, $|\Psi_+\rangle$, $|\Psi_-\rangle$, shown in Fig. 2.5. The state after the end of the laser pulse ($t \geq t_f$) is stationary for π laser pulses and non-stationary for $\pi/2$ laser pulses. This non-stationary state is the superposition of $|\Psi_0\rangle$ and $|\Psi_+\rangle$ or $|\Psi_-\rangle$ states, depending on the laser polarization, i.e. hybrid state. In this case, the electronic probability and current densities after the end of the laser pulse are no longer stationary.

Without applying the rotating wave approximation, the differential equations (2.154)–(2.156) must be solved numerically, e.g. by means of the Runge-Kutta method. Nevertheless the resulting populations $P_0(t)$, $P_+(t)$, $P_-(t)$ differ from the approximative populations (Eqs. (2.163)–(2.165)) slightly for right or left circularly polarized laser pulses (with many cycles) whereas the corresponding difference is larger for linearly polarized laser pulses because the non-zero x-component of the resonant linearly x-polarized electric field is proportional to $\cos(\omega t) = (e^{-i\omega t} + e^{i\omega t})/2$ and multiplying this factor with $e^{i\omega t}$ (cf. Eq. (2.152)) yields $(1 + e^{2i\omega t})/2$. In other words, the term $e^{2i\omega t}$ occurs in the

differential equation for the time-dependent coefficient $C_x(t)$ whereas it does not occur in the differential equation for $C_+(t)$ (Eq. (2.155)). Thus, we do not find any observable fast-oscillations with double frequency 2ω in the time-dependent population $P_+(t)$ of the $|\Psi_+\rangle$ state excited by the right circularly polarized laser pulse, even beyond the rotating wave approximation. Because the population $P_-(t)$ is negligible during the excitation, there are also no observable fast-oscillations in the population $P_0(t)$ of the $|\Psi_0\rangle$ state (cf. Eq. (2.154)). Finally, there are fast-oscillations observed in the population $P_-(t)$ of the $|\Psi_-\rangle$ state, but they are marginal.

Beyond the three-state model as well as the rotating wave approximation, the differential equations (2.122) must be solved numerically, for given laser parameters, in particular the effective pulse duration τ, the laser amplitude $\mathcal{E}_c$, the exponent of the trigonometric envelope n ($n = 2$ or $n = 20$), and the laser frequency ω_c; in the following applications, the phase η_c is set to zero for simplicity. The effective pulse duration τ_c is chosen such that it is shorter than the vibrational periods in the electronic states and larger than the time corresponding to the maximal spectral half-width $\Gamma_{max}/2$ (cf. Eqs. (2.107)–(2.109)), i.e. minimal energy gap between the target state $|\Psi_\pm\rangle$ and neighboring states with the same symmetry. For given n and τ_c, there are only two remaining laser parameters $\mathcal{E}_c$ and ω_c. Starting from the reference values of $\mathcal{E}_c$ and ω_c for the π or $\pi/2$ resonant laser pulses (Eqs. (2.171) or (2.175), and $\omega_c = \omega_{+0} = \omega_{-0}$), both parameters $\mathcal{E}_c$ and ω_c are then reoptimized to yield the optimal complete or half population transfer from the ground state $|\Psi_0\rangle$ to the target state $|\Psi_\pm\rangle$.

2.3.4 Electron circulation

Starting from the (stationary) ground state $|\Psi_0\rangle$ at the initial time t_0, the electronic state $|\Psi(t)\rangle$ (Eq. (2.120)) in the presence of the time-dependent electric field $\mathbf{E}_{c\pm}(t)$ ($t_0 \leq t \leq t_f$) is no longer stationary. The corresponding time-dependent electronic probability and current densitites in the atomic or molecular space are (extension of Eqs. (2.15) and (2.21))

$$\rho(\mathbf{r},t) = N \int \ldots \int |\Psi(t)|^2 d\sigma_1 d\mathbf{q}_2 \ldots d\mathbf{q}_N \tag{2.176}$$

$$\mathbf{j}(\mathbf{r},t) = \frac{i\hbar}{2m_e} N \int \ldots \int \left(\Psi(t)\nabla\Psi(t)^* - \Psi(t)^*\nabla\Psi(t)\right) d\sigma_1 d\mathbf{q}_2 \ldots d\mathbf{q}_N. \tag{2.177}$$

Using the ansatz for the time-dependent electronic state $|\Psi(t)\rangle$ (Eq. (2.120)), we obtain from Eqs. (2.176) and (2.177)

$$\rho(\mathbf{r},t) = \sum_{i=0}^{i_{max}} P_i(t)\rho_i(\mathbf{r}) + \sum_{\substack{i,j=0 \\ j\neq i}}^{i_{max}} C_i^*(t)C_j(t)e^{-i(E_j-E_i)(t-t_0)/\hbar}\rho_{ij}(\mathbf{r}) \tag{2.178}$$

$$\mathbf{j}(\mathbf{r},t) = \sum_{i=0}^{i_{max}} P_i(t)\,\mathbf{j}_i(\mathbf{r}) + \sum_{\substack{i,j=0 \\ j\neq i}}^{i_{max}} C_i^*(t)C_j(t)e^{-i(E_j-E_i)(t-t_0)/\hbar}\mathbf{j}_{ij}(\mathbf{r}) \tag{2.179}$$

where

$$\rho_{ij}(\mathbf{r}) = N\int\ldots\int \Psi_i^*\Psi_j\, d\sigma_1 d\mathbf{q}_2\ldots d\mathbf{q}_N \tag{2.180}$$

$$\mathbf{j}_{ij}(\mathbf{r}) = \frac{i\hbar}{2m_e}N\int\ldots\int (\Psi_j\nabla\Psi_i^* - \Psi_i^*\nabla\Psi_j)\, d\sigma_1 d\mathbf{q}_2\ldots d\mathbf{q}_N, \tag{2.181}$$

respectively. The time-dependent electronic probability and current densities (Eqs. (2.178) and (2.179)) are the sum of the time-independent electronic probability densities $\rho_i(\mathbf{r})$ (Eq. (2.15)) and current densities $\mathbf{j}_i(\mathbf{r})$ (Eq. (2.21)) of the states $|\Psi_i\rangle$ weighted by their time-dependent populations $P_i(t)$ plus the additional inference terms, respectively. After the end of the laser pulse, the coefficients $C_i(t)$ and the corresponding populations $P_i(t)$ are time-independent, i.e. $C_i(t) = C_i(t_f)$ and $P_i(t) = P_i(t_f)$ for $t \geq t_f$. For $t \geq t_f$, we obtain

$$\rho(\mathbf{r},t) = \sum_{i=0}^{i_{max}} P_i(t_f)\rho_i(\mathbf{r}) + \sum_{\substack{i,j=0 \\ j\neq i}}^{i_{max}} C_i^*(t_f)C_j(t_f)e^{-i(E_j-E_i)(t-t_0)/\hbar}\rho_{ij}(\mathbf{r}) \tag{2.182}$$

$$\mathbf{j}(\mathbf{r},t) = \sum_{i=0}^{i_{max}} P_i(t_f)\,\mathbf{j}_i(\mathbf{r}) + \sum_{\substack{i,j=0 \\ j\neq i}}^{i_{max}} C_i^*(t_f)C_j(t_f)e^{-i(E_j-E_i)(t-t_0)/\hbar}\mathbf{j}_{ij}(\mathbf{r}), \tag{2.183}$$

i.e. the first term is time-independent and the inference term is time-dependent due to the time-dependent exponential factor.

However, if the population of the target state $|\Psi_+\rangle$ at the final time t_f is approximately equal to 1, e.g. excited by a right circularly polarized reoptimized π laser pulse from the ground state $|\Psi_0\rangle$, then the interference terms in Eqs. (2.182) and (2.183) for $t \geq t_f$ are negligible because the populations of the other states are approximatley zero. In this case, we have the stationary electronic probability and current densities, i.e.

$$\rho(\mathbf{r},t) \approx \rho_+(\mathbf{r}) \tag{2.184}$$

$$\mathbf{j}(\mathbf{r},t) \approx \mathbf{j}_+(\mathbf{r}) \tag{2.185}$$

for $t \geq t_f$, together with the corresponding stationary electric ring current I_+ (Eq. (2.55)) and the induced magnetic field $\mathbf{B}_+(\mathbf{r})$ (Eq. (2.61)). Thus, the electronic ring current of the excited state $|\Psi_+\rangle$ persists after the end of the laser pulse until the excited state $|\Psi_+\rangle$ decays, e.g. by the spontaneous emission where the lifetime of the state $|\Psi_+\rangle$ (ns timescale) is typically longer than the pulse duration (fs timescale) and the mean period of an electron (as timescale).

On the other hand, if the ground $|\Psi_0\rangle$ and target $|\Psi_+\rangle$ states are approximately half populated at the final time t_f where the populations of the other states are negligible,

e.g. excited by a right circularly polarized reoptimized $\pi/2$ laser pulse, then we have the non-stationary electronic probability and current densitites, using $\omega = \omega_{+0} = (E_+ - E_0)/\hbar$ (Eq. (2.125)) and $\mathbf{j}_0(\mathbf{r}) = \mathbf{0}$ (Eq. (2.28)), and assuming $C_0(t_f) \approx 1/\sqrt{2}$ (Eq. (2.160)) and $C_+(t_f) \approx i/\sqrt{2}$ (Eq. (2.161)), i.e.

$$\rho(\mathbf{r},t) \approx \frac{1}{2}\left(\rho_0(\mathbf{r}) + \rho_+(\mathbf{r})\right) + \mathrm{Re}\left(i\, e^{-i\omega(t-t_0)}\rho_{0+}(\mathbf{r})\right) \tag{2.186}$$

$$\mathbf{j}(\mathbf{r},t) \approx \frac{1}{2}\mathbf{j}_+(\mathbf{r}) + \mathrm{Re}\left(i\, e^{-i\omega(t-t_0)}\mathbf{j}_{0+}(\mathbf{r})\right) \tag{2.187}$$

for $t \geq t_f$.

Using the CIS approximation of the wavefunctions $\Psi_0 \approx \Psi_0^{CIS} = \Phi_0^{HF}$ (Eq. (2.8)) and $\Psi_+ \approx \Psi_{+,a\to b}^{CIS} = {}^S\Phi_a^b$ (Eqs. (2.10) and (2.14)), i.e. dominated by the transition of an electron from an occupied orbital φ_a to an unoccupied orbital φ_b (for example the LUMO-HOMO transition), we obtain (Eqs. (2.20), (2.27), (2.28), (2.180), (2.181))

$$\rho(\mathbf{r},t) \approx \rho_0^{CIS}(\mathbf{r}) + \frac{1}{2}\left(|\varphi_b|^2 - |\varphi_a|^2\right) + \sqrt{2}\,\mathrm{Re}\left(i\, e^{-i\omega(t-t_0)}\,\varphi_a^*\varphi_b\right) \tag{2.188}$$

$$\mathbf{j}(\mathbf{r},t) \approx \frac{1}{2}\left(\mathbf{j}_{\varphi_b}(\mathbf{r}) - \mathbf{j}_{\varphi_a}(\mathbf{r})\right) + \sqrt{2}\,\mathrm{Re}\left(i\, e^{-i\omega(t-t_0)}\,\mathbf{j}_{\varphi_a\varphi_b}(\mathbf{r})\right) \tag{2.189}$$

for $t \geq t_f$, where

$$\mathbf{j}_{\varphi_a\varphi_b}(\mathbf{r}) = \frac{i\hbar}{2m_e}\left(\varphi_b\nabla\varphi_a^* - \varphi_a^*\nabla\varphi_b\right). \tag{2.190}$$

The difference of the electronic density is defined as

$$\Delta\rho(\mathbf{r},t) = \rho(\mathbf{r},t) - \rho(\mathbf{r},t_0) \tag{2.191}$$

and can be used for the graphical representation. Since $\rho(\mathbf{r},t_0) \approx \rho_0^{CIS}(\mathbf{r})$, we obtain

$$\Delta\rho(\mathbf{r},t) \approx \frac{1}{2}\left(|\varphi_b|^2 - |\varphi_a|^2\right) + \sqrt{2}\,\mathrm{Re}\left(i\, e^{-i\omega(t-t_0)}\,\varphi_a^*\varphi_b\right) \tag{2.192}$$

for $t \geq t_f$.

For example, if the state $|\Psi_+\rangle$ has the dominant electronic transition from an occupied non-degenerate real orbital $\varphi_a = \varphi_a^*$ to an unoccupied degenerate complex orbital $\varphi_b = (\varphi_{b,x} + i\varphi_{b,y})/\sqrt{2}$ (Eq. (2.32)), then the time-dependent probability and current densities for $t \geq t_f$, using Eq. (2.33), are

$$\Delta\rho(\mathbf{r},t) \approx \frac{1}{4}\left(\varphi_{b,x}^2 + \varphi_{b,y}^2\right) - \frac{1}{2}\varphi_a^2 + \varphi_a\left(\varphi_{b,x}\sin(\omega(t-t_0)) - \varphi_{b,y}\cos(\omega(t-t_0))\right) \tag{2.193}$$

$$\mathbf{j}(\mathbf{r},t) \approx \frac{\hbar}{2m_e}\Big[\frac{1}{2}\left(\varphi_{b,x}\nabla\varphi_{b,y} - \varphi_{b,y}\nabla\varphi_{b,x}\right) - \left(\varphi_{b,x}\nabla\varphi_a - \varphi_a\nabla\varphi_{b,x}\right)\cos(\omega(t-t_0)) \tag{2.194}$$

$$- \left(\varphi_{b,y}\nabla\varphi_a - \varphi_a\nabla\varphi_{b,y}\right)\sin(\omega(t-t_0))\Big].$$

For the special case $\varphi_b = \tilde{\varphi}_b\, e^{i\phi}$ (Eq. (2.34)) in which $\tilde{\varphi}_b$ is real and independent of the azimuthal angle ϕ, i.e. p_+ or π_+ orbitals in atoms, atomic ions, or linear molecules, respectively, then the densities (2.193) and (2.194), using $\varphi_{b,x} = \sqrt{2}\,\tilde{\varphi}_b \cos\phi$ and $\varphi_{b,y} = \sqrt{2}\,\tilde{\varphi}_b \sin\phi$, are simplified to

$$\Delta\rho(\mathbf{r},t) \approx \frac{1}{2}\,\tilde{\varphi}_b^2 - \frac{1}{2}\,\varphi_a^2 + \sqrt{2}\,\varphi_a\tilde{\varphi}_b\,\sin(\omega(t-t_0)-\phi) \tag{2.195}$$

$$\begin{aligned}\mathbf{j}(\mathbf{r},t) \approx \frac{\hbar}{m_e}\Bigg[&\frac{\tilde{\varphi}_b^2}{2\rho}\,\mathbf{e}_\phi + \frac{\varphi_a\tilde{\varphi}_b}{\sqrt{2}\,\rho}\,\sin(\omega(t-t_0)-\phi)\,\mathbf{e}_\phi \\ &+\frac{\varphi_a\nabla\tilde{\varphi}_b - \tilde{\varphi}_b\nabla\varphi_a}{\sqrt{2}}\,\cos(\omega(t-t_0)-\phi)\Bigg]\end{aligned} \tag{2.196}$$

for $t \geq t_f$ where $\rho = r\sin\theta$ is the cylindrical coordinate. Eqs. (2.195) and (2.196) demonstrate that the non-stationary electronic probability and current densities are periodic in $\omega t - \phi$, i.e. after the end of the laser pulse ($t \geq t_f$), the electron in the hybrid state (superposition of $|\Psi_0\rangle$ and $|\Psi_+\rangle$ states) circulates about the axis of symmetry periodically. In contrast to the stationary current density in atoms, atomic ions, and linear molecules, the ρ- and z-components of the circulating current density $\mathbf{j}(\mathbf{r},t)$ do not vanish (last term in Eq. (2.196)) and are also periodic in $\omega t - \phi$. The corresponding ϕ-component of the current density $\mathbf{j}(\mathbf{r},t)$ (2.196) is

$$j_\phi(\mathbf{r},t) \approx \frac{\hbar}{2m_e\rho}\left[\tilde{\varphi}_b^2 + \sqrt{2}\,\varphi_a\tilde{\varphi}_b\,\sin(\omega(t-t_0)-\phi)\right]. \tag{2.197}$$

Hence the electric current also depends on $\omega t - \phi$, i.e. it depends on the choice of the half plane $\mathbf{S}_\phi$ at the azimuthal angle ϕ. The corresponding time- and angle-dependent electric current is (extension of Eq. (2.55))

$$\begin{aligned} I(\phi,t) &= -e\int\int \mathbf{j}(\mathbf{r},t)\cdot d\mathbf{S}_\phi \\ &= -e\int_0^\infty d\rho\int_{-\infty}^\infty j_\phi(\mathbf{r},t)\,dz \\ &\approx \frac{I_+}{2} - \frac{e\hbar}{\sqrt{2}\,m_e}\,\sin(\omega(t-t_0)-\phi)\int_0^\infty\frac{d\rho}{\rho}\int_\infty^\infty \varphi_a(\rho,z)\tilde{\varphi}_b(\rho,z)\,dz \end{aligned} \tag{2.198}$$

where I_+ is the electric current of the state $|\Psi_+\rangle$ and the corresponding factor $\frac{1}{2}$ is due to the half population of this state. The last term of Eq. (2.198) is periodic in $\omega t - \phi$, i.e the corresponding strength is largest for $\phi = \omega(t-t_0) + \pi/2$ and $\phi = \omega(t-t_0) + 3\pi/2$ with opposite signs. The time- or angle-averaging electric ring current is thus approximately equal to $I_+/2$. Furthermore, the corresponding time-dependent non-relativistic induced magnetic field $\mathbf{B}(\mathbf{r},t)$ (extension of Eq. (2.61))

$$\mathbf{B}(\mathbf{r},t) = -\frac{\mu_0 e}{4\pi}\int\int\int\frac{\mathbf{j}(\mathbf{r}',t)\times(\mathbf{r}-\mathbf{r}')}{|\mathbf{r}-\mathbf{r}'|^3}\,dV' \tag{2.199}$$

is in general periodic in $\omega t - \phi$ but its z-component along the z-axis is stationary. Using Eq. (2.79) and

$$\left(\mathbf{j}(\mathbf{r}',t)\times(\mathbf{r}-\mathbf{r}')\right)_z = j_{\phi'}(\mathbf{r}',t)\rho' \tag{2.200}$$

(cf. Eq. (2.80)) for $\mathbf{r} = z\mathbf{e}_z$, we obtain

$$B_z(z,t) = -\frac{\mu_0 e}{2}\int_0^\infty \rho'^2\, d\rho' \int_{-\infty}^\infty \frac{\overline{j_{\phi'}(\mathbf{r}',t)}}{(\rho'^2+(z-z')^2)^{3/2}}\, dz' \tag{2.201}$$

where

$$\overline{j_{\phi'}(\mathbf{r}',t)} = \frac{1}{2\pi}\int_0^{2\pi} j_{\phi'}(\mathbf{r}',t)\, d\phi' \tag{2.202}$$

(cf. Eqs. (2.85) and (2.86)). Inserting Eq. (2.197) into Eq. (2.202) yields

$$\overline{j_{\phi'}(\mathbf{r}',t)} \approx \frac{\hbar}{2m_e\rho'}\,\tilde{\varphi}_b^2(\rho',z') \tag{2.203}$$

and thus ($B_z(z) = B_z(z,t)$)

$$\begin{aligned} B_z(z) &\approx -\frac{\mu_0 e\hbar}{4m_e}\int_0^\infty \rho'\, d\rho' \int_{-\infty}^\infty \frac{\tilde{\varphi}_b^2(\rho',z')}{(\rho'^2+(z-z')^2)^{3/2}}\, dz' \\ &\approx \frac{B_{z,+}(z)}{2} \end{aligned} \tag{2.204}$$

(cf. Eq. (2.90)), i.e. the z-component of the induced magnetic field along the z-axis is time-independent and equal to the half of the z-component of the induced magnetic field of the state $|\Psi_+\rangle$ where the factor $\frac{1}{2}$ is due to the half population of this state. Further analysis shows that the absolute value of the orthogonal component of the induced magnetic field along the z-axis is also time-independent and in general non-zero, i.e. $B_\perp(z,t) = B_\perp(z) = \sqrt{B_x^2(z,t)+B_y^2(z,t)} \geq 0$, but its direction varies with time periodically, i.e. $B_x(z,t)$ and $B_y(z,t)$ are time-dependent. Thus the magnitude of the total induced magnetic field along the z-axis $|\mathbf{B}(z,t)| = \sqrt{B_z^2(z)+B_\perp^2(z)}$ is time-independent and in general larger than $|B_z(z)|$.

2.4 Vibrational and pseudorotational states

2.4.1 Time-independent nuclear Schrödinger equation

The time-independent Schrödinger equation for the molecule with N' nuclei and N electrons is given by

$$\hat{H}_{tot}|\Psi_{vi}^{tot}\rangle = E_{vi}^{tot}|\Psi_{vi}^{tot}\rangle \tag{2.205}$$

where the total Hamiltonian

$$\begin{aligned} \hat{H}_{tot} &= \hat{T}_{nu} + \hat{H}_{el} \\ &= -\frac{\hbar^2}{2}\sum_{\alpha=1}^{N'}\frac{\nabla_{\mathbf{R}_\alpha}^2}{M_\alpha} + \hat{H}_{el} \end{aligned} \tag{2.206}$$

is the sum of the kinetic operator $\hat{T}_{nu}$ of the nuclei with masses $M_\alpha\,(\alpha = 1, \ldots, N')$ and the electronic Hamiltonian $\hat{H}_{el}$ (Eq. (2.2)). Note that the repulsive Coulomb potential between nuclei is already included in $\hat{H}_{el}$ (cf. Eq. (2.2)). The total (nuclear and electronic) eigenstate and eigenenergy are $|\Psi_{vi}^{tot}\rangle$ and E_{vi}^{tot}, respectively, with corresponding sets of nuclear (v) and electronic (i) quantum numbers.

Furthermore we use the Born-Oppenheimer approximation, i.e. the total wavefunction Ψ_{vi}^{tot} is the product of the nuclear Ψ_v^{nu} and electronic Ψ_i^{el} wavefunctions,

$$\Psi_{vi}^{tot}(\mathbf{R}_1, \ldots, \mathbf{R}_{N'}, \mathbf{q}_1, \ldots, \mathbf{q}_N) \;=\; \Psi_v^{nu}(\mathbf{R}_1, \ldots, \mathbf{R}_{N'})\Psi_i^{el}(\mathbf{q}_1, \ldots, \mathbf{q}_N; \mathbf{R}_1, \ldots, \mathbf{R}_{N'}) \quad (2.207)$$

where the electronic wavefunction Ψ_i^{el} depends parametically on the nuclear positions $\mathbf{R}_\alpha\,(\alpha = 1, \ldots, N')$. This approximation is made because the masses of electrons and nuclei are very different, i.e. the electronic and nuclear motions can be approximately treated independently. Inserting the Born-Oppenheimer ansatz (2.207) into the Schrödinger equation (2.205), using Eq. (2.206), neglecting the nonadiabatic coupling term, i.e.

$$-\frac{\hbar^2}{2}\sum_{\alpha=1}^{N'}\frac{1}{M_\alpha}\left[2\left(\nabla_{\mathbf{R}_\alpha}|\Psi_v^{nu}\rangle\right)\nabla_{\mathbf{R}_\alpha}|\Psi_i^{el}\rangle + |\Psi_v^{nu}\rangle\nabla_{\mathbf{R}_\alpha}^2|\Psi_i^{el}\rangle\right] \;\approx\; 0, \quad (2.208)$$

and applying $\langle\Psi_i^{el}|$ yield the time-independent nuclear Schrödinger equation

$$\left(\hat{T}_{nu} + V_i\right)|\Psi_v^{nu}\rangle \;=\; E_{vi}^{tot}|\Psi_v^{nu}\rangle \quad (2.209)$$

where

$$V_i(\mathbf{R}_1, \ldots, \mathbf{R}_{N'}) \;=\; \langle\Psi_i^{el}|\hat{H}_{el}|\Psi_i^{el}\rangle \quad (2.210)$$

is the PES of the electronic state $|\Psi_i^{el}\rangle$ (cf. Eq. (2.1)).

2.4.2 Nuclear wavefunction

Now, we focus on the aligned linear triatomic molecule ABA ($D_{\infty h}$ symmetry) in the electronic non-degenerate singlet ground state $|\Psi_0^{el}\rangle = |X\,{}^1\Sigma_g^+\rangle$. The masses of the nuclei A and B are M_A and M_B, respectively, and the total mass of the molecule is $M = 2M_A + M_B$. The equilibrium bond length between nuclei A and B is R_e. The corresponding time-independent nuclear Schrödinger equation (Eq. (2.209)) is

$$\left(-\frac{\hbar^2}{2M_A}(\nabla_{\mathbf{R}_{A_1}}^2 + \nabla_{\mathbf{R}_{A_2}}^2) - \frac{\hbar^2}{2M_B}\nabla_{\mathbf{R}_B}^2 + V_0(\mathbf{R}_{A_1}, \mathbf{R}_{A_2}, \mathbf{R}_B)\right)|\Psi_v^{nu}\rangle \;=\; E_{v0}^{tot}|\Psi_v^{nu}\rangle \quad (2.211)$$

where V_0 is the potential energy surface of the electronic ground state $|\Psi_0\rangle$ depending on the positions $\mathbf{R}_1 = \mathbf{R}_{A_1}$, $\mathbf{R}_2 = \mathbf{R}_{A_2}$, and $\mathbf{R}_3 = \mathbf{R}_B$ of the nuclei A_1 = A(left),

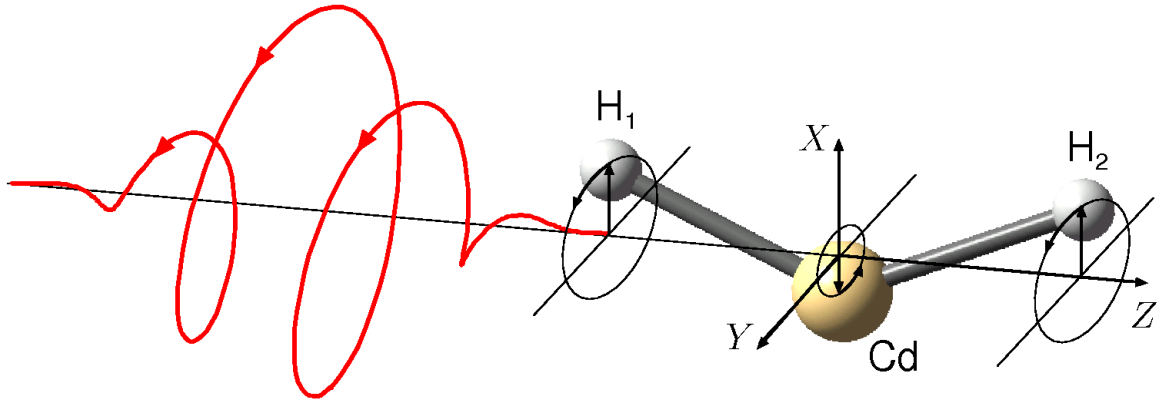

Figure 2.6: A right (+) circularly polarized laser pulse impinging on the aligned linear triatomic molecule $^{114}CdH_2$ and propagating along the Z-axis. The arrows indicate the central sequence of laser cycles as they would be "seen" by the molecule when the pulse passes by. The straight and curvilinear arrows correspond to bend and pseudorotation of the linear molecule represented by polar coordinates ρ_i and ϕ_i $(i = 1, 2, 3)$ of the nuclei A_1=H_1, A_2=H_2 and B=Cd, respectively.

A_2 =A(right), and B, respectively. These positions can be represented in Cartesian or cylindrical coordinates, i.e. $\mathbf{R}_i = (X_i, Y_i, Z_i) = (\rho_i \cos\phi_i, \rho_i \sin\phi_i, Z_i)$ $(i = 1, 2, 3)$, see Fig. 2.6, and are related to normal coordinates for the symmetric stretch

$$Q_s = Z_2 - Z_1 - 2R_e, \tag{2.212}$$

for the antisymmetric stretch

$$Q_a = Z_3 - \frac{1}{2}(Z_1 + Z_2), \tag{2.213}$$

for the degenerate bends

$$\begin{aligned} Q_{b,X} &= X_3 - \frac{1}{2}(X_1 + X_2) \qquad (2.214)\\ &= \rho_3 \cos\phi_3 - \frac{1}{2}(\rho_1 \cos\phi_1 + \rho_2 \cos\phi_2) \\ Q_{b,Y} &= Y_3 - \frac{1}{2}(Y_1 + Y_2) \qquad (2.215)\\ &= \rho_3 \sin\phi_3 - \frac{1}{2}(\rho_1 \sin\phi_1 + \rho_2 \sin\phi_2), \end{aligned}$$

for the translation of the center of mass

$$\begin{aligned} Q_{c,X} &= \frac{M_A}{M}(X_1 + X_2) + \frac{M_B}{M} X_3 \qquad (2.216)\\ &= \frac{M_A}{M}(\rho_1 \cos\phi_1 + \rho_2 \cos\phi_2) + \frac{M_B}{M} \rho_3 \cos\phi_3 \end{aligned}$$

$$
\begin{aligned}
Q_{c,Y} &= \frac{M_A}{M}(Y_1 + Y_2) + \frac{M_B}{M}\, Y_3 && (2.217)\\
&= \frac{M_A}{M}(\rho_1 \sin\phi_1 + \rho_2 \sin\phi_2) + \frac{M_B}{M}\, \rho_3 \sin\phi_3 \\
Q_{c,Z} &= \frac{M_A}{M}(Z_1 + Z_2) + \frac{M_B}{M}\, Z_3, && (2.218)
\end{aligned}
$$

and for the rotation of the molecule

$$
\begin{aligned}
Q_{r,X} &= X_2 - X_1 && (2.219)\\
&= \rho_2 \cos\phi_2 - \rho_1 \cos\phi_1 \\
Q_{r,Y} &= Y_2 - Y_1 && (2.220)\\
&= \rho_2 \sin\phi_2 - \rho_1 \sin\phi_1.
\end{aligned}
$$

Using these normal coordinates (2.212)–(2.220), the nuclear Schrödinger equation (2.211) is then rewritten as [207, 208]

$$
\begin{aligned}
&\left(-\frac{\hbar^2}{2m_s}\frac{\partial^2}{\partial Q_s^2} - \frac{\hbar^2}{2m_a}\frac{\partial^2}{\partial Q_a^2} - \frac{\hbar^2}{2m_b}\left(\frac{\partial^2}{\partial Q_{b,X}^2} + \frac{\partial^2}{\partial Q_{b,Y}^2}\right) - \frac{\hbar^2}{2m_r}\left(\frac{\partial^2}{\partial Q_{r,X}^2} + \frac{\partial^2}{\partial Q_{r,Y}^2}\right)\right. \quad (2.221)\\
&\left. -\frac{\hbar^2}{2M}\left(\frac{\partial^2}{\partial Q_{c,X}^2} + \frac{\partial^2}{\partial Q_{c,Y}^2} + \frac{\partial^2}{\partial Q_{c,Z}^2}\right) + V_0(Q_s, Q_a, Q_{b,X}, Q_{b,Y})\right)|\Psi_v^{nu}\rangle = E_{v0}^{tot}|\Psi_v^{nu}\rangle
\end{aligned}
$$

with reduced masses

$$
\begin{aligned}
m_s = m_r &= \frac{M_A M_A}{M_A + M_A} = \frac{M_A}{2} && (2.222)\\
m_a = m_b &= \frac{2M_A M_B}{M} && (2.223)
\end{aligned}
$$

where the potential energy surface V_0 depends only on the vibrational coordinates $Q_s, Q_a, Q_{b,X}, Q_{b,Y}$. Using the polar coordinates Q_b and δ instead of the Cartesian bend coordinates $Q_{b,X} = Q_b \cos\delta$ and $Q_{b,Y} = Q_b \sin\delta$ (Eqs. (2.214), (2.215)), i.e.

$$
\begin{aligned}
Q_b &= \sqrt{Q_{b,X}^2 + Q_{b,Y}^2} && (2.224)\\
&= \sqrt{\left(\rho_3 \cos\phi_3 - \frac{\rho_1 \cos\phi_1 + \rho_2 \cos\phi_2}{2}\right)^2 + \left(\rho_3 \sin\phi_3 - \frac{\rho_1 \sin\phi_1 + \rho_2 \sin\phi_2}{2}\right)^2} \\
&= \sqrt{\rho_3^2 + \frac{\rho_1^2 + \rho_2^2}{4} + \frac{\rho_1\rho_2 \cos(\phi_1 - \phi_2)}{2} - \rho_1\rho_3 \cos(\phi_1 - \phi_3) - \rho_2\rho_3 \cos(\phi_2 - \phi_3)} \\
\delta &= \arccos\left(\frac{Q_{b,X}}{Q_b}\right) && (2.225)\\
&= \arccos\left(\frac{\rho_3 \cos\phi_3 - \frac{1}{2}(\rho_1 \cos\phi_1 + \rho_2 \cos\phi_2)}{Q_b}\right),
\end{aligned}
$$

the nuclear Schrödinger equation (2.221) becomes [207, 208]

$$\left(-\frac{\hbar^2}{2m_s}\frac{\partial^2}{\partial Q_s^2} - \frac{\hbar^2}{2m_a}\frac{\partial^2}{\partial Q_a^2} - \frac{\hbar^2}{2m_b}\frac{1}{Q_b}\frac{\partial}{\partial Q_b}\left(Q_b\frac{\partial}{\partial Q_b}\right) + \frac{\hat{L}_{pr}^2}{2m_b Q_b^2} \right. \tag{2.226}$$
$$-\frac{\hbar^2}{2M}\left(\frac{\partial^2}{\partial Q_{c,X}^2}+\frac{\partial^2}{\partial Q_{c,Y}^2}+\frac{\partial^2}{\partial Q_{c,Z}^2}\right) - \frac{\hbar^2}{2m_r}\left(\frac{\partial^2}{\partial Q_{r,X}^2}+\frac{\partial^2}{\partial Q_{r,Y}^2}\right)$$
$$\left. + V_0(Q_s,Q_a,Q_b)\right)|\Psi_v^{nu}\rangle = E_{v0}^{tot}|\Psi_v^{nu}\rangle$$

where

$$\hat{L}_{pr} = -i\hbar\frac{\partial}{\partial\delta} \tag{2.227}$$

denotes the angular momentum operator for the pseudorotation δ. For symmetry reasons, the potential energy surface V_0 depends only on the stretches Q_s, Q_a and bend Q_b of the triatomic molecule but not on the pseudorotation δ.

Since each translational $Q_{c,X}, Q_{c,Y}, Q_{c,Z}$ and rotational $Q_{r,X}, Q_{r,Y}$ coordinate appears only in one term of the Schrödinger equation (2.226), we use the separation ansatz for the nuclear wavefunction (cf. Eq. (2.207))

$$\Psi_v^{nu}(\mathbf{R}_1,\mathbf{R}_2,\mathbf{R}_3) = \Phi_{c,X}(Q_{c,X})\Phi_{c,Y}(Q_{c,Y})\Phi_{c,Z}(Q_{c,Z})\Phi_{r,X}(Q_{r,X})\Phi_{r,Y}(Q_{r,Y}) \tag{2.228}$$
$$\Phi_v(Q_s,Q_a,Q_b,\delta).$$

In the following application, we assume that the molecule ABA does not rotate, i.e. $Q_{r,X} = Q_{r,Y} = 0$, and its center of mass does not move and remains at the origin, i.e. $Q_{c,X} = Q_{c,Y} = Q_{c,Z} = 0$, on the short timescale below a few picoseconds. In this case, the square-integrable wavefunctions for the translation of the center of mass and for the rotation of the molecule along the X-axis are given by

$$\Phi_{c,X}(Q_{c,X}) = \sqrt{\delta(Q_{c,X})} \tag{2.229}$$
$$\Phi_{r,X}(Q_{r,X}) = \sqrt{\delta(Q_{r,X})} \tag{2.230}$$

where the corresponding densities $\Phi_{c,X}^2(Q_{c,X}) = \delta(Q_{c,X})$ and $\Phi_{r,X}^2(Q_{r,X}) = \delta(Q_{r,X})$ are already normalized, i.e. $\int \Phi_{c,X}^2(Q_{c,X})\,dQ_{c,X} = 1$ and $\int \Phi_{r,X}^2(Q_{r,X})\,dQ_{r,X} = 1$, respectively. The other wavefunctions $\Phi_{c,Y}(Q_{c,Y})$, $\Phi_{c,Z}(Q_{c,Z})$ and $\Phi_{r,Y}(Q_{r,Y})$ are defined in an analogous manner as in Eqs. (2.229) and (2.230), respectively. Their mean energies are defined as

$$E_{c,X} = -\frac{\hbar^2}{2M}\left\langle \Phi_{c,X}\left|\frac{\partial^2}{\partial Q_{c,X}^2}\right|\Phi_{c,X}\right\rangle \tag{2.231}$$
$$E_{r,X} = -\frac{\hbar^2}{2m_r}\left\langle \Phi_{r,X}\left|\frac{\partial^2}{\partial Q_{r,X}^2}\right|\Phi_{r,X}\right\rangle \tag{2.232}$$

where the definitions for $E_{c,Y}, E_{c,Z}$ and $E_{r,Y}$ are analogous. The total translational and rotational mean energies are thus $E_c = E_{c,X}+E_{c,Y}+E_{c,Z} = 3E_{c,X}$ and $E_r = E_{r,X}+E_{r,Y} = 2E_{r,X}$, respectively.

Inserting the ansatz (2.228) into Eq. (2.226) and applying $\langle\Phi_{c,X}\Phi_{c,Y}\Phi_{c,Z}\Phi_{r,X}\Phi_{r,Y}|$ yield the Schrödinger equation for the vibrational eigenfunction $\Phi_v(Q_s, Q_a, Q_b, \delta)$

$$\left(-\frac{\hbar^2}{2m_s}\frac{\partial^2}{\partial Q_s^2} - \frac{\hbar^2}{2m_a}\frac{\partial^2}{\partial Q_a^2} - \frac{\hbar^2}{2m_b}\frac{1}{Q_b}\frac{\partial}{\partial Q_b}\left(Q_b\frac{\partial}{\partial Q_b}\right) + \frac{\hat{L}_{pr}^2}{2m_b Q_b^2}\right. \tag{2.233}$$
$$\left. + V_0(Q_s, Q_a, Q_b)\right)|\Phi_v\rangle = E_{v0}|\Phi_v\rangle$$

where $E_{v0} = E_{v0}^{tot} - E_c - E_r$ is the eigenenergy of the vibrational state $|\Phi_v\rangle$ in the electronic ground state $|\Psi_0^{el}\rangle$. Since the coordinate for the pseudorotation δ appears only in the fourth term of Eq. (2.233), we further make the separation ansatz

$$\Phi_v(Q_s, Q_a, Q_b, \delta) = \Phi_{v|l|}(Q_s, Q_a, Q_b)\Phi_l(\delta) \tag{2.234}$$

where v and l are the vibrational and pseudorotational quantum numbers, respectively. The solutions of the equation for the pseudorotational wavefunction $\Phi_l(\delta)$ (cf. Eq. (2.227))

$$\hat{L}_{pr}^2|\Phi_l\rangle = -\hbar^2\frac{\partial^2}{\partial\delta^2}|\Phi_l\rangle = a_l|\Phi_l\rangle \tag{2.235}$$

are the normalized eigenfunctions

$$\Phi_l(\delta) = \frac{1}{\sqrt{2\pi}}e^{il\delta} \tag{2.236}$$

and the eigenvalues

$$a_l = l^2\hbar^2 \tag{2.237}$$

with quantum numbers $l = 0, \pm1, \pm2, \ldots$. Inserting the ansatz (2.234) into Eq. (2.233), using Eqs. (2.235)–(2.237), and applying $\langle\Phi_l|$ yield the differential equation for the vibrational wavefunction $\Phi_{v|l|}(Q_s, Q_a, Q_b)$

$$\left(-\frac{\hbar^2}{2m_s}\frac{\partial^2}{\partial Q_s^2} - \frac{\hbar^2}{2m_a}\frac{\partial^2}{\partial Q_a^2} - \frac{\hbar^2}{2m_b}\frac{1}{Q_b}\frac{\partial}{\partial Q_b}\left(Q_b\frac{\partial}{\partial Q_b}\right) + \frac{l^2\hbar^2}{2m_b Q_b^2}\right. \tag{2.238}$$
$$\left. + V_0(Q_s, Q_a, Q_b)\right)|\Phi_{v|l|}\rangle = E_{v|l|,0}|\Phi_{v|l|}\rangle$$

where $E_{v|l|,0} = E_{v0}$. Note that the pseudorotational quantum number l appears in Eq. (2.238) only as l^2, i.e. the vibrational eigenenergy $E_{v|l|,0}$ and wavefunction $\Phi_{v|l|}(Q_s, Q_a, Q_b)$ are independent of the sign of l. The (anharmonic) vibrational state for $l \neq 0$ is therefore twofold degenerate.

The potential energy surface $V_0(Q_s, Q_a, Q_b)$ of the electronic ground state $|\Psi_0^{el}\rangle$ may be separated into the harmonic (h) and anharmonic (ah) parts, i.e.

$$V_0(Q_s, Q_a, Q_b) = V_0^h(Q_s, Q_a, Q_b) + V_0^{ah}(Q_s, Q_a, Q_b) \tag{2.239}$$

where the harmonic part for the linear triatomic molecule ABA

$$V_0^h(Q_s,Q_a,Q_b) = \frac{1}{2}\,m_s\omega_s^2Q_s^2+\frac{1}{2}\,m_a\omega_a^2Q_a^2+\frac{1}{2}\,m_b\omega_b^2Q_b^2 \tag{2.240}$$

is the sum of the harmonic potentials with corresponding harmonic frequencies ω_s for the symmetric stretch, ω_a for the antisymmetric stretch, and ω_b for the bend. For the calculation of the nuclear probability and current densities, nuclear ring currents and associated induced magnetic fields, we use the harmonic approximation, i.e. $V_0 \approx V_0^h$. In this case, the vibrational wavefunction $\Phi_{v|l|}(Q_s,Q_a,Q_b) \approx \Phi^h_{v|l|}(Q_s,Q_a,Q_b)$ is separable, i.e.

$$\Phi^h_{v|l|}(Q_s,Q_a,Q_b) = \Phi^h_{v_s}(Q_s)\Phi^h_{v_a}(Q_a)\Phi^h_{v_b|l|}(Q_b) \tag{2.241}$$

with quantum numbers v_s for the symmetric stretch, v_a for the antisymmetric stretch, and v_b for the bend. Inserting the ansatz (2.241) into Eq. (2.238) within the harmonic approximation yields three uncoupled differential equations for the wavefunctions $\Phi^h_{v_s}(Q_s)$, $\Phi^h_{v_a}(Q_a)$, and $\Phi^h_{v_b|l|}(Q_b)$

$$\left(-\frac{\hbar^2}{2m_s}\frac{\partial^2}{\partial Q_s^2}+\frac{1}{2}\,m_s\omega_s^2Q_s^2\right)|\Phi^h_{v_s}\rangle = E_{v_s,0}|\Phi^h_{v_s}\rangle \tag{2.242}$$

$$\left(-\frac{\hbar^2}{2m_a}\frac{\partial^2}{\partial Q_a^2}+\frac{1}{2}\,m_a\omega_a^2Q_a^2\right)|\Phi^h_{v_a}\rangle = E_{v_a,0}|\Phi^h_{v_a}\rangle \tag{2.243}$$

$$\left(-\frac{\hbar^2}{2m_b}\frac{1}{Q_b}\frac{\partial}{\partial Q_b}\left(Q_b\,\frac{\partial}{\partial Q_b}\right)+\frac{l^2\hbar^2}{2m_bQ_b^2}+\frac{1}{2}\,m_b\omega_b^2Q_b^2\right)|\Phi^h_{v_b|l|}\rangle = E_{v_b,0}|\Phi^h_{v_b|l|}\rangle \tag{2.244}$$

with corresponding eigenenergies $E_{v_s,0}$, $E_{v_a,0}$, and $E_{v_b,0}$, respectively, where $E_{v|l|,0} = E_{v_s,0}+E_{v_a,0}+E_{v_b,0}$. The solutions of the Schrödinger equations for one-dimensional harmonic oscillators (Eqs. (2.242) and (2.243)) are well-known one-dimensional normalized harmonic wavefunctions for the symmetric and antisymmetric stretches [207, 208]

$$\Phi^h_{v_s}(Q_s) = \left(\frac{s}{\pi}\right)^{1/4}\frac{1}{\sqrt{2^{v_s}v_s!}}\,H_{v_s}(\sqrt{s}Q_s)e^{-\frac{1}{2}sQ_s^2} \tag{2.245}$$

$$\Phi^h_{v_a}(Q_a) = \left(\frac{a}{\pi}\right)^{1/4}\frac{1}{\sqrt{2^{v_a}v_a!}}\,H_{v_a}(\sqrt{a}Q_a)e^{-\frac{1}{2}aQ_a^2} \tag{2.246}$$

where $H_n(x)$ are the Hermite polynomials and

$$s = \frac{m_s\omega_s}{\hbar} = \frac{M_A\omega_s}{2\hbar} \tag{2.247}$$

$$a = \frac{m_a\omega_a}{\hbar} = \frac{2M_AM_B\omega_a}{M\hbar} \tag{2.248}$$

(cf. Eqs. (2.222), (2.223)). The corresponding eigenenergies are

$$E_{v_s} = \left(v_s+\frac{1}{2}\right)\hbar\omega_s \tag{2.249}$$

$$E_{v_a} = \left(v_a+\frac{1}{2}\right)\hbar\omega_a \tag{2.250}$$

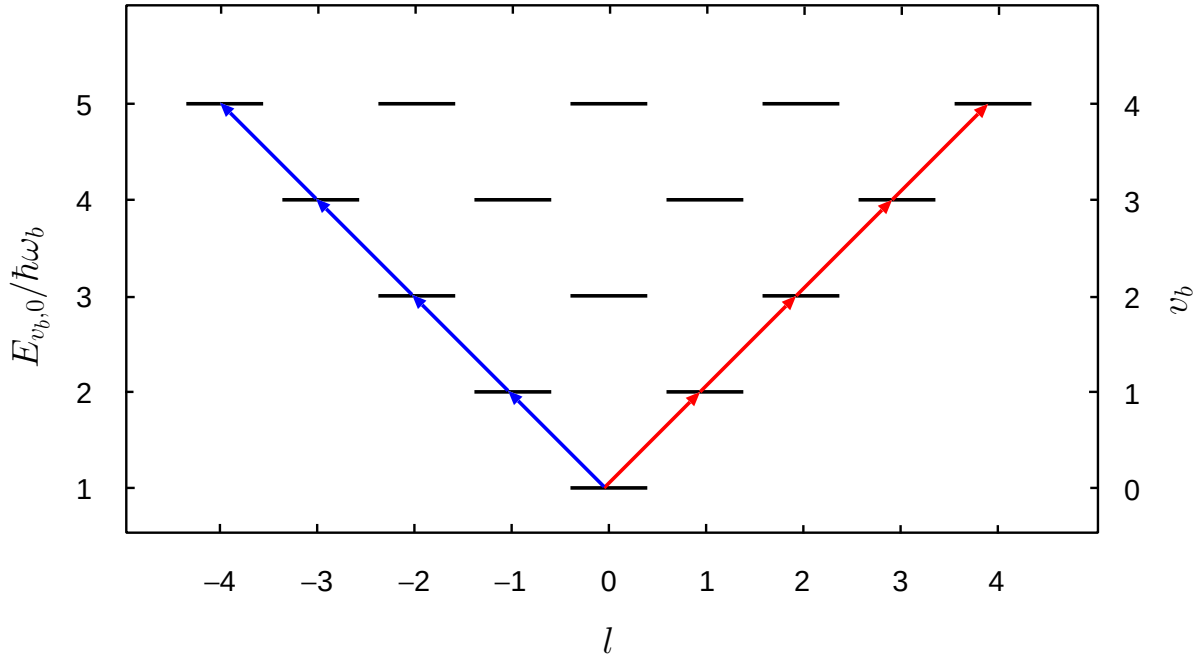

Figure 2.7: Bending and pseudorotational states of the linear triatomic molecule ABA with corresponding harmonic eigenenergies $E_{v_b,0} = (v_b + 1)\hbar\omega_b$ (Eq. (2.254)) for $v_s = v_a = 0$ and $0 \leq v_b \leq 4$. Red and blue arrows indicate the dominant ladder climbing to excited vibrational and pseudorotational states according to the selection rules $v_b \to v_b + 1$, $l \to l + 1$ and $l \to l - 1$ for absorption by a right and left circularly polarized laser pulse, respectively, see Section 2.5.2.

with quantum numbers $v_s = 0, 1, 2, \ldots$ and $v_a = 0, 1, 2, \ldots$, respectively. Solving the Schrödinger equation for the harmonic bend oscillator (Eq. (2.244)) leads to the harmonic wavefunction for the bend [207, 208, 250–252]

$$\Phi^h_{v_b|l|}(Q_b) \;=\; \sqrt{2}b^{\frac{|l|+1}{2}} \sqrt{\frac{\left(\frac{v_b-|l|}{2}\right)!}{\left(\frac{v_b+|l|}{2}\right)!}} Q_b^{|l|} e^{-\frac{1}{2}bQ_b^2} L^{|l|}_{\frac{v_b-|l|}{2}}(bQ_b^2) \tag{2.251}$$

where $L^k_n(x)$ are the associated Laguerre polynomials (for another notation, see e.g. Ref. [250]) and

$$b \;=\; \frac{m_b\omega_b}{\hbar} \;=\; \frac{2M_AM_B\omega_b}{M\hbar} \tag{2.252}$$

(cf. Eq. (2.223)). The wavefunction (2.251) is already normalized, i.e.

$$\int_0^\infty \left(\Phi^h_{v_b|l|}(Q_b)\right)^2 Q_b\, dQ_b \;=\; 1, \tag{2.253}$$

see Appendix A.2.2. The corresponding eigenenergy

$$E_{v_b,0} \;=\; (v_b + 1)\hbar\omega_b \tag{2.254}$$

with quantum number $v_b = 0, 1, 2, \ldots$ is independent of the pseudorotational quantum number $l = -v_b, -v_b+2, \ldots, v_b-2, v_b$. Thus, the harmonic vibrational state for $v_b \neq 0$ is (v_b+1)-fold degenerate, i.e. the total vibrational energy in the harmonic approximation (Eqs. (2.249), (2.250), (2.254))

$$E^h_{v|l|,0} = \left(v_s + \frac{1}{2}\right)\hbar\omega_s + \left(v_a + \frac{1}{2}\right)\hbar\omega_a + (v_b+1)\hbar\omega_b \tag{2.255}$$

is independent of l, see Fig. 2.7. Finally, the total wavefunction in the harmonic approximation $\Psi^{tot}_{v0} \approx \Psi^{tot}_{v_s v_a v_b l 0}$ (Eq. (2.207)) of the linear triatomic molecule ABA in the electronic ground state $|\Psi^{el}_0\rangle$ is

$$\begin{aligned}\Psi^{tot}_{v_s v_a v_b l 0}(\mathbf{R}_1, \mathbf{R}_2, \mathbf{R}_3, \mathbf{q}_1, \ldots, \mathbf{q}_N) &= \sqrt{\delta(Q_{c,X})\delta(Q_{c,Y})\delta(Q_{c,Z})\delta(Q_{r,X})\delta(Q_{r,Y})} \\ &\quad \Phi^h_{v_s}(Q_s)\Phi^h_{v_a}(Q_a)\Phi^h_{v_b|l|}(Q_b)\Phi_l(\delta) \\ &\quad \Psi^{el}_0(\mathbf{q}_1, \ldots, \mathbf{q}_N; \mathbf{R}_1, \mathbf{R}_2, \mathbf{R}_3),\end{aligned} \tag{2.256}$$

using Eqs. (2.228)–(2.230), (2.234), (2.241).

2.4.3 Nuclear probability density

The nuclear probability density $\rho_{A_1}(\mathbf{R} = \mathbf{R}_1)$ of the nucleus $A_1 = A(\text{left})$ in the electronic ground state $|\Psi^{el}_0\rangle$ within the Born-Oppenheimer and harmonic approximations is given by

$$\begin{aligned}\rho_{A_1}(\mathbf{R}) &= \int\int\int d\mathbf{R}_2 \int\int\int d\mathbf{R}_3 \\ &\quad \int \ldots \int |\Psi^{tot}_{v_s v_a v_b l 0}(\mathbf{R}, \mathbf{R}_2, \mathbf{R}_3, \mathbf{q}_1, \ldots, \mathbf{q}_N)|^2 \, d\mathbf{q}_1 \ldots d\mathbf{q}_N.\end{aligned} \tag{2.257}$$

Using Eq. (2.256) and the fact that the electronic wavefunction is normalized, i.e.

$$\int \ldots \int |\Psi^{el}_0(\mathbf{q}_1, \ldots, \mathbf{q}_N; \mathbf{R}_1, \mathbf{R}_2, \mathbf{R}_3)|^2 \, d\mathbf{q}_1 \ldots d\mathbf{q}_N = 1, \tag{2.258}$$

that the vibrational wavefunctions for the stretches $\Phi^h_{v_s}(Q_s)$, $\Phi^h_{v_a}(Q_a)$ (Eqs. (2.245), (2.246)) and for the bend $\Phi^h_{v_b|l|}(Q_b)$ (Eq. (2.251)) are real, and that $|\Phi_l(\delta)|^2 = 1/(2\pi)$ (Eq. (2.236)), we obtain

$$\begin{aligned}\rho_{A_1}(\mathbf{R}) &= \frac{1}{2\pi}\int_{-\infty}^{\infty}\delta(Q_{r,X})\,dX_2 \int_{-\infty}^{\infty}\delta(Q_{c,X})\,dX_3 \int_{-\infty}^{\infty}\delta(Q_{r,Y})\,dY_2 \\ &\quad \int_{-\infty}^{\infty}\delta(Q_{c,Y})\left(\Phi^h_{v_b|l|}(Q_b)\right)^2 dY_3 \int_{-\infty}^{\infty} dZ_2 \int_{-\infty}^{\infty}\delta(Q_{c,Z})\left(\Phi^h_{v_s}(Q_s)\right)^2\left(\Phi^h_{v_a}(Q_a)\right)^2 dZ_3.\end{aligned} \tag{2.259}$$

Using $Q_{r,X} = X_2 - X$ and $Q_{r,Y} = Y_2 - Y$ (Eqs. (2.219), (2.220)), we have

$$\begin{aligned}\rho_{A_1}(\mathbf{R}) &= \frac{1}{2\pi}\int_{-\infty}^{\infty}\delta(Q_{c,X})\,dX_3 \int_{-\infty}^{\infty}\delta(Q_{c,Y})\left(\Phi^h_{v_b|l|}(Q_b)\right)^2 dY_3\Big|_{X_2=X, Y_2=Y} \\ &\quad \int_{-\infty}^{\infty} dZ_2 \int_{-\infty}^{\infty}\delta(Q_{c,Z})\left(\Phi^h_{v_s}(Q_s)\right)^2\left(\Phi^h_{v_a}(Q_a)\right)^2 dZ_3.\end{aligned} \tag{2.260}$$

Again, using $Q_{c,X} = (2M_A X + M_B X_3)/M$ for $X_2 = X$ and $Q_{c,Y} = (2M_A Y + M_B Y_3)/M$ for $Y_2 = Y$ (Eqs. (2.216), (2.217)) yields

$$\rho_{A_1}(\mathbf{R}) = \frac{1}{2\pi}\frac{M^2}{M_B^2}\left(\Phi^h_{v_b|l|}(Q_b)\right)^2\Big|_{\substack{X_2=X,Y_2=Y \\ X_3=-\frac{2M_A}{M_B}X \\ Y_3=-\frac{2M_A}{M_B}Y}} \int_{-\infty}^{\infty} dZ_2 \int_{-\infty}^{\infty} \delta(Q_{c,Z}) \left(\Phi^h_{v_s}(Q_s)\right)^2 \left(\Phi^h_{v_a}(Q_a)\right)^2 dZ_3. \tag{2.261}$$

Since for $X_2 = X$, $X_3 = -2M_A X/M_B$ and $Y_2 = Y$, $Y_3 = -2M_A Y/M_B$

$$Q_{b,X} = -\frac{M}{M_B} X \tag{2.262}$$

$$Q_{b,Y} = -\frac{M}{M_B} Y \tag{2.263}$$

$$Q_b = \frac{M}{M_B} \rho \tag{2.264}$$

(Eqs. (2.214), (2.215), (2.224) and $\rho = \sqrt{X^2 + Y^2}$), we get

$$\rho_{A_1}(\mathbf{R}) = \frac{1}{2\pi}\frac{M^2}{M_B^2}\left(\Phi^h_{v_b|l|}\left(\frac{M}{M_B}\rho\right)\right)^2 \int_{-\infty}^{\infty} dZ_2 \int_{-\infty}^{\infty} \delta(Q_{c,Z}) \left(\Phi^h_{v_s}(Q_s)\right)^2 \left(\Phi^h_{v_a}(Q_a)\right)^2 dZ_3. \tag{2.265}$$

Then, using $Q_{c,Z} = (M_A(Z + Z_2) + M_B Z_3)/M$ (Eq. (2.218)) yields

$$\rho_{A_1}(\mathbf{R}) = \frac{1}{2\pi}\frac{M^3}{M_B^3}\left(\Phi^h_{v_b|l|}\left(\frac{M}{M_B}\rho\right)\right)^2 \int_{-\infty}^{\infty} \left(\Phi^h_{v_s}(Q_s)\right)^2 \left(\Phi^h_{v_a}(Q_a)\right)^2 dZ_2\Big|_{Z_3=-\frac{M_A}{M_B}(Z+Z_2)} \tag{2.266}$$

and for $Z_3 = -M_A(Z + Z_2)/M_B$

$$Q_a = -\frac{M}{2M_B}(Z + Z_2) \tag{2.267}$$

(Eq. (2.213)), i.e.

$$\rho_{A_1}(\mathbf{R}) = \frac{1}{2\pi}\frac{M^3}{M_B^3}\left(\Phi^h_{v_b|l|}\left(\frac{M}{M_B}\rho\right)\right)^2 \int_{-\infty}^{\infty} \left(\Phi^h_{v_s}(Z_2 - Z - 2R_e)\right)^2 \left(\Phi^h_{v_a}\left(-\frac{M}{2M_B}(Z + Z_2)\right)\right)^2 dZ_2 \tag{2.268}$$

where $Q_s = Z_2 - Z - 2R_e$ (Eq. (2.212)) was used. With the definition of the integral

$$I_{v_s v_a}(Q) = \frac{M}{M_B}\int_{-\infty}^{\infty} \left(\Phi^h_{v_s}(Q' - Q)\right)^2 \left(\Phi^h_{v_a}\left(-\frac{M}{2M_B}(Q + Q')\right)\right)^2 dQ', \tag{2.269}$$

we obtain the simple form for the nuclear probability density of the nucleus A_1, using $Q = Z + R_e$ and $Q' = Z_2 - R_e$, i.e.

$$\rho_{A_1}(\mathbf{R}) = \frac{1}{2\pi}\frac{M^2}{M_B^2} I_{v_s v_a}(Z + R_e)\left(\Phi^h_{v_b|l|}\left(\frac{M}{M_B}\rho\right)\right)^2. \tag{2.270}$$

For symmetry reasons the nuclear probability density $\rho_{A_2}(\mathbf{R} = \mathbf{R}_2)$ of the nucleus $A_2 = A(\text{right})$ is

$$\rho_{A_2}(\mathbf{R}) = \frac{1}{2\pi}\frac{M^2}{M_B^2} I_{v_s v_a}(Z - R_e) \left(\Phi^h_{v_b|l|}\left(\frac{M}{M_B}\rho\right)\right)^2. \tag{2.271}$$

Since the total wavefunction $\Psi^{tot}_{v_s v_a v_b l 0}$ is normalized, the integrals of the nuclear probabilites densities $\rho_{A_1}(\mathbf{R})$ and $\rho_{A_2}(\mathbf{R})$ over the whole space must be equal to 1, i.e.

$$\int\int\int \rho_{A_1}(\mathbf{R})\, d\mathbf{R} = 1 \tag{2.272}$$

$$\int\int\int \rho_{A_2}(\mathbf{R})\, d\mathbf{R} = 1 \tag{2.273}$$

(cf. Eq. (2.257)). Using Eqs. (2.270), (2.271), $d\mathbf{R} = \rho\, d\rho\, dZ\, d\phi$ and the normalized wavefunction $\Phi^h_{v_b|l|}(Q_b)$ (Eq. (2.253)), we get

$$\begin{aligned} & \int\int\int \rho_{A_{1/2}}(\mathbf{R})\, d\mathbf{R} \qquad (2.274)\\ = \; & \frac{1}{2\pi}\frac{M^2}{M_B^2}\int_0^{2\pi} d\phi \int_{-\infty}^{\infty} I_{v_s v_a}(Z \pm R_e)\, dZ \int_0^{\infty} \left(\Phi^h_{v_b|l|}\left(\frac{M}{M_B}\rho\right)\right)^2 \rho\, d\rho \\ = \; & \int_{-\infty}^{\infty} I_{v_s v_a}(Z \pm R_e)\, dZ \int_0^{\infty} \left(\Phi^h_{v_b|l|}(Q_b)\right)^2 Q_b\, dQ_b \\ = \; & \int_{-\infty}^{\infty} I_{v_s v_a}(Z \pm R_e)\, dZ = 1, \end{aligned}$$

thus

$$\int_{-\infty}^{\infty} I_{v_s v_a}(Q)\, dQ = 1 \tag{2.275}$$

for all quantum numbers $v_s = 0, 1, 2, \ldots$ and $v_a = 0, 1, 2, \ldots$. For example, for $v_s = v_a = 0$, the harmonic wavefunctions for the symmetric and antisymmetric stretches (Eq. (2.245), (2.246)) are

$$\Phi^h_{v_s=0}(Q_s) = \left(\frac{s}{\pi}\right)^{1/4} e^{-\frac{1}{2}sQ_s^2} \tag{2.276}$$

$$\Phi^h_{v_a=0}(Q_a) = \left(\frac{a}{\pi}\right)^{1/4} e^{-\frac{1}{2}aQ_a^2}. \tag{2.277}$$

The corresponding integral $I_{00}(Q)$ (Eq. (2.269)) is

$$\begin{aligned} I_{00}(Q) &= \frac{1}{\sqrt{\pi}}\sqrt{\frac{4asM^2}{4sM_B^2 + aM^2}}\, e^{-\frac{4asM^2}{4sM_B^2+aM^2}Q^2} \qquad (2.278)\\ &= \sqrt{\frac{4aM^2}{4sM_B^2 + aM^2}}\left[\Phi^h_{v_s=0}\left(\sqrt{\frac{4aM^2}{4sM_B^2 + aM^2}}\, Q\right)\right]^2 \end{aligned}$$

(see Appendix A.1) and satisfies the normalization condition (2.275) automatically. Hence, for $v_s = v_a = 0$, the nuclear probability densities of the nuclei A_1 and A_2 (Eqs.

(2.270), (2.271)) are

$$\rho_{A_1}(\mathbf{R}) = \frac{1}{2\pi^{3/2}}\frac{M^2}{M_B^2}\sqrt{\frac{4asM^2}{4sM_B^2+aM^2}}\, e^{-\frac{4asM^2}{4sM_B^2+aM^2}(Z+R_e)^2}\left(\Phi^h_{v_b|l|}\left(\frac{M}{M_B}\,\rho\right)\right)^2 \quad (2.279)$$

$$\rho_{A_2}(\mathbf{R}) = \frac{1}{2\pi^{3/2}}\frac{M^2}{M_B^2}\sqrt{\frac{4asM^2}{4sM_B^2+aM^2}}\, e^{-\frac{4asM^2}{4sM_B^2+aM^2}(Z-R_e)^2}\left(\Phi^h_{v_b|l|}\left(\frac{M}{M_B}\,\rho\right)\right)^2. \quad (2.280)$$

The nuclear probability density $\rho_B(\mathbf{R}=\mathbf{R}_3)$ of the nucleus B in the electronic ground state $|\Psi_0^{el}\rangle$ is defined as

$$\rho_B(\mathbf{R}) = \int\int\int d\mathbf{R}_1 \int\int\int d\mathbf{R}_2 \int\ldots\int |\Psi^{tot}_{v_s v_a v_b l 0}(\mathbf{R}_1,\mathbf{R}_2,\mathbf{R},\mathbf{q}_1,\ldots,\mathbf{q}_N)|^2\, d\mathbf{q}_1\ldots d\mathbf{q}_N. \quad (2.281)$$

With the same procedure of the derivation for $\rho_{A_1}(\mathbf{R})$ we have

$$\begin{aligned}\rho_B(\mathbf{R}) = \frac{1}{2\pi}&\int_{-\infty}^{\infty} dX_1 \int_{-\infty}^{\infty} \delta(Q_{c,X})\delta(Q_{r,X})\, dX_2 \\ &\int_{-\infty}^{\infty} dY_1 \int_{-\infty}^{\infty} \delta(Q_{c,Y})\delta(Q_{r,Y}) \left(\Phi^h_{v_b|l|}(Q_b)\right)^2 dY_2 \\ &\int_{-\infty}^{\infty} dZ_1 \int_{-\infty}^{\infty} \delta(Q_{c,Z}) \left(\Phi^h_{v_s}(Q_s)\right)^2 \left(\Phi^h_{v_a}(Q_a)\right)^2 dZ_2,\end{aligned} \quad (2.282)$$

using $Q_{r,X} = X_2 - X_1$, $Q_{r,Y} = Y_2 - Y_1$ (Eqs. (2.219), (2.220))

$$\begin{aligned}\rho_B(\mathbf{R}) = \frac{1}{2\pi}&\int_{-\infty}^{\infty} \delta(Q_{c,X})\, dX_1 \int_{-\infty}^{\infty} \delta(Q_{c,Y}) \left(\Phi^h_{v_b|l|}(Q_b)\right)^2 dY_1\Big|_{X_2=X_1,Y_2=Y_1} \\ &\int_{-\infty}^{\infty} dZ_1 \int_{-\infty}^{\infty} \delta(Q_{c,Z}) \left(\Phi^h_{v_s}(Q_s)\right)^2 \left(\Phi^h_{v_a}(Q_a)\right)^2 dZ_2,\end{aligned} \quad (2.283)$$

and using $Q_{c,X} = (2M_A X_1 + M_B X)/M$ for $X_2 = X_1$ and $Q_{c,Y} = (2M_A Y_1 + M_B Y)/M$ for $Y_2 = Y_1$ (Eqs. (2.216), (2.217))

$$\begin{aligned}\rho_B(\mathbf{R}) = \frac{1}{8\pi}\frac{M^2}{M_A^2}&\left(\Phi^h_{v_b|l|}(Q_b)\right)^2\Big|_{\substack{X_2=X_1,Y_2=Y_1\\ X_1=-\frac{M_B}{2M_A}X\\ Y_1=-\frac{M_B}{2M_A}Y}} \\ &\int_{-\infty}^{\infty} dZ_1 \int_{-\infty}^{\infty} \delta(Q_{c,Z}) \left(\Phi^h_{v_s}(Q_s)\right)^2 \left(\Phi^h_{v_a}(Q_a)\right)^2 dZ_2.\end{aligned} \quad (2.284)$$

Since for $X_2 = X_1$, $X_1 = -M_B X/(2M_A)$ and $Y_2 = Y_1$, $Y_1 = -M_B Y/(2M_A)$

$$Q_{b,X} = \frac{M}{2M_A}\,X \quad (2.285)$$

$$Q_{b,Y} = \frac{M}{2M_A}\,Y \quad (2.286)$$

$$Q_b = \frac{M}{2M_A}\,\rho \quad (2.287)$$

(Eqs. (2.214), (2.215), (2.224) and $\rho = \sqrt{X^2 + Y^2}$), we obtain

$$\rho_B(\mathbf{R}) = \frac{1}{8\pi}\frac{M^2}{M_A^2}\left(\Phi^h_{v_b|l|}\left(\frac{M}{2M_A}\rho\right)\right)^2 \int_{-\infty}^{\infty} dZ_1 \int_{-\infty}^{\infty} \delta(Q_{c,Z})\left(\Phi^h_{v_s}(Q_s)\right)^2\left(\Phi^h_{v_a}(Q_a)\right)^2 dZ_2. \tag{2.288}$$

Using $Q_{c,Z} = (M_A(Z_1 + Z_2) + M_B Z)/M$ (Eq. (2.218)) yields

$$\rho_B(\mathbf{R}) = \frac{1}{8\pi}\frac{M^3}{M_A^3}\left(\Phi^h_{v_b|l|}\left(\frac{M}{2M_A}\rho\right)\right)^2 \int_{-\infty}^{\infty}\left(\Phi^h_{v_s}(Q_s)\right)^2\left(\Phi^h_{v_a}(Q_a)\right)^2 dZ_1\Big|_{Z_2=-\frac{M_B}{M_A}Z-Z_1} \tag{2.289}$$

and for $Z_2 = -M_B Z/M_A - Z_1$

$$Q_s = -\frac{M_B}{M_A}Z - 2Z_1 - 2R_e \tag{2.290}$$

$$Q_a = \frac{M}{2M_A}Z \tag{2.291}$$

(Eqs. (2.212), (2.213)), i.e.

$$\begin{aligned}\rho_B(\mathbf{R}) &= \frac{1}{8\pi}\frac{M^3}{M_A^3}\left(\Phi^h_{v_a}\left(\frac{M}{2M_A}Z\right)\right)^2\left(\Phi^h_{v_b|l|}\left(\frac{M}{2M_A}\rho\right)\right)^2 \\ &\qquad \int_{-\infty}^{\infty}\left(\Phi^h_{v_s}\left(-\frac{M_B}{M_A}Z - 2Z_1 - 2R_e\right)\right)^2 dZ_1 \\ &= \frac{1}{16\pi}\frac{M^3}{M_A^3}\left(\Phi^h_{v_a}\left(\frac{M}{2M_A}Z\right)\right)^2\left(\Phi^h_{v_b|l|}\left(\frac{M}{2M_A}\rho\right)\right)^2 \int_{-\infty}^{\infty}\left(\Phi^h_{v_s}(Q_s)\right)^2 dQ_s.\end{aligned} \tag{2.292}$$

Since the wavefunction $\Phi^h_{v_s}(Q_s)$ (Eq. (2.212)) is normalized, we have the final form for the nuclear probability density of the nucleus B

$$\rho_B(\mathbf{R}) = \frac{1}{16\pi}\frac{M^3}{M_A^3}\left(\Phi^h_{v_a}\left(\frac{M}{2M_A}Z\right)\right)^2\left(\Phi^h_{v_b|l|}\left(\frac{M}{2M_A}\rho\right)\right)^2 \tag{2.293}$$

where the normalization condition

$$\int\int\int \rho_B(\mathbf{R})\, d\mathbf{R} = 1 \tag{2.294}$$

is fulfilled automatically. Note that all stationary nuclear probability densities $\rho_{A_1}(\mathbf{R})$, $\rho_{A_2}(\mathbf{R})$ and $\rho_B(\mathbf{R})$ (Eqs. (2.270), (2.271), (2.293)) are independent of the azimuthal angle ϕ. Their densities along the Z-axis ($\rho = 0$) are zero for $l \neq 0$ (cf. Eq. (2.251)), i.e. they have toroidal structures with a nodal line along the Z-axis. However, for $l = 0$, the densities along the Z-axis ($\rho = 0$) are non-zero, and in addition for $v_b = 0$, they have ellipsoidal structures. The centers of the densities are located at $Z = \mp R_e$ and $Z = 0$ for nuclei A_1, A_2, and B, respectively. Furthermore, the densities $\rho_{A_1}(\mathbf{R})$ and $\rho_{A_2}(\mathbf{R})$ depend on all harmonic vibrational frequencies ω_s, ω_a, and ω_b (cf. Eqs. (2.270), (2.271), (2.247), (2.248), (2.251), (2.252)) whereas the density $\rho_B(\mathbf{R})$ (Eq. (2.293)) is independent of the quantum

number v_s and the vibrational frequency ω_s for the symmetric stretch since, in this mode, the nucleus B does not vibrate, i.e. Q_s is independent of Z_3 (cf. Eq. (2.212)). For the heavy nucleus B, i.e. $M_B \gg M_A$, the corresponding density $\rho_B(\mathbf{R})$ is strongly localized at the origin ($Z = 0$) whereas the distributions of the densities $\rho_{A_1}(\mathbf{R})$ and $\rho_{A_2}(\mathbf{R})$ of the other light nuclei A_1 and A_2 are broad. In the reverse case, i.e. $M_A \gg M_B$, the densities $\rho_{A_1}(\mathbf{R})$ and $\rho_{A_2}(\mathbf{R})$ are strongly localized at $Z = -R_e$ and $Z = R_e$, respectively, whereas the distribution of the density $\rho_B(\mathbf{R})$ of the light nucleus B is broad.

Finally, the total nuclear probability density within the Born-Oppenheimer and harmonic approximations is the sum of the probability densities of the nuclei A_1, A_2, and B, i.e.

$$\begin{aligned}\rho_{tot}(\mathbf{R}) &= \rho_{A_1}(\mathbf{R}) + \rho_{A_2}(\mathbf{R}) + \rho_B(\mathbf{R}) \\ &= \frac{1}{2\pi}\frac{M^2}{M_B^2}\left(I_{v_s v_a}(Z+R_e) + I_{v_s v_a}(Z-R_e)\right)\left(\Phi^h_{v_b|l|}\left(\frac{M}{M_B}\,\rho\right)\right)^2 \\ &\quad + \frac{1}{16\pi}\frac{M^3}{M_A^3}\left(\Phi^h_{v_a}\left(\frac{M}{2M_A}\,Z\right)\right)^2\left(\Phi^h_{v_b|l|}\left(\frac{M}{2M_A}\,\rho\right)\right)^2\end{aligned} \tag{2.295}$$

(cf. Eqs. (2.270), (2.271), (2.293)) where

$$\int\int\int \rho_{tot}(\mathbf{R})\, d\mathbf{R} = 3 \tag{2.296}$$

(cf. Eqs. (2.272), (2.273), (2.294)). Three nuclei exist in the molecular space.

2.4.4 Nuclear current density

The nuclear current density $\mathbf{j}_{A_1}(\mathbf{R} = \mathbf{R}_1)$ of the nucleus A_1 =A(left) in the electronic ground state $|\Psi_0^{el}\rangle$ within the Born-Oppenheimer and harmonic approximations is given by

$$\begin{aligned}\mathbf{j}_{A_1}(\mathbf{R}) &= \frac{i\hbar}{2M_A}\int\int\int d\mathbf{R}_2 \int\int\int d\mathbf{R}_3 \int\ldots\int d\mathbf{q}_1 \ldots d\mathbf{q}_N \\ &\quad \Big\{\Psi^{tot}_{v_s v_a v_b l 0}(\mathbf{R},\mathbf{R}_2,\mathbf{R}_3,\mathbf{q}_1,\ldots,\mathbf{q}_N)\nabla_{\mathbf{R}}\left[\Psi^{tot}_{v_s v_a v_b l 0}(\mathbf{R},\mathbf{R}_2,\mathbf{R}_3,\mathbf{q}_1,\ldots,\mathbf{q}_N)\right]^* \\ &\quad - \left[\Psi^{tot}_{v_s v_a v_b l 0}(\mathbf{R},\mathbf{R}_2,\mathbf{R}_3,\mathbf{q}_1,\ldots,\mathbf{q}_N)\right]^* \nabla_{\mathbf{R}}\Psi^{tot}_{v_s v_a v_b l 0}(\mathbf{R},\mathbf{R}_2,\mathbf{R}_3,\mathbf{q}_1,\ldots,\mathbf{q}_N)\Big\}.\end{aligned} \tag{2.297}$$

Since the nuclear wavefunctions $\Phi^h_{v_s}(Q_s)$, $\Phi^h_{v_a}(Q_a)$, $\Phi^h_{v_b|l|}(Q_b)$ (Eqs. (2.245), (2.246), (2.251)) are real and the electronic wavefunction $\Psi_0^{el}(\mathbf{q}_1,\ldots,\mathbf{q}_N;\mathbf{R}_1,\mathbf{R}_2,\mathbf{R}_3)$ of the electronic non-degenerate ground state $|\Psi_0^{el}\rangle$ can be designed as a real function (using real orbitals), we obtain, using Eqs. (2.256), (2.258) and $\nabla_{\mathbf{R}} = (\nabla_{\mathbf{R}}\delta)\partial/\partial\delta$,

$$\begin{aligned}\mathbf{j}_{A_1}(\mathbf{R}) &= \frac{i\hbar}{2M_A}\int_{-\infty}^{\infty}\delta(Q_{r,X})\,dX_2\int_{-\infty}^{\infty}\delta(Q_{c,X})\,dX_3\int_{-\infty}^{\infty}\delta(Q_{r,Y})\,dY_2 \\ &\int_{-\infty}^{\infty}\delta(Q_{c,Y})\left(\Phi^h_{v_b|l|}(Q_b)\right)^2\left[\Phi_l(\delta)\frac{\partial}{\partial\delta}\Phi_l^*(\delta)-\Phi_l^*(\delta)\frac{\partial}{\partial\delta}\Phi_l(\delta)\right](\nabla_{\mathbf{R}}\delta)\,dY_3 \\ &\int_{-\infty}^{\infty}dZ_2\int_{-\infty}^{\infty}\delta(Q_{c,Z})\left(\Phi^h_{v_s}(Q_s)\right)^2\left(\Phi^h_{v_a}(Q_a)\right)^2 dZ_3.\end{aligned} \tag{2.298}$$

With $\Phi_l = e^{il\delta}/\sqrt{2\pi}$ (Eq. (2.236)) we have

$$\begin{aligned}\mathbf{j}_{A_1}(\mathbf{R}) &= \frac{l\hbar}{2\pi M_A}\int_{-\infty}^{\infty}\delta(Q_{r,X})\,dX_2\int_{-\infty}^{\infty}\delta(Q_{c,X})\,dX_3\int_{-\infty}^{\infty}\delta(Q_{r,Y})\,dY_2 \\ &\int_{-\infty}^{\infty}\delta(Q_{c,Y})\left(\Phi^h_{v_b|l|}(Q_b)\right)^2(\nabla_{\mathbf{R}}\delta)\,dY_3 \\ &\int_{-\infty}^{\infty}dZ_2\int_{-\infty}^{\infty}\delta(Q_{c,Z})\left(\Phi^h_{v_s}(Q_s)\right)^2\left(\Phi^h_{v_a}(Q_a)\right)^2 dZ_3.\end{aligned} \tag{2.299}$$

With $Q_{r,X} = X_2 - X$, $Q_{r,Y} = Y_2 - Y$, $Q_{c,X} = (2M_AX + M_BX_3)/M$ for $X_2 = X$, and $Q_{c,Y} = (2M_AY + M_BY_3)/M$ for $Y_2 = Y$ (Eqs. (2.219), (2.220), (2.216), (2.217)), it leads to

$$\begin{aligned}\mathbf{j}_{A_1}(\mathbf{R}) &= \frac{l\hbar}{2\pi M_A}(\nabla_{\mathbf{R}}\delta)\Big|_{\substack{X_2=X,Y_2=Y\\ X_3=-\frac{2M_A}{M_B}X\\ Y_3=-\frac{2M_A}{M_B}Y}} \\ &\int_{-\infty}^{\infty}\delta(Q_{r,X})\,dX_2\int_{-\infty}^{\infty}\delta(Q_{c,X})\,dX_3\int_{-\infty}^{\infty}\delta(Q_{r,Y})\,dY_2 \\ &\int_{-\infty}^{\infty}\delta(Q_{c,Y})\left(\Phi^h_{v_b|l|}(Q_b)\right)^2 dY_3\int_{-\infty}^{\infty}dZ_2\int_{-\infty}^{\infty}\delta(Q_{c,Z})\left(\Phi^h_{v_s}(Q_s)\right)^2\left(\Phi^h_{v_a}(Q_a)\right)^2 dZ_3 \\ &= \frac{l\hbar}{M_A}\rho_{A_1}(\mathbf{R})(\nabla_{\mathbf{R}}\delta)\Big|_{\substack{X_2=X,Y_2=Y\\ X_3=-\frac{2M_A}{M_B}X\\ Y_3=-\frac{2M_A}{M_B}Y}}\end{aligned} \tag{2.300}$$

where the expression for the nuclear probability density $\rho_{A_1}(\mathbf{R})$ (Eq. (2.259), (2.270)) was used in the last step. Now, let us evaluate $\nabla_{\mathbf{R}}\delta$ using the definition of the Nabla operator in Cartesian coordinates ($\mathbf{R} = \mathbf{R}_1$)

$$\nabla_{\mathbf{R}} = \frac{\partial}{\partial X}\mathbf{e}_X + \frac{\partial}{\partial Y}\mathbf{e}_Y + \frac{\partial}{\partial Z}\mathbf{e}_Z. \tag{2.301}$$

Since $\delta = \arccos(Q_{b,X}/Q_b)$ (Eq. (2.225)) is independent of Z, we obtain

$$\nabla_{\mathbf{R}}\delta = \frac{\partial\delta}{\partial X}\mathbf{e}_X + \frac{\partial\delta}{\partial Y}\mathbf{e}_Y. \tag{2.302}$$

Using the derivation for the inverse trigonometric function $d\arccos(x)/dx = -1/\sqrt{1-x^2}$ [253] we have

$$\nabla_{\mathbf{R}}\delta = -\frac{1}{\sqrt{1-\left(\frac{Q_{b,X}}{Q_b}\right)^2}}\left(\frac{\partial}{\partial X}\left(\frac{Q_{b,X}}{Q_b}\right)\mathbf{e}_X + \frac{\partial}{\partial Y}\left(\frac{Q_{b,X}}{Q_b}\right)\mathbf{e}_Y\right) \tag{2.303}$$

$$
\begin{aligned}
&= -\frac{Q_b}{\sqrt{Q_b^2 - Q_{b,X}^2}} \left(\left(\frac{1}{Q_b} \frac{\partial Q_{b,X}}{\partial X} - \frac{Q_{b,X}}{Q_b^2} \frac{\partial Q_b}{\partial X} \right) \mathbf{e}_X + \left(\frac{1}{Q_b} \frac{\partial Q_{b,X}}{\partial Y} - \frac{Q_{b,X}}{Q_b^2} \frac{\partial Q_b}{\partial Y} \right) \mathbf{e}_Y \right) \\
&= -\frac{1}{Q_{b,Y}} \left(\left(\frac{\partial Q_{b,X}}{\partial X} - \frac{Q_{b,X}}{Q_b} \frac{\partial Q_b}{\partial X} \right) \mathbf{e}_X - \frac{Q_{b,X}}{Q_b} \frac{\partial Q_b}{\partial Y} \mathbf{e}_Y \right)
\end{aligned}
$$

since $Q_{b,Y} = \sqrt{Q_b^2 - Q_{b,X}^2}$ (Eq. (2.224)) and $Q_{b,X}$ (Eq. (2.214)) is independent of Y. With $Q_b = \sqrt{Q_{b,X}^2 + Q_{b,Y}^2}$ (Eq. (2.224)) it yields

$$
\begin{aligned}
\nabla_{\mathbf{R}} \delta &= -\frac{1}{Q_{b,Y}} \left(\left(\frac{\partial Q_{b,X}}{\partial X} - \frac{Q_{b,X}}{2Q_b^2} \frac{\partial \left(Q_{b,X}^2 + Q_{b,Y}^2 \right)}{\partial X} \right) \mathbf{e}_X - \frac{Q_{b,X}}{2Q_b^2} \frac{\partial \left(Q_{b,X}^2 + Q_{b,Y}^2 \right)}{\partial Y} \mathbf{e}_Y \right) \qquad (2.304) \\
&= -\frac{1}{Q_{b,Y}} \left(\left(\frac{\partial Q_{b,X}}{\partial X} - \frac{Q_{b,X}^2}{Q_b^2} \frac{\partial Q_{b,X}}{\partial X} \right) \mathbf{e}_X - \frac{Q_{b,X} Q_{b,Y}}{Q_b^2} \frac{\partial Q_{b,Y}}{\partial Y} \mathbf{e}_Y \right) \\
&= -\frac{1}{Q_{b,Y}} \left(\frac{Q_{b,Y}^2}{Q_b^2} \frac{\partial Q_{b,X}}{\partial X} \mathbf{e}_X - \frac{Q_{b,X} Q_{b,Y}}{Q_b^2} \frac{\partial Q_{b,Y}}{\partial Y} \mathbf{e}_Y \right) \\
&= -\frac{1}{Q_b^2} \left(Q_{b,Y} \frac{\partial Q_{b,X}}{\partial X} \mathbf{e}_X - Q_{b,X} \frac{\partial Q_{b,Y}}{\partial Y} \mathbf{e}_Y \right),
\end{aligned}
$$

again using the fact that $Q_{b,X}$ and $Q_{b,Y}$ (Eqs. (2.214) and (2.215)) are independent of Y and X, respectively, and $Q_{b,Y}^2 = Q_b^2 - Q_{b,X}^2$ (Eq. (2.224)). With $Q_{b,X} = X_3 - (X + X_2)/2$ (Eq. (2.214)) and $Q_{b,Y} = Y_3 - (Y + Y_2)/2$ (Eq. (2.215)) it reduces to

$$
\nabla_{\mathbf{R}} \delta = \frac{1}{2Q_b^2} \left(Q_{b,Y} \mathbf{e}_X - Q_{b,X} \mathbf{e}_Y \right). \qquad (2.305)
$$

Thus, for $X_2 = X$, $X_3 = -2M_A X/M_B$ and $Y_2 = Y$, $Y_3 = -2M_A Y/M_B$, i.e. using Eqs. (2.262)–(2.264)),

$$
\begin{aligned}
(\nabla_{\mathbf{R}} \delta)\Big|_{\substack{X_2 = X, Y_2 = Y \\ X_3 = -\frac{2M_A}{M_B} X \\ Y_3 = -\frac{2M_A}{M_B} Y}} &= -\frac{M_B}{2M\rho^2} \left(Y \mathbf{e}_X - X \mathbf{e}_Y \right) \qquad (2.306) \\
&= -\frac{M_B}{2M\rho} \left(\sin\phi \, \mathbf{e}_X - \cos\phi \, \mathbf{e}_Y \right) \\
&= \frac{M_B}{2M\rho} \mathbf{e}_\phi
\end{aligned}
$$

where $X = \rho \cos\phi$, $Y = \rho \sin\phi$, and $\mathbf{e}_\phi = -\sin\phi \, \mathbf{e}_X + \cos\phi \, \mathbf{e}_Y$ were used. Hence, the nuclear current density $\mathbf{j}_{A_1}(\mathbf{R})$ (Eq. (2.300)) of the nucleus A_1 is

$$
\mathbf{j}_{A_1}(\mathbf{R}) = \frac{l\hbar M_B}{2MM_A} \frac{\rho_{A_1}(\mathbf{R})}{\rho} \mathbf{e}_\phi. \qquad (2.307)
$$

For symmetry reasons, the nuclear current density of the nucleus A_2 is

$$
\mathbf{j}_{A_2}(\mathbf{R}) = \frac{l\hbar M_B}{2MM_A} \frac{\rho_{A_2}(\mathbf{R})}{\rho} \mathbf{e}_\phi. \qquad (2.308)
$$

The corresponding nuclear current density $\mathbf{j}_B(\mathbf{R} = \mathbf{R}_3)$ of the nucleus B in the electronic ground state $|\Psi_0^{el}\rangle$ is

$$\begin{aligned}\mathbf{j}_B(\mathbf{R}) &= \frac{i\hbar}{2M_B} \int\int\int d\mathbf{R}_1 \int\int\int d\mathbf{R}_2 \int \ldots \int d\mathbf{q}_1 \ldots d\mathbf{q}_N \\ &\Big\{\Psi^{tot}_{v_s v_a v_b l 0}(\mathbf{R}_1, \mathbf{R}_2, \mathbf{R}, \mathbf{q}_1, \ldots, \mathbf{q}_N) \nabla_{\mathbf{R}} \Big[\Psi^{tot}_{v_s v_a v_b l 0}(\mathbf{R}_1, \mathbf{R}_2, \mathbf{R}, \mathbf{q}_1, \ldots, \mathbf{q}_N)\Big]^* \\ &- \Big[\Psi^{tot}_{v_s v_a v_b l 0}(\mathbf{R}_1, \mathbf{R}_2, \mathbf{R}, \mathbf{q}_1, \ldots, \mathbf{q}_N)\Big]^* \nabla_{\mathbf{R}} \Psi^{tot}_{v_s v_a v_b l 0}(\mathbf{R}_1, \mathbf{R}_2, \mathbf{R}, \mathbf{q}_1, \ldots, \mathbf{q}_N)\Big\} .\end{aligned} \tag{2.309}$$

In an analogous way (cf. Eqs. (2.297)–(2.300), (2.282)–(2.284)), the current density reduces to

$$\mathbf{j}_B(\mathbf{R}) = \frac{l\hbar}{M_B} \rho_B(\mathbf{R}) \left(\nabla_{\mathbf{R}} \delta\right)\Big|_{\substack{X_2 = X_1, Y_2 = Y_1 \\ X_1 = -\frac{M_B}{2M_A} X \\ Y_1 = -\frac{M_B}{2M_A} Y}} . \tag{2.310}$$

For $\mathbf{R} = \mathbf{R}_3$ the evaluation of $\nabla_{\mathbf{R}} \delta$ is the same as in Eqs. (2.302)–(2.304) but for $Q_{b,X} = X - (X_1 + X_2)/2$ (Eq. (2.214)) and $Q_{b,Y} = Y - (Y_1 + Y_2)/2$ (Eq. (2.215)) we obtain

$$\begin{aligned}\nabla_{\mathbf{R}} \delta &= -\frac{1}{Q_b^2} \left(Q_{b,Y} \frac{\partial Q_{b,X}}{\partial X} \mathbf{e}_X - Q_{b,X} \frac{\partial Q_{b,Y}}{\partial Y} \mathbf{e}_Y \right) \\ &= -\frac{1}{Q_b^2} \left(Q_{b,Y} \mathbf{e}_X - Q_{b,X} \mathbf{e}_Y \right) .\end{aligned} \tag{2.311}$$

For $X_2 = X_1$, $X_1 = -M_B X/(2M_A)$ and $Y_2 = Y_1$, $Y_1 = -M_B Y/(2M_A)$, i.e. using Eqs. (2.285)–(2.287)), $X = \rho \cos\phi$, $Y = \rho \sin\phi$, and $\mathbf{e}_\phi = -\sin\phi\, \mathbf{e}_X + \cos\phi\, \mathbf{e}_Y$, we obtain

$$\begin{aligned}\left(\nabla_{\mathbf{R}} \delta\right)\Big|_{\substack{X_2 = X_1, Y_2 = Y_1 \\ X_1 = -\frac{M_B}{2M_A} X \\ Y_1 = -\frac{M_B}{2M_A} Y}} &= -\frac{2M_A}{M\rho^2} \left(Y \mathbf{e}_X - X \mathbf{e}_Y \right) \\ &= -\frac{2M_A}{M\rho} \left(\sin\phi\, \mathbf{e}_X - \cos\phi\, \mathbf{e}_Y \right) \\ &= \frac{2M_A}{M\rho} \mathbf{e}_\phi .\end{aligned} \tag{2.312}$$

Thus, the nuclear current density $\mathbf{j}_B(\mathbf{R})$ (Eq. (2.310)) of the nucleus B is

$$\mathbf{j}_B(\mathbf{R}) = \frac{2l\hbar M_A}{M M_B} \frac{\rho_B(\mathbf{R})}{\rho} \mathbf{e}_\phi \tag{2.313}$$

and independent of the quantum number v_s and the vibrational frequency ω_s for the symmetric stretch (cf. Eq. (2.293)). Note that the expressions for the nuclear current densities $\mathbf{j}_{A_1}(\mathbf{R})$, $\mathbf{j}_{A_2}(\mathbf{R})$, and $\mathbf{j}_B(\mathbf{R})$ (Eqs. (2.307), (2.308), (2.313)) are similar to the one for the electronic current density in atoms, atomic ions, and linear molecules (cf. Eq. (2.38)). The total nuclear current density can be written as

$$\begin{aligned}\mathbf{j}_{tot}(\mathbf{R}) &= \mathbf{j}_{A_1}(\mathbf{R}) + \mathbf{j}_{A_2}(\mathbf{R}) + \mathbf{j}_B(\mathbf{R}) \\ &= \frac{l\hbar}{M\rho} \left(\frac{M_B}{2M_A} \left(\rho_{A_1}(\mathbf{R}) + \rho_{A_2}(\mathbf{R}) \right) + \frac{2M_A}{M_B} \rho_B(\mathbf{R}) \right) \mathbf{e}_\phi .\end{aligned} \tag{2.314}$$

2.4.5 Nuclear ring currents

As in the theory of electronic ring currents in atoms, atomic ions, and linear molecules (cf. Eq. (2.38)), the total nuclear current density $\mathbf{j}_{tot}(\mathbf{R})$ (Eq. (2.314)) is proportional to the pseudorotational quantum number l and vanishes for $l = 0$. Its ϕ-component is the only one which does not vanish, and it is independent of the azimuthal angle ϕ because the probability densities $\rho_{A_1}(\mathbf{R})$, $\rho_{A_2}(\mathbf{R})$, and $\rho_B(\mathbf{R})$ (Eqs. (2.270), (2.271), (2.293)) are also independent of ϕ. Thus, the state $|\Psi^{tot}_{v_s v_a v_b l 0}\rangle$ with $l \neq 0$ represents the stationary toroidal ring currents of the nuclei A_1, A_2, and B about the Z-axis where the sign of l determines the direction of these nuclear ring currents.

Now, let us first calculate the mean angular momenta of the nuclei A_1, A_2, and B, to show that the Z-component of the total angular momentum is in fact equal to $l\hbar$ and that the corresponding X- and Y-components are zero. The formula for the mean angular momentum of the the nucleus A_1 is given as

$$\begin{aligned}\langle \hat{\mathbf{L}}_{A_1} \rangle &= \int\int\int d\mathbf{R}_1 \int\int\int d\mathbf{R}_2 \int\int\int d\mathbf{R}_3 \int \ldots \int d\mathbf{q}_1 \ldots d\mathbf{q}_N \\ &\quad \left[\Psi^{tot}_{v_s v_a v_b l 0}(\mathbf{R}_1, \mathbf{R}_2, \mathbf{R}_3, \mathbf{q}_1, \ldots, \mathbf{q}_N)\right]^* \hat{\mathbf{L}}_{A_1} \Psi^{tot}_{v_s v_a v_b l 0}(\mathbf{R}_1, \mathbf{R}_2, \mathbf{R}_3, \mathbf{q}_1, \ldots, \mathbf{q}_N)\end{aligned} \tag{2.315}$$

where the angular momentum operator $\hat{\mathbf{L}}_{A_1}$ is defined as

$$\hat{\mathbf{L}}_{A_1} = -i\hbar \left(\mathbf{R}_1 \times \nabla_{\mathbf{R}_1}\right). \tag{2.316}$$

Since the expectation value $\langle \hat{\mathbf{L}}_{A_1} \rangle$ is real, Eq. (2.315) can be rewritten as

$$\langle \hat{\mathbf{L}}_{A_1} \rangle = \frac{1}{2}\left(\langle \hat{\mathbf{L}}_{A_1} \rangle + \langle \hat{\mathbf{L}}_{A_1} \rangle^*\right) \tag{2.317}$$

$$\begin{aligned}&= \frac{i\hbar}{2} \int\int\int d\mathbf{R}_1 \int\int\int d\mathbf{R}_2 \int\int\int d\mathbf{R}_3 \int \ldots \int d\mathbf{q}_1 \ldots d\mathbf{q}_N \\ &\quad \Big\{\Psi^{tot}_{v_s v_a v_b l 0}(\mathbf{R}_1, \mathbf{R}_2, \mathbf{R}_3, \mathbf{q}_1, \ldots, \mathbf{q}_N) \\ &\qquad (\mathbf{R}_1 \times \nabla_{\mathbf{R}_1}) \left[\Psi^{tot}_{v_s v_a v_b l 0}(\mathbf{R}_1, \mathbf{R}_2, \mathbf{R}_3, \mathbf{q}_1, \ldots, \mathbf{q}_N)\right]^* \\ &\quad - \left[\Psi^{tot}_{v_s v_a v_b l 0}(\mathbf{R}_1, \mathbf{R}_2, \mathbf{R}_3, \mathbf{q}_1, \ldots, \mathbf{q}_N)\right]^* \\ &\qquad (\mathbf{R}_1 \times \nabla_{\mathbf{R}_1}) \Psi^{tot}_{v_s v_a v_b l 0}(\mathbf{R}_1, \mathbf{R}_2, \mathbf{R}_3, \mathbf{q}_1, \ldots, \mathbf{q}_N)\Big\}.\end{aligned}$$

The evaluation of this equation is similar to the one of the equation for $\mathbf{j}_{A_1}(\mathbf{R})$ (cf. Eqs. (2.297)–(2.300)), i.e. the intermediate result, using $\mathbf{R}_1 \times \nabla_{\mathbf{R}_1} = (\mathbf{R}_1 \times \nabla_{\mathbf{R}_1}\delta)\partial/\partial\delta$, is

$$\langle \hat{\mathbf{L}}_{A_1} \rangle = l\hbar \int_{-\infty}^{\infty} dX_1 \int_{-\infty}^{\infty} dY_1 \int_{-\infty}^{\infty} \rho_{A_1}(\mathbf{R}_1) \left(\mathbf{R}_1 \times \nabla_{\mathbf{R}_1}\delta\right) \Big|_{\substack{X_2 = X_1, Y_2 = Y_1 \\ X_3 = -\frac{2M_A}{M_B} X_1 \\ Y_3 = -\frac{2M_A}{M_B} Y_1}} dZ_1. \tag{2.318}$$

Using Eq. (2.306), $\mathbf{R}_1 = \rho_1 \mathbf{e}_\rho + Z_1 \mathbf{e}_Z$, and $dX_1\, dY_1\, dZ_1 = \rho_1\, d\rho_1\, dZ_1\, d\phi_1$ expressed in cylindrial coordinates, we obtain

$$\langle \hat{\mathbf{L}}_{A_1} \rangle = \frac{l\hbar M_B}{2M} \int_0^{\infty} d\rho_1 \int_{-\infty}^{\infty} dZ_1 \int_0^{2\pi} \rho_{A_1}(\mathbf{R}_1)(\rho_1 \mathbf{e}_\rho + Z_1 \mathbf{e}_Z) \times \mathbf{e}_\phi\, d\phi_1 \tag{2.319}$$

$$= \frac{\pi l\hbar M_B}{M}\int_0^\infty d\rho_1 \int_{-\infty}^\infty \rho_{A_1}(\mathbf{R}_1)(\rho_1\mathbf{e}_Z - Z_1\mathbf{e}_\rho)\,dZ_1$$

where $\mathbf{e}_\rho \times \mathbf{e}_\phi = \mathbf{e}_Z$, $\mathbf{e}_Z \times \mathbf{e}_\phi = -\mathbf{e}_\rho$, and the ϕ_1-integration was easily carried out because the integrand is independent of ϕ_1. With Eq. (2.270) we obtain

$$\begin{aligned}\langle\hat{\mathbf{L}}_{A_1}\rangle &= \frac{l\hbar M}{2M_B}\int_0^\infty \left(\Phi^h_{v_b|l|}\left(\frac{M}{M_B}\,\rho_1\right)\right)^2 d\rho_1 \int_{-\infty}^\infty I_{v_s v_a}(Z_1+R_e)(\rho_1\mathbf{e}_Z - Z_1\mathbf{e}_\rho)\,dZ_1 \qquad (2.320)\\ &= \frac{l\hbar M}{2M_B}\int_0^\infty \left(\Phi^h_{v_b|l|}\left(\frac{M}{M_B}\,\rho_1\right)\right)^2 d\rho_1 \\ &\qquad \left(\rho_1\int_{-\infty}^\infty I_{v_s v_a}(Z_1+R_e)\,dZ_1\mathbf{e}_Z - \int_{-\infty}^\infty I_{v_s v_a}(Z_1+R_e)Z_1\,dZ_1\mathbf{e}_\rho\right).\end{aligned}$$

The integrands $I_{v_s v_a}(Z_1+R)$ (Eq. (2.269)) and $I_{v_s v_a}(Z_1+R)Z_1$ are even and odd functions in Z_1, thus the corresponding integrals are 1 (Eq. (2.275)) and 0, respectively, i.e.

$$\begin{aligned}\langle\hat{\mathbf{L}}_{A_1}\rangle &= \frac{l\hbar M}{2M_B}\int_0^\infty \left(\Phi^h_{v_b|l|}\left(\frac{M}{M_B}\,\rho_1\right)\right)^2 \rho_1\,d\rho_1\mathbf{e}_Z \qquad (2.321)\\ &= \frac{l\hbar M_B}{2M}\int_0^\infty \left(\Phi^h_{v_b|l|}\left(Q_b\right)\right)^2 Q_b\,dQ_b\mathbf{e}_Z \\ &= \frac{M_B}{2M}\,l\hbar\,\mathbf{e}_Z\end{aligned}$$

since $\Phi^h_{v_b|l|}(Q_b)$ is normalized (Eq. (2.253)). For symmetry reasons, the mean angular momentum of the nucleus A_2 is

$$\langle\hat{\mathbf{L}}_{A_2}\rangle = \frac{M_B}{2M}\,l\hbar\,\mathbf{e}_Z. \qquad (2.322)$$

The mean angular momentum of the nucleus B is evaluated in the almost same manner but using Eq. (2.312) instead of Eq. (2.306), i.e.

$$\langle\hat{\mathbf{L}}_B\rangle = \frac{4\pi l\hbar M_A}{M}\int_0^\infty d\rho_3\int_{-\infty}^\infty \rho_B(\mathbf{R}_3)(\rho_3\mathbf{e}_Z - Z_3\mathbf{e}_\rho)\,dZ_3 \qquad (2.323)$$

(cf. Eq. (2.319)). With Eq. (2.293) we obtain

$$\langle\hat{\mathbf{L}}_B\rangle = \frac{l\hbar M^2}{4M_A^2}\int_0^\infty \left(\Phi^h_{v_b|l|}\left(\frac{M}{2M_A}\,\rho_3\right)\right)^2 d\rho_3\int_{-\infty}^\infty \left(\Phi^h_{v_a}\left(\frac{M}{2M_A}\,Z_3\right)\right)^2 (\rho_3\mathbf{e}_Z - Z_3\mathbf{e}_\rho)\,dZ_3 \qquad (2.324)$$

$$\begin{aligned}&= \frac{l\hbar M^2}{4M_A^2}\int_0^\infty \left(\Phi^h_{v_b|l|}\left(\frac{M}{2M_A}\,\rho_3\right)\right)^2 d\rho_3 \\ &\qquad \left(\rho_3\int_{-\infty}^\infty \left(\Phi^h_{v_a}\left(\frac{M}{2M_A}\,Z_3\right)\right)^2 dZ_3\mathbf{e}_Z - \int_{-\infty}^\infty \left(\Phi^h_{v_a}\left(\frac{M}{2M_A}\,Z_3\right)\right)^2 Z_3\,dZ_3\mathbf{e}_\rho\right)\\ &= \frac{l\hbar M^2}{4M_A^2}\int_0^\infty \left(\Phi^h_{v_b|l|}\left(\frac{M}{2M_A}\,\rho_3\right)\right)^2 \rho_3\,d\rho_3\int_{-\infty}^\infty \left(\Phi^h_{v_a}\left(\frac{M}{2M_A}\,Z_3\right)\right)^2 dZ_3\mathbf{e}_Z\end{aligned}$$

since the integrand of the third integral is an odd function in Z_3. The functions $\Phi^h_{v_a}(Q_a)$ and $\Phi^h_{v_b|l|}(Q_b)$ are normalized, thus

$$\begin{aligned}\langle\hat{\mathbf{L}}_B\rangle &= \frac{2l\hbar M_A}{M}\int_0^\infty \left(\Phi^h_{v_b|l|}\left(Q_b\right)\right)^2 Q_b\,dQ_b\int_{-\infty}^\infty \left(\Phi^h_{v_a}\left(Q_a\right)\right)^2 dQ_a\mathbf{e}_Z \qquad (2.325)\\ &= \frac{2M_A}{M}\,l\hbar\,\mathbf{e}_Z.\end{aligned}$$

Finally, the total angular momentum is

$$\begin{aligned}\langle\hat{\mathbf{L}}_{tot}\rangle &= \langle\hat{\mathbf{L}}_{A_1}\rangle + \langle\hat{\mathbf{L}}_{A_2}\rangle + \langle\hat{\mathbf{L}}_B\rangle \\ &= \frac{1}{M}\left(\frac{M_B}{2} + \frac{M_B}{2} + 2M_A\right) l\hbar\,\mathbf{e}_Z \\ &= l\hbar\,\mathbf{e}_Z\end{aligned} \tag{2.326}$$

since $M = 2M_A + M_B$, i.e. its Z-component is equal to $l\hbar$ as expected.

The electric ring current of the nuclei in the stationary state $|\Psi^{tot}_{v_s v_a v_b l 0}\rangle$ is determined by

$$\begin{aligned}I_{tot} &= I_{A_1} + I_{A_2} + I_B \\ &= \tilde{Z}_A e \int\int (\mathbf{j}_{A_1}(\mathbf{R}) + \mathbf{j}_{A_2}(\mathbf{R})) \cdot d\mathbf{S} + \tilde{Z}_B e \int\int \mathbf{j}_B(\mathbf{R}) \cdot d\mathbf{S}\end{aligned} \tag{2.327}$$

(cf. Eq. (2.55)) where $\tilde{Z}_A$ and $\tilde{Z}_B$ are the nuclear charges of the nuclei A and B, respectively. The integral is over the half plane perpendicular to the X/Y plane at a fixed arbitrary azimuthal angle ϕ with domains $\rho \in [0,\infty)$, $Z \in (-\infty,\infty)$ ($d\mathbf{S} = d\rho\, dZ\, \mathbf{e}_\phi$) since the nuclear current densities $\mathbf{j}_{A_1}(\mathbf{R})$, $\mathbf{j}_{A_2}(\mathbf{R})$, $\mathbf{j}_B(\mathbf{R})$ (Eqs. (2.307), (2.308), (2.313)) are independent of ϕ. Note that for $l = 0$, the electric ring current is zero, i.e. $I_{tot} = 0$. With Eqs. (2.307), (2.308), (2.313) and (2.270), (2.271), (2.293) we have for $l \neq 0$

$$I_{tot} = \tilde{Z}_A e \int_0^\infty d\rho \int_{-\infty}^\infty (\mathbf{j}_{A_1}(\mathbf{R}) + \mathbf{j}_{A_2}(\mathbf{R})) \cdot \mathbf{e}_\phi\, dZ + \tilde{Z}_B e \int_0^\infty d\rho \int_{-\infty}^\infty \mathbf{j}_B(\mathbf{R}) \cdot \mathbf{e}_\phi\, dZ \tag{2.328}$$

$$\begin{aligned}&= \frac{el\hbar}{M}\left(\frac{\tilde{Z}_A M_B}{2M_A}\int_0^\infty \frac{d\rho}{\rho}\int_{-\infty}^\infty (\rho_{A_1}(\mathbf{R}) + \rho_{A_2}(\mathbf{R}))\, dZ + \frac{2\tilde{Z}_B M_A}{M_B}\int_0^\infty \frac{d\rho}{\rho}\int_{-\infty}^\infty \rho_B(\mathbf{R})\, dZ\right) \\ &= \frac{el\hbar M}{4\pi M_A M_B}\left(\tilde{Z}_A \int_0^\infty \left(\Phi^h_{v_b|l|}\left(\frac{M}{M_B}\rho\right)\right)^2 \frac{d\rho}{\rho}\int_{-\infty}^\infty (I_{v_s v_a}(Z + R_e) + I_{v_s v_a}(Z - R_e))\, dZ \right. \\ &\qquad \left. + \frac{\tilde{Z}_B M}{2M_A}\int_0^\infty \left(\Phi^h_{v_b|l|}\left(\frac{M}{2M_A}\rho\right)\right)^2 \frac{d\rho}{\rho}\int_{-\infty}^\infty \left(\Phi^h_{v_a}\left(\frac{M}{2M_A}Z\right)\right)^2 dZ\right).\end{aligned}$$

Using Eq. (2.275) and the normalized wavefunction $\Phi^h_{v_a}(Q_a)$, we obtain

$$I_{tot} = \frac{el\hbar M}{4\pi M_A M_B}(2\tilde{Z}_A + \tilde{Z}_B)\int_0^\infty \left(\Phi^h_{v_b|l|}(Q_b)\right)^2 Q_b^{-1}\, dQ_b. \tag{2.329}$$

The integral is evaluated as

$$I_{-1} = \int_0^\infty \left(\Phi^h_{v_b|l|}(Q_b)\right)^2 Q_b^{-1}\, dQ_b = \frac{b}{|l|} \tag{2.330}$$

(see Appendix A.2.4). Hence, the electric ring current, using Eq. (2.252),

$$I_{tot} = \mathrm{sgn}(l)\,\frac{e\omega_b}{2\pi}\,(2\tilde{Z}_A + \tilde{Z}_B) \tag{2.331}$$

and the corresponding components

$$I_A = I_{A_1} = I_{A_2} = \mathrm{sgn}(l)\,\frac{\tilde{Z}_A e\omega_b}{2\pi} \tag{2.332}$$

$$I_B = \mathrm{sgn}(l)\,\frac{\tilde{Z}_B e\omega_b}{2\pi} \tag{2.333}$$

for $l \neq 0$ are independent of all quantum numbers except for the sign of the pseudorotational number l which determines the direction of the nuclear ring currents. Thus, the magnitudes of the corresponding electric ring currents in the harmonic approximation are equal in all vibrational and pseudorotational states of the linear triatomic ABA molecule with non-zero pseudorotational quantum number ($l \neq 0$). Furthermore, the magnitudes are proportional to the harmonic bending frequency ω_b but they are independent of the harmonic frequencies for the stretches ω_s and ω_a, and also of the equilibrium bond length R_e. The electric ring currents of the nuclei A_1 and A_2 (Eq. (2.332)) are equal and proportional to their nuclear charge $\tilde{Z}_A$ whereas that of the nucleus B (Eq. (2.333)) is proportional to its nuclear charge $\tilde{Z}_B$. Thus, the corresponding electric ring currents are strong for nuclei with large nuclear charges $\tilde{Z}_A$ and $\tilde{Z}_B$, and for high harmonic bending frequency ω_b.

The periods of the nuclei A_1, A_2, and B about the Z-axis in the harmonic approximation are equal, i.e.

$$T = T_{A_1} = T_{A_2} = T_B = \frac{\tilde{Z}_A e}{|I_{A_1}|} = \frac{\tilde{Z}_B e}{|I_B|} = \frac{2\pi}{\omega_b} \tag{2.334}$$

(cf. Eq. (2.60)), as expected in classical mechanics.

2.4.6 Induced magnetic fields

The stationary nuclear ring currents with non-zero pseudorotational quantum number ($l \neq 0$) induce magnetic fields according to the Biot-Savart law. The induced magnetic fields along the Z-axis are calculated as

$$\mathbf{B}_{A_1}(Z) = \frac{\tilde{Z}_A e\mu_0}{2}\int_0^\infty \rho'^2\,d\rho' \int_{-\infty}^\infty \frac{j_{\phi' A_1}(\rho', Z')}{(\rho'^2 + (Z-Z')^2)^{3/2}}\,dZ'\,\mathbf{e}_Z \tag{2.335}$$

$$\mathbf{B}_{A_2}(Z) = \frac{\tilde{Z}_A e\mu_0}{2}\int_0^\infty \rho'^2\,d\rho' \int_{-\infty}^\infty \frac{j_{\phi' A_2}(\rho', Z')}{(\rho'^2 + (Z-Z')^2)^{3/2}}\,dZ'\,\mathbf{e}_Z \tag{2.336}$$

$$\mathbf{B}_B(Z) = \frac{\tilde{Z}_B e\mu_0}{2}\int_0^\infty \rho'^2\,d\rho' \int_{-\infty}^\infty \frac{j_{\phi' B}(\rho', Z')}{(\rho'^2 + (Z-Z')^2)^{3/2}}\,dZ'\,\mathbf{e}_Z \tag{2.337}$$

(cf. Eq. (2.87)) where $j_{\phi' A_1}(\rho', Z')$, $j_{\phi' A_2}(\rho', Z')$, and $j_{\phi' B}(\rho', Z')$ are the ϕ-components of the ϕ-independent nuclear current densities $\mathbf{j}_{A_1}(\mathbf{R}')$, $\mathbf{j}_{A_2}(\mathbf{R}')$, and $\mathbf{j}_B(\mathbf{R}')$ (Eqs. (2.307),

(2.308), (2.313)), respectively. The total induced magnetic field along the Z-axis is

$$\mathbf{B}_{tot}(Z) \;=\; \mathbf{B}_{A_1}(Z) + \mathbf{B}_{A_2}(Z) + \mathbf{B}_B(Z) \tag{2.338}$$

which must be calculated numerically for arbitrary values of Z. Note that for symmetry reasons, $\mathbf{B}_{A_1}(-Z) = \mathbf{B}_{A_2}(Z)$ and $\mathbf{B}_B(-Z) = \mathbf{B}_B(Z)$, thus $\mathbf{B}_{tot}(-Z) = \mathbf{B}_{tot}(Z)$. The approximations for $Z = -R_e$, $Z = R_e$, and $Z = 0$

$$\mathbf{B}_{tot}(-R_e) \;=\; \mathbf{B}_{tot}(R_e) \;\approx\; \mathbf{B}_{A_1}(-R_e) \;=\; \mathbf{B}_{A_2}(R_e) \tag{2.339}$$

$$\mathbf{B}_{tot}(0) \;\approx\; \mathbf{B}_B(0) \tag{2.340}$$

are valid because the magnetic fields at the equilibrium position of the nucleus induced by ring currents of the other nuclei are negligible due to large separation between the nuclei. The evaluation of the induced magnetic fields $\mathbf{B}_{A_1}(-R_e) = \mathbf{B}_{A_2}(R_e)$ and $\mathbf{B}_B(0)$ (Eqs. (2.339), (2.340)) is rather difficult, hence, we restrict the evaluation to the lowest quantum numbers for the stretches, i.e. $v_s = v_a = 0$, since in this case the induced magnetic fields at the equilibrium positions of the nuclei are expected to be strongest because the corresponding nuclear probability and current densities for $v_s = v_a = 0$ with respect to the Z-axis are localized rather compactly at the equilibrium positions of the nuclei. In general, the induced magnetic field $\mathbf{B}_B(\mathbf{R})$ is independent of v_s because the corresponding current density $\mathbf{j}_B(\mathbf{R})$ (Eq. (2.313)) is also independent of v_s whereas the induced magnetic field $\mathbf{B}_{A_1}(-R_e) = \mathbf{B}_{A_2}(R_e)$ depends on both the quantum numbers v_s and v_a; of course, they also depend on the quantum numbers v_b and l.

We have for $v_s = v_a = 0$ (Eq. (2.335)), using Eqs. (2.307), (2.270), (2.278), $u = ((Z' + R_e)/\rho')^2$,

$$\begin{aligned}
\mathbf{B}_{A_1}(-R_e) \;&=\; \frac{\tilde{Z}_A e\mu_0}{2} \int_0^\infty \rho'^2\, d\rho' \int_{-\infty}^\infty \frac{j_{\phi' A_1}(\rho', Z')}{(\rho'^2 + (Z' + R_e)^2)^{3/2}}\, dZ'\, \mathbf{e}_Z \qquad (2.341)\\
&=\; \frac{\tilde{Z}_A el\hbar\mu_0 M_B}{4MM_A} \int_0^\infty \rho'\, d\rho' \int_{-\infty}^\infty \frac{\rho_{A_1}(\rho', Z')}{(\rho'^2 + (Z' + R_e)^2)^{3/2}}\, dZ'\, \mathbf{e}_Z\\
&=\; \frac{\tilde{Z}_A el\hbar\mu_0 M}{8\pi M_A M_B} \int_0^\infty \left(\Phi^h_{v_b|l|}\left(\frac{M}{M_B}\,\rho'\right)\right)^2 \rho'\, d\rho' \int_{-\infty}^\infty \frac{I_{00}(Z' + R_e)}{(\rho'^2 + (Z' + R_e)^2)^{3/2}}\, dZ'\, \mathbf{e}_Z\\
&=\; \frac{\tilde{Z}_A el\hbar\mu_0 M m_{A_1}}{8\pi^{3/2} M_A M_B} \int_0^\infty \left(\Phi^h_{v_b|l|}\left(\frac{M}{M_B}\,\rho'\right)\right)^2 \rho'\, d\rho'\\
&\qquad\qquad \int_{-\infty}^\infty \frac{e^{-m_{A_1}^2 (Z' + R_e)^2}}{(\rho'^2 + (Z' + R_e)^2)^{3/2}}\, dZ'\, \mathbf{e}_Z\\
&=\; \frac{\tilde{Z}_A el\hbar\mu_0 M m_{A_1}}{8\pi^{3/2} M_A M_B} \int_0^\infty \left(\Phi^h_{v_b|l|}\left(\frac{M}{M_B}\,\rho'\right)\right)^2 \frac{d\rho'}{\rho'} \int_0^\infty \frac{e^{-m_{A_1}^2 \rho'^2 u}}{\sqrt{u}\,(1+u)^{3/2}}\, du\, \mathbf{e}_Z
\end{aligned}$$

where

$$m_{A_1} \;=\; \sqrt{\frac{4asM^2}{4sM_B^2 + aM^2}} \tag{2.342}$$

and for $v_a = 0$ (Eq. (2.337)), using Eqs. (2.313), (2.293), (2.246), $u = (Z'/\rho')^2$,

$$\begin{aligned}
\mathbf{B}_B(0) &= \frac{\tilde{Z}_B e\mu_0}{2}\int_0^\infty \rho'^2\, d\rho' \int_{-\infty}^\infty \frac{j_{\phi' B}(\rho', Z')}{(\rho'^2+Z'^2)^{3/2}}\, dZ'\, \mathbf{e}_Z \qquad (2.343)\\
&= \frac{\tilde{Z}_B el\hbar\mu_0 M_A}{M M_B}\int_0^\infty \rho'\, d\rho' \int_{-\infty}^\infty \frac{\rho_B(\rho', Z')}{(\rho'^2+Z'^2)^{3/2}}\, dZ'\, \mathbf{e}_Z\\
&= \frac{\tilde{Z}_B el\hbar\mu_0 M^2}{16\pi M_A^2 M_B}\int_0^\infty \left(\Phi^h_{v_b|l|}\left(\frac{M}{2M_A}\,\rho'\right)\right)^2 \rho'\, d\rho' \int_{-\infty}^\infty \frac{\left(\Phi^h_{v_a=0}\left(\frac{M}{2M_A}\,Z'\right)\right)^2}{(\rho'^2+Z'^2)^{3/2}}\, dZ'\, \mathbf{e}_Z\\
&= \frac{\tilde{Z}_B el\hbar\mu_0 M m_B}{8\pi^{3/2} M_A M_B}\int_0^\infty \left(\Phi^h_{v_b|l|}\left(\frac{M}{2M_A}\,\rho'\right)\right)^2 \rho'\, d\rho' \int_{-\infty}^\infty \frac{e^{-m_B^2 Z'^2}}{(\rho'^2+Z'^2)^{3/2}}\, dZ'\, \mathbf{e}_Z\\
&= \frac{\tilde{Z}_B el\hbar\mu_0 M m_B}{8\pi^{3/2} M_A M_B}\int_0^\infty \left(\Phi^h_{v_b|l|}\left(\frac{M}{2M_A}\,\rho'\right)\right)^2 \frac{d\rho'}{\rho'} \int_0^\infty \frac{e^{-m_B^2\rho'^2 u}}{\sqrt{u}\,(1+u)^{3/2}}\, du\, \mathbf{e}_Z
\end{aligned}$$

where

$$m_B = \frac{\sqrt{a}M}{2M_A}. \qquad (2.344)$$

Using the integral representation of the confluent hypergeometric function of the second kind $U(\alpha,\beta,z)$ [253, 254]

$$U(\alpha,\beta,z) = \frac{1}{\Gamma(\alpha)}\int_0^\infty e^{-zu}u^{\alpha-1}(1+u)^{\beta-\alpha-1}du, \qquad (2.345)$$

the Gamma function $\Gamma\left(\frac{1}{2}\right) = \sqrt{\pi}$, and $l = \mathrm{sgn}(l)|l|$, Eqs. (2.341) and (2.343) are then rewritten as

$$\begin{aligned}
\mathbf{B}_{A_1}(-R_e) &= \frac{\tilde{Z}_A el\hbar\mu_0 M m_{A_1}}{8\pi M_A M_B}\int_0^\infty \left(\Phi^h_{v_b|l|}\left(\frac{M}{M_B}\,\rho'\right)\right)^2 U\left(\frac{1}{2},0,m_{A_1}^2\rho'^2\right)\frac{d\rho'}{\rho'}\,\mathbf{e}_Z \qquad (2.346)\\
&= \mathrm{sgn}(l)\,\frac{\tilde{Z}_A e\hbar\mu_0 M^2 b^{3/2}}{8\pi M_A M_B^2}\,|l|\sqrt{\frac{\tilde{a}}{b^3}}\int_0^\infty \left(\Phi^h_{v_b|l|}\left(Q_b\right)\right)^2 U\left(\frac{1}{2},0,\tilde{a}Q_b^2\right) Q_b^{-1}\, dQ_b\, \mathbf{e}_Z
\end{aligned}$$

where

$$\tilde{a} = \frac{M_B^2}{M^2}\,m_{A_1}^2 = \frac{4asM_B^2}{4sM_B^2 + aM^2} = \frac{1}{\frac{1}{a}+\frac{M^2}{4sM_B^2}} \qquad (2.347)$$

and

$$\begin{aligned}
\mathbf{B}_B(0) &= \frac{\tilde{Z}_B el\hbar\mu_0 M m_B}{8\pi M_A M_B}\int_0^\infty \left(\Phi^h_{v_b|l|}\left(\frac{M}{2M_A}\,\rho'\right)\right)^2 U\left(\frac{1}{2},0,m_B^2\rho'^2\right)\frac{d\rho'}{\rho'}\,\mathbf{e}_Z \qquad (2.348)\\
&= \mathrm{sgn}(l)\,\frac{\tilde{Z}_B e\hbar\mu_0 M^2 b^{3/2}}{16\pi M_A^2 M_B}\,|l|\sqrt{\frac{a}{b^3}}\int_0^\infty \left(\Phi^h_{v_b|l|}\left(Q_b\right)\right)^2 U\left(\frac{1}{2},0,aQ_b^2\right) Q_b^{-1}\, dQ_b\, \mathbf{e}_Z,
\end{aligned}$$

respectively. With the definition of the integral

$$I_U\left(v_b,|l|,\frac{b}{c}\right) = |l|\sqrt{\frac{c}{b^3}}\int_0^\infty \left(\Phi^h_{v_b|l|}\left(Q_b\right)\right)^2 U\left(\frac{1}{2},0,cQ_b^2\right) Q_b^{-1}\, dQ_b, \qquad (2.349)$$

Eqs. (2.346) and (2.348) lead to

$$\mathbf{B}_{A_1}(-R_e) = \mathrm{sgn}(l)\,\frac{\tilde{Z}_A e\mu_0}{2\pi\sqrt{2\hbar}}\sqrt{\frac{MM_A}{M_B}}\,\omega_b^{3/2}\,I_U\left(v_b,|l|,\frac{\omega_b}{\omega_{\tilde{a}}}\right)\mathbf{e}_Z \tag{2.350}$$

and

$$\mathbf{B}_B(0) = \mathrm{sgn}(l)\,\frac{\tilde{Z}_B e\mu_0}{4\pi\sqrt{2\hbar}}\sqrt{\frac{MM_B}{M_A}}\,\omega_b^{3/2}\,I_U\left(v_b,|l|,\frac{\omega_b}{\omega_a}\right)\mathbf{e}_Z \tag{2.351}$$

where Eq. (2.252) was used. In Eq. (2.349), the dimensionless values b/c for $c=\tilde{a}$ and $c=a$, using Eqs. (2.247), (2.248), (2.252), (2.347), are rewritten as

$$\frac{b}{\tilde{a}} = \omega_b\left(\frac{1}{\omega_a}+\frac{M}{M_B\omega_s}\right) = \frac{\omega_b}{\omega_{\tilde{a}}} \tag{2.352}$$

where

$$\omega_{\tilde{a}} = \left(\frac{1}{\omega_a}+\frac{M}{M_B\omega_s}\right)^{-1} \tag{2.353}$$

and

$$\frac{b}{a} = \frac{\omega_b}{\omega_a}, \tag{2.354}$$

respectively (cf. Eqs. (2.350), (2.351)). Note that $b/a < b/\tilde{a}$.

For $|l|\neq 0$ the prefactors in Eqs. (2.350) and (2.351) are independent of the quantum numbers v_b, $|l|$ and of the harmonic frequencies for the stretches ω_s and ω_a. The dependences on $v_b, |l|, \omega_s$, and ω_a are determined only by the integral I_U (2.349) but for $c=a$ the integral I_U and the corresponding induced magnetic field $\mathbf{B}_B(0)$ are independent of ω_s as expected (cf. Eq. (2.354)). Since the integral I_U and the prefactors except for $\mathrm{sgn}(l)$ are positive, the direction of the induced magnetic fields along the Z-axis is determined by the sign of the pseudorotational quantum number l or, equivalently, by the sign of the Z-component of the total angular momentum $l\hbar$, i.e. if $l>0$ or $l<0$, then the induced magnetic fields along the Z-axis are directed to the positive or negative Z-axis, respectively. The analytical solutions of the integrals I_U for $v_b\leq 3$ and $|l|\neq 0$, using Eq. (2.352) for $c=\tilde{a}$ and Eq. (2.354) for $c=a$, are (see Appendix A.3 for the evaluation of these integrals)

$$I_U\left(v_b=|l|=1,\frac{\omega_b}{\omega_c}\right) = \frac{2}{\sqrt{\pi}}\frac{1}{1-\frac{\omega_b}{\omega_c}}\left(\frac{\arcsin\sqrt{1-\frac{\omega_b}{\omega_c}}}{\sqrt{1-\frac{\omega_b}{\omega_c}}}-\sqrt{\frac{\omega_b}{\omega_c}}\right) \tag{2.355}$$

$$I_U\left(v_b=|l|=2,\frac{\omega_b}{\omega_c}\right) = \frac{1}{\sqrt{\pi}}\frac{1}{\left(1-\frac{\omega_b}{\omega_c}\right)^2} \left[\left(1-\frac{4\omega_b}{\omega_c}\right)\frac{\arcsin\sqrt{1-\frac{\omega_b}{\omega_c}}}{\sqrt{1-\frac{\omega_b}{\omega_c}}}+\left(1+\frac{2\omega_b}{\omega_c}\right)\sqrt{\frac{\omega_b}{\omega_c}}\right] \tag{2.356}$$

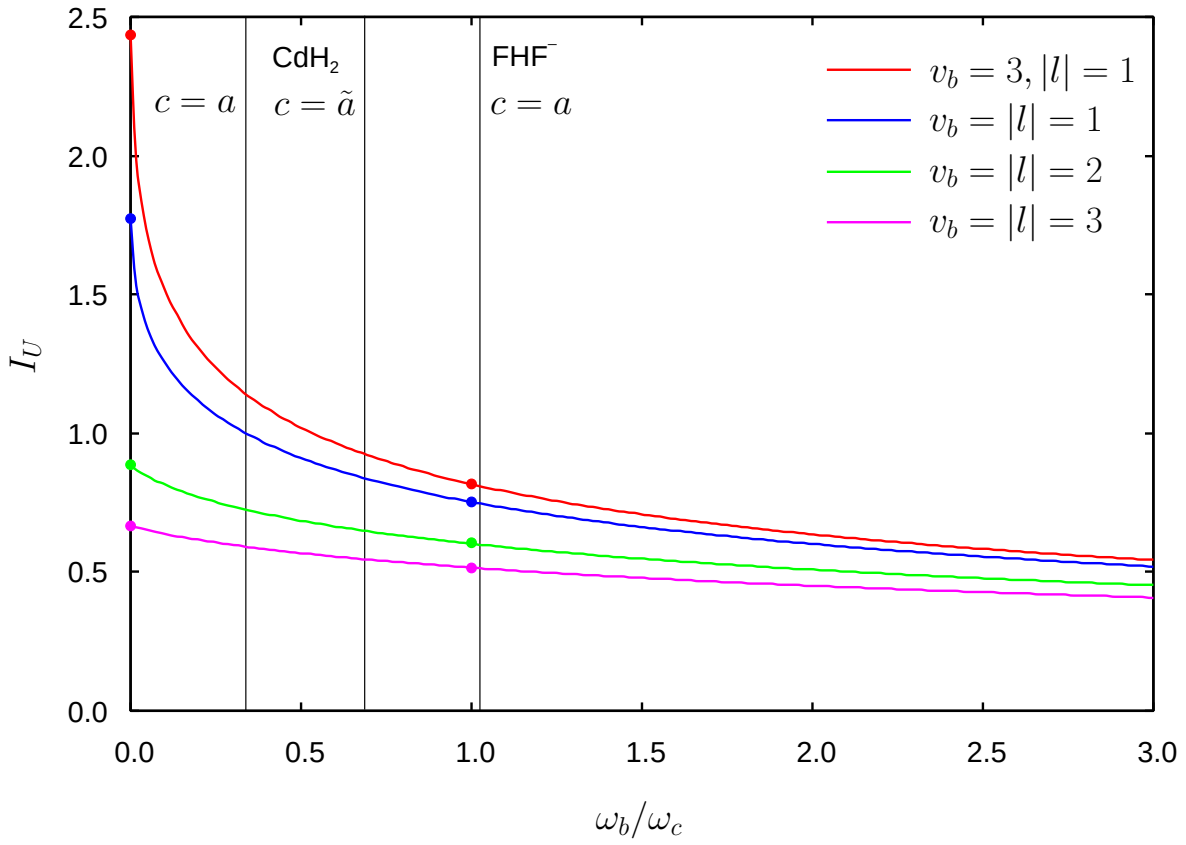

Figure 2.8: Integrals I_U for $v_b \leq 3$ and $|l| \neq 0$ (Eqs. (2.355)–(2.358)) versus ω_b/ω_c: $v_b = 3, |l| = 1$ (red), $v_b = |l| = 1$ (blue), $v_b = |l| = 2$ (green), $v_b = |l| = 3$ (magenta). The integral values I_U for different v_b and $|l|$ marked by circles at $\omega_b/\omega_c = 0$ and $\omega_b/\omega_c = 1$ are given in Eqs. (2.360)–(2.367). The vertical lines for $^{114}CdH_2$ and FHF^- (see Section 3.5) are also drawn, i.e. $\omega_b/\omega_{\tilde{a}} \approx 0.68$ and $\omega_b/\omega_a \approx 0.34$ for $^{114}CdH_2$ and $\omega_b/\omega_a \approx 1.03$ for FHF^- whereas the corresponding line at $\omega_b/\omega_{\tilde{a}} \approx 83.66$ for FHF^- is outside of the range of this figure.

$$I_U\left(v_b = |l| = 3, \frac{\omega_b}{\omega_c}\right) = \frac{3}{4\sqrt{\pi}} \frac{1}{\left(1 - \frac{\omega_b}{\omega_c}\right)^3} \left[\left(1 - \frac{4\omega_b}{\omega_c} + \frac{8\omega_b^2}{\omega_c^2}\right) \frac{\arcsin\sqrt{1 - \frac{\omega_b}{\omega_c}}}{\sqrt{1 - \frac{\omega_b}{\omega_c}}} + \left(1 - \frac{10\omega_b}{3\omega_c} - \frac{8\omega_b^2}{3\omega_c^2}\right) \sqrt{\frac{\omega_b}{\omega_c}}\right] \tag{2.357}$$

$$I_U\left(v_b = 3, |l| = 1, \frac{\omega_b}{\omega_c}\right) = \frac{1}{\sqrt{\pi}} \frac{1}{\left(1 - \frac{\omega_b}{\omega_c}\right)^3} \left[\left(\frac{11}{4} - \frac{\omega_b}{\omega_c} + \frac{2\omega_b^2}{\omega_c^2}\right) \frac{\arcsin\sqrt{1 - \frac{\omega_b}{\omega_c}}}{\sqrt{1 - \frac{\omega_b}{\omega_c}}} + \left(-\frac{21}{4} + \frac{7\omega_b}{2\omega_c} - \frac{2\omega_b^2}{\omega_c^2}\right) \sqrt{\frac{\omega_b}{\omega_c}}\right]. \tag{2.358}$$

Note that the integral I_U for $v_b = 3, |l| = 1$ (Eq. (2.358)) can be written as the linear combination of the remaining three integrals, i.e.

$$I_U\left(v_b = 3, |l| = 1, \frac{\omega_b}{\omega_c}\right) = 2I_U\left(v_b = |l| = 1, \frac{\omega_b}{\omega_c}\right) - 2I_U\left(v_b = |l| = 2, \frac{\omega_b}{\omega_c}\right) + I_U\left(v_b = |l| = 3, \frac{\omega_b}{\omega_c}\right) \tag{2.359}$$

(see Appendix A.3.4). The integrals (2.355)–(2.358) versus ω_b/ω_c are plotted in Fig. 2.8.

Hence, the induced magnetic fields are strongest for $|l| = 1$, and weaker for $|l| = 2, 3, \ldots$. The smallest mean current radius is obtained for $|l| = 1$ and larger radii are obtained for $|l| = 2, 3, \ldots$, see Section 2.4.7, while the magnitudes of the electric ring currents (Eqs. (2.331)–(2.333)) for $|l| \neq 0$ in the harmonic approximation are independent of all vibrational and pseudorotational quantum numbers. This finding is in accord with the Biot-Savart law in the current loop model, cf. Eq. (2.93). Furthermore, for fixed $|l| = 1$, the induced magnetic fields for $v_b = 3$ are stronger than for $v_b = 1$. In general, one can show by further evaluation of integrals for $v_b > 3$ that the induced magnetic fields are strongest for $|l| = 1$ and $v_b \gg 1$, due to a decrease in the mean current radii for fixed $|l|$ with increasing v_b, see Section 2.4.7. The corresponding integral values I_U examplarily for $\omega_b/\omega_c = 0$ (easily calculated from Eqs. (2.355)–(2.358)) and $\omega_b/\omega_c = 1$ (see Appendix A.3) are

$$I_U\left(v_b = 3, |l| = 1, \frac{\omega_b}{\omega_c} = 0\right) = \frac{11\sqrt{\pi}}{8} \approx 2.4371 \tag{2.360}$$

$$I_U\left(v_b = |l| = 1, \frac{\omega_b}{\omega_c} = 0\right) = \sqrt{\pi} \approx 1.7725 \tag{2.361}$$

$$I_U\left(v_b = |l| = 2, \frac{\omega_b}{\omega_c} = 0\right) = \frac{\sqrt{\pi}}{2} \approx 0.8862 \tag{2.362}$$

$$I_U\left(v_b = |l| = 3, \frac{\omega_b}{\omega_c} = 0\right) = \frac{3\sqrt{\pi}}{8} \approx 0.6647 \tag{2.363}$$

and

$$I_U\left(v_b = 3, |l| = 1, \frac{\omega_b}{\omega_c} = 1\right) = \frac{152}{105\sqrt{\pi}} \approx 0.8167 \tag{2.364}$$

$$I_U\left(v_b = |l| = 1, \frac{\omega_b}{\omega_c} = 1\right) = \frac{4}{3\sqrt{\pi}} \approx 0.7523 \tag{2.365}$$

$$I_U\left(v_b = |l| = 2, \frac{\omega_b}{\omega_c} = 1\right) = \frac{16}{15\sqrt{\pi}} \approx 0.6018 \tag{2.366}$$

$$I_U\left(v_b = |l| = 3, \frac{\omega_b}{\omega_c} = 1\right) = \frac{32}{35\sqrt{\pi}} \approx 0.5158, \tag{2.367}$$

respectively, which are marked by circles in Fig. 2.8. However, their asymptotic limits for $\omega_b/\omega_c \to \infty$ are zero and in this limit the integral $I_U \to 0$ is independent of all vibrational and pseudorotational quantum numbers (see Appendix A.3). In general, for $\omega_b/\omega_c \gg 1$,

the dependence of the integral I_U on the quantum numbers v_b and $|l|$ is less important, but for small ω_b/ω_c the dependence on the quantum numbers v_b and $|l|$ is no longer negligible, see also Fig. 2.8. For example, for FHF^-, the integral I_U for $c = \tilde{a}$, which is necessary for the calculation of the induced magnetic fields at $Z = \pm R_e$ (cf. Eq. (2.350)), is almost independent of v_b and $|l|$ because $\omega_b/\omega_{\tilde{a}} \approx 83.66$ is large due to the relatively small mass of the hydrogen nucleus, i.e. $M \gg M_B$ (cf. Eq. (2.352) and Sectoin 3.5). In this case the integral values I_U range only from 0.1165 for $v_b = |l| = 3$ to 0.1208 for $v_b = 3, |l| = 1$. But for $^{114}CdH_2$ the corresponding mass ratio is $M/M_B \approx 1$, thus the value $\omega_b/\omega_{\tilde{a}} \approx 0.68$ is not as large as it is for FHF^- (cf. Eq. (2.352)) and the corresponding integral I_U for $c = \tilde{a}$ is still strongly dependent on v_b and $|l|$, see also Fig. 2.8. Furthermore, the integral I_U for $c = a$, which is necessary for the calculation of the induced magnetic field at $Z = 0$ (cf. Eq. (2.351)), is larger than the one for $c = \tilde{a}$ because of $\omega_a > \omega_{\tilde{a}}$ (cf. Eqs. (2.352)–(2.354) and Fig. 2.8). Obviously, the integral I_U increases with the harmonic frequencies for the antisymmetric ω_a (for $c = \tilde{a}$ and $c = a$) and symmetric ω_s (only for $c = \tilde{a}$) stretches (cf. Eqs. (2.352) and (2.354)). For small frequencies ω_a and ω_s, i.e. $\omega_b/\omega_c \gg 1$, the nuclear ring currents with respect to the Z-axis are no longer compactly localized at the equilibrium positions of the nuclei, thus the corresponding integrals I_U and the induced magnetic fields are smaller than the ones for high frequencies ω_a and ω_s. This fact also confirms indirectly that the induced magnetic fields are strongest for the lowest quantum numbers for the stretches $v_a = v_s = 0$.

To investigate the dependence of the induced magnetic fields $\mathbf{B}_{A_1}(-R_e) = \mathbf{B}_{A_2}(R_e)$ and $\mathbf{B}_B(0)$ on the harmonic bending frequency ω_b, we must consider the product $\omega_b^{3/2} I_U$ (cf. Eqs. (2.350), (2.351)). Although, the integral I_U decreases with increasing ω_b, see Fig. 2.8, the additional factor $\omega_b^{3/2}$ leads to the strong dependence on ω_b. The product $\omega_b^{3/2} I_U$ and thus the induced magnetic fields increase with the harmonic bending frequency ω_b. While I_U goes to zero if $\omega_b \to \infty$, we will show for the example $v_b = |l| = 1$ that the product $\omega_b^{3/2} I_U$ instead goes to infinity if $\omega_b \to \infty$. Using Eq. (2.355), $z = 1 - \omega_b/\omega_c$, i.e. $\omega_b = (1-z)\omega_c$, L'Hospital's rule, and $d \arcsin(z)/dz = 1/\sqrt{1-z^2}$, we have

$$
\begin{aligned}
\lim_{\omega_b \to \infty} \omega_b^{3/2} I_U &= \frac{2\omega_c^{3/2}}{\sqrt{\pi}} \lim_{z \to -\infty} (1-z)^{3/2} \left[\frac{\arcsin\sqrt{z}}{z^{3/2}} - \frac{\sqrt{1-z}}{z} \right] \\
&= \frac{2\omega_c^{3/2}}{\sqrt{\pi}} \lim_{z \to -\infty} \frac{(1-z)^{3/2} \arcsin\sqrt{z} - (1-z)^2\sqrt{z}}{z^{3/2}} \\
&= \frac{2\omega_c^{3/2}}{\sqrt{\pi}} \lim_{z \to -\infty} \frac{\frac{d}{dz}(1-z)^{3/2} \arcsin\sqrt{z} - \frac{d}{dz}(1-z)^2\sqrt{z}}{\frac{d}{dz} z^{3/2}} \\
&= \frac{4\omega_c^{3/2}}{3\sqrt{\pi}} \lim_{z \to -\infty} \frac{-\frac{3}{2}\sqrt{1-z} \arcsin\sqrt{z} + \frac{1-z}{2\sqrt{z}} + 2(1-z)\sqrt{z} - \frac{(1-z)^2}{2\sqrt{z}}}{\sqrt{z}} \\
&= \frac{4\omega_c^{3/2}}{3\sqrt{\pi}} \lim_{z \to -\infty} \frac{-\frac{3}{2}\sqrt{1-z} \arcsin\sqrt{z} + \frac{5}{2}(1-z)\sqrt{z}}{\sqrt{z}}
\end{aligned}
\tag{2.368}
$$

$$= \frac{4\omega_c^{3/2}}{3\sqrt{\pi}} \lim_{z\to-\infty} \left[-\frac{3}{2}\sqrt{\frac{1}{z}-1}\arcsin\left(i\sqrt{-z}\right) + \frac{5}{2}(1-z) \right].$$

Using [253]

$$\arcsin(iz) = i\,\mathrm{arcsinh}(z) \tag{2.369}$$

and $\lim_{z\to\infty}\mathrm{arcsinh}(z) \to \infty$, we obtain

$$\begin{aligned} \lim_{\omega_b\to\infty} \omega_b^{3/2} I_U &= \frac{4\omega_c^{3/2}}{3\sqrt{\pi}} \lim_{z\to-\infty} \left[-\frac{3i}{2}\sqrt{\frac{1}{z}-1}\,\mathrm{arcsinh}\left(\sqrt{-z}\right) + \frac{5}{2}(1-z) \right] \\ &= \frac{4\omega_c^{3/2}}{3\sqrt{\pi}} \left[\frac{3}{2} \lim_{z\to-\infty} \mathrm{arcsinh}\left(\sqrt{-z}\right) + \frac{5}{2} \lim_{z\to-\infty}(1-z) \right] \\ &\to \infty. \end{aligned} \tag{2.370}$$

In general, for arbitrary quantum numbers v_b and $|l|$, one can show in an analogous way for $v_b = |l| = 1$ that the induced magnetic fields $\mathbf{B}_{A_1}(-R_e) = \mathbf{B}_{A_2}(R_e)$ and $\mathbf{B}_B(0)$ go to infinity if $\omega_b \to \infty$. The reason for the strong increase of the induced magnetic fields by increasing the harmonic bending frequency ω_b is that the electric ring currents (Eqs. (2.331)–(2.333)) and the corresponding mean ring current radii (see Section 2.4.7) are proportional to ω_b and $\omega_b^{-1/2}$, respectively, and the induced magnetic field in the current loop model (Eq. 2.93) is thus proportional to $\omega_b^{3/2}$ which is in accord with the factor $\omega_b^{3/2}$ in Eqs. (2.350) and (2.351). Note that the electric ring current in the current loop model (2.94) is proportional to the inverse square of the mean ring current radius and hence proportional to ω_b, again in accord with Eqs. (2.331)–(2.333).

The physical properties of the nuclei of the ABA molecule also play an important role in the determination of the induced magnetic fields, i.e. the nuclear charges $\tilde{Z}_A$, $\tilde{Z}_B$ and masses M_A, M_B. The magnetic fields induced by ring currents of the nuclei A and B at their ring centers $\mathbf{B}_{A_1}(-R_e) = \mathbf{B}_{A_2}(R_e)$ (Eq. (2.350)) and $\mathbf{B}_B(0)$ (Eq. (2.351)) are proportional to their nuclear charges $\tilde{Z}_A$ and $\tilde{Z}_B$, respectively. The dependence of the magnetic fields on the nuclear masses is determined by the factors

$$\sqrt{\frac{MM_A}{M_B}} = \sqrt{M_A}\sqrt{\frac{2M_A+M_B}{M_B}} = \sqrt{M_A}\sqrt{\frac{2M_A}{M_B}+1} \tag{2.371}$$

for $Z = \pm R_e$ and

$$\sqrt{\frac{MM_B}{M_A}} = \sqrt{M_B}\sqrt{\frac{2M_A+M_B}{M_A}} = \sqrt{M_B}\sqrt{2+\frac{M_B}{M_A}} \tag{2.372}$$

for $Z = 0$. In addition, the integral I_U in $\mathbf{B}_{A_1}(-R_e) = \mathbf{B}_{A_2}(R_e)$ also depends on the nuclear masses, i.e. $\omega_{\tilde{a}}$ (Eq. (2.353)) depends on M_A and M_B as

$$\omega_{\tilde{a}}(M_A, M_B) = \left(\frac{1}{\omega_a} + \left(\frac{2M_A}{M_B} + 1 \right) \frac{1}{\omega_s} \right)^{-1}. \tag{2.373}$$

Thus, the induced magnetic fields at $Z = \pm R_e$, i.e. $\mathbf{B}_{A_1}(-R_e) = \mathbf{B}_{A_2}(R_e)$, increase with increasing M_A, even if the relative mass ratio M_A/M_B remains unchanged or if M_B decreases. Note that the inverse dependence of the integral I_U on $\omega_{\tilde{a}}(M_A, M_B)$ (Eq. (2.373)) is still weak compared to the stronger dependence of Eq. (2.371). Similarly, the induced magnetic field at $Z = 0$, i.e. $\mathbf{B}_B(0)$, increases with increasing M_B, even if M_B/M_A remains unchanged or if M_A decreases.

2.4.7 Mean ring current radius

The mean ring current radii of the nuclei A_1 ($i = 1$), A_2 ($i = 2$), and B ($i = 3$) for $|l| \neq 0$ are calculated as

$$R_{n,i} \;=\; \langle \rho^n \rangle_{j,i}^{1/n} \;=\; \left(\frac{\tilde{Z}_i e}{I_i} \int\int \rho^n \mathbf{j}_i(\mathbf{R}) \cdot d\mathbf{S} \right)^{1/n} \tag{2.374}$$

where $d\mathbf{S} = d\rho\, dZ\, \mathbf{e}_\phi$ and $n = 1, -1, -2$, cf. Eqs. (2.95)–(2.97); for choosing n see the discussion in Section 2.2.7. Note that for symmetry reasons, the mean ring current radii of the nuclei A_1 and A_2 are equal, i.e. $R_{n,A} = R_{n,A_1} = R_{n,A_2}$. Using Eqs. (2.307), (2.332), $\mathrm{sgn}(l)l = (\mathrm{sgn}(l))^2|l| = |l|$, (2.270), (2.275), they are evaluated as

$$\begin{aligned}
R_{n,A} &= \left(\frac{\tilde{Z}_A e}{I_A} \int\int \rho^n \mathbf{j}_{A_1}(\mathbf{R}) \cdot d\mathbf{S} \right)^{1/n} \qquad (2.375)\\
&= \left(\frac{\pi |l| \hbar M_B}{\omega_b M M_A} \int_0^\infty \rho^{n-1}\, d\rho \int_{-\infty}^{\infty} \rho_{A_1}(\mathbf{R})\, dZ \right)^{1/n} \\
&= \left(\frac{|l| \hbar M}{2\omega_b M_A M_B} \int_0^\infty \left(\Phi^h_{v_b|l|} \left(\frac{M}{M_B}\, \rho \right) \right)^2 \rho^{n-1}\, d\rho \int_{-\infty}^{\infty} I_{v_s v_a}(Z + R_e)\, dZ \right)^{1/n} \\
&= \left(\frac{|l| \hbar M^{1-n}}{2\omega_b M_A M_B^{1-n}} \int_0^\infty \left(\Phi^h_{v_b|l|}(Q_b) \right)^2 Q_b^{n-1}\, dQ_b \right)^{1/n} \\
&= \left(\frac{|l| \hbar M^{1-n} I_{n-1}(v_b, |l|)}{2\omega_b M_A M_B^{1-n}} \right)^{1/n}
\end{aligned}$$

where the integral $I_m(v_b, |l|)$ is defined as

$$I_m(v_b, |l|) \;=\; \int_0^\infty \left(\Phi^h_{v_b|l|}(Q_b) \right)^2 Q_b^m\, dQ_b, \tag{2.376}$$

see Appendix A.2. In an analogous way, using Eqs. (2.313), (2.333), (2.293), (2.376), and normalized wavefunction $\Phi^h_{v_a}(Q_a)$ (2.246), we can evaluate the mean ring current radius of the nucleus B as

$$
\begin{aligned}
R_{n,B} &= \left(\frac{\tilde{Z}_B e}{I_B} \int\int \rho^n \mathbf{j}_B(\mathbf{R}) \cdot d\mathbf{S} \right)^{1/n} \qquad (2.377)\\
&= \left(\frac{4\pi |l| \hbar M_A}{\omega_b M M_B} \int_0^\infty \rho^{n-1}\, d\rho \int_{-\infty}^{\infty} \rho_B(\mathbf{R})\, dZ \right)^{1/n} \\
&= \left(\frac{|l| \hbar M^2}{4\omega_b M_A^2 M_B} \int_0^\infty \left(\Phi^h_{v_b|l|} \left(\frac{M}{2M_A}\, \rho \right) \right)^2 \rho^{n-1}\, d\rho \int_{-\infty}^{\infty} \left(\Phi^h_{v_a} \left(\frac{M}{2M_A}\, Z \right) \right)^2 dZ \right)^{1/n} \\
&= \left(\frac{|l| \hbar M^{1-n}}{2^{1-n} \omega_b M_A^{1-n} M_B} \int_0^\infty \left(\Phi^h_{v_b|l|}(Q_b) \right)^2 Q_b^{n-1}\, dQ_b \right)^{1/n} \\
&= \left(\frac{|l| \hbar M^{1-n} I_{n-1}(v_b, |l|)}{2^{1-n} \omega_b M_A^{1-n} M_B} \right)^{1/n} .
\end{aligned}
$$

By comparing the mean ring current radii $R_{n,A}$ and $R_{n,B}$ (Eqs. (2.375), (2.377)), we obtain

$$
\frac{R_{n,A}^n}{R_{n,B}^n} = \frac{M_B^n}{2^n M_A^n}, \qquad (2.378)
$$

thus in accord with the condition of the center of mass (in the X/Y-plane)

$$
2M_A R_{n,A} = M_B R_{n,B} \qquad (2.379)
$$

which holds for all n.

The mean ring current radii of the nuclei A and B for $n = 1$ and $|l| \neq 0$, using the integral $I_0(v_b, |l|)$ (Eq. (2.376), Appendix A.2.3) and Eq. (2.252), are

$$
\begin{aligned}
R_{1,A}(v_b = |l|) &= \sqrt{\frac{\hbar M_B}{2\omega_b M M_A}}\, \frac{\Gamma\left(|l| + \frac{1}{2}\right)}{(|l|-1)!} \qquad (2.380)\\
R_{1,A}(v_b = |l| + 2) &= \sqrt{\frac{\hbar M_B}{2\omega_b M M_A}}\, \frac{\Gamma\left(|l| + \frac{1}{2}\right)}{(|l|-1)!}\, \frac{|l| + \frac{3}{4}}{|l| + 1} \qquad (2.381)\\
&\vdots
\end{aligned}
$$

and

$$
\begin{aligned}
R_{1,B}(v_b = |l|) &= \sqrt{\frac{2\hbar M_A}{\omega_b M M_B}}\, \frac{\Gamma\left(|l| + \frac{1}{2}\right)}{(|l|-1)!} \qquad (2.382)\\
R_{1,B}(v_b = |l| + 2) &= \sqrt{\frac{2\hbar M_A}{\omega_b M M_B}}\, \frac{\Gamma\left(|l| + \frac{1}{2}\right)}{(|l|-1)!}\, \frac{|l| + \frac{3}{4}}{|l| + 1}, \qquad (2.383)\\
&\vdots
\end{aligned}
$$

respectively. Since $|l| + \frac{3}{4} < |l| + 1$, the mean ring current radii for $v_b = |l| + 2$ are smaller than the ones for $v_b = |l|$, i.e. for fixed $|l|$ they decrease with increasing v_b. By further analysis, one can show that for $v_b = |l|$, $v_b = |l| + 2, \ldots$, and for combinations also involving fixed v_b, the mean current radii increase with $|l|$, see Table 2.1.

v_b	$\|l\|$	R_1	R_{-1}	R_{-2}	$\tilde{R}$
0	0	-	-	-	0.886
1	1	0.886	0.564	-	1.329
2	0	-	-	-	1.551
2	2	1.329	1.128	1.000	1.662
3	1	0.775	0.410	-	1.828
3	3	1.662	1.505	1.414	1.939
4	0	-	-	-	2.008
4	2	1.219	0.903	0.775	2.077
4	4	1.939	1.805	1.732	2.181

Table 2.1: Mean ring current radii R_n of the nuclear ring current depending on the quantum numbers $0 \leq v_b \leq 4$ and $|l|$ for $n = 1, -1, -2$ (Eqs. (2.380)–(2.389)) but without prefactors (Eqs. (2.390), (2.391)). For comparison, the mean radii $\tilde{R}$ (Eqs. (2.396)–(2.399)) without prefactors (Eqs. (2.390), (2.391)) are also listed.

For the estimation of the induced magnetic fields in the current loop model (Eq. (2.93)), the mean ring current radii for $n = -1$ and $|l| \neq 0$ should be used, i.e. with the integral $I_{-2}(v_b, |l|)$ (Appendix A.2.5) and Eq. (2.252),

$$R_{-1,A}(v_b = |l|) = \sqrt{\frac{\hbar M_B}{2\omega_b M M_A}} \frac{(|l|-1)!}{\Gamma\left(|l| - \frac{1}{2}\right)} \tag{2.384}$$

$$R_{-1,A}(v_b = |l|+2) = \sqrt{\frac{\hbar M_B}{2\omega_b M M_A}} \frac{(|l|-1)!}{\Gamma\left(|l| - \frac{1}{2}\right)} \frac{|l|+1}{|l|+\frac{7}{4}} \tag{2.385}$$

$$\vdots$$

and

$$R_{-1,B}(v_b = |l|) = \sqrt{\frac{2\hbar M_A}{\omega_b M M_B}} \frac{(|l|-1)!}{\Gamma\left(|l| - \frac{1}{2}\right)} \tag{2.386}$$

$$R_{-1,B}(v_b = |l|+2) = \sqrt{\frac{2\hbar M_A}{\omega_b M M_B}} \frac{(|l|-1)!}{\Gamma\left(|l| - \frac{1}{2}\right)} \frac{|l|+1}{|l|+\frac{7}{4}} \tag{2.387}$$

$$\vdots$$

Again, because of $|l| + 1 < |l| + \frac{7}{4}$, the mean ring current radii for fixed $|l|$ decrease with increasing v_b. By further analysis, for $v_b = |l|$, $v_b = |l| + 2$, ..., and also for fixed v_b, they increase with $|l|$ as for $n = 1$, see also Table 2.1.

The integrals $I_0(v_b, |l|)$ for $n = 1$ and $I_{-2}(v_b, |l|)$ for $n = -1$ do not have the simple analytical expressions depending on v_b and $|l|$, but the integral $I_{-3}(v_b, |l|)$ for $n = -2$ does

have the closed analytical form (see Appendix A.2.6). However, the mean ring current radii for $n = -3$ are usually used to estimate the approximate electric ring currents in the current loop model (Eq. (2.94)). For $|l| \neq 0, 1$, they are

$$R_{-2,A} = \sqrt{\frac{\hbar M_B}{2\omega_b M M_A}} \sqrt{\frac{|l|^2 - 1}{v_b + 1}} \tag{2.388}$$

and

$$R_{-2,B} = \sqrt{\frac{2\hbar M_A}{\omega_b M M_B}} \sqrt{\frac{|l|^2 - 1}{v_b + 1}}. \tag{2.389}$$

Note that the radii would be zero if $|l| = 1$ because the integral $I_{-2}(v_b, |l| = 1)$ is infinite, thus the estimation of the electric ring currents for $|l| = 1$ in the current loop model cannot be used. The mean ring current radii increase with $|l|$, and decrease with increasing v_b, see also Table 2.1. Thus, the ring current radii are smallest for $|l| = 1$ and $v_b \gg 1$, and the corresponding induced magnetic fields are strongest, see also the discussion in Section 2.4.6. Furthermore, Table 2.1 shows us that the mean ring current radii for $n = 1$ are larger than the ones for $n = -1$ which are in turn larger than the ones for $n = -2$.

The prefactors in Eqs. (2.380)–(2.389) for nuclei A and B are rewritten as

$$\sqrt{\frac{\hbar M_B}{2\omega_b M M_A}} = \sqrt{\frac{\hbar}{2\omega_b \left(\frac{2M_A}{M_B} + 1\right) M_A}} \tag{2.390}$$

and

$$\sqrt{\frac{2\hbar M_A}{\omega_b M M_B}} = \sqrt{\frac{2\hbar}{\omega_b \left(2 + \frac{M_B}{M_A}\right) M_B}} \tag{2.391}$$

respectively. It is obvious that the mean ring current radii decrease with increasing harmonic bending frequency according to $\omega_b^{-1/2}$. For the nuclei A and B, the radii decrease with an increase in their own respective masses M_A and M_B, or for a decrease in the masses M_B and M_A, respectively. However, they are independent of the nuclear charges $\tilde{Z}_A$, $\tilde{Z}_B$ and of the harmonic frequencies for the stretches ω_s, ω_a. For heavy nuclei and high harmonic bending frequency, the mean ring current radius can be very small, even in the range of $0.001\, a_0$, and the corresponding strong induced magnetic field is sharply localized inside of the nuclear ring current whereas it decreases rapidly outside of the nuclear ring current. This behavior indicates that the strong magnetic field interacts only with the nuclear spin and 1s electrons.

For comparison, instead of the nuclear currrent densities, we calculate the mean radii $\tilde{R}_{A_1}$, $\tilde{R}_{A_2}$, and $\tilde{R}_B$ of the nuclear probability densities $\rho_{A_1}(\mathbf{R})$, $\rho_{A_2}(\mathbf{R})$, and $\rho_B(\mathbf{R})$, respectively. For symmetry reasons $\tilde{R}_A = \tilde{R}_{A_1} = \tilde{R}_{A_2}$ and the mean radius for the nucleus

A is defined as

$$\begin{aligned}\tilde{R}_A \;=\; \langle\rho_1\rangle \;&=\; \int\int\int d\mathbf{R}_1 \int\int\int d\mathbf{R}_2 \int\int\int d\mathbf{R}_3 \int\ldots\int d\mathbf{q}_1\ldots d\mathbf{q}_N \\ &\quad \left[\Psi^{tot}_{v_s v_a v_b l 0}(\mathbf{R}_1,\mathbf{R}_2,\mathbf{R}_3,\mathbf{q}_1,\ldots,\mathbf{q}_N)\right]^* \rho_1 \Psi^{tot}_{v_s v_a v_b l 0}(\mathbf{R}_1,\mathbf{R}_2,\mathbf{R}_3,\mathbf{q}_1,\ldots,\mathbf{q}_N) \\ &=\; \int\int\int \rho_1 \rho_{A_1}(\mathbf{R}_1)\, d\mathbf{R}_1\end{aligned} \tag{2.392}$$

where Eq. (2.257) was used. With $d\mathbf{R}_1 = \rho_1\, d\rho_1\, dZ_1\, d\phi_1$ and Eqs. (2.270), (2.275), (2.376), we obtain

$$\begin{aligned}\tilde{R}_A \;&=\; \frac{M^2}{M_B^2}\int_0^\infty \left(\Phi^h_{v_b|l|}\left(\frac{M}{M_B}\,\rho_1\right)\right)^2 \rho_1^2\, d\rho_1 \int_{-\infty}^{\infty} I_{v_s v_a}(Z_1+R_e)\, dZ_1 \\ &=\; \frac{M_B}{M}\int_0^\infty \left(\Phi^h_{v_b|l|}(Q_b)\right)^2 Q_b^2\, dQ_b \\ &=\; \frac{M_B}{M}\, I_2(v_b,|l|).\end{aligned} \tag{2.393}$$

The corresponding mean radius for nucleus B, using Eqs. (2.281), (2.293), (2.376), is given by

$$\begin{aligned}\tilde{R}_B \;=\; \langle\rho_3\rangle \;&=\; \int\int\int d\mathbf{R}_1 \int\int\int d\mathbf{R}_2 \int\int\int d\mathbf{R}_3 \int\ldots\int d\mathbf{q}_1\ldots d\mathbf{q}_N \\ &\quad \left[\Psi^{tot}_{v_s v_a v_b l 0}(\mathbf{R}_1,\mathbf{R}_2,\mathbf{R}_3,\mathbf{q}_1,\ldots,\mathbf{q}_N)\right]^* \rho_3 \Psi^{tot}_{v_s v_a v_b l 0}(\mathbf{R}_1,\mathbf{R}_2,\mathbf{R}_3,\mathbf{q}_1,\ldots,\mathbf{q}_N) \\ &=\; \int\int\int \rho_3 \rho_B(\mathbf{R}_3)\, d\mathbf{R}_3 \\ &=\; \frac{1}{8}\frac{M^3}{M_A^3}\int_0^\infty \left(\Phi^h_{v_b|l|}\left(\frac{M}{2M_A}\,\rho_3\right)\right)^2 \rho_3^2\, d\rho_3 \int_{-\infty}^{\infty}\left(\Phi^h_{v_a}\left(\frac{M}{2M_A}\,Z_3\right)\right)^2 dZ_3 \\ &=\; \frac{2M_A}{M}\int_0^\infty \left(\Phi^h_{v_b|l|}(Q_b)\right)^2 Q_b^2\, dQ_b \\ &=\; \frac{2M_A}{M}\, I_2(v_b,|l|).\end{aligned} \tag{2.394}$$

It is obvious that the condition of the center of mass is also satisfied for the mean radii, i.e.

$$2M_A\tilde{R}_A \;=\; M_B\tilde{R}_B, \tag{2.395}$$

cf. Eq. (2.379).

Using the integral $I_2(v_b,|l|)$ (Appendix A.2.1) and Eq. (2.252), the results for all $|l|$ are

$$\tilde{R}_A(v_b=|l|) \;=\; \sqrt{\frac{\hbar M_B}{2\omega_b M M_A}}\,\frac{\Gamma\left(|l|+\frac{3}{2}\right)}{|l|!} \tag{2.396}$$

$$\tilde{R}_A(v_b=|l|+2) \;=\; \sqrt{\frac{\hbar M_B}{2\omega_b M M_A}}\,\frac{\Gamma\left(|l|+\frac{3}{2}\right)}{|l|!}\,\frac{|l|+\frac{7}{4}}{|l|+1} \tag{2.397}$$

$$\vdots$$

and

$$\tilde{R}_B(v_b = |l|) = \sqrt{\frac{2\hbar M_A}{\omega_b M M_B}} \frac{\Gamma\left(|l| + \frac{3}{2}\right)}{|l|!} \tag{2.398}$$

$$\tilde{R}_B(v_b = |l| + 2) = \sqrt{\frac{2\hbar M_A}{\omega_b M M_B}} \frac{\Gamma\left(|l| + \frac{3}{2}\right)}{|l|!} \frac{|l| + \frac{7}{4}}{|l| + 1} \tag{2.399}$$

$$\vdots$$

Note that the prefactors in Eqs. (2.396)–(2.399) are the same as the ones for the mean ring current radii (cf. Eqs. (2.390), (2.391)). In contrast to the mean ring current radii, the mean radii increase with $|l|$ and also with v_b since $|l| + \frac{7}{4} > |l| + 1$, see also Table (2.1). In particular, the mean radii for $|l| = 0$ are non-zero but there are no nuclear currents. The mean radii are larger than the corresponding mean ring current radii because the nuclear current densities contain the additional factor $1/\rho$ (cf. Eqs. (2.270), (2.271), (2.293)).

2.4.8 Electronic ring currents in pseudorotating molecules

For the stationary pseudorotation of the linear triatomic molecule ABA, we have considered the stationary non-degenerate electronic state. Of course, the electronic and nuclear probability and current densities are stationary but we showed that the current densities of the nuclei are non-zero for $|l| \neq 0$ which carry stationary toroidal ring currents of the nuclei about the Z-axis. One expects intuitively that the electrons follow the nuclear motion even in the stationary state such that the electrons should also circulate with the nuclei about the Z-axis although the electronic state is non-degenerate. But in the Born-Oppenheimer approximation $\Psi_{vi}^{tot} = \Psi_v^{nu}\Psi_i^{el}$ (Eq. (2.207)), the corresponding electronic current density $\mathbf{j}_{el}(\mathbf{r})$ (cf. Eq. (2.21)) is exactly zero, i.e.

$$\begin{aligned}
\mathbf{j}_{el}(\mathbf{r}) &= \frac{i\hbar N}{2m_e} \int\int\int d\mathbf{R}_1 \int\int\int d\mathbf{R}_2 \int\int\int d\mathbf{R}_3 \\
&\qquad \int\cdots\int \left(\Psi_{vi}^{tot} \nabla_{\mathbf{r}} (\Psi_{vi}^{tot})^* - (\Psi_{vi}^{tot})^* \nabla_{\mathbf{r}} \Psi_{vi}^{tot}\right) d\sigma_1 d\mathbf{q}_2 \ldots \mathbf{q}_N \\
&= \frac{i\hbar N}{2m_e} \int\int\int d\mathbf{R}_1 \int\int\int d\mathbf{R}_2 \int\int\int |\Psi_v^{nu}|^2 \, d\mathbf{R}_3 \\
&\qquad \int\cdots\int \left(\Psi_i^{el} \nabla_{\mathbf{r}} (\Psi_i^{el})^* - (\Psi_i^{el})^* \nabla_{\mathbf{r}} \Psi_i^{el}\right) d\sigma_1 d\mathbf{q}_2 \ldots \mathbf{q}_N \\
&= \mathbf{0}
\end{aligned} \tag{2.400}$$

because the nuclear wavefunction Ψ_v^{nu} is independent of the positions of the electrons, and the electronic wavefunction Ψ_i^{el} of the non-degenerate electronic state can be designed as a real function using real orbitals.

One can go beyond the Born-Oppenheimer approximation and use first-order perturbation theory to obtain the first-order term of the total wavefunction which can describe the non-zero electronic current due to nuclear motion even in the stationary state, see e.g. Refs. [255,256]. This implies that the electronic wavefunction has an additional phase factor due to moving nuclei, in general, depending on time and electronic as well as nuclear coordinates. In the semi-classical picture, in particular for application of atomic collisions, this phase is called travelling atomic orbital (TAO) or electron translation factor (ETF), see e.g. Refs. [257, 258]. Recently, an alternative approach for calculating electronic and nuclear fluxes (currents) in vibrating molecule H_2^+ was developed [259].

Nevertheless, the influence of the electronic ring currents on induced magnetic fields in pseudorotating molecules at $Z = 0, \pm R_e$ should be negligible. The reason is the broad distribution of the electronic probability density in the range of several a_0 which is larger than the typically very small mean ring current radii of the pseudorotating nuclei. For example, the maximal mean current radius of the light hydrogen nucleus of an XHX or HXH molecule for $v_b = |l| = 1$ is about $0.2\,a_0$. Hence, if the pseudorotating nucleus at $X = 0$, $Y > 0$ moves in the negative X-direction, then the broadly distributed electronic wavepacket at $X = 0$ but $Y \geq 0$ as well as $Y \leq 0$ moves in the same negative X-direction. After the half period, the nucleus at $X = 0$, $Y < 0$ and the electronic wavepacket at $X = 0$ and $Y \geq 0$ as well as $Y \leq 0$ move in the positive X-direction. This switch in direction leads to the oscillation of the electronic current densities at each point where its magnitudes (positive and negative directions) are slightly different due to the small displacement of the double mean ring current radii of the nucleus $2R_n$. Averaging the electronic current density over the stationary nuclear probability density yields the relatively weak toroidal electronic ring current with a corresponding relatively weak induced magnetic field at the ring center.

2.5 Nuclear dynamics

2.5.1 Circularly polarized laser pulses

The concept for the generation of nuclear ring currents and pseudorotation is the same as for the generation of electronic ring currents and circulation, see Fig. 2.6 (cf. Fig. 2.4 and Section 2.3). In particular, a right (+) or left (−) circularly polarized laser pulse propagating along the molecular axis of the linear triatomic molecule ABA (Z-axis) is used for the excitation from the vibrational non-degenerate ground state $|\Psi^{nu}_{v=0}\rangle$ to vibrational degenerate excited states $|\Psi^{nu}_{v\neq 0}\rangle$ carrying anti-clockwise (+) or clockwise (−) nuclear ring

currents with a non-zero Z-component of the total angular momentum $\langle\hat{\mathbf{L}}_{tot}\rangle \neq 0$ ($|l| \neq 0$). All formulae for the circularly polarized laser pulses given in Section 2.3.1 can be adopted here, for example the time-dependent circularly polarized vector potential (Eq. (2.98)) and electric field (Eq. (2.99)), laser envelope (Eq. (2.100)), and time-dependent intensity (Eq. (2.114)). Note that the linear triatomic non-polar molecule ABA has to be pre-aligned by means of a linearly polarized laser pulse [210, 213] and that the effective pulse duration of the circularly polarized laser pulse τ_c should be shorter than the rotational period of the linear molecule, i.e. the linear molecule should be aligned during the vibrational excitation. Furthermore, the laser frequency of the circularly polarized laser pulse ω_c should be near-resonant to the harmonic bending vibrational frequency ω_b such that the electronic and rotational transitions are off-resonant, i.e. the electronic state remains in the electronic non-degenerate singlet ground state $|\Psi_0^{el}\rangle = |X\,^1\Sigma_g^+\rangle$, and the time-dependent field-free rotational state after the alignment is not changed during the vibrational excitation.

2.5.2 Time-dependent nuclear Schrödinger equation

The laser driven vibrational and pseudorotational dynamics in the electronic ground state $|\Psi_0^{el}\rangle$ is described by the time-dependent nuclear Schrödinger equation (TDSE) within the electric dipole and Born-Oppenheimer (Eq. (2.207)) approximations,

$$i\hbar\frac{\partial}{\partial t}|\Phi(t)\rangle = \hat{H}_{vib}(t)|\Phi(t)\rangle \tag{2.401}$$

where $\hat{H}_{vib}(t)$ is the time-dependent vibrational Hamiltonian

$$\hat{H}_{vib}(t) = \hat{H}_{vib} - \tilde{\mathbf{M}}\cdot\mathbf{E}_{c\pm}(t). \tag{2.402}$$

The vibrational Hamiltonian $\hat{H}_{vib}$ is the nuclear Hamiltonian $\hat{T}_{nu} + V_0$ (Eq. (2.209)) but without kinetic operators for translation and rotation of the molecule, i.e.

$$\hat{H}_{vib} = -\frac{\hbar^2}{2m_s}\frac{\partial^2}{\partial Q_s^2} - \frac{\hbar^2}{2m_a}\frac{\partial^2}{\partial Q_a^2} - \frac{\hbar^2}{2m_b}\frac{1}{Q_b}\frac{\partial}{\partial Q_b}\left(Q_b\frac{\partial}{\partial Q_b}\right) + \frac{\hat{L}_{pr}^2}{2m_bQ_b^2} + V_0(Q_s, Q_a, Q_b) \tag{2.403}$$

(cf. Eq. (2.233)). The right (+) or left (−) circularly polarized electric field $\mathbf{E}_{c\pm}(t)$ is given in Eqs. (2.118) and (2.99), respectively. The dipole function $\tilde{\mathbf{M}}$ is defined as

$$\tilde{\mathbf{M}}(Q_s, Q_a, Q_b, \delta) = \langle\Psi_0^{el}|\mathbf{M}|\Psi_0^{el}\rangle \tag{2.404}$$

where the dipole operator $\mathbf{M}$ is given in Eq. (2.118). For symmetry reasons, the X- and Y- components of the dipole function $\tilde{\mathbf{M}}$ in polar coordinates are

$$\tilde{M}_X = \tilde{M}_\perp\cos\delta \tag{2.405}$$

$$\tilde{M}_Y = \tilde{M}_\perp\sin\delta \tag{2.406}$$

where $\tilde{M}_\perp(Q_s, Q_a, Q_b) = \tilde{M}_X(Q_s, Q_a, Q_b, \delta = 0) = \tilde{M}_Y(Q_s, Q_a, Q_b, \delta = \pi/2)$ denotes the component of the dipole function perpendicular to the Z-axis and depends, in principle, on the vibrational coordinates Q_s, Q_a, and Q_b but not on the pseudorotational coordinate δ. Since the Z-component of the electric field is zero, the interaction term is rewritten as

$$-\tilde{\mathbf{M}} \cdot \mathbf{E}_{c\pm}(t) \quad = \quad -\tilde{M}_\perp \left(E_{c\pm,X}(t) \cos\delta + E_{c\pm,Y}(t) \sin\delta \right), \tag{2.407}$$

cf. Eq. (2.119).

The ansatz for the time-dependent vibrational state $|\Phi(t)\rangle$ is

$$|\Phi(t)\rangle \quad = \quad \sum_{v=0}^{v'_{max}} C_v(t) |\Phi_v\rangle e^{-iE_{v0}(t-t_0)/\hbar} \tag{2.408}$$

where $|\Phi_v\rangle$ and E_{v0} are the vibrational eigenstates and eigenenergies of $\hat{H}_{vib}$ with vibrational quantum numbers $v = 0, 1, 2, \ldots$ in the electronic ground state $|\Psi_0^{el}\rangle$ (Eq. (2.233)). $C_v(t)$ and $v'_{max} + 1$ are the time-dependent coefficients and total number of vibrational states $|\Phi_v\rangle$ included in this expansion, respectively. Using $|\Phi_v\rangle = |\Phi_{v|l|}\rangle|\Phi_l\rangle$ (Eq. (2.234)), the ansatz (2.408) is then rewritten as

$$|\Phi(t)\rangle \quad = \quad \sum_{v=0}^{v_{max}} \sum_{l=-l_{max}}^{l_{max}} C_{vl}(t) |\Phi_{v|l|}\rangle|\Phi_l\rangle e^{-iE_{v|l|,0}(t-t_0)/\hbar} \tag{2.409}$$

where $v = 0, 1, 2, \ldots, v_{max}$ and $l = -l_{max}, \ldots, l_{max}$ are now the pure vibrational and pseudorotational quantum numbers, respectively, $E_{v|l|,0} = E_{v0}$ and $C_{vl}(t) = C_v(t)$. At the initial time t_0, the system is in the vibrational ground state $v = l = 0$, i.e.

$$|\Phi(t_0)\rangle \quad = \quad |\Phi_{v=0,|l|=0}\rangle|\Phi_{l=0}\rangle. \tag{2.410}$$

Inserting the ansatz (2.409) and (2.410) into the Schrödinger equation (2.401) and (2.402) yields the equivalent set of differential equations for the time-dependent coefficients

$$i\hbar \frac{d}{dt} C_{vl}(t) \quad = \quad \sum_{v'=0}^{v_{max}} \sum_{l'=-l_{max}}^{l_{max}} H_{vl,v'l'}(t) C_{v'l'}(t) \tag{2.411}$$

with initial condition

$$C_{vl}(t_0) \quad = \quad \delta_{v0}\delta_{l0} \tag{2.412}$$

($v = 0, \ldots, v_{max}; l = -l_{max}, \ldots, l_{max}$), cf. Eqs. (2.122), (2.123). The time-dependent matrix elements $H_{vl,v'l'}(t)$ are evaluated as

$$H_{vl,v'l'}(t) \quad = \quad -\tilde{\mathbf{M}}_{vl,v'l'} \cdot \mathbf{E}_{c\pm}(t) e^{-i\omega_{v'|l'|,v|l|}(t-t_0)} \tag{2.413}$$

with transition frequencies

$$\omega_{v'|l'|,v|l|} \quad = \quad \frac{E_{v'|l'|,0} - E_{v|l|,0}}{\hbar} \tag{2.414}$$

and transition dipole matrix elements

$$\tilde{\mathbf{M}}_{vl,v'l'} = \langle\Phi_{v|l|}|\langle\Phi_l|\tilde{\mathbf{M}}|\Phi_{l'}\rangle|\Phi_{v'|l|'}\rangle \tag{2.415}$$

$(v, v' = 0, \ldots, v_{max}; l, l' = -l_{max}, \ldots, l_{max})$. Since the wavefunction $\Phi_{v|l|}$ is independent of the pseudorotation δ, the corresponding X- and Y- components of the transition dipole matrix elements, using Eqs. (2.405), (2.406), (2.236), are evaluated as

$$\begin{aligned}
\tilde{M}_{vl,v'l',X} &= \langle\Phi_{v|l|}|\tilde{M}_\perp|\Phi_{v'|l'|}\rangle\langle\Phi_l|\cos\delta|\Phi_{l'}\rangle \\
&= \frac{1}{2\pi}\langle\Phi_{v|l|}|\tilde{M}_\perp|\Phi_{v'|l'|}\rangle\int_0^{2\pi} e^{i(l'-l)\delta}\cos\delta\, d\delta \\
&= \frac{1}{4\pi}\langle\Phi_{v|l|}|\tilde{M}_\perp|\Phi_{v'|l'|}\rangle\int_0^{2\pi} e^{i(l'-l)\delta}\left(e^{i\delta}+e^{-i\delta}\right) d\delta \\
&= \frac{1}{4\pi}\langle\Phi_{v|l|}|\tilde{M}_\perp|\Phi_{v'|l'|}\rangle\left(\int_0^{2\pi} e^{i(l'-l+1)\delta}\, d\delta + \int_0^{2\pi} e^{i(l'-l-1)\delta}\, d\delta\right) \\
&= \frac{1}{2}\langle\Phi_{v|l|}|\tilde{M}_\perp|\Phi_{v'|l'|}\rangle\left(\delta_{l'l-1}+\delta_{l'l+1}\right)
\end{aligned} \tag{2.416}$$

and

$$\begin{aligned}
\tilde{M}_{vl,v'l',Y} &= \langle\Phi_{v|l|}|\tilde{M}_\perp|\Phi_{v'|l'|}\rangle\langle\Phi_l|\sin\delta|\Phi_{l'}\rangle \\
&= \frac{1}{2\pi}\langle\Phi_{v|l|}|\tilde{M}_\perp|\Phi_{v'|l'|}\rangle\int_0^{2\pi} e^{i(l'-l)\delta}\sin\delta\, d\delta \\
&= \frac{1}{4i\pi}\langle\Phi_{v|l|}|\tilde{M}_\perp|\Phi_{v'|l'|}\rangle\int_0^{2\pi} e^{i(l'-l)\delta}\left(e^{i\delta}-e^{-i\delta}\right) d\delta \\
&= -\frac{i}{4\pi}\langle\Phi_{v|l|}|\tilde{M}_\perp|\Phi_{v'|l'|}\rangle\left(\int_0^{2\pi} e^{i(l'-l+1)\delta}\, d\delta - \int_0^{2\pi} e^{i(l'-l-1)\delta}\, d\delta\right) \\
&= -\frac{i}{2}\langle\Phi_{v|l|}|\tilde{M}_\perp|\Phi_{v'|l'|}\rangle\left(\delta_{l'l-1}-\delta_{l'l+1}\right),
\end{aligned} \tag{2.417}$$

respectively. Thus, the matrix elements (Eq. (2.413)) are rewritten as

$$\begin{aligned}
H_{vl,v'l'}(t) = -\frac{1}{2}\langle\Phi_{v|l|}|\tilde{M}_\perp|\Phi_{v'|l'|}\rangle\,[&(E_{c\pm,X}(t) - iE_{c\pm,Y}(t))\,\delta_{l'l-1} \\
&+ (E_{c\pm,X}(t) + iE_{c\pm,Y}(t))\,\delta_{l'l+1}]
\end{aligned} \tag{2.418}$$

$(v, v' = 0, \ldots, v_{max}; l, l' = -l_{max}, \ldots, l_{max})$. Since the Z-component of the electric field is zero, the Z-component of the transition dipole matrix element is irrelevant. Because of the factors $\delta_{l'l-1}$ and $\delta_{l'l+1}$ in Eq. (2.418), the diagonal matrix elements $H_{vl,vl}(t)$ are exactly zero. Moreover, the selection rule $l \rightarrow l \pm 1$ holds for pseudorotational transitions, by analogy with the selection rule for laser-induced electron circulation and electronic ring currents in atoms, atomic ions, and aligned linear molecules, see Section 2.3.2. Thus, we expect that the right (+) and left (−) circularly polarized laser pulses will induce dominant pseudorotational transitions $l \rightarrow l+1$ and $l \rightarrow l-1$ for absorption, or $l \rightarrow l-1$ and $l \rightarrow l+1$ for stimulated emission, respectively, see Fig. 2.7.

In the so-called double harmonic approximation (DHA), one uses the harmonic potential $V_0^h(Q_s, Q_a, Q_b)$ (Eq. (2.240)) for the potential energy surface together with the linear approximation for the dipole function [207, 208]

$$\tilde{M}_\perp^h(Q_b) = \left.\frac{\partial \tilde{M}_\perp(Q_s, Q_a, Q_b)}{\partial Q_b}\right|_{Q_s=Q_a=Q_b=0} Q_b \tag{2.419}$$

where the zeroth-order term $\tilde{M}_\perp(Q_s = 0, Q_a = 0, Q_b = 0)$ for a linear triatomic molecule ABA is zero due to symmetry. The DHA matrix elements $\langle \Phi_{v|l|} | \tilde{M}_\perp^h | \Phi_{v'|l'|} \rangle \approx \langle \Phi_{v|l|} | \tilde{M}_\perp | \Phi_{v'|l'|} \rangle$ for $l' = l \pm 1$ (cf. Eq. (2.418)), using Eqs. (2.241), (2.245), (2.246), (2.251), (2.419), are

$$\langle \Phi_{v|l|} | \tilde{M}_\perp^h | \Phi_{v'|l'|} \rangle = \left.\frac{\partial \tilde{M}_\perp(Q_s, Q_a, Q_b)}{\partial Q_b}\right|_{Q_s=Q_a=Q_b=0} \delta_{v_s v_s'} \delta_{v_a v_a'} \langle \Phi_{v_b|l|} | Q_b | \Phi_{v_b'|l'|} \rangle \tag{2.420}$$

where [207, 208]

$$\begin{aligned} \langle \Phi_{v_b|l|} | Q_b | \Phi_{v_b'|l'|} \rangle = {} & \delta_{v_b' v_b + 1} \left(\delta_{|l'||l|+1} \sqrt{\frac{v_b + |l|}{2} + 1} - \delta_{|l'||l|-1} \sqrt{\frac{v_b - |l|}{2} + 1} \right) \\ & + \delta_{v_b' v_b - 1} \left(\delta_{|l'||l|-1} \sqrt{\frac{v_b' + |l'|}{2} + 1} - \delta_{|l'||l|+1} \sqrt{\frac{v_b' - |l'|}{2} + 1} \right) \end{aligned} \tag{2.421}$$

for $l' = l \pm 1$. Thus, the DHA yields selection rules

$$v_s' = v_s \tag{2.422}$$

$$v_a' = v_a \tag{2.423}$$

$$v_b' = v_b \pm 1 \tag{2.424}$$

$$l' = l \pm 1. \tag{2.425}$$

Starting from the ground state $v_s = v_a = v_b = l = 0$, the dominant absorption processes ($v_b \to v_b + 1$, $l \to l + 1$ and $l \to l - 1$, "double" ladder climbing) by means of a right and left circularly polarized laser pulse are illustrated schematically by red and blue arrows in Fig. 2.7, respectively.

In the anharmonic model where the harmonic and anharmonic eigenenergies are different, i.e. $E_{v|l|,0}^h \neq E_{v|l|,0}$, we use quantum numbers v_s, v_a, v_b, and l for the dominant contribution of the harmonic vibrational wavefunctions, denoted as $v, l = (v_s, v_b^l, v_a)$. According to the DHA selection rules (Eqs. (2.422)–(2.425)), we neglect the transitions from anharmonic vibrational states $|v, l\rangle = |(v_s = 0, v_b^l, v_a = 0)\rangle$ to other states $|v', l'\rangle = |(v_s', v_b'^{l'}, v_a')\rangle$ where $l' = l \pm 1$ and $v_s' + v_a' > 0$. In this approximation, the ansatz (2.409) and the propagation of the set of equations (2.411) for the time-dependent coefficients $C_{vl}(t) = C_{v_b l}(t)$ are, therefore, restricted to quantum numbers $v, l = (v_s = 0, v_b^l, v_a = 0)$.

The differential equations (2.411) together with the initial condition (2.412) are then solved by the same Runge-Kutta method [245] as for electron dynamics, but with larger time step sizes. For example, $\Delta t = 1\,\mathrm{fs}$ for $^{114}CdH_2$ and $\Delta t = 5\,\mathrm{fs}$ for FHF^-. Of course, the convergence of the results is tested with respect to the number of bending and pseudorotational states which are included in the expansion (Eq. (2.409)), for example $0 \leq v_b \leq 10$ for $^{114}CdH_2$ [207] and $0 \leq v_b \leq 4$ for FHF^- [208]. Finally, the resulting time-dependent coefficients yield time-dependent populations of bending and pseudorotational states, i.e.

$$P_{v_b l}(t) = |C_{v_b l}(t)|^2, \tag{2.426}$$

and the corresponding time-dependent mean values of quantum numbers for the bend and pseudorotation

$$\langle v_b(t)\rangle = \sum_{v_b=0}^{v_{b,max}} \sum_{l=-l_{max}}^{l_{max}} v_b P_{v_b l}(t) \tag{2.427}$$

$$\langle l(t)\rangle = \sum_{v_b=0}^{v_{b,max}} \sum_{l=-l_{max}}^{l_{max}} l P_{v_b l}(t). \tag{2.428}$$

The latter corresponds to the time-dependent mean value of the Z-component of the total angular momentum, i.e.

$$\langle \hat{L}_{tot,Z}(t)\rangle = \langle l(t)\rangle \hbar, \tag{2.429}$$

cf. Eq. (2.326).

2.5.3 Nuclear pseudorotation

In an analogous way as in Section 2.3.4, the expressions for the time-dependent nuclear probability and current densities are similar, i.e. by inserting the time variable t in Eqs. (2.257), (2.281), (2.297), (2.309), cf. Eqs. (2.176), (2.177), and using the ansatz (2.409) for the time-dependent vibrational state $|\Phi(t)\rangle$ while the electronic state remains in the ground state $|\Psi_0^{el}\rangle$ and therefore time-independent. For $t \leq t_0$, the molecule is in the vibrational and electronic ground state and the corresponding nuclear probability and current densities are stationary. While the electric field is turned on at time t_0, the nuclear probability and current densities for $t \geq t_0$ are, in general, no longer stationary. In the harmonic approximation and assuming that the symmetric and antisymmetric stretches are not excited ($v_s = v_a = 0$), the time-dependent probability densities of the nuclei A_1, A_2, and B are

$$\rho_{A_1}(\mathbf{R},t) = \frac{1}{2\pi}\frac{M^2}{M_B^2}\, I_{00}(Z+R_e) \left| \sum_{v_b=0}^{v_{b,max}} \sum_{l=-l_{max}}^{l_{max}} C_{v_b l}(t)\Phi^h_{v_b|l|}\left(\frac{M}{M_B}\,\rho\right) e^{il(\phi+\pi)} e^{-iE_{v_b|l|,0}(t-t_0)/\hbar} \right|^2, \tag{2.430}$$

$$\rho_{A_2}(\mathbf{R},t) = \frac{1}{2\pi}\frac{M^2}{M_B^2}\, I_{00}(Z-R_e) \left| \sum_{v_b=0}^{v_{b,max}} \sum_{l=-l_{max}}^{l_{max}} C_{v_b l}(t)\Phi^h_{v_b|l|}\left(\frac{M}{M_B}\,\rho\right) e^{il(\phi+\pi)} e^{-iE_{v_b|l|,0}(t-t_0)/\hbar} \right|^2, \tag{2.431}$$

and

$$\rho_B(\mathbf{R},t) = \frac{1}{16\pi}\frac{M^3}{M_A^3}\left(\Phi^h_{v_a=0}\left(\frac{M}{2M_A}\,Z\right)\right)^2 \left| \sum_{v_b=0}^{v_{b,max}} \sum_{l=-l_{max}}^{l_{max}} C_{v_b l}(t)\Phi^h_{v_b|l|}\left(\frac{M}{2M_A}\,\rho\right) e^{il\phi} e^{-iE_{v_b|l|,0}(t-t_0)/\hbar} \right|^2, \tag{2.432}$$

respectively, cf. Eqs. (2.270), (2.271), (2.293). Note that the pseudorotation δ was replaced by $\phi+\pi$ for nuclei A_1 and A_2, and by ϕ for nucleus B since $\cos\delta = Q_{b,X}/Q_b = -X/\rho = -\cos\phi$ for nuclei A_1 and A_2, and $\cos\delta = Q_{b,X}/Q_b = X/\rho = \cos\phi$ for nucleus B (cf. Eqs. (2.225), (2.262), (2.264), (2.285), (2.287)). As in Section 2.3.4, the time-dependent nuclear probability densities (Eqs. (2.430)–(2.432)) are the sum of the nuclear probability densities of vibrational stationary states weighted by their time-dependent populations $P_{v_b l}(t)$ plus the interference terms. After the end of the laser pulse, i.e. $t \geq t_f$, the coefficients $C_{v_b l}(t) = C_{v_b l}(t_f)$ and corresponding populations $P_{v_b l}(t) = P_{v_b l}(t_f)$ are time-independent but the nuclear probability densities and also current densities are, in general, time-dependent because of the time-dependent exponential factors in the interference terms in Eqs. (2.430)–(2.432), cf. Eqs. (2.182), (2.183). In this case, the exponential factors depending on the azimuthal angle ϕ and time t lead to the non-stationary nuclear pseudorotation about the Z-axis. Moreover, in the harmonic approximation, the l-independent vibrational eigenenergies $E_{v_b|l|,0} \approx E^h_{v_b|l|,0} = \frac{1}{2}\hbar\omega_s + \frac{1}{2}\hbar\omega_a + (v_b+1)\hbar\omega_b$ (Eq. (2.255)) are equidistant, i.e. the transition frequency of all neighboring states with respect to v_b is $\omega = \omega_b$. With this approximation, the nuclear probability and current densities (cf. Eqs. (2.195), (2.196)) as well as the electric currents and induced magnetic fields (cf. Eqs. (2.198), (2.199)) are periodic in ωt. In the anharmonic model, however, this periodicity is no longer strictly valid, i.e. the distribution of the nuclear densities circulating about the Z-axis changes slowly with time and has revival structures, cf. Refs. [260–266].

In the special case in which the population of the target vibrational state $|(0, v_b^l, 0)\rangle$ ($l \neq 0$) at the final time t_f is approximately equal to 1, the interference terms in Eqs. (2.430)–(2.432) for $t \geq t_f$ are negligible due to almost no populations of other vibrational states. The nuclear pseudorotation and ring currents as well as electric ring currents and

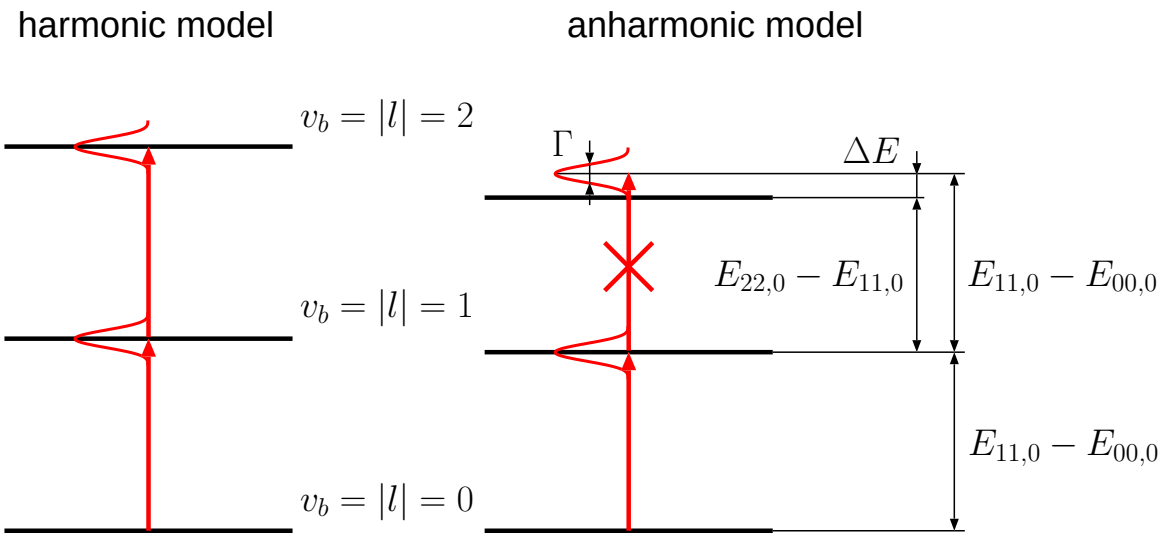

Figure 2.9: Vibrational levels ($v_b = |l| = 0, 1, 2$) and resonant excitations (red arrows) in the harmonic and anharmonic models with equidistant and non-equidistant energies $E^h_{v_b|l|,0}$ and $E_{v_b|l|,0}$, respectively, where the anharmonic energies $E_{v_b|l|,0}$ are shifted to $E_{v_b|l|,0} + E^h_{00,0} - E_{00,0}$. Multiphoton transitions ("double" ladder climbing, see Fig. 2.7) in the harmonic model by means of the right circularly polarized laser pulse can be supressed in the anharmonic model where the spectral width Γ of the laser pulse must be smaller than the anharmonicity ΔE, see Eq. (2.436). This condition implies that the effective pulse duration τ_c must be sufficiently long, but on the other hand, it must be much shorter than the rotational revival time τ_{rev} of the linear triatomic molecule ABA.

induced magnetic fields after the end of the laser pulse are stationary. For example, the nuclear current densities for $t \geq t_f$ are

$$\rho_{A_1}(\mathbf{R}, t) \approx \rho_{A_1}(\mathbf{R}) \tag{2.433}$$

$$\rho_{A_2}(\mathbf{R}, t) \approx \rho_{A_2}(\mathbf{R}) \tag{2.434}$$

$$\rho_B(\mathbf{R}, t) \approx \rho_B(\mathbf{R}). \tag{2.435}$$

The nuclear ring currents of the excited vibrational state $|(0, v^l_b, 0)\rangle$ $(l \neq 0)$ persist after the laser pulse until they decay by means of spontaneous emission with the corresponding lifetime (ms timescale) which is typically longer than the effective pulse duration (fs/ps timescale) and the periods of nuclei about the Z-axis (fs timescale).

The complete population transfer from the vibrational ground state $|(0, 0^0, 0)\rangle$ to the first degenerate state $|(0, 1^1, 0)\rangle$ can be achieved by means of a right circularly polarized reoptimized π laser pulse, see Section 2.3.3, but with the following important considerations for vibrational excitations. We know that in the harmonic approximation with equidistant level spacings there are sequential multiphoton transitions to higher states due to double ladder climbing, see Figs. 2.7 and 2.9. To avoid this, we must take an anhar-

monic model into account with non-equidistant vibrational energies $E_{v|l|,0}$. In particular, the transition from the state $|(0,1^1,0)\rangle$ to the higher state $|(0,2^2,0)\rangle$ can be supressed by the suitable choice of the spectral width Γ of the laser pulse. The spectral width Γ should be smaller than the absolute difference between two transition energies, denoted as the anharmonicity ΔE,

$$\Gamma \;<\; \Delta E \;=\; |(E_{v_b=2,|l|=2,0} - E_{v_b=1,|l|=1,0}) - (E_{v_b=1,|l|=1,0} - E_{v_b=0,|l|=0,0})|, \quad (2.436)$$

see Fig. 2.9. Since the anharmonicity ΔE is, in general, small, the effective pulse duration τ_c of the circularly polarized laser pulse (Eq. (2.99)) must be sufficiently long, typically a few ps. On the other hand, τ_c must be much shorter than the rotational revival time τ_{rev}, see Section 2.6.3, because the molecule must be aligned during the vibrational excitation. Moreover, the rotational revival time for the HXH molecule is shorter than the one for the XHX molecule, where X is the heavy nucleus. Thus, the complete population transfer can be achieved for the XHX molecule, but it can also be achieved for the HXH molecule if the anharmonicity ΔE (2.436) is sufficiently large.

2.6 Nonadiabatic orientation of a linear molecule

For all applications described in this work, i.e. the generation of electron or nuclear circulations with corresponding ring currents and induced magnetic fields, linear or ring-shaped molecules must be aligned or oriented during short electronic or vibrational excitations. The nonadiabatic alignment [210–214] and orientation [113,146,215–217] of the non-polar and polar molecules can be achieved by means of a linearly polarized HCP. After the HCP, the rotational wavepacket evolves under field-free conditions similar to the field-free non-stationary electron circulation and nuclear pseudorotation after the circularly polarized laser pulse. In addition, the wavepacket dephases due to non-equidistant rotational level spacings but it will be reconstructed periodically at intervals of the rotational revival time τ_{rev} [225]. However, in this work only the nonadiabatic orientation of linear polar molecules, such as BeO [146] and AlCl [145], is investigated, whereas the nonadiabatic alignment of non-polar molecules can be achieved according to Refs. [210–214], in which the polarizability α plays a dominant role since the permanent dipole moments of the non-polar molecules are zero. Furthermore, the typically weak rotational-vibrational coupling is neglected in this work, since the time scales on which the effects of such interactions are observable are much longer (ns timescale) [226] than the pulse durations of the laser pulses and than the time scales of electron circulation and nuclear pseudorotations, see Sections 2.3.4 and 2.5.3.

2.6.1 Rotational states

At the initial time $t = 0$, the linear polar molecule BeO or AlCl is in the vibrational and electronic non-degenerate ground state at a rotational temperature $T > 0\,\mathrm{K}$, hence the inital state is the $|X\,^1\Sigma^+(v = 0)\rangle$ vibronic state with a Boltzmann distribution of the rotational states $|JM\rangle$ where $J = 0, 1, 2, \ldots, J_{max}$ and $M = -J, -J{+}1, \ldots, J{-}1, J$ are the corresponding rotational quantum numbers. In the rigid-rotor limit where the rotational-vibrational coupling is neglected, the $(2J + 1)$-fold degenerate rotational energies of the $X\,^1\Sigma^+(v = 0)$ state are

$$E_X^J \;=\; B_{e,X} J(J+1) \tag{2.437}$$

where $B_{e,X}$ denotes the rotational constant of the molecule. The Boltzmann weights of the states $|JM\rangle$ are then calculated as

$$P(J,M) \;=\; \tilde{P}(J) \;=\; \frac{e^{-B_{e,X}J(J+1)/k_BT}}{\sum_{J=0}^{J_{max}}(2J+1)e^{-B_{e,X}J(J+1)/k_BT}} \tag{2.438}$$

where k_B is the Boltzmann constant.

2.6.2 Linearly polarized laser pulses

Linearly (l) polarized HCPs have been applied to achieve molecular orientation [113, 215–217], but most reported pulses do not satisfy the corresponding condition (2.111) for the linearly polarized laser pulse, i.e. [141, 242, 243]

$$\int_{-\infty}^{\infty} \mathbf{E}_l(t)\,dt \;=\; \mathbf{0}. \tag{2.439}$$

Hence, the time-dependent linearly polarized electric field with non-zero z-component propagating along the axis perpendicular to the laboratory-fixed z-axis is constructed as

$$\mathbf{E}_l(t) \;=\; \begin{cases} \mathbf{0} & (t \le 0) \\ -\mathcal{E}_{1,l}\cos^2\left(\frac{\omega_l(t-t_{p,l})}{2}\right)\sin(\omega_l(t-t_{p,l}))\,\mathbf{e}_z & (0 \le t \le t_{p,l}) \\ -\mathcal{E}_{2,l}(1-e^{-(t-t_{p,l})/\tau_{1,l}})e^{-(t-t_{p,l})/\tau_{2,l}}\,\mathbf{e}_z & (t \ge t_{p,l}), \end{cases} \tag{2.440}$$

where $\mathcal{E}_{1,l}$, $\mathcal{E}_{2,l}$ are amplitudes, ω_l is the carrier frequency, $t_{p,l} = \pi/\omega_l$ is the pulse duration of the first part of the laser pulse ($0 \le t \le t_{p,l}$), $\tau_{1,l}$, $\tau_{2,l}$ are the switch-on and switch-off times of the second part of the laser pulse ($t \ge t_{p,l}$), respectively. It is obvious that the first part of the laser pulse is zero at $t = 0$ and $t = t_{p,l}$ since $\sin(-\omega_l t_{p,l}) = -\sin(\pi) = 0$ and $\sin(\omega(t_{p,l} - t_{p,l})) = 0$, respectively, and the second part of the laser pulse is also zero

at $t = t_{p,l}$ since $1 - e^{-(t_{p,l}-t_{p,l})/\tau_{1,l}} = 1 - e^0 = 1 - 1 = 0$. Moreover, the electric field (2.440) must be smooth at $t = 0$ and $t = t_{p,l}$. The derivative of the electric field is given by

$$\frac{d}{dt}\,\mathbf{E}_l(t) \;=\; \begin{cases} \mathbf{0} & (t \le 0) \\ -\mathcal{E}_{1,l}\omega_l \cos\left(\frac{\omega_l(t-t_{p,l})}{2}\right)\left[\cos\left(\frac{\omega_l(t-t_{p,l})}{2}\right)\cos(\omega_l(t-t_{p,l}))\right. & \\ \qquad\left. -\sin\left(\frac{\omega_l(t-t_{p,l})}{2}\right)\sin(\omega_l(t-t_{p,l}))\right]\,\mathbf{e}_z & (0 \le t \le t_{p,l}) \\ -\mathcal{E}_{2,l}\left[\frac{1}{\tau_{1,l}}\,e^{-(t-t_{p,l})/\tau_{1,l}}e^{-(t-t_{p,l})/\tau_{2,l}}\right. & \\ \qquad\left. -\frac{1}{\tau_{2,l}}\,(1-e^{-(t-t_{p,l})/\tau_{1,l}})e^{-(t-t_{p,l})/\tau_{2,l}}\right]\,\mathbf{e}_z & (t \ge t_{p,l}) \end{cases} . \tag{2.441}$$

At $t = 0$, we have $\cos(\omega_l(t - t_{p,l})/2) = \cos(\pi/2) = 0$, thus the electric field at $t = 0$ is always smooth. The condition that the electric field is also smooth at $t = t_{p,l}$ leads to

$$\mathcal{E}_{1,l}\omega_l \;=\; \frac{\mathcal{E}_{2,l}}{\tau_{1,l}} \tag{2.442}$$

which can be easily verified using Eq. (2.441). Thus, the formula for the switch-on time of the second part of the laser pulse is

$$\tau_{1,l} \;=\; \frac{\mathcal{E}_{2,l}}{\mathcal{E}_{1,l}\omega_l}. \tag{2.443}$$

Finally, using Eq. (2.440), $t_{p,l} = \pi/\omega_l$, and $\sin(2x) = 2\sin x \cos x$, the condition (2.439) is rewritten as

$$\begin{aligned} \int_{-\infty}^{\infty} \mathbf{E}_l(t)\,dt \;&=\; -\mathcal{E}_{1,l}\int_0^{t_{p,l}} \cos^2\left(\frac{\omega_l(t-t_{p,l})}{2}\right)\sin(\omega_l(t-t_{p,l}))\,dt\,\mathbf{e}_z \\ &\quad -\mathcal{E}_{2,l}\int_{t_{p,l}}^{\infty}(1-e^{-(t-t_{p,l})/\tau_{1,l}})e^{-(t-t_{p,l})/\tau_{2,l}}\,dt\,\mathbf{e}_z \\ &=\; -2\mathcal{E}_{1,l}\int_0^{t_{p,l}} \cos^3\left(\frac{\omega_l(t-t_{p,l})}{2}\right)\sin\left(\frac{\omega_l(t-t_{p,l})}{2}\right)\,dt\,\mathbf{e}_z \\ &\quad -\mathcal{E}_{2,l}\int_{t_{p,l}}^{\infty} e^{-(t-t_{p,l})/\tau_{2,l}}\,dt\,\mathbf{e}_z + \mathcal{E}_{2,l}\int_{t_{p,l}}^{\infty} e^{-(t-t_{p,l})\left(\frac{1}{\tau_{1,l}}+\frac{1}{\tau_{2,l}}\right)}\,dt\,\mathbf{e}_z \\ &=\; \frac{\mathcal{E}_{1,l}}{\omega_l}\,\cos^4\left(\frac{\omega_l(t-t_{p,l})}{2}\right)\Bigg|_0^{t_{p,l}}\,\mathbf{e}_z \\ &\quad +\mathcal{E}_{2,l}\tau_{2,l}\,e^{-(t-t_{p,l})/\tau_{2,l}}\Big|_{t_{p,l}}^{\infty}\,\mathbf{e}_z - \mathcal{E}_{2,l}\,\frac{\tau_{1,l}\tau_{2,l}}{\tau_{1,l}+\tau_{2,l}}\;e^{-(t-t_{p,l})\left(\frac{1}{\tau_{1,l}}+\frac{1}{\tau_{2,l}}\right)}\Bigg|_{t_{p,l}}^{\infty}\,\mathbf{e}_z \\ &=\; \left(\frac{\mathcal{E}_{1,l}}{\omega_l} - \mathcal{E}_{2,l}\tau_{2,l} + \mathcal{E}_{2,l}\,\frac{\tau_{1,l}\tau_{2,l}}{\tau_{1,l}+\tau_{2,l}}\right)\mathbf{e}_z \\ &=\; \left(\frac{\mathcal{E}_{1,l}}{\omega_l} - \frac{\mathcal{E}_{2,l}\tau_{2,l}^2}{\tau_{1,l}+\tau_{2,l}}\right)\mathbf{e}_z \;=\; \mathbf{0}, \end{aligned} \tag{2.444}$$

thus

$$\frac{\mathcal{E}_{1,l}}{\omega_l} \;=\; \frac{\mathcal{E}_{2,l}\tau_{2,l}^2}{\tau_{1,l}+\tau_{2,l}}, \tag{2.445}$$

and using Eq. (2.442)

$$\frac{1}{\omega_l^2 \tau_{1,l}} = \frac{\tau_{2,l}^2}{\tau_{1,l} + \tau_{2,l}}, \tag{2.446}$$

or

$$\tau_{2,l}^2 - \frac{\tau_{2,l}}{\omega_l^2 \tau_{1,l}} - \frac{1}{\omega_l^2} = 0. \tag{2.447}$$

The solution of this quadratic equation for the switch-off time $\tau_{2,l} > 0$ is therefore

$$\tau_{2,l} = \frac{1}{2\omega_l^2 \tau_{1,l}} + \sqrt{\frac{1}{4\omega_l^4 \tau_{1,l}^2} + \frac{1}{\omega_l^2}}. \tag{2.448}$$

Since the first part of the laser pulse ($0 \leq t \leq t_{p,l}$) is similar to a HCP, the corresponding magnitude must exceed that of the second part of the laser pulse ($t \geq t_{p,c}$), i.e. $|\mathcal{E}_{1,l}| > |\mathcal{E}_{2,l}|$. Then, the switch-on time $\tau_{1,l}$ (Eq. (2.443)) is short, and the switch-off time $\tau_{2,l}$ (Eq. (2.448)) is long, i.e. the second part of the laser pulse has a long tail. With a compromise between a large amplitude ratio $\mathcal{E}_{1,l}/\mathcal{E}_{2,l}$ and an acceptable switch-off time $\tau_{2,l}$, we use $\mathcal{E}_{1,l}/\mathcal{E}_{2,l} = 10$ in this work. The laser amplitude $\mathcal{E}_{1,l}$ and carrier frequency ω_l should be optimized to yield the best orientation of the linear molecule. Note that the carrier frequency ω_l must be small with respect to the vibrational and electronic transition frequencies from the ground state, i.e. it is off-resonant with all vibrational and electronic excitations, and hence the molecule remains in the electronic and vibrational ground state $X\,^1\Sigma^+(v = 0)$, while the moderately intense laser pulse populates a broad rotational wavepacket. The other laser parameters, i.e. pulse duration $t_{p,l}$, switch-on $\tau_{1,l}$ and switch-off $\tau_{2,l}$ times, are estimated using $t_{p,l} = \pi/\omega_l$ and Eqs. (2.443), (2.448), respectively. The time-dependent intensity of the laser pulse is given by [244]

$$I_l(t) = c\varepsilon_0 |\mathbf{E}_l(t)|^2, \tag{2.449}$$

cf. Eq. (2.114), and its maximum $I_{l,max} = \max I_l(t)$ is smaller than $c\varepsilon_0 \mathcal{E}_{1,l}^2$. In passing, we note that similar HCPs have been constructed, e.g. in Ref. [141], aiming at entirely different goals, i.e. control of unidirectional rescattering of electrons. A counterintuitive result of Ref. [141] is that the effect of the long weak second part of the HCP may be quite important.

2.6.3 Time-dependent Schrödinger equation for a rigid-rotor

In the rigid-rotor approximation, the time-dependent Schrödinger equation for the rotational state $|\Psi_{rot}(t)\rangle$ is written within the electric dipole approximation as

$$i\hbar \frac{\partial}{\partial t} |\Psi_{rot}(t)\rangle = \hat{H}_{rot}(t) |\Psi_{rot}(t)\rangle \tag{2.450}$$

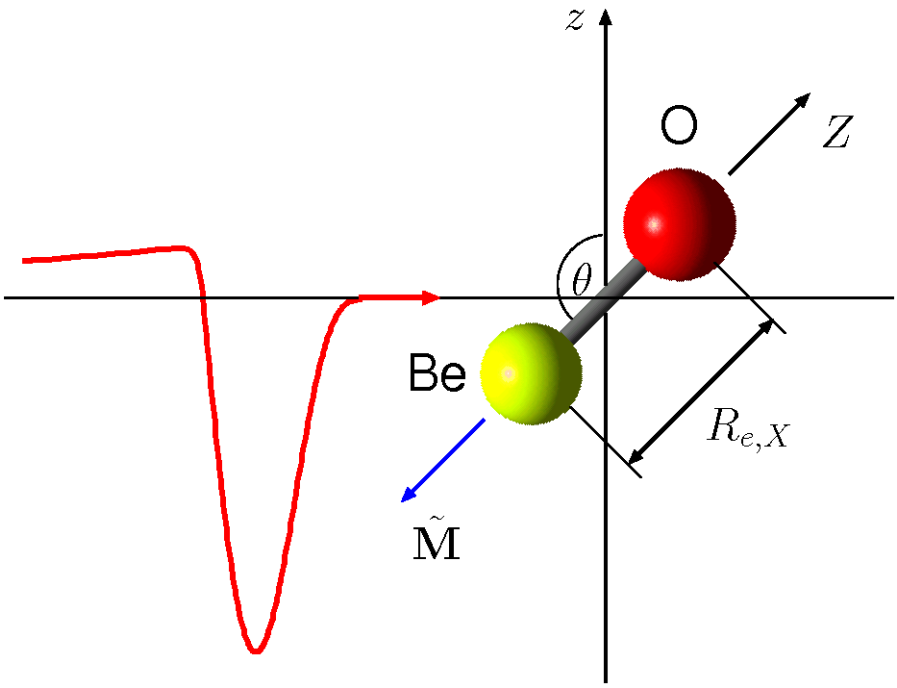

Figure 2.10: Negative orientation of the diatomic polar BeO molecule by means of a linearly polarized HCP $\mathbf{E}_l(t)$ (Eq. (2.440)) (with negative amplitudes $\mathcal{E}_{1,l}$ and $\mathcal{E}_{2,l}$) propagating along the axis perpendicular to the laboratory-fixed z-axis. The direction of the permanent electric dipole moment $\tilde{\mathbf{M}}$ (blue arrow) is from the O to the Be atom, i.e. it is the direction of the negative molecular Z-axis. In the perfect negative orientation of the BeO molecule, the laboratory-fixed z- and molecular Z-axes coincide, i.e. $\theta = 180°$.

where $\hat{H}_{rot}(t)$ is the time-dependent rotational Hamiltonian

$$\hat{H}_{rot}(t) \quad = \quad \hat{H}_{rot} - \tilde{M}(R_{e,X}) E_{l,z}(t) \cos\theta, \tag{2.451}$$

$\hat{H}_{rot}$ is the rigid-rotor rotational Hamiltonian

$$\hat{H}_{rot} \quad = \quad B_{e,X} \hat{J}^2, \tag{2.452}$$

and $\hat{J}$ is the total angular momentum operator with corresponding rotational eigenstates $|JM\rangle$ and eigenenergies $E_X^J = B_{e,X} J(J+1)$ (Eq. (2.437)). In the second term of Eq. (2.451), $\tilde{M}(R_{e,X})$ denotes the magnitude of the permanent electric dipole moment at the equilibrium bond length $R_{e,X}$ of the electronic ground state of the diatomic polar molecule, i.e.

$$\tilde{M}(R_{e,X}) \quad = \quad |\tilde{\mathbf{M}}(R_{e,X})| \quad = \quad |\langle \Psi_0^{el} | \mathbf{M} | \Psi_0^{el} \rangle|, \tag{2.453}$$

cf. Eq. (2.404), $E_{l,z}(t)$ is the z-component of the time-dependent electric field $\mathbf{E}_l(t)$ (Eq. (2.440)), and θ is the angle between the laboratory-fixed z-axis and the direction of the permanent electric dipole moment $\tilde{\mathbf{M}}(R_{e,X})$ of the molecule, see Fig. 2.10.

As for electron and vibrational dynamics, the time-dependent rotational state $|\Psi_{rot}(t)\rangle$ is expanded in terms of the rotational states $|JM\rangle$ as

$$|\Psi_{rot}^{J_iM_i}(t)\rangle \;=\; \sum_{J=0}^{J_{max}} \sum_{M=-J}^{J} C_{JM}^{J_iM_i}(t)|JM\rangle e^{-iE_X^J t/\hbar}, \tag{2.454}$$

cf. Eqs. (2.120), (2.408), with the initial condition

$$|\Psi_{rot}^{J_iM_i}(t=0)\rangle \;=\; |J_iM_i\rangle. \tag{2.455}$$

Inserting the ansatz (2.454) and (2.455) into the Schrödinger equation (2.450) yields the set of coupled differential equations for the time-dependent coefficients,

$$i\hbar \frac{d}{dt} C_{JM}^{J_iM_i}(t) \;=\; \sum_{J'=0}^{J_{max}} \sum_{M'=-J'}^{J'} H_{JM,J'M'}(t) C_{J'M'}^{J_iM_i}(t), \tag{2.456}$$

with the initial conditions

$$C_{JM}^{J_iM_i}(t=0) \;=\; \delta_{JJ_i}\delta_{MM_i} \tag{2.457}$$

($J = 0, 1, \ldots, J_{max}; M = -J, -J+1, \ldots, J-1, J$), cf. Eqs. (2.122), (2.123), (2.411), (2.412). The time-dependent matrix elements $H_{JM,J'M'}(t)$ are

$$H_{JM,J'M'}(t) \;=\; -\tilde{M}(R_{e,X}) E_{l,z}(t) \langle JM|\cos\theta|J'M'\rangle e^{-i\omega_{J'J}t} \tag{2.458}$$

with transition frequencies

$$\omega_{J'J} \;=\; \frac{E_X^{J'} - E_X^J}{\hbar} \tag{2.459}$$

and transition matrix elements [267, 268]

$$\langle JM|\cos\theta|J'M'\rangle \;=\; \delta_{MM'}(-1)^M \sqrt{(2J+1)(2J'+1)} \begin{pmatrix} J & 1 & J' \\ M & 0 & -M \end{pmatrix} \begin{pmatrix} J & 1 & J' \\ 0 & 0 & 0 \end{pmatrix} \tag{2.460}$$

($J = 0, 1, \ldots, J_{max}; M = -J, -J+1, \ldots, J-1, J$). These matrix elements yield the selection rules for the rotational transitions $J' = J \pm 1$ and $M' = M$. Thus, the differential equations (2.456) are simplified to

$$i\hbar \frac{d}{dt} C_{JM_i}^{J_iM_i}(t) \;=\; \sum_{0 \le J' = J\pm 1 \le J_{max}} H_{JM_i,J'M_i}(t) C_{J'M_i}^{J_iM_i}(t) \tag{2.461}$$

for $J = 0, 1, \ldots, J_{max}$, and

$$C_{JM}^{J_iM_i}(t=0) \;=\; 0 \tag{2.462}$$

for $M \neq M_i$. The time-dependent rotational wavepacket $|\Psi_{rot}^{J_iM_i}(t)\rangle$ (Eq. (2.454)) is then rewritten as

$$|\Psi_{rot}^{J_iM_i}(t)\rangle = \sum_{J=0}^{J_{max}} C_{JM_i}^{J_iM_i}(t)|JM_i\rangle e^{-iE_X^J t/\hbar}. \tag{2.463}$$

The differential equations (2.461) with initial condition (2.462) are solved by means of the same Runge-Kutta method [245] as for electron and vibrational dynamics, cf. Sections 2.3 and 2.5, respectively. For BeO molecule, the time step size is chosen as $\Delta t = 5\,\mathrm{fs}$ with which the convergence results are obtained for a low rotational temperature $T = 1\,\mathrm{K}$ and moderate total number $J_{max} = 13$ of rotational states which are included in the expansion (Eq. (2.463)). The resulting time-dependent coefficients depending on the initial state $|J_iM_i\rangle$ yield the time-dependent expectation value of $\cos\theta$

$$\begin{aligned} \langle\cos\theta\rangle_{J_iM_i}(t) &= \langle\Psi_{rot}^{J_iM_i}(t)|\cos\theta|\Psi_{rot}^{J_iM_i}(t)\rangle \\ &= \sum_{J,J'=0}^{J_{max}} \left[C_{JM_i}^{J_iM_i}(t)\right]^* C_{J'M_i}^{J_iM_i}(t)\langle JM_i|\cos\theta|J'M_i\rangle e^{-i\omega_{J'J}t} \end{aligned} \tag{2.464}$$

which determines the degree of molecular orientation. The corresponding thermally averaged time-dependent expectation value is given as a Boltzmann average (Eq. (2.438)) over the initial state-selected value of Eq. (2.464),

$$\langle\cos\theta\rangle_T(t) = \sum_{J_i=J_{i,min}}^{J_{i,max}} \tilde{P}(J_i) \sum_{M_i=-J_i}^{J_i} \langle\cos\theta\rangle_{J_iM_i}(t), \tag{2.465}$$

where $J_{i,min}$ and $J_{i,max}$ are chosen such that the Boltzmann weights $\tilde{P}(J_i)$ ($J_i = J_{i,min}, \ldots, J_{i,max}$) at the rotational temperature T are not negligible. Positive and negative signs of $\langle\cos\theta\rangle_T(t)$ correspond to orientation in the positive and negative z-directions, respectively, and $|\langle\cos\theta\rangle_T(t)| = 1$ corresponds to the idealized limit of perfect orientation. The laser parameters $\mathcal{E}_{1,l}$ and ω_l, see Section 2.6.2, are optimized such that the expectation value $|\langle\cos\theta\rangle_T(t^*)|$ is maximized at $t = t^*$, where t^* denotes the instant of best orientation of the molecule after the laser pulse. Since the time-dependent rotational wavepacket after the laser pulse is a superposition state, there is revival pattern, i.e. the orientation of the molecule is periodically reconstructed at intervals of the rotational revival time $\tau_{rev,X} = \pi\hbar/B_{e,X}$ of the electronic ground state [226]. The orientation duration $\Delta\tau_X$ of the molecule is determined by the peak width at times $t = t^* + n\tau_{rev,X}$ ($n = 0, 1, 2, \ldots$) and, of course, it is much smaller than the rotational revival time $\Delta\tau_X < \tau_{rev,X}$. Thus, the effective pulse duration τ_c of the applied circularly polarized laser pulse for electronic or vibrational excitations of the oriented molecule must be smaller than the orientation duration $\Delta\tau_X$. In total, the lifetimes of the electronic or vibrational excited states carrying electronic or nuclear ring currents are on the ns or ms timescale, respectively. The ring

currents will persist for a short period $\Delta\tau_X$ but will recur periodically in time, following the regular revival pattern of excited state rigid-rotors.

The time- and angle-resolved distribution of the rotational wavepacket depending on the initial state $|J_i M_i\rangle$ is obtained as an integral over the (isotropic) distribution of the azimuthal angle ϕ,

$$|\Psi_{rot}^{J_i M_i}(\theta,t)|^2 \;=\; \int_0^{2\pi} |\Psi_{rot}^{J_i M_i}(\theta,\phi,t)|^2 \, d\phi, \tag{2.466}$$

where $\Psi_{rot}^{J_i M_i}(\theta,\phi,t) = \langle\theta,\phi|\Psi_{rot}^{J_i M_i}(t)\rangle$, and the corresponding thermally averaged time-dependent angular distribution is

$$|\Psi_{rot}(\theta,t)|_T^2 \;=\; \sum_{J_i=J_{i,min}}^{J_{i,max}} \tilde{P}(J_i) \sum_{M_i=-J_i}^{J_i} |\Psi_{rot}^{J_i M_i}(\theta,t)|^2. \tag{2.467}$$

At the initial time $t = 0$, the expectation value $\langle\cos\theta\rangle_T(t=0)$ is zero and the corresponding angular distribution $|\Psi_{rot}(\theta,t=0)|_T^2$ is isotropic in θ whereas the angular distribution $|\Psi_{rot}(\theta,t)|_T^2$ at times $t = t^* + n\tau_{rev,X}$ $(n = 0,1,2,\ldots)$ is focused in the $0° - 20°$ or $160° - 180°$ ranges for best positive or negative orientation of the diatomic molecule, respectively. The thermally averaged normalized angular distribution used in Section 3.3 is defined as $|\Psi_{rot}(\theta,t)|_T^2 \sin\theta$ since

$$\int_0^{\pi} |\Psi_{rot}(\theta,t)|_T^2 \sin\theta \, d\theta \;=\; 1. \tag{2.468}$$

Finally, we note that BeO and AlCl are convenient special cases, because the z-components of electronic (orbit and spin) angular momentum in their electronic ground states $|X\,{}^1\Sigma^+\rangle$ are zero. In contrast, the electronic ground states of NO and OHF^- [113] are $|X\,{}^2\Pi\rangle$ and their z-components of electronic (orbit as well as spin) angular momenta are non-zero. In this case, there are additional complications in the derivation of equations for laser control of molecular orientation.

Chapter 3

Results

3.1 Overview

In Section 3.2, the analytical exact results are presented for electronic ring currents and associated induced magnetic fields in non-relativistic hydrogen-like atomic orbitals, i.e. in the hydrogen atom or one-electron ions with nuclear charge $Z \leq 13$, induced by left or right circularly polarized π laser pulses [144]. These exact expressions can be used as an approximation for the electronic ring currents and induced magnetic fields in many-electron systems, for example in pre-oriented polar diatomics AlCl [145] and BeO [146], see Section 3.3, and also in the pre-aligned planar molecule magnesium-porphyrin (MgP) [147–150], see Section 3.4, using left or right circularly polarized re-optimized π laser pulses. The corresponding electron circulations in superposition states induced by left or right circularly polarized re-optimized $\pi/2$ laser pulses are also presented. Finally, the nuclear ring currents and nuclear pseudorotation of the linear triatomic molecules FHF^- [208] and $^{114}CdH_2$ [207], induced by circularly polarized picosecond (ps) re-optimized π and femtosecond (fs) non-optimized laser pulses, respectively, are discussed in Section 3.5.

3.2 Atomic orbitals

3.2.1 Electronic ring currents

For the hydrogen atom or one-electron ions (He^+, Li^{2+}, ...) with nuclear charge Z, the non-relativistic atomic orbitals φ_{nlm} with principal quantum number $n = 1, 2, \ldots$, angular

momentum quantum number $l = 0, \ldots, n-1$, and magnetic or azimuthal quantum number $m = -l, -l+1, \ldots, l-1, l$ are given in spherical coordinates $\mathbf{r} = (r, \theta, \phi)$ by [144, 269]

$$\varphi_{nlm}(r, \theta, \phi) = C_{nl} \left(\frac{2Zr}{na_0}\right)^l e^{-Zr/na_0} L^{2l+1}_{n-l-1}\left(\frac{2Zr}{na_0}\right) Y_{lm}(\theta, \phi). \tag{3.1}$$

The normalization constant C_{nl} is given by

$$C_{nl} = \sqrt{\left(\frac{2Z}{na_0}\right)^3 \frac{(n-l-1)!}{2n(n+l)!}}, \tag{3.2}$$

where a_0 is the Bohr radius

$$a_0 = \frac{4\pi\varepsilon_0\hbar^2}{m_e e^2}. \tag{3.3}$$

In Eq. (3.1), $L^k_n(x)$ are the associated Laguerre polynomials,

$$Y_{lm}(\theta, \phi) = \sqrt{\frac{2l+1}{4\pi}\frac{(l-m)!}{(l+m)!}} P^m_l(\cos\theta) e^{im\phi} \tag{3.4}$$

are the spherical harmonics, and $P^m_l(x)$ are the associated Legendre polynomials. The energy of the atomic orbital φ_{nlm} (Eq. (3.1)) is

$$E_{nlm} = E_n = -m_e c^2 \frac{(Z\alpha)^2}{2n^2} = -\frac{Z^2}{2n^2} E_h \tag{3.5}$$

where

$$\alpha = \frac{e^2}{4\pi\varepsilon_0\hbar c} = \frac{\hbar}{a_0 m_e c} \tag{3.6}$$

and

$$E_h = \frac{\hbar^2}{m_e a_0^2} \tag{3.7}$$

are the dimensionless fine structure constant and the Hartree energy, respectively. The corresponding ϕ-independent electronic current density is (Eq. (2.38)) [270, 271]

$$\mathbf{j}_{nlm}(r, \theta) = \frac{m\hbar}{m_e}\frac{\rho_{nlm}(r, \theta)}{r\sin\theta}\mathbf{e}_\phi, \tag{3.8}$$

where

$$\rho_{nlm}(r, \theta) = |\varphi_{nlm}(r, \theta, \phi)|^2 \tag{3.9}$$

is the electronic probability density. For example, the electron wavefunctions of $2p_\pm$ atomic orbitals (Eqs. (3.1), (3.2), (3.4)) are given by

$$\varphi_{21\pm1}(r, \theta, \phi) = \mp\frac{1}{8\sqrt{\pi}}\left(\frac{Z}{a_0}\right)^{5/2} r e^{-Zr/2a_0} \sin\theta\, e^{\pm i\phi} \tag{3.10}$$

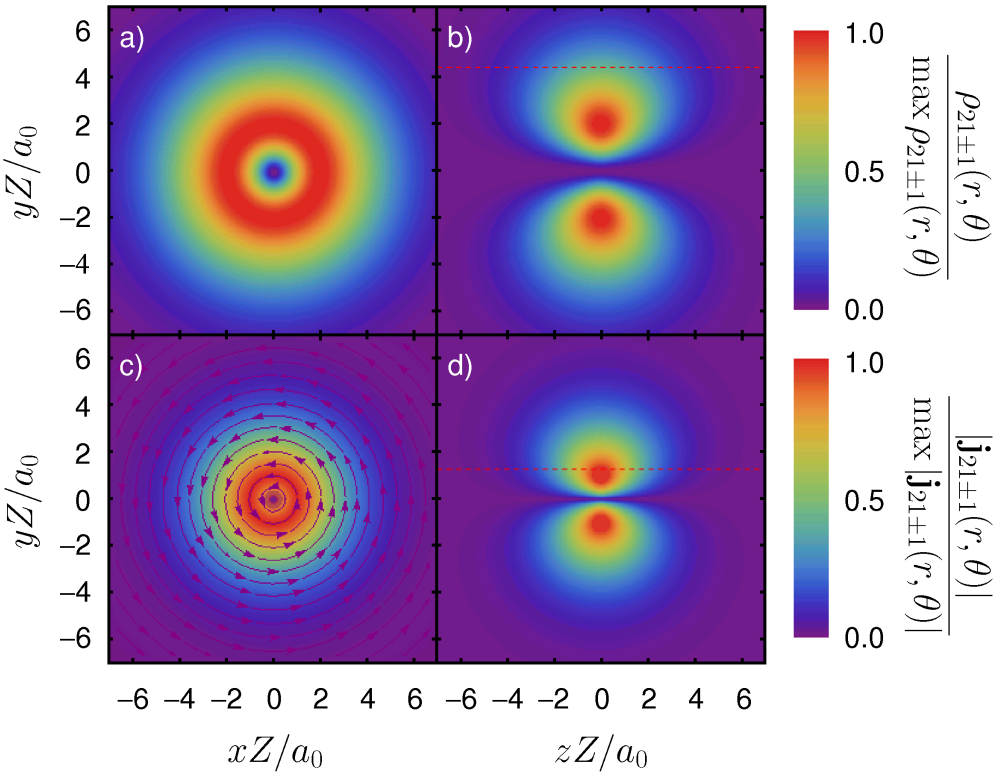

Figure 3.1: Electronic probability $\rho_{21\pm1}(r,\theta)$ (Eq. (3.11)) (panels a, b) and current densities $\mathbf{j}_{21\pm1}(r,\theta)$ (Eq. (3.12)) (panels c, d) in the x/y ($z = 0$) (panels a, c) and y/z ($x = 0$) (panels b, d) planes, for $2p_\pm$ atomic orbitals and for arbitrary nuclear charges Z due to the scaling of the axis, xZ/a_0, yZ/a_0, and zZ/a_0. Note that panel c shows the direction of the electronic current density only for the $2p_+$ orbital; the corresponding direction for the $2p_-$ orbital would be opposite. In panel d, the electron of the $2p_+$ orbital at $y > 0$ and $y < 0$ moves toward and away from the reader, respectively, and backwards for the $2p_-$ orbital. The mean radius $\tilde{R}_{21\pm1}$ (Eq. (3.52)) (see also Fig. 3.3) and mean ring current radius $R_{-1,21\pm1}$ (Eq. (3.50)) are also drawn in red dashed lines in panels b and d, respectively. Note that the mean radius $\tilde{R}_{21\pm1}$ is much larger than the most probable radius $\tilde{R}_{max,21\pm1}$ (Eq. (3.16)).

where $L_0^k(x) = 1$, $P_1^1(\cos\theta) = -\sin\theta$, and $P_1^{-1} = \frac{1}{2}\sin\theta$ [254]. The corresponding electronic probability (Eq. (3.9))

$$\rho_{21\pm1}(r,\theta) = \frac{1}{64\pi}\left(\frac{Z}{a_0}\right)^5 r^2 e^{-Zr/a_0}\sin^2\theta, \tag{3.11}$$

and current densities (Eq. (3.8))

$$\mathbf{j}_{21\pm1}(r,\theta) = \pm\frac{\hbar}{64\pi m_e}\left(\frac{Z}{a_0}\right)^5 r e^{-Zr/a_0}\sin\theta\,\mathbf{e}_\phi \tag{3.12}$$

$$|\mathbf{j}_{21\pm1}(r,\theta)| = \frac{\hbar}{64\pi m_e}\left(\frac{Z}{a_0}\right)^5 r e^{-Zr/a_0}\sin\theta \tag{3.13}$$

are illustrated in Fig. 3.1. Because of the factor $\sin\theta$, the densities are largest for $\theta = \pi/2$. The corresponding maxima $\max\rho_{21\pm1}(r,\theta)$ and $\max|\mathbf{j}_{21\pm1}(r,\theta)|$ are determined as follows.

For the electronic current density, we derive

$$\begin{aligned} 0 &= \frac{d}{dr}\,\rho_{21\pm1}\left(r,\theta=\frac{\pi}{2}\right)\Big|_{r=\tilde{R}_{max,21\pm1}} \\ &= \frac{1}{64\pi}\left(\frac{Z}{a_0}\right)^5 \frac{d}{dr}\,r^2 e^{-Zr/a_0}\Big|_{r=\tilde{R}_{max,21\pm1}} \\ &= \frac{1}{64\pi}\left(\frac{Z}{a_0}\right)^5 re^{-Zr/a_0}\left(2-\frac{Zr}{a_0}\right)\Big|_{r=\tilde{R}_{max,21\pm1}}, \end{aligned} \tag{3.14}$$

where $\rho_{21\pm1}(r,\theta)=0$ is obtained when $r=0$ or when $r\to\infty$, and the maximum

$$\max\rho_{21\pm1}(r,\theta) = \frac{1}{16\pi}\left(\frac{Z}{a_0}\right)^3 e^{-2} \tag{3.15}$$

is obtained for $\theta=\pi/2$ and the most probable radius

$$\tilde{R}_{max,21\pm1} = 2\,\frac{a_0}{Z}. \tag{3.16}$$

For the electronic current density, we have

$$\begin{aligned} 0 &= \frac{d}{dr}\,\left|\mathbf{j}_{21\pm1}\left(r,\theta=\frac{\pi}{2}\right)\right|\Big|_{r=R_{max,21\pm1}} \\ &= \frac{\hbar}{64\pi m_e}\left(\frac{Z}{a_0}\right)^5 \frac{d}{dr}\,re^{-Zr/a_0}\Big|_{r=R_{max,21\pm1}} \\ &= \frac{\hbar}{64\pi m_e}\left(\frac{Z}{a_0}\right)^5 e^{-Zr/a_0}\left(1-\frac{Zr}{a_0}\right)\Big|_{r=R_{max,21\pm1}}, \end{aligned} \tag{3.17}$$

where $|\mathbf{j}_{21\pm1}(r,\theta)|=0$ is obtained when $r=0$ or when $r\to\infty$ (cf. Eq. (3.13)), and the maximum

$$\max|\mathbf{j}_{21\pm1}(r,\theta)| = \frac{\hbar}{64\pi m_e}\left(\frac{Z}{a_0}\right)^4 e^{-1} \tag{3.18}$$

is obtained for $\theta=\pi/2$ and the most probable ring current radius

$$R_{max,21\pm1} = \frac{a_0}{Z} \tag{3.19}$$

which is smaller than the most probable radius $\tilde{R}_{max,21\pm1}$ (Eq. (3.16)).

For $m=0$, the electric ring current is zero, and for $m\neq0$ (thus $l\neq0$), we obtain, using Eqs. (2.55), (3.1), (3.2), (3.8), (3.9), and $d\mathbf{S}=r\,dr\,d\theta\,\mathbf{e}_\phi$,

$$\begin{aligned} I_{nlm} &= -e\int\int \mathbf{j}_{nlm}(r,\theta)\cdot d\mathbf{S} \\ &= -\frac{em\hbar}{m_e}\int_0^\infty dr\int_0^\pi \frac{|\varphi_{nlm}(r,\theta,\phi)|^2}{\sin\theta}\,d\theta \end{aligned} \tag{3.20}$$

$$
\begin{aligned}
&= -\frac{em\hbar}{m_e} C_{nl}^2 \int_0^\infty \left(\frac{2Zr}{na_0}\right)^{2l} e^{-2Zr/na_0} \left[L_{n-l-1}^{2l+1}\left(\frac{2Zr}{na_0}\right)\right]^2 dr \int_0^\pi \frac{|Y_{lm}(\theta,\phi)|^2}{\sin\theta}\, d\theta \\
&= -\frac{em\hbar}{m_e}\frac{na_0}{2Z} C_{nl}^2 \int_0^\infty x^{2l} e^{-x} \left[L_{n-l-1}^{2l+1}(x)\right]^2 dr \int_0^\pi \frac{|Y_{lm}(\theta,\phi)|^2}{\sin\theta}\, d\theta \\
&= -\frac{2em\hbar}{m_e a_0^2}\frac{Z^2}{n^3}\frac{(n-l-1)!}{(n+l)!} \int_0^\infty x^{2l} e^{-x} \left[L_{n-l-1}^{2l+1}(x)\right]^2 dr \int_0^\pi \frac{|Y_{lm}(\theta,\phi)|^2}{\sin\theta}\, d\theta.
\end{aligned}
$$

The first integral involving associated Laguerre polynomials can be evaluated using Eqs. (A.30), (A.32) by replacing $|l| \neq 0$ by $2l+1 \neq 0$ and v_b by $2n-1$, i.e.

$$
\frac{\left(\frac{v_b-|l|}{2}\right)!}{\left(\frac{v_b+|l|}{2}\right)!} \int_0^\infty x^{|l|-1} e^{-x} \left[L_{\frac{v_b-|l|}{2}}^{|l|}(x)\right]^2 dx = \frac{1}{|l|} \tag{3.21}
$$

$$
\frac{(n-l-1)!}{(n+l)!} \int_0^\infty x^{2l} e^{-x} \left[L_{n-l-1}^{2l+1}(x)\right]^2 dx = \frac{1}{2l+1}, \tag{3.22}
$$

hence

$$
\int_0^\infty x^{2l} e^{-x} \left[L_{n-l-1}^{2l+1}(x)\right]^2 dx = \frac{(n+l)!}{(2l+1)(n-1-l)!} \tag{3.23}
$$

for all $l = 0, \ldots, n-1$. With Eq. (3.4), the second integral in Eq. (3.20) is then rewritten as

$$
\begin{aligned}
\int_0^\pi \frac{|Y_{lm}(\theta,\phi)|^2}{\sin\theta}\, d\theta &= \frac{2l+1}{4\pi}\frac{(l-m)!}{(l+m)!} \int_0^\pi \frac{\left[P_l^m(\cos\theta)\right]^2}{\sin\theta}\, d\theta \\
&= \frac{2l+1}{4\pi}\frac{(l-m)!}{(l+m)!} \int_{-1}^1 \frac{\left[P_l^m(x)\right]^2}{1-x^2}\, dx.
\end{aligned} \tag{3.24}
$$

For $m > 0$, the last integral is [253, 254]

$$
\int_{-1}^1 \frac{\left[P_l^m(x)\right]^2}{1-x^2}\, dx = \frac{1}{m}\frac{(l+m)!}{(l-m)!}, \tag{3.25}
$$

and for $m < 0$, using

$$
P_l^m(x) = (-1)^m \frac{(l+m)!}{(l-m)!} P_l^{-m}(x), \tag{3.26}
$$

i.e.

$$
\int_{-1}^1 \frac{\left[P_l^m(x)\right]^2}{1-x^2}\, dx = -\frac{1}{m}\frac{(l+m)!}{(l-m)!}, \tag{3.27}
$$

thus for $m \neq 0$

$$
\int_{-1}^1 \frac{\left[P_l^m(x)\right]^2}{1-x^2}\, dx = \frac{1}{|m|}\frac{(l+m)!}{(l-m)!}. \tag{3.28}
$$

The integral (3.24) is then reduced to

$$
\int_0^\pi \frac{|Y_{lm}(\theta,\phi)|^2}{\sin\theta}\, d\theta = \frac{2l+1}{4\pi|m|}. \tag{3.29}
$$

atom or ion	Z	$\lvert I_{21\pm1}\rvert$ (mA)	$T_{21\pm1}$ (as)	$\lvert\mathbf{B}_{21\pm1}(\mathbf{r}=\mathbf{0})\rvert$ (T)	$R_{-1,21\pm1}$ (a_0)	$\lvert\mathbf{M}_{21\pm1;100}\rvert$ (ea_0)	$\tilde{\tau}_{21\pm1}$ (ps)
H	1	0.132	1215.9	0.52	1.273	0.745	1595.325
He^{+}	2	0.527	304.0	4.17	0.637	0.372	99.708
Li^{2+}	3	1.186	135.1	14.08	0.424	0.248	19.695
Be^{3+}	4	2.108	76.0	33.38	0.318	0.186	6.232
B^{4+}	5	3.294	48.6	65.19	0.255	0.149	2.553
C^{5+}	6	4.744	33.8	112.65	0.212	0.124	1.231
N^{6+}	7	6.457	24.8	178.89	0.182	0.106	0.664
O^{7+}	8	8.433	19.0	267.03	0.159	0.093	0.389
F^{8+}	9	10.674	15.0	380.20	0.141	0.083	0.243
Ne^{9+}	10	13.177	12.2	521.53	0.127	0.074	0.160
Na^{10+}	11	15.945	10.0	694.16	0.116	0.068	0.109
Mg^{11+}	12	18.975	8.4	901.21	0.106	0.062	0.077
Al^{12+}	13	22.270	7.2	1145.81	0.098	0.057	0.056

Table 3.1: Magnitude of the electric ring current $|I_{21\pm1}|$ (Eq. (3.31)), the mean period of an electron about the z-axis $T_{21\pm1}$ (Eq. (3.32)), the induced magnetic field at the nucleus $|\mathbf{B}_{21\pm1}(\mathbf{r}=\mathbf{0})|$ (Eq. (3.43)), the mean ring current radius $R_{-1,21\pm1}$ (Eq. (3.50)), the transition dipole moment $|\mathbf{M}_{21\pm1;100}|$ for transition between $1s$ and $2p_{\pm}$ orbitals (Eq. (3.64)), and the lifetime $\tilde{\tau}_{21\pm1}$ (Eq. (3.72)) for $2p_{\pm}$ orbitals ($n=2, l=1, m=\pm1$) depending on the nuclear charges $Z \leq 13$, see also Ref. [144].

With Eqs. (3.23), (3.29), the electric ring current for $m \neq 0$ (Eq. (3.20)) is [144]

$$I_{nlm} = -\mathrm{sgn}(m)\frac{e\hbar}{2\pi m_e a_0^2}\frac{Z^2}{n^3}. \tag{3.30}$$

The magnitude of the electric ring current $|I_{nlm}|$ is proportional to Z^2 and independent of quantum numbers l and m where the corresponding direction is determined by the sign of the quantum number m. The strongest electric ring current is obtained for $2p_{\pm}$ orbitals ($n=2, l=1, m=\pm1$), i.e.

$$I_{21\pm1} = \mp\frac{e\hbar Z^2}{16\pi m_e a_0^2}, \tag{3.31}$$

with the corresponding shortest mean period in the attosecond domain (Eq. (2.60)) of an electron about the z-axis

$$T_{21\pm1} = \frac{16\pi m_e a_0^2}{\hbar Z^2}. \tag{3.32}$$

The corresponding magnitudes $|I_{21\pm1}|$ and mean periods $T_{21\pm1}$ for $Z \leq 13$ are listed in Table 3.1.

3.2.2 Induced magnetic fields

The electronic ring current in the atomic orbital $\varphi_{nlm}(r,\theta,\phi)$ ($m \neq 0$) induces the ϕ-independent magnetic field in cylindrical coordinates (Eq. (2.78))

$$\begin{aligned}\mathbf{B}_{nlm}(\rho,z) &= -\frac{\mu_0 e}{4\pi}\int_0^\infty \rho'\,d\rho'\int_{-\infty}^{\infty}\mathbf{j}_{nlm}(\rho',z')\cdot\mathbf{e}_{\phi'}\,dz' \\ &\qquad \int_0^{2\pi}\frac{(z-z')\cos\Delta\phi\,\mathbf{e}_\rho+(\rho'-\rho\cos\Delta\phi)\mathbf{e}_z}{(\rho^2+\rho'^2-2\rho\rho'\cos\Delta\phi+(z-z')^2)^{3/2}}\,d\Delta\phi\end{aligned} \tag{3.33}$$

or in spherical coordinates, using $\rho = r\sin\theta$, $z = r\cos\theta$, $d\rho\,dz = r\,dr\,d\theta$, $\mathbf{e}_\rho = \sin\theta\,\mathbf{e}_r + \cos\theta\,\mathbf{e}_\theta$, and $\mathbf{e}_z = \cos\theta\,\mathbf{e}_r - \sin\theta\,\mathbf{e}_\theta$,

$$\begin{aligned}\mathbf{B}_{nlm}(r,\theta) &= -\frac{\mu_0 e}{4\pi}\int_0^\infty r'^2\,dr'\int_0^\pi \mathbf{j}_{nlm}(r',\theta')\cdot\mathbf{e}_{\phi'}\,\sin\theta'\,d\theta' \\ &\int_0^{2\pi}\Big(r^2+r'^2-2rr'(\sin\theta\sin\theta'\cos\Delta\phi+\cos\theta\cos\theta')\Big)^{-3/2} \\ &\quad\{r'(\sin\theta'\cos\theta-\cos\theta'\sin\theta\cos\Delta\phi)\mathbf{e}_r \\ &\quad+[r\cos\Delta\phi-r'(\sin\theta'\sin\theta+\cos\theta'\cos\theta\cos\Delta\phi)]\mathbf{e}_\theta\}\,d\Delta\phi,\end{aligned} \tag{3.34}$$

and using Eq. (3.8) [144],

$$\begin{aligned}\mathbf{B}_{nlm}(r,\theta) &= -\frac{\mu_0 e m\hbar}{4\pi m_e}\int_0^\infty r'\,dr'\int_0^\pi \rho_{nlm}(r',\theta')\,d\theta' \\ &\int_0^{2\pi}\Big(r^2+r'^2-2rr'(\sin\theta\sin\theta'\cos\Delta\phi+\cos\theta\cos\theta')\Big)^{-3/2} \\ &\quad\{r'(\sin\theta'\cos\theta-\cos\theta'\sin\theta\cos\Delta\phi)\mathbf{e}_r \\ &\quad+[r\cos\Delta\phi-r'(\sin\theta'\sin\theta+\cos\theta'\cos\theta\cos\Delta\phi)]\mathbf{e}_\theta\}\,d\Delta\phi.\end{aligned} \tag{3.35}$$

The induced magnetic field at the nucleus ($\mathbf{r} = \mathbf{0}$), using $r = 0$ and $\theta = 0$, hence $\mathbf{e}_r = \mathbf{e}_z$ and $\mathbf{e}_\theta = \mathbf{e}_\rho$, is

$$\begin{aligned}\mathbf{B}_{nlm}(\mathbf{r}=\mathbf{0}) &= -\frac{\mu_0 e m\hbar}{4\pi m_e}\int_0^\infty\frac{dr'}{r'^2}\int_0^\pi\rho_{nlm}(r',\theta')\,d\theta' \\ &\qquad\int_0^{2\pi}\{r'\sin\theta'\mathbf{e}_z-r'\cos\theta'\cos\Delta\phi\,\mathbf{e}_\rho\}\,d\Delta\phi \\ &= -\frac{\mu_0 e m\hbar}{2m_e}\int_0^\infty\frac{dr'}{r'}\int_0^\pi\rho_{nlm}(r',\theta')\sin\theta'\,d\theta'\,\mathbf{e}_z,\end{aligned} \tag{3.36}$$

and using Eqs. (3.1), (3.2), (3.9),

$$\begin{aligned}\mathbf{B}_{nlm}(\mathbf{r}=\mathbf{0}) &= -\frac{\mu_0 e m\hbar}{2m_e}C_{nl}^2\int_0^\infty\left(\frac{2Zr'}{na_0}\right)^{2l}\frac{1}{r'}\,e^{-2Zr'/na_0}\left[L_{n-l-1}^{2l+1}\left(\frac{2Zr'}{na_0}\right)\right]^2 dr' \\ &\qquad\int_0^\pi|Y_{lm}(\theta',\phi')|^2\sin\theta'\,d\theta'\,\mathbf{e}_z \\ &= -\frac{\mu_0 e m\hbar}{\pi m_e a_0^3}\frac{Z^3}{n^4}\frac{(n-l-1)!}{(n+l)!}\int_0^\infty x^{2l-1}\,e^{-x}\left[L_{n-l-1}^{2l+1}(x)\right]^2 dx\,\mathbf{e}_z\end{aligned} \tag{3.37}$$

where

$$\int_0^\pi |Y_{lm}(\theta',\phi')|^2 \sin\theta \, d\theta \;=\; \frac{1}{2\pi}. \tag{3.38}$$

Again, the integral in Eq. (3.37) can be evaluated using Eqs. (A.36), (A.37) by replacing $|l| \neq 0, 1$ by $2l+1 \neq 0, 1$ and v_b by $2n-1$, i.e.

$$\frac{\left(\frac{v_b-|l|}{2}\right)!}{\left(\frac{v_b+|l|}{2}\right)!} \int_0^\infty x^{|l|-2} e^{-x} \left[L^{|l|}_{\frac{v_b-|l|}{2}}(x)\right]^2 dx \;=\; \frac{1}{|l|}\frac{v_b+1}{|l|^2-1} \tag{3.39}$$

$$\frac{(n-l-1)!}{(n+l)!} \int_0^\infty x^{2l-1} e^{-x} \left[L^{2l+1}_{n-l-1}(x)\right]^2 dx \;=\; \frac{n}{2l(2l+1)(l+1)}, \tag{3.40}$$

hence

$$\int_0^\infty x^{2l-1} e^{-x} \left[L^{2l+1}_{n-l-1}(x)\right]^2 dx \;=\; \frac{n(n+l)!}{2l(2l+1)(l+1)(n-1-l)!} \tag{3.41}$$

for $l = 1, \ldots, n-1$. Thus, the induced magnetic field at the nucleus (Eq. (3.37)) for $l = 1, \ldots, n-1$ is [144]

$$\mathbf{B}_{nlm}(\mathbf{r}=\mathbf{0}) \;=\; -\frac{\mu_0 e\hbar}{2\pi m_e a_0^3} \frac{Z^3 m}{n^3 l(2l+1)(l+1)} \, \mathbf{e}_z, \tag{3.42}$$

in accord with the results of fine-structure splitting calculations for hydrogenlike atoms. These calculations rely on the relation between the magnetic field induced by electron motion and electronic angular momentum, i.e. $\mathbf{B}_L \sim \mathbf{L}$, and on the fine-structure interaction term which is proprortional to $\mathbf{L}\cdot\mathbf{S} \sim \mathbf{B}_L \cdot \mathbf{S}$ whre $\mathbf{S}$ is the electronic spin operator [272]. The magnitude of the induced magnetic field is proportional to Z^3 and depends on all quantum numbers n, l, m. Of course, the direction of the induced magnetic field ist determined by the sign of the azimuthal quantum number m. The strongest induced magnetic field at the nucleus (Eq. (3.42)) is obtained for $2p_\pm$ orbitals, i.e.

$$\mathbf{B}_{21\pm1}(\mathbf{r}=\mathbf{0}) \;=\; \mp\frac{\mu_0 e\hbar Z^3}{96\pi m_e a_0^3} \, \mathbf{e}_z, \tag{3.43}$$

in accord with the strongest electric ring current $I_{21\pm1}$ in $2p_\pm$ orbitals (Eq. (3.31)). The corresponding magnitudes $|\mathbf{B}_{21\pm1}(\mathbf{r}=\mathbf{0})|$ for $Z \leq 13$ are also listed in Table 3.1. Fig. 3.2 shows the induced magnetic field $\mathbf{B}_{21\pm1}(r,\theta)$ (Eq. (3.35)) for $2p_\pm$ atomic orbitals.

3.2.3 Mean ring current radius

The mean ring current radius $R_{-1,nlm}$ (Eq. (2.96)) of the electronic ring current in the atomic orbital $\varphi_{nlm}(r,\theta,\phi)$ $(m \neq 0)$, using $\rho = r\sin\theta$, is given by

$$R_{-1,nlm} \;=\; \frac{I_{nlm}}{-e\int\int (r\sin\theta)^{-1} \mathbf{j}_{nlm}(r,\theta)\cdot d\mathbf{S}}, \tag{3.44}$$

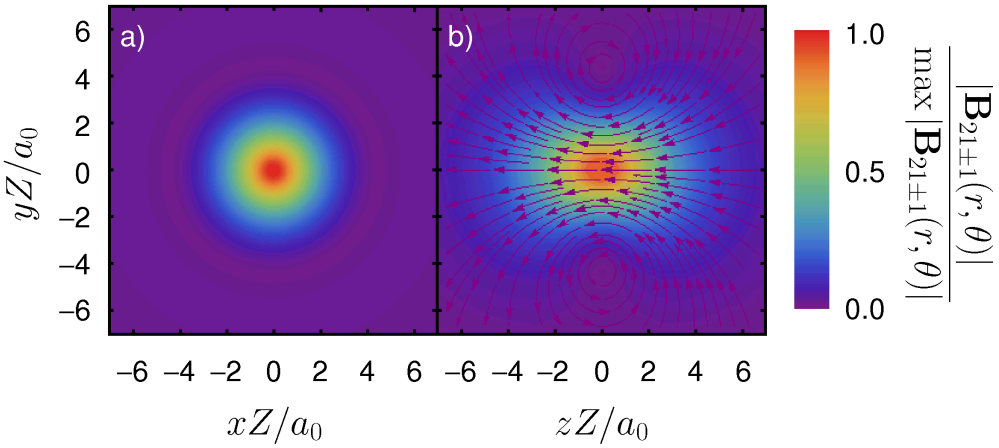

Figure 3.2: Induced magnetic field $\mathbf{B}_{21\pm1}(r,\theta)$ (Eq. (3.35)) in the x/y ($z=0$) (panel a) and y/z ($x=0$) (panel b) planes, for $2p_\pm$ atomic orbitals and for arbitrary nuclear charges Z, cf. Fig. 3.1. In panel b, the direction of the induced magnetic field is drawn only for the $2p_+$ orbital whereas the field direction for the $2p_-$ orbital is opposite. In panel a, the induced magnetic field for the $2p_+$ orbital in the center region is directed away from the reader and in the outside region (with smaller magnitudes) toward the reader. For the $2p_-$ orbital, the situation would be reversed. The maximum of the induced magnetic field is located at the nucleus, i.e. $\max|\mathbf{B}_{21\pm1}(r,\theta)| = |\mathbf{B}_{21\pm1}(\mathbf{r}=\mathbf{0})|$ (Eq. (3.43)).

and using Eqs. (3.1), (3.2), (3.8), (3.9), (3.30), (3.41), and $d\mathbf{S} = r\,dr\,d\theta\,\mathbf{e}_\phi$,

$$
\begin{aligned}
R_{-1,nlm} &= \frac{1}{2\pi a_0^2}\frac{Z^2}{|m|n^3}\left(\int_0^\infty \frac{dr}{r}\int_0^\pi \frac{|\varphi_{nlm}(r,\theta,\phi)|^2}{\sin^2\theta}\,d\theta\right)^{-1} \qquad (3.45)\\
&= \frac{1}{2\pi a_0^2}\frac{Z^2}{|m|n^3}\frac{1}{C_{nl}^2}\left(\int_0^\infty \left(\frac{2Zr}{na_0}\right)^{2l}\frac{1}{r}\,e^{-2Zr/na_0}\left[L_{n-l-1}^{2l+1}\left(\frac{2Zr}{na_0}\right)\right]^2 dr\right.\\
&\qquad\qquad \left.\int_0^\pi \frac{|Y_{lm}(\theta,\phi)|^2}{\sin^2\theta}\,d\theta\right)^{-1}\\
&= \frac{a_0}{8\pi}\frac{n}{Z|m|}\frac{(n+l)!}{(n-l-1)!}\left(\int_0^\infty x^{2l-1}e^{-x}\left[L_{n-l-1}^{2l+1}(x)\right]^2 dx\int_0^\pi \frac{|Y_{lm}(\theta,\phi)|^2}{\sin^2\theta}\,d\theta\right)^{-1}\\
&= \frac{a_0}{4\pi}\frac{l(2l+1)(l+1)}{Z|m|}\left(\int_0^\pi \frac{|Y_{lm}(\theta,\phi)|^2}{\sin^2\theta}\,d\theta\right)^{-1}.
\end{aligned}
$$

The remaining integral, using Eq. (3.4), involving powers of $\sin\theta$ and two associated Legendre polynomials, is derived from the general formula [144, 273]

$$
\begin{aligned}
\int_0^\pi \frac{|Y_{lm}(\theta,\phi)|^2}{\sin^2\theta}\,d\theta &= \frac{2l+1}{4\pi|m|!}\frac{\Gamma\left(l+\frac{1}{2}\right)\Gamma\left(|m|-\frac{1}{2}\right)}{(l-1)!} \qquad (3.46)\\
&\quad {}_4F_3\left(\frac{3}{2},-\frac{1}{2},-\frac{1}{2}(l-|m|-1),-\frac{1}{2}(l-|m|);1,\frac{1}{2}-l,|m|+1;1\right)
\end{aligned}
$$

where $\Gamma(z)$ and ${}_4F_3(a_1, a_2, a_3, a_4; b_1, b_2, b_3; z)$ are the Gamma function (Eq. (A.5)) and the generalized hypergeometric function [254]

$$\begin{aligned} {}_4F_3(a_1, a_2, a_3, a_4; b_1, b_2, b_3; z) &= \frac{\Gamma(b_1)\Gamma(b_2)\Gamma(b_3)}{\Gamma(a_1)\Gamma(a_2)\Gamma(a_3)\Gamma(a_4)} \\ &\quad \sum_{k=0}^{\infty} \frac{\Gamma(a_1+k)\Gamma(a_2+k)\Gamma(a_3+k)\Gamma(a_4+k)}{\Gamma(b_1+k)\Gamma(b_2+k)\Gamma(b_3+k)} \frac{z^k}{k!} \\ &= 1 + \frac{\Gamma(b_1)\Gamma(b_2)\Gamma(b_3)}{\Gamma(a_1)\Gamma(a_2)\Gamma(a_3)\Gamma(a_4)} \\ &\quad \sum_{k=1}^{\infty} \frac{\Gamma(a_1+k)\Gamma(a_2+k)\Gamma(a_3+k)\Gamma(a_4+k)}{\Gamma(b_1+k)\Gamma(b_2+k)\Gamma(b_3+k)} \frac{z^k}{k!} \end{aligned} \tag{3.47}$$

respectively. Note that the generalized hypergeometric function is equal to 1 if at least one of the parameters a_i $(i = 1, \ldots, 4)$ is equal to 0 since $\Gamma(0)$ is infinite and hence $1/\Gamma(0) = 0$, cf. Eq. (3.47). The mean ring current radius (Eq. (3.45)) for $m \neq 0$ is rewritten as [144]

$$\begin{aligned} R_{-1,nlm} &= \frac{a_0}{Z} \frac{l(l+1)(l-1)!(|m|-1)!}{\Gamma\left(l+\frac{1}{2}\right)\Gamma\left(|m|-\frac{1}{2}\right)} \\ &\quad \left[{}_4F_3\left(\frac{3}{2}, -\frac{1}{2}, -\frac{1}{2}(l-|m|-1), -\frac{1}{2}(l-|m|); 1, \frac{1}{2}-l, |m|+1; 1\right)\right]^{-1}. \end{aligned} \tag{3.48}$$

It can be seen already in Eq. (3.45) that the mean ring current radius $R_{-1,nlm}$ depends on Z, l, and $|m|$ but not on n. For $l = |m| \geq 1$ and $l = |m| + 1 \geq 2$, i.e. $a_3 = 0$ and $a_4 = 0$, Eq. (3.48) is simplified to

$$R_{-1,nlm} = \frac{a_0}{Z} \frac{l(l+1)(l-1)!(|m|-1)!}{\Gamma\left(l+\frac{1}{2}\right)\Gamma\left(|m|-\frac{1}{2}\right)}. \tag{3.49}$$

For $2p_\pm$ atomic orbitals $(n = 2, l = |m| = 1)$, the mean ring current radius

$$R_{-1,21\pm1} = \frac{4}{\pi}\frac{a_0}{Z} \approx 1.27\,\frac{a_0}{Z} \tag{3.50}$$

is a bit larger than the most probable ring current radius $R_{max,21\pm1} = a_0/Z$ (Eq. (3.19)), see also Fig. 3.1. The corresponding values for $Z \leq 13$ are also listed in Table 3.1. The mean ring current radius is smaller than the mean radius $\tilde{R}_{nlm} = \langle\rho\rangle = \langle r \sin\theta\rangle$, exemplarily for $2p_\pm$ atomic orbitals, using Eqs. (3.11), (A.5), (A.7),

$$\int_0^\pi \sin^4 \, d\theta = \frac{3\pi}{8} \tag{3.51}$$

[254], and $dV = r^2 \sin\theta \, dr \, d\theta \, d\phi$,

$$\begin{aligned} \tilde{R}_{21\pm1} &= \int\int\int r \sin\theta \, \rho_{21\pm1}(r,\theta) \, dV \\ &= 2\pi \int_0^\infty r^3 \, dr \int_0^\pi \rho_{21\pm1}(r,\theta) \, \sin^2\theta \, d\theta \end{aligned} \tag{3.52}$$

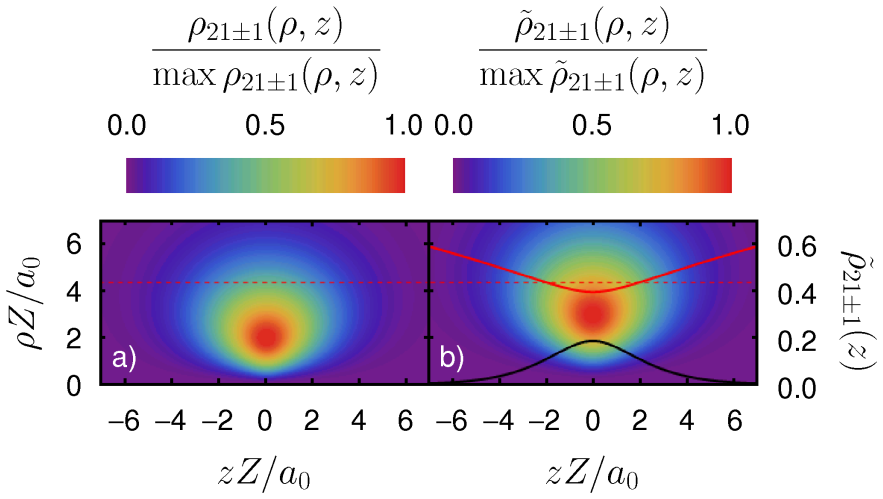

Figure 3.3: Electronic probability density $\rho_{21\pm1}(\rho,z) = \rho_{21\pm1}(r,\theta)$ (Eq. (3.11)) (panel a, cf. Fig. 3.1b) in the cylindrical coordinate sytem ($\rho = r\sin\theta, z = r\cos\theta, \phi$), for $2p_\pm$ atomic orbitals and for arbitrary azimuthal angles ϕ and nuclear charges Z, and after integration over the azimuthal angle $\tilde{\rho}_{21\pm1}(\rho,z) = \int_0^{2\pi} \rho_{21\pm1}(\rho,z)\,\rho\,d\phi = 2\pi\rho\,\rho_{21\pm1}(\rho,z)$ (panel b). Further integration over the radial coordinate ρ yields the one-dimensional electronic probability density, $\tilde{\rho}_{21\pm1}(z) = \int_0^\infty \tilde{\rho}_{21\pm1}(\rho,z)\,d\rho$ (black curve in panel b), i.e. the electrons of $2p_\pm$ orbitals are located most probably at $z = 0$. In panel b, the curve of the mean radius depending on z, i.e. $\langle\rho\rangle(z) = \int_0^\infty \rho\tilde{\rho}_{21\pm1}(\rho,z)\,d\rho/\tilde{\rho}_{21\pm1}(z)$, is plotted in red. It has its minimum at $\langle\rho\rangle(z=0) = 4\,a_0/Z$ and almost linearly increases with $|z|$. Averaging $\langle\rho\rangle(z)$ (red curve) over z with weight $\tilde{\rho}_{21\pm1}(z)$ (black curve) yields the larger value of the mean radius $\langle\rho\rangle = \int_{-\infty}^\infty \langle\rho\rangle(z)\tilde{\rho}_{21\pm1}(z)\,dz = \int_{-\infty}^\infty dz \int_0^\infty \rho\tilde{\rho}_{21\pm1}(\rho,z)\,d\rho = \tilde{R}_{21\pm1} \approx 4.42\,a_0/Z$ (cf. Eq. (3.52), red dashed lines in panels a and b, and in Fig. 3.1b).

$$
\begin{aligned}
&= \frac{1}{32}\left(\frac{Z}{a_0}\right)^5 \int_0^\infty r^5 e^{-Zr/a_0}\,dr \int_0^\pi \sin^4\theta\,d\theta \\
&= \frac{1}{32}\frac{a_0}{Z}\int_0^\infty x^5 e^{-x}\,dx \int_0^\pi \sin^4\theta\,d\theta \\
&= \frac{45\pi}{32}\frac{a_0}{Z} \;\approx\; 4.42\,\frac{a_0}{Z}.
\end{aligned}
$$

Furthermore, the mean radius $\tilde{R}_{21\pm1}$ is about twice as large as the most probable radius $\tilde{R}_{max,21\pm1} = 2a_0/Z$ (Eq. (3.16)). The large value of $\tilde{R}_{21\pm1}$ compared to $\tilde{R}_{max,21\pm1}$ (Eq. (3.16)) and $R_{-1,21\pm1}$ (Eq. (3.50)) can be explained in Fig. 3.3, see also Fig. 3.1.

3.2.4 Complete population transfer

The complete excitation of an electron from the ground state atomic orbital $1s$ to the target excited orbital $2p_+$ or $2p_-$, representing the strongest electric ring currents and

induced magnetic fields, can be achieved by means of a right (+) or left (−) circularly polarized π laser pulse $\mathbf{E}_{c+}(t)$ or $\mathbf{E}_{c-}(t)$, propagating along the z-axis (Eq. (2.99)), respectively, see Section 2.3.3. Here, the laser envelope $s_n(t)$ (Eq. (2.100)) is a $\cos^2$ envelope function ($n = 2$) and the number of laser cycles during the total pulse duration $t_{p,c}$,

$$m_c(t_{p,c}) \;=\; \frac{\omega_c t_{p,c}}{2\pi} \;=\; 500, \tag{3.53}$$

is chosen to be very large such that the second term of the electric field (Eq. (2.99)) can be neglected (cf. Eq. (2.112)) and that the three-state model with the RWA (cf. Section 2.3.3) can be applied, see below. The laser frequency ω_c is chosen to be resonant with the excitation frequency between $1s$ and $2p_\pm$ atomic orbitals, using Eq. (3.5),

$$\omega_c \;=\; \omega_{21\pm1;100} \;=\; \frac{E_{n=2} - E_{n=1}}{\hbar} \;=\; \frac{3}{8}\frac{m_e c^2}{\hbar}\,(Z\alpha)^2, \tag{3.54}$$

see Table 3.2. Hence, with Eq. (3.53), the total pulse duration $t_{p,c}$ and the effective pulse duration τ_c are given by

$$t_{p,c} \;=\; \frac{2\pi m_c(t_{p,c})}{\omega_c} \;=\; \frac{16\pi}{3}\,\frac{\hbar}{m_e c^2}\,\frac{m_c(t_{p,c})}{(Z\alpha)^2} \tag{3.55}$$

and

$$\begin{aligned} \tau_c \;=\; \tau \;&=\; \frac{2}{\pi}\arccos\left(2^{-1/4}\right)\, t_{p,c} \;\approx\; 0.364\, t_{p,c} \\ &=\; \frac{32}{3}\arccos\left(2^{-1/4}\right)\,\frac{\hbar}{m_e c^2}\frac{m_c(t_{p,c})}{(Z\alpha)^2}, \end{aligned} \tag{3.56}$$

cf. Eqs. (2.101), (2.102), respectively, see Table 3.2. The transition dipole element $\mathbf{M}_{21\pm;100}$ (Eqs. (2.118), (2.126)) of the $1s \to 2p_\pm$ transition is given by

$$\begin{aligned} \mathbf{M}_{21\pm1;100} \;&=\; \langle\varphi_{21\pm1}|\mathbf{M}|\varphi_{100}\rangle \\ &=\; -e\int_0^\infty r^2\,dr\int_0^\pi \sin\theta\,d\theta\int_0^{2\pi}\varphi^*_{21\pm1}(r,\theta,\phi)\,\mathbf{r}\,\varphi_{100}(r,\theta,\phi)\,d\phi \end{aligned} \tag{3.57}$$

where the nucleus is located at the center ($\mathbf{R} = \mathbf{0}$). With Eq. (3.10),

$$\varphi_{100}(r,\theta,\phi) \;=\; \frac{1}{\sqrt{\pi}}\left(\frac{Z}{a_0}\right)^{3/2} e^{-Zr/a_0}, \tag{3.58}$$

and

$$\mathbf{r} \;=\; r\sin\theta\,\cos\phi\,\mathbf{e}_x + r\sin\theta\,\sin\phi\,\mathbf{e}_y + r\cos\theta\,\mathbf{e}_z, \tag{3.59}$$

we obtain

$$\begin{aligned} \mathbf{M}_{21\pm1;100} \;&=\; \pm\frac{e}{8\pi}\left(\frac{Z}{a_0}\right)^4\int_0^\infty r^3 e^{-3Zr/2a_0}\,dr\int_0^\pi \sin^2\theta\,d\theta\int_0^{2\pi} e^{\mp i\phi}\,\mathbf{r}\,d\phi \\ &=\; \pm\frac{e}{8\pi}\left(\frac{Z}{a_0}\right)^4\int_0^\infty r^4 e^{-3Zr/2a_0}\,dr\int_0^\pi \sin^3\theta\,d\theta \\ &\qquad\qquad \int_0^{2\pi}(\cos\phi \mp i\sin\phi)(\cos\phi\,\mathbf{e}_x + \sin\phi\,\mathbf{e}_y)\,d\phi \\ &=\; \pm\frac{4}{243\pi}\frac{ea_0}{Z}\int_0^\infty x^4 e^{-x}\,dx\int_0^\pi \sin^3\theta\,d\theta\int_0^{2\pi}(\cos^2\phi\,\mathbf{e}_x \mp i\sin^2\phi\,\mathbf{e}_y)\,d\phi, \end{aligned} \tag{3.60}$$

atom or ion	Z	$\hbar\omega_c$ (eV)	$t_{p,c}$ (fs)	τ_c (fs)	$\lvert\mathcal{E}_c\rvert$ (Vm^{-1})	$I_{max,c}$ (Wcm^{-2})
H	1	10.2	202.6	73.77	3.66×10^8	3.56×10^{10}
He^+	2	40.8	50.66	18.44	2.93×10^9	2.28×10^{12}
Li^{2+}	3	91.8	22.52	8.197	9.88×10^9	2.59×10^{13}
Be^{3+}	4	163.3	12.67	4.611	2.34×10^{10}	1.46×10^{14}
B^{4+}	5	255.1	8.106	2.951	4.58×10^{10}	5.56×10^{14}
C^{5+}	6	367.4	5.629	2.049	7.91×10^{10}	1.66×10^{15}
N^{6+}	7	500.0	4.136	1.506	1.26×10^{11}	4.19×10^{15}
O^{7+}	8	653.1	3.166	1.153	1.87×10^{11}	9.33×10^{15}
F^{8+}	9	826.5	2.502	0.911	2.67×10^{11}	1.89×10^{16}
Ne^{9+}	10	1020.4	2.026	0.738	3.66×10^{11}	3.56×10^{16}
Na^{10+}	11	1234.7	1.675	0.610	4.87×10^{11}	6.30×10^{16}
Mg^{11+}	12	1469.4	1.407	0.512	6.33×10^{11}	1.06×10^{17}
Al^{12+}	13	1724.5	1.199	0.437	8.04×10^{11}	1.72×10^{17}

Table 3.2: Laser parameters of the right (+) or left (−) circularly polarized π laser pulses (Eq. (2.99)) with a $\cos^2$ envelope ($n = 2$) (Eq. (2.100)), for complete population transfer from $1s$ to $2p_\pm$ atomic orbitals for $Z \leq 13$. The laser parameters are listed for total number of laser cycles $m_c(t_{p,c}) = 500$ (Eq. (3.53)), i.e. resonant laser frequency ω_c (Eq. (3.54)), total pulse duration $t_{p,c}$ (Eq. (3.55)) with corresponding effective pulse duration τ_c (Eq. (3.56)), magnitude of the electric field amplitude $|\mathcal{E}_c|$ (Eq. (3.66)) with corresponding maximum intensity $I_{max,c}$ (Eq. (3.67)).

and using Eqs. (A.5), (A.7),

$$\int_0^\pi \sin^3\theta\, d\theta = \frac{4}{3}, \tag{3.61}$$

$$\int_0^{2\pi} \cos^2\phi\, d\phi = \int_0^{2\pi} \sin^2\phi\, d\phi = \pi \tag{3.62}$$

[254], i.e.

$$\mathbf{M}_{21\pm1;100} = \pm\frac{128}{243}\frac{ea_0}{Z}(\mathbf{e}_x \mp i\mathbf{e}_y). \tag{3.63}$$

The corresponding magnitudes

$$|\mathbf{M}_{21\pm1;100}| = \sqrt{2}\,\frac{128}{243}\frac{ea_0}{Z} \tag{3.64}$$

for $Z \leq 13$ are listed in Table 3.1. The condition for circularly polarized π laser pulses (Eq. (2.171)) must be satisfied, where M is defined as

$$M = \frac{\mathbf{M}_{21\pm1;100}\cdot(\mathbf{e}_x \mp i\mathbf{e}_y)^*}{|\mathbf{e}_x \mp i\mathbf{e}_y|^2} = \pm\frac{128}{243}\frac{ea_0}{Z}, \tag{3.65}$$

cf. Eqs. (2.128) and (2.150). Therefore, the magnitude of the electric field amplitude $|\mathcal{E}_c|$ and the corresponding maximum intensity $I_{max,c}$, using Eqs. (2.171), (3.6), (3.55), (3.65), are

$$|\mathcal{E}_c| = \frac{\pi\hbar}{|M|t_{p,c}} = \frac{729}{2048}\frac{m_e^2c^3}{e\hbar}\frac{(Z\alpha)^3}{m_c(t_{p,c})} \tag{3.66}$$

and

$$I_{max,c} = c\varepsilon_0\mathcal{E}_c^2 = \frac{531441}{4194304}\frac{\varepsilon_0 m_e^4c^7}{e^2\hbar^2}\frac{(Z\alpha)^6}{m_c^2(t_{p,c})}, \tag{3.67}$$

respectively, see Table 3.2. Since $I_{max,c} \leq 10^{18}\,\mathrm{Wcm}^{-2}$, the laser pulses are still in the non-relativistic regime. Regardless of the laser-matter interaction, the electric ring currents and induced magnetic fields for small nuclear charges $Z \leq 13$ can be calculated using non-relativistic (Schrödinger) theory, see Sections 3.2.1 and 3.2.2, whereas for large nuclear charges $Z > 13$, the relativistic Dirac theory [274] must be used to calculate corresponding relativistic currents and magnetic fields, since the mean kinetic energy of the electron in ions is then in the relativistic regime, see also discussion in Ref. [144]. The time-dependent populations of three states $|\Psi_0\rangle = |\varphi_{1s}\rangle$ and $|\Psi_\pm\rangle = |\varphi_{2p_\pm}\rangle$ for $n = 2$ are given in Eqs. (2.163)–(2.165), (2.166), (2.171), i.e.

$$P_0(t) = \cos^2\left[\frac{\pi(t-t_0)}{2t_{p,c}} + \frac{1}{4}\sin\left(2\pi\left(\frac{t-t_0}{t_{p,c}} - \frac{1}{2}\right)\right)\right] \tag{3.68}$$

$$P_+(t) = \sin^2\left[\frac{\pi(t-t_0)}{2t_{p,c}} + \frac{1}{4}\sin\left(2\pi\left(\frac{t-t_0}{t_{p,c}} - \frac{1}{2}\right)\right)\right] \tag{3.69}$$

$$P_-(t) = 0 \tag{3.70}$$

for $t_0 \leq t \leq t_f = t_0 + t_{p,c}$, and illustrated in Fig. 2.5a, exemplarily for a right circularly polarized π laser pulse. After the end of the laser pulse ($t \geq t_f$), the populations of these three states are constant, i.e. $P_+(t) = 1$, $P_0(t) = P_-(t) = 0$ for $t \geq t_f$. Thus, the stationary electronic ring current and induced magnetic field for the atomic orbital $2p_+$ (Figs. 3.1 and 3.2) persist after the end of the laser pulse until they decay by spontaneous emission, see below.

The very large number of laser cycles $m_c(t_{p,c}) = 500$ (Eq. (3.53)) and therefore large total pulse duration $t_{p,c}$ (Eq. (3.55)) ensure that the competing transitions from the $1s$ ground atomic orbital to other excited atomic orbitals, e.g. $3p_\pm$, are neglected because the spectral width of the $\cos^2$ laser pulse is much smaller than the energy gap between the excited orbitals $2p_\pm$ and $3p_\pm$. The spectral width parameter for $m_c(t_{p,c}) = 500$ laser cycles, using Eqs. (2.108), (3.5), (3.56),

$$\gamma = \frac{\Gamma_2}{E_{n=3} - E_{n=2}} \approx 47.45\,\frac{\hbar}{\tau_c m_e c^2 (Z\alpha)^2} \approx \frac{7.78}{m_c(t_{p,c})} \approx 0.0156 \tag{3.71}$$

is much smaller than 1, i.e. the three-state model (Section 2.3.3) can be applied. For comparison, the corresponding laser parameters for $\gamma = 0.1$ ($m_c(t_{p,c}) \approx 78$) and $\gamma = 0.01$ ($m_c(t_{p,c}) \approx 778$) are listed in Ref. [144].

Of course, the lifetime $\tilde{\tau}_{21\pm1}$ of excited atomic orbitals $2p_\pm$ by spontaneous emission [144, 240]

$$\tilde{\tau}_{21\pm1} \approx \frac{3\pi\varepsilon_0 c^3\hbar}{\omega_{21\pm1;100}^3 |\mathbf{M}_{21\pm1;100}|^2} \approx \frac{6561\pi}{64}\frac{\varepsilon_0 m_e^3 c^3 a_0^4}{e^2\hbar^2}\frac{1}{Z^4}, \tag{3.72}$$

see Table 3.1, should be larger than the total pulse duration $t_{p,c}$ (Eq. (3.55)), i.e., with Eqs. (3.3) and (3.6),

$$\begin{aligned} \frac{\tilde{\tau}_{21\pm1;100}}{t_{p,c}} &\approx \frac{19683}{1024}\frac{\varepsilon_0 m_e^4 c^5 a_0^4 \alpha^2}{e^2\hbar^3}\frac{1}{m_c(t_{p,c})Z^2} \\ &\approx \frac{19683}{4096\pi}\frac{1}{\alpha^3 m_c(t_{p,c})Z^2} \\ &\approx \frac{7872.5}{Z^2}. \end{aligned} \tag{3.73}$$

Thus, for $Z \leq 13$, this ratio is larger than 46 and clearly satisfies the condition $\tilde{\tau}_{21\pm1;100}/t_{p,c} \gg 1$.

Finally, the maximum ionization probability P_{ion} which depends on the magnitude of the electric field $|\mathcal{E}_c|$, given by [39, 109]

$$P_{ion} = 4\omega_a Z^5 \frac{\mathcal{E}_a}{|\mathcal{E}_c|} \exp\left(-\frac{2Z^3}{3}\frac{\mathcal{E}_a}{|\mathcal{E}_c|}\right), \tag{3.74}$$

should be neglected to avoid competing ionization of an electron from the electronic ground state. Here, $\omega_a = \hbar/(m_e a_0^2) \approx 4.134 \times 10^{16}\,\mathrm{s}^{-1}$ and $\mathcal{E}_a = \hbar^2/(e m_e a_0^3) \approx 514.221\,\mathrm{GVm}^{-1}$ are atomic units of frequency and electric field, respectively. Using Eq. (3.66), we obtain for $m_c(t_{p,c}) = 500$ laser cycles

$$P_{ion} \approx 4.721 \times 10^{-396}\, Z^2\,\mathrm{s}^{-1}. \tag{3.75}$$

Thus, the ionization probability can be neglected for all known nuclear charges Z.

3.2.5 Electron circulation

Non-stationary electron circulation after the end of the laser pulse can be achieved, for example, by means of a right (+) or left (−) circularly polarized resonant $\pi/2$ laser pulse (Eq. (2.99)) with a $\cos^2$ envelope (Eq. (2.100)) and many laser cycles, where the condition

for $\pi/2$ pulses (Eq. (2.175)) must be satisfied, see Section 2.3.3. This condition implies that the factor $|\mathcal{E}_c t_{p,c}|$ for $\pi/2$ laser pulses is half of the one for π laser pulses (Table 3.2). For example, the total pulse duration $t_{p,c}$ or the magnitude of the electric field $|\mathcal{E}_c|$ is halved while the other laser parameter $|\mathcal{E}_c|$ or $t_{p,c}$ remains unchanged, respectively [147,149,150]. Dividing the magnitude of the electric field $|\mathcal{E}_c|$ by 2 is preferred because halving the total pulse duration $t_{p,c}$ would double the spectral width Γ (cf. Eq. (3.71)). The resulting time-dependent populations of three states $|\Psi_0\rangle = |\varphi_{1s}\rangle$ and $|\Psi_\pm\rangle = |\varphi_{2p_\pm}\rangle$ for a $\cos^2$ laser envelope are given in Eqs. (2.163)–(2.165), (2.166), (2.175), i.e.

$$P_0(t) = \cos^2\left[\frac{\pi(t-t_0)}{4t_{p,c}} + \frac{1}{8}\sin\left(2\pi\left(\frac{t-t_0}{t_{p,c}} - \frac{1}{2}\right)\right)\right] \tag{3.76}$$

$$P_+(t) = \sin^2\left[\frac{\pi(t-t_0)}{4t_{p,c}} + \frac{1}{8}\sin\left(2\pi\left(\frac{t-t_0}{t_{p,c}} - \frac{1}{2}\right)\right)\right] \tag{3.77}$$

$$P_-(t) = 0 \tag{3.78}$$

for $t_0 \le t \le t_f = t_0 + t_{p,c}$, and illustrated in Fig. 2.5b, exemplarily for a right circularly polarized $\pi/2$ laser pulse.

After the end of this laser pulse ($t \ge t_f$), the time-dependent wavefunction $\varphi(r,\theta,\phi,t)$ is the superposition state with dominant contributions of $1s$ and $2p_+$ atomic orbitals with equal weights, i.e.

$$\varphi(r,\theta,\phi,t) = \frac{1}{\sqrt{2}}\,\varphi_{100}(r,\theta,\phi)e^{-iE_1(t-t_0)/\hbar} + \frac{i}{\sqrt{2}}\,\varphi_{21+1}(r,\theta,\phi)e^{-iE_2(t-t_0)/\hbar}e^{i\omega_c t_{p,c}/2}, \tag{3.79}$$

cf. Eqs. (2.146), (2.160), (2.161), (2.167), (2.175), (3.65). With Eqs. (3.10), (3.54), and (3.58), the wavefunction is rewritten as

$$\varphi(r,\theta,\phi,t) = \frac{e^{-iE_1(t-t_0)/\hbar}}{\sqrt{2\pi}}\left(\frac{Z}{a_0}\right)^{3/2}\left[e^{-Zr/a_0} - \frac{i}{8}\,\frac{Zr}{a_0}\,e^{-Zr/2a_0}\sin\theta\,e^{-i(\omega_c(t-t_f)-\phi)}\right] \tag{3.80}$$

where $\omega_c(t-t_0+t_{p,c}/2) = \omega_c(t-t_f+t_f-t_0+t_{p,c}/2) = \omega_c(t-t_f+3t_{p,c}/2) = \omega_c(t-t_f) + 3\pi m_c(t_{p,c})$ and the number of laser cycles $m_c(t_{p,c}) = 500$ (cf. Eq. (3.53)) have been used.

The corresponding time-dependent electronic probability (Eqs. (2.176), (2.186)) and current (Eqs. (2.177), (2.187)) densities, using (Eqs. (2.36), (3.10)), are

$$\begin{aligned}
\rho(r,\theta,\phi,t) &= |\varphi(r,\theta,\phi,t)|^2 \qquad (3.81)\\
&= \frac{1}{2\pi}\left(\frac{Z}{a_0}\right)^3\left|e^{-Zr/a_0} - \frac{i}{8}\,\frac{Zr}{a_0}\,e^{-Zr/2a_0}\sin\theta\,e^{-i(\omega_c(t-t_f)-\phi)}\right|^2\\
&= \frac{1}{2\pi}\left(\frac{Z}{a_0}\right)^3\left[e^{-2Zr/a_0} + \frac{1}{64}\left(\frac{Zr}{a_0}\right)^2 e^{-Zr/a_0}\sin^2\theta\right.\\
&\qquad\left. -\frac{1}{4}\,\frac{Zr}{a_0}\,e^{-3Zr/2a_0}\sin\theta\,\sin(\omega_c(t-t_f)-\phi)\right]
\end{aligned}$$

and

$$\begin{aligned}
\mathbf{j}(r,\theta,\phi,t) &= \frac{i\hbar}{2m_e}\left[\varphi(r,\theta,\phi,t)\nabla\varphi(r,\theta,\phi,t)^* - \varphi(r,\theta,\phi,t)^*\nabla\varphi(r,\theta,\phi,t)\right] \qquad (3.82)\\
&= \frac{\hbar}{16\pi m_e}\left(\frac{Z}{a_0}\right)^4\Big[\frac{1}{8}\frac{Zr}{a_0}\,e^{-Zr/a_0}\,\sin\theta\,\mathbf{e}_\phi\\
&\qquad -e^{-Zr/a_0}\,\nabla r e^{-Zr/2a_0}\,\sin\theta\,\cos(\omega_c(t-t_f)-\phi)\\
&\qquad +re^{-Zr/2a_0}\sin\theta\,\cos(\omega_c(t-t_f)-\phi)\nabla e^{-Zr/a_0}\Big]\\
&= \frac{\hbar}{16\pi m_e}\left(\frac{Z}{a_0}\right)^4\Big[\Big(\frac{1}{8}\frac{Zr}{a_0}\,e^{-Zr/a_0}\,\sin\theta - e^{-3Zr/2a_0}\,\sin(\omega_c(t-t_f)-\phi)\Big)\,\mathbf{e}_\phi\\
&\quad +\Big(re^{-Zr/2a_0}\sin\theta\,\nabla e^{-Zr/a_0} - e^{-Zr/a_0}\,\nabla r e^{-Zr/2a_0}\sin\theta\Big)\cos(\omega_c(t-t_f)-\phi)\Big]\\
&= \frac{\hbar}{16\pi m_e}\left(\frac{Z}{a_0}\right)^4 e^{-3Zr/2a_0}\Big[\Big(\frac{1}{8}\frac{Zr}{a_0}\,e^{Zr/2a_0}\,\sin\theta - \sin(\omega_c(t-t_f)-\phi)\Big)\,\mathbf{e}_\phi\\
&\qquad -\Big(\frac{1}{2}\frac{Zr}{a_0}+1\Big)\,\sin\theta\,\cos(\omega_c(t-t_f)-\phi)\,\mathbf{e}_r\\
&\qquad -\cos\theta\,\cos(\omega_c(t-t_f)-\phi)\,\mathbf{e}_\theta\Big]\,,
\end{aligned}$$

respectively, see Figs. 3.4 and 3.5. Note that the additional factor $\sqrt{2}$ occuring in interference terms of Eqs. (2.195) and (2.196) does not appear in Eqs. (3.81) and (3.82) because there are no singlet configuration state functions (CSFs) (Eq. (2.10)) for the hydrogen atom and one-electron ions, cf. Eqs. (2.180), (2.181), (2.188), and (2.189).

The time-dependent electronic probability and current densities (Eqs. (3.81), (3.82)) oscillate with resonant frequency $\omega_c = \omega_{21\pm1;100}$, i.e. the electronic wavepacket in the hybrid (superposition) state after the end of the laser pulse ($t \geq t_f$) circulates about the z-axis with the same frequency ω_c, see Fig. 3.4. In contrast to the current-loop-like stationary ring currents of $2p_+$ atomic orbitals (Fig. 3.1), the time-dependent electronic currents of $1s+2p_+$ hybrid orbitals look like circulating, nearly rectilinear currents (Figs. 3.4 and 3.5). Furthermore, the time-dependent current density has, in general, non-zero r- and θ-components, and, in particular, non-zero current density at the nucleus ($\mathbf{r}=\mathbf{0}$), using $r=0$ and $\theta=0$, hence $\mathbf{e}_r = \mathbf{e}_z$, $\mathbf{e}_\theta = \cos\phi\,\mathbf{e}_x + \sin\phi\,\mathbf{e}_y$, $\mathbf{e}_\phi = -\sin\phi\,\mathbf{e}_x + \cos\phi\,\mathbf{e}_y$,

$$\begin{aligned}
\mathbf{j}(\mathbf{r}=\mathbf{0},t) &= \frac{\hbar}{16\pi m_e}\left(\frac{Z}{a_0}\right)^4\left[-\sin(\omega_c(t-t_f)-\phi)(-\sin\phi\,\mathbf{e}_x+\cos\phi\,\mathbf{e}_y)\right. \qquad (3.83)\\
&\qquad \left. -\cos(\omega_c(t-t_f)-\phi)(\cos\phi\,\mathbf{e}_x+\sin\phi\,\mathbf{e}_y)\right]\\
&= \frac{\hbar}{16\pi m_e}\left(\frac{Z}{a_0}\right)^4\left[(\sin(\omega_c(t-t_f)-\phi)\sin\phi - \cos(\omega_c(t-t_f)-\phi)\cos\phi)\,\mathbf{e}_x\right.\\
&\qquad \left. -(\sin(\omega_c(t-t_f)-\phi)\cos\phi + \cos(\omega_c(t-t_f)-\phi)\sin\phi)\,\mathbf{e}_y\right]\\
&= -\frac{\hbar}{16\pi m_e}\left(\frac{Z}{a_0}\right)^4\left[\cos(\omega_c(t-t_f))\,\mathbf{e}_x + \sin(\omega_c(t-t_f))\,\mathbf{e}_y\right].
\end{aligned}$$

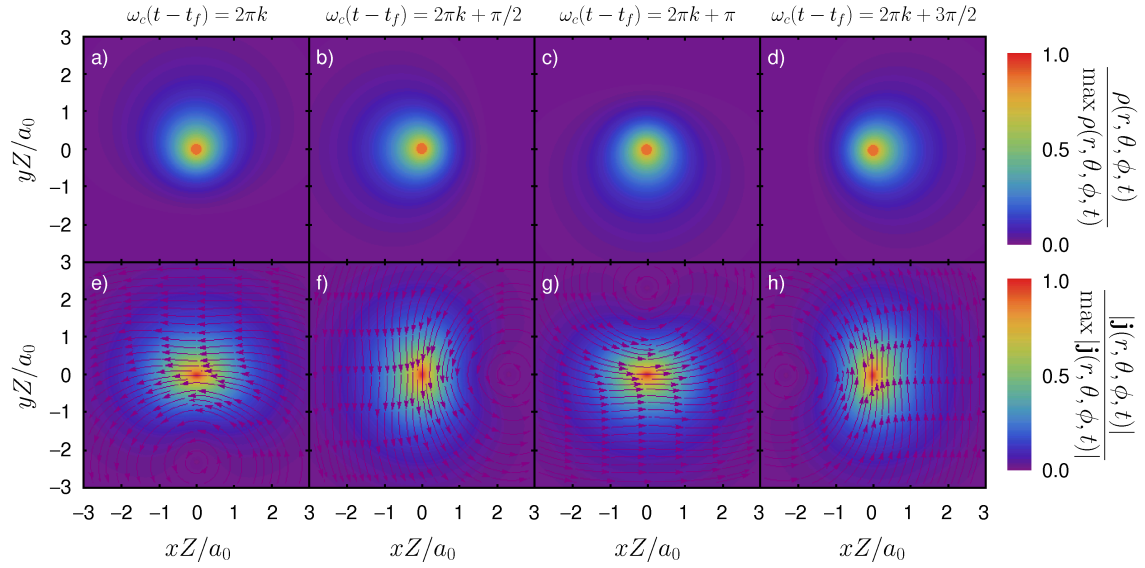

Figure 3.4: Time-dependent electronic probability $\rho(r,\theta,\phi,t)$ (Eq. (3.81)) (panels a–d) and current densities $\mathbf{j}(r,\theta,\phi,t)$ (Eq. (3.82)) (panels e–h) in the x/y ($z = 0$) plane, for superposition states of $1s$ and $2p_+$ atomic orbitals with equal weights and for arbitrary nuclear charges Z due to the scaling of the axis, xZ/a_0 and yZ/a_0. The snapshots after the end of a right circularly polarized $\pi/2$ laser pulse at times $t = t_f + 2\pi k/\omega_c$, $t = t_f + (2\pi k + \pi/2)/\omega_c$, $t = t_f + (2\pi k + \pi)/\omega_c$, and $t = t_f + (2\pi k + 3\pi/2)/\omega_c$ ($k = 0, 1, 2, \ldots$) are shown in panels a, b, c, and d, for probability and e, f, g, and h, for current densities, respectively.

The corresponding time-independent magnitude

$$|\mathbf{j}(\mathbf{r} = \mathbf{0}, t)| = \frac{\hbar}{16\pi m_e}\left(\frac{Z}{a_0}\right)^4 = \max|\mathbf{j}(\mathbf{r}, t)| \tag{3.84}$$

is the maximum current density and is about 11 times larger than the maximum current density of the stationary electronic ring current $\max|\mathbf{j}_{21\pm1}(r,\theta)|$ (Eq. (3.18)). Note that, in general, the current density

$$|\mathbf{j}(\mathbf{r} = \mathbf{0}, t)| = \frac{\hbar\sqrt{P_0 P_+}}{8\pi m_e}\left(\frac{Z}{a_0}\right)^4 = \max|\mathbf{j}(\mathbf{r}, t)| \tag{3.85}$$

is maximal if $1s$ and $2p_+$ atomic orbitals are equally weighted, i.e. $P_0 = P_+ = \frac{1}{2}$, cf. Eq. (3.84). Because of the contribution of the 1s atomic orbital, the maximum electronic probability density (Eq. (3.81)) is located at the nucleus ($\mathbf{r} = \mathbf{0}$)

$$\rho(\mathbf{r} = \mathbf{0}, t) = \frac{1}{2\pi}\left(\frac{Z}{a_0}\right)^3 = \max\rho(\mathbf{r}, t). \tag{3.86}$$

The density is non-zero, time-independent, and about 59 times larger than the maximum probability density of the $2p_\pm$ orbital $\max\rho_{21\pm1}(r,\theta)$ (Eq. (3.15)).

In contrast to the stationary ring currents for which the nodal line of the electronic probability and current densities is along the z-axis, the nodal curves ($\rho(\mathbf{r}, t) = 0$) ($r < \infty$)

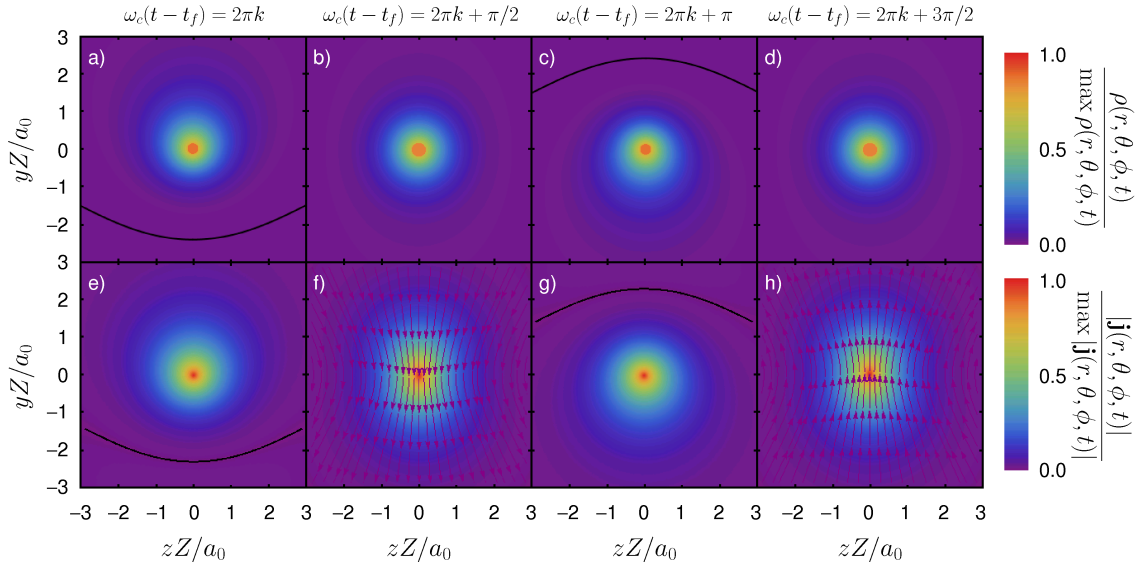

Figure 3.5: As in Fig. 3.4, but the time-dependent probability (Eq. (3.81)) and current densities (Eq. (3.82)) are shown in the y/z ($x = 0$) plane. Since the r- and θ-components of the current densities for $\phi = \omega_c(t - t_f) + \pi/2$ and $\phi = \omega_c(t - t_f) + 3\pi/2$ are zero (cf. Eq. (3.82)), no arrows are drawn in panels e and g, but the corresponding ϕ-component is, in general, non-zero. The electron above and below the (circulating) nodal (black) curves (Eq. (3.90)) in panels a, c, e, and g moves toward and away from the reader, respectively.

and ($\mathbf{j}(\mathbf{r}, t) = \mathbf{0}$) ($r < \infty$) of the time-dependent probability and current densities (Eqs. (3.81), (3.82)) are beside the z-axis. The location of the nodal curve of the current density can be derived as follows. The condition for the θ-component $j_\theta(\mathbf{r}, t) = 0$ (Eq. (3.82)) is fulfilled if $\theta = \pi/2$, $\phi = \omega_c(t - t_f) + \pi/2$, or $\phi = \omega_c(t - t_f) + 3\pi/2$. But the condition for the r-component $j_r(\mathbf{r}, t) = 0$ is not true for $\theta = \pi/2$ and $\phi \neq \omega_c(t - t_f) + \pi/2$ or $\phi \neq \omega_c(t - t_f) + 3\pi/2$, hence $\phi = \omega_c(t - t_f) + \pi/2$ or $\phi = \omega_c(t - t_f) + 3\pi/2$ must be satisfied. The last condition $j_\phi(\mathbf{r}, t) = 0$ yields

$$\frac{1}{8}\frac{Zr}{a_0} e^{Zr/2a_0} \sin\theta \pm 1 \quad = \quad 0 \tag{3.87}$$

where the signs + and − correspond to $\phi = \omega_c(t - t_f) + \pi/2$ and $\phi = \omega_c(t - t_f) + 3\pi/2$, respectively. Using cylindrical coordinates, i.e. $r\sin\theta = \rho = \sqrt{x^2 + y^2}$ and $r = \sqrt{\rho^2 + z^2}$, Eq. (3.87) becomes

$$\frac{1}{8}\frac{Z\rho}{a_0} e^{Z\sqrt{\rho^2+z^2}/2a_0} \pm 1 \quad = \quad 0 \tag{3.88}$$

and can be rewritten as

$$\frac{Z\sqrt{\rho^2 + z^2}}{2a_0} \quad = \quad \ln\left(\mp\frac{8a_0}{Z\rho}\right). \tag{3.89}$$

Since the argument of the logarithm must be positive, the nodal curve is only given by $\phi = \omega_c(t - t_f) + 3\pi/2$ and

$$z = \pm\sqrt{\frac{4a_0^2}{Z^2}\left(\ln\frac{8a_0}{Z\rho}\right)^2 - \rho^2}, \tag{3.90}$$

which is in accord with the nodal curve of the probability density, obtained from $\rho(\mathbf{r}, t) = 0$ (Eq. (3.81)). That is, using $\rho = r\sin\theta$ and $r = \sqrt{\rho^2 + z^2}$,

$$\begin{aligned} 0 &= e^{-Zr/a_0} + \frac{1}{64}\left(\frac{Zr}{a_0}\right)^2 \sin^2\theta - \frac{1}{4}\frac{Zr}{a_0}\, e^{-Zr/2a_0} \sin\theta\, \sin(\omega_c(t - t_f) - \phi) \qquad (3.91)\\ &= e^{-Z\sqrt{\rho^2+z^2}/a_0} + \frac{1}{64}\left(\frac{Z}{a_0}\right)^2 \rho^2 - \frac{1}{4}\frac{Z}{a_0}\,\rho\, e^{-Z\sqrt{\rho^2+z^2}/2a_0}\, \sin(\omega_c(t - t_f) - \phi)\\ &= \left(e^{-Z\sqrt{\rho^2+z^2}/2a_0} - \frac{1}{8}\frac{Z}{a_0}\,\rho\right)^2 + \frac{1}{4}\frac{Z}{a_0}\,\rho\, e^{-Z\sqrt{\rho^2+z^2}/2a_0}(1 - \sin(\omega_c(t - t_f) - \phi)). \end{aligned}$$

Since the first and second terms are positive or equal to zero, both terms must vanish for $\rho, |z| < \infty$, i.e. $\phi = \omega_c(t - t_f) + 3\pi/2$ and

$$e^{-Z\sqrt{\rho^2+z^2}/2a_0} - \frac{1}{8}\frac{Z}{a_0}\,\rho = 0 \tag{3.92}$$

or equivalently

$$z = \pm\sqrt{\frac{4a_0^2}{Z^2}\left(\ln\frac{Z\rho}{8a_0}\right)^2 - \rho^2}, \tag{3.93}$$

which is also equal to Eq. (3.90) since $(\ln x)^2 = (\ln x^{-1})^2$. To yield the corresponding formula for ρ as a function of z, one has to solve Eqs. (3.90) or (3.93) numerically. The solution at $z = 0$ is $\rho \approx 2.404\, a_0/Z$ and goes to zero if $z \to \pm\infty$. Since $\phi = \omega_c(t - t_f) + 3\pi/2$ is time-dependent, the nodal curve circulates about the z-axis with the same resonant frequency ω_c.

The time- and angle-dependent electric current (Eq. (2.198) without the factor $\sqrt{2}$), using $d\mathbf{S}_\phi = r\, dr\, d\theta\, \mathbf{e}_\phi$, Eqs. (3.82), (A.5), (A.7), is evaluated as

$$\begin{aligned} I(\phi, t) &= -e\int\int \mathbf{j}(r, \theta, \phi, t) \cdot d\mathbf{S}_\phi \qquad (3.94)\\ &= -e\int_0^\infty r\, dr \int_0^\pi j_\phi(r, \theta, \phi, t)\, d\theta\\ &= -\frac{e\hbar}{128\pi m_e}\left(\frac{Z}{a_0}\right)^5 \int_0^\infty r^2 e^{-Zr/a_0}\, dr \int_0^\pi \sin\theta\, d\theta\\ &\quad + \frac{e\hbar}{16\pi m_e}\left(\frac{Z}{a_0}\right)^4 \sin(\omega_c(t - t_f) - \phi) \int_0^\infty r e^{-3Zr/2a_0}\, dr \int_0^\pi d\theta\\ &= -\frac{e\hbar Z^2}{64\pi m_e a_0^2}\int_0^\infty x^2 e^{-x}\, dx + \frac{e\hbar Z^2}{36 m_e a_0^2}\sin(\omega_c(t - t_f) - \phi)\int_0^\infty x e^{-x}\, dx\\ &= -\frac{e\hbar Z^2}{32\pi m_e a_0^2} + \frac{e\hbar Z^2}{36 m_e a_0^2}\sin(\omega_c(t - t_f) - \phi), \end{aligned}$$

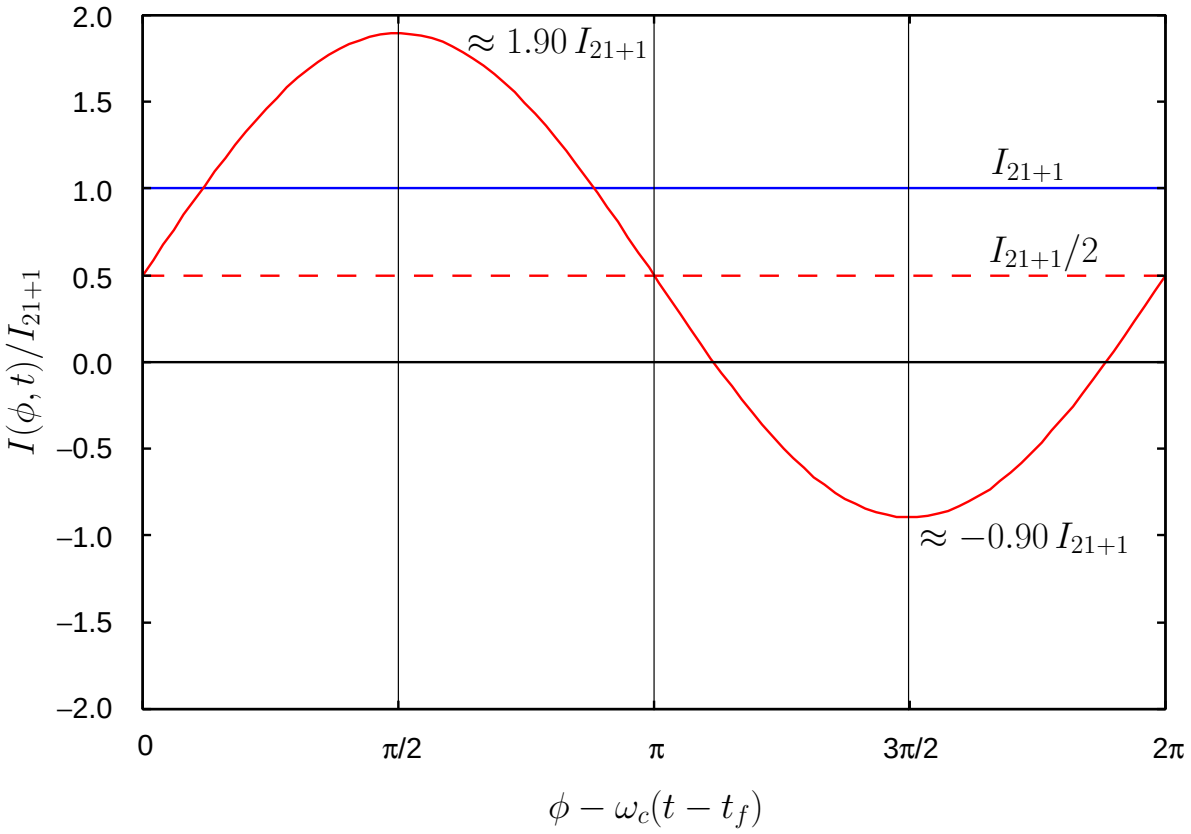

Figure 3.6: Time- and angle-dependent electric current $I(\phi,t)$ (red curve, Eq. (3.95)) with corresponding average current $I_{21+1}/2$ (dashed red line) for superposition states of $1s$ and $2p_+$ atomic orbitals with equal weights. The electric currents at $\phi=\omega_c(t-t_f)+\pi/2$ and $\phi=\omega_c(t-t_f)+3\pi/2$ are approximately $1.90\,I_{21+1}$ and $-0.90\,I_{21+1}$, respectively, cf. Fig. 3.4e–h. For comparison, the stationary electric ring current I_{21+1} (Eq. (3.31)) of $2p_+$ atomic orbitals is also shown (blue line).

and using Eq. (3.31),

$$I(\phi,t) \;=\; \frac{I_{21+1}}{2}\left(1+\frac{8\pi}{9}\sin(\phi-\omega_c(t-t_f))\right), \tag{3.95}$$

see Fig. 3.6. Thus, the electric current is periodic. Since $8\pi/9>1$, its direction is not only determined by the sign of the azimuthal quantum number $m=+1$ but also by the time t and the azimuthal angle ϕ. Its magnitude is largest for $\phi=\omega_c(t-t_f)+\pi/2$ with the same direction as that of the stationary electric ring current I_{21+1}, i.e. $\approx 1.90\,I_{21+1}$. However, the magnitude at the other extremum $\phi=\omega_c(t-t_f)+3\pi/2$ is smaller than the magnitude at $\phi=\omega_c(t-t_f)+\pi/2$ but largest for the opposite direction, i.e. $\approx -0.90\,I_{21+1}$, cf. Fig. 3.4e–h.

The time-dependent electronic current density (Eq. (3.82)) induces the time-dependent magnetic field $\mathbf{B}(\mathbf{r},t)$ (Eq. (2.199)), see Fig. 3.7. We will show that the x- and y-

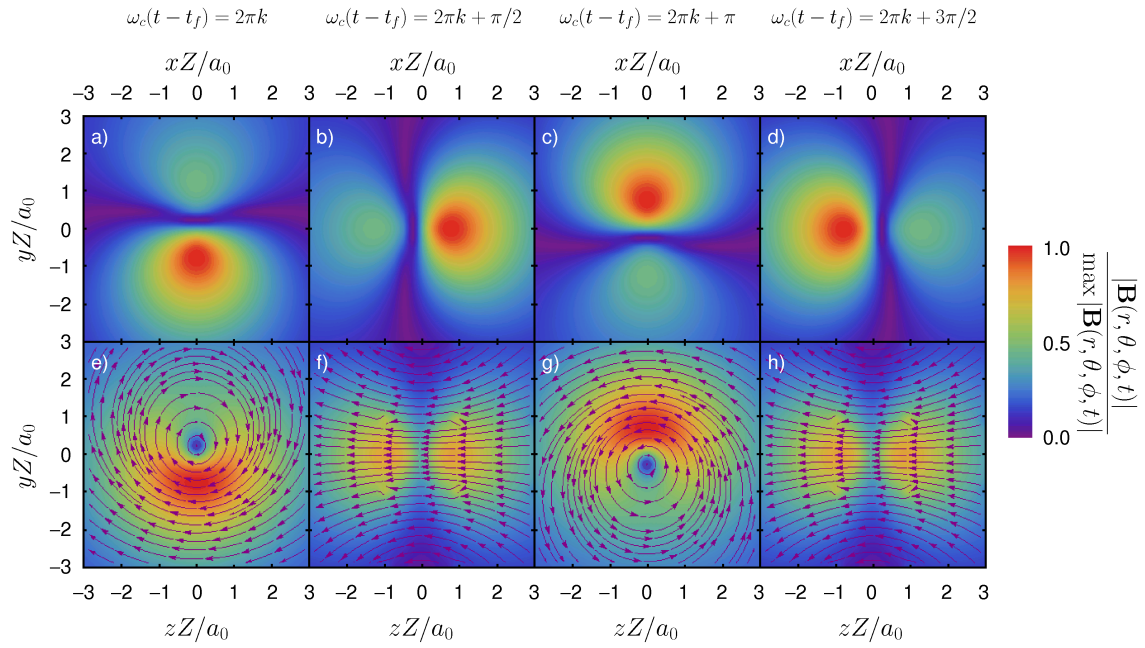

Figure 3.7: Time-dependent induced magnetic field $\mathbf{B}(r,\theta,\phi,t)$ (Eq. (2.199)) in the x/y ($z=0$) (panels a–d) and y/z ($x=0$) (panels e–h) planes, for superposition states of $1s$ and $2p_+$ atomic orbitals with equal weights and for arbitrary nuclear charges Z, cf. Figs. 3.4 and 3.5. The snapshots are taken at times $t = t_f + 2\pi k/\omega_c$ (panels a, e), $t = t_f + (2\pi k + \pi/2)/\omega_c$ (panels b, f), $t = t_f + (2\pi k + \pi)/\omega_c$ (panels c, g), and $t = t_f + (2\pi k + 3\pi/2)/\omega_c$ (panels d, h) ($k = 0, 1, 2, \ldots$). In panels a–d, the induced magnetic field has zero x- and y-components due to z-symmetry. The most intense region (red) is directed away from the reader and the least intense region (green) toward the reader. However, the induced magnetic field at the nucleus is time-independent, i.e. $\mathbf{B}(\mathbf{r}=\mathbf{0},t) = \mathbf{B}_{21+1}(\mathbf{r}=\mathbf{0})/2$ (Eq. (3.99)), cf. panels f and h.

components of the induced magnetic field at the nucleus ($\mathbf{r} = \mathbf{0}$) are zero due to z-symmetry of the electronic current density. The induced magnetic field at the nucleus ($\mathbf{r} = \mathbf{0}$), using Eqs. (2.199), (3.82), $dV' = r'^2 \sin\theta'\, dr'\, d\theta'\, d\phi'$, is evaluated as

$$
\begin{aligned}
\mathbf{B}(\mathbf{r}=\mathbf{0},t) &= \frac{\mu_0 e}{4\pi} \int_0^\infty \frac{dr'}{r'} \int_0^\pi \sin\theta'\, d\theta' \int_0^{2\pi} \mathbf{j}(\mathbf{r}',t) \times \mathbf{r}'\, d\phi' \qquad (3.96)\\
&= \frac{\mu_0 e\hbar}{64\pi^2 m_e} \left(\frac{Z}{a_0}\right)^4 \int_0^\infty e^{-3Zr'/2a_0}\, dr' \int_0^\pi \sin\theta'\, d\theta' \int_0^{2\pi} d\phi' \\
&\quad \left[\left(\frac{1}{8}\frac{Zr'}{a_0}\, e^{Zr'/2a_0} \sin\theta' - \sin(\omega_c(t-t_f)-\phi')\right)\mathbf{e}_{\phi'} \right.\\
&\quad - \left(\frac{1}{2}\frac{Zr'}{a_0} + 1\right) \sin\theta' \cos(\omega_c(t-t_f)-\phi')\, \mathbf{e}_{r'} \\
&\quad \left. - \cos\theta' \cos(\omega_c(t-t_f)-\phi')\, \mathbf{e}_{\theta'}\right] \times \mathbf{e}_{r'}
\end{aligned}
$$

$$= \frac{\mu_0 e\hbar}{64\pi^2 m_e}\left(\frac{Z}{a_0}\right)^4 \int_0^\infty e^{-3Zr'/2a_0}\,dr' \int_0^\pi \sin\theta'\,d\theta' \int_0^{2\pi} d\phi' \left[\left(\frac{1}{8}\frac{Zr'}{a_0}\,e^{Zr'/2a_0}\,\sin\theta' - \sin(\omega_c(t-t_f)-\phi')\right)\mathbf{e}_{\theta'} + \cos\theta'\,\cos(\omega_c(t-t_f)-\phi')\,\mathbf{e}_{\phi'}\right].$$

With

$$\mathbf{e}_{\theta'} = \cos\theta'\,\cos\phi'\,\mathbf{e}_x + \cos\theta'\,\sin\phi'\,\mathbf{e}_y - \sin\theta'\,\mathbf{e}_z \tag{3.97}$$

$$\mathbf{e}_{\phi'} = -\sin\phi'\,\mathbf{e}_x + \cos\phi'\,\mathbf{e}_y, \tag{3.98}$$

we obtain

$$\begin{aligned}\mathbf{B}(\mathbf{r}=\mathbf{0},t) &= \frac{\mu_0 e\hbar}{64\pi^2 m_e}\left(\frac{Z}{a_0}\right)^4 \int_0^\infty e^{-3Zr'/2a_0}\,dr' \int_0^\pi \sin\theta'\,d\theta' \int_0^{2\pi} d\phi' \qquad (3.99)\\ &\quad \left[\cos\theta'\left(\frac{1}{8}\frac{Zr'}{a_0}\,e^{Zr'/2a_0}\,\sin\theta' - \sin(\omega_c(t-t_f)-\phi')\right)(\cos\phi'\,\mathbf{e}_x + \sin\phi'\,\mathbf{e}_y)\right.\\ &\quad -\sin\theta'\left(\frac{1}{8}\frac{Zr'}{a_0}\,e^{Zr'/2a_0}\,\sin\theta' - \sin(\omega_c(t-t_f)-\phi')\right)\mathbf{e}_z\\ &\quad \left.+\cos\theta'\,\cos(\omega_c(t-t_f)-\phi')(-\sin\phi'\,\mathbf{e}_x + \cos\phi'\,\mathbf{e}_y)\right]\\ &= -\frac{\mu_0 e\hbar}{256\pi m_e}\left(\frac{Z}{a_0}\right)^5 \int_0^\infty r' e^{-Zr'/a_0}\,dr' \int_0^\pi \sin^3\theta'\,d\theta'\,\mathbf{e}_z\\ &= -\frac{\mu_0 e\hbar}{192\pi m_e}\left(\frac{Z}{a_0}\right)^3 \int_0^\infty x e^{-x}\,dx\,\mathbf{e}_z\\ &= -\frac{\mu_0 e\hbar Z^3}{192\pi m_e a_0^3}\,\mathbf{e}_z \;=\; \frac{1}{2}\,\mathbf{B}_{21+1}(\mathbf{r}=\mathbf{0})\end{aligned}$$

where

$$\int_0^\pi \sin^n\theta\,\cos\theta\,d\theta = 0 \qquad (n=0,1,2,\ldots) \tag{3.100}$$

$$\int_0^{2\pi} \sin\phi\,d\phi = 0 \tag{3.101}$$

and Eqs. (3.61), (3.43), (A.5), (A.7) have been used. Therefore, the magnetic field at the nucleus induced by the time-dependent electronic current density has zero x- and y-components, and its z-component is time-independent. This field is half of the one induced by the stationary electronic ring current (cf. Eqs. (2.204), (3.43)). Of course, the induced magnetic field at any location ($\mathbf{r} \neq \mathbf{0}$) is time- and angle-dependent, and circulates about the z-axis with the same frequency ω_c, see Fig. 3.7. The magnitude of the induced magnetic field along the z-axis is time-independent, cf. Fig. 3.7e–h. Because of the z-symmetry, the x- as well as the y-components of the induced magnetic field are also zero on the symmetric plane, i.e. $z = 0$ or $\theta = \pi/2$, see Fig. 3.7a–d. For $|z| \neq 0$, all

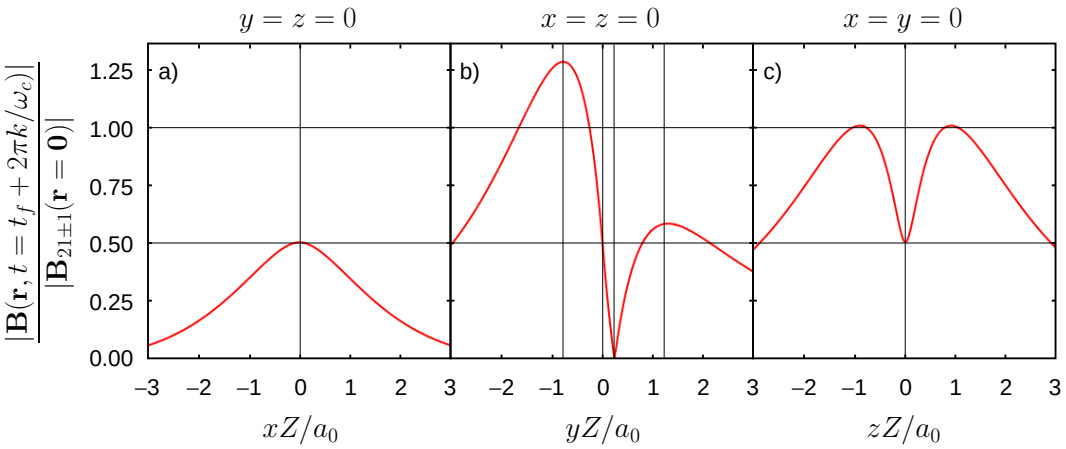

Figure 3.8: Magnitudes of the induced magnetic field $|\mathbf{B}(r, \theta, \phi, t = t_f + 2\pi k/\omega_c)|$ ($k = 0, 1, 2, \ldots$) (Eq. (2.199)) along x- ($y = z = 0$) (panel a), y- ($x = z = 0$) (panel b), and z- ($x = y = 0$) (panel c) axes, for superposition states of $1s$ and $2p_+$ atomic orbitals with equal weights and for arbitrary nuclear charges Z, cf. panels a and e of Fig. 3.7. The curves in panels a (x-axis) and c (z-axis) are along the horizontal section lines in panels a and e of Fig. 3.7, respectively, whereas the curve in panel b (y-axis) is along identical vertical section lines in panels a and e of Fig. 3.7. In contrast to the time-dependent magnitudes of the magnetic field along x- and y-axes with zero x- and y-components (panels a and b), the corresponding magnitude along the z-axis (panel c) is time-independent but with time-dependent x- and y-components, cf. Fig. 3.7e–h. The magnitudes of the induced magnetic field at $t = t_f + 2\pi k/\omega_c$ ($k = 0, 1, 2, \ldots$), $x = z = 0$ (panel b), and $y = -0.795\, a_0/Z$, $y = 0$, $y = 0.217\, a_0/Z$, and $y = 1.200\, a_0/Z$ are $1.28\, |\mathbf{B}_{21+1}(\mathbf{r} = \mathbf{0})|$, $0.5\, |\mathbf{B}_{21+1}(\mathbf{r} = \mathbf{0})|$, 0, and $0.58\, |\mathbf{B}_{21+1}(\mathbf{r} = \mathbf{0})|$, respectively.

components of the induced magnetic fields are in general non-zero. It is very interesting that the maximum of the induced magnetic field

$$\max |\mathbf{B}(\mathbf{r}, t)| \approx 1.28\, |\mathbf{B}_{21\pm1}(\mathbf{r} = \mathbf{0})|, \tag{3.102}$$

located at $\phi = \omega_c(t - t_f) + 3\pi/2$, $\theta = \pi/2$, and $r \approx 0.795\, a_0/Z$ is 2.56 times larger than the induced magnetic field at the nucleus $|\mathbf{B}(\mathbf{r} = \mathbf{0}, t)|$ (Eq. (3.99)). It is even 1.28 times larger than that of the stationary ring current $\max |\mathbf{B}_{21\pm1}(\mathbf{r})| = |\mathbf{B}_{21\pm1}(\mathbf{r} = \mathbf{0})|$ (Eq. (3.43)). This maximum magnetic field has a negative z-component, i.e. it is directed toward the negative z-axis where its other components are zero since $z = 0$. However, there is another maximum of the z-component of the induced magnetic field which is exactly directed toward the positive z-axis. The magnitude of this maximum is $0.58\, |\mathbf{B}_{21\pm1}(\mathbf{r} = \mathbf{0})|$, located at $\phi = \omega_c(t - t_f) + \pi/2$, $\theta = \pi/2$, and $r \approx 1.200\, a_0/Z$, which is still larger than the one at the nucleus $|\mathbf{B}(\mathbf{r} = \mathbf{0}, t)|$ (Eq. (3.99)). Note that the induced magnetic field at $\phi = \omega_c(t - t_f) + \pi/2$, $\theta = \pi/2$, and $r \approx 0.217\, a_0/Z$, i.e. close to the nucleus, is zero. Fig. 3.8 shows the magnitudes of the induced magnetic field $|\mathbf{B}(\mathbf{r}, t = t_f + 2\pi k/\omega_c)|$ ($k = 0, 1, 2, \ldots$) along the x-, y-, and z-axes, cf. panels a and e of Fig. 3.7.

3.2.6 Approximations for many-electron systems

The stationary electric ring currents for the atomic orbitals in the hydrogen atom and one-electron ions (Eq. (3.30)) and associated induced magnetic fields at their centers (Eq. (3.42)) can be generalized within the approximation for atomic and molecular orbitals carrying electronic ring currents in many-electron systems, such as atoms, ions, and molecules. For the estimate of these magnitudes in twofold degenerate states $|\Psi_{\pm}\rangle$ of atoms, atomic ions, and linear molecules, the following approximations are used:

1. The state $|\Psi_{\pm}\rangle$ is approximately equal to the CIS state $|\Psi_{\pm}^{CIS}\rangle$ where the electronic transitions from different occupied non-degenerate orbitals φ_a to an unoccupied twofold degenerate orbital $\varphi_{b\pm}$ or from an occupied twofold degenerate orbital $\varphi_{a\mp}$ to different unoccupied non-degenerate orbitals φ_b are dominant. The corresponding electronic current densities were given in Eqs. (2.40) and (2.41), i.e.

$$\mathbf{j}_{\pm}(\mathbf{r}) \approx \mathbf{j}_{\pm}^{CIS}(\mathbf{r}) \approx \mathbf{j}_{\pm,\rightarrow b\pm}^{CIS}(\mathbf{r}) = \mathbf{j}_{\varphi_{b\pm}}(\mathbf{r}) \tag{3.103}$$

and

$$\mathbf{j}_{\pm}(\mathbf{r}) \approx \mathbf{j}_{\pm}^{CIS}(\mathbf{r}) \approx \mathbf{j}_{\pm,a\mp\rightarrow}^{CIS}(\mathbf{r}) = \mathbf{j}_{\varphi_{a\pm}}(\mathbf{r}), \tag{3.104}$$

where $\mathbf{j}_{\varphi_{b\pm}}(\mathbf{r})$ and $\mathbf{j}_{\varphi_{a\pm}}(\mathbf{r})$ are the electronic current densities of the unoccupied $\varphi_{b\pm}$ and occupied $\varphi_{a\pm}$ atomic or molecular orbitals, respectively. Note that the special case of the single dominant electronic transition (for example the HOMO-LUMO transition) is already included in this approximation. Thus, the electric ring current and induced magnetic field in the degenerate state are independent of the non-degenerate orbital contribution to dominant electronic transitions. For example, two degenerate states with corresponding dominant transitions $1s \rightarrow 3p_{\pm}$ and $2s \rightarrow 3p_{\pm}$ are different but their electric ring currents and induced magnetic fields are very similar. However, one can also go beyond the CIS approximation, e.g. CISD approximation in which the double electronic transitions are also included, see examples below.

2. For molecules, the linear combination of atomic orbitals - molecular orbital (LCAO-MO) approximation is used, i.e. the degenerate molecular orbital consists of several degenerate atomic orbitals with associated quantum numbers n, l, m. In particular for linear molecules, there are electronic ring currents of these atomic orbitals about the corresponding nuclei. These electric ring currents and associated induced magnetic fields at the nuclei are then weighted by the corresponding weights for the expansion coefficients of the LCAO-MO.

3. The electric ring currents and induced magnetic fields (Eqs. (3.30), (3.42)) can be estimated for each contributed degenerate atomic orbital with corresponding quantum numbers n, l, m but the nuclear charge Z should be replaced by the effective one Z_{eff}, using simple Slater rules [275, 276].

For example, the first excited state $|A^1\Pi_\pm\rangle$ of the AlCl molecule does not correspond only to the dominant HOMO-LUMO transition $9\sigma \rightarrow 4\pi_\pm$ (83.9%), but also to another single transition $8\sigma \rightarrow 4\pi_\pm$ (3.6%) and, beyond the CIS approximation, double and triple transitions $9\sigma^2 \rightarrow 4\pi_\pm, 10\sigma$ (5.2%), $8\sigma, 9\sigma^2 \rightarrow 4\pi_\pm^2, 4\pi_\mp$ (0.4%), and $8\sigma, 9\sigma \rightarrow 4\pi_\pm, 10\sigma$ (0.3%) [145]. All of these transitions contribute to the electronic ring current of the molecular orbital $4\pi_\pm$ with the weight $\geq 93.4\%$, hence $\mathbf{j}_{A^1\Pi_\pm}(\mathbf{r}) \approx \mathbf{j}_{4\pi_\pm}(\mathbf{r})$. The molecular orbital $4\pi_\pm$ has the LCAO-MO expansion $4\pi_\pm \approx c_{3p_\pm(\mathrm{Al})} 3p_\pm(\mathrm{Al}) + c_{3p_\pm(\mathrm{Cl})} 3p_\pm(\mathrm{Cl})$ with dominant weights for the coefficients $|c_{3p_\pm(\mathrm{Al})}|^2 \approx 0.9$ and $|c_{3p_\pm(\mathrm{Cl})}|^2 \approx 0.1$ [145]. The effective nuclear charges for $3p_\pm$ orbitals of Al and Cl atoms are $Z_{eff}(\mathrm{Al}) = 13 - 2 - 8 \cdot 0.85 - 2 \cdot 0.35 = 3.5$ and $Z_{eff}(\mathrm{Cl}) = 17 - 2 - 8 \cdot 0.85 - 6 \cdot 0.35 = 6.1$, respectively [144,145,275,276]. The approximate electric ring currents (Eq. (3.30)) for electronic ring currents of atomic orbitals $3p_\pm(\mathrm{Al})$ and $3p_\pm(\mathrm{Cl})$, using $n = 3, l = 1, m = \pm 1$, are

$$I_{31\pm1}(\mathrm{Al}) = \mp \frac{e\hbar}{54\pi m_e a_0^2} Z_{eff}^2(\mathrm{Al}) |c_{3p_\pm(\mathrm{Al})}|^2 \approx \mp 430\,\mu\mathrm{A} \tag{3.105}$$

$$I_{31\pm1}(\mathrm{Cl}) = \mp \frac{e\hbar}{54\pi m_e a_0^2} Z_{eff}^2(\mathrm{Cl}) |c_{3p_\pm(\mathrm{Cl})}|^2 \approx \mp 145\,\mu\mathrm{A}, \tag{3.106}$$

which are similar to the CASSCF results $I_\pm(\mathrm{Al}) \approx \mp 313\,\mu\mathrm{A}$ and $I_\pm(\mathrm{Cl}) \approx \mp 92\,\mu\mathrm{A}$ [145], respectively, see also Section 3.3.2. Likewise, the approximate magnitudes of the induced magnetic fields at nuclei Al and Cl (Eq. (3.42)) are

$$|\mathbf{B}_{31\pm1}(\mathbf{r} = \mathbf{r}_{\mathrm{Al}})| = \frac{\mu_0 e\hbar}{324\pi m_e a_0^3} Z_{eff}^3(\mathrm{Al}) |c_{3p_\pm(\mathrm{Al})}|^2 \approx 6.0\,\mathrm{T} \tag{3.107}$$

$$|\mathbf{B}_{31\pm1}(\mathbf{r} = \mathbf{r}_{\mathrm{Cl}})| = \frac{\mu_0 e\hbar}{324\pi m_e a_0^3} Z_{eff}^3(\mathrm{Cl}) |c_{3p_\pm(\mathrm{Cl})}|^2 \approx 3.5\,\mathrm{T}, \tag{3.108}$$

again in accord with the CASSCF results $|\mathbf{B}(\mathbf{r} = \mathbf{r}_{\mathrm{Al}})| \approx 7.7\,\mathrm{T}$ and $|\mathbf{B}(\mathbf{r} = \mathbf{r}_{\mathrm{Cl}})| \approx 4.1\,\mathrm{T}$ [145], see also Section 3.3.2.

Another example is the first excited state $|A^1\Pi_\pm\rangle$ of the BeO molecule which corresponds the dominant HOMO-LUMO transition $1\pi_\mp \rightarrow 5\sigma$ (96.1%) [146], hence $\mathbf{j}_{A^1\Pi_\pm}(\mathbf{r}) \approx \mathbf{j}_{1\pi_\pm}(\mathbf{r})$. Furthermore, the molecular orbital $1\pi_\pm$ has the LCAO-MO expansion $1\pi_\pm \approx c_{2p_\pm(\mathrm{O})} 2p_\pm(\mathrm{O}) + c_{2p_\pm(\mathrm{Be})} 2p_\pm(\mathrm{Be})$ with dominant weights for the coefficients $|c_{2p_\pm(\mathrm{O})}|^2 \approx 0.96$ and $|c_{2p_\pm(\mathrm{Be})}|^2 \approx 0.03$ [146]. Thus, there is only a dominant electronic ring current of the $2p_\pm$ atomic orbital about the O nucleus. The effective nuclear charge for the $2p_\pm$ orbital of the O atom is $Z_{eff}(\mathrm{O}) = 8 - 2 \cdot 0.85 - 5 \cdot 0.35 = 4.55$. Therefore,

the approximate electric ring current (Eq. (3.30)) and magnitude of the induced magnetic field (Eq. (3.42)) at the O nucleus, using $n = 2, l = 1, m = \pm 1$ (cf. Eqs. (3.31), (3.43)), are

$$I_{21\pm1}(\mathrm{O}) \;=\; \mp\frac{e\hbar}{16\pi m_e a_0^2}\, Z_{eff}^2(\mathrm{O})|c_{2p_\pm(\mathrm{O})}|^2 \;\approx\; \mp 2.62\,\mathrm{mA} \tag{3.109}$$

and

$$|\mathbf{B}_{21\pm1}(\mathbf{r}=\mathbf{r}_\mathrm{O})| \;=\; \frac{\mu_0 e\hbar}{96\pi m_e a_0^3}\, Z_{eff}^3(\mathrm{O})|c_{2p_\pm(\mathrm{O})}|^2 \;\approx\; 47.2\,\mathrm{T}, \tag{3.110}$$

which are in quite good agreement with the CASSCF results $I_\pm(\mathrm{O}) \approx \mp 2.49\,\mathrm{mA}$ and $|\mathbf{B}(\mathbf{r}=\mathbf{r}_\mathrm{O})| \approx 52.1\,\mathrm{T}$ [146], respectively, see also Section 3.3.2.

The induced magnetic fields are strongest for $2p_\pm$ atomic orbitals and for large effective nuclear charges Z_{eff}, cf. Section 3.2.2. Thus, these strong magnetic fields can be achieved also for atoms, in particular, for O and F atoms. The lowest singlet states $|1^1D_{M_L}\rangle$ ($M_L = \pm1, \pm2$) of the O atom carry non-zero electronic ring currents. They correspond to the dominant electronic configurations $\ldots(2p_-)(2p_0)(2p_+)^2$ for $M_L = 1$, $\ldots(2p_-)^2(2p_0)(2p_+)$ for ($M_L = -1$), $\ldots(2p_0)^2(2p_+)^2$ for ($M_L = +2$), and $(2p_-)^2(2p_0)^2$ for ($M_L = -2$). For $M_L = \pm1$, the electronic ring currents are dominated by $2p_\pm$ atomic orbitals. For $M_L = \pm2$, the electric ring currents and induced magnetic fields are twice as large as the ones for $M_L = \pm1$ because two (rather than a single) electrons with opposite spins and the same spatial atomic orbital $2p_\pm$ circulate about the O nucleus. Using the effective nuclear charge for the O atom ($Z_{eff} = 4.55$, see above), the approximate induced magnetic fields at the O nucleus (Eq. (3.110) but without the factor $|c_{2p_\pm(\mathrm{O})}|^2$) are $|\mathbf{B}_{21\pm1}(\mathbf{r}=\mathbf{r}_\mathrm{O})| \approx 49.1\,\mathrm{T}$ for $M_L = \pm1$ and $2|\mathbf{B}_{21\pm1}(\mathbf{r}=\mathbf{r}_\mathrm{O})| \approx 98.3\,\mathrm{T}$ for $M_L = \pm2$. These approximate values are compared to the CASSCF results $|\mathbf{B}(\mathbf{r}=\mathbf{r}_\mathrm{O})| \approx 62.0\,\mathrm{T}$ for $M_L = \pm1$ and $|\mathbf{B}(\mathbf{r}=\mathbf{r}_\mathrm{O})| \approx 124.0\,\mathrm{T}$ for $M_L = \pm2$ [146].

A final example is the doublet twofold degenerate ground states $|1^2P_{M_L}\rangle$ ($M_L = \pm1$) of the F atom which correspond to the dominant electronic configurations $\ldots(2p_-)(2p_0)^2(2p_+)^2$ for $M_L = +1$ and $\ldots(2p_-)^2(2p_0)^2(2p_+)$ for $M_L = -1$. These degenerate states carry non-zero electronic ring currents of the atomic orbitals $2p_\pm$ about the F nucleus, even in the electronic ground state. Since the effective nuclear charge of the F atom ($Z_{eff} = 9 - 2\cdot0.85 - 6\cdot0.35 = 5.2$) is larger than that of the O atom, the associated induced magnetic fields are, of course, stronger. The approximate magnitude is $|\mathbf{B}_{21\pm1}(\mathbf{r}=\mathbf{r}_\mathrm{F})| \approx 73.3\,\mathrm{T}$ compared to the CASSCF result $|\mathbf{B}(\mathbf{r}=\mathbf{r}_\mathrm{F})| \approx 95.2\,\mathrm{T}$, see conclusion in Ref. [146].

Note that the approximate induced magnetic fields in all of the above examples are nevertheless underestimated. Thus, one can consider the approximate magnitudes of the induced magnetic fields as the lower bounds of the exact ones.

3.3 Linear molecules AlCl and BeO

3.3.1 Nonadiabatic orientation

Before applying right or left circularly polarized laser pulses propagating along the laboratory-fixed z-axis in order to generate electronic ring currents and electron circulation in excited electronic degenerate states $|A\,^1\Pi_\pm\rangle$ of linear polar AlCl and BeO molecules (see Sections 3.3.2 and 3.3.3, and Refs. [145, 146]), these molecules have to be oriented along the laboratory-fixed z-axis, e.g. by means of a linearly polarized laser pulse (see Section 2.6). We first present the results for the nonadiabatic orientation of the BeO molecule [146], and then for the AlCl molecule in which the simple scalings for laser parameters are used to obtain equivalent quantum dynamical results as for the BeO molecule.

We consider the BeO molecule in the electronic and vibrational ground state $|X\,^1\Sigma^+(\nu = 0)\rangle$ at the rotational temperature $T = 1\,\mathrm{K}$. The BeO molecule has the rotational constant $B_{e,X} = 1.619\,hc\,\mathrm{cm}^{-1}$ and the permanent dipole moment $\tilde{M}(R_{e,X}) = 2.56\,ea_0 = 6.50\,\mathrm{D}$ (Eq. (2.453), calculated at the CASPT2 level) at the equilibrium bond length $R_{e,X} = 2.54\,a_0$ of the electronic ground state $|X\,^1\Sigma^+\rangle$ [146]. Note that the dipole vector points from the O to the Be atom, see Fig. 2.10. The first three rotational eigenenergies (Eq. (2.437)) are $E_X^{J=0} = 0\,hc\,\mathrm{cm}^{-1}$, $E_X^{J=1} = 3.24\,hc\,\mathrm{cm}^{-1}$, and $E_X^{J=2} = 9.71\,hc\,\mathrm{cm}^{-1}$, and the corresponding Boltzmann weights at $T = 1\,\mathrm{K}$ (Eq. (2.438)) are $\tilde{P}(0) = 0.972$, $\tilde{P}(1) = 0.009$, and $\tilde{P}(2) = 10^{-6}$. Since other Boltzmann weights at $T = 1\,\mathrm{K}$ are negligible, only initial rotational states $|J_i M_i\rangle$ with $J_{i,min} = 0 \leq J_i \leq J_{i,max} = 2$, $M_i = -J_i, \ldots, J_i$ and the total number of rotational states $J_{max} = 13$ were used for the time-propagation of the time-dependent rotational state $|\Psi_{rot}^{J_i M_i}(t)\rangle$ (Eq. (2.120)).

A HCP-like linearly z-polarized laser pulse (Eq. (2.440)) propagating along the axis perpendicular to the laboratory-fixed z-axis is applied for the nonadiabatic orientation of the BeO molecule. While the ratio of field amplitudes $\mathcal{E}_{1,l}/\mathcal{E}_{2,l} = 10$ of the laser pulse is constant, the laser amplitude $\mathcal{E}_{1,l}$ (with negative amplitude) and carrier frequency ω_l are optimized to yield the maximum negative orientation of the BeO molecule (see Fig. 2.10). The optimized laser parameters are $\mathcal{E}_{1,l} = -100\,\mathrm{MV\,m}^{-1}$ and $\hbar\omega_l = 12.0\,hc\,\mathrm{cm}^{-1}$, thus $\mathcal{E}_{2,l} = -10.0\,\mathrm{MV\,m}^{-1}$. Note that the optimized carrier frequency ω_l is off-resonant with the experimental vibrational frequency of the electronic ground state $\hbar\omega_{e,X} = 1487.3\,hc\,\mathrm{cm}^{-1}$ [277] and with the excitation frequency of the first excited electronic state $|A\,^1\Pi_\pm\rangle$ at $R_{e,X}$, i.e. $\Delta E_1(R_{e,X}) = \hbar\omega_{10} = 1.2367\,\mathrm{eV} = 9974.7\,hc\,\mathrm{cm}^{-1}$ [146], hence the BeO molecule remains in the electronic and vibrational ground state $|X\,^1\Sigma^+(\nu = 0)\rangle$. The other laser pa-

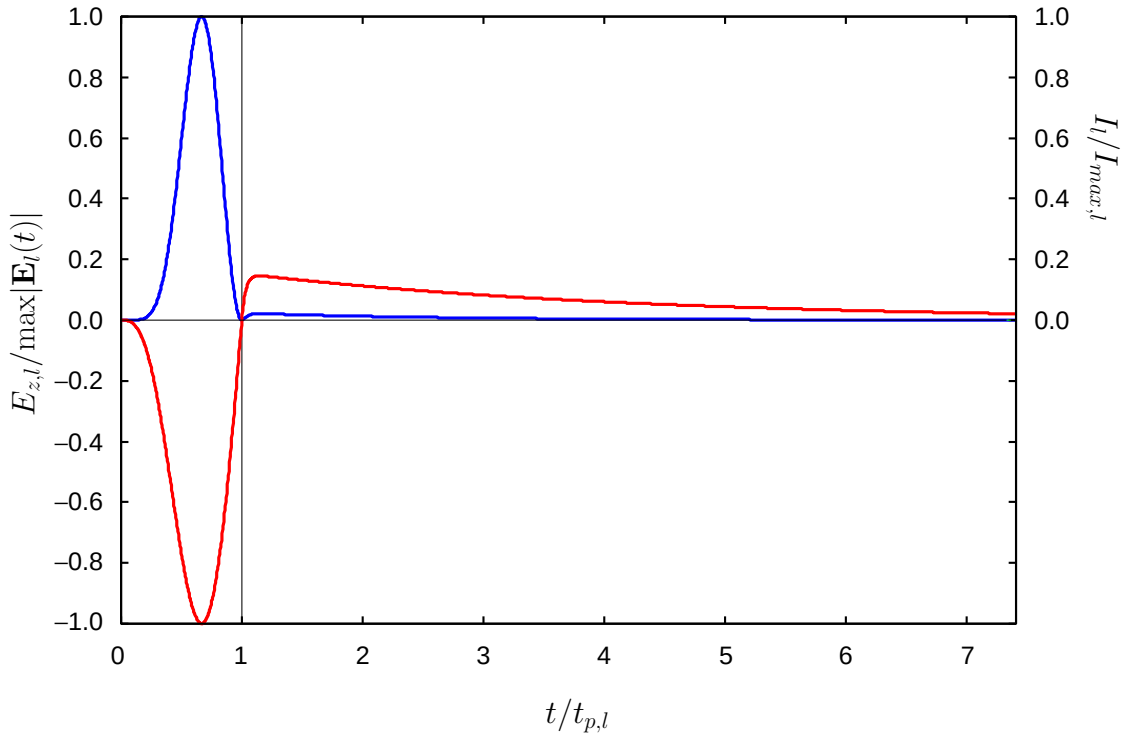

Figure 3.9: z-component of the time-dependent electric field $E_{z,l}(t)$ (Eq. (2.440), red curve) and its intensity $I_l(t)$ (Eq. (2.449), blue curve) of the optimized linearly z-polarized laser pulse propagating along the axis perpendicular to the laboratory-fixed z-axis for maximum negative orientation of BeO and AlCl molecules, cf. Fig. 2.10. The laser parameters are $\mathcal{E}_{1,l} = -100\,\mathrm{MV\,m^{-1}}$, $\mathcal{E}_{2,l} = -10.0\,\mathrm{MV\,m^{-1}}$, $\hbar\omega_l = 12.0\,hc\,\mathrm{cm^{-1}}$, $t_{p,l} = \pi/\omega_l = 1.39\,\mathrm{ps}$, $\tau_{1,l} = 44.2\,\mathrm{fs}$, $\tau_{2,l} = 4.47\,\mathrm{ps}$ for the BeO molecule and $\mathcal{E}_{1,l} = -64.0\,\mathrm{MV\,m^{-1}}$, $\mathcal{E}_{2,l} = -6.40\,\mathrm{MV\,m^{-1}}$, $\hbar\omega_l = 1.81\,hc\,\mathrm{cm^{-1}}$, $t_{p,l} = \pi/\omega_l = 9.22\,\mathrm{ps}$, $\tau_{1,l} = 294\,\mathrm{fs}$, $\tau_{2,l} = 29.6\,\mathrm{ps}$ for the AlCl molecule. The vertical line indicates the pulse duration $t_{p,l}$ of the first part of the laser pulse and the maximum time shown in this figure is the rotational revival time $\tau_{rev,X} = 7.41\,t_{p,l}$.

rameters are then estimated, i.e. the laser pulse duration of the first part of the laser pulse is $t_{p,l} = \pi/\omega_l = 1.39\,\mathrm{ps}$, and the switch-on (Eq. (2.443)) and switch-off times (Eq. (2.448)) of the second part of the laser pulse are $\tau_{1,l} = 44.2\,\mathrm{fs}$ and $\tau_{2,l} = 4.47\,\mathrm{ps}$, respectively. The maximum intensity of the laser pulse is $I_{max,l} = \max I_l(t) = 1.12\,\mathrm{GV\,cm^{-2}}$, cf. Eq. (2.449). Note that the maximum amplitude $\max|\mathbf{E}_l(t)| = 65.0\,\mathrm{MV\,m^{-1}}$ is smaller than $|\mathcal{E}_{1,l}|$. Fig. 3.9 presents the z-component of the time-dependent electric field $\mathbf{E}_l(t) = E_{z,l}(t)\mathbf{e}_z$ and the corresponding intensity $I_l(t)$ (Eq. (2.449)). Note that this laser pulse is very similar to the experimental laser pulse shown in Fig. 2 of Ref. [278], i.e. with almost the same pulse shape and duration, but with lower intensity.

Fig. 3.10 shows the thermally averaged time-dependent expectation value $\langle\cos\theta\rangle_T(t)$ (Eq. (2.465)) at $T = 1\,\mathrm{K}$ for the optimized laser pulse. The orientation reaches a minimum value of $\langle\cos\theta\rangle_{T=1\,\mathrm{K}}(t = 1.27\,\mathrm{ps}) = -0.850$ immediately before the turn off of the first

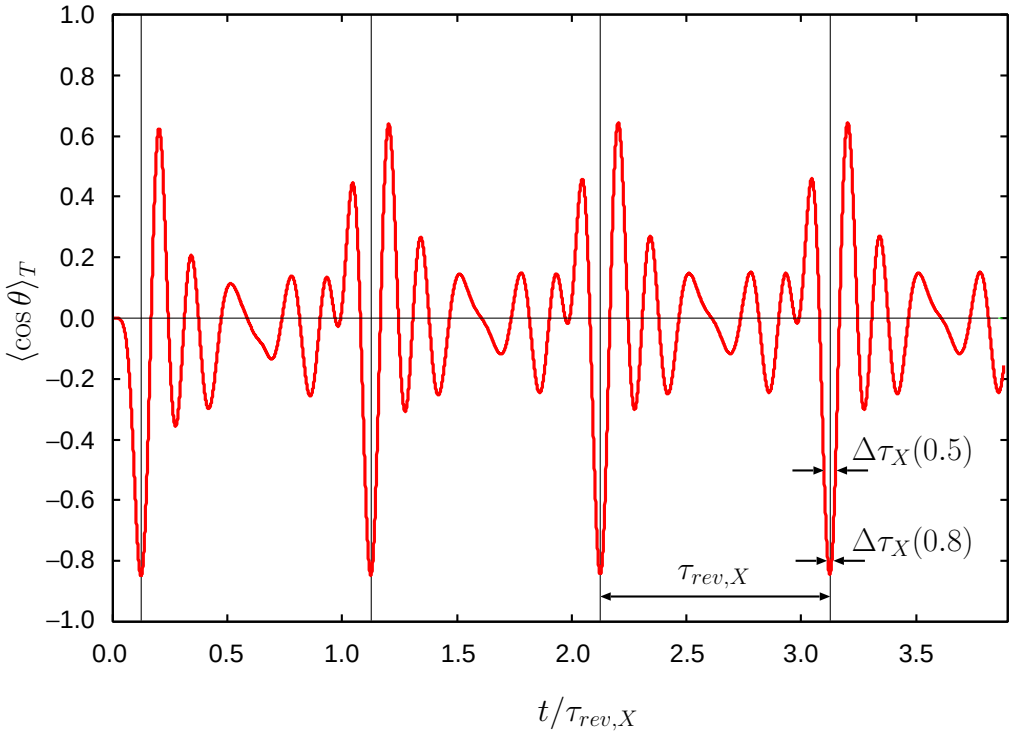

Figure 3.10: Thermally averaged time-dependent expectation value $\langle\cos\theta\rangle_T(t)$ at $T = 1\,\mathrm{K}$ for the BeO molecule and $T = 0.151\,\mathrm{K}$ for the AlCl molecule. The orientation revivals (marked by vertical lines) are spaced by the rotational revival time $\tau_{rev,X}$ of the electronic ground state $|X\,^1\Sigma^+\rangle$, i.e. $\tau_{rev,X} = 10.30\,\mathrm{ps}$ for the BeO molecule and $\tau_{rev,X} = 68.4\,\mathrm{ps}$ for the AlCl molecule. The orientation durations $\Delta\tau_X$ are $0.050\,\tau_{rev,X}$ (i.e. 0.52 ps for BeO and 3.4 ps for AlCl) and $0.017\,\tau_{rev,X}$ (i.e. 0.17 ps for BeO and 1.1 ps for AlCl) for absolute values of $\langle\cos\theta\rangle_T(t)$ larger than 0.5 and 0.8, respectively.

part of the laser pulse, implying strong orientation of the BeO molecule in the negative z-direction. As expected, the rotational revival pattern is observed, i.e. the rotational wavepacket dephases and rephases periodically at intervals of the rotational revival time $\tau_{rev,X} = \pi\hbar/B_{e,X} = 10.30\,\mathrm{ps} = 7.41\,t_{p,l}$ of the electronic ground state $|X\,^1\Sigma^+\rangle$ of the BeO molecule because the pulse duration $t_{p,l}$ is much smaller than the revival time $\tau_{rev,X}$, i.e. the orientation is nonadiabatic. The maximum negative orientation of the BeO molecule after the switch-off of the laser pulse recurs at times $t = t^* + n\tau_{rev,X}$ $(n = 0, 1, 2, \ldots)$ where $t^* = 21.88\,\mathrm{ps} = 2.12\,\tau_{rev,X}$. Note that the orientation of the BeO molecule also recurs at $t = 11.58\,\mathrm{ps} = 1.12\,\tau_{rev,X}$ but the electric field of the laser pulse is still not negligible, see also Fig. 3.9. At times $t = t^* + n\tau_{rev,X} = (2.12 + n)\tau_{rev,X}$ $(n = 0, 1, 2, \ldots)$, the thermally averaged expectation value $\langle\cos\theta\rangle_T(t)$ is -0.844 and the orientation durations $\Delta\tau_X$ are $0.52\,\mathrm{ps} = 0.050\,\tau_{rev,X}$ and $0.17\,\mathrm{ps} = 0.017\,\tau_{rev,X}$ for absolute values of $\langle\cos\theta\rangle_T(t)$ larger than 0.5 and 0.8, respectively. These durations $\Delta\tau_X$ should be larger than the pulse durations of applied circularly polarized laser pulses for the induction of electronic ring currents.

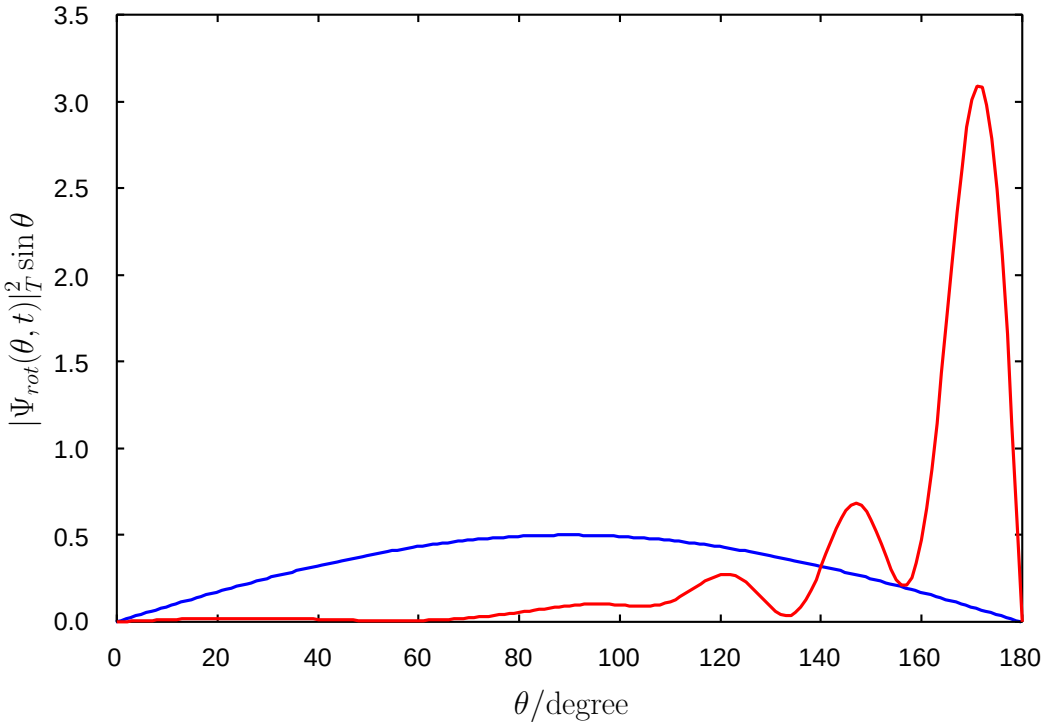

Figure 3.11: Thermally averaged normalized angular distribution $|\Psi_{rot}(\theta,t)|^2_T \sin\theta$ of the rotational wavepacket at $T = 1\,\mathrm{K}$ for the BeO molecule and $T = 0.151\,\mathrm{K}$ for the AlCl molecule, and at times $t = (2.12+n)\tau_{rev,X}$ ($n = 0,1,2,\ldots$, $\tau_{rev,X} = 10.30\,\mathrm{ps}$ for BeO and $\tau_{rev,X} = 68.4\,\mathrm{ps}$ for AlCl) (red curve) compared with the initial distribution at $t = 0$ (blue curve).

Fig. 3.11 shows the thermally averaged normalized angular distribution $|\Psi_{rot}(\theta,t)|^2_T \sin\theta$ at $T = 1\,\mathrm{K}$ and at the instances of almost perfect negative orientation of the BeO molecule $t = (2.12+n)\tau_{rev,X}$ ($n = 0,1,2,\ldots$), where the angular distribution is focused in the 160° to 180° range. The initial normalized angular distribution at $t = 0$ is also shown in Fig. 3.11, where the corresponding expectation value $\langle\cos\theta\rangle_T(t=0)$ is zero.

Now, we consider the AlCl molecule in the same ground state $|X\,^1\Sigma^+(\nu=0)\rangle$ as for the BeO molecule. The AlCl molecule has the rotational constant $B_{e,X} = 0.244\,hc\,\mathrm{cm}^{-1}$ and the permanent dipole moment $\tilde{M}(R_{e,X}) = 0.60\,ea_0 = 1.53\,\mathrm{D}$ (Eq. (2.453), calculated at the CASPT2 level [279]) at the experimental equilibrium bond length $R_{e,X} = 4.03\,a_0$ of the electronic ground state $|X\,^1\Sigma^+\rangle$ [145, 277]. The dipole vector points from the Cl to the Al atom, thus the AlCl molecule has to be oriented in the negative z-direction as for the BeO molecule. Since the rotation constant of the AlCl molecule is smaller than that of the BeO molecule, the rotational eigenenergies (Eq. (2.437)) are reduced by the factor $B_{e,X}(\mathrm{AlCl})/B_{e,X}(\mathrm{BeO}) = 0.151$, i.e. $E_X^{J=0} = 0\,hc\,\mathrm{cm}^{-1}$, $E_X^{J=1} = 0.49\,hc\,\mathrm{cm}^{-1}$, and $E_X^{J=2} = 1.46\,hc\,\mathrm{cm}^{-1}$. To obtain the equivalent Boltzmann weights for the AlCl molecule

as for the BeO molecule, the rotational temperature for the AlCl molecule is reduced to $T = B_{e,X}(\mathrm{AlCl})/B_{e,X}(\mathrm{BeO}) \cdot 1\,\mathrm{K} = 0.151\,\mathrm{K}$ (cf. Eq. (2.438)), where $J_{i,min} = 0$, $J_{i,max} = 2$, and $J_{max} = 13$ remain unchanged (see above).

Equivalent quantum dynamics for the nonadiabatic orientation of the AlCl molecule, shown in Figs. 3.9–3.11, can be obtained using the simple scalings for laser parameters. Since the rotational revival time is larger for the AlCl molecule, i.e. $\tau_{rev,X} = \pi\hbar/B_{e,X} = 68.4\,\mathrm{ps}$, by the factor $B_{e,X}(\mathrm{BeO})/B_{e,X}(\mathrm{AlCl}) = 6.64$, all other time variables for the laser pulse have to be raised by the same factor, i.e. $t_{p,l} = 9.22\,\mathrm{ps}$, $\tau_{1,l} = 294\,\mathrm{fs}$, and $\tau_{2,l} = 29.6\,\mathrm{ps}$. Thus, the carrier frequency is reduced to $\omega_l = \pi/t_{p,l} = 1.81\,hc\,\mathrm{cm}^{-1}$, which is also off-resonant with the experimental vibrational frequency of the electronic ground state $\hbar\omega_{e,X} = 481.3\,hc\,\mathrm{cm}^{-1}$ [277,280] and with the excitation frequency of the first excited electronic state $|A\,^1\Pi_\pm\rangle$ at $R_{e,X}$, i.e. $\Delta E_1(R_{e,X}) = \hbar\omega_{10} = 4.6323\,\mathrm{eV} = 37362\,hc\,\mathrm{cm}^{-1}$ [145]. Furthermore, if $\tilde{M}(R_{e,X})\mathcal{E}_{1,l}t_{p,l}$ is equal for BeO and AlCl molecules, then the quantum dynamical results are exactly equal (cf. Eqs. (2.458) and (2.461), also compared with Eqs. (2.171) and (2.175)). Thus, the laser amplitudes $\mathcal{E}_{1,l}$ and $\mathcal{E}_{2,l}$ for the AlCl molecule are reduced by the factor $B_{e,X}(\mathrm{AlCl})/B_{e,X}(\mathrm{BeO}) \cdot \tilde{M}(R_{e,X},\mathrm{BeO})/\tilde{M}(R_{e,X},\mathrm{AlCl}) = 0.640$, i.e. $\mathcal{E}_{1,l} = -64.0\,\mathrm{MV\,m}^{-1}$ and $\mathcal{E}_{2,l} = -6.40\,\mathrm{MV\,m}^{-1}$. The corresponding maximum amplitude is $\max|\mathbf{E}_l(t)| = 41.6\,\mathrm{MV\,m}^{-1}$. The maximum intensity of the laser pulse is reduced by the factor $(0.640)^2$, i.e. $I_{max,l} = 0.459\,\mathrm{GV\,cm}^{-2}$. These laser paramters are also listed in Fig. 3.9.

The thermally averaged expectation value $\langle\cos\theta\rangle_T(t)$ at $T = 0.151\,\mathrm{K}$ for the AlCl molecule is the same as for the BeO molecule at $T = 1\,\mathrm{K}$ (see Fig. 3.10), but the rotational revival time and orientation durations are raised by the factor $B_{e,X}(\mathrm{Be})/B_{e,X}(\mathrm{Al}) = 6.64$, i.e. $\tau_{rev,X} = 68.4\,\mathrm{ps}$, $\Delta\tau_X = 3.4\,\mathrm{ps}$ and $\Delta\tau_X = 1.1\,\mathrm{ps}$ for absolute values of $\langle\cos\theta\rangle_T(t)$ larger than 0.5 and 0.8, respectively. The thermally averaged normalized angular distribution $|\Psi_{rot}(\theta,t)|^2_T(t)\sin\theta$ at $T = 0.151\,\mathrm{K}$ and at times $t = (2.12+n)\tau_{rev,X}$ $(n = 0,1,2,\ldots)$ for the AlCl molecule is the same as for the BeO molecule at $T = 1\,\mathrm{K}$, but with a different rotational revival time $\tau_{rev,X}$, see Fig. 3.11.

3.3.2 Electronic ring currents in excited $|A\,^1\Pi_\pm\rangle$ states

First, we summarize the quantum chemistry results for the AlCl and BeO molecules, given in Refs. [145] and [146], respectively. The quantum chemical calculations were done at CASSCF(8,11)/CASPT2 and CASSCF(6,12)/CASPT2 levels for AlCl and BeO molecules, using the MOLCAS 6.0 program package, respectively [281–286]. For AlCl, 8 electrons and 11 orbitals were included in the active space and an atomic natural orbital

state (AlCl)	dominant configuration (AlCl)		ΔE_i (eV)	$\lvert\mathbf{M}_{ij}\rvert$ (ea_0)						
$X\,^1\Sigma^+$	$\ldots(8\sigma)^2(3\pi)^4(9\sigma)^2$	(87.8 %)	0.0000	A: 1.313	G: 0.431	H: 1.102	J: 0.182	K: 0.007		
$A\,^1\Pi_\pm$	$(9\sigma) \to (4\pi_\pm)$	(83.9 %)	4.6323	X: 1.313	B: 0.032	C: 0.082	D: 0.183	E: 0.092	F: 1.575	I: 1.359
$B\,^1\Sigma^+$	$(9\sigma) \to (10\sigma)$	(51.6 %)	6.4649	A: 0.032	G: 0.040	H: 0.091	J: 0.856	K: 0.017		
	$(3\pi_+) \to (4\pi_+)$	(17.9 %)								
	$(3\pi_-) \to (4\pi_-)$	(17.9 %)								
$C\,^1\Delta_\pm$	$(3\pi_\mp) \to (4\pi_\pm)$	(90.6 %)	6.4816	A: 0.082	G: 0.164	H: 0.195	J: 0.376	K: 1.113		
$D\,^1\Sigma^-$	$(3\pi_-) \to (4\pi_+)$	(45.9 %)	6.5461	A: 0.183	G: 0.184	H: 0.068	J: 0.666	K: 0.009		
	$(3\pi_+) \to (4\pi_-)$	(45.9 %)								
$E\,^1\Sigma^+$	$(9\sigma) \to (10\sigma)$	(31.0 %)	7.1413	A: 0.092	G: 0.070	H: 0.362	J: 0.174	K: 0.004		
	$(3\pi_+) \to (4\pi_+)$	(25.3 %)								
	$(3\pi_-) \to (4\pi_-)$	(25.3 %)								
$F\,^1\Delta_\pm$	$(9\sigma)^2 \to (4\pi_\pm)^2$	(90.6 %)	7.8580	A: 1.575	G: 0.069	H: 0.014	J: 0.133	K: 0.486		
$G\,^1\Pi_\pm$	$(3\pi_\mp) \to (10\sigma)$	(81.4 %)	8.4586	X: 0.431	B: 0.040	C: 0.164	D: 0.184	E: 0.070	F: 0.069	I: 0.116
$H\,^1\Pi_\pm$	$(8\sigma) \to (4\pi_\pm)$	(66.0 %)	8.6738	X: 1.102	B: 0.091	C: 0.195	D: 0.068	E: 0.362	F: 0.014	I: 0.101
$I\,^1\Sigma^+$	$(9\sigma)^2 \to (4\pi_+)(4\pi_-)$	(76.4 %)	8.9655	A: 1.359	G: 0.116	H: 0.101	J: 0.318	K: 0.007		
$X\,^2\Sigma^+$	$(9\sigma) \to$ ionized		9.1959							
$J\,^1\Pi_\pm$	$(3\pi_\pm)(9\sigma) \to (4\pi_\pm)^2$	(50.7 %)	9.6454	X: 0.182	B: 0.856	C: 0.376	D: 0.666	E: 0.174	F: 0.133	I: 0.318
	$(9\sigma)^2 \to (4\pi_\pm)(10\sigma)$	(25.9 %)								
$K\,^1\Pi_\pm$	$(3\pi_\mp)(9\sigma) \to (4\pi_+)(4\pi_-)$	(90.4 %)	9.7273	X: 0.007	B: 0.017	C: 1.113	D: 0.009	E: 0.004	F: 0.486	I: 0.007

Table 3.3: Quantum chemistry CASSCF(8,11)/CASPT2 results for the AlCl molecule at the experimental equilibrium bond length $R_{e,X} = 4.03\,a_0$ of the electronic ground state $|X\,^1\Sigma^+\rangle$, adapted from Ref. [145].

relativistic core correlated (ANO-RCC) $6s5p3d2f$ contracted basis set for Al and Cl was used; for BeO, 6 electrons and 12 orbitals were included in the active space and an ANO-RCC $5s4p2d1f$ contracted basis set for Be and O was used. Furthermore, scalar relativistic effects by means of the Douglas-Kroll transformation were also included [287].

Tables 3.3 and 3.4 list the dominant electronic configurations of electronic states, the excitation energies $\Delta E_i = E_i - E_0 = \hbar\omega_{i0}$, and the absolute values of all non-zero dipole transition matrix elements $|\mathbf{M}_{ij}|$ with zero z-component of $\mathbf{M}_{ij}$ for both the AlCl and BeO molecules. These results were computed at the equilibrium bond length of the electronic ground state $|X\,^1\Sigma^+\rangle$, i.e. $R_{e,X} = 4.03\,a_0$ for the AlCl molecule (experimental [145,277,280]) and $R_{e,X} = 2.54\,a_0$ for the BeO molecule (estimated [146]). The first excited states of AlCl and BeO are twofold degenerate states $|A\,^1\Pi_\pm\rangle$ carrying electronic ring currents but with different dominant electronic configurations $\ldots(3\pi)^4(9\sigma)(4\pi_\pm)$ (83.9 %) and $\ldots(1\pi_\pm)^2(1\pi_\mp)(5\sigma)$ (96.1 %) corresponding to the dominant HOMO-LUMO transitions $9\sigma \to 4\pi_\pm$ and $1\pi_\mp \to 5\sigma$, respectively. The $|A\,^1\Pi_\pm\rangle$ states of AlCl and BeO are energetically well separated from other electronic states. Furthermore, these states are bound states and have corresponding equilibrium bond lengths $R_{e,A} = 4.07\,a_0$ for the AlCl molecule [280] and $R_{e,A} = 2.78\,a_0$ for the BeO molecule [146] with corresponding small equilibrium displacements $\Delta R_e = R_{e,A} - R_{e,X} = 0.04\,a_0$ and $\Delta R_e = 0.24\,a_0$, respectively. Note that the potential curves of several electronic states for AlCl and BeO can be found in Refs. [280] and [146, 288], respectively. Because of small displacements

state (BeO)	dominant configuration (BeO)		ΔE_i (eV)	$\lvert\mathbf{M}_{ij}\rvert$ (ea_0)				
$X\,^1\Sigma^+$	$\ldots(4\sigma)^2(1\pi)^4$	(67.4 %)	0.0000	A: 0.686	E: 0.851	G: 0.717		
$A\,^1\Pi_\pm$	$(1\pi_\mp) \rightarrow (5\sigma)$	(96.1 %)	1.2367	X: 0.686	B: 0.371	C: 1.349	D: 0.948	F: 0.693
$B\,^1\Sigma^+$	$(4\sigma) \rightarrow (5\sigma)$	(80.2 %)	2.4852	A: 0.371	E: 1.154	G: 0.246		
$C\,^1\Delta_\pm$	$(1\pi_\mp) \rightarrow (2\pi_\pm)$	(95.7 %)	5.5636	A: 1.349	E: 0.074	G: 0.518		
$D\,^1\Sigma^-$	$(1\pi_-) \rightarrow (2\pi_+)$	(48.4 %)	5.5773	A: 0.948	E: 0.004	G: 0.400		
	$(1\pi_+) \rightarrow (2\pi_-)$	(48.4 %)						
$E\,^1\Pi_\pm$	$(4\sigma) \rightarrow (2\pi_\pm)$	(95.5 %)	6.7417	X: 0.851	B: 1.154	C: 0.074	D: 0.004	F: 0.275
$F\,^1\Sigma^+$	$(1\pi_+) \rightarrow (2\pi_+)$	(31.0 %)	7.5513	A: 0.693	E: 0.275	G: 0.145		
	$(1\pi_-) \rightarrow (2\pi_-)$	(31.0 %)						
$G\,^1\Pi_\pm$	$(1\pi_\mp) \rightarrow (6\sigma)$	(94.7 %)	7.7462	X: 0.717	B: 0.246	C: 0.518	D: 0.400	F: 0.145
$X\,^2\Pi_\pm$	$(1\pi_\mp) \rightarrow$ ionized		9.88					

Table 3.4: Quantum chemistry CASSCF(6,12)/CASPT2 results for the BeO molecule at the estimated equilibrium bond length $R_{e,X} = 2.54\,a_0$ of the electronic ground state $|X\,^1\Sigma^+\rangle$, adapted from Ref. [146].

ΔR_e and the short pulse duration of the applied circularly polarized laser pulse (a few fs) compared to the vibrational periods $\tau_{vib,A} = 69.3\,\text{fs}$ [145] and $\tau_{vib,A} = 29.2\,\text{fs}$ [146] in the electronic excited states $|A\,^1\Pi_\pm\rangle$ of AlCl and BeO, the nuclei can be considered as frozen during FC-type electronic excitations from the vibrational and electronic ground state $|X\,^1\Sigma^+(\nu = 0)\rangle$ to the vibrational and electronic excited states $|A\,^1\Pi_\pm(\nu' = 0)\rangle$ and $|A\,^1\Pi_\pm(\nu' = 0, \ldots, 5)\rangle$ of AlCl [145, 280] and BeO [146], respectively.

The stationary electronic excited states $|A\,^1\Pi_\pm\rangle$ of AlCl and BeO carry anti-clockwise $(+)$ and clockwise $(-)$ electronic ring currents about the molecular axis. As already shown in Section 3.2.6, the electronic ring currents of excited states $|A\,^1\Pi_\pm\rangle$ are dominated by those of $4\pi_\pm$ and $1\pi_\pm$ molecular orbitals of AlCl and BeO with corresponding weights of at least 93 % and 96 %, respectively. Furthermore, the molecular orbital $4\pi_\pm$ of the AlCl molecule has the LCAO-MO expansion $4\pi_\pm \approx c_{3p_\pm(\text{Al})} 3p_\pm(\text{Al}) + c_{3p_\pm(\text{Cl})} 3p_\pm(\text{Cl})$ with dominant weights for the coefficients $|c_{3p_\pm(\text{Al})}|^2 \approx 0.9$ and $|c_{3p_\pm(\text{Cl})}|^2 \approx 0.1$ [145], and the molecular orbital $1\pi_\pm$ of the BeO molecule has the LCAO-MO expansion $1\pi_\pm \approx c_{2p_\pm(\text{O})} 2p_\pm(\text{O}) + c_{2p_\pm(\text{Be})} 2p_\pm(\text{Be})$ with dominant weights for the coefficients $|c_{2p_\pm(\text{O})}|^2 \approx 0.96$ and $|c_{2p_\pm(\text{Be})}|^2 \approx 0.03$ [146]. Hence, the electronic ring currents of excited states $|A\,^1\Pi_\pm\rangle$ of AlCl and BeO are dominated by those of $3p_\pm(\text{Al})$ and $2p_\pm(\text{O})$ atomic orbitals about Al and O nuclei, respectively. The corresponding toroidal electronic current densities in cylindrical coordinates are

$$\mathbf{j}_{A\,^1\Pi_\pm}(\rho, z) \approx \mathbf{j}_{4\pi_\pm}(\rho, z) = \pm \frac{\hbar}{m_e} \frac{|\varphi_{4\pi_\pm}|^2}{\rho} \mathbf{e}_\phi \tag{3.111}$$

for AlCl and

$$\mathbf{j}_{A\,^1\Pi_\pm}(\rho, z) \approx \mathbf{j}_{1\pi_\pm}(\rho, z) = \pm \frac{\hbar}{m_e} \frac{|\varphi_{1\pi_\pm}|^2}{\rho} \mathbf{e}_\phi \tag{3.112}$$

for BeO, cf. Eq. (2.38). Figs. 3.12 and 3.13 show the electronic probability densities

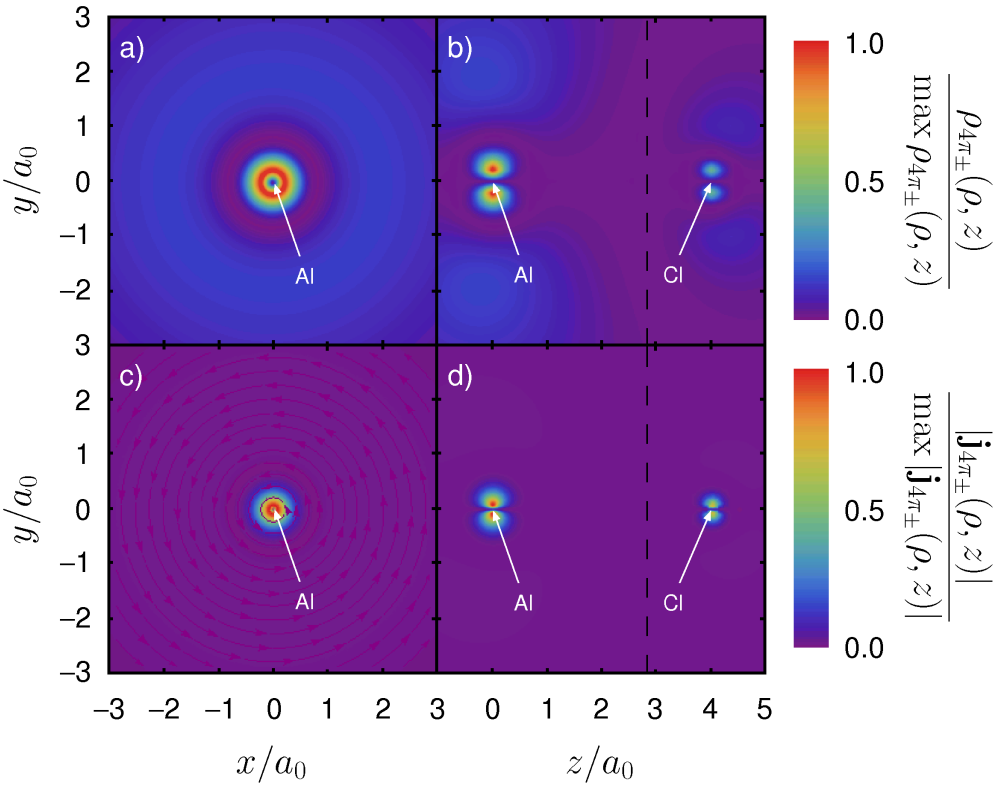

Figure 3.12: Electronic probability $\rho_{4\pi_\pm}(\rho, z)$ (panels a, b) and current densities $\mathbf{j}_{4\pi_\pm}(\rho, z)$ (Eq. (3.111)) (panels c, d) in the x/y ($z = 0$) (panels a, c) and y/z ($x = 0$) (panels b, d) planes, for $4\pi_\pm$ molecular orbitals of the AlCl molecule. The Al and Cl nuclei are located at $\mathbf{r}_{\mathrm{Al}} = (0, 0, 0)$ and $\mathbf{r}_{\mathrm{Cl}} = (0, 0, R_{e,X})$ where $R_{e,X} = 4.03\, a_0$, respectively. Note that panel c shows the direction of the electronic current density only for the $4\pi_+$ orbital; the corresponding direction for the $4\pi_-$ orbital would be opposite. In panel d, the electron of the $4\pi_+$ orbital at $y > 0$ and $y < 0$ moves toward and away from the reader, respectively, and backwards for the $4\pi_-$ orbital. The electronic ring currents about the Al and Cl nuclei are separated by the surface $\mathbf{r} = (x, y, 2.84\, a_0)$ shown as the vertical dashed line in panel d.

$\rho_{4\pi_\pm}(\rho, z) = |\varphi_{4\pi_\pm}|^2$ and $\rho_{1\pi_\pm}(\rho, z) = |\varphi_{1\pi_\pm}|^2$ of $4\pi_\pm$ and $1\pi_\pm$ molecular orbitals, and the corresponding electronic current densities $\mathbf{j}_{4\pi_\pm}(\rho, z)$ and $\mathbf{j}_{1\pi_\pm}(\rho, z)$ of AlCl and BeO, respectively. Since the maximum electronic current density of the $1\pi_\pm$ molecular orbital of the BeO molecule is approximately four times larger than that of the $4\pi_\pm$ molecular orbital of the AlCl molecule, i.e. $\max |\mathbf{j}_{1\pi_\pm}(\rho, z)| \approx 4 \max |\mathbf{j}_{4\pi_\pm}(\rho, z)|$, the current density of the $1\pi_\pm$ molecular orbital of BeO in the excited state $|A\,{}^1\Pi_\pm\rangle$ is much stronger. Since $1\pi_\pm \approx 2p_\pm(\mathrm{O})$, the corresponding current density is strongly localized at the O nucleus with large effective nuclear charge $Z_{eff} = 4.55$ (see Section 3.2.6) and is very similar to that of the atomic orbital $2p_\pm$ shown in Fig. 3.1. Since $2p_\pm$ atomic orbitals give rise to stronger effects than $3p_\pm$ orbitals, see Sections 3.2.1 and 3.2.2, the corresponding electric ring currents and induced magnetic fields of $1\pi_\pm \approx 2p_\pm(\mathrm{O})$ orbitals of BeO are stronger

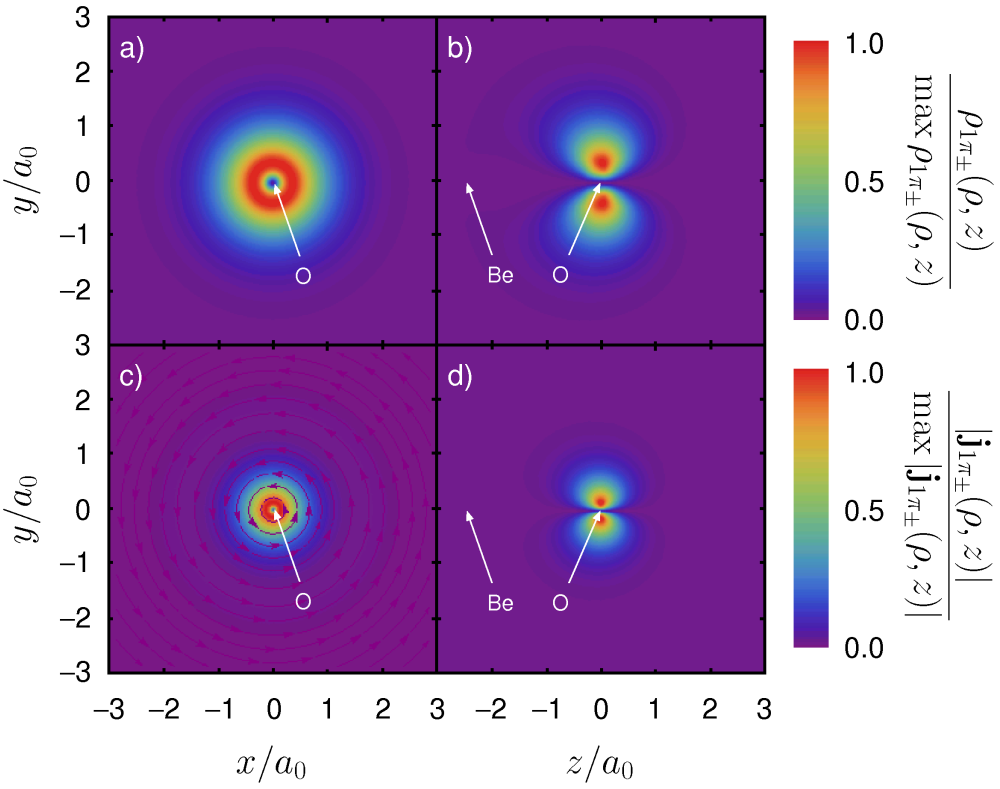

Figure 3.13: Electronic probability $\rho_{1\pi_\pm}(\rho, z)$ (panels a, b) and current densities $\mathbf{j}_{1\pi_\pm}(\rho, z)$ (Eq. (3.112)) (panels c, d) in the x/y ($z = 0$) (panels a, c) and y/z ($x = 0$) (panels b, d) planes, for $1\pi_\pm$ molecular orbitals of the BeO molecule, cf. Fig. 3.1. The Be and O nuclei are located at $\mathbf{r}_{\mathrm{Be}} = (0, 0, -R_{e,X})$ and $\mathbf{r}_{\mathrm{O}} = (0, 0, 0)$ where $R_{e,X} = 2.54\, a_0$, respectively. Note that panel c shows the direction of the electronic current density only for the $1\pi_+$ orbital; the corresponding direction for the $1\pi_-$ orbital would be opposite. In panel d, the electron of the $1\pi_+$ orbital at $y > 0$ and $y < 0$ moves toward and away from the reader, respectively, and backwards for the $1\pi_-$ orbital.

than those of $4\pi_\pm \approx 3p_\pm(\mathrm{Al})$ orbitals of AlCl. The corresponding total electric ring currents (Eq. (2.55)) of electronic states $|A\,^1\Pi_\pm\rangle$ of AlCl and BeO are estimated as

$$I_{A\,^1\Pi_\pm} \approx I_{4\pi_\pm} = \mp 0.405\,\mathrm{mA} \tag{3.113}$$

and

$$I_{A\,^1\Pi_\pm} \approx I_{1\pi_\pm} = \mp 2.490\,\mathrm{mA}, \tag{3.114}$$

respectively. Furthermore, the electric ring current of the $4\pi_\pm$ molecular orbital of the AlCl molecule can be divided approximately into two separate electric ring currents about the Al and Cl nuclei, see Fig. 3.12. Using the separation surface $\mathbf{r} = (x, y, 2.84\, a_0)$, the electric ring currents about Al and Cl nuclei are $I_{\mathrm{Al}} = \mp 0.313\,\mathrm{mA}$ and $I_{\mathrm{Cl}} = \mp 0.092\,\mathrm{mA}$, respectively. These electric ring currents are in accord with the approximate values given

in Section 3.2.6 based on the theory of electronic ring currents of atomic orbitals. The corresponding mean periods of an electron circulating about the z-axis (Eq. (2.60)) are

$$T_{A\,^1\Pi_\pm} \approx T_{4\pi_\pm} = 396\,\text{as} \tag{3.115}$$

for AlCl and

$$T_{A\,^1\Pi_\pm} \approx T_{1\pi_\pm} = 64.4\,\text{as} \tag{3.116}$$

for BeO which are, of course, much shorter than the lifetimes of eletronic ring currents of excited states $|A\,^1\Pi_\pm\rangle$, which are limited by the radiative decay of excited states, i.e. $\tau_{rad,A\,^1\Pi_\pm} = 5.5\,\text{ns}$ for AlCl [145] and $\tau_{rad,A\,^1\Pi_\pm} = 1.1\,\mu\text{s}$ for BeO [146].

The toroidal electronic ring currents of excited states $|A\,^1\Pi_\pm\rangle$, circulating about the molecular z-axis, induce magnetic fields $\mathbf{B}_{A\,^1\Pi_\pm}(\mathbf{r}) \approx \mathbf{B}_{4\pi_\pm}(\mathbf{r})$ for the AlCl molecule and $\mathbf{B}_{A\,^1\Pi_\pm}(\mathbf{r}) \approx \mathbf{B}_{1\pi_\pm}(\mathbf{r})$ for the BeO molecule, cf. Eq. (2.78). These induced magnetic fields are illustrated in Fig. 3.14. For the AlCl molecule, the induced magnetic field achieves peak values at both the Al and Cl nuclei, i.e.

$$|\mathbf{B}_{A\,^1\Pi_\pm}(\mathbf{r} = \mathbf{r}_{\text{Al}})| \approx |\mathbf{B}_{4\pi_\pm}(\mathbf{r} = \mathbf{r}_{\text{Al}})| = 7.7\,\text{T} \tag{3.117}$$

$$|\mathbf{B}_{A\,^1\Pi_\pm}(\mathbf{r} = \mathbf{r}_{\text{Cl}})| \approx |\mathbf{B}_{4\pi_\pm}(\mathbf{r} = \mathbf{r}_{\text{Cl}})| = 4.1\,\text{T}, \tag{3.118}$$

respectively. For the BeO molecule, the induced magnetic field has only one large peak at the O nucleus because $1\pi_\pm \approx 2p_\pm(\text{O})$. The induced magnetic fields at Be and O nuclei are

$$|\mathbf{B}_{A\,^1\Pi_\pm}(\mathbf{r} = \mathbf{r}_{\text{Be}})| \approx |\mathbf{B}_{1\pi_\pm}(\mathbf{r} = \mathbf{r}_{\text{Be}})| = 1.2\,\text{T} \tag{3.119}$$

$$|\mathbf{B}_{A\,^1\Pi_\pm}(\mathbf{r} = \mathbf{r}_{\text{O}})| \approx |\mathbf{B}_{1\pi_\pm}(\mathbf{r} = \mathbf{r}_{\text{O}})| = 52.1\,\text{T}, \tag{3.120}$$

respectively. These values of the magnetic fields are again in accord with the approximate values estimated in Section 3.2.6.

The mean ring current radii (Eq. (2.96)) of the electronic ring currents of excited states $|A\,^1\Pi_\pm\rangle$ of AlCl and BeO molecules are estimated as

$$R_{-1,A\,^1\Pi_\pm} \approx R_{-1,4\pi_\pm} = 0.18\,a_0 \tag{3.121}$$

and

$$R_{-1,A\,^1\Pi_\pm} \approx R_{-1,1\pi_\pm} = 0.25\,a_0, \tag{3.122}$$

respectively.

In the following application, see also Section 2.3, we assume that the AlCl and BeO molecules in the electronic ground state $|X\,^1\Sigma^+\rangle$ are perfectly oriented along the

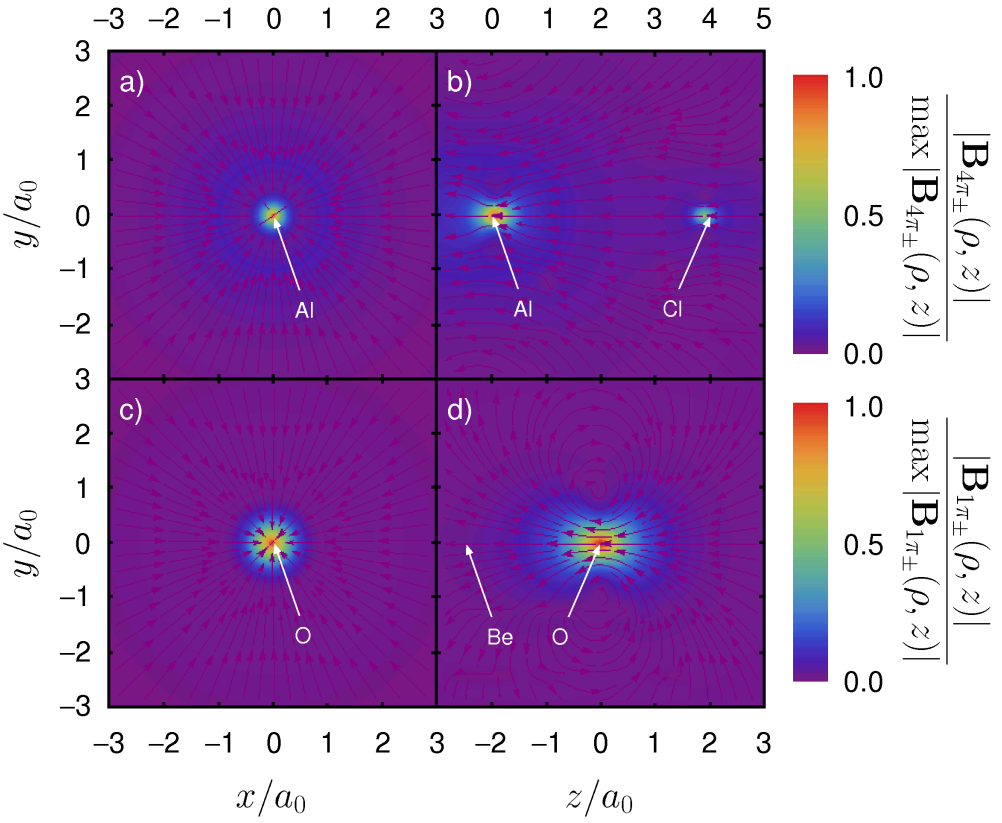

Figure 3.14: Induced magnetic fields $\mathbf{B}_{4\pi_\pm}(\rho,z)$ (panels a, b) and $\mathbf{B}_{1\pi_\pm}(\rho,z)$ (panels c, d) (Eq. (2.78)) in the x/y ($z=0$) (panels a, c) and y/z ($x=0$) (panels b, d) planes, for $4\pi_\pm$ and $1\pi_\pm$ molecular orbitals of AlCl and BeO, respectively. The arrows are drawn only for $4\pi_+$ and $1\pi_+$ molecular orbitals. The locations of the nuclei are the same as in Figs. 3.12 and 3.13. In panels a and c, the induced magnetic fields in the center regions are directed away from the reader (large negative z-component of the magnetic field) where the arrows drawn in these panels are only for very small ρ-components of the magnetic fields. The maxima of the induced magnetic fields $\max|\mathbf{B}_{4\pi_\pm}(\rho,z)| = |\mathbf{B}_{4\pi_\pm}(\mathbf{r}=\mathbf{r}_{\mathrm{Al}})| = 7.70\,\mathrm{T}$ and $\max|\mathbf{B}_{1\pi_\pm}(\rho,z)| = |\mathbf{B}_{1\pi_\pm}(\mathbf{r}=\mathbf{r}_{\mathrm{O}})| = 52.1\,\mathrm{T}$ are located at the Al and O nuclei, respectively.

laboratory-fixed z-axis, a condition that can be approximately achieved using the method described in Section 3.3.1. We showed that almost perfect orientation $|\langle\cos\theta\rangle_T| \geq 0.8$ is achieved at the revival times $t = (2.12+n)\tau_{rev,X}$ ($n = 0, 1, 2, \ldots$), for about $\Delta\tau_X = 0.17\,\mathrm{ps}$. Thus, this orientation time is much larger than the total pulse duration of the subsequent circularly polarized laser pulse, $t_{p,c} = 21.2\,\mathrm{fs}$. The circularly polarized laser pulse (Eq. (2.99)) is centered at a selected revival time, for example $t_c = t^* = 2.12\,\tau_{rev,X}$, i.e. $t_c = 145.18\,\mathrm{ps}$ for AlCl and $t_c = 21.88\,\mathrm{ps}$ for BeO.

For the given total pulse duration $t_{p,c} = 21.2\,\mathrm{fs}$, the laser parametes of the right (or left) circularly polarized reoptimized π laser pulse (Eq. (2.99)) with $\cos^{20}$ envelope (Eq. (2.100)) are determined in order to achieve an almost complete population transfer from

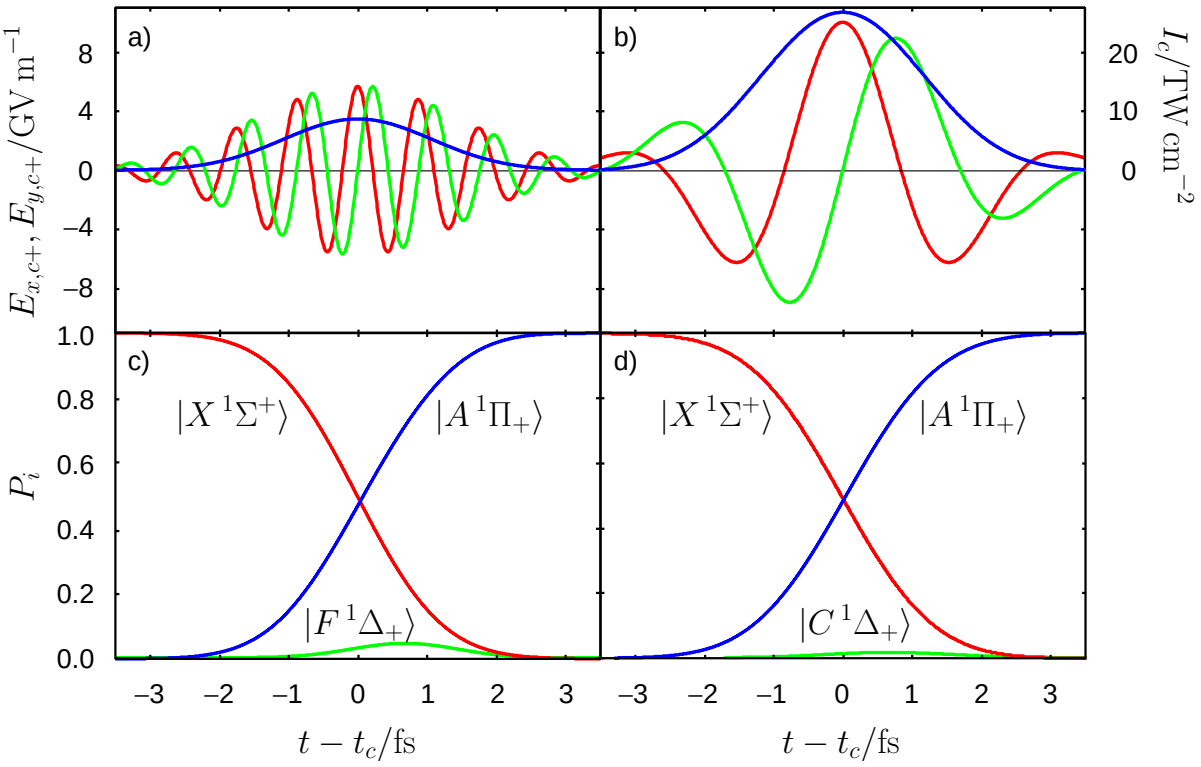

Figure 3.15: Complete population transfer $|X\,^1\Sigma^+\rangle \rightarrow |A\,^1\Pi_+\rangle$ of AlCl (left panels) and BeO (right panels) by means of a right circularly reoptimized π laser pulse centered at $t_c = 2.12\,\tau_{rev,X}$. Panels a and b show the x- (red) and y- (green) components of the time-dependent electric field $\mathbf{E}_{c+}(t)$ (Eq. (2.99)) and the corresponding time-dependent intensity $I_c(t)$ (Eq. (2.114)) (blue). In panels c and d, the time-dependent populations $P_i(t)$ (Eq. (2.130)) of dominant electronic states $|X\,^1\Sigma^+\rangle$ (red) and $|A\,^1\Pi_+\rangle$ (blue) are drawn; minor contributions of electronic states $|F\,^1\Delta_+\rangle$ (green) of the AlCl molecule and $|C\,^1\Delta_+\rangle$ (green) of the BeO molecule are also observed.

the electronic ground state $|X\,^1\Sigma^+\rangle$ to the excited state $|A\,^1\Pi_+\rangle$ (or $|A\,^1\Pi_-\rangle$) of AlCl and BeO at the equilibrium bond length $R_{e,X}$. For the AlCl molecule, the optimized laser parameters are the field amplitude $\mathcal{E}_c = 5.72\,\mathrm{GV\,m^{-1}}$ and the laser frequency $\hbar\omega_c = 4.65\,\mathrm{eV}$, with the corresponding maximum intensity $I_{max,c} = 8.68\,\mathrm{TW\,cm^{-2}}$, the effective pulse duration $\tau_c = 2.5\,\mathrm{fs}$, and the optical cycle period $\Delta t_c = 2\pi/\omega_c = 889\,\mathrm{as}$. For the BeO molecule, the corresponding laser parameters are $\mathcal{E}_c = 10.05\,\mathrm{GV\,m^{-1}}$, $\hbar\omega_c = 1.04\,\mathrm{eV}$, $I_{max,c} = 26.8\,\mathrm{TW\,cm^{-2}}$, $\tau_c = 2.74\,\mathrm{fs}$, and $\Delta t_c = 3.98\,\mathrm{fs}$, see Refs. [145, 146]. Fig. 3.15 shows the x- and y-components of the time-dependent right circularly polarized electric field $\mathbf{E}_{c+}(t) = E_{x,c+}(t)\mathbf{e}_x + E_{y,c+}(t)\mathbf{e}_y$ (Eq. (2.99)) centered at $t_c = 2.12\,\tau_{rev,X}$ and the associated time-dependent intensity $I_c(t)$ (Eq. (2.114)) for AlCl and BeO.

The corresponding resulting population dynamics are also shown in Fig. 3.15, see Refs. [145, 146], which are very similar to the population dynamics in the three-state

model, see Fig. 2.5. This figure clearly shows that a right circularly polarized reoptimized π laser pulse for AlCl and BeO induces an almost complete population transfer from the electronic ground state $|X\,^1\Sigma^+\rangle$ to the target excited state $|A\,^1\Pi_+\rangle$ carrying an electronic ring current shown in Figs. 3.12 and 3.13. The population of the degenerate state $|A\,^1\Pi_+\rangle$ at the final time $t_f = t_c + t_{p,c}/2$ reaches the value 1, i.e. $P_A(t_f) = 1 - 3 \cdot 10^{-4}$ for AlCl and $P_A(t_f) = 1 - 6 \cdot 10^{-7}$ for BeO. There are also small fractions of high-lying excited states $|F\,\Delta_+\rangle$ and $|C\,\Delta_+\rangle$ of AlCl and BeO molecules, due to strong two-photon dipole-allowed transitions $|X\,^1\Sigma^+\rangle \rightarrow |A\,^1\Pi_+\rangle \rightarrow |F\,^1\Delta_+\rangle$ and $|X\,^1\Sigma^+\rangle \rightarrow |A\,^1\Pi_+\rangle \rightarrow |C\,^1\Delta_+\rangle$, respectively, but the populations of these states after the end of the laser pulses are negligible. Note that all other states listed in Tab. 3.3 and 3.4 are also included in the calculation and these states have negligible populations during the electronic excitation.

3.3.3 Electron circulation

A right circularly polarized reoptimized $\pi/2$ laser pulse (Eq. (2.99)) with $\cos^{20}$ envelope (Eq. (2.100)) is applied in order to achieve a half population transfer from the electronic ground state $|X\,^1\Sigma^+\rangle$ to the excited state $|A\,^1\Pi_+\rangle$ of AlCl or BeO molecules. Starting from the reference values for reoptimized π laser pulses shown in Fig. 3.15, three possible laser parameters can be adjusted to achieve half population transfer. As already predicted in Section 2.3.3, cf. Eqs. (2.171) and (2.175), the amplitude of the electric field $\mathcal{E}_c$ or the total pulse duration $t_{p,c}$ of the laser pulse can be reduced by the factor $\frac{1}{2}$. Another possibility is the modification of the laser frequency ω_c which also leads to the reduction of the population of the excited state $|A\,^1\Pi_+\rangle$ from 1 to 0.5, see Ref. [149]. In this Section, the amplitude of the electric field $\mathcal{E}_c$ is reduced by the factor $\frac{1}{2}$. Then, the amplitude $\mathcal{E}_c$ and the laser frequency ω_c are reoptimized in order to achieve an almost exact half popoulation transfer from $|X\,^1\Sigma^+\rangle$ to $|A\,^1\Pi_+\rangle$ states where the total pulse duration $t_{p,c} = 21.2\,\mathrm{fs}$, which is already sufficiently short compared to vibrational periods and orientation durations of AlCl and BeO, remains unchanged. For AlCl, the reoptimized amplitude of the electric field is $\mathcal{E}_c = 2.84\,\mathrm{GV\,m^{-1}}$ and the laser frequency $\hbar\omega_c = 4.65\,\mathrm{eV}$ is the same as for the reoptimized π laser pulse, hence $\Delta t_c = 889\,\mathrm{as}$ and $\tau_c = 2.5\,\mathrm{fs}$. The corresponding maximum intensity $I_{max,c} = 2.14\,\mathrm{TW\,cm^{-2}}$ is about four times smaller than the maximum intensity of the reoptimized π laser pulse. For BeO, the field amplitude is $\mathcal{E}_c = 5.01\,\mathrm{GV\,m^{-1}}$ and the laser frequency is modified slightly from $\hbar\omega_c = 1.04\,\mathrm{eV}$ to $1.06\,\mathrm{eV}$, corresponding to $\Delta t_c = 3.90\,\mathrm{fs}$ and $\tau_c = 2.73\,\mathrm{fs}$. The corresponding maximum intensity is $I_{max,c} = 6.66\,\mathrm{TW\,cm^{-2}}$. Fig. 3.16 shows the x- and y-components of the right circularly polarized electric field $\mathbf{E}_{c+}(t) = E_{x,c+}(t)\mathbf{e}_x + E_{y,c+}(t)\mathbf{e}_y$ (Eq. (2.99)) centered at $t_c = 2.12\,\tau_{rev,X}$ and the corresponding time-dependent intensity $I_c(t)$ (Eq. (2.114)).

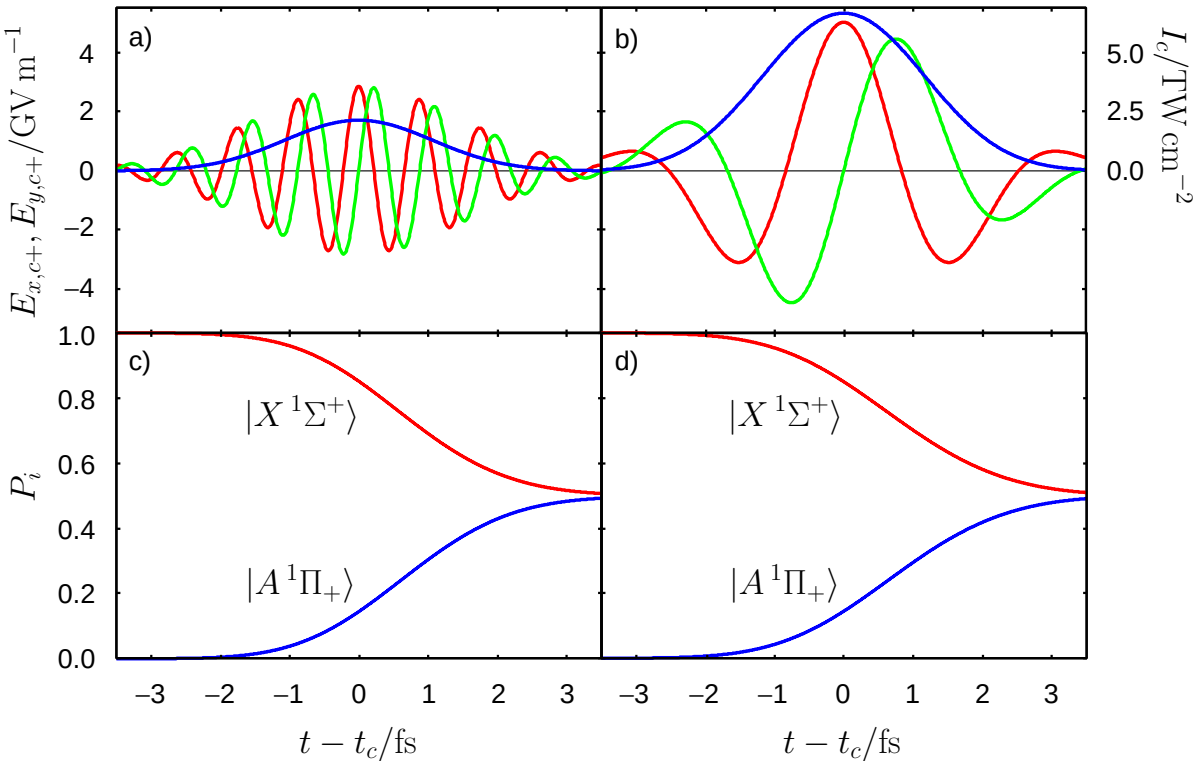

Figure 3.16: Half population transfer $|X\,^1\Sigma^+\rangle \rightarrow |A\,^1\Pi_+\rangle$ of AlCl (left panels) and BeO (right panels) molecules by means of a right circularly polarized reoptimized $\pi/2$ laser pulse centered at $t_c = 2.12\,\tau_{rev,X}$. For further details, see Fig. 3.15. Note that the populations of excited states $|F\,^1\Delta_+\rangle$ and $|C\,^1\Delta_+\rangle$ of AlCl and BeO molecules are much smaller than the corresponding populations for the right circularly polarized reoptimized π laser pulses shown in Fig. 3.15 because of small intensities of the reoptimized $\pi/2$ laser pulses shown as blue curves in panels a and b, respectively.

The resulting population dynamics of electronic states $|X\,^1\Sigma^+\rangle$ and $|A\,^1\Pi_+\rangle$ of AlCl and BeO molecules shown in Fig. 3.16 are very similar to the population dynamics in the three-state model, see Fig. 2.5. In particluar, there are negligible populations of other electronic states including $|F\,^1\Delta_+\rangle$ and $|C\,^1\Delta_+\rangle$ states of AlCl and BeO, respectively, compare Figs. 3.15 and 3.16, because the intensities of the reoptimized $\pi/2$ laser pulses are reduced by the factor $\frac{1}{4}$. The populations of the states $|X\,^1\Sigma^+\rangle$ and $|A\,^1\Pi_+\rangle$ at the final time $t_f = t_c + t_{p,c}/2$ are $P_X(t_f) = 0.5 + 3 \cdot 10^{-4}$ and $P_A(t_f) = 0.5 - 4 \cdot 10^{-4}$ for AlCl and $P_X(t_f) = 0.5 + 9 \cdot 10^{-5}$ and $P_A(t_f) = 0.5 - 9 \cdot 10^{-5}$ for BeO, respectively. Hence, a right circularly polarized reoptimized $\pi/2$ laser pulse shown in Fig. 3.16 induces an almost exact half population transfer from the electronic ground state $|X\,^1\Sigma^+\rangle$ to the excited state $|A\,^1\Pi_+\rangle$ of AlCl and BeO molecules.

After the end of the reoptimized $\pi/2$ laser pulse, the electronic state is the superposition of electronic ground $|X\,^1\Sigma^+\rangle$ and excited $|A\,^1\Pi_+\rangle$ states of AlCl or BeO. The

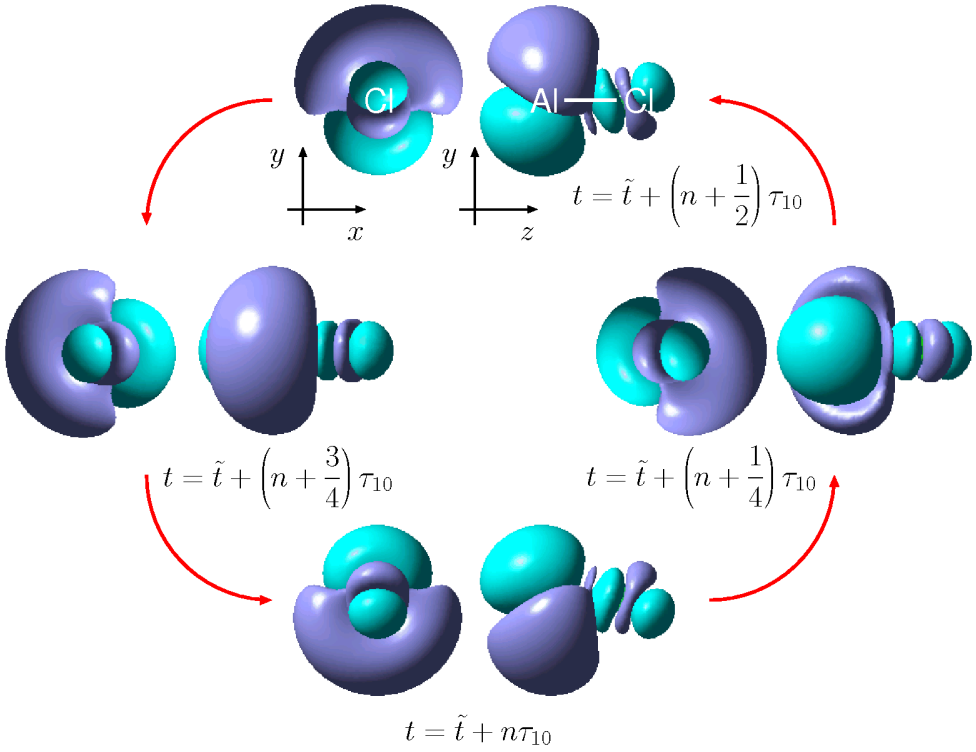

Figure 3.17: Electron circulation in the superposition of $|X\,^1\Sigma^+\rangle$ and $|A\,^1\Pi_+\rangle$ states of the AlCl molecule after a right circularly polarized reoptimized $\pi/2$ laser pulse, see Fig. 3.16. This hybrid state has the dominant contribution of the hybrid orbital, $9\sigma + 4\pi_+$, corresponding to the HOMO-LUMO transition $9\sigma \rightarrow 4\pi_+$. The snapshots are illustrated as the difference of the electronic density $\Delta\rho(\mathbf{r},t) = \rho(\mathbf{r},t) - \rho(\mathbf{r},t_0)$ (Eqs. (2.191) and (2.195)) at times $t = \tilde{t} + (n+k)\tau_{10}$ ($n = 0, 1, 2, \ldots$, $k = 0, 1/4, 1/2, 3/4$). Here, $\tilde{t}$ is the time after the end of the laser pulse at which the difference of the electron density is the same as shown in the bottom panel ($t = \tilde{t} + n\tau_{10}$), and $\tau_{10} = 2\pi/\omega_{10} = 892\,\text{as}$ is the period of the time-dependent electronic density $\rho(\mathbf{r},t)$ circulating about the molecular z-axis. The blue and cyan regions show positive and negative differences $\Delta\rho(\mathbf{r},t)$, respectively.

corresponding electronic probability and current densities are time-dependent and circulate about the molecular z-axis. Since the electronic ground state $|X\,^1\Sigma^+\rangle$ of BeO is dominated by the corresponding HF wave function with weight of only 67.4 %, see Table 3.4, we consider the electron circulation only for the AlCl molecule. We calculate the difference of the electronic probability density $\Delta\rho(\mathbf{r},t) = \rho(\mathbf{r},t) - \rho(\mathbf{r},t_0)$ (Eqs. (2.191) and (2.195)) after the end of the laser pulse ($t > t_f$), using the CIS approximation (see Section 2.3.4) with the dominant HOMO-LUMO transition $9\sigma \rightarrow 4\pi_+$. The corresponding snapshots are illustrated in Fig. 3.17. The electronic probability density, i.e. the electron wavepacket, circulates about the z-axis with period $\tau_{10} = 2\pi/\omega_{10} = 892\,\text{as}$, where ω_{10} is the excitation frequency of the electronic state $|A\,^1\Pi_+\rangle$. The corresponding period for the BeO molecule is $\tau_{10} = 3.34\,\text{fs}$. Note that this period τ_{10} of the time-dependent electronic

probability density about the z-axis should not be confused with the period T (Eq. (2.60)) of an electron about the z-axis. These times are, in general, different. For example, the electronic density in the stationary degenerate state is time-independent and the corresponding period is thus not defined whereas the period of an electron about the z-axis is non-zero for non-zero stationary electronic ring currents. These different times can also be understood in classical mechanics. For example, the velocity of water particles (molecules) in the ocean and the velocity of water waves are, in general, different. A further analogous example is the steady flow of water in the tube where the density of water is time-independent (the corresponding period is not defined) but the stationary velocity of water particles (molecules) is non-zero.

3.4 Ring-shaped molecule Mg-porphyrin

3.4.1 Electronic ring currents in excited $|2\,^1E_{u\pm}\rangle$ and $|4\,^1E_{u\pm}\rangle$ states

Now, let us consider the ring-shaped molecule magnesium-porphyrin, shown in Fig. 3.18 [147–150]. Mg-porphyrin is an important biomolecule, for example a core molecule of chlorophyll. The molecule's optimized geometry in the electronic ground state $|X\,^1A_{1g}\rangle$ is planar and has D_{4h} symmetry. Although the molecule is not axial-symmetric, there are twofold degenerate electronic states $|E_{\pm}\rangle$ carrying opposite electronic ring currents. The quantum chemistry results of electronic states $|X\,^1A_{1g}\rangle$, $|n\,^1E_{u\pm}\rangle$ $(n = 1-4)$ and $|n\,^1E_{u\pm}\rangle$ $(n = 5, 6)$ that are used in this work are adapted from CASSCF(14,16)/CASPT2 and TDDFT calculations by Rubio et al. [289] and by Sundholm [290], respectively. However, the optimized geometry and orbitals are calculated at HF level with the 6-31G(d) basis set, using the GAUSSIAN03 program package. These HF orbitals are primarily used for calculating electronic current densities of degenerate molecular orbitals, corresponding electric ring currents and induced magnetic fields in Mg-porphyrin. Other quantum chemical SAC/SAC-CI and TDDFT results for Mg-porphyrin can also be found in Refs. [291] and [292], respectively.

Table 3.5 lists the dominant electronic configurations of electronic ground $|X\,^1A_{1g}\rangle$ and excited $|n\,^1E_{u\pm}\rangle$ $(n = 1-6)$ states at the equilibrium geometry of Mg-porphyrin, the corresponding excitation energies $\Delta E_i = E_i - E_0 = \hbar\omega_{i0}$, and the absolute values of dipole transition matrix elements $|\mathbf{M}_{ij}|$ between $|X\,^1A_{1g}\rangle$ and $|n\,^1E_{u\pm}\rangle$ states, adapted from Refs. [289, 290]. Note that there are other non-degenerate excited $|A\rangle$ and $|B\rangle$ states but we use the approximation that these states and corresponding additional electronic transitions

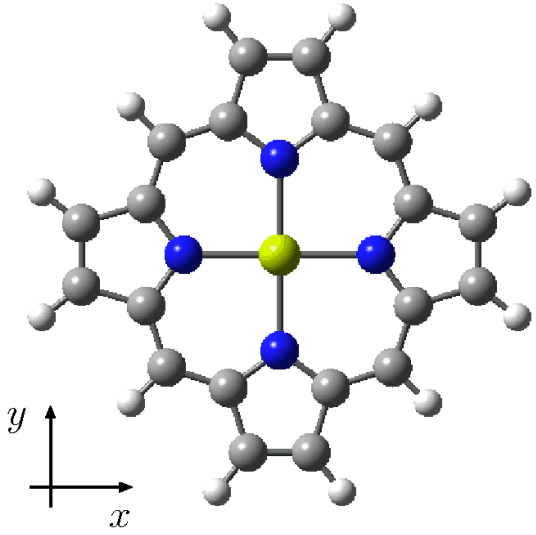

Figure 3.18: Molecular structure of Mg-porphyrin at the optimized geometry of the electronic ground state $|X\,^1A_{1g}\rangle$. The planar molecule has D_{4h} symmetry and consists of four pyrrole fragments connected to four carbon bridges and to one central atom. The axis of symmetry is the z-axis. The molecule has 37 atoms including one magnesium atom (yellow), four nitrogen atoms (blue), twenty carbon atoms (gray), and twelve hydrogen atoms (white).

are not included in the quantum dynamics calculations since the non-degenerate excited states cannot be excited by circularly polarized laser pulses directly from the electronic ground state $|X\,^1A_{1g}\rangle$. The energy of the ionized state $|X\,^2A_{1u}\rangle$ of Mg-porphyrin is $E_0 + 6.91\,\mathrm{eV}$ [293]. Furthermore, we assume that the nuclei are frozen during FC-type electronic excitations from the electronic ground $|X\,^1A_{1g}\rangle$ to excited $|n\,^1E_{u\pm}\rangle$ states of Mg-porpyhrin due to the sufficiently short pulse duration of the applied circularly polarized laser pulse.

In this work, the electronic ring currents of excited states $|2\,^1E_{u\pm}\rangle$, $|4\,^1E_{u\pm}\rangle$ and $|5\,^1E_{u\pm}\rangle$ about the axis of symmetry (z-axis) are investigated in this Section and Section 3.4.2. The degenerate electronic state $|2\,^1E_{u\pm}\rangle$ has dominant electronic configurations $\ldots(4a_{2u})^2(1a_{1u})(4e_{g\pm})$ (35 %), $\ldots(4a_{2u})(1a_{1u})^2(4e_{g\pm})$ (27 %), and $\ldots(3a_{2u})(3e_g)^4(2b_{2u})^2(4a_{2u})^2(1a_{1u})^2(4e_{g\pm})$ (6 %) corresponding to dominant transitions $1a_{1u} \rightarrow 4e_{g\pm}$, $4a_{2u} \rightarrow 4e_{g\pm}$, and $3a_{2u} \rightarrow 4e_{g\pm}$, respectively, whereas the state $|4\,^1E_{u\pm}\rangle$ has the dominant electronic configuration $\ldots(3a_{2u})(3e_g)^4(2b_{2u})^2(4a_{2u})^2(1a_{1u})^2(4e_{g\pm})$ (57 %) corresponding to the dominant transition $3a_{2u} \rightarrow 4e_{g\pm}$. Although the electronic structures of excited states $|2\,^1E_{u\pm}\rangle$ and $|4\,^1E_{u\pm}\rangle$ are different, the electronic ring currents of these states are very similar due to the similar dominant contribution of the electronic ring current of the molecular orbital $4e_{g\pm}$ with corresponding weights of at least 68 % and 57 %, respectively. Note that the TDDFT results by Sundholm [290] predict that

state (MgP)	dominant configuration (MgP)		ΔE_i (eV)	$\lvert\mathbf{M}_{ij}\rvert$ (ea_0)
$X\,^1A_{1g}$	$\ldots(4a_{2u})^2(1a_{1u})^2$	(80 %)	0.00	
$1\,^1E_{u\pm}$	$(4a_{2u}) \rightarrow (4e_{g\pm})$	(39 %)	1.66	X: 0.31
	$(1a_{1u}) \rightarrow (4e_{g\pm})$	(36 %)		
$2\,^1E_{u\pm}$	$(1a_{1u}) \rightarrow (4e_{g\pm})$	(35 %)	2.66	X: 3.55
	$(4a_{2u}) \rightarrow (4e_{g\pm})$	(27 %)		
	$(3a_{2u}) \rightarrow (4e_{g\pm})$	(6 %)		
$3\,^1E_{u\pm}$	$(2b_{2u}) \rightarrow (4e_{g\mp})$	(61 %)	3.11	X: 1.40
$4\,^1E_{u\pm}$	$(3a_{2u}) \rightarrow (4e_{g\pm})$	(57 %)	3.42	X: 2.60
$5\,^1E_{u\pm}$	$(3e_{g\pm}) \rightarrow (2b_{1u})$	(94 %)	4.56	X: 1.00
$6\,^1E_{u\pm}$	$(1b_{1u}) \rightarrow (4e_{g\mp})$	(73 %)	5.12	X: 0.24
	$(2e_{g\pm}) \rightarrow (2b_{1u})$	(23 %)		

Table 3.5: Quantum chemistry CASSCF(14,16)/CASPT2 and TDDFT results for electronic states $|X\,^1A_{1g}\rangle$, $|n\,^1E_{u\pm}\rangle$ ($n = 1-4$) and $|n\,^1E_{u\pm}\rangle$ ($n = 5, 6$) of Mg-porphyrin (MgP) at the optimized geometry of the electronic ground state $|X\,^1A_{1g}\rangle$, adapted from Refs. [289] and [290], respectively.

the corresponding minimum weights of the electronic ring current of the molecular orbital $4e_{g\pm}$ for excited states $|2\,^1E_{u\pm}\rangle$ and $|4\,^1E_{u\pm}\rangle$ are 85 % and 96 %, respectively. Thus, the electronic current densities of electronic states $|2\,^1E_{u\pm}\rangle$ and $|4\,^1E_{u\pm}\rangle$ are

$$\mathbf{j}_{2\,^1E_{u\pm}}(\mathbf{r}) \approx \mathbf{j}_{4e_{g\pm}}(\mathbf{r}) \tag{3.123}$$

$$\mathbf{j}_{4\,^1E_{u\pm}}(\mathbf{r}) \approx \mathbf{j}_{4e_{g\pm}}(\mathbf{r}). \tag{3.124}$$

Of course, the electronic ring current of the excited state $|1\,^1E_{u\pm}\rangle$ is also dominated by that of the molecular orbital $4e_{g\pm}$ with weight of at least 75 % but it is difficult to excite this state due to the small transition dipole moment. Furthermore, the excited state $|3\,^1E_{u\pm}\rangle$ has the dominant electronic configuration $\ldots(2b_{2u})(4a_{2u})^2(1a_{1u})^2(4e_{g\mp})$ (61 %) corresponding to the dominant transition $2b_{2u} \rightarrow 4e_{g\mp}$, see also the discussion after Eq. (2.52). Hence, the electronic ring current of the excited state $|3\,^1E_{u\pm}\rangle$ is dominated by that of the molecular orbital $4e_{g\mp}$. For ring-shaped molecules, the magnetic quantum number M_L is not a good quantum number, i.e. the direction of the electronic ring current in ring-shaped molecules cannot be determined by the sign of M_L, thus the opposite direction of the electronic ring current of the molecular orbital $4e_{g\mp}$ for the state $|3\,^1E_{u\pm}\rangle$ is not contradictory. Another example is the excited state $|5\,^1E_{u\pm}\rangle$, see Section 3.4.2.

Fig. 3.19 shows the electronic probability $\rho_{4e_{g\pm}}(\mathbf{r}) = |\varphi_{4e_{g\pm}}|^2$ and current densities $\mathbf{j}_{4e_{g\pm}}(\mathbf{r})$ of the molecular orbital $4e_{g\pm}$ of Mg-porphyrin. The corresponding maxima are

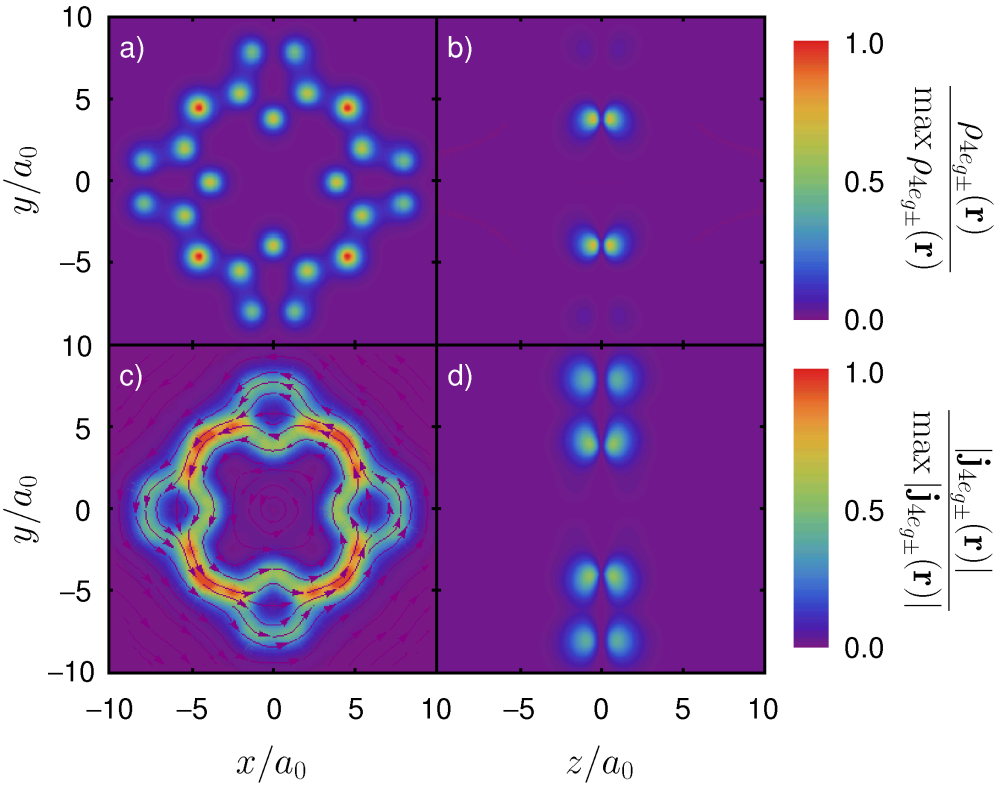

Figure 3.19: Electronic probability $\rho_{4e_{g\pm}}(\mathbf{r})$ (panels a, b) and current densities $\mathbf{j}_{4e_{g\pm}}(\mathbf{r})$ (panels c, d) in the x/y ($z = \pm 0.55\,a_0$ (panel a) and $z = \pm 0.79\,a_0$ (panel c)) and y/z ($x = 0$) (panels b, d) planes, for $4e_{g\pm}$ molecular orbitals of Mg-porphyrin. The Mg nucleus is located at $\mathbf{r}_{\mathrm{Mg}} = (0, 0, 0)$. The maxima of $\rho_{4e_{g\pm}}(\mathbf{r})$ are located near four carbon bridges, i.e. $x = y = \pm 4.5\,a_0$ and $z = \pm 0.55\,a_0$, and the maxima of $|\mathbf{j}_{4e_{g\pm}}(\mathbf{r})|$ are located at $x = y = \pm 4.5\,a_0$ and $z = \pm 0.79\,a_0$. Note that panel c shows the direction of the electronic current density only for the $4e_{g+}$ orbital; the corresponding direction for the $4e_{g-}$ orbital would be opposite. In panel d, the electron of the $4e_{g+}$ orbital at $y > 0$ and $y < 0$ moves toward and away from the reader, respectively, and backwards for the $4e_{g-}$ orbital.

located near four carbon bridges, i.e. $x = y = \pm 4.5\,a_0$, $z = \pm 0.55\,a_0$ for probability and $z = \pm 0.79\,a_0$ for current densities. This electronic ring current is unidirectional, i.e. anti-clockwise and clockwise for molecular orbital $4e_{g+}$ and $4e_{g-}$, respectively. The electric ring currents (Eq. (2.55)) of electronic states $|2\,^1E_{u\pm}\rangle$ and $|4\,^1E_{u\pm}\rangle$ of Mg-porphyrin are similar, i.e. [148]

$$I_{2\,^1E_{u\pm}} \approx I_{4\,^1E_{u\pm}} \approx I_{4e_{g\pm}} = \mp 85\,\mu\mathrm{A}. \tag{3.125}$$

These currents are, of course, weaker than the electric ring currents in one-electron ions (Tab. 3.1) and linear molecules AlCl and BeO (Eqs. (3.113) and (3.114)). Furthermore, there are branch zones of the electronic ring current of the molecular orbital $4e_{g\pm}$ located near eight neighbouring carbon atoms of carbon bridges. In pyrrole fragments, the electronic currents are divided into inner and outer currents along C–N–C

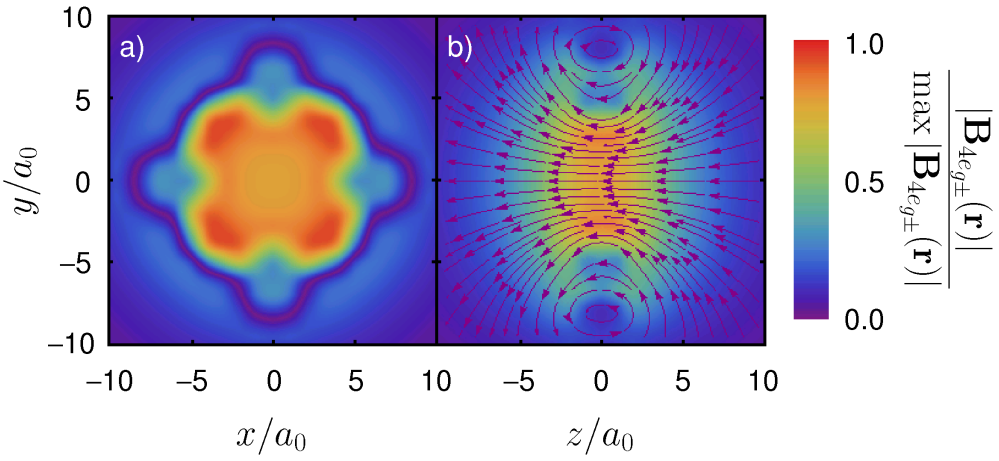

Figure 3.20: Induced magnetic field $\mathbf{B}_{4e_{g\pm}}(\mathbf{r})$ (Eq. (2.61)) in the x/y ($z = 0$) (panel a) and y/z ($x = 0$) (panel b) planes, for $4e_{g\pm}$ molecular orbitals of Mg-porphyrin. In panel a, the induced magnetic field for the $4e_{g+}$ orbital in the center region is directed away from the reader and in the outside region (with smaller magnitudes) toward the reader. In panel b, the direction of the induced magnetic field is drawn only for the $4e_{g+}$ orbital. For the $4e_{g-}$ orbital, the situation would be reversed. The maxima of the induced magnetic field $\max|\mathbf{B}_{4e_{g\pm}}(\mathbf{r})| = 0.21\,\mathrm{T}$ are located at $x = y = \pm 3.5\,a_0$ and $z = \pm 0.9\,a_0$. The induced magnetic field at the Mg nucleus is $|\mathbf{B}_{4e_{g\pm}}(\mathbf{r} = \mathbf{r}_{\mathrm{Mg}} = \mathbf{0})| = 0.16\,\mathrm{T}$.

and C–C–C–C bonds, respectively. The corresponding values are $I_{in,4e_{g\pm}} = \mp 44\,\mu\mathrm{A}$ and $I_{out,4e_{g\pm}} = \mp 41\,\mu\mathrm{A}$ which are obtained by integration of the electronic current density $\mathbf{j}_{4e_{g\pm}}(\mathbf{r})$ over separated half planes, e.g. $x = 0$, $0 \le y \le 6.1\,a_0$ and $y \ge 6.1\,a_0$, respectively. The mean period of an electron circulating about the z-axis (Eq. (2.60)) is

$$T_{2\,^1E_{u\pm}} \approx T_{4\,^1E_{u\pm}} \approx T_{4e_{g\pm}} = 1.9\,\mathrm{fs}, \tag{3.126}$$

which is typically much shorter than the corresponding lifetime of the eletronic ring current, which is limited by the radiative decay of excited states $|2\,^1E_{u\pm}\rangle$ and $|4\,^1E_{u\pm}\rangle$ on the ns-timescale.

The electronic ring currents of excited states $|2\,^1E_{u\pm}\rangle$ and $|4\,^1E_{u\pm}\rangle$ of Mg-porphyrin, circulating about the z-axis, induce magnetic fields $\mathbf{B}_{2\,^1E_{u\pm}}(\mathbf{r}) \approx \mathbf{B}_{4\,^1E_{u\pm}}(\mathbf{r}) \approx \mathbf{B}_{4e_{g\pm}}(\mathbf{r})$, cf. Eq. (2.61) and see Fig. 3.20. The induced magnetic field at the Mg nucleus ($\mathbf{r}_{\mathrm{Mg}} = \mathbf{0}$) [148]

$$|\mathbf{B}_{2\,^1E_{u\pm}}(\mathbf{r} = \mathbf{r}_{\mathrm{Mg}})| \approx |\mathbf{B}_{4\,^1E_{u\pm}}(\mathbf{r} = \mathbf{r}_{\mathrm{Mg}})| \approx |\mathbf{B}_{4e_{g\pm}}(\mathbf{r} = \mathbf{r}_{\mathrm{Mg}})| = 0.16\,\mathrm{T} \tag{3.127}$$

is somewhat smaller than the maximum of the induced magnetic field

$$\max|\mathbf{B}_{2\,^1E_{u\pm}}(\mathbf{r})| \approx \max|\mathbf{B}_{4\,^1E_{u\pm}}(\mathbf{r})| \approx \max|\mathbf{B}_{4e_{g\pm}}(\mathbf{r})| = 0.21\,\mathrm{T} \tag{3.128}$$

located at $x = y = \pm 3.5\,a_0$ and $z = \pm 0.9\,a_0$, because the currrent density flowing near carbon bridges is strong and, hence, the induced magnetic field around it is also strong

(similar to the magnetic field in a rectilinear current). Again, the induced magnetic fields in Mg-porphyrin are weaker than the induced magnetic fields in one-electron ions (Tab. 3.1) and linear molecules AlCl and BeO (Eqs. (3.117)–(3.120)). The mean ring current radii (Eqs. (2.95) and (2.96)) of the electronic ring currents of excited states $|2\,^1E_{u\pm}\rangle$ and $|4\,^1E_{u\pm}\rangle$ of Mg-porphyrin averaged over the azimuthal angle are

$$R_{1,2\,^1E_{u\pm}} \approx R_{1,4\,^1E_{u\pm}} \approx R_{1,4e_{g\pm}} = 5.9\,a_0 \tag{3.129}$$

and

$$R_{-1,2\,^1E_{u\pm}} \approx R_{-1,4\,^1E_{u\pm}} \approx R_{-1,4e_{g\pm}} = 5.2\,a_0, \tag{3.130}$$

hence $R_{1,4e_{g\pm}} \approx R_{-1,4e_{g\pm}}$, see also the discussion in Section 2.2.7.

For the induction of electronic ring currents of excited states $|2\,^1E_{u\pm}\rangle$ and $|4\,^1E_{u\pm}\rangle$ by means of right or left circularly polarized laser pulses, we assume that the ring-shaped molecule Mg-porphyrin is pre-aligned along the laboratory-fixed z-axis, using techniques of nonadiabatic alignment of non-polar molecules, see also Refs. [210, 213]. Furthermore, we assume that the alignment duration is longer than the total pulse duration of the circularly polarized laser pulse, here $t_{p,c} = 21.2\,\text{fs}$, the same as for AlCl and BeO molecules, and that the laser pulse (Eq. (2.99)) is centered at the revival time of the rotational wavepacket, i.e. $t_c = t^*$.

The laser parameters of the right circularly polarized laser pulse (Eq. (2.99)) with $\cos^{20}$ envelope (Eq. (2.100)) are then optimized in order to achieve a complete population transfer from the electronic ground state $|X\,^1A_{1g}\rangle$ to the excited state $|2\,^1E_{u+}\rangle$ or $|4\,^1E_{u+}\rangle$ of Mg-porphyrin. For the target state $|2\,^1E_{u+}\rangle$, the optimized laser parameters are $\mathcal{E}_c = 1.99\,\text{GV m}^{-1}$, $\hbar\omega_c = 2.61\,\text{eV}$, $I_{max,c} = 1.05\,\text{TW cm}^{-2}$, $\tau_c = 2.53\,\text{fs}$, and $\Delta t_c = 2\pi/\omega_c = 1.58\,\text{fs}$. For the target state $|4\,^1E_{u+}\rangle$, the corresponding laser parameters are $\mathcal{E}_c = 2.80\,\text{GV m}^{-1}$, $\hbar\omega_c = 3.32\,\text{eV}$, $I_{max,c} = 2.08\,\text{TW cm}^{-2}$, $\tau_c = 2.52\,\text{fs}$, and $\Delta t_c = 1.25\,\text{fs}$. For laser parameters with longer effective pulse duration $\tau_c = 3.52\,\text{fs}$, see Ref. [148]. Fig. 3.21 shows the x- and y-components of the time-dependent right circularly polarized electric field $\mathbf{E}_{c+}(t) = E_{x,c+}(t)\mathbf{e}_x + E_{y,c+}(t)\mathbf{e}_y$ (Eq. (2.99)) centered at the revival time $t_c = t^*$ and the corresponding time-dependent intensity $I_c(t)$ (Eq. (2.114)) for nearly complete population transfer from the ground state $|X\,^1A_{1g}\rangle$ to the excited state $|2\,^1E_{u+}\rangle$ or $|4\,^1E_{u+}\rangle$ of Mg-porphyrin.

Fig. 3.21 also shows the corresponding time-dependent populations $P_i(t)$ of electronic states $|X\,^1A_{1g}\rangle$, $|2\,^1E_{u+}\rangle$, $|3\,^1E_{u+}\rangle$, $|4\,^1E_{u+}\rangle$, and $|5\,^1E_{u+}\rangle$ whereas other electronic states such as $|1\,^1E_{u+}\rangle$ and $|6\,^1E_{u+}\rangle$ states have negligible populations during the electronic excitation. For optimal population transfer $|X\,^1A_{1g}\rangle \rightarrow |2\,^1E_{u+}\rangle$, a right circularly polarized reoptimized π laser pulse excites the target state $|2\,^1E_{u+}\rangle$ with its fi-

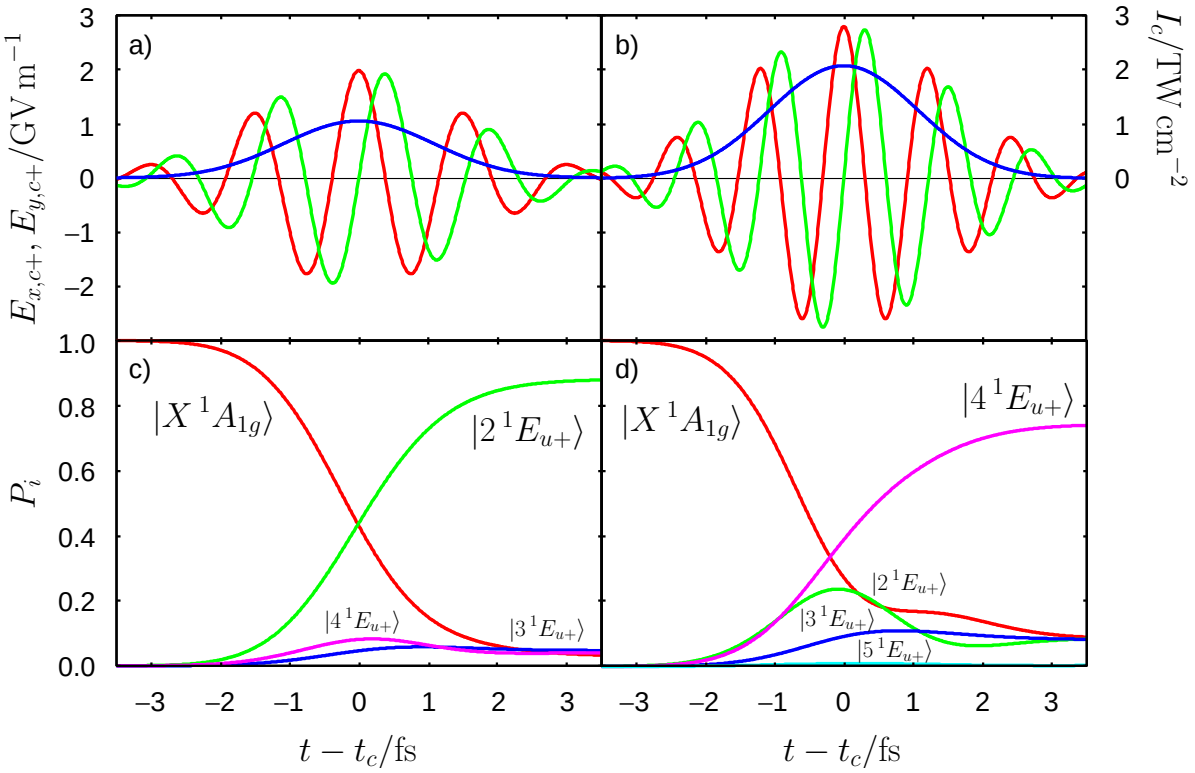

Figure 3.21: Population transfers $|X\,^1A_{1g}\rangle \rightarrow |2\,^1E_{u+}\rangle$ (left panels) and $|X\,^1A_{1g}\rangle \rightarrow |4\,^1E_{u+}\rangle$ (right panels) by means of a right circularly polarized reoptimized π laser pulse centered at the revival time $t_c = t^*$. Panels a and b show the x- (red) and y- (green) components of the time-dependent electric field $\mathbf{E}_{c+}(t)$ (Eq. (2.99)) and the corresponding time-dependent intensity $I_c(t)$ (Eq. (2.114)) (blue). In panels c and d, the time-dependent populations $P_i(t)$ (Eq. (2.130)) of electronic states $|X\,^1A_{1g}\rangle$ (red), $|2\,^1E_{u+}\rangle$ (green), $|3\,^1E_{u+}\rangle$ (blue), $|4\,^1E_{u+}\rangle$ (magenta), and $|5\,^1E_{u+}\rangle$ (cyan) are drawn.

nal population $P_2(t_f) = 0.881$. The final populations of other electronic states are marginal, i.e. $P_X(t_f) = 0.030$, $P_3(t_f) = 0.047$, and $P_4(t_f) = 0.041$. For the other optimal population transfer $|X\,^1A_{1g}\rangle \rightarrow |4\,^1E_{u+}\rangle$, the final population of the target state $|4\,^1E_{u+}\rangle$ is $P_4(t_f) = 0.745$ whereas other electronic states have small final populations, i.e. $P_X(t_f) = 0.085$, $P_2(t_f) = 0.085$, $P_3(t_f) = 0.082$, and $P_5(t_f) = 0.003$. The non-negligible populations of these undesirable electronic states are due to the large spectral width of the laser pulse. For sufficiently long pulse durations, e.g. $\tau_c \gg 10\,\mathrm{fs}$, these side effects will disappear.

Finally, the excited state $|4\,^1E_{u\pm}\rangle$ has the mean electronic angular momentum $\langle \hat{L}_z \rangle = \langle \hat{L}_{z,el} \rangle = \pm 2.5\,\hbar$ calculated at the CISD level [148]. Since a right (+) or left (−) circularly polarized laser pulse transfers the photonic angular momentum $\pm\hbar$ to the molecule during the electronic excitation, i.e. the total angular momentum of the molecule after the excitation is equal to $\pm\hbar$. This conservation of the total angular momentum implies that

the mean nuclear angular momentum is $\langle \hat{L}_{z,nu} \rangle = \mp 1.5\,\hbar$. Thus, there are nuclear ring currents in Mg-porphyrin (e.g. nuclear pseudorotations or rotations) associated with electronic ring currents. These nuclear pseudorotations and rotations are rather slow, with periods on fs- and ps-timescales, respectively. These timescales are much longer than the effective pulse duration $\tau_c \approx 2.5\,\text{fs}$ of the circularly polarized laser pulses and, hence, the nuclei can be considered frozen during the FC-type electronic excitation. Analogous excitations of nuclear rotations associated with electronic currents through helical molecules between electrodes have been discovered in Ref. [294].

3.4.2 Electronic ring currents in excited $|5\,^1E_{u\pm}\rangle$ states

Now, let us investigate electronic ring currents in electronic excited $|5\,^1E_{u\pm}\rangle$ states of Mg-porphyrin. The electronic state $|5\,^1E_{u\pm}\rangle$ has the dominant electronic configuration $(3e_{g\pm})(3e_{g\mp})^2(2b_{2u})^2(4a_{2u})^2(1a_{1u})^2(2b_{1u})$ (94 %) corresponding to the dominant transition $3e_{g\pm} \rightarrow 2b_{1u}$, see Table 3.5 and the discussion after Eqs. (2.52) and (3.124). Due to removal of an electron from the $3e_{g\pm}$ orbital, the electronic ring current of the $|5\,^1E_{u\pm}\rangle$ is dominated by that of the $3e_{g\mp}$ molecular orbital of Mg-porphyrin with the weight of at least 94 %. Thus, the electronic current density of the electronic state $|5\,^1E_{u\pm}\rangle$ is

$$\mathbf{j}_{5\,^1E_{u\pm}}(\mathbf{r}) \approx \mathbf{j}_{3e_{g\mp}}(\mathbf{r}). \tag{3.131}$$

Fig. 3.22 shows the electronic probability $\rho_{3e_{g\pm}}(\mathbf{r}) = |\varphi_{3e_{g\pm}}|^2$ and current densities $\mathbf{j}_{3e_{g\pm}}(\mathbf{r})$ of the molecular orbital $3e_{g\pm}$ of Mg-porphyrin. The corresponding maxima are located near the four nitrogen atoms, i.e. $x = 0$, $y = \pm 3.8\,a_0$ and $y = 0$, $x = \pm 3.8\,a_0$, $z = \pm 0.46\,a_0$ for the probability density and $x = \pm 0.41\,a_0$, $y = \pm 4.1\,a_0$ and $y = \pm 0.41\,a_0$, $x = \pm 4.1\,a_0$, $z = \pm 0.73\,a_0$ for the current density. Note that the panel c of Fig. 3.22 shows the current density of the molecular orbital $3e_{g-}$, not of the other one, i.e. $3e_{g+}$. The electronic ring currents of the $3e_{g\pm}$ and $4e_{g\pm}$ molecular orbitals are very different, cf. Figs. 3.19 and 3.22. For $3e_{g\pm}$ orbitals, the electronic ring current is no longer unidirectional, i.e. there are several richly structured ring currents in Mg-porphyrin. For the $3e_{g-}$ molecular orbital, the net electronic ring current is anti-clockwise along carbon bridges and nitrogen atoms of Mg-porphyrin. However, there are four strong clockwise ring currents in pyrrole fragments and four weak anti-clockwise ring currents between carbon bridges and the Mg atom. Furthermore, there are also two very weak clockwise ring currents around the Mg atom inside and outside of Mg-porphyrin. The net electric ring current (Eq. (2.55)) of the electronic state $|5\,^1E_{u\pm}\rangle$ of Mg-porphyrin is

$$I_{5\,^1E_{u\pm}} \approx I_{3e_{g\mp}} = \mp 6\,\mu\text{A} \tag{3.132}$$

which is much weaker than the electric ring currents of the $|2\,^1E_{u\pm}\rangle$ and $|4\,^1E_{u\pm}\rangle$ states of Mg-porphyrin, i.e. $I_{2\,^1E_{u\pm}} \approx I_{4\,^1E_{u\pm}} \approx \mp 85\,\mu\text{A}$ (Eq. (3.125)). However, the electric

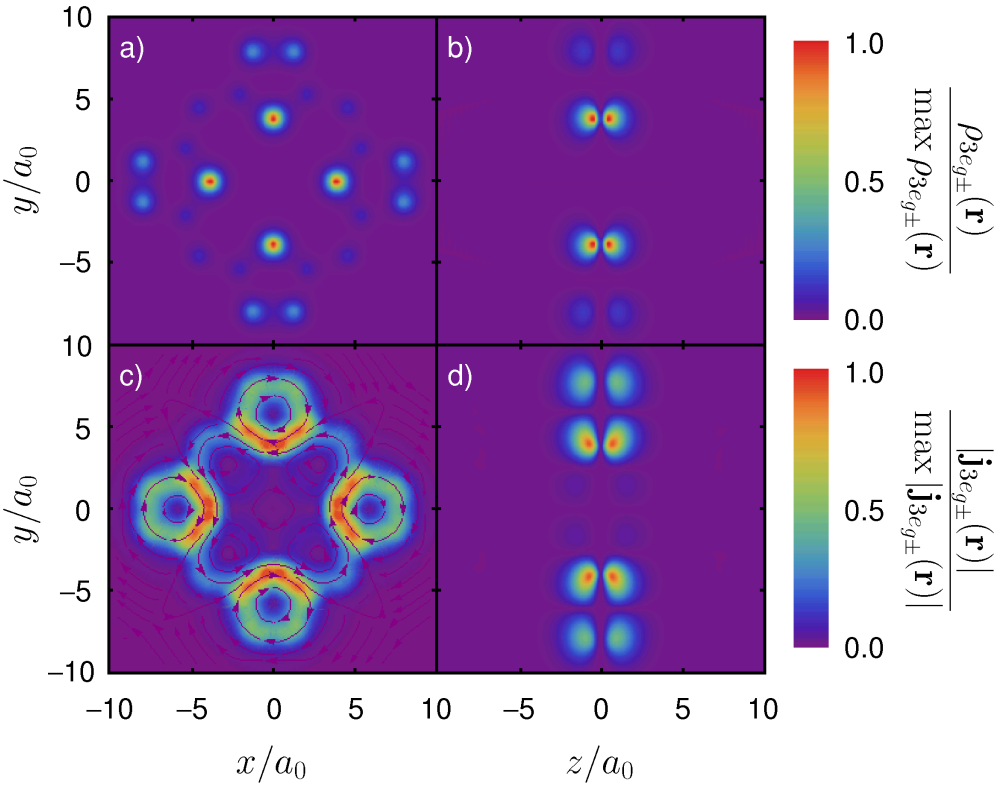

Figure 3.22: Electronic probability $\rho_{3e_{g\pm}}(\mathbf{r})$ (panels a, b) and current densities $\mathbf{j}_{3e_{g\pm}}(\mathbf{r})$ (panels c, d) in the x/y ($z = \pm 0.46\,a_0$ (panel a), $z = \pm 0.73\,a_0$ (panel c)) and y/z ($x = 0$) (panels b, d) planes, for $3e_{g\pm}$ molecular orbitals of Mg-porphyrin. The corresponding maxima are located near the four nitrogen atoms, i.e. $x = 0$, $y = \pm 3.8\,a_0$ and $y = 0$, $x = \pm 3.8\,a_0$, $z = \pm 0.46\,a_0$ for $\rho_{3e_{g\pm}}(\mathbf{r})$ and $x = \pm 0.41\,a_0$, $y = \pm 4.1\,a_0$ and $y = \pm 0.41\,a_0$, $x = \pm 4.1\,a_0$, $z = \pm 0.73\,a_0$ for $|\mathbf{j}_{3e_{g\pm}}(\mathbf{r})|$. Panel c shows the direction of the electronic current density only for the $3e_{g-}$ orbital. In panel d, there are three different regions, i.e. the electron of the $3e_{g-}$ orbital at $0 < y < 2.4\,a_0$, $y > 6.1\,a_0$ and $2.4\,a_0 < y < 6.1\,a_0$ moves away from and toward the reader, respectively. For $y < 0$, the corresponding directions are opposite. For the $3e_{g+}$ orbital, the situation would be reversed.

ring currents in pyrrole fragments are stronger. The inner and outer electric currents along C–N–C and C–C–C–C bonds are $I_{in,3e_{g\mp}} = \mp 35\,\mu$A and $I_{out,3e_{g\mp}} = \pm 27\,\mu$A which are obtained by integration of the electronic current density $\mathbf{j}_{3e_{g\mp}}(\mathbf{r})$ over separated half planes, e.g. $x = 0$, $2.4\,a_0 \leq y \leq 6.1\,a_0$ and $y \geq 6.1\,a_0$, respectively. The weak ring current around the Mg atom (inside of Mg-porphyrin) $I_{\mathrm{Mg},3e_{g\mp}} = \pm 2\,\mu$A is obtained using the remaining half plane, e.g. $x = 0$, $0 \leq y \leq 2.4\,a_0$, cf. panel d of Fig. 3.22. The mean period of an electron circulating about the z-axis (Eq. (2.60)) is

$$T_{5\,^1E_{u\pm}} \approx T_{3e_{g\mp}} = 26\,\mathrm{fs}, \tag{3.133}$$

which is typically shorter than the corresponding lifetime of the electronic ring current, which is limited by the radiative decay of the excited state $|5\,^1E_{u\pm}\rangle$ on the ns-timescale.

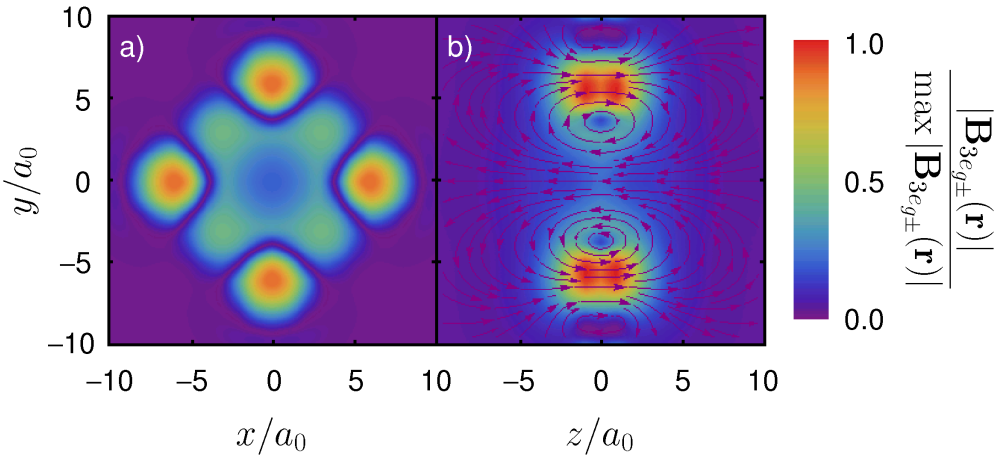

Figure 3.23: Induced magnetic field $\mathbf{B}_{3e_{g\pm}}(\mathbf{r})$ (Eq. (2.61)) in the x/y ($z = 0$) (panel a) and y/z ($x = 0$) (panel b) planes, for $3e_{g\pm}$ molecular orbitals of Mg-porphyrin. In panel a, the induced magnetic field for the $3e_{g-}$ orbital inside the pyrrole fragments is directed toward the reader and outside of these fragments (with smaller magnitudes) away from the reader. In panel b, the direction of the induced magnetic field is drawn only for the $3e_{g-}$ orbital. For the $3e_{g+}$ orbital, the situation would be reversed. The maxima of the induced magnetic field $\max|\mathbf{B}_{3e_{g\pm}}(\mathbf{r})| = 0.11\,\mathrm{T}$ are located at $x = 0$, $y = \pm 5.8\,a_0$, $z = \pm 1.0\,a_0$ and $x = \pm 5.8\,a_0$, $y = 0$, $z = \pm 1.0\,a_0$. The induced magnetic field at the Mg nucleus is $|\mathbf{B}_{3e_{g\pm}}(\mathbf{r} = \mathbf{r}_{\mathrm{Mg}} = \mathbf{0})| = 0.02\,\mathrm{T}$.

The electronic ring current of the excited state $|5\,^1E_{u\pm}\rangle$ of Mg-porphyrin induces the magnetic field $\mathbf{B}_{5\,^1E_{u\pm}}(\mathbf{r}) \approx \mathbf{B}_{3e_{g\mp}}(\mathbf{r})$, cf. Eq. (2.61) and see Fig. 3.23. The induced magnetic field at the Mg nucleus ($\mathbf{r}_{\mathrm{Mg}} = \mathbf{0}$)

$$|\mathbf{B}_{5\,^1E_{u\pm}}(\mathbf{r} = \mathbf{r}_{\mathrm{Mg}})| \approx |\mathbf{B}_{3e_{g\mp}}(\mathbf{r} = \mathbf{r}_{\mathrm{Mg}})| = 0.02\,\mathrm{T} \tag{3.134}$$

is much smaller than the maximum of the induced magnetic field

$$\max|\mathbf{B}_{5\,^1E_{u\pm}}(\mathbf{r})| \approx \max|\mathbf{B}_{3e_{g\mp}}(\mathbf{r})| = 0.11\,\mathrm{T} \tag{3.135}$$

located inside the pyrrole fragments, i.e. $x = 0$, $y = \pm 5.8\,a_0$ and $y = 0$, $x = \pm 5.8\,a_0$, $z = \pm 1.0\,a_0$, due to the strong electronic ring currents in pyrrole fragments. Nevertheless, this maximum of the induced magnetic field is still smaller than the corresponding maxima for excited $|2\,^1E_{u\pm}\rangle$ and $|4\,^1E_{u\pm}\rangle$ states (Eq. (3.128)). Since the formulae for the mean ring current radii (Eqs. (2.95)–(2.97)) are only defined for unidirectional ring currents, these formulae cannot be used for the electronic excited state $|5\,^1E_{u\pm}\rangle$ where the electronic ring current is not unidirectional, see Fig. 3.22.

As for electronic excitations of the $|2\,^1E_{u\pm}\rangle$ and $|4\,^1E_{u\pm}\rangle$ states, we assume that the molecule Mg-porphyrin is pre-aligned along the laboratory-fixed z-axis [210, 213], that the alignment duration is longer than the total pulse duration of the subsequent right or

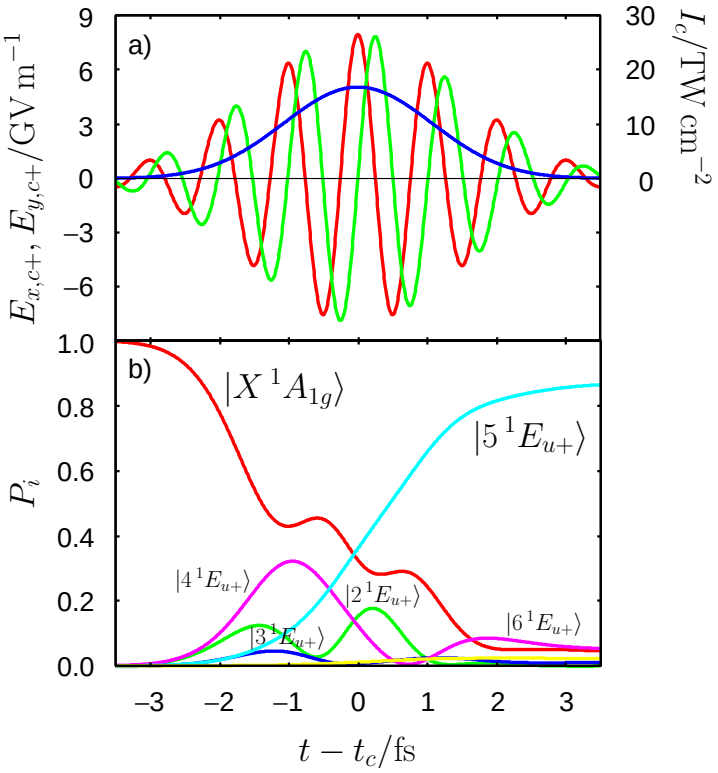

Figure 3.24: Population transfer $|X\,^1A_{1g}\rangle \rightarrow |5\,^1E_{u+}\rangle$ by means of a right circularly reoptimized π laser pulse centered at the revival time $t_c = t^*$. Panel a shows the x- (red) and y- (green) components of the time-dependent electric field $\mathbf{E}_{c+}(t)$ (Eq. (2.99)) and the corresponding time-dependent intensity $I_c(t)$ (Eq. (2.114)) (blue). In panel b, the time-dependent populations $P_i(t)$ (Eq. (2.130)) of electronic states $|X\,^1A_{1g}\rangle$ (red), $|2\,^1E_{u+}\rangle$ (green), $|3\,^1E_{u+}\rangle$ (blue), $|4\,^1E_{u+}\rangle$ (magenta), $|5\,^1E_{u+}\rangle$ (cyan), and $|6\,^1E_{u+}\rangle$ (yellow) are drawn.

left circularly polarized laser pulse, $t_{p,c} = 21.2\,\mathrm{fs}$, and that the laser pulse (Eq. (2.99)) is centered at the revival time $t_c = t^*$. Again, the laser parameters of the right circularly polarized laser pulse (Eq. (2.99)) with $\cos^{20}$ envelope (Eq. (2.100)) are optimized in order to achieve a complete population transfer from the electronic ground state $|X\,^1A_{1g}\rangle$ to the excited state $|5\,^1E_{u+}\rangle$ of Mg-porphyrin. They are $\mathcal{E}_c = 7.97\,\mathrm{GV\,m^{-1}}$, $\hbar\omega_c = 4.03\,\mathrm{eV}$, $I_{max,c} = 16.9\,\mathrm{TW\,cm^{-2}}$, $\tau_c = 2.51\,\mathrm{fs}$, and $\Delta t_c = 2\pi/\omega_c = 1.03\,\mathrm{fs}$. Fig. 3.24 shows the x- and y-components of the time-dependent right circularly polarized electric field $\mathbf{E}_{c+}(t) = E_{x,c+}(t)\mathbf{e}_x + E_{y,c+}(t)\mathbf{e}_y$ (Eq. (2.99)) centered at the revival time $t_c = t^*$ and the corresponding time-dependent intensity $I_c(t)$ (Eq. (2.114)) for selective population transfer from the ground state $|X\,^1A_{1g}\rangle$ to the excited state $|5\,^1E_{u+}\rangle$ of Mg-porphyrin.

In Fig. 3.24, the time-dependent populations $P_i(t)$ of electronic states $|X\,^1A_{1g}\rangle$ and $|n\,^1E_{u+}\rangle$ $(n = 2-6)$ are shown whereas other electronic states, i.e. $|1\,^1E_{u+}\rangle$ and $|n\,^1E_{u-}\rangle$ $(n = 1-6)$, have negligible populations during the electronic excitation. Thus, a right

circularly polarized reoptimized π laser pulse induces selective population transfer from the electronic ground $|X\,^1A_{1g}\rangle$ to the excited $|5\,^1E_{u+}\rangle$ states. The corresponding final populations are $P_X(t_f) = 0.042$ and $P_5(t_f) = 0.869$. The final populations of other excited states are small, i.e. $P_2(t_f) = 0.001$, $P_3(t_f) = 0.013$, $P_4(t_f) = 0.051$, and $P_6(t_f) = 0.023$. These results would be improved for long pulse durations of circularly polarized laser pulses with smaller spectral widths.

We note that the excited state $|5\,^1E_{u\pm}\rangle$, represented by the dominant transition $3e_{g\pm} \rightarrow 2b_{1u}$ (94 %), has the mean electronic angular momentum $\langle\hat{L}_z\rangle = \langle\hat{L}_{z,el}\rangle = \mp 0.08\,\hbar$ calculated at the HF level. Since the angular momentum is proportional to the angular velocity of the circulating electron and to the corresponding radius, the outer electronic current of the $3e_{g-}$ orbital in pyrrole fragments with large radius contributes more to the negative angular momentum ($\sim -27\,\mu\text{A}\cdot 8\,a_0 \approx -216\,a_0\,\mu\text{A}$) than does the opposite inner electronic current with small radius ($\sim 35\,\mu\text{A}\cdot 4\,a_0 \approx 140\,a_0\,\mu\text{A}$) plus the electronic current along carbon bridges ($\sim 6\,\mu\text{A}\cdot 6\,a_0 \approx 36\,a_0\,\mu\text{A}$). In contrast to the positive mean electronic angular momentum of the $|4\,^1E_{u+}\rangle$ state, the mean electronic angular momentum of the $|5\,^1E_{u+}\rangle$ state is negative. Since the total angular momentum of the molecule after the excitation by means of a right (+) or left (−) circularly polarized laser pulse (with photonic angular momentum $\pm\hbar$) is equal to $\pm\hbar$, the mean nuclear angular momentum of the state $|5\,^1E_{u\pm}\rangle$ must be $\langle\hat{L}_{z,nu}\rangle = \pm 1.08\,\hbar$, i.e. it is positive for the state $|5\,E_{u+}\rangle$ in contrast to the negative mean nuclear angular momentum of the state $|4\,^1E_{u+}\rangle$. There are also nuclear ring currents in excited states $|5\,^1E_{u\pm}\rangle$, represented by nuclear pseudorotations or rotations induced by electronic ring currents, see also the discussion at the end of Section 3.4.1.

3.4.3 Electron circulation

A superposition of the ground state $|X\,^1A_{1g}\rangle$ and the excited state $|2\,^1E_{u+}\rangle$, $|4\,^1E_{u+}\rangle$, or $|5\,^1E_{u+}\rangle$ of Mg-porphyrin, with approximately equal populations (≈ 0.5), is achieved by means of a right circularly polarized reoptimized $\pi/2$ laser pulse (Eq. (2.99)) with $\cos^{20}$ envelope (Eq. (2.100)). As for AlCl and BeO molecules, the total pulse duration $t_{p,c} = 21.2\,\text{fs}$ is chosen to be fixed whereas the amplitude of the electric field $\mathcal{E}_c$ and the laser frequency ω_c are reoptimized in order to achieve almost exact half population transfer from the electronic ground $|X\,^1A_{1g}\rangle$ to the excited $|n\,^1E_{u+}\rangle$ ($n = 2, 4, 5$) states. The optimized laser parameters are $\mathcal{E}_c = 1.56\,\text{GV m}^{-1}$, $\hbar\omega_c = 2.30\,\text{eV}$, $I_{max,c} = 0.65\,\text{TW cm}^{-2}$, $\tau_c = 2.54\,\text{fs}$, $\Delta t_c = 2\pi/\omega_c = 1.80\,\text{fs}$ for the half population transfer $|X\,^1A_{1g}\rangle \rightarrow |2\,^1E_{u+}\rangle$, $\mathcal{E}_c = 2.31\,\text{GV m}^{-1}$, $\hbar\omega_c = 3.63\,\text{eV}$, $I_{max,c} = 1.42\,\text{TW cm}^{-2}$, $\tau_c = 2.52\,\text{fs}$, $\Delta t_c = 2\pi/\omega_c = 1.14\,\text{fs}$ for the half population transfer $|X\,^1A_{1g}\rangle \rightarrow |4\,^1E_{u+}\rangle$, and $\mathcal{E}_c = 3.98\,\text{GV m}^{-1}$,

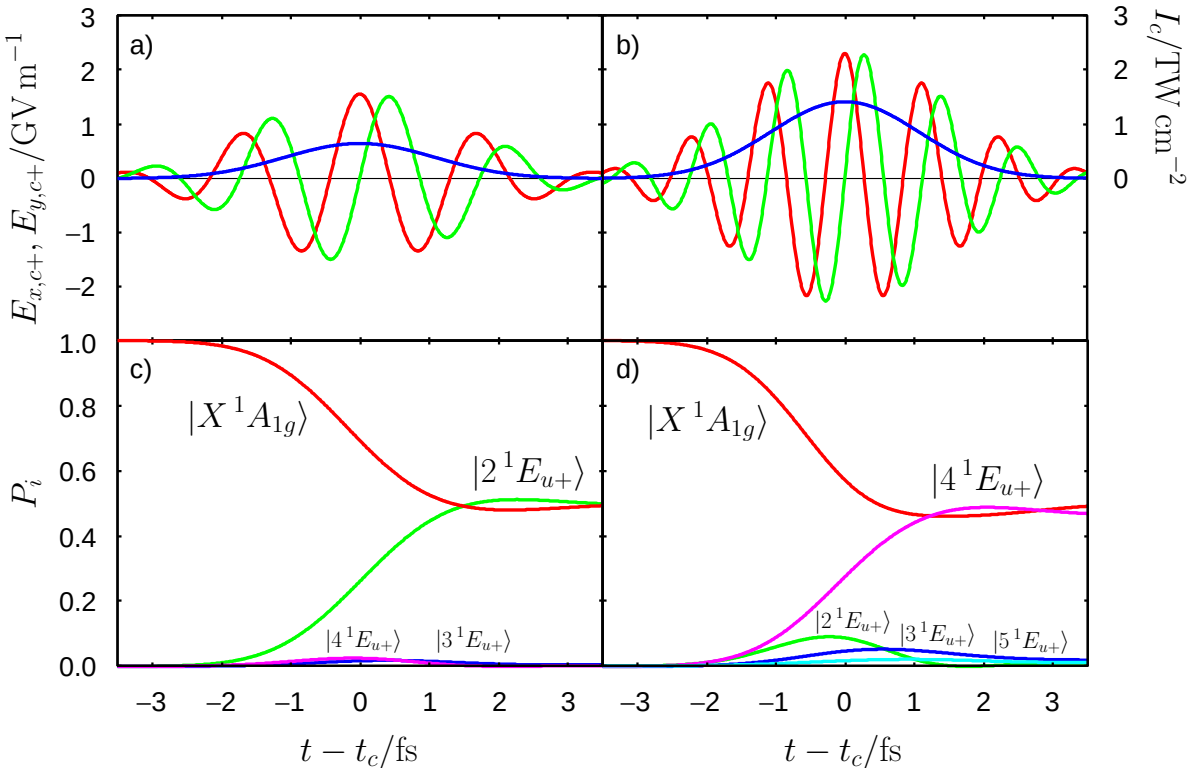

Figure 3.25: Half population transfers $|X\,^1A_{1g}\rangle \rightarrow |2\,^1E_{u+}\rangle$ (left panels) and $|X\,^1A_{1g}\rangle \rightarrow |4\,^1E_{u+}\rangle$ (right panels) by means of a right circularly polarized reoptimized $\pi/2$ laser pulse centered at the revival time $t_c = t^*$. For further details, see Fig. 3.21.

$\hbar\omega_c = 4.31\,\mathrm{eV}$, $I_{max,c} = 4.20\,\mathrm{TW\,cm^{-2}}$, $\tau_c = 2.51\,\mathrm{fs}$, $\Delta t_c = 2\pi/\omega_c = 0.98\,\mathrm{fs}$ for the half population transfer $|X\,^1A_{1g}\rangle \rightarrow |5\,^1E_{u+}\rangle$. Figs. 3.25 and 3.26 show the x- and y-components of the right circularly polarized electric fields $\mathbf{E}_{c+}(t) = E_{x,c+}(t)\mathbf{e}_x + E_{y,c+}(t)\mathbf{e}_y$ (Eq. (2.99)) centered at the revival time $t_c = t^*$ and the corresponding time-dependent intensities $I_c(t)$ (Eq. (2.114)) for almost exact half population transfers from the electronic ground state $|X\,^1A_{1g}\rangle$ to the excited states $|2\,^1E_{u+}\rangle$, $|4\,^1E_{u+}\rangle$, and $|5\,^1E_{u+}\rangle$ of Mg-porphyrin. The optimized parameters of the right circularly polarized laser pulses with other effective pulse durations τ_c are given in Refs. [147,150] for the half population transfer $|X\,^1A_{1g}\rangle \rightarrow |2\,^1E_{u+}\rangle$ ($\tau_c = 0.91\,\mathrm{fs}$ and $\tau_c = 1.37\,\mathrm{fs}$), [149] for the half population transfer $|X\,^1A_{1g}\rangle \rightarrow |4\,^1E_{u+}\rangle$ ($\tau_c = 1.82\,\mathrm{fs}$ and $\tau_c = 3.64\,\mathrm{fs}$), and [147] for the half population transfer $|X\,^1A_{1g}\rangle \rightarrow |5\,^1E_{u+}\rangle$ ($\tau_c = 2.00\,\mathrm{fs}$).

Figs. 3.25 and 3.26 also show the time-dependent populations of electronic states $|X\,^1A_{1g}\rangle$ and $|n\,^1E_{u+}\rangle$ ($n = 2-5$) of Mg-porphyrin. They clearly show that the populations of all excited states for half population transfers are smaller than the corresponding populations for complete population transfers, shown in Figs. 3.21 and 3.24, due to smaller intensities of the right circularly polarized reoptimized $\pi/2$ laser pulses. The final popula-

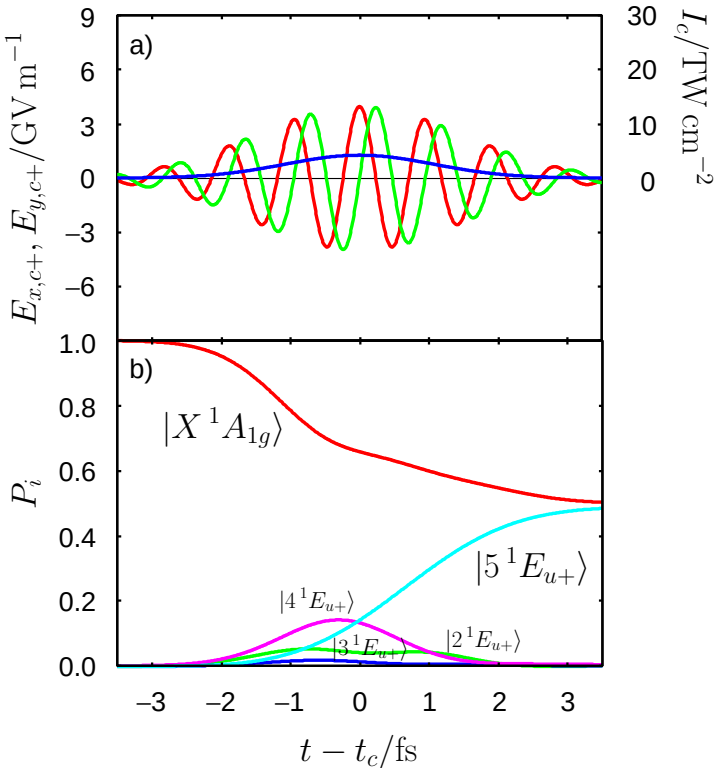

Figure 3.26: Half population transfer $|X\,^1A_{1g}\rangle \rightarrow |5\,^1E_{u+}\rangle$ by means of a right circularly polarized reoptimized $\pi/2$ laser pulse centered at the revival time $t_c = t^*$. For further details, see Fig. 3.24.

tions of the dominant electronic states at $t_f = t_c + t_{p,c}$ are $P_X(t_f) = 0.499$, $P_2(t_f) = 0.493$ for the half population transfer $|X\,^1A_{1g}\rangle \rightarrow |2\,^1E_{u+}\rangle$, $P_X(t_f) = 0.499$, $P_4(t_f) = 0.462$ for the half population transfer $|X\,^1A_{1g}\rangle \rightarrow |4\,^1E_{u+}\rangle$, and $P_X(t_f) = 0.499$, $P_5(t_f) = 0.491$ for the half population transfer $|X\,^1A_{1g}\rangle \rightarrow |5\,^1E_{u+}\rangle$, where the other electronic states have negligible final populations.

After the end of the right circularly polarized reoptimized $\pi/2$ laser pulses shown in Figs. 3.25 and 3.26, there are electron circulations of the probability density about the z-axis. Here, we consider only the superposition of the electronic ground $|X\,^1A_{1g}\rangle$ and excited $|5\,^1E_{u+}\rangle$ states of Mg-porphyrin since the ground state $|X\,^1A_{1g}\rangle$ is dominated by the corresponding HF wavefunction with weight of 80 % and the excited state $|5\,^1E_{u+}\rangle$ is dominated by the corresponding transition $3e_{g+} \rightarrow 2b_{1u}$ with weight of 94 %, see Table 3.5. Thus, the CIS approximation for this superposition state is better than the other superposition states involving $|2\,^1E_{u+}\rangle$ and $|4\,^1E_{u+}\rangle$ states. The difference of the electronic probability density $\Delta\rho(\mathbf{r}, t) = \rho(\mathbf{r}, t) - \rho(\mathbf{r}, t_0)$ (Eqs. (2.191) and (2.192)) after the end of the laser pulse ($t > t_f$), using the CIS approximation (see Section 2.3.4) with dominant transition $3e_{g+} \rightarrow 2b_{1u}$, is shown in Fig. 3.27, see also Ref. [147]. The electronic probability density circulates about the z-axis with period $\tau_{50} = 2\pi/\omega_{50} = 907\,\mathrm{as}$, where ω_{50} is the

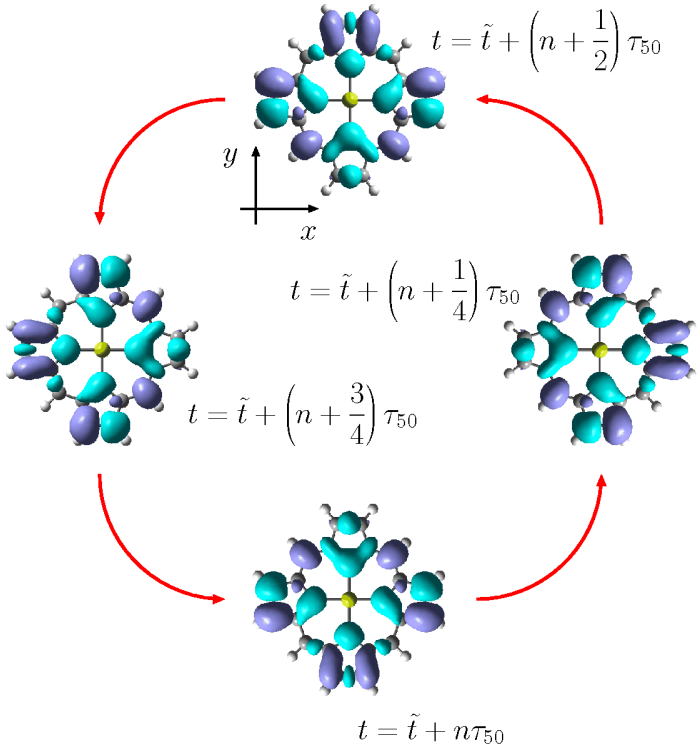

Figure 3.27: Electron circulation in the superposition of $|X\,^1A_{1g}\rangle$ and $|5\,^1E_{u+}\rangle$ states of Mg-porphyrin after a right circularly polarized reoptimized $\pi/2$ laser pulse, see Fig. 3.26. This hybrid state has the dominant contribution of the hybrid orbital, $3e_{g+}+2b_{1u}$, corresponding to the dominant transition $3e_{g+} \rightarrow 2b_{1u}$. The snapshots are illustrated as the difference of the electronic density $\Delta\rho(\mathbf{r},t) = \rho(\mathbf{r},t) - \rho(\mathbf{r},t_0)$ (Eqs. (2.191) and (2.192)) at times $t = \tilde{t} + (n+k)\tau_{50}$ ($n = 0, 1, 2, \ldots$, $k = 0, 1/4, 1/2, 3/4$), cf. Ref. [147]. Here, $\tilde{t}$ is the time after the end of the laser pulse at which the difference of the electron density is the same as shown in the bottom panel ($t = \tilde{t} + n\tau_{50}$), and $\tau_{50} = 2\pi/\omega_{50} = 907\,\text{as}$ is the period of the time-dependent electronic density $\rho(\mathbf{r},t)$ circulating about the z-axis. The blue and cyan regions show positive and negative differences $\Delta\rho(\mathbf{r},t)$, respectively.

excitation frequency of the electronic state $|5\,^1E_{u+}\rangle$. For the superposition of the ground $|X\,^1A_{1g}\rangle$ and excited $|4\,^1E_{u+}\rangle$ states, the electron circulation with period $\tau_{40} = 2\pi/\omega_{40} = 1.21\,\text{fs}$ is illustrated in Ref. [149]. The corresponding period for the electron circulation in the superposition of $|X\,^1A_{1g}\rangle$ and $|2\,^1E_{u+}\rangle$ states is $\tau_{20} = 2\pi/\omega_{20} = 1.55\,\text{fs}$. Note that the period τ_{i0} of the time-dependent electronic probability density should not be confused with the period T (Eq. (2.60)) of an electron about the z-axis, see also the discussion at the end of Section 3.3.

3.5 Linear triatomic molecules FHF^- and $^{114}CdH_2$

3.5.1 Nuclear ring currents

In this Section, we apply the concepts for nuclear ring currents and pseudorotation in bending and pseudorotational states to linear triatomic molecules FHF^- [208] and $^{114}CdH_2$ [207] in the electronic ground state $|X\,^1\Sigma_g^+\rangle$, see also Section 2.4. These linear molecules have $D_{\infty h}$ symmetry. The physical properties of FHF^- and $^{114}CdH_2$ molecules are listed in Table 3.6. The equilibrium bond lengths R_e between nuclei A and B, here A=F, B=H for FHF^- and A=H, B=Cd for $^{114}CdH_2$, and harmonic vibrational frequencies ω_s for the symmetric stretch, ω_a for the antisymmetric stretch, and ω_b for the bend are determined by ab initio calculations, where the corresponding details can be found in Refs. [207, 208]. The rotational constants $B_{e,X}$ for FHF^- and $^{114}CdH_2$ are different, see Table 3.6, due to the different locations of the light hydrogen nucleus, i.e. at $Z = 0$ for FHF^- and at $Z = \pm R_e$ for $^{114}CdH_2$. Thus, the rotational revival time for FHF^-, i.e. $\tau_{rev,X} = 48.8\,\text{ps}$, is much larger than for $^{114}CdH_2$, i.e. $\tau_{rev,X} = 5.6\,\text{ps}$. In the subsequent application, the linear triatomic molecule with its molecular Z-axis has to be pre-aligned along the laboratory-fixed z-axis, cf. Fig. 2.10, again using techniques of nonadiabatic alignment of non-polar molecules [210, 213]. One expects that the maximum of the alignment duration of the linear triatomic molecule is about 10 % of the rotational revival time, cf. Section 3.3.1, i.e. $\Delta\tau_{X,max} \approx 0.1\,\tau_{rev,X}$. Hence, $\Delta\tau_{X,max}$ is approximately 5 ps for FHF^- and 500 fs for $^{114}CdH_2$.

Let us investigate nuclear ring currents and induced magnetic fields in bending and pseudorotational excited degenerate states $|v_b = 1^{l=\pm1}\rangle = |(v_s = 0, v_b = 1^{l=\pm1}, v_a = 0)\rangle$ of the electronic ground state $|X\,^1\Sigma_g^+\rangle$ of linear triatomic molecules FHF^- and $^{114}CdH_2$. We use the harmonic approximation in order to calculate nuclear probability and current densities, electric ring currents, and induced magnetic fields, see Section 2.4. In this approximation, the total vibrational energy of twofold degenerate states $|1^{\pm1}\rangle$ is

$$E^h_{v_s=v_a=0,v_b=1,l=\pm1} = \frac{\hbar\omega_s}{2} + \frac{\hbar\omega_a}{2} + 2\hbar\omega_b, \tag{3.136}$$

cf. Eq. (2.255). The corresponding total angular momentum is $\langle\hat{\mathbf{L}}_{tot}\rangle = \pm\hbar\mathbf{e}_Z$ (Eq. (2.326)). Figs. 3.28 and 3.29 show the total nuclear probability $\rho_{tot}(\mathbf{R})$ (Eq. (2.295)) and current densities $\mathbf{j}_{tot}(\mathbf{R})$ (Eq. (2.314)) of vibrational states $|1^{\pm1}\rangle$ of FHF^- and $^{114}CdH_2$ molecules. For FHF^-, the maxima of the nuclear probability and current densities are located at $Z = \pm R_e = \pm 2.15\,a_0$, $\rho = 0.0077\,a_0$ and $\rho = 0.0055\,a_0$, respectively. For $^{114}CdH_2$, the maxima of the nuclear probability and current densities are located at $Z = 0$, $\rho = 0.0054\,a_0$ and $\rho = 0.0038\,a_0$, respectively. The toroidal shapes of the probability and

	FHF^-	$^{114}CdH_2$
M_A/u	18.998	1.0078
M_B/u	1.0078	113.903
$\tilde{Z}_A$	9	1
$\tilde{Z}_B$	1	48
R_e/a_0	2.15	3.16
$B_{e,X}/(hc\,\mathrm{cm}^{-1})$	0.342	3.00
$\tau_{rev,X}$/ps	48.8	5.6
$\omega_s/(2\pi c\,\mathrm{cm}^{-1})$	640.3	1864.0
$\omega_a/(2\pi c\,\mathrm{cm}^{-1})$	1333.7	1849.5
$\omega_b/(2\pi c\,\mathrm{cm}^{-1})$	1367.2	629.2

Table 3.6: Properties of linear triatomic molecules FHF^- and $^{114}CdH_2$ in the electronic ground state $|X\,^1\Sigma_g^+\rangle$, i.e. nuclear masses M_A and M_B in unified atomic mass unit ($1\,\mathrm{u} = 1.66054 \cdot 10^{-27}\,\mathrm{kg}$), nuclear charges $\tilde{Z}_A$ and $\tilde{Z}_B$ where A=F, B=H for FHF^- and A=H, B=Cd for $^{114}CdH_2$, equilibrium bond lengths R_e between nuclei A and B, rotational constants $B_{e,X}$, corresponding rotational revival times $\tau_{rev,X} = \pi\hbar/B_{e,X}$, and vibrational harmonic frequencies ω_s for the symmetric stretch, ω_a for the antisymmetric stretch, and ω_b for the bend, adapted from Refs. [208] for FHF^- (cf. Ref. [295]) and [207] for $^{114}CdH_2$.

current densities representing the rotations of the H and F/Cd nuclei about the Z-axis are large and small due to different masses of the light and heavy nucleus, respectively. The nodal lines of the probability and current densities coincide with the molecular Z-axis. For FHF^-, the hydrogen bond in excited states $|1^{\pm1}\rangle$ is no longer located along the Z-axis ("linear hydrogen bond"), but around it — this means that we have discovered a new type of hydrogen bond, denoted as "toroidal hydrogen bond" [208]. We recognize that the ratio of widths of nuclear probability and current densities along ρ- and Z-axes is determined by the factor $f = \omega_b/\omega_{\tilde{a}}$ (Eq. (2.352)) for the nucleus A and $f = \omega_b/\omega_a$ (Eq. (2.354)) for the nucleus B. The toroidal shapes are spherical for $f \approx 1$, oblate for $f < 1$, and prolate for $f > 1$. For FHF^-, the toroidal shapes of H and F nuclei are spherical ($f = 1.03$) and strongly prolate ($f = 83.7$), respectively, cf. Figs. 2.8 and 3.28. For $^{114}CdH_2$, the toroidal shapes of the H nuclei are oblate ($f = 0.68$), where the corresponding shape of the Cd nucleus is a little more oblate ($f = 0.34$), cf. Figs. 2.8 and 3.29. Due to the factor $1/\rho$ in Eq. (2.314), the nuclear current density approaches the Z-axis more closely than the nuclear probability density, cf. Figs. 3.28 and 3.29.

The bending and pseudorotational states $|1^{\pm1}\rangle$ represent unidirectional anti-clockwise (+) and clockwise (−) toroidal ring currents of the nuclei about the molecular Z-axis. They have strong electric ring currents of the F and Cd nuclei and the weak ones of

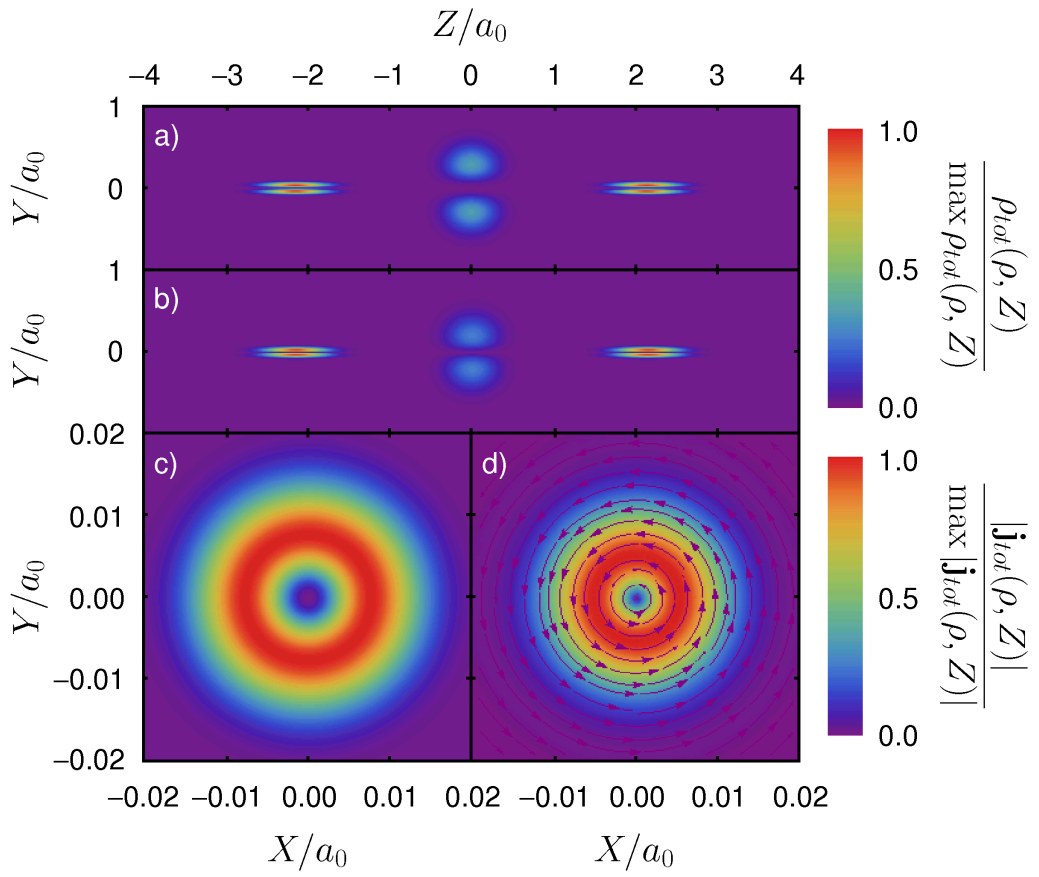

Figure 3.28: Nuclear probability $\rho_{tot}(\rho, Z)$ (Eq. (2.295)) (a, c) and current densities $\mathbf{j}_{tot}(\rho, Z)$ (Eq. (2.314)) (b, d) in the Y/Z ($X = 0$) (a, b) and X/Y ($Z = \pm R_e = \pm 2.15\, a_0$) (c, d) planes, for vibrational states $|1^{\pm 1}\rangle$ of FHF^-. The F and H nuclei are located in the left/right and middle regions (a, b), respectively. For better visualization, $\rho_F(\rho, z)$ and $\mathbf{j}_F(\rho, z)$ are enlarged by a factor 5, whereas $\rho_H(\rho, z)$ and $\mathbf{j}_H(\rho, z)$ are increased by factors 2000 and 40, respectively. Panel d shows the direction of $\mathbf{j}_F(\rho, z)$ only for $|1^1\rangle$; the corresponding direction for $|1^{-1}\rangle$ would be opposite. In panel b, the nuclei of the state $|1^1\rangle$ at $Y > 0$ and $Y < 0$ move toward and away from the reader, respectively, and backwards for $|1^{-1}\rangle$.

the H nuclei (Eqs. (2.332) and (2.333)) because of the large nuclear charges $\tilde{Z}_F = 9$ and $\tilde{Z}_{Cd} = 48$ compared to $\tilde{Z}_H = 1$, i.e.

$$I_F = \pm 59.1\, \mu A \quad (3.137)$$

$$I_H = \pm 6.6\, \mu A \quad (3.138)$$

and

$$I_{Cd} = \pm 145.1\, \mu A \quad (3.139)$$

$$I_H = \pm 3.0\, \mu A \quad (3.140)$$

for FHF^- and $^{114}CdH_2$, respectively. The corresponding total electric ring currents (Eq. (2.331)) and mean periods of the nuclei (Eq. (2.334)) circulating about the molecular

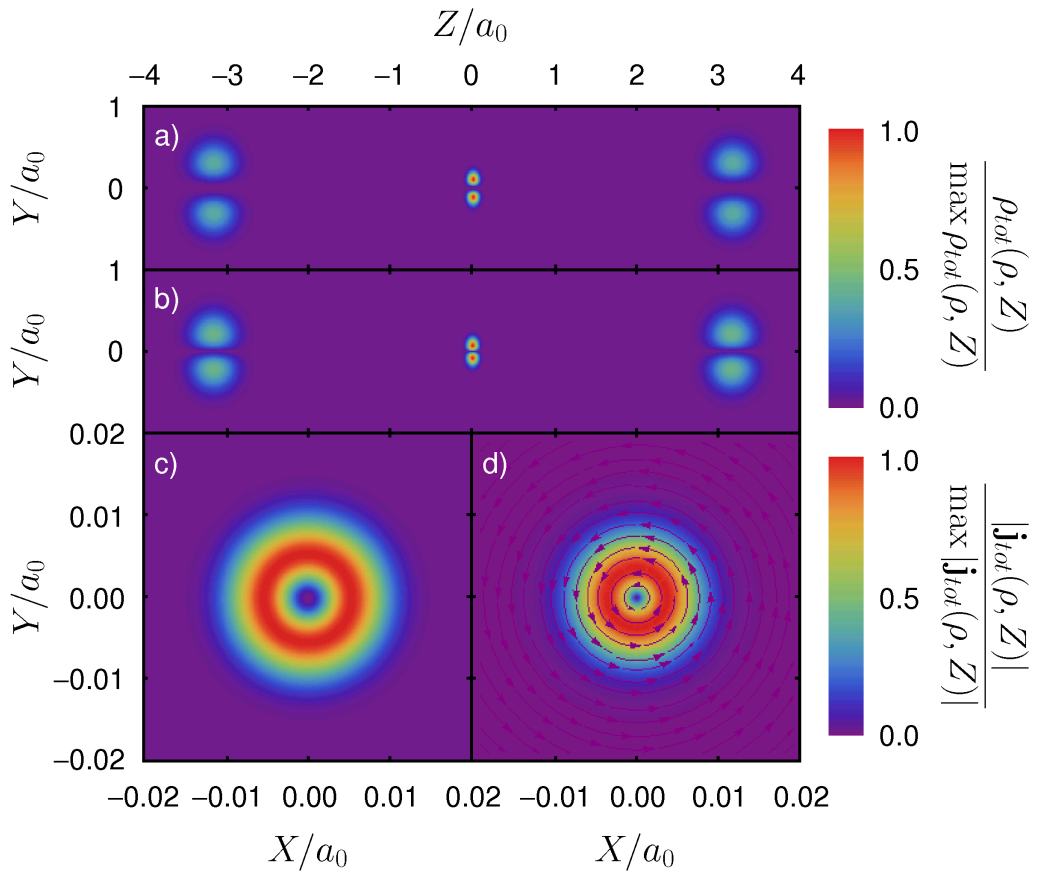

Figure 3.29: Nuclear probability $\rho_{tot}(\rho, Z)$ (Eq. (2.295)) (a, c) and current densities $\mathbf{j}_{tot}(\rho, Z)$ (Eq. (2.314)) (b, d) in the Y/Z ($X = 0$) (a, b) and X/Y ($Z = 0$) (c, d) planes, for vibrational states $|1^{\pm 1}\rangle$ of $^{114}CdH_2$. The Cd and H nuclei are located in the middle and left/right regions (a, b), respectively. For better visualization, $\rho_{Cd}(\rho, z)$ and $\mathbf{j}_{Cd}(\rho, z)$ are enlarged by a factor 20, whereas $\rho_H(\rho, z)$ and $\mathbf{j}_H(\rho, z)$ are increased by factors 10^5 and 2000, respectively. Panel d shows the direction of $\mathbf{j}_{Cd}(\rho, z)$ only for $|1^1\rangle$; the corresponding direction for $|1^{-1}\rangle$ would be opposite. In panel b, the nuclei of the state $|1^1\rangle$ at $Y > 0$ and $Y < 0$ move toward and away from the reader, respectively, and backwards for $|1^{-1}\rangle$.

Z-axis are

$$I_{FHF^-} = \pm 124.8\,\mu A \tag{3.141}$$
$$I_{^{114}CdH_2} = \pm 151.1\,\mu A \tag{3.142}$$

and

$$T_{FHF^-} = 24.4\,fs \tag{3.143}$$
$$T_{^{114}CdH_2} = 53.0\,fs, \tag{3.144}$$

respectively.

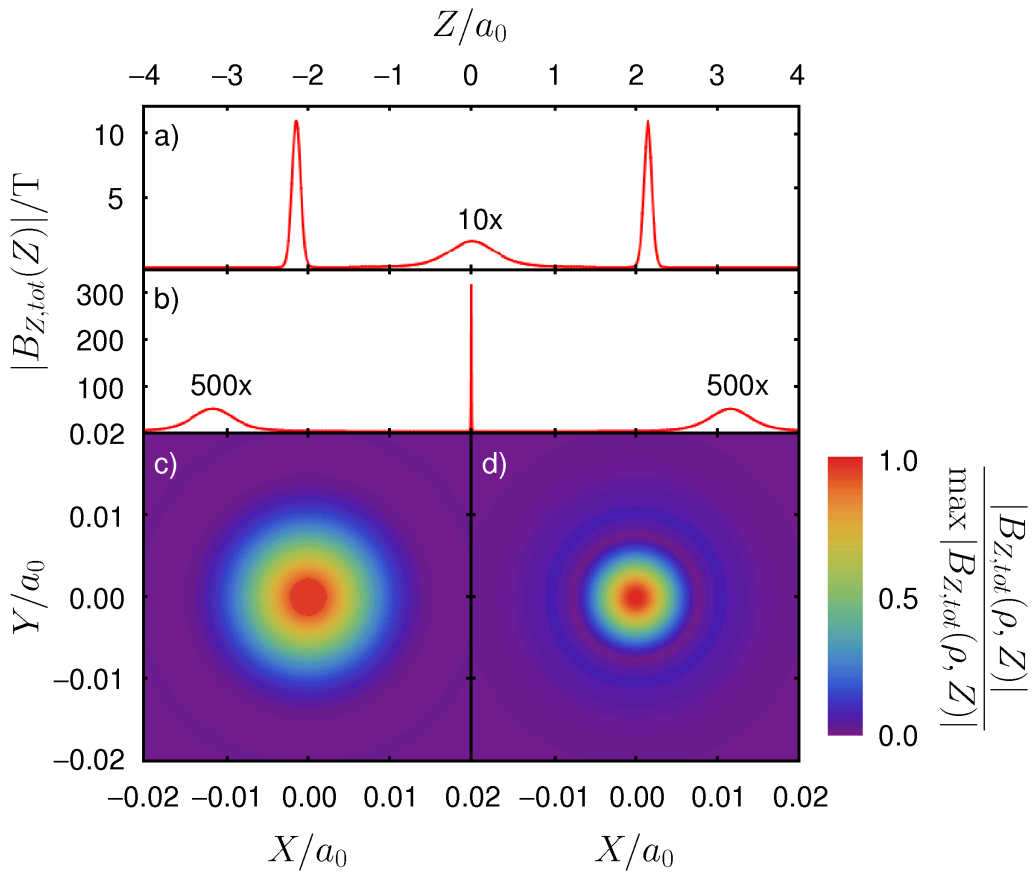

Figure 3.30: Induced magnetic fields $\mathbf{B}_{tot}(\rho, Z)$ along the Z-axis (a, b) and in the X/Y plane ($Z = \pm R_e = \pm 2.15\,a_0$ for FHF^- (c) and $Z = 0$ for $^{114}CdH_2$ (d)), for vibrational states $|1^{\pm 1}\rangle$ of FHF^- (a, c) and $^{114}CdH_2$ (b, d). The locations of the nuclei are the same as in Figs. 3.28 and 3.29. For better visualization in panels a and b, $\mathbf{B}_{\mathrm{H}}(Z)$ is increased by factors 10 and 500, respectively. In panels c and d, the ρ-component of $\mathbf{B}_{tot}(\rho, Z)$ is very small and thus negligible. For $|1^1\rangle$, the induced magnetic fields in the center regions of panels c and d are directed away from the reader. For $|1^{-1}\rangle$, the situation would be reversed. The maxima of the induced magnetic fields are given in Eqs. (3.145) and (3.146).

The nuclear ring currents of vibrational states $|1^{\pm 1}\rangle$ induce magnetic fields $\mathbf{B}_{tot}(\mathbf{R})$; the corresponding induced magnetic fields along the Z-axis, i.e. $\mathbf{B}_{tot}(Z)$, are given in Eqs. (2.335)–(2.338). Fig. 3.30 shows the induced magnetic fields for linear triatomic molecules FHF^- and $^{114}CdH_2$. The induced magnetic fields are independent of the azimuthal angle ϕ and strongest at the centers of the ring currents of the heavy nuclei, i.e. $\rho = 0$, $Z = \pm R_e = \pm 2.15\,a_0$ for FHF^- and $\rho = 0$, $Z = 0$ for $^{114}CdH_2$. The corresponding maxima of the induced magnetic fields of excited states $|1^{\pm 1}\rangle$ (cf. Eqs. (2.350) and (2.351)) are

$$\max|\mathbf{B}_{tot}(\mathbf{R})| \;=\; |\mathbf{B}_{tot}(\pm R_e)| \;=\; 10.9\,\mathrm{T} \;\approx\; |\mathbf{B}_{\mathrm{F}}(\pm R_e)| \tag{3.145}$$

and

$$\max|\mathbf{B}_{tot}(\mathbf{R})| \;=\; |\mathbf{B}_{tot}(0)| \;=\; 318\,\mathrm{T} \;\approx\; |\mathbf{B}_{\mathrm{Cd}}(0)| \tag{3.146}$$

for FHF^- and $^{114}CdH_2$, respectively. If the shape of the current density of the F nucleus would be not prolate, i.e. spherical or oblate, then the maximum of the corresponding induced magnetic field would be on the order of $50\,\mathrm{T} - 100\,\mathrm{T}$, because the integral I_U for $v_b = |l| = 1$ and $f = \omega_b/\omega_{\tilde{a}} = 1$ (spherical), i.e. $I_U = 0.7523$ (Eq. (2.365)), is larger than that for $f = \omega_b/\omega_{\tilde{a}} = 83.7$ (oblate), i.e. $I_U = 0.1205$, cf. Fig. 2.8. The induced magnetic fields at the centers of the ring currents of the hydrogen nuclei are comparatively very small, i.e.

$$|\mathbf{B}_{tot}(0)| \;=\; 200\,\mathrm{mT} \;\approx\; |\mathbf{B}_{\mathrm{H}}(0)| \tag{3.147}$$

and

$$|\mathbf{B}_{tot}(\pm R_e)| \;=\; 99\,\mathrm{mT} \;\approx\; |\mathbf{B}_{\mathrm{H}}(\pm R_e)| \tag{3.148}$$

for FHF^- and $^{114}CdH_2$, respectively, cf. Eqs. (2.350) and (2.351). Furthermore, the approximations (2.339) and (2.340) are very good, since the magnetic field induced by the nuclear ring current, strongly localized at the corresponding center, is approximately zero at the centers of the other nuclear ring currents, cf. Fig. 3.30. However, the width of the magnetic field induced by the ring current of the F nucleus along the Z-axis is broader than for Cd, because of the prolate shape of the toroidal ring current of the F nucleus.

The mean ring current radii of excited states $|1^{\pm 1}\rangle$, using Eqs. (2.380), (2.382), (2.384), and (2.386), are

$$R_{1,\mathrm{F}} \;=\; 0.0069\,a_0 \tag{3.149}$$
$$R_{-1,\mathrm{F}} \;=\; 0.0044\,a_0 \tag{3.150}$$
$$R_{1,\mathrm{H}} \;=\; 0.26\,a_0 \tag{3.151}$$
$$R_{-1,\mathrm{H}} \;=\; 0.16\,a_0 \tag{3.152}$$

for FHF^- and

$$R_{1,\mathrm{Cd}} \;=\; 0.0048\,a_0 \tag{3.153}$$
$$R_{-1,\mathrm{Cd}} \;=\; 0.0030\,a_0 \tag{3.154}$$
$$R_{1,\mathrm{H}} \;=\; 0.27\,a_0 \tag{3.155}$$
$$R_{-1,\mathrm{H}} \;=\; 0.17\,a_0 \tag{3.156}$$

for $^{114}CdH_2$, cf. Table 2.1. Note that the ring current radius $R_{-1,\mathrm{F}}$ for the F nucleus is about 67 times larger than the nuclear radius of F. However, for the Cd nucleus, the current radius $R_{-1,\mathrm{Cd}}$ is only 25 times larger than its radius, implying that the strong induced magnetic fields are sharply located inside these nuclear ring currents, cf. Fig. 3.30.

state	$\Delta E_{v_b\|l\|,0}$ $(hc\,\mathrm{cm}^{-1})$
0^0	0.0
$1^{\pm1}$	1304.6
2^0	2602.5
$2^{\pm2}$	2613.2
$3^{\pm1}$	3867.5
$3^{\pm3}$	3925.3
4^0	5335.3
$4^{\pm2}$	5342.7
$4^{\pm4}$	5240.0

Table 3.7: Anharmonic excitation energies $\Delta E_{v_b|l|,0} = E_{(v_s=0,v_b^l,v_a=0),0} - E_{(0,0^0,0),0}$ of bending and pseudorotational states $|v_b^l\rangle = |(v_s = 0, v_b^l, v_a = 0)\rangle$ in the electronic ground state $|X\,^1\Sigma_g^+\rangle$ of the FHF^- molecule [208].

The different effects of the induced magnetic fields at the centers of the nuclear ring currents of Cd in $^{114}CdH_2$ and F in FHF^- can be understood simply by using Biot-Savart law in the current loop model. Using Eqs. (2.93), (2.94), and (2.334) with nuclear charge Q, the result is $|\mathbf{B}| = \mu_0 Q/(2RT) = \mu_0 Q\omega/(4\pi R)$. This approximation shows that the induced magnetic fields are strong for heavy atoms (large nuclear charge Q and small ring current radius R) and for high degenerate vibrational frequencies ω. It can also be applied to non-linear pseudorotating molecules such as the tetrahedral UH_4 molecule in pseudorotational excited degenerate antisymmetric vibrational states, see also conclusions in Chapter 4.

For the complete population transfer from the vibrational ground state $|0^0\rangle$ to the first excited pseudorotational state $|1^1\rangle$ by means of a right circularly polarized laser pulse, we employ an anharmonic model to avoid multiphoton transitions to higher excited vibrational levels (ladder climbing), see also Fig. 2.9. For the electronic ground state $|X\,^1\Sigma_g^+\rangle$ of the FHF^- molecule, the anharmonic excitation energies $\Delta E_{v_b|l|,0} = E_{(v_s=0,v_b^l,v_a=0),0} - E_{(0,0^0,0),0}$ of bending and pseudorotational states $|v_b^l\rangle = |(v_s = 0, v_b^l, v_a = 0)\rangle$ are listed in Table 3.7, adapted from Ref. [208]. However, for FHF^-, we use the linear approximation of the dipole function (Eq. (2.419)) in order to calculate the transition dipole matrix elements (Eq. (2.415)). We use $\partial\tilde{M}_\perp(Q_s, Q_a, Q_b)/\partial Q_b|_{Q_s=Q_a=Q_b=0} = 0.0869\,e$, which is determined from ab initio calculations [208]. For the choice of the effective pulse duration of the laser pulse, we calculate the anharmonicity of the FHF^- molecule, $\Delta E = 4\,hc\,\mathrm{cm}^{-1}$ (Eq. (2.436)), i.e. the spectral width Γ of the laser pulse must be smaller than ΔE. Hence,

the effective pulse duration τ of the $\cos^{20}$ envelope must satisfy the condition

$$\tau = \frac{2.826\,\hbar}{\Gamma_{20}} > \frac{2.826\,\hbar}{\Delta E} = 3.75\,\text{ps}, \tag{3.157}$$

cf. Eqs. (2.109) and (2.436). On the other hand, the effective pulse duration τ must be shorter than the maximum of the alignment duration of the FHF^- molecule, i.e.

$$\tau < \Delta\tau_{X,max} \approx 5\,\text{ps}. \tag{3.158}$$

For FHF^-, we use $\tau = 4\,\text{ps}$. The corresponding total pulse duration is $t_{p,c} = 33.8\,\text{ps}$.

Note that for $^{114}CdH_2$, the anharmonicity is $\Delta E = 4.7\,hc\,\text{cm}^{-1}$ (cf. Eq. (2.436) and Table 3.8). For the complete population transfer $|0^0\rangle \rightarrow |1^1\rangle$ of the $^{114}CdH_2$ molecule, the spectral width must be smaller than $4.7\,hc\,\text{cm}^{-1}$ and the corresponding effective pulse duration of the $\cos^{20}$ envelope must be larger than 3.19 ps which does not satisfy the other condition $\tau < \Delta\tau_{X,max} \approx 500\,\text{fs}$. Thus, the complete population transfer $|0^0\rangle \rightarrow |1^1\rangle$ for $^{114}CdH_2$ cannot be achieved by means of a right circularly polarized laser pulse, given by Eq. (2.99), with effective pulse duration less than 500 fs; for further details, see Section 3.5.2.

Assuming that the molecule FHF^- is pre-aligned along the laboratory-fixed z-axis and that the laser pulse is centered at the revival time $t_c = t^*$, we reoptimize the laser parameters of the right circularly polarized IR laser pulse (Eq. (2.99)) with $\cos^{20}$ envelope (Eq. (2.100)) in order to achieve a complete population transfer $|0^0\rangle \rightarrow |1^1\rangle$. The reoptimized laser parameters, starting from the reference values $\mathcal{E}_c = 81.8\,\text{MV m}^{-1}$ and $\hbar\omega_c = 1304.6\,hc\,\text{cm}^{-1}$ for the resonant π laser pulse, are $\mathcal{E}_c = 81.9\,\text{MV m}^{-1}$ and $\hbar\omega_c = 1303.8\,hc\,\text{cm}^{-1}$. The corresponding maximum intensity is $I_{max,c} = 1.78\,\text{GW cm}^{-2}$. Because of the short optical cycle period $\Delta t_c = 2\pi/\omega_c = 25.6\,\text{fs}$ compared to the effective pulse duration $\tau = \tau_c = 4\,\text{ps}$, i.e. there are about 156 laser cylces during 4 ps, only the time-dependent intensity $I_c(t)$ (Eq. (2.114)) of a right circularly polarized reoptimized π laser pulse is shown in Fig. 3.31.

The time-dependent populations $P_{v_b l}(t)$ of bending and pseudorotational states $|0^0\rangle$, $|1^1\rangle$, and $|2^2\rangle$ are also shown in Fig. 3.31, where the other states have negligible populations during the vibrational excitation. This figure clearly shows that a right circularly polarized reoptimized π laser pulse excites the state $|1^1\rangle$ almost completely from the ground state $|0^0\rangle$. The corresponding final populations $P_{v_b l}(t_f)$ (Eq. (2.426)) of vibrational states $|0^0\rangle$, $|1^1\rangle$, and $|2^2\rangle$ are 0.011, 0.951, and 0.038, respectively. The non-zero transient population of the bending and pseudorotational state $|2^2\rangle$ is due to the double ladder climbing $(v_b, l \rightarrow v_b + 1, l + 1)$, see Fig. 2.9. As a consequence of the double ladder climbing, the mean values $\langle v_b(t)\rangle$ and $\langle l(t)\rangle$ (Eqs. (2.427)) and (2.428)) are indistinguishable in Fig. 3.31,

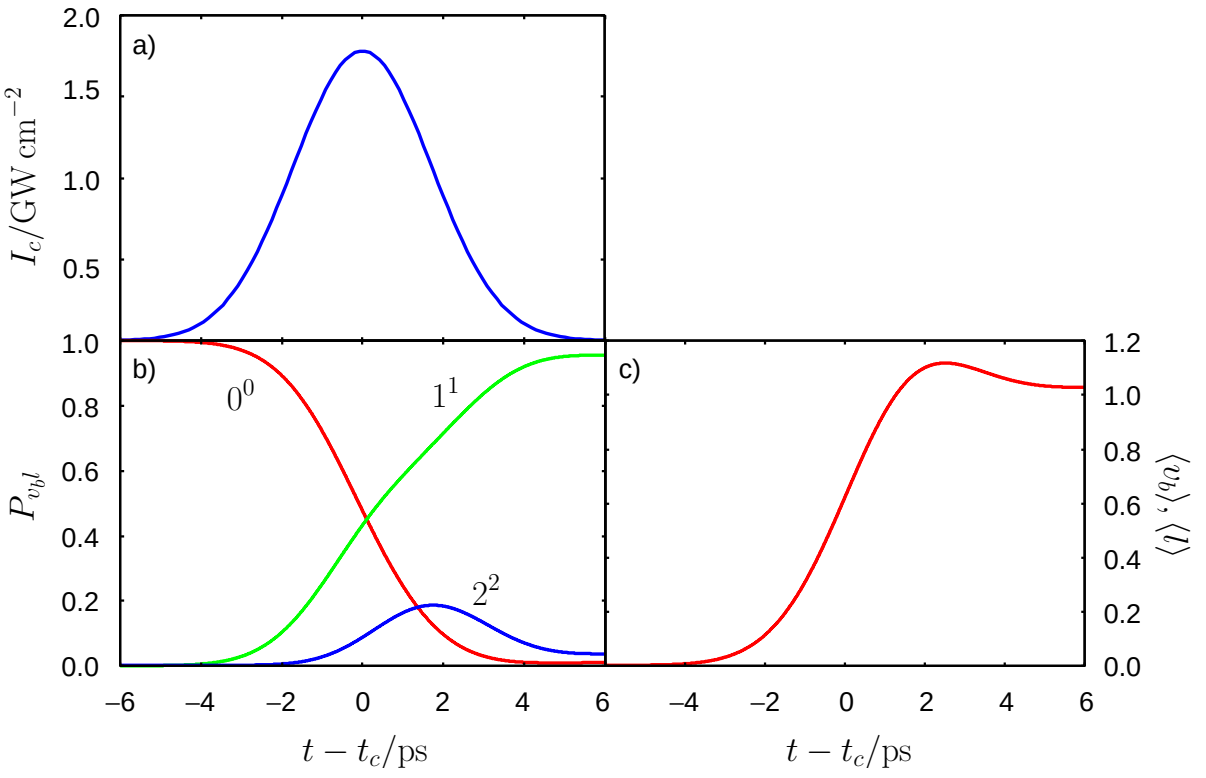

Figure 3.31: Selective population transfer $|0^0\rangle \rightarrow |1^1\rangle$ of FHF^- by means of a right circularly reoptimized π laser pulse centered at the revival time $t_c = t^*$. Panels a, b, and c show the time-dependent intensity $I_c(t)$ (Eq. (2.114)) of the laser pulse, the time-dependent populations $P_{v_b l}(t)$ (Eq. (2.426)) of bending and pseudorotational states $|0^0\rangle$ (red), $|1^1\rangle$ (green), $|2^2\rangle$ (blue), and the corresponding mean values $\langle v_b(t)\rangle$ (Eq. (2.427)) and $\langle l(t)\rangle$ (Eq. (2.428)), respectively. Note that the magnitudes of $\langle v_b(t)\rangle$ and $\langle l(t)\rangle$ are on the same scale, i.e. $\langle v_b(t)\rangle \approx \langle l(t)\rangle$.

i.e. $\langle v_b(t)\rangle \approx \langle l(t)\rangle$. At the final time t_f, these mean values are equal to 1.03, i.e. the corresponding mean value of the Z-component of the total angular momentum at the final time is $\langle \hat{L}_{tot,Z}(t_f)\rangle = 1.03\,\hbar$ (Eq. (2.429)).

3.5.2 Nuclear pseudorotation

For the vibrational excitation of anharmonic bending and pseudorotational states $|v_b^l\rangle = |(v_s = 0, v_b^l, v_a = 0)\rangle$ ($v_b \leq 10$) in the electronic ground state $|X\,^1\Sigma_g^+\rangle$ of $^{114}CdH_2$ by means of a right circularly polarized laser pulse, the anharmonic excitation energies $\Delta E_{v_b|l|,0} = E_{(v_s=0,v_b^l,v_a=0),0} - E_{(0,0^0,0),0}$ for $v_b \leq 10$ (see Table 3.8) and anharmonic dipole matrix elements $\langle v_b^l|\tilde{M}_\perp|v_b^{l'}\rangle$ (cf. Eqs. (2.416) and (2.417)) adapted from Ref. [207] are used in the following quantum dynamical calculations. As discussed in Section 3.5.1, the complete

state	$\Delta E_{v_b\|l\|,0}$ ($hc\,\mathrm{cm}^{-1}$)	state	$\Delta E_{v_b\|l\|,0}$ ($hc\,\mathrm{cm}^{-1}$)	state	$\Delta E_{v_b\|l\|,0}$ ($hc\,\mathrm{cm}^{-1}$)	state	$\Delta E_{v_b\|l\|,0}$ ($hc\,\mathrm{cm}^{-1}$)
0^0	0.0	$5^{\pm1}$	2941.3	$7^{\pm5}$	4107.1	$9^{\pm5}$	5205.8
$1^{\pm1}$	605.9	$5^{\pm3}$	2955.5	$7^{\pm7}$	4148.0	$9^{\pm7}$	5245.1
2^0	1199.5	$5^{\pm5}$	2983.9	8^0	4617.5	$9^{\pm9}$	5297.5
$2^{\pm2}$	1207.1	6^0	3505.2	$8^{\pm2}$	4624.2	10^0	5706.4
$3^{\pm1}$	1788.9	$6^{\pm2}$	3512.2	$8^{\pm4}$	4644.3	$10^{\pm2}$	5712.8
$3^{\pm3}$	1803.7	$6^{\pm4}$	3533.1	$8^{\pm6}$	4677.7	$10^{\pm4}$	5732.3
4^0	2366.9	$6^{\pm6}$	3567.9	$8^{\pm8}$	4724.5	$10^{\pm6}$	5764.4
$4^{\pm2}$	2374.1	$7^{\pm1}$	4066.1	$9^{\pm1}$	5166.3	$10^{\pm8}$	5809.4
$4^{\pm4}$	2395.9	$7^{\pm3}$	4079.8	$9^{\pm3}$	5179.5	$10^{\pm10}$	5867.2

Table 3.8: Anharmonic excitation energies $\Delta E_{v_b|l|,0} = E_{(v_s=0,v_b^l,v_a=0),0} - E_{(0,0^0,0),0}$ of bending and pseudorotational states $|v_b^l\rangle = |(v_s = 0, v_b^l, v_a = 0)\rangle$ in the electronic ground state $|X\,^1\Sigma_g^+\rangle$ of the $^{114}CdH_2$ molecule [207].

population transfer from the vibrational ground state $|0^0\rangle$ to the excited state $|1^1\rangle$ cannot be achieved by means of a right circularly polarized laser pulse. The reason is that the $^{114}CdH_2$ molecule rotates faster than FHF^-, due to the light masses of the H nuclei. The maximum alignment duration of $^{114}CdH_2$ is only about 500 fs whereas the condition of the spectral width of the laser pulse (Eq. (2.436)) implies $\tau \geq 3.19\,\mathrm{ps}$.

Here, we use a right circularly polarized IR laser pulse (Eq. (2.99)) with $\cos^{20}$ envelope (Eq. (2.100)) and short pulse duration, $\tau = 50\,\mathrm{fs}$, in order to achieve field-free nuclear pseudorotation of $^{114}CdH_2$. The corresponding total pulse duration is $t_{p,c} = 423.1\,\mathrm{fs}$. As for the FHF^- molecule, the $^{114}CdH_2$ molecule is aligned during the vibrational excitation ($x = X$ and $y = Y$), where the circularly polarized laser pulse is centered at the revival time $t_c = t^*$. We optimize the amplitude of the electric field $\mathcal{E}_c$ and laser frequency ω_c so that the sum of final populations of excited states $|v_b^l\rangle$ ($1 \leq v_b \leq 4$) is maximal. Thus, the final populations of higher-lying vibrational states $v_b \geq 5$ are supressed, using non-resonant laser frequency ω_c to avoid double ladder climbing to higher excited states. The optimized laser parameters are $\mathcal{E}_c = 6.00\,\mathrm{GV\,m^{-1}}$ and $\hbar\omega_c = 777.0\,hc\,\mathrm{cm}^{-1}$ (compare $\hbar\omega_b = 629.9\,hc\,\mathrm{cm}^{-1}$). The corresponding maximum intensity is $I_{max,c} = 9.56\,\mathrm{TW\,cm^{-2}}$. Fig. 3.32 shows the X- and Y-components of the right circularly polarized electric field $\mathbf{E}_{c+}(t) = E_{X,c+}\mathbf{e}_X + E_{Y,c+}(t)\mathbf{E}_Y$ (Eq. (2.99)) and the corresponding time-dependent intensity $I_c(t)$ (Eq. (2.114)).

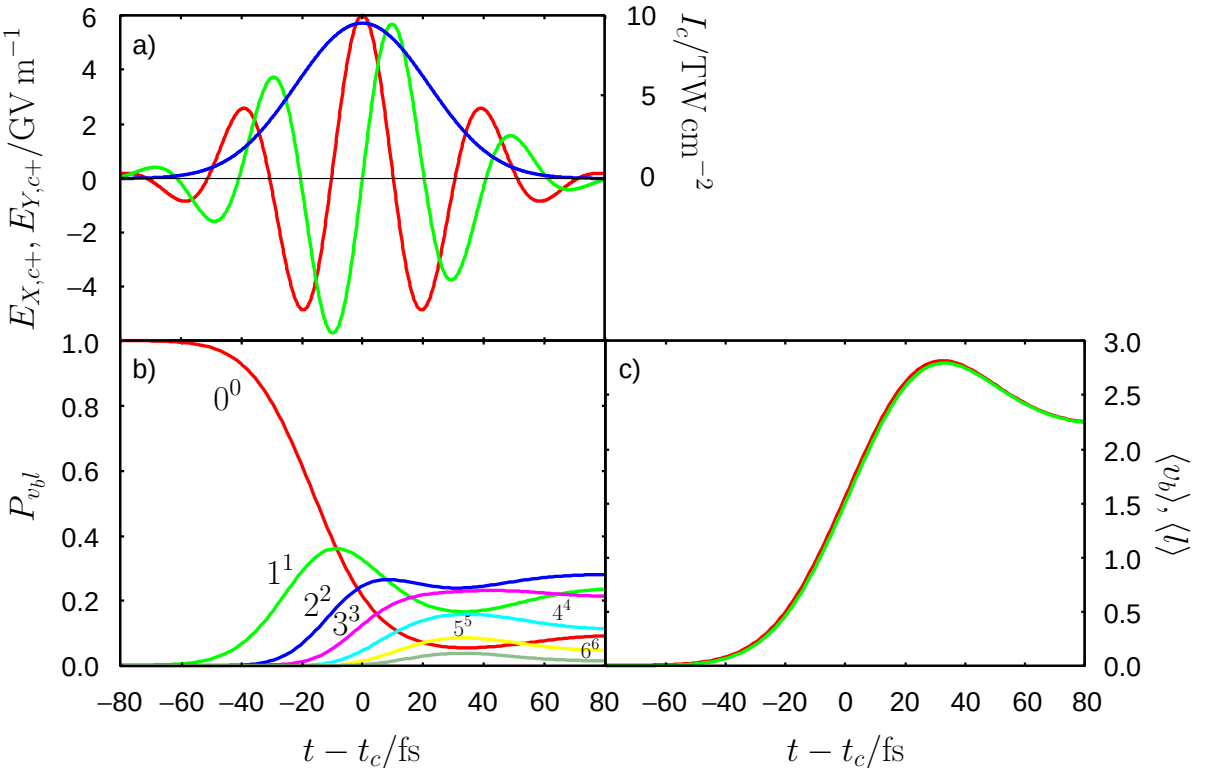

Figure 3.32: Vibrational dynamics of $^{114}CdH_2$ by means of a right circularly polarized 50 fs laser pulse centered at the revival time $t_c = t^*$. Panel a shows the X- (red) and Y- (green) components of the time-dependent electric field $\mathbf{E}_{c+}(t)$ (Eq. (2.99)) and the corresponding time-dependent intensity $I_c(t)$ (Eq. (2.114)) (blue). In panel b, the time-dependent populations $P_{v_b l}(t)$ (Eq. (2.426)) of bending and pseudorotational states $|0^0\rangle$ (red), $|1^1\rangle$ (green), $|2^2\rangle$ (blue), $|3^3\rangle$ (magenta), $|4^4\rangle$ (cyan), $|5^5\rangle$ (yellow), and $|6^6\rangle$ (gray) are drawn. Panel c shows the corresponding mean values $\langle v_b(t)\rangle$ (red, Eq. (2.427)) and $\langle l(t)\rangle$ (green, Eq. (2.428)).

Fig. 3.32 also shows the time-dependent populations $P_{v_b l}(t)$ of bending and pseudorotational states $|v_b^l\rangle$ $(0 \leq v_b = l \leq 6)$. Because of the non-resonant laser pulse, the high-lying excited states $|v_b^l\rangle$ $(7 \leq v_b = l \leq 10)$ have negligible populations during the vibrational excitation. Furthrmore, the populations of the other states $|v_b^l\rangle$ $(v_b \neq l)$ are also negligible due to double ladder climbing $(v_b, l \rightarrow v_b + 1, l + 1)$, see Fig. 2.9. The vibrational ground state $|0^0\rangle$ is therefore transferred sequentially to the dominant excited bending and pseudorotational states $|v_b^l\rangle$ $(1 \leq v_b = l \leq 4)$, by dominant absorption processes $|0^0\rangle \rightarrow |1^1\rangle \rightarrow |2^2\rangle \rightarrow |3^3\rangle \rightarrow |4^4\rangle \rightarrow \ldots$, cf. Refs. [98, 296] for simple vibrational ladder climbing in one-dimensional oscillator models. The transient stimulated emission processes, i.e. $|3^3\rangle \rightarrow |2^2\rangle$, $|2^2\rangle \rightarrow |1^1\rangle$, and $|1^1\rangle \rightarrow |0^0\rangle$, after ca. 30 fs are also observed. The final populations of dominant states $|v_b^l\rangle$ $(1 \leq v_b = l \leq 4)$ are $P_{00}(t_f) = 0.095$, $P_{11}(t_f) = 0.238$, $P_{22}(t_f) = 0.282$, $P_{33}(t_f) = 0.210$, and $P_{44}(t_f) = 0.111$. The other vibrational states $|5^5\rangle$, $|6^6\rangle$, and $|7^7\rangle$ have negligible final populations $P_{55}(t_f) = 0.046$,

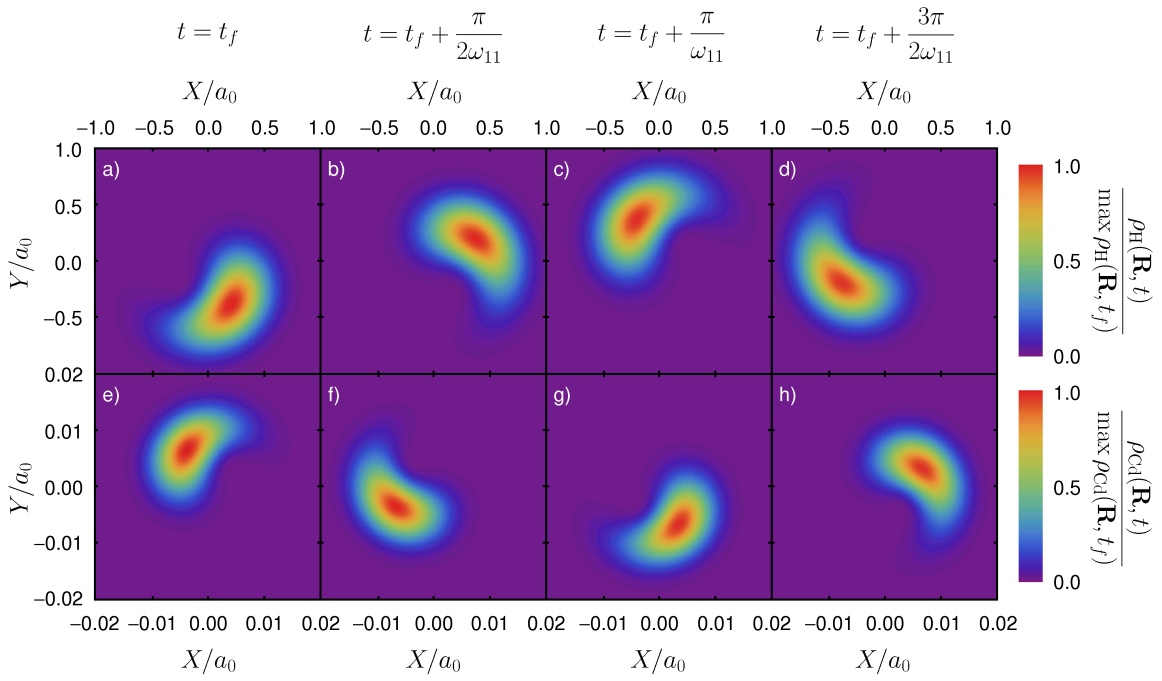

Figure 3.33: Nuclear pseudorotation of the $^{114}CdH_2$ molecule after the end of the right circularly polarized laser pulse (see Fig. 3.32). Panels a–d and e–h show the time-dependent probability densities $\rho_{\mathrm{H}}(\mathbf{R},t)$ and $\rho_{\mathrm{Cd}}(\mathbf{R},t)$ of the H and Cd nuclei at $Z = \pm R_e = 3.16\,a_0$ and $Z = 0$ (Eqs. (2.430)–(2.432)), respectively. The corresponding snapshots are shown at times $t = t_f + 2\pi k/\omega_{11}$ $(k = 0, 1/4, 1/2, 3/4)$, where $\omega_{11} = \Delta E_{11,0}/\hbar = 605.9\,(2\pi c)\,\mathrm{cm}^{-1}$ is the anharmonic frequency of the state $|1^1\rangle$ (see Table 3.8).

$P_{66}(t_f) = 0.014$, and $P_{77}(t_f) = 0.003$, respectively. The sum of final populations of excited states $|v_b^l\rangle$ $(1 \leq v_b \leq 4)$ is 0.841, which also implies that the final populations of excited states $|v_b^l\rangle$ $(1 \leq v_b \leq 4, v_b \neq l)$ are negligible $(\sum_{v_b,l=1}^{4} P_{v_b l}(t_f) - \sum_{v_b=l=1}^{4} P_{v_b l}(t_f) = 0.841 - 0.841 = 0.000)$. This fact is also supported by the time-dependent mean values $\langle v_b(t)\rangle$ (Eq. (2.427)) and $\langle l(t)\rangle$ (Eq. (2.428)), illustrated in Fig. 3.32. Thus, the double ladder climbing is confirmed by almost perfect agreement $\langle v_b(t)\rangle \approx \langle l(t)\rangle$. Furthermore, initial absorption processes and subsequent competitions with stimulated emission processes (after ca. 30 fs) lead to the non-monotonic time evolution of $\langle v_b(t)\rangle$ and $\langle l(t)\rangle$. At the final time, these mean values are $\langle v_b(t_f)\rangle = \langle l(t_f)\rangle = 2.22$, and the corresponding mean value of the Z-component of the total angular momentum is $\langle \hat{L}_{tot,Z}(t_f)\rangle = 2.22\,\hbar$ (Eq. (2.429)).

After the end of the right circularly polarized 50 fs laser pulse, the vibrational state $|\Phi(t)\rangle$ after the final time t_f consists of bending and pseudorotational states $|v_b^l\rangle$ $(v_b = l)$, where the corresponding coefficients $C_{v_b l}(t)$ for $t \geq t_f$ are time-independent. The bending and pseudorotational wavepacket $|\Phi(t)\rangle$ is, however, time-dependent due to the time-dependent exponential factors in Eqs. (2.430)–(2.432). The snapshots of the time-

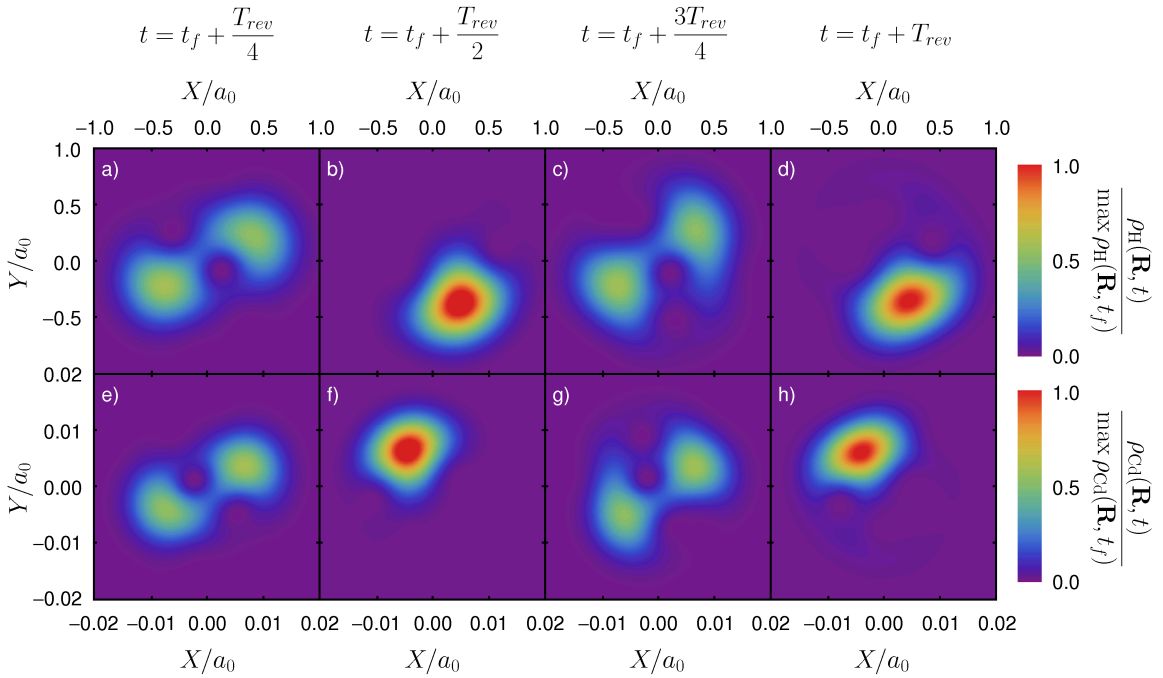

Figure 3.34: Revival structures of the nuclear pseudorotation of the $^{114}CdH_2$ molecule after the end of the right circularly polarized laser pulse (see Fig. 3.32). Same as in Fig. 3.34, but the time-dependent probability densities are shown at longer times $t = t_f + kT_{rev}$ ($k = 1/4, 1/2, 3/4, 1$), where $T_{rev} = 14.2\,\mathrm{ps}$ is the pseudorotational revival time. Panels d and h are similar to panels a and e of Fig. 3.33, respectively.

dependent probability densities $\rho_{\mathrm{H}}(\mathbf{R},t)$ and $\rho_{\mathrm{Cd}}(\mathbf{R},t)$ of the H and Cd nuclei at $Z = \pm R_e = \pm 3.16\,a_0$ and $Z = 0$, and at times $t = t_f + 2\pi k/\omega_{11}$ ($k = 0, 1/4, 1/2, 3/4$) (one cycle) are shown in Fig. 3.33, respectively. Here, the anharmonic vibrational energies $E_{v_b|l|,0}$ (see Table 3.8) and harmonic approximation of vibrational wave functions are used. Fig. 3.33 clearly shows that the H and Cd nuclei at opposite locations circulate anti-clockwise about the Z-axis with the anharmonic frequency $\omega_{11} = \Delta E_{11,0}/\hbar = 605.9\,(2\pi c)\,\mathrm{cm}^{-1}$ of the state $|1^1\rangle$, corresponding to the anharmonic peseudorotational period $\tau_{11} = 55.1\,\mathrm{fs}$.

Because of the anharmonicity of bending and pseudorotational levels, the vibrational wavepacket dephases after several cycles and recurs at intervals of the pseudorotating revival time T_{rev},

$$T_{rev} \;=\; 4\pi\hbar \left| \frac{\partial^2 E_{v_b=|l|,0}}{\partial {v_b}^2} \right|^{-1}_{v_b=\langle v_b(t_f)\rangle} \;\approx\; 14 - 15\,\mathrm{ps}, \tag{3.159}$$

cf. Ref. [263, 264, 266]. For Morse potentials, the revival time T_{rev} is constant because the anharmonic energies have only terms with exponents $n = 0, 1, 2$ of v_b. However, for exact anharmonic systems, the second-order derivative in Eq. (3.159) is no longer constant and the revival time T_{rev} is dependent on $\langle v_b(t)\rangle$. In this case, the vibrational wavepackets at times t_f and $t_f + T_{rev}$ are not exactly equal but similar, cf. Refs. [264, 266]. Using

anharmonic energies of $^{114}CdH_2$ from Table 3.8, the pseudorotating revival time T_{rev} (Eq. (3.159)) is estimated between 14 ps and 15 ps. In numerical calculations, we found that the probability densities at times t_f and $t_f + T_{rev}$ are similar, if $T_{rev} = 14.2$ ps. Fig. 3.34 shows the time-dependent probability densities of the H and Cd nuclei at times $t_f + T_{rev}/4$, $t + T_{rev}/2$, $t + 3T_{rev}/4$, and $t + T_{rev}$. As predicted in Ref. [263], the vibrational wavepacket recurs also at $t_f + T_{rev}/2$, but the relative phase of the wavepackets at t_f and $t_f + T_{rev}/2$ is π. At times $t_f + T_{rev}/4$ and $t_f + 3T_{rev}/4$, the pseudorotation of the $^{114}CdH_2$ molecule is separated into two regions with the corresponding probabilities of about 0.5.

However, the alignment duration $\Delta\tau_{X,max} \approx 500$ fs of the $^{114}CdH_2$ molecule is much shorter than the pseudorotational revival time $T_{rev} = 14.2$ fs. Since the rotational revival time of $^{114}CdH_2$ is $\tau_{rev,X} = 5.6$ ps (still shorter than the pseudorotational revival time), the rotational wavepacket recurs at times $t_0 + n\tau_{rev,X} \approx t_f + n\tau_{rev,X}$ ($n = 1, 2, \ldots$). The ratio of the pseudorotational and rotational revival times is $T_{rev}/\tau_{rev,X} \approx 2.5 = 5/2$. This ratio implies that the total (rotational and vibrational) wavefunction recurs at the time $t_f + 2T_{rev} \approx t_f + 5\tau_{rev,X} \approx 28$ ps, where the difference of $2T_{rev}$ and $5\tau_{rev,X}$ is less than the maximum of the alignment duration $\Delta\tau_{X,max} \approx 500$ fs of the $^{114}CdH_2$ molecule.

Chapter 4

Conclusions and Outlook

In this work, concepts for the generation of electron circulations, nuclear pseudorotations, electronic and nuclear ring currents, and associated induced magnetic fields in atoms, ions, and aligned/oriented molecules by means of circularly polarized laser pulses have been developed, with demonstrations by quantum dynamics simulations for exemplary model systems, see also Refs. [144–150]. The four main challenges of this work, listed in Section 1.3, were accomplished:

1. Stationary electronic and nuclear ring currents and associated induced magnetic fields can be controlled by means of circularly polarized UV/visible and IR optimized π laser pulses, respectively, where the direction of ring currents is determined by the sense of circular polarization. Ring currents occur in electronic and vibrational degenerate states. In this work, twofold degenerate excited states $|\Psi_\pm\rangle$ in the complex representation were used, which are easily obtained from degenerate states $|\Psi_x\rangle$ and $|\Psi_y\rangle$ in the real representation by simple transformation (Eq. (2.29)). We have investigated electronic ring currents in atomic orbitals of the hydrogen atom and one-electron ions (Section 3.2), in excited states $|A\,^1\Pi_\pm\rangle$ of oriented linear molecules AlCl and BeO (Section 3.3), and in excited states $|n\,^1E_{u\pm}\rangle$ $(n = 2, 4, 5)$ of the aligned ring-shaped molecule Mg-porphyrin (Section 3.4), and nuclear ring currents in excited bending and pseudorotational degenerate states $(v_b = 1, l = \pm 1)$ of linear triatomic molecules FHF^- and $^{114}CdH_2$ (Section 3.5).

   By means of a circularly polarized optimized π laser pulse, the population of the excited degenerate target state is transferred selectively from the electronic or vibrational non-degenerate initial state. For electronic excitation, the effective pulse duration, typically of the order of $\tau_c = 2.5\,\text{fs}$, is shorter than vibrational and rotational periods of the molecule. Thus, the molecule was considered frozen during

the electronic FC-type excitation. For vibrational (bending and pseudorotational) excitation, the electronic states are not excited due to off-resonance of the laser pulse and the linear triatomic molecule is aligned during the excitation. The anharmonicity of the bending and pseudorotational state, and the alignment duration of the linear triatomic molecule play an important role for the selective population transfer from the vibrational ground state ($v_b = 0, l = 0$) to the excited bending and pseudorotational state ($v_b = 1, l = \pm 1$). For FHF^-, the effective pulse duration of $\tau_c = 4\,\text{ps}$ is sufficient in order to achieve an optimal final population of the excited state. However, for $^{114}CdH_2$, the first excited pseudorotational state cannot be selectively populated from the vibrational ground state because the rotational revival time of $^{114}CdH_2$ is too short and the anharmonicity of bending and pseudorotational states is too small. In this case, the full optimization of the ultrashort laser pulse (with effective pulse duration less than the alignment duration of the molecule) through an evolutionary algorithm would overcome this problem.

2. Analytical results for electronic probability and current densities, corresponding electric ring currents, mean ring current radii, and induced magnetic fields in atomic orbitals of the hydrogen atom and one-electron ions show that the effects are strongest for $2p_\pm$ atomic orbitals and high nuclear charges Z, see Section 3.2. Electric ring current and induced magnetic field at the nucleus are proportional to Z^2 and Z^3, respectively, whereas the mean ring current radius is proportonal to Z^{-1}. The corresponding non-relativistic magnitudes for $2p_\pm$ atomic orbitals range from 0.132 mA, 0.52 T, and $1.273\,a_0$ for H ($Z = 1$) to 22.3 mA, 1146 T, and $0.098\,a_0$ for Al^{12+} ($Z = 13$). The huge induced magnetic fields in $2p_\pm$ atomic orbitals of Al^{12+} are obviously much stronger than the currently available experimental permanent magnetic fields, ca. 90 T [230].

   As demonstrated in Section 3.2.6, the electric ring currents and induced magnetic fields can be estimated for electronic ring currents in many-electron atomic and molecular systems, using CIS and LCAO-MO approximations and Slater rules for estimation of the effective nuclear charge Z_{eff}. The corresponding approximate values compare well with the exact values, using CASSCF orbitals carrying electronic ring currents. The exact induced magnetic fields in excited states $|1\,^1D_{\pm1}\rangle$ and $|1\,^1D_{\pm2}\rangle$ of singlet oxygen are 62.0 T and $2 \cdot 62.0\,\text{T} = 124.0\,\text{T}$, respectively. However, these states cannot be excited directly from the ground state $|1\,^3P_{\pm1}\rangle$ of triplet oxygen by means of a circularly polarized laser pulse due to different spin states. Another example is the electronic ground state $|1\,^2P_{\pm1}\rangle$ of the F atom, carrying electronic ring currents with induced magnetic fields of 95.2 T at the nucleus. In this case, the ring currents in ground states cannot be achieved from the 1 : 1 mixture of $|1\,^2P_{+1}\rangle$ and $|1\,^2P_{-1}\rangle$ states by a single circularly polarized laser pulse.

The accessible electronic ring currents induced by a circularly polarized UV/visible laser pulse are those of the excited electronic degenerate states with a dipole allowed transition from the ground state with the same spin multiplicity. Examples are the excited states $|A\,^1\Pi_\pm\rangle$ of linear molecules AlCl and BeO as well as excited states $|n\,^1E_{u\pm}\rangle$ $(n = 2, 4, 5)$ of the ring-shaped molecule Mg-porphyrin, see Sections 3.3 and 3.4. The LUMO $4\pi_\pm$ and HOMO $1\pi_\pm$ of excited states $|A\,^1\Pi_\pm\rangle$ of AlCl and BeO carry the dominant electronic ring currents, respectively. For AlCl, the corresponding electric ring currents and maxima of induced magnetic fields are 0.405 mA and 7.7 T located at the Al nucleus, respectively, whereas for BeO, they are 2.490 mA and 52.1 T located at the O nucleus. For Mg-porphyrin, we found that the electronic ring current, in general, depends on the electronic state, but the ring currents are similar for $|2\,^1E_{u\pm}\rangle$ and $|4\,^1E_{u\pm}\rangle$ states because these states carry dominant electronic ring currents of the same HOMO $4e_{g\pm}$. For these orbitals, the electric ring currents and maximum of induced magnetic fields located near carbon bridges are 85 μA and 0.21 T, respectively. Note that the electronic ring current can also be generated by means of a permanent magnetic field, but a magnetic field of the order of about 8000 T would be required in order to achieve the same electric ring current [148, 170, 179], i.e. the required magnetic field is about 100 times stronger than the permanent magnetic fields which can be produced with present-day technology [230]. Thus, the generation of electronic ring currents by means of circularly polarized laser pulses is more efficient than the traditional approach based on permanent magnetic fields. Furthermore, the laser pulse can control the structure of the electronic ring current. For example, the nature of the electronic ring current in excited states $|5\,^1E_{u\pm}\rangle$ is totally different. These states carry dominant electronic ring currents of $3e_{g\mp}$ molecular orbitals, having net electric ring currents of only 6 μA. But there are strong electric ring currents of about 30 μA along the bonds of pyrrole fragments, which induce magnetic fields of 0.11 T, located at the centers of the pyrrole fragments.

We also investigated nuclear ring currents in the first excited bending and pseudorotational states ($v_b = 1, l = \pm 1$) of linear triatomic molecules FHF^- and $^{114}CdH_2$ (Section 3.5). The net electric ring currents are similar, i.e. 125 μA for FHF^- and 151 μA for $^{114}CdH_2$. But the induced magnetic fields for FHF^- and $^{114}CdH_2$ are very different and can be explained based on analytical results for linear triatomic molecules, see Section 2.4.6. In fact, $^{114}CdH_2$ has the strong induced magnetic field of 318 T located at the center of the ring current of the Cd nucleus, whereas the maximum of the induced magnetic field for FHF^- reaches only 10.9 T located at centers of ring currents of the F nuclei. We conclude that the induced magnetic fields for HXH are stronger than for XHX, for heavy atoms X (large nuclear charge Q and small ring current radius R), and for high bending frequencies ω_b, in accord

with the Biot-Savart law in the current loop model where the induced magnetic field is proportional to $Q\omega/R$. Unfortunately, the rotational revival time of HXH is shorter than that of XHX, thus the vibrational bending and pseudorotational state ($v_b = 1, l = \pm 1$) of HXH cannot be excited completely by a circularly polarized IR optimized π laser pulse, if the anharmonicity of bending and pseudorotational states is too small.

3. Unidirectional electron circulation in the superposition of electronic non-degenerate ground and degenerate excited states is achieved by means of a circularly polarized UV/visible optimized $\pi/2$ laser pulse. After the end of the laser pulse, the electronic wavepacket is time-dependent. The corresponding probability and current densities as well as electric ring current and induced magnetic field are periodic in time and azimuthal angle, i.e. the electron circulates about the axis of symmetry. We have extensively investigated electron circulation in the superposition state consisting of $1s$ and $2p_+$ atomic orbitals with equal weights (Section 3.2.5), in the superposition of $|X\,^1\Sigma^+\rangle$ and $|A\,^1\Pi_+\rangle$ states of oriented AlCl and BeO (Section 3.3.3), and in the superposition of $|X\,^1A_{1g}\rangle$ and $|n\,^1E_{u+}\rangle$ ($n = 2, 4, 5$) states of aligned Mg-porpyhrin (Section 3.4.3). For electron circulation in a superposition of two electronic excited degenerate states, e.g. $|4\,^1E_{u+}\rangle$ and $|5\,^1E_{u+}\rangle$ of Mg-porphyrin, induced by means of two time-delayed circularly polarized optimized $\pi/2$ laser pulses, see Ref. [149].

   For the aligned linear triatomic molecule $^{114}CdH_2$, nuclear pseudorotation, representing several dominant bending and pseudorotational states ($v_b = l = 0, \ldots, 4$), can be induced by means of a right circularly polarized IR 50 fs laser pulse (Section 3.5.2). We showed that double ladder climbing ($v_b \rightarrow v_b + 1$, $l \rightarrow l + 1$) for right circular polarization is the reason for the excitation of vibrational states with the same bending and pseudorotational quantum numbers ($v_b = l$), starting from the vibrational ground state ($v_b = l = 0$). After the end of the laser pulse, the Cd and H nuclei circulate about the pre-aligned molecular Z-axis with a period of about 55 fs. But the nuclear pseudorotation does not persist for a long time, due to dephasing of vibrational wavepacket in the superposition of anharmonic vibrational states. This anharmonicity leads to the bending and pseudorotational revival pattern. The corresponding revival time for $^{114}CdH_2$ is estimated as $T_{rev} = 14.2$ ps, whereas the rotational revival time is $\tau_{rev,X} = 5.6$ ps, i.e. the nuclear pseudorotation of aligned $^{114}CdH_2$ will recur at $2T_{rev} \approx 5\tau_{rev,X} \approx 28$ ps after the end of the laser pulse.

4. Finally, we also demonstrated the nonadiabatic field-free orientation of polar AlCl and BeO molecules by means of a HCP-like linearly polarized laser pulse (Sections 2.6 and 3.3.1). In this work, we have considered the requirement that the integral of the electric field over time is zero, cf. Eq. (2.439) and Refs. [141,242,243]. Thus, the laser pulse consists of two parts, i.e. a strong short HCP-like laser pulse following

by a weak long switch-off laser pulse. For BeO at the rotational temperature of 1 K, the HCP-like laser pulse was optimized in order to yield the maximum (negative) orientation of BeO along the polarization axis. The pulse duration of the first part of the laser pulse is 1.39 ps, i.e. much shorter than the rotational revival time of BeO, $\tau_{rev,X} = 10.30$ ps. Hence, the rotational wavepacket evolves nonadiabatically after the end of the laser pulse under field-free conditions and the rotational revival pattern is observed. The thermally averaged expectation value of $\cos\theta$ reaches -0.850 at intervals of the rotational revival time, implying strong orientation of BeO in the negative z-direction. At these times, the normalized angular distribution is strongly located between 160° and 180°. The corresponding orientation duration is estimated as 0.52 ps. For AlCl, we use the simple scalings for laser parameters to obtain equivalent quantum dynamics of the rotational wavepacket. Since the rotational revival time of AlCl is $\tau_{rev,X} = 68.4$ ps, determined by the rotational constant of the molecule [225], all times for AlCl can be estimated from those for BeO by multiplying the latter by $68.4/10.30 = 6.64$. For example, the pulse duration of the first part of the laser pulse and orientation duration are 9.22 ps and 3.4 ps, respectively, but the rotational temperature is reduced by the same factor, i.e. 0.151 K for AlCl.

The basic concept of the laser control of electronic and nuclear ring currents, introduced in this work, opens different interesting research projects for future work:

1. In various quantum chemistry packages, one can compute electronic probability densities of molecular electronic states, but to the best of my knowledge, the computation of stationary electronic current densities of degenerate states, associated electric ring currents, and induced magnetic fields has not been implemented yet. One could develop corresponding routines in quantum chemistry packages to investigate electronic ring currents in different symmetric molecules, depending on the electronic state. Stationary electronic ring currents do not only occur in atoms, ions [144], and linear molecules [145, 146], but also in non-linear molecules, including ring-shaped molecules such as benzene [297] with D_{6h} symmetry, metal-porphyrins [147–150, 292, 298, 299], metal-porphyrazines [292, 298], metal-tetrabenzoporphyrins [298,299], and metal-phthalocyanines [298,300] with D_{4h} symmetry as well as corresponding sandwiches with C_{4v} [301] or D_{4d} [302] symmetries. Furthermore, electronic ring currents also exist in non-ring-shaped molecules such as planar XY_4 (D_{4h}), tetrahedral XY_4 (T_d), and octahedral XY_6 (O_h) molecules because of their existence of twofold and threefold (only for T_d and O_h) degenerate states. Investigation of electronic ring currents in n-fold ($n = 2 - 5$) degenerate states of high-symmetric fullerene C_{60} (I_h) [303] would be very interesting.

2. Since Mg-porphyrin (D_{4h}) (for direct synthesis of Mg-porhpyrin, see [304]) is the core molecule of the important biomolecule chlorophyll [305,306] with lowest molecular symmetry C_1, one could compute non-stationary electronic ring currents in the superposition of near-degenerate states of chlorophyll, with comparison of corresponding ring currents in Mg-porphyrin to investigate the influence of the symmetry-breaking of the molecule on electronic ring currents.

3. In most cases, after the FC-type electronic transition by a circularly polarized laser pulse, the molecule vibrates in the degenerate state because of different equilibrium structures of the electronic ground and excited states. The corresponding electronic ring current is no longer stationary and vibrates with the vibrational period of the molecule, i.e. the circulating electron travels with the vibrating nuclei. For linear molecules, the z-component of the electronic current density $j_z(\mathbf{r}, t)$ is no longer zero, i.e. the approach for calculating electronic and nuclear fluxes (currents) [259] could be extended to electronic degenerate states. The corresponding electric ring currents and induced magnetic fields are also time-dependent. For longer times, there is vibrational revival pattern, i.e. the electronic ring current follows this revival pattern with the same vibrational revival time. Research in this field, i.e. electronic ring currents in vibrating molecules, would also be very interesting, in particular for probing electron dynamics in excited degenerate states.

4. Long-lived electronic ring currents in electronic degenerate ground states of atoms and molecules could be achieved by different techniques. For example, the LiF molecule has a dissociative excited state $|A\,^1\Pi_+\rangle$ that can be excited by an optimized right circularly polarized laser pulse from the ground state $|X\,^1\Sigma^+\rangle$. After the complete electronic transition, the LiF molecule dissociates into atomic fragments Li and F in corresponding $|X\,^2S\rangle$ and $|X\,^2P_+\rangle$ electronic states, respectively. Regardless of spin effects, the ground state of the Li atom carries no electronic ring current, but the ground state of the F atom carries a long-lived electronic ring current, dominated by the $2p_+$ atomic orbital, with an induced magnetic field of about 95.2 T at the nucleus. Another example are the electronic ground states $|X\,^2\Pi_\pm\rangle$ of the NO molecule carrying opposite electronic ring currents. At the initial time, the weights of these degenerates states are equal, i.e. the net electronic ring current is zero. By means of a right circularly polarized pump laser pulse, the electronic and vibrational ground state $|X\,^2\Pi_-(\nu = 0)\rangle$ is transferred to the first excited state $|1\,^2\Sigma^+(\nu' > 0)\rangle$ whereas the other state $|X\,^2\Pi_+(\nu = 0)\rangle$ cannot be affected. Then, the molecule in the excited state $|1\,^2\Sigma^+(\nu' > 0)\rangle$ vibrates and has no electronic ring current. After a delay time, the left circularly polarized dump laser pulse with smaller laser frequency induces the population transfer from the excited state $|1\,^2\Sigma^+(\nu' > 0)\rangle$ to the electronic ground but vibrational excited state $|X\,^2\Pi_+(\nu > 0)\rangle$, via induced

emission. After the dump laser pulse, the NO molecule is in a superposition of the electronic ground and vibrational excited state $|X\,^2\Pi_+(\nu > 0)\rangle$ and the remaining electronic and vibrational ground state $|X\,^2\Pi_+(\nu = 0)\rangle$. This superposition state carries non-stationary but long-lived electronic ring current in the electronic ground state of the vibrating molecule NO. This control is analogous to the selective preparation of enantiomers from a racemate by a series of circularly polarized laser pulses, see Ref. [107].

5. In this work, the non-relativistic approximation was used, i.e. some relativistic effects of electronic ring currents were neglected. This approximation can be applied to electronic ring currents in excited singlet states, where spin effects are neglected, and with low effective nuclear charge Z_{eff}. In the relativistic regime, the current density always exists in all spin-orbitals due to the fact that it contains not only the orbit but also spin current densities, see the decomposition of the relativistic current density in its orbital and spin parts in Refs. [189, 307, 308]. Thus, the degenerate states with non-zero spin quantum numbers $S \neq 0$ and $M_S \neq 0$ also carry electronic ring currents, even if the magnetic quantum number M_L is zero. Using the Dirac theory for the hydrogen atom and one-electron ions, one can show that the expressions for the electric ring current (Eq. (3.30)) and induced magnetic fields (Eq. (3.42)) for quantum numbers $j = n - \frac{1}{2}$ are modified, by replacing l by j and m by m_j, and by multiplying relativistic correction factors which are important for large nuclear charges Z. Because m_j is always non-zero, there are relativistic electronic ring currents in all atomic spin-orbitals. For ground state degenerate spin-orbitals $1s_{\frac{1}{2},\pm\frac{1}{2}}$ of the H atom, the electric ring current is 1.05 mA and the associated induced magnetic field at the nucleus is 16.7 T which are about 8 and 32 times stronger than the corresponding non-relativistic results for $2p_\pm$ atomic orbitals, respectively. The relativistic results can also be applied to highly charged ions such as one-electron U^{91+} ions with nuclear charge $Z = 92$. The electric ring current in the ground state is very strong, i.e. 12.0 A, corresponding to the mean period of 13.4 zs (zeptosecond, $1\,\text{zs} = 10^{-21}\,\text{s}$). The associated induced magnetic field at the nucleus, 36.4 MT, is comparable to the magnetic fields in neutron stars, ca. 100 MT. Note that the Dirac theory is valid only for Z below 100 because there are quantum electrodynamics effects for Z above 100. The results of relativistic ring currents and associated induced magnetic fields in atomic spin-orbitals will be published elsewhere. One still has to consider the generation of relativistic electronic ring currents in the ground state by means of a series of linearly and circularly polarized laser pulses, even in the relativistic regime [309], see also the work on quantum dynamics of relativistic electrons [310]. In a similar context, the spin asymmetry in the ionization of the H atom by means of intense circularly polarized laser fields is already predicted in Ref. [311].

6. For the generation of electronic ring currents by means of circularly polarized laser pulses, we have assumed that the nuclei are fixed in space because of extremely large differences in the masses of nuclei and electrons. However, for electronic ring currents in $2p_\pm$ atomic orbitals of the H atom or He^+ ion with light nuclear masses, the center of mass is no longer located at the nucleus, i.e. it is located outside the nucleus. This leads to the electronic and nuclear ring currents of the $2p_\pm$ atomic orbitals about the center of mass. The electric ring currents for nuclei are estimated as $0.132\,\mathrm{mA}$ for H ($Z = 1$) and $2 \cdot 0.527\,\mathrm{mA} = 1.05\,\mathrm{mA}$ for He^+ ($Z = 2$), see Table 3.1. Since the corresponding mean radii of the nuclear ring currents are much smaller than those of the electronic ring currents, i.e. about $0.0007\,a_0$ for H and $0.00009\,a_0$ for He^+, the associated magnetic fields induced by nuclear ring currents at the center of mass are on the order of about $1000\,\mathrm{T}$ for H and $60000\,\mathrm{T}$ for He^+, i.e. they clearly exceed the magnetic fields induced by the corresponding electronic ring currents. Work on this topic is in progress and will be published elsewhere.

7. Nuclear pseudorotations and stationary nuclear ring currents in electronic non-degenerate ground states appear in all vibrational degenerate states of symmetric molecules, cf. Ref. [206]. They can be induced by means of circularly polarized laser pulses, starting from vibrational non-degenerate ground states. The vibrational degenerate states carrying nuclear ring currents are not necessarily bending states, e.g. for linear triatomic molecules, but also other degenerate states, exemplarily for antisymmetric vibrational T_2 modes of tetrahedral (T_d) molecules XY_4. The advantage of the antisymmetric stretches is the high vibrational frequency $\nu_3 = \omega_a$ compared to the bending frequency $\nu_4 = \omega_b$ with the same symmetry T_2, see e.g. Ref. [312]. Since the vibrational T_2 state is threefold degenerate, the pre-alignment of the XY_4 molecule is not necessary for the estimation of electric ring currents and magnetic fields induced by nuclear ring currents in the harmonic approximation. To achieve the small mean ring current radius R_X of the central nucleus X with high vibrational frequency ω_a and, hence, strong induced magnetic fields at the center of the molecule, the XH_4 molecule in the electronic non-degenerate singlet ground state $|X\,{}^1A_1\rangle$ is considered where the mass M_X and charge Q_X of the nucleus X are large, e.g. X=U. This is in accord with the Biot-Savart law in the current loop model, i.e. the induced magnetic field is proportional to $Q_X\omega_a/R_X$. Examples are the ReH_4^-, OsH_4 [313], and UH_4 [314, 315] molecules with T_d symmetry. First approximations of the magnetic fields induced by stationary nuclear ring currents in the first excited antisymmetric vibrational T_2 states of these molecules leads to the result of the order of about $5000\,\mathrm{T}$ at the center of the molecule. Work on this topic is currently in progress.

8. In this work, we have assumed perfect alignment/orientation of the molecule during the electronic or vibrational excitation by means of a circularly polarized laser pulse. In reality, as discussed in Section 3.3.1, laser induced alignment/orientation can be rather sharp but it is never perfect, see also Figs. 3.10 and 3.11. Application of the same circularly polarized laser pulse to the non-perfectly aligned/oriented molecule gives rise to additional dipole allowed transitions. For example, the electronic $|\Sigma^+\rangle \leftrightarrow |\Sigma^+\rangle$ and vibrational $|(v_s, v_b^l, v_a)\rangle \leftrightarrow |(v_s, v_b^l, v_a \pm 1)\rangle$ transitions for linear triatomic molecules become allowed because the projection of the molecular Z-axis on the laboratory-fixed x- or y-axis is non-zero. Therefore, the electronic and nuclear ring currents are no longer perfect, i.e. the corresponding electric ring currents and induced magnetic fields are no longer maximal, see also the discussion in Ref. [146]. The influence of non-perfect molecular alignment/orientation on the generation of electronic and nuclear ring currents should also be investigated in the future.

9. Finally, there are several suggestions for experimental detections of electronic and nuclear ring currents with associated induced magnetic fields. For example, the electronic ring currents and, in particular, their directions could be monitored by HHG by means of elliptically polarized laser pulses [77], by asymmetric photoelectron spectra [243, 316, 317], or by momentum imaging techniques, e.g. cold target recoil ion momentum spectroscopy (COLTRIMS) [318, 319]. Perhaps, the strong magnetic fields induced by electronic or nuclear ring currents could be used for nuclear magnetic resonance (NMR) and electron spin resonance (ESR) spectroscopy. Another suggested detection of the induced magnetic field is the depolarisation of neutron spins by collisions of neutrons and atomic or molecular systems carrying ring currents due to the interaction of neutron spins and induced magnetic fields. The strong magnetic fields induced by nuclear ring currents in pseudorotating molecules could be used for the detection of new interactions, i.e. nuclear spin - nuclear orbit interaction, which would lead to additonal energy splitting, in analogy to electron spin - electron orbit interaction which causes the well-known fine structure splitting.

Appendix A

Integrals

A.1 Integrals involving Gaussian functions

The integral $I_{v_s v_a}(Q)$ (Eq. (2.269)) for $v_s = v_a = 0$

$$I_{00}(Q) = \frac{M}{M_B}\int_{-\infty}^{\infty}\left(\Phi^h_{v_s=0}(Q'-Q)\right)^2\left(\Phi^h_{v_a=0}\left(-\frac{M}{2M_B}(Q+Q')\right)\right)^2 dQ' \tag{A.1}$$

with

$$\Phi^h_{v_s=0}(Q_s) = \left(\frac{s}{\pi}\right)^{1/4} e^{-\frac{1}{2}sQ_s^2} \tag{A.2}$$

$$\Phi^h_{v_a=0}(Q_a) = \left(\frac{a}{\pi}\right)^{1/4} e^{-\frac{1}{2}aQ_a^2} \tag{A.3}$$

(Eqs. (2.245) and (2.246)) is evaluated as

$$\begin{aligned}
I_{00}(Q) &= \frac{\sqrt{as}}{\pi}\frac{M}{M_B}\int_{-\infty}^{\infty} e^{-s(Q'-Q)^2-\frac{aM^2}{4M_B^2}(Q+Q')^2} dQ' \qquad (A.4)\\
&= \frac{\sqrt{as}}{\pi}\frac{M}{M_B}\, e^{-\left(s+\frac{aM^2}{4M_B^2}\right)Q^2}\int_{-\infty}^{\infty} e^{-\left(s+\frac{aM^2}{4M_B^2}\right)Q'^2+2\left(s-\frac{aM^2}{4M_B^2}\right)Q'Q} dQ'\\
&= \frac{\sqrt{as}}{\pi}\frac{M}{M_B}\, e^{-\frac{4sM_B^2+aM^2}{4M_B^2}Q^2}\int_{-\infty}^{\infty} e^{-\frac{4sM_B^2+aM^2}{4M_B^2}\left[Q'^2-2\frac{4sM_B^2-aM^2}{4sM_B^2+aM^2}Q'Q\right]} dQ'\\
&= \frac{\sqrt{as}}{\pi}\frac{M}{M_B}\, e^{\frac{4sM_B^2+aM^2}{4M_B^2}\left[\left(\frac{4sM_B^2-aM^2}{4sM_B^2+aM^2}\right)^2-1\right]Q^2}\\
&\qquad \int_{-\infty}^{\infty} e^{-\frac{4sM_B^2+aM^2}{4M_B^2}\left[Q'^2-2\frac{4sM_B^2-aM^2}{4sM_B^2+aM^2}Q'Q+\left(\frac{4sM_B^2-aM^2}{4sM_B^2+aM^2}\right)^2Q^2\right]} dQ'
\end{aligned}$$

$$
\begin{aligned}
&= \frac{\sqrt{as}}{\pi}\frac{M}{M_B}\, e^{\frac{1}{4M_B^2}\left[\frac{\left(4sM_B^2-aM^2\right)^2-\left(4sM_B^2+aM^2\right)^2}{4sM_B^2+aM^2}\right]Q^2}\int_{-\infty}^{\infty} e^{-\frac{4sM_B^2+aM^2}{4M_B^2}\left(Q'-\frac{4sM_B^2-aM^2}{4sM_B^2+aM^2}\,Q\right)^2} dQ' \\
&= \frac{\sqrt{as}}{\pi}\frac{M}{M_B}\, e^{-\frac{4asM^2}{4sM_B^2+aM^2}\,Q^2}\int_{-\infty}^{\infty} e^{-\frac{4sM_B^2+aM^2}{4M_B^2}Q''^2} dQ'' \\
&= \frac{1}{\pi}\sqrt{\frac{4asM^2}{4sM_B^2+aM^2}}\, e^{-\frac{4asM^2}{4sM_B^2+aM^2}\,Q^2}\int_{-\infty}^{\infty} e^{-y^2} dy \\
&= \frac{1}{\sqrt{\pi}}\sqrt{\frac{4asM^2}{4sM_B^2+aM^2}}\, e^{-\frac{4asM^2}{4sM_B^2+aM^2}\,Q^2} \\
&= \sqrt{\frac{4aM^2}{4sM_B^2+aM^2}}\left[\Phi^h_{v_s=0}\left(\sqrt{\frac{4aM^2}{4sM_B^2+aM^2}}\,Q\right)\right]^2
\end{aligned}
$$

where the formula for the Gamma function $\Gamma(z)$ $(z>0)$ [253, 254]

$$\Gamma(z) = \int_0^{\infty} x^{z-1}e^{-x}\,dx \tag{A.5}$$

was used, hence

$$\int_{-\infty}^{\infty} e^{-y^2}dy = 2\int_0^{\infty} e^{-y^2}dy = \int_0^{\infty}\frac{1}{\sqrt{x}}\,e^{-x}dx = \Gamma\left(\frac{1}{2}\right) = \sqrt{\pi}. \tag{A.6}$$

Note that if z is a positive integer, then [253, 254]

$$\Gamma(z) = (z-1)!. \tag{A.7}$$

A.2 Integrals involving associated Laguerre polynomials

Let us evaluate the integral

$$I_m = \int_0^{\infty}\left(\Phi^h_{v_b|l|}(Q_b)\right)^2 Q_b^m\, dQ_b \tag{A.8}$$

where

$$\Phi^h_{v_b|l|}(Q_b) = \sqrt{2}b^{\frac{|l|+1}{2}}\sqrt{\frac{\left(\frac{v_b-|l|}{2}\right)!}{\left(\frac{v_b+|l|}{2}\right)!}}Q_b^{|l|}e^{-\frac{1}{2}bQ_b^2}L^{|l|}_{\frac{v_b-|l|}{2}}(bQ_b^2) \tag{A.9}$$

for $l=-v_b,-v_b+2,\ldots,v_b-2,v_b$ (Eq. (2.251)), i.e.

$$I_m = 2b^{|l|+1}\frac{\left(\frac{v_b-|l|}{2}\right)!}{\left(\frac{v_b+|l|}{2}\right)!}\int_0^{\infty} Q_b^{2|l|+m}e^{-bQ_b^2}\left[L^{|l|}_{\frac{v_b-|l|}{2}}(bQ_b^2)\right]^2 dQ_b \tag{A.10}$$

or, using $x = bQ_b^2$,

$$I_m = b^{\frac{1-m}{2}} \frac{\left(\frac{v_b-|l|}{2}\right)!}{\left(\frac{v_b+|l|}{2}\right)!} \int_0^\infty x^{|l|+\frac{m-1}{2}} e^{-x} \left[L^{|l|}_{\frac{v_b-|l|}{2}}(x)\right]^2 dx. \tag{A.11}$$

The important relations for the associated Laguerre polynomials $L_n^k(x)$ with positive integers n and k [253, 254]

$$L_n^k(x) = \sum_{\nu=0}^{n} (-1)^\nu \left(\begin{array}{c} n+k \\ n-\nu \end{array} \right) \frac{x^\nu}{\nu!} \tag{A.12}$$

are the orthogonality relation [253, 254]

$$\int_0^\infty x^k e^{-x} L_n^k(x) L_m^k(x)\, dx = \frac{(n+k)!}{n!}\, \delta_{mn} \tag{A.13}$$

and the recurrence relation [253, 254]

$$L_n^k(x) = L_n^{k+1}(x) - L_{n-1}^{k+1}(x). \tag{A.14}$$

Eq. (A.14) leads to the other recurrence relation [254]

$$L_n^{k+1}(x) = \sum_{\nu=0}^{n} L_\nu^k(x) \tag{A.15}$$

since

$$\begin{aligned} \sum_{\nu=0}^{n} L_\nu^k(x) &= \sum_{\nu=0}^{n} L_\nu^{k+1}(x) - \sum_{\nu=1}^{n} L_{\nu-1}^{k+1}(x) \\ &= \sum_{\nu=0}^{n} L_\nu^{k+1}(x) - \sum_{\nu=0}^{n-1} L_\nu^{k+1}(x) \\ &= \sum_{\nu=0}^{n} L_\nu^{k+1}(x) - \sum_{\nu=0}^{n} L_\nu^{k+1}(x) + L_n^{k+1}(x) \\ &= L_n^{k+1}(x). \end{aligned} \tag{A.16}$$

Furthermore, in Eq. (A.12) the binomial coefficient for positive integers n and k is defined as [253, 254]

$$\left(\begin{array}{c} n \\ k \end{array} \right) = \left(\begin{array}{c} n \\ n-k \end{array} \right) = \frac{n!}{k!(n-k)!} \qquad (0 \le k \le n). \tag{A.17}$$

The corresponding recurrence relation is [253]

$$\left(\begin{array}{c} n+1 \\ k+1 \end{array} \right) = \left(\begin{array}{c} n \\ k \end{array} \right) + \left(\begin{array}{c} n \\ k+1 \end{array} \right) \tag{A.18}$$

which similarly leads to the other recurrence relation [254]

$$\sum_{j=k}^{n} \begin{pmatrix} j \\ k \end{pmatrix} = \begin{pmatrix} n+1 \\ k+1 \end{pmatrix} \tag{A.19}$$

proved by induction, i.e.

$$\sum_{j=k}^{k} \begin{pmatrix} j \\ k \end{pmatrix} = \begin{pmatrix} k \\ k \end{pmatrix} = \frac{k!}{k!} = \frac{(k+1)!}{(k+1)!} = \begin{pmatrix} k+1 \\ k+1 \end{pmatrix} \tag{A.20}$$

and

$$\sum_{j=k}^{n+1} \begin{pmatrix} j \\ k \end{pmatrix} = \sum_{j=k}^{n} \begin{pmatrix} j \\ k \end{pmatrix} + \begin{pmatrix} n+1 \\ k \end{pmatrix} = \begin{pmatrix} n+1 \\ k+1 \end{pmatrix} + \begin{pmatrix} n+1 \\ k \end{pmatrix} = \begin{pmatrix} n+2 \\ k+1 \end{pmatrix}. \tag{A.21}$$

We use Eqs. (A.11), (A.12), (A.17), and (A.5) to obtain

$$\begin{aligned} I_m &= b^{\frac{1-m}{2}} \frac{\left(\frac{v_b-|l|}{2}\right)!}{\left(\frac{v_b+|l|}{2}\right)!} \sum_{\nu_1=0}^{\frac{v_b-|l|}{2}} \sum_{\nu_2=0}^{\frac{v_b-|l|}{2}} (-1)^{\nu_1+\nu_2} \frac{1}{\nu_1!\nu_2!} \begin{pmatrix} \frac{v_b+|l|}{2} \\ \frac{v_b-|l|}{2}-\nu_1 \end{pmatrix} \begin{pmatrix} \frac{v_b+|l|}{2} \\ \frac{v_b-|l|}{2}-\nu_2 \end{pmatrix} \\ &\qquad \int_0^\infty x^{|l|+\frac{m-1}{2}+\nu_1+\nu_2} e^{-x}\, dx \\ &= b^{\frac{1-m}{2}} \frac{\left(\frac{v_b-|l|}{2}\right)!}{\left(\frac{v_b+|l|}{2}\right)!} \sum_{\nu_1=0}^{\frac{v_b-|l|}{2}} \sum_{\nu_2=0}^{\frac{v_b-|l|}{2}} (-1)^{\nu_1+\nu_2} \frac{1}{\nu_1!\nu_2!} \begin{pmatrix} \frac{v_b+|l|}{2} \\ |l|+\nu_1 \end{pmatrix} \begin{pmatrix} \frac{v_b+|l|}{2} \\ |l|+\nu_2 \end{pmatrix} \\ &\qquad \Gamma\left(|l|+\frac{m+1}{2}+\nu_1+\nu_2\right) \end{aligned} \tag{A.22}$$

for $|l| > -(m+1)/2$. In general, it is difficult to obtain a simple analytical result for arbitrary v_b and $|l|$. However, the evaluation of Eq. (A.22) is useful for several integrals I_m, in particular for even $|m|$ since, in this case, the exponent of x is real.

A.2.1 $m = 2$

For $m = 2$, the integral I_2 (Eq. (A.11)) for all $|l|$ is given by

$$\begin{aligned} I_2 &= \frac{1}{\sqrt{b}} \frac{\left(\frac{v_b-|l|}{2}\right)!}{\left(\frac{v_b+|l|}{2}\right)!} \sum_{\nu_1=0}^{\frac{v_b-|l|}{2}} \sum_{\nu_2=0}^{\frac{v_b-|l|}{2}} (-1)^{\nu_1+\nu_2} \frac{1}{\nu_1!\nu_2!} \begin{pmatrix} \frac{v_b+|l|}{2} \\ |l|+\nu_1 \end{pmatrix} \begin{pmatrix} \frac{v_b+|l|}{2} \\ |l|+\nu_2 \end{pmatrix} \\ &\qquad \Gamma\left(|l|+\frac{3}{2}+\nu_1+\nu_2\right). \end{aligned} \tag{A.23}$$

For $v_b = |l|$, we obtain

$$I_2 = \frac{1}{\sqrt{b}\,|l|!}\,\Gamma\left(|l|+\frac{3}{2}\right) \qquad (v_b = |l|). \tag{A.24}$$

Using Eq. (A.17), we have for $v_b = |l| + 2$

$$\begin{aligned} I_2 &= \frac{1}{\sqrt{b}\,(|l|+1)!}\sum_{\nu_1=0}^{1}\sum_{\nu_2=0}^{1}(-1)^{\nu_1+\nu_2}\frac{1}{\nu_1!\nu_2!}\begin{pmatrix} |l|+1 \\ |l|+\nu_1 \end{pmatrix}\begin{pmatrix} |l|+1 \\ |l|+\nu_2 \end{pmatrix} \\ &\qquad\qquad \Gamma\left(|l|+\frac{3}{2}+\nu_1+\nu_2\right) \\ &= \frac{1}{\sqrt{b}\,(|l|+1)!}\left[(|l|+1)^2\Gamma\left(|l|+\frac{3}{2}\right)-2(|l|+1)\Gamma\left(|l|+\frac{5}{2}\right)+\Gamma\left(|l|+\frac{7}{2}\right)\right] \\ &= \frac{1}{\sqrt{b}\,(|l|+1)!}\left[(|l|+1)^2-2(|l|+1)\left(|l|+\frac{3}{2}\right)+\left(|l|+\frac{5}{2}\right)\left(|l|+\frac{3}{2}\right)\right]\Gamma\left(|l|+\frac{3}{2}\right) \\ &= \frac{1}{\sqrt{b}\,(|l|+1)!}\left[|l|^2+2|l|+1-2|l|^2-5|l|-3+|l|^2+4|l|+\frac{15}{4}\right]\Gamma\left(|l|+\frac{3}{2}\right) \\ &= \frac{1}{\sqrt{b}\,(|l|+1)!}\left(|l|+\frac{7}{4}\right)\Gamma\left(|l|+\frac{3}{2}\right) \qquad (v_b = |l|+2) \end{aligned} \tag{A.25}$$

where the relation $\Gamma(z+1) = z\Gamma(z)$ [253, 254] was used.

A.2.2 $m = 1$

For $m = 1$, the integral I_1 (Eq. (A.11)) is easily carried out, i.e.

$$\begin{aligned} I_1 &= \frac{\left(\frac{v_b-|l|}{2}\right)!}{\left(\frac{v_b+|l|}{2}\right)!}\int_0^\infty x^{|l|}e^{-x}\left[L^{|l|}_{\frac{v_b-|l|}{2}}(x)\right]^2 dx \\ &= \frac{\left(\frac{v_b-|l|}{2}\right)!}{\left(\frac{v_b+|l|}{2}\right)!}\frac{\left(\frac{v_b+|l|}{2}\right)!}{\left(\frac{v_b-|l|}{2}\right)!} \\ &= 1 \end{aligned} \tag{A.26}$$

for all $|l|$ where the orthogonality relation (Eq. (A.13)) was used.

A.2.3 $m = 0$

For $m = 0$, the integral I_0 (Eq. (A.22)) for all $|l|$ is

$$I_0 = \sqrt{b}\,\frac{\left(\frac{v_b-|l|}{2}\right)!}{\left(\frac{v_b+|l|}{2}\right)!}\sum_{\nu_1=0}^{\frac{v_b-|l|}{2}}\sum_{\nu_2=0}^{\frac{v_b-|l|}{2}}(-1)^{\nu_1+\nu_2}\frac{1}{\nu_1!\nu_2!}\begin{pmatrix} \frac{v_b+|l|}{2} \\ |l|+\nu_1 \end{pmatrix}\begin{pmatrix} \frac{v_b+|l|}{2} \\ |l|+\nu_2 \end{pmatrix}\Gamma\left(|l|+\frac{1}{2}+\nu_1+\nu_2\right). \tag{A.27}$$

For $v_b = |l|$, it reduces to

$$I_0 = \frac{\sqrt{b}}{|l|!}\,\Gamma\left(|l|+\frac{1}{2}\right) \qquad (v_b = |l|). \tag{A.28}$$

For $v_b = |l| + 2$, we have, using Eq. (A.17),

$$I_0 = \frac{\sqrt{b}}{(|l|+1)!} \sum_{\nu_1=0}^{1} \sum_{\nu_2=0}^{1} (-1)^{\nu_1+\nu_2} \frac{1}{\nu_1!\nu_2!} \begin{pmatrix} |l|+1 \\ |l|+\nu_1 \end{pmatrix} \begin{pmatrix} |l|+1 \\ |l|+\nu_2 \end{pmatrix} \Gamma\left(|l| + \frac{1}{2} + \nu_1 + \nu_2\right) \tag{A.29}$$

$$= \frac{\sqrt{b}}{(|l|+1)!} \left[(|l|+1)^2 \Gamma\left(|l|+\frac{1}{2}\right) - 2(|l|+1)\Gamma\left(|l|+\frac{3}{2}\right) + \Gamma\left(|l|+\frac{5}{2}\right)\right]$$

$$= \frac{\sqrt{b}}{(|l|+1)!} \left[(|l|+1)^2 - 2(|l|+1)\left(|l|+\frac{1}{2}\right) + \left(|l|+\frac{3}{2}\right)\left(|l|+\frac{1}{2}\right)\right] \Gamma\left(|l|+\frac{1}{2}\right)$$

$$= \frac{\sqrt{b}}{(|l|+1)!} \left[|l|^2 + 2|l| + 1 - 2|l|^2 - 3|l| - 1 + |l|^2 + 2|l| + \frac{3}{4}\right] \Gamma\left(|l|+\frac{1}{2}\right)$$

$$= \frac{\sqrt{b}}{(|l|+1)!} \left(|l|+\frac{3}{4}\right) \Gamma\left(|l|+\frac{1}{2}\right) \qquad (v_b = |l|+2).$$

A.2.4 $m = -1$

For $m = -1$, the integral I_{-1} (Eq. (A.11)) for $|l| \neq 0$ is

$$I_{-1} = b \frac{\left(\frac{v_b-|l|}{2}\right)!}{\left(\frac{v_b+|l|}{2}\right)!} \int_0^\infty x^{|l|-1} e^{-x} \left[L^{|l|}_{\frac{v_b-|l|}{2}}(x)\right]^2 dx. \tag{A.30}$$

Using Eqs. (A.15), (A.13), (A.17), and (A.19), we obtain

$$I_{-1} = b \frac{\left(\frac{v_b-|l|}{2}\right)!}{\left(\frac{v_b+|l|}{2}\right)!} \int_0^\infty x^{|l|-1} e^{-x} \left[\sum_{\nu=0}^{\frac{v_b-|l|}{2}} L_\nu^{|l|-1}(x)\right]^2 dx \tag{A.31}$$

$$= b \frac{\left(\frac{v_b-|l|}{2}\right)!}{\left(\frac{v_b+|l|}{2}\right)!} \sum_{\nu=0}^{\frac{v_b-|l|}{2}} \int_0^\infty x^{|l|-1} e^{-x} \left[L_\nu^{|l|-1}(x)\right]^2 dx$$

$$= b \frac{\left(\frac{v_b-|l|}{2}\right)!}{\left(\frac{v_b+|l|}{2}\right)!} \sum_{\nu=0}^{\frac{v_b-|l|}{2}} \frac{(\nu+|l|-1)!}{\nu!}$$

$$= b\,(|l|-1)! \frac{\left(\frac{v_b-|l|}{2}\right)!}{\left(\frac{v_b+|l|}{2}\right)!} \sum_{\nu=0}^{\frac{v_b-|l|}{2}} \begin{pmatrix} \nu+|l|-1 \\ |l|-1 \end{pmatrix}$$

$$= b\,(|l|-1)! \frac{\left(\frac{v_b-|l|}{2}\right)!}{\left(\frac{v_b+|l|}{2}\right)!} \sum_{\nu=|l|-1}^{\frac{v_b+|l|}{2}-1} \begin{pmatrix} \nu \\ |l|-1 \end{pmatrix}$$

$$= b\,(|l|-1)! \frac{\left(\frac{v_b-|l|}{2}\right)!}{\left(\frac{v_b+|l|}{2}\right)!} \begin{pmatrix} \frac{v_b+|l|}{2} \\ |l| \end{pmatrix}$$

$$= b \frac{(|l|-1)!}{|l|!} \frac{\left(\frac{v_b-|l|}{2}\right)!}{\left(\frac{v_b+|l|}{2}\right)!} \frac{\left(\frac{v_b+|l|}{2}\right)!}{\left(\frac{v_b-|l|}{2}\right)!},$$

thus

$$I_{-1} = \frac{b}{|l|} \qquad (|l| \neq 0). \tag{A.32}$$

A.2.5 $m = -2$

For $m = -2$, the integral I_{-2} (Eq. (A.22)) for $|l| \neq 0$ is

$$I_{-2} = b^{3/2} \frac{\left(\frac{v_b-|l|}{2}\right)!}{\left(\frac{v_b+|l|}{2}\right)!} \sum_{\nu_1=0}^{\frac{v_b-|l|}{2}} \sum_{\nu_2=0}^{\frac{v_b-|l|}{2}} (-1)^{\nu_1+\nu_2} \frac{1}{\nu_1!\nu_2!} \begin{pmatrix} \frac{v_b+|l|}{2} \\ |l|+\nu_1 \end{pmatrix} \begin{pmatrix} \frac{v_b+|l|}{2} \\ |l|+\nu_2 \end{pmatrix} \Gamma\left(|l| - \frac{1}{2} + \nu_1 + \nu_2\right). \tag{A.33}$$

For $v_b = |l|$, it becomes

$$I_{-2} = \frac{b^{3/2}}{|l|!} \Gamma\left(|l| - \frac{1}{2}\right) \qquad (v_b = |l|, |l| \neq 0). \tag{A.34}$$

Using Eq. (A.17), we obtain for $v_b = |l| + 2$

$$I_{-2} = \frac{b^{3/2}}{(|l|+1)!} \sum_{\nu_1=0}^{1} \sum_{\nu_2=0}^{1} (-1)^{\nu_1+\nu_2} \frac{1}{\nu_1!\nu_2!} \begin{pmatrix} |l|+1 \\ |l|+\nu_1 \end{pmatrix} \begin{pmatrix} |l|+1 \\ |l|+\nu_2 \end{pmatrix} \Gamma\left(|l| - \frac{1}{2} + \nu_1 + \nu_2\right) \tag{A.35}$$

$$= \frac{b^{3/2}}{(|l|+1)!} \left[(|l|+1)^2 \Gamma\left(|l| - \frac{1}{2}\right) - 2(|l|+1)\Gamma\left(|l| + \frac{1}{2}\right) + \Gamma\left(|l| + \frac{3}{2}\right)\right]$$

$$= \frac{b^{3/2}}{(|l|+1)!} \left[(|l|+1)^2 - 2(|l|+1)\left(|l| - \frac{1}{2}\right) + \left(|l| + \frac{1}{2}\right)\left(|l| - \frac{1}{2}\right)\right] \Gamma\left(|l| - \frac{1}{2}\right)$$

$$= \frac{b^{3/2}}{(|l|+1)!} \left[|l|^2 + 2|l| + 1 - 2|l|^2 - |l| + 1 + |l|^2 - \frac{1}{4}\right] \Gamma\left(|l| - \frac{1}{2}\right)$$

$$= \frac{b^{3/2}}{(|l|+1)!} \left(|l| + \frac{7}{4}\right) \Gamma\left(|l| - \frac{1}{2}\right) \qquad (v_b = |l| + 2, |l| \neq 0).$$

A.2.6 $m = -3$

For $m = -3$, the integral I_{-3} (Eq. (A.11)) for $|l| \neq 0, 1$ is

$$I_{-3} = b^2 \frac{\left(\frac{v_b-|l|}{2}\right)!}{\left(\frac{v_b+|l|}{2}\right)!} \int_0^\infty x^{|l|-2} e^{-x} \left[L^{|l|}_{\frac{v_b-|l|}{2}}(x)\right]^2 dx. \tag{A.36}$$

The simple result

$$I_{-3} = \frac{b^2}{|l|} \frac{v_b + 1}{|l|^2 - 1} \qquad (|l| \neq 0, 1) \tag{A.37}$$

can be proven by induction. For $v_b = |l|$, we have, using Eqs. (A.12), (A.5), and (A.7),

$$\begin{aligned} I_{-3} &= \frac{b^2}{|l|!}\int_0^\infty x^{|l|-2}e^{-x}\left[L_0^{|l|}(x)\right]^2\,dx \qquad (A.38)\\ &= \frac{b^2}{|l|!}\int_0^\infty x^{|l|-2}e^{-x}\,dx \\ &= \frac{b^2}{|l|!}\,\Gamma(|l|-1) \\ &= \frac{b^2}{|l|}\frac{1}{|l|-1} \\ &= \frac{b^2}{|l|}\frac{|l|+1}{|l|^2-1} \qquad (|l|\neq 0,1). \end{aligned}$$

For $v_b = v_b' + 2 = |l| + 2n + 2$ (n is a positive integer), we obtain, using Eq. (A.15),

$$\begin{aligned} I_{-3} &= b^2\,\frac{\left(\frac{v_b'-|l|}{2}+1\right)!}{\left(\frac{v_b'+|l|}{2}+1\right)!}\int_0^\infty x^{|l|-2}e^{-x}\left[L^{|l|}_{\frac{v_b'-|l|}{2}+1}(x)\right]^2\,dx \qquad (A.39)\\ &= b^2\,\frac{\left(\frac{v_b'-|l|}{2}+1\right)!}{\left(\frac{v_b'+|l|}{2}+1\right)!}\int_0^\infty x^{|l|-2}e^{-x}\left[\sum_{\nu=0}^{\frac{v_b'-|l|}{2}+1} L_\nu^{|l|-1}(x)\right]^2\,dx \\ &= b^2\,\frac{\left(\frac{v_b'-|l|}{2}+1\right)!}{\left(\frac{v_b'+|l|}{2}+1\right)!}\int_0^\infty x^{|l|-2}e^{-x}\left[\sum_{\nu=0}^{\frac{v_b'-|l|}{2}+1}\sum_{\nu'=0}^{\nu} L_{\nu'}^{|l|-2}(x)\right]^2\,dx \\ &= b^2\,\frac{\left(\frac{v_b'-|l|}{2}+1\right)!}{\left(\frac{v_b'+|l|}{2}+1\right)!}\int_0^\infty x^{|l|-2}e^{-x}\left[\sum_{\nu=0}^{\frac{v_b'-|l|}{2}+1}\left(\frac{v_b'-|l|}{2}+2-\nu\right)L_\nu^{|l|-2}(x)\right]^2\,dx \end{aligned}$$

since

$$\begin{aligned} \sum_{\nu=0}^{n}\sum_{\nu'=0}^{\nu} L_{\nu'}^k(x) &= \sum_{\nu=0}^{n}\Big(L_0^k(x)+L_1^k(x)+\ldots+L_\nu^k(x)\Big) \qquad (A.40)\\ &= (n+1)L_0^k(x)+nL_1^k(x)+\ldots+L_n^k(x) \\ &= \sum_{\nu=0}^{n}(n+1-\nu)L_\nu^k(x). \end{aligned}$$

Using Eqs. (A.13), (A.36), (A.37), (A.39), and $(n+1)^2 = n^2 + (2n+1)$, we have

$$I_{-3} = b^2\,\frac{\left(\frac{v_b'-|l|}{2}+1\right)!}{\left(\frac{v_b'+|l|}{2}+1\right)!}\sum_{\nu=0}^{\frac{v_b'-|l|}{2}+1}\left(\frac{v_b'-|l|}{2}+2-\nu\right)^2\int_0^\infty x^{|l|-2}e^{-x}\left[L_\nu^{|l|-2}(x)\right]^2\,dx \qquad (A.41)$$

$$
\begin{aligned}
&= b^2 \frac{\left(\frac{v_b'-|l|}{2}+1\right)!}{\left(\frac{v_b'+|l|}{2}+1\right)!} \left\{ \sum_{\nu=0}^{\frac{v_b'-|l|}{2}} \left(\frac{v_b'-|l|}{2}+2-\nu\right)^2 \int_0^\infty x^{|l|-2} e^{-x} \left[L_\nu^{|l|-2}(x)\right]^2 dx \right. \\
&\qquad \left. + \int_0^\infty x^{|l|-2} e^{-x} \left[L^{|l|-2}_{\frac{v_b'-|l|}{2}+1}(x)\right]^2 dx \right\} \\
&= b^2 \frac{\left(\frac{v_b'-|l|}{2}+1\right)!}{\left(\frac{v_b'+|l|}{2}+1\right)!} \left\{ \sum_{\nu=0}^{\frac{v_b'-|l|}{2}} \left(\frac{v_b'-|l|}{2}+1-\nu\right)^2 \int_0^\infty x^{|l|-2} e^{-x} \left[L_\nu^{|l|-2}(x)\right]^2 dx \right. \\
&\qquad + \sum_{\nu=0}^{\frac{v_b'-|l|}{2}} (v_b'-|l|+3-2\nu) \int_0^\infty x^{|l|-2} e^{-x} \left[L_\nu^{|l|-2}(x)\right]^2 dx \\
&\qquad \left. + \int_0^\infty x^{|l|-2} e^{-x} \left[L^{|l|-2}_{\frac{v_b'-|l|}{2}+1}(x)\right]^2 dx \right\} \\
&= b^2 \frac{\left(\frac{v_b'-|l|}{2}+1\right)!}{\left(\frac{v_b'+|l|}{2}+1\right)!} \left\{ \int_0^\infty x^{|l|-2} e^{-x} \left[L^{|l|}_{\frac{v_b'-|l|}{2}}(x)\right]^2 dx + \int_0^\infty x^{|l|-2} e^{-x} \left[L^{|l|-2}_{\frac{v_b'-|l|}{2}+1}(x)\right]^2 dx \right. \\
&\qquad \left. + \sum_{\nu=0}^{\frac{v_b'-|l|}{2}} (v_b'-|l|+3-2\nu) \int_0^\infty x^{|l|-2} e^{-x} \left[L_\nu^{|l|-2}(x)\right]^2 dx \right\} \\
&= b^2 \frac{\left(\frac{v_b'-|l|}{2}+1\right)!}{\left(\frac{v_b'+|l|}{2}+1\right)!} \left\{ \frac{\left(\frac{v_b'+|l|}{2}\right)!}{\left(\frac{v_b'-|l|}{2}\right)!} \frac{v_b'+1}{|l|(|l|^2-1)} + \frac{\left(\frac{v_b'+|l|}{2}-1\right)!}{\left(\frac{v_b'-|l|}{2}+1\right)!} \right. \\
&\qquad \left. + \sum_{\nu=0}^{\frac{v_b'-|l|}{2}} (v_b'-|l|+3-2\nu) \frac{(\nu+|l|-2)!}{\nu!} \right\}.
\end{aligned}
$$

With Eqs. (A.17) and (A.19), it leads to

$$
\begin{aligned}
I_{-3} &= \frac{\frac{v_b'-|l|}{2}+1}{\frac{v_b'+|l|}{2}+1} \frac{b^2}{|l|} \frac{v_b'+1}{|l|^2-1} + \frac{b^2}{\frac{v_b'+|l|}{2}\left(\frac{v_b'+|l|}{2}+1\right)} \\
&\quad + b^2 (v_b'-|l|+3) \frac{\left(\frac{v_b'-|l|}{2}+1\right)!}{\left(\frac{v_b'+|l|}{2}+1\right)!} \sum_{\nu=0}^{\frac{v_b'-|l|}{2}} \frac{(\nu+|l|-2)!}{\nu!} \\
&\quad - 2b^2 \frac{\left(\frac{v_b'-|l|}{2}+1\right)!}{\left(\frac{v_b'+|l|}{2}+1\right)!} \sum_{\nu=0}^{\frac{v_b'-|l|}{2}} \frac{(\nu+|l|-2)!}{(\nu-1)!}
\end{aligned} \tag{A.42}
$$

$$
\begin{aligned}
&= \frac{\frac{v_b'-|l|}{2}+1}{\frac{v_b'+|l|}{2}+1}\frac{b^2}{|l|}\frac{v_b'+1}{|l|^2-1}+\frac{b^2}{\frac{v_b'+|l|}{2}\left(\frac{v_b'+|l|}{2}+1\right)}\\
&\quad +b^2(|l|-2)!\,(v_b'-|l|+3)\,\frac{\left(\frac{v_b'-|l|}{2}+1\right)!}{\left(\frac{v_b'+|l|}{2}+1\right)!}\sum_{\nu=0}^{\frac{v_b'-|l|}{2}}\begin{pmatrix}\nu+|l|-2\\ |l|-2\end{pmatrix}\\
&\quad -2b^2(|l|-1)!\frac{\left(\frac{v_b'-|l|}{2}+1\right)!}{\left(\frac{v_b'+|l|}{2}+1\right)!}\sum_{\nu=1}^{\frac{v_b'-|l|}{2}}\begin{pmatrix}\nu+|l|-2\\ |l|-1\end{pmatrix}\\
&= \frac{\frac{v_b'-|l|}{2}+1}{\frac{v_b'+|l|}{2}+1}\frac{b^2}{|l|}\frac{v_b'+1}{|l|^2-1}+\frac{b^2}{\frac{v_b'+|l|}{2}\left(\frac{v_b'+|l|}{2}+1\right)}\\
&\quad +b^2(|l|-2)!\,(v_b'-|l|+3)\,\frac{\left(\frac{v_b'-|l|}{2}+1\right)!}{\left(\frac{v_b'+|l|}{2}+1\right)!}\sum_{\nu=|l|-2}^{\frac{v_b'+|l|}{2}-2}\begin{pmatrix}\nu\\ |l|-2\end{pmatrix}\\
&\quad -2b^2(|l|-1)!\frac{\left(\frac{v_b'-|l|}{2}+1\right)!}{\left(\frac{v_b'+|l|}{2}+1\right)!}\sum_{\nu=|l|-1}^{\frac{v_b'+|l|}{2}-2}\begin{pmatrix}\nu\\ |l|-1\end{pmatrix}\\
&= \frac{\frac{v_b'-|l|}{2}+1}{\frac{v_b'+|l|}{2}+1}\frac{b^2}{|l|}\frac{v_b'+1}{|l|^2-1}+\frac{b^2}{\frac{v_b'+|l|}{2}\left(\frac{v_b'+|l|}{2}+1\right)}\\
&\quad +b^2(|l|-2)!\,(v_b'-|l|+3)\,\frac{\left(\frac{v_b'-|l|}{2}+1\right)!}{\left(\frac{v_b'+|l|}{2}+1\right)!}\begin{pmatrix}\frac{v_b'+|l|}{2}-1\\ |l|-1\end{pmatrix}\\
&\quad -2b^2(|l|-1)!\frac{\left(\frac{v_b'-|l|}{2}+1\right)!}{\left(\frac{v_b'+|l|}{2}+1\right)!}\begin{pmatrix}\frac{v_b'+|l|}{2}-1\\ |l|\end{pmatrix}\\
&= \frac{\frac{v_b'-|l|}{2}+1}{\frac{v_b'+|l|}{2}+1}\frac{b^2}{|l|}\frac{v_b'+1}{|l|^2-1}+\frac{b^2}{\frac{v_b'+|l|}{2}\left(\frac{v_b'+|l|}{2}+1\right)}\\
&\quad +\frac{b^2\,(v_b'-|l|+3)}{|l|-1}\frac{\frac{v_b'-|l|}{2}+1}{\frac{v_b'+|l|}{2}\left(\frac{v_b'+|l|}{2}+1\right)}-\frac{2b^2}{|l|}\frac{\frac{v_b'-|l|}{2}\left(\frac{v_b'-|l|}{2}+1\right)}{\frac{v_b'+|l|}{2}\left(\frac{v_b'+|l|}{2}+1\right)}.
\end{aligned}
$$

Finally, with $v_b' = |l|+2n$, we obtain

$$
\begin{aligned}
I_{-3} &= \frac{n+1}{|l|+n+1}\frac{b^2}{|l|}\frac{|l|+2n+1}{|l|^2-1}+\frac{b^2}{(|l|+n)\,(|l|+n+1)} \qquad \text{(A.43)}\\
&\quad +\frac{b^2\,(2n+3)}{|l|-1}\frac{n+1}{(|l|+n)\,(|l|+n+1)}-\frac{2b^2}{|l|}\frac{n\,(n+1)}{(|l|+n)\,(|l|+n+1)}\\
&= \frac{b^2}{|l|(|l|^2-1)}\frac{1}{(|l|+n)(|l|+n+1)}\,[(|l|+n)(|l|+2n+1)(n+1)\\
&\qquad +|l|(|l|^2-1)+|l|(|l|+1)(n+1)(2n+3)-2(|l|^2-1)n\,(n+1)\big]
\end{aligned}
$$

$$
\begin{aligned}
&= \frac{b^2}{|l|(|l|^2-1)}\frac{1}{(|l|+n)(|l|+n+1)}\Big[(|l|+n)(|l|n+|l|+2n^2+3n+1)\\
&\qquad +|l|^3+3|l|^2n+3|l|^2+2|l|n^2+5|l|n+2|l|+2n^2+2n\Big]\\
&= \frac{b^2}{|l|(|l|^2-1)}\frac{1}{(|l|+n)(|l|+n+1)}\Big[(|l|+n)(|l|n+|l|+2n^2+3n+1)\\
&\qquad +(|l|+n)(|l|^2+2|l|n+3|l|+2n+2)\Big]\\
&= \frac{b^2}{|l|(|l|^2-1)}\frac{|l|^2+3|l|n+4|l|+2n^2+5n+3}{|l|+n+1}\\
&= \frac{b^2}{|l|}\frac{|l|+2n+3}{|l|^2-1}\\
&= \frac{b^2}{|l|}\frac{v_b+1}{|l|^2-1} \qquad (|l|\neq 0,1).
\end{aligned}
$$

A.3 Integrals involving confluent hypergeometric functions

We solve the integral

$$I_U = |l|\sqrt{\frac{c}{b^3}}\int_0^\infty \left(\Phi^h_{v_b|l|}(Q_b)\right)^2 U\left(\frac{1}{2},0,cQ_b^2\right) Q_b^{-1}\,dQ_b \tag{A.44}$$

where $U(\alpha,\beta,z)$ is the confluent hypergeometric function of the second kind [253, 254]. With Eq. (2.251), we have

$$I_U = 2|l|b^{|l|-1/2}\sqrt{c}\,\frac{\left(\frac{v_b-|l|}{2}\right)!}{\left(\frac{v_b+|l|}{2}\right)!}\int_0^\infty Q_b^{2|l|-1}e^{-bQ_b^2}\left[L^{|l|}_{\frac{v_b-|l|}{2}}(bQ_b^2)\right]^2 U\left(\frac{1}{2},0,cQ_b^2\right)\,dQ_b \tag{A.45}$$

(cf. Eq. (A.10)), using $x=bQ_b^2$,

$$I_U = |l|\sqrt{\frac{c}{b}}\,\frac{\left(\frac{v_b-|l|}{2}\right)!}{\left(\frac{v_b+|l|}{2}\right)!}\int_0^\infty x^{|l|-1}e^{-x}\left[L^{|l|}_{\frac{v_b-|l|}{2}}(x)\right]^2 U\left(\frac{1}{2},0,\frac{c}{b}\,x\right)\,dx \tag{A.46}$$

(cf. Eq. (A.30)), with Eqs. (A.12) and (A.17),

$$
\begin{aligned}
I_U = |l|\sqrt{\frac{c}{b}}\,\frac{\left(\frac{v_b-|l|}{2}\right)!}{\left(\frac{v_b+|l|}{2}\right)!}\sum_{\nu_1=0}^{\frac{v_b-|l|}{2}}\sum_{\nu_2=0}^{\frac{v_b-|l|}{2}}(-1)^{\nu_1+\nu_2}\frac{1}{\nu_1!\nu_2!}\begin{pmatrix}\frac{v_b+|l|}{2}\\ |l|+\nu_1\end{pmatrix}\begin{pmatrix}\frac{v_b+|l|}{2}\\ |l|+\nu_2\end{pmatrix} \\
\int_0^\infty x^{|l|-1+\nu_1+\nu_2}e^{-x}\,U\left(\frac{1}{2},0,\frac{c}{b}\,x\right)\,dx
\end{aligned} \tag{A.47}
$$

(cf. Eq. (A.22)), and using $u=cx/b$,

$$
\begin{aligned}
I_U = |l|\frac{b^{|l|-1/2}}{c^{|l|-1/2}}\,\frac{\left(\frac{v_b-|l|}{2}\right)!}{\left(\frac{v_b+|l|}{2}\right)!}\sum_{\nu_1=0}^{\frac{v_b-|l|}{2}}\sum_{\nu_2=0}^{\frac{v_b-|l|}{2}}(-1)^{\nu_1+\nu_2}\frac{1}{\nu_1!\nu_2!}\begin{pmatrix}\frac{v_b+|l|}{2}\\ |l|+\nu_1\end{pmatrix}\begin{pmatrix}\frac{v_b+|l|}{2}\\ |l|+\nu_2\end{pmatrix}\frac{b^{\nu_1+\nu_2}}{c^{\nu_1+\nu_2}} \\
\int_0^\infty u^{|l|-1+\nu_1+\nu_2}e^{-\frac{b}{c}u}\,U\left(\frac{1}{2},0,u\right)\,du.
\end{aligned} \tag{A.48}
$$

This integral is already known [254], i.e. for $\beta > 0$ and $s > 0$

$$\int_0^\infty u^{\beta-1} e^{-su}\, U(\alpha, 0, u)\, du \;=\; \frac{\Gamma(\beta)\Gamma(\beta+1)}{\Gamma(\alpha+\beta+1)}\, {}_2F_1(\beta, \beta+1; \alpha+\beta+1; 1-s) \tag{A.49}$$

where ${}_2F_1(\alpha, \beta; \gamma; z)$ is the hypergeometric function [253, 254]

$$\begin{aligned} {}_2F_1(\alpha, \beta; \gamma; z) &= \frac{\Gamma(\gamma)}{\Gamma(\alpha)\Gamma(\beta)} \sum_{k=0}^{\infty} \frac{\Gamma(\alpha+k)\Gamma(\beta+k)}{\Gamma(\gamma+k)} \frac{z^k}{k!} \\ &= 1 + \frac{\Gamma(\gamma)}{\Gamma(\alpha)\Gamma(\beta)} \sum_{k=1}^{\infty} \frac{\Gamma(\alpha+k)\Gamma(\beta+k)}{\Gamma(\gamma+k)} \frac{z^k}{k!}. \end{aligned} \tag{A.50}$$

Thus, we obtain for $|l| \neq 0$ and $b, c > 0$

$$\begin{aligned} I_U \;=\; & |l| \frac{b^{|l|-1/2}}{c^{|l|-1/2}} \frac{\left(\frac{v_b-|l|}{2}\right)!}{\left(\frac{v_b+|l|}{2}\right)!} \sum_{\nu_1=0}^{\frac{v_b-|l|}{2}} \sum_{\nu_2=0}^{\frac{v_b-|l|}{2}} (-1)^{\nu_1+\nu_2} \frac{1}{\nu_1!\nu_2!} \begin{pmatrix} \frac{v_b+|l|}{2} \\ |l|+\nu_1 \end{pmatrix} \begin{pmatrix} \frac{v_b+|l|}{2} \\ |l|+\nu_2 \end{pmatrix} \frac{b^{\nu_1+\nu_2}}{c^{\nu_1+\nu_2}} \\ & \frac{\Gamma(|l|+\nu_1+\nu_2)\Gamma(|l|+\nu_1+\nu_2+1)}{\Gamma\left(|l|+\nu_1+\nu_2+\frac{3}{2}\right)} \\ & {}_2F_1\left(|l|+\nu_1+\nu_2, |l|+\nu_1+\nu_2+1; |l|+\nu_1+\nu_2+\frac{3}{2}; 1-\frac{b}{c}\right). \end{aligned} \tag{A.51}$$

For the speical case $v_b = |l|$, Eq. (A.51) simplifies to

$$I_U \;=\; \frac{b^{|l|-1/2}}{c^{|l|-1/2}} \frac{|l|!}{\Gamma\left(|l|+\frac{3}{2}\right)}\, {}_2F_1\left(|l|, |l|+1; |l|+\frac{3}{2}; 1-\frac{b}{c}\right). \tag{A.52}$$

A.3.1 $v_b = |l| = 1$

For $v_b = |l| = 1$, Eq. (A.52) becomes

$$I_U \;=\; \frac{4}{3\sqrt{\pi}} \sqrt{\frac{b}{c}}\, {}_2F_1\left(1, 2; \frac{5}{2}; 1-\frac{b}{c}\right) \tag{A.53}$$

where $\Gamma(\frac{5}{2}) = \frac{3}{4}\sqrt{\pi}$. Using the linear transformation formula for the hypergeometric function [253, 254]

$${}_2F_1(\alpha, \beta; \gamma; z) \;=\; \frac{1}{(1-z)^\alpha}\, {}_2F_1\left(\alpha, \gamma-\beta; \gamma; \frac{z}{z-1}\right) \tag{A.54}$$

we have

$$I_U \;=\; \frac{4}{3\sqrt{\pi}} \sqrt{\frac{c}{b}}\, {}_2F_1\left(1, \frac{1}{2}; \frac{5}{2}; 1-\frac{c}{b}\right). \tag{A.55}$$

With the Gaussian recursion relation for the hypergeometric function [253, 254]

$$\begin{aligned} & \gamma\left[\gamma - 1 - (2\gamma - \alpha - \beta - 1)z\right]\, {}_2F_1(\alpha, \beta; \gamma; z) \\ & +(\gamma-\alpha)(\gamma-\beta)z\, {}_2F_1(\alpha, \beta; \gamma+1; z) + \gamma(\gamma-1)(z-1)\, {}_2F_1(\alpha, \beta; \gamma-1; z) \;=\; 0, \end{aligned} \tag{A.56}$$

or equivalently

$$
\begin{aligned}
{}_2F_1(\alpha,\beta;\gamma+1;z) &= -\frac{\gamma\left[\gamma-1-(2\gamma-\alpha-\beta-1)z\right]}{(\gamma-\alpha)(\gamma-\beta)z}\,{}_2F_1(\alpha,\beta;\gamma;z) \\
&\quad -\frac{\gamma(\gamma-1)(z-1)}{(\gamma-\alpha)(\gamma-\beta)z}\,{}_2F_1(\alpha,\beta;\gamma-1;z),
\end{aligned} \tag{A.57}
$$

Eq. (A.55) can be rewritten as

$$
I_U = \frac{2}{\sqrt{\pi}}\frac{1}{\sqrt{\frac{b}{c}\left(1-\frac{b}{c}\right)}}\left[{}_2F_1\left(1,\frac{1}{2};\frac{3}{2};1-\frac{c}{b}\right)-{}_2F_1\left(1,\frac{1}{2};\frac{1}{2};1-\frac{c}{b}\right)\right]. \tag{A.58}
$$

Again with Eq. (A.54) and ${}_2F_1(\alpha,\beta;\gamma;z) = {}_2F_1(\beta,\alpha;\gamma;z)$, it yields

$$
I_U = \frac{2}{\sqrt{\pi}}\frac{1}{1-\frac{b}{c}}\left[{}_2F_1\left(\frac{1}{2},\frac{1}{2};\frac{3}{2};1-\frac{b}{c}\right)-\sqrt{\frac{c}{b}}\,{}_2F_1\left(1,\frac{1}{2};\frac{1}{2};1-\frac{c}{b}\right)\right]. \tag{A.59}
$$

Finally, with [253, 254]

$$
{}_2F_1\left(\frac{1}{2},\frac{1}{2};\frac{3}{2};z^2\right) = \frac{\arcsin z}{z} \tag{A.60}
$$

$$
{}_2F_1(\alpha,\beta;\beta;z) = \frac{1}{(1-z)^\alpha} \qquad (z<1), \tag{A.61}
$$

the result for $v_b = |l| = 1$ in the conventional form is

$$
I_U = \frac{2}{\sqrt{\pi}}\frac{1}{1-\frac{b}{c}}\left(\frac{\arcsin\sqrt{1-\frac{b}{c}}}{\sqrt{1-\frac{b}{c}}}-\sqrt{\frac{b}{c}}\right). \tag{A.62}
$$

Note that in the limit $b/c \to 1$, the integral I_U is finite, i.e. using L'Hospital's rule and $z = 1 - b/c$,

$$
\begin{aligned}
\lim_{\frac{b}{c}\to 1} I_U &= \frac{2}{\sqrt{\pi}}\lim_{z\to 0}\frac{\arcsin\sqrt{z}-\sqrt{z(1-z)}}{z^{3/2}} \\
&= \frac{2}{\sqrt{\pi}}\lim_{z\to 0}\frac{\frac{d}{dz}\arcsin\sqrt{z}-\frac{d}{dz}\sqrt{z(1-z)}}{\frac{d}{dz}z^{3/2}} \\
&= \frac{4}{3\sqrt{\pi}}\lim_{z\to 0}\frac{\frac{1}{\sqrt{1-z}}\frac{1}{2\sqrt{z}}-\frac{1-2z}{2\sqrt{z(1-z)}}}{\sqrt{z}} \\
&= \frac{4}{3\sqrt{\pi}}\lim_{z\to 0}\frac{1}{\sqrt{1-z}} \\
&= \frac{4}{3\sqrt{\pi}},
\end{aligned} \tag{A.63}
$$

which can also be obtained easily using Eqs. (A.50) and (A.53). The corresponding asymptotic limit for $b/c \to \infty$, i.e. $z = 1 - b/c \to -\infty$, is

$$
\lim_{\frac{b}{c}\to\infty} I_U = \frac{4}{3\sqrt{\pi}}\lim_{z\to-\infty}\frac{1}{\sqrt{1-z}} = 0. \tag{A.64}
$$

A.3.2 $v_b = |l| = 2$

For $v_b = |l| = 2$ we obtain from Eq. (A.52)

$$I_U = \frac{16}{15\sqrt{\pi}} \frac{b^{3/2}}{c^{3/2}} {}_2F_1\left(2, 3; \frac{7}{2}; 1 - \frac{b}{c}\right) \tag{A.65}$$

where $\Gamma(\frac{7}{2}) = \frac{5}{2}\,\Gamma(\frac{5}{2}) = \frac{5}{2}\,\frac{3}{4}\,\sqrt{\pi} = \frac{15}{8}\,\sqrt{\pi}$. Using the other Gaussian recursion relation for the hypergeometric function [254]

$${}_2F_1(\alpha+1, \beta+1; \gamma+1; z) = \frac{\gamma}{\beta z}\left[{}_2F_1(\alpha+1, \beta; \gamma; z) - {}_2F_1(\alpha, \beta; \gamma; z)\right] \tag{A.66}$$

yields

$$I_U = \frac{4}{3\sqrt{\pi}} \frac{b^{3/2}}{c^{3/2}} \frac{1}{1-\frac{b}{c}} \left[{}_2F_1\left(2, 2; \frac{5}{2}; 1 - \frac{b}{c}\right) - {}_2F_1\left(1, 2; \frac{5}{2}; 1 - \frac{b}{c}\right)\right]. \tag{A.67}$$

Using Eq. (A.54) twice, we get

$$I_U = \frac{4}{3\sqrt{\pi}} \frac{1}{1-\frac{b}{c}} \left[{}_2F_1\left(\frac{1}{2}, \frac{1}{2}; \frac{5}{2}; 1 - \frac{b}{c}\right) - \frac{b^{3/2}}{c^{3/2}} {}_2F_1\left(1, 2; \frac{5}{2}; 1 - \frac{b}{c}\right)\right], \tag{A.68}$$

and using Eq. (A.57),

$$\begin{aligned} I_U = \frac{1}{\sqrt{\pi}} \frac{1}{\left(1-\frac{b}{c}\right)^2} \Bigg[& \left(1 - \frac{2b}{c}\right) {}_2F_1\left(\frac{1}{2}, \frac{1}{2}; \frac{3}{2}; 1 - \frac{b}{c}\right) + \frac{b}{c} {}_2F_1\left(\frac{1}{2}, \frac{1}{2}; \frac{1}{2}; 1 - \frac{b}{c}\right) \\ & - \frac{4}{3} \frac{b^{3/2}}{c^{3/2}} \left(1 - \frac{b}{c}\right) {}_2F_1\left(1, 2; \frac{5}{2}; 1 - \frac{b}{c}\right)\Bigg]. \end{aligned} \tag{A.69}$$

Finally, using Eqs. (A.60), (A.61), (A.53), and (A.62), the result for $v_b = |l| = 2$ in the conventional form is

$$I_U = \frac{1}{\sqrt{\pi}} \frac{1}{\left(1-\frac{b}{c}\right)^2} \left[\left(1 - \frac{4b}{c}\right) \frac{\arcsin\sqrt{1-\frac{b}{c}}}{\sqrt{1-\frac{b}{c}}} + \left(1 + \frac{2b}{c}\right)\sqrt{\frac{b}{c}}\right]. \tag{A.70}$$

In the limit $b/c \to 1$, we have, using L'Hospital's rule twice and $z = 1 - b/c$,

$$\begin{aligned} \lim_{\frac{b}{c}\to 1} I_U &= \frac{1}{\sqrt{\pi}} \lim_{z\to 0} \frac{(4z-3)\arcsin\sqrt{z} + (3-2z)\sqrt{z(1-z)}}{z^{5/2}} \\ &= \frac{1}{\sqrt{\pi}} \lim_{z\to 0} \frac{\frac{d}{dz}(4z-3)\arcsin\sqrt{z} + \frac{d}{dz}(3-2z)\sqrt{z(1-z)}}{\frac{d}{dz} z^{5/2}} \\ &= \frac{2}{5\sqrt{\pi}} \lim_{z\to 0} \frac{4\arcsin\sqrt{z} + \frac{4z-3}{2\sqrt{z(1-z)}} - 2\sqrt{z(1-z)} + \frac{(3-2z)(1-2z)}{2\sqrt{z(1-z)}}}{z^{3/2}} \\ &= \frac{2}{5\sqrt{\pi}} \lim_{z\to 0} \frac{\frac{d}{dz} 4\arcsin\sqrt{z} - \frac{d}{dz} 2\sqrt{z(1-z)} + \frac{d}{dz} \frac{2z^2-2z}{\sqrt{z(1-z)}}}{\frac{d}{dz} z^{3/2}} \end{aligned} \tag{A.71}$$

$$
\begin{aligned}
&= \frac{4}{15\sqrt{\pi}} \lim_{z\to 0} \frac{\frac{2}{\sqrt{z(1-z)}} - \frac{1-2z}{\sqrt{z(1-z)}} + \frac{4z-2}{\sqrt{z(1-z)}} + \frac{1-2z}{\sqrt{z(1-z)}}}{\sqrt{z}} \\
&= \frac{4}{15\sqrt{\pi}} \lim_{z\to 0} \frac{4}{\sqrt{1-z}} \\
&= \frac{16}{15\sqrt{\pi}},
\end{aligned}
$$

which is in accord with the result for $b/c = 1$ using Eqs. (A.50) and (A.65). The asymptotic limit is

$$\lim_{\frac{b}{c}\to\infty} I_U = \frac{4}{15\sqrt{\pi}} \lim_{z\to-\infty} \frac{4}{\sqrt{1-z}} = 0. \tag{A.72}$$

A.3.3 $v_b = |l| = 3$

The integral for $v_b = |l| = 3$ is (Eq. (A.52))

$$I_U = \frac{32}{35\sqrt{\pi}} \frac{b^{5/2}}{c^{5/2}} {}_2F_1\left(3,4;\frac{9}{2};1-\frac{b}{c}\right) \tag{A.73}$$

where $\Gamma(\frac{9}{2}) = \frac{7}{2}\Gamma(\frac{7}{2}) = \frac{7}{2}\frac{15}{8}\sqrt{\pi} = \frac{105}{16}\sqrt{\pi}$. With the same procedure as for $v_b = |l| = 2$, we have, using Eq. (A.66),

$$I_U = \frac{16}{15\sqrt{\pi}} \frac{b^{5/2}}{c^{5/2}} \frac{1}{1-\frac{b}{c}} \left[{}_2F_1\left(3,3;\frac{7}{2};1-\frac{b}{c}\right) - {}_2F_1\left(2,3;\frac{7}{2};1-\frac{b}{c}\right)\right], \tag{A.74}$$

using Eq. (A.54) twice,

$$I_U = \frac{16}{15\sqrt{\pi}} \frac{1}{1-\frac{b}{c}} \left[{}_2F_1\left(\frac{1}{2},\frac{1}{2};\frac{7}{2};1-\frac{b}{c}\right) - \frac{b^{5/2}}{c^{5/2}} {}_2F_1\left(2,3;\frac{7}{2};1-\frac{b}{c}\right)\right], \tag{A.75}$$

and using Eq. (A.57) twice,

$$
\begin{aligned}
I_U &= \frac{1}{\sqrt{\pi}} \frac{1}{\left(1-\frac{b}{c}\right)^2} \left[\left(1-\frac{2b}{c}\right) {}_2F_1\left(\frac{1}{2},\frac{1}{2};\frac{5}{2};1-\frac{b}{c}\right) + \frac{b}{c} {}_2F_1\left(\frac{1}{2},\frac{1}{2};\frac{3}{2};1-\frac{b}{c}\right) \right. \qquad (A.76) \\
&\qquad \left. - \frac{16}{15}\frac{b^{5/2}}{c^{5/2}} \left(1-\frac{b}{c}\right) {}_2F_1\left(2,3;\frac{7}{2};1-\frac{b}{c}\right)\right] \\
&= \frac{3}{4\sqrt{\pi}} \frac{1}{\left(1-\frac{b}{c}\right)^3} \left[\left(1-\frac{8b}{3c}+\frac{8b^2}{3c^2}\right) {}_2F_1\left(\frac{1}{2},\frac{1}{2};\frac{3}{2};1-\frac{b}{c}\right) \right. \\
&\qquad \left. + \frac{b}{c}\left(1-\frac{2b}{c}\right) {}_2F_1\left(\frac{1}{2},\frac{1}{2};\frac{1}{2};1-\frac{b}{c}\right) - \frac{64}{45}\frac{b^{5/2}}{c^{5/2}} \left(1-\frac{b}{c}\right)^2 {}_2F_1\left(2,3;\frac{7}{2};1-\frac{b}{c}\right)\right].
\end{aligned}
$$

Finally, using Eqs. (A.60), (A.61), (A.65), and (A.70), the result for $v_b = |l| = 3$ is

$$I_U = \frac{3}{4\sqrt{\pi}} \frac{1}{\left(1-\frac{b}{c}\right)^3} \left[\left(1-\frac{4b}{c}+\frac{8b^2}{c^2}\right) \frac{\arcsin\sqrt{1-\frac{b}{c}}}{\sqrt{1-\frac{b}{c}}} + \left(1-\frac{10b}{3c}-\frac{8b^2}{3c^2}\right)\sqrt{\frac{b}{c}}\right]. \tag{A.77}$$

The limit at $b/c = 1$, using L'Hospital's rule threefold and $z = 1 - b/c$, is

$$\begin{aligned}
\lim_{\frac{b}{c}\to 1} I_U &= \frac{3}{4\sqrt{\pi}} \lim_{z\to 0} \frac{(8z^2-12z+5)\arcsin\sqrt{z} + \left(\frac{26}{3}z - \frac{8}{3}z^2 - 5\right)\sqrt{z(1-z)}}{z^{7/2}} \qquad \text{(A.78)}\\
&= \frac{3}{4\sqrt{\pi}} \lim_{z\to 0} \frac{\frac{d}{dz}\,(8z^2-12z+5)\arcsin\sqrt{z} + \frac{d}{dz}\,\left(\frac{26}{3}z - \frac{8}{3}z^2 - 5\right)\sqrt{z(1-z)}}{\frac{d}{dz}\,z^{7/2}}\\
&= \frac{3}{14\sqrt{\pi}} \lim_{z\to 0} \frac{(16z-12)\arcsin\sqrt{z} + \left(\frac{26}{3} - \frac{16}{3}z\right)\sqrt{z(1-z)} + \frac{\frac{8}{3}z^3-6z^2+\frac{10}{3}z}{\sqrt{z(1-z)}}}{z^{5/2}}\\
&= \frac{3}{14\sqrt{\pi}} \lim_{z\to 0} \frac{\frac{d}{dz}(16z-12)\arcsin\sqrt{z} + \frac{d}{dz}\left(\frac{26}{3} - \frac{16}{3}z\right)\sqrt{z(1-z)} + \frac{d}{dz}\frac{\frac{8}{3}z^3-6z^2+\frac{10}{3}z}{\sqrt{z(1-z)}}}{\frac{d}{dz}\,z^{5/2}}\\
&= \frac{3}{35\sqrt{\pi}} \lim_{z\to 0} \frac{16\arcsin\sqrt{z} - \frac{16}{3}\sqrt{z(1-z)} + \frac{\frac{32}{3}z^2-\frac{32}{3}z}{\sqrt{z(1-z)}}}{z^{3/2}}\\
&= \frac{3}{35\sqrt{\pi}} \lim_{z\to 0} \frac{\frac{d}{dz}\,16\arcsin\sqrt{z} - \frac{d}{dz}\,\frac{16}{3}\sqrt{z(1-z)} + \frac{d}{dz}\,\frac{\frac{32}{3}z^2-\frac{32}{3}z}{\sqrt{z(1-z)}}}{\frac{d}{dz}\,z^{3/2}}\\
&= \frac{2}{35\sqrt{\pi}} \lim_{z\to 0} \frac{\frac{8}{\sqrt{z(1-z)}} + \frac{\frac{16}{3}z-\frac{8}{3}}{\sqrt{z(1-z)}} + \frac{\frac{64}{3}z-\frac{32}{3}}{\sqrt{z(1-z)}} + \frac{\frac{16}{3}-\frac{32}{3}z}{\sqrt{z(1-z)}}}{\sqrt{z}}\\
&= \frac{2}{35\sqrt{\pi}} \lim_{z\to 0} \frac{16}{\sqrt{1-z}}\\
&= \frac{32}{35\sqrt{\pi}},
\end{aligned}$$

again in accord with the result obtained by Eqs. (A.50) and (A.73). The asymptotic limit is

$$\lim_{\frac{b}{c}\to\infty} I_U = \frac{2}{35\sqrt{\pi}} \lim_{z\to -\infty} \frac{16}{\sqrt{1-z}} = 0. \qquad \text{(A.79)}$$

A.3.4 $v_b = 3, |l| = 1$

For $v_b = 3, |l| = 1$, the simplest case of $v_b = |l|+2$, the evaluation of the integral I_U (A.51) is, at first glance, rather difficult but using the previous results for $v_b = |l| = 1, 2, 3$, it can be easily simplified as follows

$$\begin{aligned}
I_U &= \frac{1}{2}\sqrt{\frac{b}{c}} \sum_{\nu_1=0}^{1}\sum_{\nu_2=0}^{1} (-1)^{\nu_1+\nu_2} \frac{1}{\nu_1!\nu_2!} \begin{pmatrix} \frac{v_b+1}{2} \\ \nu_1+1 \end{pmatrix} \begin{pmatrix} \frac{v_b+1}{2} \\ \nu_2+1 \end{pmatrix} \frac{b^{\nu_1+\nu_2}}{c^{\nu_1+\nu_2}} \qquad \text{(A.80)}\\
&\quad \frac{\Gamma(\nu_1+\nu_2+1)\Gamma(\nu_1+\nu_2+2)}{\Gamma\left(\nu_1+\nu_2+\frac{5}{2}\right)}\, {}_2F_1\left(\nu_1+\nu_2+1, \nu_1+\nu_2+2; \nu_1+\nu_2+\frac{5}{2}; 1-\frac{b}{c}\right)
\end{aligned}$$

$$= \frac{8}{3\sqrt{\pi}}\sqrt{\frac{b}{c}}\,{}_2F_1\left(1,2;\frac{5}{2};1-\frac{b}{c}\right) - \frac{32}{15\sqrt{\pi}}\frac{b^{3/2}}{c^{3/2}}\,{}_2F_1\left(2,3;\frac{7}{2};1-\frac{b}{c}\right) + \frac{32}{35\sqrt{\pi}}\frac{b^{5/2}}{c^{5/2}}\,{}_2F_1\left(3,4;\frac{9}{2};1-\frac{b}{c}\right).$$

Using Eqs. (A.53), (A.62), (A.65), (A.70), (A.73), and (A.77), we have

$$\begin{aligned} I_U &= 2I_U(v_b=|l|=1) - 2I_U(v_b=|l|=2) + I_U(v_b=|l|=3) \qquad \text{(A.81)}\\ &= \frac{4}{\sqrt{\pi}}\frac{1}{1-\frac{b}{c}}\left(\frac{\arcsin\sqrt{1-\frac{b}{c}}}{\sqrt{1-\frac{b}{c}}} - \sqrt{\frac{b}{c}}\right)\\ &\quad -\frac{2}{\sqrt{\pi}}\frac{1}{\left(1-\frac{b}{c}\right)^2}\left[\left(1-\frac{4b}{c}\right)\frac{\arcsin\sqrt{1-\frac{b}{c}}}{\sqrt{1-\frac{b}{c}}} + \left(1+\frac{2b}{c}\right)\sqrt{\frac{b}{c}}\right]\\ &\quad +\frac{3}{4\sqrt{\pi}}\frac{1}{\left(1-\frac{b}{c}\right)^3}\left[\left(1-\frac{4b}{c}+\frac{8b^2}{c^2}\right)\frac{\arcsin\sqrt{1-\frac{b}{c}}}{\sqrt{1-\frac{b}{c}}} + \left(1-\frac{10b}{3c}-\frac{8b^2}{3c^2}\right)\sqrt{\frac{b}{c}}\right]\\ &= \frac{1}{\sqrt{\pi}}\frac{1}{\left(1-\frac{b}{c}\right)^3}\left[\left(4-\frac{8b}{c}+\frac{4b^2}{c^2}\right)\frac{\arcsin\sqrt{1-\frac{b}{c}}}{\sqrt{1-\frac{b}{c}}} + \left(-4+\frac{8b}{c}-\frac{4b^2}{c^2}\right)\sqrt{\frac{b}{c}}\right]\\ &\quad +\frac{1}{\sqrt{\pi}}\frac{1}{\left(1-\frac{b}{c}\right)^3}\left[\left(-2+\frac{10b}{c}-\frac{8b^2}{c^2}\right)\frac{\arcsin\sqrt{1-\frac{b}{c}}}{\sqrt{1-\frac{b}{c}}} + \left(-2-\frac{2b}{c}+\frac{4b^2}{c^2}\right)\sqrt{\frac{b}{c}}\right]\\ &\quad +\frac{1}{\sqrt{\pi}}\frac{1}{\left(1-\frac{b}{c}\right)^3}\left[\left(\frac{3}{4}-\frac{3b}{c}+\frac{6b^2}{c^2}\right)\frac{\arcsin\sqrt{1-\frac{b}{c}}}{\sqrt{1-\frac{b}{c}}} + \left(\frac{3}{4}-\frac{5b}{2c}-\frac{2b^2}{c^2}\right)\sqrt{\frac{b}{c}}\right], \end{aligned}$$

thus

$$I_U = \frac{1}{\sqrt{\pi}}\frac{1}{\left(1-\frac{b}{c}\right)^3}\left[\left(\frac{11}{4}-\frac{b}{c}+\frac{2b^2}{c^2}\right)\frac{\arcsin\sqrt{1-\frac{b}{c}}}{\sqrt{1-\frac{b}{c}}} + \left(-\frac{21}{4}+\frac{7b}{2c}-\frac{2b^2}{c^2}\right)\sqrt{\frac{b}{c}}\right]. \qquad \text{(A.82)}$$

Finally, the corresponding limit at $b/c = 1$, using Eqs. (A.81), (A.63), (A.71), and (A.78), is

$$\begin{aligned} \lim_{\frac{b}{c}\to 1} I_U &= \frac{8}{3\sqrt{\pi}} - \frac{32}{15\sqrt{\pi}} + \frac{32}{35\sqrt{\pi}} \qquad \text{(A.83)}\\ &= \frac{152}{105\sqrt{\pi}}. \end{aligned}$$

Since the asymptotic limits ($b/c \to \infty$) for $v_b = |l| = 1, 2, 3$ are zero (Eqs. (A.64), (A.72), and (A.79)), the corresponding asymptotic limit for $v_b = 3, |l| = 1$ is also zero, i.e.

$$\lim_{\frac{b}{c}\to\infty} I_U = 0. \qquad \text{(A.84)}$$

Bibliography

[1] P. Agostini, L. F. DiMauro, Rep. Prog. Phys. **67**, 813 (2004).

[2] A. Scrinzi, M. Y. Ivanov, R. Kienberger, D. M. Villeneuve, J. Phys. B **39**, R1 (2006).

[3] A. D. Bandrauk, S. Chelkowski, G. L. Yudin, in J. J. Dubowski, S. Tanev, eds., *Photon-based Nanoscience and Nanobiotechnology* (Springer, Dordrecht, 2006), p. 31.

[4] P. B. Corkum, F. Krausz, Nature Phys. **3**, 381 (2007).

[5] P. H. Bucksbaum, Science **317**, 766 (2007).

[6] F. Krausz, M. Ivanov, Rev. Mod. Phys. **81**, 163 (2009).

[7] M. Born, R. Oppenheimer, Ann. Phys. **84**, 457 (1927).

[8] L. S. Cederbaum, J. Chem. Phys. **128**, 124101 (2008).

[9] S. Chelkowski, G. L. Yudin, A. D. Bandrauk, J. Phys. B **39**, S409 (2006).

[10] A. L. Cavalieri, N. Müller, Th. Uphues, V. S. Yakovlev, A. Baltuška, B. Horvath, B. Schmidt, L. Blümel, R. Holzwarth, S. Hendel, M. Drescher, U. Kleineberg, P. M. Echenique, R. Kienberger, F. Krausz, U. Heinzmann, Nature **449**, 1029 (2007).

[11] R. Kienberger, M. Hentschel, M. Uiberacker, Ch. Spielmann, M. Kitzler, A. Scrinzi, M. Wieland, Th. Westerwalbesloh, U. Kleineberg, U. Heinzmann, M. Drescher, F. Krausz, Science **297**, 1144 (2002).

[12] M. Uiberacker, Th. Uphues, M. Schultze, A. J. Verhoef, V. Yakovlev, M. F. Kling, J. Rauschenberger, N. M. Kabachnik, H. Schröder, M. Lezius, K. L. Kompa, H.-G. Muller, M. J. J. Vrakking, S. Hendel, U. Kleineberg, U. Heinzmann, M. Drescher, F. Krausz, Nature **446**, 627 (2007).

[13] F. Remacle, R. D. Levine, PNAS **103**, 6793 (2006).

[14] T. Pfeifer, M. J. Abel, P. M. Nagel, A. Jullien, Z.-H. Loh, M. J. Bell, D. M. Neumark, S. R. Leone, Chem. Phys. **463**, 11 (2008).

[15] P. B. Corkum, N. H. Burnett, M. Y. Ivanov, Opt. Lett. **19**, 1870 (1994).

[16] M. Y. Ivanov, P. B. Corkum, T. Zuo, A. D. Bandrauk, Phys. Rev. Lett. **74**, 2933 (1995).

[17] M. Drescher, M. Hentschel, R. Kienberger, G. Tempea, Ch. Spielmann, G. A. Reider, P. B. Corkum, F. Krausz, Science **291**, 1923 (2001).

[18] M. Hentschel, R. Kienberger, Ch. Spielmann, G. A. Reider, N. Milosevic, T. Brabec, P. B. Corkum, U. Heinzmann, M. Drescher, F. Krausz, Nature **414**, 509 (2001).

[19] J. Itatani, J. Levesque, D. Zeidler, H. Niikura, H. Pépin, J. C. Kieffer, P. B. Corkum, D. M. Villeneuve, Nature **432**, 867 (2004).

[20] S. Patchovskii, Z. Zhao, T. Brabec, D. M. Villeneuve, J. Chem. Phys. **126**, 114306 (2007).

[21] M. Lein, J. Phys. B **40**, R135 (2007).

[22] E. V. van der Zwan, C. C. Chirilă, M. Lein, Phys. Rev. A **78**, 033410 (2008).

[23] S. Baker, J. S. Robinson, C. A. Haworth, H. Teng, R. A. Smith, C. C. Chirilă, M. Lein, J. W. G. Tisch, J. P. Marangos, Science **312**, 424 (2006).

[24] J. P. Marangos, S. Baker, N. Kajumba, J. S. Robinson, J. W. G. Tisch, R. Torres, Phys. Chem. Chem. Phys. **10**, 35 (2008).

[25] N. L. Wagner, A. Wüest, I. P. Christov, T. Popmintchev, X. Zhou, M. M. Murnane, H. C. Kapteyn, PNAS **103**, 13279 (2006).

[26] W. Li, X. Zhou, R. Lock, S. Patchovskii, A. Stolow, H. C. Kapteyn, M. M. Murnane, Science **322**, 1207 (2008).

[27] A. D. Bandrauk, S. Chelkowski, H. Lu, J. Phys. B **42**, 075602 (2009).

[28] S. Ramakrishna, T. Seideman, Phys. Rev. Lett. **99**, 113901 (2007).

[29] S. Ramakrishna, T. Seideman, Phys. Rev. A **77**, 053411 (2008).

[30] A. Abdurrouf, F. H. M. Faisal, Phys. Rev. A **79**, 023405 (2009).

[31] P. B. Corkum, Phys. Rev. Lett. **71**, 1994 (1993).

[32] M. Lewenstein, Ph. Balcou, M. Y. Ivanov, A. L'Huillier, P. B. Corkum, Phys. Rev. A **49**, 2117 (1994).

[33] M. Y. Kuchiev, V. N. Ostrovsky, Phys. Rev. A **60**, 3111 (1999).

[34] R. Santra, A. Gordon, Phys. Rev. Lett. **96**, 073906 (2006).

[35] L. V. Keldysh, Zh. Eksp. Teor. Fiz. **47**, 1945 (1964).

[36] K. Mishima, M. Hayashi, J. Yi, S. H. Lin, H. L. Selzle, E. W. Schlag, Phys. Rev. A **66**, 033401 (2002).

[37] X. M. Tong, Z. X. Zhao, C. D. Lin, Phys. Rev. A **66**, 033402 (2002).

[38] H. R. Reiss, Phys. Rev. Lett. **101**, 043002 (2008).

[39] P. B. Corkum, N. H. Burnett, F. Brunel, Phys. Rev. Lett. **62**, 1259 (1989).

[40] D. B. Milošević, G. G. Paulus, D. Bauer, W. Becker, J. Phys. B **39**, R203 (2006).

[41] O. E. Alon, V. Averbukh, N. Moiseyev, Phys. Rev. Lett. **80**, 3743 (1998).

[42] R. Baer, D. Neuhauser, P. R. Ždánská, N. Moiseyev, Phys. Rev. A **68**, 043406 (2003).

[43] P. R. Ždánská, V. Averbukh, N. Moiseyev, J. Chem. Phys. **118**, 8726 (2003).

[44] D. Bauer, F. Ceccherini, Laser Part. Beams **19**, 85 (2001).

[45] F. Ceccherini, D. Bauer, Phys. Rev. A **64**, 033423 (2001).

[46] O. E. Alon, V. Averbukh, N. Moiseyev, Phys. Rev. Lett. **85**, 5218 (2000).

[47] J. Sun, W.-Z. Liang, Y. Liu, J. Theo. Comp. Chem. **7**, 579 (2008).

[48] V. V. Strelkov, Phys. Rev. A **74**, 013405 (2006).

[49] F. He, C. Ruiz, A. Becker, Opt. Lett. **32**, 3224 (2007).

[50] K. C. Kulander, B. W. Shore, Phys. Rev. Lett. **62**, 524 (1989).

[51] J. H. Eberly, Q. Su, J. Javanainen, Phys. Rev. Lett. **62**, 881 (1989).

[52] K. Burnett, V. C. Reed, J. Cooper, P. L. Knight, Phys. Rev. A **45**, 3347 (1992).

[53] D. J. Diestler, Phys. Rev. A **78**, 033814 (2008).

[54] C. C. Chirilă, M. Lein, J. Mod. Opt. **54**, 1039 (2007).

[55] A. D. Bandrauk, S. Chelkowski, D. J. Diestler, J. Manz, K.-J. Yuan, Phys. Rev. A **79**, 023403 (2009).

[56] M. Lein, N. Hay, R. Velotta, J. P. Marangos, P. L. Knight, Phys. Rev. A **66**, 023805 (2002).

[57] M. Lein, P. P. Corso, J. P. Marangos, P. L. Knight, Phys. Rev. A **67**, 023819 (2003).

[58] B. Zimmermann, M. Lein, J. M. Rost, Phys. Rev. A **71**, 033401 (2005).

[59] S. Baker, J. S. Robinson, M. Lein, C. C. Chirilă, R. Torres, H. C. Bandulet, D. Comtois, J. C. Kieffer, D. M. Villeneuve, J. W. G. Tisch, J. P. Marangos, Phys. Rev. Lett. **101**, 053901 (2008).

[60] S. Odžak, D. B. Milošević, Phys. Rev. A **79**, 023414 (2009).

[61] S. Odžak, D. B. Milošević, J. Phys. B **42**, 071001 (2009).

[62] R. de Nalda, E. Heesel, M. Lein, N. Hay, R. Velotta, E. Springate, M. Castillejo, J. P. Marangos, Phys. Rev. A **69**, 031804(R) (2004).

[63] X. X. Zhou, X. M. Tong, Z. X. Zhao, C. D. Lin, Phys. Rev. A **71**, 061801(R) (2005).

[64] C. B. Madsen, L. B. Madsen, Phys. Rev. A **74**, 023403 (2006).

[65] C. B. Madsen, L. B. Madsen, Phys. Rev. A **76**, 043419 (2007).

[66] B. K. McFarland, J. P. Farrell, P. H. Bucksbaum, M. Gühr, Science **322**, 1232 (2008).

[67] A. D. Bandrauk, S. Baramaki, Chem. Phys. **338**, 312 (2007).

[68] A. D. Bandrauk, S. Barmaki, G. L. Kamta, Phys. Rev. Lett. **98**, 013001 (2007).

[69] A. D. Bandrauk, S. Barmaki, S. Chelkowski, G. L. Kamta, in K. Yamanouchi, S. L. Chin, P. Agostini, G. Ferrante, eds., *Progress in Ultrafast Intense Laser Science III* (Springer, Berlin, 2008), vol. 89 of *Springer Series in Chemical Physics*, p. 171.

[70] E. Goulielmakis, M. Schultze, M. Hofstetter, V. S. Yakovlev, J. Gagnon, M. Uiberacker, A. L. Aquila, E. M. Gullikson, D. T. Attwood, R. Kienberger, F. Krausz, U. Kleineberg, Science **320**, 1614 (2008).

[71] A. D. Bandrauk, S. Chelkowski, N. H. Shon, Phys. Rev. A **68**, 041802 (2003).

[72] A. Baltuška, Th. Udem, M. Uiberacker, M. Hentschel, E. Goulielmakis, Ch. Gohle, R. Holzwarth, V. S. Yakovlev, A. Scrinzi, T. W. Hänsch, F. Krausz, Nature **421**, 611 (2003).

[73] R. Kienberger, E. Goulielmakis, M. Uiberacker, A. Baltuška, V. S. Yakovlev, F. Bammer, A. Scrinzi, Th. Westerwalbesloh, U. Kleineberg, U. Heinzmann, M. Drescher, F. Krausz, Nature **427**, 817 (2004).

[74] E. Goulielmakis, M. Uiberacker, R. Kienberger, A. Baltuška, V. S. Yakovlev, A. Scrinzi, Th. Westerwalbesloh, U. Kleineberg, U. Heinzmann, M. Drescher, F. Krausz, Science **305**, 1267 (2004).

[75] E. Goulielmakis, V. S. Yakovlev, A. L. Cavalieri, M. Uiberacker, V. Pervak, A. Apolonski, R. Kienberger, U. Kleineberg, F. Krausz, Science **317**, 769 (2007).

[76] D. B. Milošević, W. Becker, R. Kopold, Phys. Rev. A **61**, 063404 (2000).

[77] X. Xie, A. Scrinzi, M. Wickenhauser, A. Baltuška, I. Barth, M. Kitzler, Phys. Rev. Lett. **101**, 033901 (2008).

[78] O. Smirnova, S. Patchovskii, Y. Mairesse, N. Dudovich, D. Villeneuve, P. B. Corkum, M. Y. Ivanov, Phys. Rev. Lett. **102**, 063601 (2009).

[79] X. Zhou, R. Lock, N. Wagner, W. Li, H. C. Kapteyn, M. M. Murnane, Phys. Rev. Lett. **102**, 073902 (2009).

[80] U. Graf, M. Fieß, M. Schultze, R. Kienberger, F. Krausz, E. Goulielmakis, Opt. Express **16**, 18956 (2008).

[81] M. Shapiro, P. Brumer, *Principles of the Quantum Control of Molecular Processes* (Wiley, Hoboken, 2003).

[82] O. Kühn, L. Wöste, eds., *Analysis and Control of Ultrafast Photoinduced Reactions*, vol. 87 of *Springer Series in Chemical Physics* (Springer, Berlin, 2007).

[83] M. Dantus, V. V. Lozovoy, Chem. Rev. **104**, 1813 (2004).

[84] V. V. Lozovoy, M. Dantus, ChemPhysChem **6**, 1970 (2005).

[85] A. Stolow, A. E. Bragg, D. M. Neumark, Chem. Rev. **104**, 1719 (2004).

[86] D. J. Tannor, S. A. Rice, J. Chem. Phys. **83**, 5013 (1985).

[87] R. Kosloff, S. A. Rice, P. Gaspard, S. Tersigni, D. J. Tannor, Chem. Phys. **139**, 201 (1989).

[88] P. Brumer, M. Shapiro, Chem. Phys. Lett. **126**, 541 (1986).

[89] J. Joseph, J. Manz, Mol. Phys. **58**, 1149 (1986).

[90] S. Shi, A. Woody, H. Rabitz, J. Chem. Phys. **88**, 6870 (1988).

[91] A. P. Peirce, M. A. Dahleh, H. Rabitz, Phys. Rev. A **37**, 4950 (1988).

[92] R. S. Judson, H. Rabitz, Phys. Rev. Lett. **68**, 1500 (1992).

[93] Q. Ren, G. G. Balint-Kurti, F. R. Manby, M. Artamonov, T.-S. Ho, H. Rabitz, J. Chem. Phys. **124**, 014111 (2006).

[94] J. Werschnik, E. K. U. Gross, J. Phys. B **40**, R175 (2007).

[95] U. Gaubatz, P. Rudecki, M. Becker, S. Schiemann, M. Külz, K. Bergmann, Chem. Phys. Lett. **149**, 463 (1988).

[96] K. Bergmann, H. Theuer, B. W. Shore, Rev. Mod. Phys. **70**, 1003 (1998).

[97] N. V. Vitanov, T. Hlafmann, B. W. Shore, K. Bergmann, Annu. Rev. Phys. Chem. **52**, 763 (2001).

[98] S. Chelkowski, A. D. Bandrauk, P. B. Corkum, Phys. Rev. Lett. **65**, 2355 (1990).

[99] B. Amstrup, N. E. Henriksen, J. Chem. Phys. **97**, 8285 (1992).

[100] J. E. Combariza, B. Just, J. Manz, G. K. Paramonov, J. Phys. Chem. **95**, 10351 (1991).

[101] M. V. Korolkov, J. Manz, G. K. Paramonov, J. Chem. Phys. **105**, 10874 (1996).

[102] N. Došlić, O. Kühn, J. Manz, K. Sudermann, J. Phys. Chem. A **102**, 9645 (1998).

[103] M. Holthaus, B. Just, Phys. Rev. A **49**, 1950 (1994).

[104] J. L. Herek, A. Materny, A. H. Zewail, Chem. Phys. Lett. **228**, 15 (1994).

[105] A. H. Zewail, J. Phys. Chem. **100**, 12701 (1996).

[106] Y. Fujimura, L. González, K. Hoki, D. Kröner, J. Manz, Y. Ohtsuki, Angew. Chem. Int. Ed. **39**, 4586 (2000), Angew. Chem. **112**, 4785 (2000).

[107] K. Hoki, D. Kröner, J. Manz, Chem. Phys. **267**, 59 (2001).

[108] C. B. Madsen, L. B. Madsen, S. S. Viftrup, M. P. Johansson, T. B. Poulsen, L. Holmegaard, V. Kumarappan, K. A. Jørgensen, H. Stapelfeldt, Phys. Rev. Lett. **102**, 073007 (2009).

[109] A. D. Bandrauk, E.-W. S. Sedik, C. F. Matta, J. Chem. Phys. **121**, 7764 (2004).

[110] C. P. Koch, J. P. Palao, R. Kosloff, F. Masnou-Seeuws, Phys. Rev. A **70**, 013402 (2004).

[111] N. Elghobashi, L. González, J. Manz, J. Chem. Phys. **120**, 8002 (2004).

[112] N. Elghobashi, L. González, Phys. Chem. Chem. Phys. **6**, 4071 (2004).

[113] N. Elghobashi-Meinhardt, L. González, I. Barth, T. Seideman, J. Chem. Phys. **130**, 024310 (2009).

[114] N. F. Scherer, R. J. Carlson, A. Matro, M. Du, A. J. Ruggiero, V. Romero-Rochin, J. A. Cina, G. R. Fleming, S. A. Rice, J. Chem. Phys. **95**, 1487 (1991).

[115] K. Ohmori, Annu. Rev. Phys. Chem. **60**, 487 (2009).

[116] G. Kurizki, M. Shapiro, P. Brumer, Phys. Rev. B **39**, 3435 (1989).

[117] P. Krause, T. Klamroth, P. Saalfrank, J. Chem. Phys. **123**, 074105 (2005).

[118] J. C. Tremblay, T. Klamroth, P. Saalfrank, J. Chem. Phys. **129**, 084302 (2008).

[119] A. S. Moskalenko, A. Matos-Abiague, J. Berakdar, Phys. Rev. B **74**, 161303(R) (2006).

[120] T. Klamroth, J. Chem. Phys. **124**, 144310 (2006).

[121] K. A. Pronin, A. D. Bandrauk, Phys. Rev. B **69**, 195308 (2004).

[122] I. Franco, M. Shapiro, P. Brumer, J. Chem. Phys. **128**, 244906 (2008).

[123] S. S. Skourtis, D. N. Beratan, R. Naaman, A. Nitzan, D. H. Waldeck, Phys. Rev. Lett. **101**, 238103 (2008).

[124] R. J. Cave, Science **323**, 1435 (2009).

[125] M. V. Korolkov, J. Manz, J. Chem. Phys. **120**, 11522 (2004).

[126] A. B. H. Yedder, C. Le Bris, O. Atabek, S. Chelkowski, A. D. Bandrauk, Phys. Rev. A **69**, 041802(R) (2004).

[127] A. D. Bandrauk, N. H. Shon, Phys. Rev. A **66**, 031401(R) (2002).

[128] Z. Zhai, R.-F. Yu, X.-S. Liu, Y.-J. Yang, Phys. Rev. A **78**, 041402(R) (2008).

[129] R. A. Bartels, M. M. Murnane, H. C. Kapteyn, I. Christov, H. Rabitz, Phys. Rev. A **70**, 043404 (2004).

[130] C. Winterfeldt, Ch. Spielmann, G. Gerber, Rev. Mod. Phys. **80**, 117 (2008).

[131] M. Kitzler, K. O'Keeffe, M. Lezius, J. Mod. Opt. **53**, 57 (2006).

[132] M. Kitzler, X. Xie, S. Roither, A. Scrinzi, A. Baltuška, New J. Phys. **10**, 025029 (2008).

[133] M. Wollenhaupt, A. Präkelt, C. Sarpe-Tudoran, D. Liese, T. Baumert, J. Opt. B **7**, S270 (2005).

[134] T. Bayer, M. Wollenhaupt, T. Baumert, J. Phys. B **41**, 074007 (2008).

[135] T. Brixner, G. Krampert, T. Pfeifer, R. Selle, G. Gerber, M. Wollenhaupt, O. Graefe, C. Horn, D. Liese, T. Baumert, Phys. Rev. Lett. **92**, 208301 (2004).

[136] F. He, A. Becker, J. Phys. B **41**, 074017 (2008).

[137] S. Gräfe, V. Engel, M. Y. Ivanov, Phys. Rev. Lett. **101**, 103001 (2008).

[138] D. Geppert, P. von den Hoff, R. de Vivie-Riedle, J. Phys. B **41**, 074006 (2008).

[139] M. F. Kling, Ch. Siedschlag, I. Znakovskaya, A. J. Verhoef, S. Zherebtsov, F. Krausz, M. Lezius, M. J. J. Vrakking, Mol. Phys. **106**, 455 (2008).

[140] F. Martín, J. Fernández, T. Havermeier, L. Foucar, Th. Weber, K. Kreidi, M. Schöffler, L. Schmidt, T. Jahnke, O. Jagutzki, A. Czasch, E. P. Benis, T. Osipov, A. L. Landers, A. Belkacem, M. H. Prior, H. Schmidt-Böcking, C. L. Cocke, R. Dörner, Science **315**, 629 (2007).

[141] A. D. Bandrauk, S. Chelkowski, D. J. Diestler, J. Manz, K.-J. Yuan, Int. J. Mass Spectrom. **277**, 189 (2008).

[142] C. P. J. Martiny, L. B. Madsen, Phys. Rev. Lett. **97**, 093001 (2006).

[143] S. X. Hu, L. A. Collins, Phys. Rev. A **73**, 023405 (2006).

[144] I. Barth, J. Manz, Phys. Rev. A **75**, 012510 (2007).

[145] I. Barth, J. Manz, L. Serrano-Andrés, Chem. Phys. **347**, 263 (2008).

[146] I. Barth, L. Serrano-Andrés, T. Seideman, J. Chem. Phys. **129**, 164303 (2008).

[147] I. Barth, J. Manz, Angew. Chem. Int. Ed. **45**, 2962 (2006), Angew. Chem. **118**, 3028 (2006).

[148] I. Barth, J. Manz, Y. Shigeta, K. Yagi, J. Am. Chem. Soc. **128**, 7043 (2006).

[149] I. Barth, J. Manz, in A. W. Castleman, Jr., M. L. Kimble, eds., *Femtochemistry VII: Fundamental Ultrafast Processes in Chemistry, Physics, and Biology* (Elsevier, Amsterdam, 2006), p. 441.

[150] I. Barth, L. González, C. Lasser, J. Manz, T. Rozgonyi, in B. Lasorne, G. A. Worth, eds., *Coherent Control of Molecules* (CCP6, Daresbury, 2006), p. 18.

[151] K. Nobusada, K. Yabana, Phys. Rev. A **75**, 032518 (2007).

[152] K. Nobusada, K. Yabana, Comp. Phys. Comm. **177**, 54 (2007).

[153] A. Matos-Abiague, J. Beradkar, Phys. Rev. Lett. **94**, 166801 (2005).

[154] Y. V. Pershin, C. Piermarocchi, Phys. Rev. B **72**, 125348 (2005).

[155] Y. V. Pershin, C. Piermarocchi, Phys. Rev. B **72**, 245331 (2005).

[156] E. Räsänen, A. Castro, J. Werschnik, A. Rubio, E. K. U. Gross, Phys. Rev. Lett. **98**, 157404 (2007).

[157] M. Kanno, H. Kono, Y. Fujimura, Angew. Chem. Int. Ed. **45**, 7995 (2006).

[158] M. Kanno, K. Hoki, H. Kono, Y. Fujimura, J. Chem. Phys. **127**, 204314 (2007).

[159] M. Nest, F. Remacle, R. D. Levine, New J. Phys. **10**, 025019 (2008).

[160] F. Remacle, R. Kienberger, F. Krausz, R. D. Levine, Chem. Phys. **338**, 342 (2007).

[161] T. Minami, H. Fukui, H. Nagai, K. Yoneda, R. Kishi, H. Takahashi, M. Nakano, J. Phys. Chem. C **113**, 3332 (2009).

[162] J. A. Yeazell, C. R. Stroud, Jr., Phys. Rev. A **35**, 2806 (1987).

[163] J. A. Yeazell, C. R. Stroud, Jr., Phys. Rev. Lett. **60**, 1494 (1988).

[164] J. J. Mestayer, B. Wyker, J. C. Lancaster, F. B. Dunning, C. O. Reinhold, S. Yoshida, J. Burgdörfer, Phys. Rev. Lett. **100**, 243004 (2008).

[165] J. J. Mestayer, B. Wyker, F. B. Dunning, C. O. Reinhold, S. Yoshida, J. Burgdörfer, Phys. Rev. A **78**, 045401 (2008).

[166] J. J. Mestayer, B. Wyker, F. B. Dunning, S. Yoshida, C. O. Reinhold, J. Burgdörfer, Phys. Rev. A **79**, 033417 (2009).

[167] H. Maeda, J. H. Gurian, T. F. Gallagher, Phys. Rev. Lett. **102**, 103001 (2009).

[168] J. A. Yeazell, M. Mallalieu, C. R. Stroud, Jr., Phys. Rev. Lett. **64**, 2007 (1990).

[169] J. A. Yeazell, C. R. Stroud, Jr., Phys. Rev. A **43**, 5153 (1991).

[170] J. Jusélius, D. Sundholm, J. Org. Chem. **65**, 5233 (2000).

[171] E. Steiner, P. W. Fowler, J. Phys. Chem. A **105**, 9553 (2001).

[172] E. Steiner, P. W. Fowler, L. W. Jenneskens, Angew. Chem. Int. Ed. **40**, 362 (2001).

[173] E. Steiner, P. W. Fowler, ChemPhysChem **1**, 114 (2002).

[174] E. Steiner, P. W. Fowler, Org. Biomol. Chem. **1**, 1785 (2003).

[175] J. Jusélius, D. Sundholm, J. Gauss, J. Chem. Phys. **121**, 3952 (2004).

[176] E. Steiner, P. W. Fowler, Org. Biomol. Chem. **2**, 34 (2004).

[177] A. Soncini, P. W. Fowler, Chem. Phys. Lett. **400**, 213 (2004).

[178] A. Soncini, P. W. Fowler, F. Zerbetto, Chem. Phys. Lett. **405**, 136 (2005).

[179] E. Steiner, A. Soncini, P. W. Fowler, Org. Biomol. Chem. **3**, 4053 (2005).

[180] E. Steiner, P. W. Fowler, Org. Biomol. Chem. **4**, 2473 (2006).

[181] E. Steiner, A. Soncini, P. W. Fowler, J. Phys. Chem. A **110**, 12882 (2006).

[182] R. W. A. Havenith, P. W. Fowler, Chem. Phys. Lett. **449**, 347 (2007).

[183] A. Soncini, P. W. Fowler, Chem. Phys. Lett. **450**, 431 (2008).

[184] G. Periyasamy, N. A. Burton, I. H. Hillier, J. M. H. Thomas, J. Phys. Chem. A **112**, 5960 (2008).

[185] S. Pelloni, P. Lazzeretti, Chem. Phys. **356**, 153 (2009).

[186] P. Lazzeretti, Prog. Nucl. Magn. Res. Spec. **36**, 1 (2000).

[187] J. A. N. F. Gomes, R. B. Mallion, Chem. Rev. **101**, 1349 (2001).

[188] T. Heine, C. Corminboeuf, G. Seifert, Chem. Rev. **105**, 3889 (2005).

[189] R. Bast, J. Jusélius, T. Saue, Chem. Phys. **356**, 187 (2009).

[190] N. F. Hinsche, A. S. Moskalenko, J. Berakdar, Phys. Rev. A **79**, 023822 (2009).

[191] J.-P. Sauvage, ed., *Molecular Machines and Motors, Structure and Bonding*, vol. 99 (Springer, Berlin, 2001).

[192] V. Balzani, M. Venturi, A. Credi, *Molecular Devices and Machines – A Journey into the Nanoworld* (Wiley-VCH, Weinheim, 2003).

[193] G. S. Kottas, L. I. Clarke, D. Horinek, J. Michl, Chem. Rev. **105**, 1281 (2005).

[194] R. A. van Delden, M. K. J. ter Wiel, M. M. Pollard, J. Vicario, N. Koumura, B. L. Feringa, Nature **437**, 1337 (2005).

[195] K. Hoki, M. Yamaki, Y. Fujimura, Angew. Chem. Int. Ed. **42**, 2975 (2003), Angew. Chem. **115**, 3084 (2003).

[196] K. Hoki, M. Yamaki, S. Koseki, Y. Fujimura, J. Chem. Phys. **118**, 497 (2003).

[197] M. Yamaki, K. Hoki, Y. Ohtsuki, H. Kono, Y. Fujimura, J. Am. Chem. Soc. **127**, 7300 (2005).

[198] M. Yamaki, K. Hoki, H. Kono, Y. Fujimura, Chem. Phys. **347**, 272 (2008).

[199] M. Yamaki, S. Nakayama, K. Hoki, H. Kono, Y. Fujimura, Phys. Chem. Chem. Phys. **11**, 1662 (2009).

[200] Y. Fujimura, L. González, D. Kröner, J. Manz, I. Mehdaoui, B. Schmidt, Chem. Phys. Lett. **386**, 248 (2004).

[201] J. Gaus, K. Kobe, V. Bonačić-Koutecký, H. Kühling, J. Manz, B. Reischl, S. Rutz, E. Schreiber, L. Wöste, J. Phys. Chem. **97**, 12509 (1993).

[202] T. Baumert, R. Thalweiser, G. Gerber, Chem. Phys. Lett. **209**, 29 (1993).

[203] J. Schön, H. Köppel, Chem. Phys. Lett. **231**, 55 (1994).

[204] J. Schön, H. Köppel, J. Chem. Phys. **103**, 9292 (1995).

[205] R. de Vivie-Riedle, J. Gaus, V. Bonačić-Koutecký, J. Manz, B. Reischl-Lenz, P. Saalfrank, Chem. Phys. **223**, 1 (1997).

[206] A. F. Sax, Chem. Phys. **349**, 9 (2008).

[207] I. Barth, J. Manz, P. Sebald, Chem. Phys. **346**, 89 (2008).

[208] I. Barth, J. Manz, G. Pérez-Hernández, P. Sebald, Z. Phys. Chem. **222**, 1311 (2008).

[209] A. D. Buckingham, J. E. Del Bene, S. A. C. McDowell, Chem. Phys. Lett. **463**, 1 (2008).

[210] H. Stapelfeldt, T. Seideman, Rev. Mod. Phys. **75**, 543 (2003).

[211] M. Leibscher, I. Sh. Averbukh, H. Rabitz, Phys. Rev. A **69**, 013402 (2004).

[212] E. Hamilton, T. Seideman, T. Ejdrup, M. D. Poulsen, C. Z. Bisgaard, S. S. Viftrup, H. Stapelfeldt, Phys. Rev. A **72**, 043402 (2005).

[213] T. Seideman, E. Hamilton, Adv. At. Mol. Opt. Phys. **52**, 289 (2006).

[214] S. Fleischer, I. Sh. Averbukh, Y. Prior, J. Phys. B **41**, 074018 (2008).

[215] C. M. Dion, A. Keller, O. Atabek, Eur. Phys. J. D **14**, 249 (2001).

[216] M. Machholm, N. E. Henriksen, Phys. Rev. Lett. **87**, 193001 (2001).

[217] A. B. H. Yedder, A. Auger, C. M. Dion, E. Cancès, A. Keller, C. Le Bris, O. Atabek, Phys. Rev. A **66**, 063401 (2002).

[218] K. F. Lee, D. M. Villeneuve, P. B. Corkum, A. Stolow, J. G. Underwood, Phys. Rev. Lett. **97**, 173001 (2006).

[219] M. D. Poulsen, T. Ejdrup, H. Stapelfeldt, E. Hamilton, T. Seideman, Phys. Rev. A **73**, 033405 (2006).

[220] C. Z. Bisgaard, S. S. Viftrup, H. Stapelfeldt, Phys. Rev. A **73**, 053410 (2006).

[221] S. S. Viftrup, V. Kumarappan, L. Holmegaard, C. Z. Bisgaard, H. Stapelfeldt, M. Artamonov, E. Hamilton, T. Seideman, Phys. Rev. A **79**, 023404 (2009).

[222] J. J. Larsen, K. Hald, N. Bjerre, H. Stapeldfeldt, T. Seideman, Phys. Rev. Lett. **85**, 2470 (2000).

[223] M. Artamonov, T. Seideman, J. Chem. Phys. **128**, 154313 (2008).

[224] A. Rouzée, E. Hertz, B. Lavorel, O. Faucher, J. Phys. B **41**, 074002 (2008).

[225] T. Seideman, Phys. Rev. Lett. **83**, 4971 (1999).

[226] S. C. Althorpe, T. Seideman, J. Chem. Phys. **113**, 7901 (2000).

[227] J. P. van der Ziel, P. S. Pershan, L. D. Malmstrom, Phys. Rev. Lett. **15**, 190 (1965).

[228] P. S. Pershan, J. P. van der Ziel, L. D. Malmstrom, Phys. Rev. **143**, 574 (1966).

[229] R. Hertel, J. Magn. Magn. Mater. **303**, L1 (2006).

[230] F. Pobell, A. D. Bianchi, T. Herrmannsdörfer, H. Krug, S. Zherlitsyn, S. Zvyagin, J. Wosnitza, in *AIP Conference Proceedings* (2006), vol. 850, p. 1649.

[231] P. Krause, T. Klamroth, P. Saalfrank, J. Chem. Phys. **127**, 034107 (2007).

[232] J. B. Foresman, M. Head-Gordon, J. A. Pople, M. J. Frisch, J. Phys. Chem. **96**, 135 (1992).

[233] P. Krause, T. Klamroth, J. Chem. Phys. **128**, 234307 (2008).

[234] R. Paunz, *Spin Eigenfunctions* (Plenum, New York, 1979).

[235] I. N. Levine, *Quantum Chemistry* (Prentice Hall, New Jersey, 2000), 5th ed.

[236] N. Sukumar, B. M. Deb, Int. J. Quant. Chem. **40**, 501 (1991).

[237] O. D. Jefimenko, *Electricity and Magnetism* (Electret Scientific, Star City, 1989).

[238] D. J. Griffiths, M. A. Heald, Am. J. Phys. **59**, 111 (1991).

[239] J. A. Heras, Am. J. Phys. **63**, 928 (1995).

[240] A. Hinchliffe, R. W. Munn, *Molecular Electromagnetism* (Wiley, Chichester, 1985).

[241] I. Barth, C. Lasser, Phys. Rev. A (2009), in preparation.

[242] J. Rauch, G. Mourou, Proc. Am. Math. Soc. **134**, 851 (2005).

[243] S. Chelkowski, A. D. Bandrauk, Phys. Rev. A **71**, 053815 (2005).

[244] W. H. Flygare, *Molecular Structure and Dynamics* (Prentice-Hall, Englewood Cliffs, 1978).

[245] P. Deuflhard, F. Bornemann, *Numerische Mathematik II: Gewöhnliche Differentialgleichungen* (de Gruyter, Berlin, 2002).

[246] M. Sargent III, M. O. Scully, W. E. Lamb, Jr., *Laser Physics* (Addison-Wesley, London, 1974).

[247] L. Allen, J. H. Eberly, *Optical resonance and two-level atoms* (Wiley, New York, 1975).

[248] G. F. Thomas, Phys. Rev. A **27**, 2744 (1983).

[249] A. Salam, W. J. Meath, Chem. Phys. **228**, 115 (1998).

[250] W. H. Shaffer, J. Chem. Phys. **9**, 607 (1941).

[251] L. D. Landau, E. M. Lifshitz, *Quantum Mechanics* (Pergamon, New York, 1977).

[252] P. K. Kennedy, D. H. Kobe, J. Phys. A **16**, 521 (1983).

[253] M. Abramowitz, I. A. Stegun, *Handbook of Mathematical Functions* (Dover, New York, 1972).

[254] I. S. Gradshteyn, I. M. Ryzhik, *Table of Integrals, Series, and Products* (Academic Press, New York, 1965).

[255] L. A. Nafie, J. Chem. Phys. **79**, 4950 (1983).

[256] T. H. Walnut, Int. J. Quant. Chem. **22**, 99 (1988).

[257] J. B. Delos, Rev. Mod. Phys. **53**, 287 (1981).

[258] E. Deumens, A. Diz, R. Longo, Y. Öhrn, Rev. Mod. Phys. **66**, 917 (1994).

[259] I. Barth, H.-C. Hege, H. Ikeda, A. Kenfack, M. Koppitz, J. Manz, F. Marquardt, G. K. Paramonov, Science (2009), submitted.

[260] J. Parker, C. R. Stroud, Jr., Phys. Rev. Lett. **56**, 716 (1986).

[261] I. Sh. Averbukh, N. F. Perelman, Phys. Lett. A **139**, 449 (1989).

[262] C. Leichtle, I. Sh. Averbukh, W. P. Schleich, Phys. Rev. A **54**, 5299 (1996).

[263] I. Sh. Averbukh, M. J. J. Vrakking, D. M. Villeneuve, A. Stolow, Phys. Rev. Lett. **77**, 3518 (1996).

[264] W. P. Schleich, *Quantum Optics in Phase Space* (Wiley-VCH, Berlin, 2001).

[265] P. Földi, M. G. Benedict, A. Czirják, B. Molnár, Fortschr. Phys. **51**, 122 (2003).

[266] D. J. Tannor, *Introduction to Quantum Mechanics: A Time-Dependent Perspective* (University Science Books, Sausalito, 2007).

[267] A. R. Edmonds, *Angular Momentum in Quantum Mechanics* (Princeton University Press, Princeton, 1957).

[268] R. N. Zare, *Angular Momentum* (Wiley, New York, 1988).

[269] P. A. Tipler, R. A. Llewellyn, *Modern Physics* (Freeman, New York, 2003).

[270] P. Bronner, Master's thesis, Universität Karlsrhue (2004), http://www.hydrogenlab.de.

[271] W. Greiner, *Theoretische Physik, Bd. 4: Quantenmechanik: Einführung* (Harri Deutsch, Frankfurt am Main, 2005).

[272] H. Haken, H. C. Wolf, *Atom- und Quantenphysik* (Springer, Berlin, 1993).

[273] M. A. Rashid, J. Phys. A **19**, 2505 (1986).

[274] F. Schwabl, *Quantenmechanik für Fortgeschrittene* (Springer, Berlin, 1997).

[275] C. Zener, Phys. Rev. **36**, 51 (1930).

[276] J. C. Slater, Phys. Rev. **36**, 57 (1930).

[277] K. P. Huber, G. Herzberg, *Molecular Spectra and Molecular Structure* (Van Nostrand Reinhold, New York, 1979).

[278] B. Fischer, M. Hoffmann, H. Helm, G. Modjesch, P. U. Jepsen, Semicond. Sci. Technol. **20**, S246 (2005).

[279] L. Serrano-Andrés (2009), private communication.

[280] S. R. Langhoff, C. W. Bauschlicher, Jr., J. Chem. Phys. **88**, 5715 (1988).

[281] K. Andersson, P.-Å. Malmqvist, B. O. Roos, J. Chem. Phys. **96**, 1218 (1992).

[282] L. Serrano-Andrés, M. Merchán, I. Nebot-Gil, R. Lindh, B. O. Roos, J. Chem. Phys. **98**, 3151 (1993).

[283] B. O. Roos, K. Andersson, M. P. Fülscher, P.-Å. Malmqvist, L. Serrano-Andrés, K. Pierloot, M. Merchán, Adv. Chem. Phys. **93**, 219 (1996).

[284] L. Serrano-Andrés, N. Forsberg, P.-Å. Malmqvist, J. Chem. Phys. **108**, 7202 (1998).

[285] A. C. Borin, L. Serrano-Andrés, Chem. Phys. **262**, 253 (2000).

[286] L. Serrano-Andrés, M. Merchán, A. C. Borin, Chem. Eur. J. **12**, 6559 (2006).

[287] B. O. Roos, P.-Å. Malmqvist, Phys. Chem. Chem. Phys. **6**, 2919 (2004).

[288] R. J. Buenker, H.-P. Liebermann, L. Pichl, M. Tachikawa, M. Kimura, J. Chem. Phys. **126**, 104305 (2007).

[289] M. Rubio, B. O. Roos, L. Serrano-Andrés, M. Merchán, J. Chem. Phys. **110**, 7202 (1999).

[290] D. Sundholm, Chem. Phys. Lett. **317**, 392 (2000).

[291] J. Hasegawa, M. Hada, M. Nonoguchi, H. Nakatsuji, Chem. Phys. Lett. **250**, 159 (1996).

[292] E. J. Baerends, G. Ricciardi, A. Rosa, S. J. A. van Gisbergen, Coord. Chem. Rev. **230**, 5 (2002).

[293] O. Dolgounitcheva, V. G. Zakrzewski, J. V. Ortiz, J. Phys. Chem. A **109**, 11596 (2005).

[294] P. Král, T. Seideman, J. Chem. Phys. **123**, 184702 (2005).

[295] J. E. Del Bene, M. J. T. Jordan, Spect. Acta Part A **55**, 719 (1999).

[296] L. Windhorn, J. S. Yeston, T. Witte, W. Fuß, M. Motzkus, D. Proch, K.-L. Kompa, C. B. Moore, J. Chem. Phys. **119**, 641 (2003).

[297] A. Bernhardsson, N. Forsberg, P.-Å. Malmqvist, B. O. Roos, L. Serrano-Andrés, J. Chem. Phys. **112**, 2798 (2000).

[298] A. Rosa, G. Ricciardi, E. J. Baerends, S. J. A. van Gisbergen, J. Phys. Chem. A **105**, 3311 (2001).

[299] X. Liu, E. K. L. Yeow, S. Velate, R. P. Steer, Phys. Chem. Chem. Phys. **8**, 1298 (2006).

[300] G. Ricciardi, A. Rosa, E. J. Baerends, J. Phys. Chem. A **105**, 5242 (2001).

[301] G. Ricciardi, A. Rosa, S. J. A. van Gisbergen, E. J. Baerends, J. Phys. Chem. A **104**, 635 (2000).

[302] G. Ricciardi, A. Rosa, E. J. Baerends, S. J. A. van Gisbergen, J. Am. Chem. Soc. **124**, 12319 (2002).

[303] J. Feng, J. Li, Z. Wang, M. C. Zerner, Int. J. Quant. Chem. **37**, 599 (1990).

[304] D. K. Dogutan, M. Ptaszek, J. S. Lindsey, J. Org. Chem. **72**, 5008 (2007).

[305] D. Sundholm, Chem. Phys. Lett. **302**, 480 (1999).

[306] A. B. J. Parusel, S. Grimme, J. Phys. Chem. B **104**, 5395 (2000).

[307] W. Gordon, Z. Phys. **50**, 630 (1928).

[308] A. K. Rajagopal, J. Callaway, Phys. Rev. B **7**, 1912 (1973).

[309] G. A. Mourou, T. Tajima, S. V. Bulanov, Rev. Mod. Phys. **78**, 309 (2006).

[310] G. R. Mocken, C. H. Keitel, J. Comp. Phys. **199**, 558 (2004).

[311] F. H. M. Faisal, S. Bhattacharyya, Phys. Rev. Lett. **93**, 053002 (2004).

[312] A. W. Potts, W. C. Price, Proc. R. Soc. Lond. A **326**, 165 (1972).

[313] T. Hisashima, T. Matsushita, T. Asada, S. Koseki, A. Toyota, Theor. Chem. Acc. **120**, 85 (2008).

[314] P. F. Souter, G. P. Kushto, L. Andrews, Chem. Commun. p. 2401 (1996).

[315] P. F. Souter, G. P. Kushto, L. Andrews, M. Neurock, J. Am. Chem. Soc. **119**, 1682 (1997).

[316] A. D. Bandrauk, H. S. Nguyen, Can. J. Chem. **82**, 831 (2004).

[317] G. L. Yudin, A. D. Bandrauk, P. B. Corkum, Phys. Rev. Lett. **96**, 063002 (2006).

[318] J. Ullrich, R. Moshammer, R. Dörner, O. Jagutzki, V. Mergel, H. Schmidt-Böcking, L. Spielberger, J. Phys. B **30**, 2917 (1997).

[319] R. Dörner, V. Mergel, O. Jagutzki, L. Spielberger, J. Ullrich, R. Moshammer, H. Schmidt-Böcking, Phys. Rep. **330**, 95 (2000).

List of Acronyms

AlCl	aluminium monochloride
ANO-RCC	atomic natural orbital relativistic core correlated
AO	atomic orbital
ATI	above-threshold ionization
BeO	beryllium oxide
CASPT2	complete active space with second-order perturbation theory
CASSCF	complete active space self-consistent field
CEP	carrier envelope phase
CI	configuration interaction
CIS	configuration interaction singles
COLTRIMS	cold target recoil ion momentum spectroscopy
CSF	configuration state function
DHA	double harmonic approximation
ESR	electron spin resonance
ETR	electron translation factor
FC	Franck-Condon
FWHM	full width at half maximum
HCP	half-cycle (laser) pulse
HF	Hartree-Fock
HHG	high harmonic generation
IR	infrared
LCAO	linear combination of atomic orbitals
LIET	laser induced electron transfer
MgP	magnesium porphyrin
MO	molecular orbital
NMR	nuclear magnetic resonance

PES	potential energy surface
RWA	rotating wave approximation
SAC	symmetry adapted cluster
SFCL	strong field control of landscapes
SPODS	selective population of dressed states
STIRAP	stimulated Raman adiabatic passage
TAO	travelling atomic orbital
TDDFT	time-dependent density functional theory
TDSE	time-dependent Schrödinger equation
TISE	time-independent Schrödinger equation
UV	ultraviolet
XUV	extreme ultraviolet

List of Tables

List of Figures

Acknowledgement

This work was completed between November 2004 and March 2009 at the Institut für Chemie und Biochemie of the Freie Universität Berlin. I would like to express my gratidude to those who have supported me throughout the past four and a half years.

My first thanks are specially directed to my supervisor, Jörn Manz, who kindly accepted me in his workgroup and provided me with a hot research project. I enjoyed many fruitful and stimulating discussions with him on challenging topics, which have now opened the door to other interesting projects. I also would like to acknowledge his kindness, patience, and personal support. I shall not forget numerous workshops and conferences that I have participated together with him.

I am grateful to Luis Serrano-Andrés and Tamar Seideman for a great cooperation, including my welcome visits in their workgroups in Valencia (Spain) in October 2007 and Evanston, Illinois (USA) in March 2008, respectively. I would like to thank Caroline Lasser for a good cooperation on the trigonometric pulse envelopes that are discussed in Section 2.3.1 of this work. Furthermore, I also thank the coordinator of the Attosecond Science Workshop, André Dieter Bandrauk, who encouraged me to participate in that workshop which took place at the Kavli Institute for Theoretical Physics (KITP) of the University of Califorina at Santa Barbara (UCSB) in August/September 2006.

I would like to express my thanks to my interpreters, namely Oya Ataman, Kathleen Bieling, Silke Brendel-Evan, Sabine Gossner, Christjane Kreuter, Carola Otto, and Ralf Wiebel. They have done a wonderful job, translating spoken English into German Sign Language and vice versa. They did so during talks and discussions in seminars, workshops, and conferences for two and a half years. I am very grateful to the Integrationsamt Berlin, Agentur für Arbeit Berlin-Nord, and Bundesagentur für Arbeit for generous financial support for these hard-working interpreters and also for assistive technology such as a laptop.

Because of my deafness, my native language is neither English nor German, but German Sign Language with a different grammar structure. Thus, I would like to thank Nadia Elghobashi-Meinhardt and Anatole Kenfack very much for their careful English proofreading.

I also would like to thank all workgroup members of Jörn Manz and Beate Paulus for their helpfulness and kindness. They made the working environment so friendly and open. Special thanks go to my office mates David Ambrosek, Nadia Elghobashi-Meinhardt, Anatole Kenfack, and Guillermo Pérez-Hernández.

Financial support by the Deutsche Forschungsgemeinschaft (project Ma 515/23-1 “Modelle für die selektive Quantendynamik von durch Attosekunden-Laserpulse getriebenen Elektronen”, coordinated by Jörn Manz from October 2005 to June 2007, and subsequently Sfb 450 “Analysis and control of ultrafast photoinduced reations”, subproject TPC1 “Theory for the control of chemical reactions by ultrashort laser pulses”, coordinated by Jörn Manz and Robert Benny Gerber since July 2007) is gratefully acknowledged.

The topic and scientific environment of the Graduiertenkolleg 788 “Hydrogen Bonding and Hydrogen Transfer”, project A1 “Quantenchemie und Quantendynamik von Modell-Wasserstofftransfersystemen” (coordinated by Jörn Manz and Leticia González and supported by the Deutsche Forschungsgemeinschaft) has also served as strong motivation for part of this work, see Sections 2.4, 2.5, and 3.5, and it has been a pleasure to contribute to the success of the GK 788. Helpful cooperation with Peter Sebald and Guillermo Pérez-Hernández for these sections is gratefully acknowledged.

I would like to thank my parents, my children, and other family members for their support and patience. Finally, I would like to convey special thanks to my wife Tanja for her great contribution to the success of this work.

Erklärung

Hiermit versichere ich, dass ich die vorliegende Arbeit mit den angegebenen Hilfsmitteln selbständig angefertigt habe.

Berlin, den 02.04.2009